REVIEW

Cavity–polariton dispersion and polarization splitting in single and coupled semiconductor microcavities

G. Panzarini and L. C. Andreani

Instituto Nazionale per la Fisica della Materia-Dipartimento di Fisica ''A. Volta,'' Universitá di Pavia, via Bassi 6, 27100 Pavia, Italy

A. Armitage, D. Baxter, M. S. Skolnick, V. N. Astratov, and J. S. Roberts

Department of Physics, University of Sheffield, Sheffield S3 7RH, United Kingdom

A. V. Kavokin and M. R. Vladimirova

LASMEA, Université Blaise Pascal Clermont II, Complexe Scientifique des Cézeaux, 24, Avenue des Landais, 63177 Aubiere Cedex, France

M. A. Kaliteevski

A. F. Ioffe Physicotechnical Institute, Russian Academy of Sciences, 194024 St. Petersburg, Russia
(Submitted February 9, 1999)
Fiz. Tverd. Tela (St. Petersburg) **41**, 1337–1353 (August 1999)

Recent theoretical and experimental work on linear exciton-light coupling in single and coupled semiconductor microcavities is reviewed: emphasis is given to angular dispersion and polarization effects in the strong-coupling regime, where cavity-polariton states are formed. The theoretical formulation is based on semiclassical theory. The energy of single-cavity modes is determined by the Fabry–Pérot frequency ω_c as well as by the center of the stop band ω_s of the dielectric mirrors; the phase delay in the dielectric mirrors carries a nontrivial angle- and polarization dependence. The polarization splitting of cavity modes depends on the mismatch between ω_c and ω_s, and increases with internal angle as $\sin^2\theta_{\rm eff}$. Interaction between the cavity mode and quantum-well (QW) excitons is described at each angle by a two-oscillator model, whose parameters are expressed in terms of microscopic quantities. Weak and strong coupling regimes and the formation of cavity polaritons are described. Comparison with experimental results on a GaAs-based cavity with $In_{0.13}Ga_{0.87}As$ QWs shows that a quantitative understanding of polariton dispersion and polarization splitting has been achieved. Coupling of two identical cavities thorugh a central dielectric mirror induces an optical splitting between symmetric and antisymmetric modes. When QW excitons are embedded in both cavities at antinode positions, the system behaves as four coupled oscillators, leading to a splitting of otherwise degenerate exciton states and to separate anticrossing of symmetric and antisymmetric modes. These features are confirmed by experimental results on coupled GaAs cavities with $In_{0.06}Ga_{0.94}As$ QWs. An analysis of reflectivity lineshapes requires the inclusion of the effect of resonance narrowing of cavity polaritons. Finally, the polarization splitting in a coupled cavity depends both on the single-cavity factors and on the angle- and polarization dependence of the optical coupling between the cavities. Inclusion of all these effects provides a good description of the experimental findings. © *1999 American Institute of Physics.* [S1063-7834(99)00108-2]

1. INTRODUCTION

The physics of quantum-well excitons embedded in semiconductor microcavities is characterized by two regimes. In the weak-coupling case the decay rate and emission pattern of the exciton may be modified, but a radiative decay still occurs; in the strong-coupling regime, instead, a reversible energy exchange between exciton and cavity mode takes place. This is related to the formation of mixed exciton-photon states, usually termed cavity polaritons, since they are the analog of the (quasi-) stationary exciton-polariton states occurring in bulk semiconductors.[1]

The strong-coupling regime of quantum-well (QW) excitons in microcavities (MCs) is a peculiar and interesting phenomenon, which allows cavity quantum-electrodynamic effects to be studied in a solid-state environment, and which has been the subject of numerous investigations in recent years. After the pioneering observation of a Rabi (polariton) splitting in III–V Fabry–Pérot MCs,[2] important develop-

ments include the measurement of the polariton dispersion by angle-resolved photoluminescence,[3] demonstration of a Rabi splitting at room temperature[4] and of Rabi oscillations in real time,[5] tuning of the exciton-cavity coupling by electric[6] and magnetic[7–10] fields or temperature,[6] saturation and bleaching effects,[11] studies of relaxation and time-resolved photoluminescence,[12–15] effects of disorder and motional narrowing.[16–22] Crossover from polariton doublet to Mollow triplet under high excitation has been demonstrated.[23] Larger Rabi splittings have been observed in II–VI microcavities,[24,25] where stimulation effects have also been reported,[25] and in organic microcavities.[26,27] Reviews of these and related topics, as well as of semiclassical and quantum treatments, can be found in Refs. 28–30.

Recently the system of two coupled MCs with embedded QWs has also been investigated,[31–33] as a way to further increase the flexibility in controlling both radiation and material degrees of freedom. In particular, coupled MCs allow a sizeable and measurable radiative splitting of excitons in QWs separated by a macroscopic distance ($>2\ \mu$m) to be achieved.[33] A radiative splitting between excitons in electronically uncoupled QWs exists in principle also for QWs without MCs[34] or in a single cavity,[35] but in this case the effect is very small and easily washed out by disorder. Coupled cavities made of porous silicon have also been studied.[36] Angle- and polarization-resolved reflectivity experiments on coupled cavities yield detailed information on exciton–photon interactions, which call for accurate yet sufficiently simple theoretical treatments.

A basic piece of information for all the above-mentioned studies is a precise knowledge of polariton dispersion for MCs containing QW excitons. A difficulty which must be faced by a theoretical treatment is to give a realistic description of the phase delay in penetration depth of light in the dielectric mirrors. A derivation of the phase delay[37] and of an accurate secular equation for mixed cavity modes in single cavities[38] have been given previously only for normal incidence. In extending these treatments to oblique incidence, the different polarizations of light (transverse electric, TE, and transverse magnetic, TM) must be considered. Theoretically, the difference in TE and TM polatized reflectivity spectra of quantum well microcavities was discussed in Refs. 39 and 40; the only experimental reports of a polarization splitting of cavity polaritons are those of Refs. 41 and 33.

In this paper we present a comprehensive theoretical and experimental study of cavity-polariton dispersion in single and coupled MCs containing embedded QWs. By the use of linear semiclassical theory we derive analytic equations for cavity-mode dispersion and cavity-polariton eigenfrequencies for both TE and TM light polarizations. Angle- and polarization-resolved reflectivity results on single and coupled GaAs cavities with InGaAs QWs are presented and compared with theoretical predictions; in particular, the effect of cavity mismatch and absorption of the intensity of reflectivity features, as well as the different factors which influence the polarization splitting, are studied in detail. A full theoretical analysis of the single-cavity results of Ref. 41 is presented, which is found to be in good agreement with experiment. A careful analysis of reflectivity results for coupled cavities produces evidence of line narrowing of cavity polaritons in the resonance region.

The rest of this paper is organized as follows. In Sec. 2 we give a brief account of the theoretical framework. In Sec. 3 we derive equations for reflection phase delay and penetration depth in dielectric mirrors when the frequency is close to the center of the stop band, thereby extending the results of Ref. 37 to the case of oblique incidence. In Sec. 4 we study a single cavity and obtain results for the empty-cavity mode, polariton dispersion, and polarization splitting; the role of energy-dependent refractive index in determining the polariton dispersion is emphasized. Experimental results are then presented and compared with theory. In Sec. 5 we treat coupled cavities, and derive analytic formulas for optical splitting of the two modes, empty-cavity dispersion and polariton energies; experimental results on coupled cavities are presented and discussed. Section 6 contains concluding remarks. Some derivations and results of the analytic treatment are given in the Appendices.

2. THEORETICAL FRAMEWORK

The present treatment is based on the semiclassical theory of exciton-radiation interaction. This approach,[42] which consists in solving Maxwell equations together with a constitutive relation between electric and displacement fields, yields the same results as a purely quantum-mechanical theory as far as linear polariton properties are concerned; this follows from the fact that the quantum exciton-radiation Hamiltonian is quadratic in the exciton and photon operators.[28]

For a layered system it is useful to formulate Maxwell equations in terms of a transfer matrix approach.[43–45] We take the z-axis to coincide with the growth direction; for any incidence angle and for TE (or s) and TM (or p) polarizations the transfer matrix $T(z_l \rightarrow z_r)$ is a 2×2 matrix which acts on the basis of right- and left-travelling waves and which propagates the electric field from a point z_l to a point z_r in the structure. The transfer matrix is unimodular, when the refractive indices n_l, n_r of left and right media are the same, otherwise $\det(T)=n_l/n_r$. Evaluation of the transfer matrix T of the whole structure — which is simply obtained by multiplying from the left the transfer matrices of the different regions — provides the reflection and transmission coefficients, which in this paper are always considered for light incident from the left:

$$r=-\frac{T_{21}}{T_{22}}, \quad t=\frac{\det(T)}{T_{22}}=\frac{n_l}{n_r}\frac{1}{T_{22}}; \tag{1}$$

the reflectivity R and transmittivity T are then given by

$$R=|r|^2, \quad T=\frac{n_r}{n_l}|t|^2=\frac{n_l}{n_r}\frac{1}{|T_{22}|^2}. \tag{2}$$

Absorption is given by $A=1-R-T$. The poles of the reflection and transmission coefficients, namely the complex frequencies ω which satisfy the equation $T_{22}(\omega)=0$, give finally the energies and halfwidths of a resonance.

Useful parametrized forms of the transfer matrix can be given for the special cases of a non-absorbing or of a sym-

metric structure; they are derived by imposing the requirements of invariance under the time-reversal operation, or under specular reflection, respectively. The most general transfer matrix of a non-absorbing structure is expressed as[38]

$$T_{\text{non-abs}}=\frac{n_l}{n_r}\begin{pmatrix} 1/t^* & -r^*/t^* \\ -r/t & 1/t \end{pmatrix} \tag{3}$$

in terms of the reflection and transmission coefficients. The mirror image of the structure has a transfer matrix $\tilde{T}$ given by

$$\tilde{T}_{\text{non-abs}}=\begin{pmatrix} 1/t^* & r/t \\ r^*/t^* & 1/t \end{pmatrix}. \tag{4}$$

If in addition the structure is symmetric, the two matrices T and $\tilde{T}$ are identical, therefore $t/t^*=-r/r^*$. For a general symmetric structure (but which may be absorbing, so that time reversal is not a good symmetry operation) the transfer matrix can be expressed as[43,44]

$$T_{\text{sym}}=\frac{1}{t}\begin{pmatrix} t^2-r^2 & r \\ -r & 1 \end{pmatrix}, \tag{5}$$

where again r and t represent the reflection and transmission coefficients from the left side.

We describe each layer in the structure by a local dielectric constant, the only exception being the QW regions. For the QWs we use a nonlocal susceptibility evaluated by linear response theory, which incorporates the microscopic details of the exciton envelope function. The QW transfer matrix at oblique incidence for TE and TM polarizations has the form (5). The difference between TE and TM polarized light appears in reflection and transmission coefficients. These depend on the scattering amplitudes of the e.m. field modes coupled to the exciton polarized along different directions: *T*-mode (in-plane polarized, transverse), *L*-mode (in-plane polarized, longitudinal), and *Z*-mode (polarized along the growth direction).[39,46] For TE polarization

$$r_{\text{QW}}^{\text{TE}}=-\frac{i\Gamma_T}{\Delta+i\Gamma_T}, \quad t_{\text{QW}}^{\text{TE}}=1+r_{\text{QW}}^{\text{TE}}, \tag{6}$$

while for TM polarization

$$r_{\text{QW}}^{\text{TM}}=r_L-r_Z, \quad t_{\text{QW}}^{\text{TM}}=1+r_L+r_Z, \tag{7}$$

with

$$r_L=-\frac{i\Gamma_L}{\Delta+i\Gamma_L}, \quad r_Z=-\frac{i\Gamma_Z}{\Delta-\delta_{ZT}+i\Gamma_Z}; \tag{8}$$

the case of TM polarization is more complex since the scattering amplitudes of *L*- and *Z*-modes interfere. In the above formulas $\Delta=\omega-\omega_{\text{ex}}+i\gamma_{\text{ex}}$ (we neglect the weak dependence of the exciton frequency ω_{ex} on in-plane wavevector and polarization), δ_{ZT} is the splitting between Z and T exciton polaritons in the QW,[45] γ_{ex} is the non radiative exciton broadening. A radiative broadening follows from coupling of the QW exciton to the radiation field through Maxwell equations,[47–49] and it depends on the angle θ_c in the medium. For the in-plane polarized T and L modes it is given by $\Gamma_T=\Gamma_0/\cos\theta_c$, $\Gamma_L=\Gamma_0\cos\theta_c$, where $\Gamma_0=(\pi/n_c)(e^2/4\pi\varepsilon_0 mc)f_{xy}$ is the radiative decay rate of the QW exciton amplitude at zero in-plane wavevector (f_{xy} is the oscillator per unit area, m is the free electron mass and ε_0 is the vacuum permittivity). Concerning the *z*-polarized mode, for the heavy hole exciton resonance $\Gamma_Z=0$, while for the light hole exciton $\Gamma_Z=4\Gamma_0((\cos\theta_c)^{-1}-\cos\theta_c)$. In the following we will only consider the heavy hole excitons. Substituting the above coefficients r and t into the general transfer matrix (5), for a symmetric structure one can obtain in this case:

$$T_{\text{QW}}^{\alpha}=\frac{1}{\Delta}\begin{pmatrix} \Delta-i\Gamma^{\alpha} & -i\Gamma^{\alpha} \\ i\Gamma^{\alpha} & \Delta+i\Gamma^{\alpha} \end{pmatrix}, \quad \alpha=\text{TE,TM}. \tag{9}$$

Here $\Gamma^{(\text{TE})}\equiv\Gamma_T$, $\Gamma^{(\text{TM})}\equiv\Gamma_L=\Gamma_T\cos^2\theta_c$. The angle θ_c in the cavity is related to the external angle θ by $\sin\theta_c=(\sin\theta)/n_c$.

3. DIELECTRIC MIRRORS

The simplest semiconductor microcavity structure is a planar Fabry–Pérot cavity, bounded by dielectric mirrors termed distributed Bragg reflectors (DBRs).[50–52] A DBR is a periodic quarter wave stack consisting of alternating layers of high and low refractive index materials, with the optical thickness of each layer a quarter wave at the operating wavelength. The most useful feature of a DBR, which is a consequence of propagation of e.m. waves in periodic layered media, is the existence of a ''stop band'' region in which radiation cannot propagate; in this frequency region constructive interference between rays reflected from successive periods leads to reflectivity values close to unity. The center of the stop band (denoted by ω_s in this paper) is determined by the $\lambda/4$ condition, whereas the fractional bandwidth depends on the refractive indices n_1 and n_2 of the two materials according to $\Delta\omega_s/\omega_s=(4/\pi)\arcsin(|n_2-n_1|/(n_2+n_1))$. A proper treatment of the phase delay on reflection by a DBR is a preliminary issue in order to calculate the angular dispersion of cavity polaritons for TE and TM polarizations. Previous work on angular dependence of phase delay in Fabry–Pérot filters (but neglecting the difference of polarizations) is described in Ref. 53.

We consider a DBR with layer thicknesses a,b, and refractive indices n_1,n_2 which can be either in the order $n_1<n_2$ (as exemplified in Fig. 1) or $n_1>n_2$; our treatment applies to both situations. First we consider the periodic structure with N periods of Fig. 1a and calculate its transfer matrix T_N (see e.g. Ref. 52). Then we take a DBR surrounded from the left by a cavity medium with refractive index n_c and from the right, by an external medium with refractive index n_{ext} (Fig. 1b), which is our structure of interest, and evaluate its transfer matrix by multiplying T_N with appropriate interface matrices. The resulting transfer matrix is expressed in the general form (3) for nonabsorbing materials.

We now derive an approximate, parametrized expression for the reflection coefficient of the DBR showing its dependence on angle and polarization. At frequencies close to the center of the stop band $\omega_s^{\alpha}(\theta)$, $\alpha=\text{TE, TM}$, the reflection coefficient of a DBR at a fixed angle may be assumed to have a constant amplitude and a phase which is linear in $[\omega-\omega_s^{\alpha}(\theta)]$:

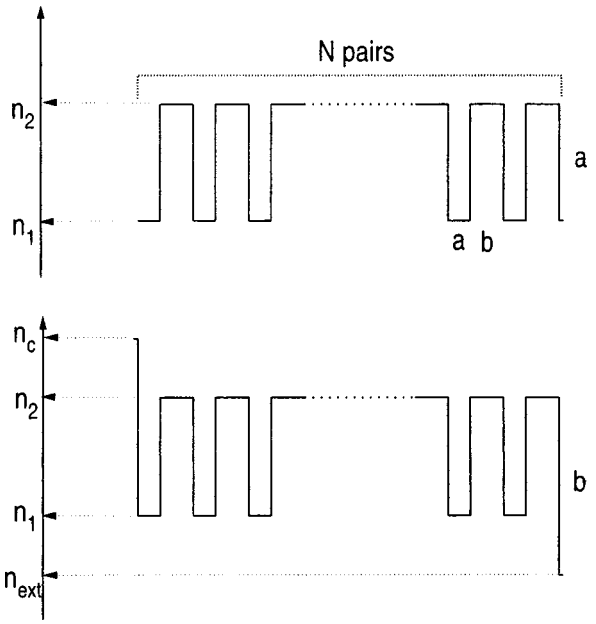

FIG. 1. Refractive index profiles of (a) the periodic DBR structure, and (b) the DBR surrounded on the left by a cavity with refractive index n_c and on the right by an external medium with refractive index n_{ext}.

$$r^{\alpha}_{\text{DBR}}(\omega)=\pm\sqrt{R^{\alpha}}\exp\left[i\frac{n_c}{c}L^{\alpha}_{\text{DBR}}(\omega-\omega^{\alpha}_s)\cos\theta_c\right]. \quad (10)$$

The upper (lower) sign holds for $n_1<n_2$ $(n_1>n_2)$. Thus when $n_1<n_2$ the phase of the reflection coefficient is zero at the center of the stop band, and the electric field has a maximum at the boundary between cavity and DBR. This case is realized, e.g., for a GaAs cavity with AlAs/GaAs Bragg mirrors, in this case we have $n_c=n_2=n(\text{GaAs})$, $n_1=n(\text{AlAs})$. In the opposite case $n_1>n_2$ the phase of the reflection coefficient equals π at the center of the stop band (like for a metallic mirror), and the electric field vanishes at the boundary.

The quantity $L^{\alpha}_{\text{DBR}}(\theta)$ represents a penetration depth of the field in the dielectric mirror, dependent on both angle and polarization. At normal incidence it equals $2L_{\tau}$, where L_{τ} is defined in Ref. 37 as the distance at which a fixed-phase mirror has to be displaced in order to produce the same phase delay on reflection. For TE-polarization this kind of parametrization has been used in Ref. 40. Expressions for the parameters $R^{\alpha}(\theta)$, $L^{\alpha}_{\text{DBR}}(\theta)$, $\omega^{\alpha}_s(\theta)$ appearing in Eq. (10) are given in Appendix A.

In Fig. 2 we show the phase of the reflection coefficient of a AlAs/GaAs DBR, calculated with the equations of Appendix A, compared with the results of a numerical simulation. The parameters are close to those of the experimental results to be shown later. We have assumed the $\lambda/4$ condition to be satisfied at $\hbar\omega_s=1.4$ eV, with refractive indices $n_1=3.01$ for AlAs and $n_2=3.55$ for GaAs. We have considered the cases of normal incidence, and of $\theta=60°$ for TE and TM polarizations. The comparison shows that the assumed linear dependence of the phase of the DBR is a very good approximation in a wide range of frequencies around the center of the stop band. For the chosen parameters the stop band extends from 1.28 to 1.52 eV: the phase of the reflection coefficient varies from $-\pi$ to π in this interval. The inset shows the penetration depth for both polarizations as a function of angle. The penetration depth increases for TM, and decreases for TE polarization; this angular dependence will play an important role in determining the polarization splitting of cavity polaritons.

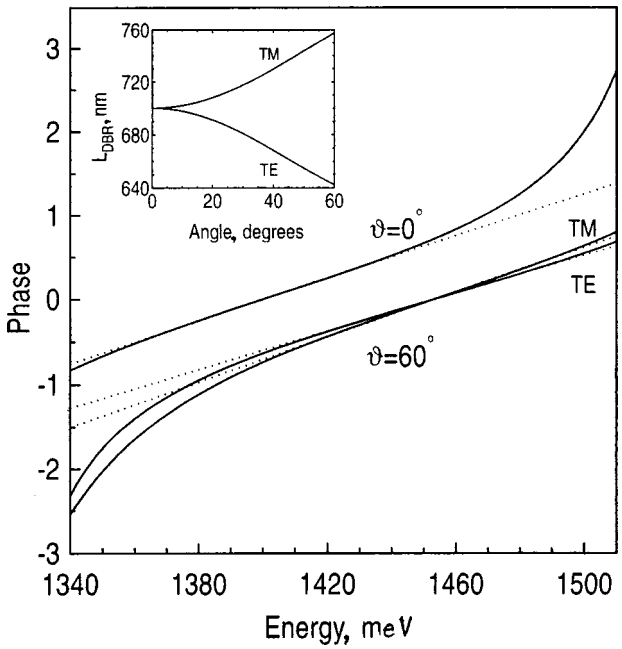

FIG. 2. Phase of the reflection coefficient of a AlAs/GaAs DBR close to the center of the stop band ($\omega_s=1.4$ eV at normal incidence), at $\theta=0$ and at $\theta=60°$ for TE and TM polarizations. Solid lines — numerical simulations with $N=12$. Dotted lines — analytic equation [see Eq. (10)]. Inset — angular dependence of mirror penetration depth for the two polarizations.

4. SINGLE MICROCAVITY

We consider a symmetric Fabry-Pérot cavity structure of length L_c with a symmetric layer characterized by reflection and transmission coefficients r_c, t_c placed at its center. The transfer matrices of the right and left mirrors are expressed in the forms (3) and (4), respectively, and that of the central structure in the form (5) with $r=r_c$ and $t=t_c$; the transfer matrix T of the whole structure is easily found by multiplying from the left the transfer matrices of the various layers. The eigenmodes are found from the poles of the transmission coefficient (1), i.e., by setting the element T_{22} equal to zero. The equation $T_{22}(\omega)=0$ for the eigenfrequencies can be put in the following form[39] (with $k_z=(n_c\omega/c)\cos\theta_c$):

$$[r_{\text{DBR}}(r_c+t_c)\,e^{ik_zL_c}][r_{\text{DBR}}(r_c-t_c)\,e^{ik_zL_c}-1]=0. \quad (11)$$

This is an equation for the frequency ω in the complex plane. One can easily prove[40] that the first bracket in Eq. (11) is equal to zero at the eigenfrequency of a mode even with respect to the center of the cavity, while the zero of the second bracket corresponds to an odd cavity mode. The above equation is general and applies to several specific situations, e.g. an empty cavity ($r_c=0$, $t_c=1$), a cavity with one quantum well ($r_c=r_{\text{QW}}$, $t_c=t_{\text{QW}}$), a cavity with two sets of QWs in symmetric positions,[35,40] or even a coupled cavity if the central object is another DBR.

4.1. Empty cavity

By specifying Eq. (11) to the case of an empty cavity, the eigenfrequencies of the cavity modes are determined by the equation $r_{\mathrm{DBR}}^2 \exp(2ik_z L_c)=1$. By using the parametrization (10) and taking the logarithm, the equation for the complex frequency becomes (for simplicity the polarization index is understood in all subsequent formulas)

$$2\frac{n_c}{c}[L_c\omega + L_{\mathrm{DBR}}(\theta)(\omega-\omega_s(\theta))]\cos\theta_c = 2\pi m + i\ln R, \tag{12}$$

where $R=|r_{\mathrm{DBR}}|^2$ is the mirror reflectivity and the integer m represents the number of half wavelengths contained in the cavity region. The complex frequency is denoted by $\omega_m^{\alpha}(\theta) - i\gamma_m^{\alpha}(\theta)$ (α=TE,TM), where ω_m is the real frequency of the mode and γ_m is the mode halfwidth (HWHM); they are determined by the real and imaginary parts of Eq. (12), respectively. The real part of (12) gives the phase-matching condition, and leads to a cavity–mode frequency ω_m which can be expressed in the form

$$\omega_m(\theta) = \frac{L_c\omega_c(\theta) + L_{\mathrm{DBR}}(\theta)\omega_s\theta}{L_{\mathrm{eff}}(\theta)}, \tag{13}$$

where $L_{\mathrm{eff}}=L_c+L_{\mathrm{DBR}}$ is an effective cavity length, and $\omega_c = m\pi c/(n_c L_c\cos\theta_c)$ is the Fabry-Pérot frequency if there is no phase delay in the mirrors. This expression shows that the cavity mode frequency is a weighted average of ω_c and ω_s; in most cases L_{DBR} is much larger than L_c, so that ω_m is mostly determined by the center of the stop band. This often unappreciated result implies that the frequency of the cavity mode has only a weak dependence on cavity thickness, while it depends more sensitively on the DBR layer thicknesses: this behavior is verified in numerical simulations as well as in experiments. A useful approximate formula for the dependence of mode energy on cavity length L_c is $\delta\omega_m/\omega_m \simeq \delta L_c/L_{\mathrm{eff}}$. The imaginary part of (12) gives the halfwidth in the limit $R\to 1$, when $\ln R \simeq -(1-R)$ as

$$\gamma_m(\theta) = \frac{e(1-R(\theta))}{2n_c L_{\mathrm{eff}}(\theta)\cos\theta_c}. \tag{14}$$

The above results are given in more general form in Appendix B, where the case of an asymmetric cavity is also considered. The main difference in optical properties of an asymmetric compared to a symmetric cavity is that the minima of reflectivity do not reach zero, i.e., reflectivity dips are much less pronounced.

Although the results of Appendix A are valid for any values of the refractive indices, simpler expressions for the cavity mode dispersion can be given for the common case in which n_c, n_1, n_2 are close to each other. Let us denote by n_{eff} the common value of the refractive index: then the center of the stop band is very closely the same for the two polarizations (as seen from the formulas of Appendix A, and also found numerically), and behaves as $\omega_s(\theta)=\pi c/(n_{\mathrm{eff}}(a+b)\cos\theta_{\mathrm{eff}})$, where a,b are the DBR layer thicknesses: it has therefore the same angular dependence as the Fabry–Pérot frequency $\omega_c(\theta)$. When the cavity-mode frequency at $\theta=0$ is factorized, this leads to the frequently used dispersion relation $\omega_m(\theta)=\omega_m(0)/\cos\theta_{\mathrm{eff}}$: this relation also can be viewed as a definition for the effective refractive index.[51,53–55] However the definition implicitly assumes that the refractive index is a constant, i.e., independent of energy. When the energy-dependence of the refractive index is taken into account, it is easy to show that the cavity mode dispersion becomes

$$\omega_m(\theta) = \frac{n_{\mathrm{eff}}[\omega_m(0)]\omega_m(0)}{n_{\mathrm{eff}}[\omega_m(\theta)]\cos\theta_{\mathrm{eff}}}. \tag{15}$$

Although the energy dependence of the refractive index is small, it has an important effect on the angular dependence of the cavity-mode and therefore on the polariton dispersion, as will be shown in Sec. 4.3 by the comparison with the experiments.

An approximate relation for the polarization splitting can also be given for the case $n_c \simeq n_1 \simeq n_2$. While ω_s is very nearly the same for both polarizations, the penetration depth L_{DBR} depends markedly on polarization, as it increases with angle for TM and it decreases for TE polarization (see inset of Fig. 2). From Eq. (13) it can be seen that if $\omega_c=\omega_s$, the cavity mode frequency is independent of L_{eff} and thus it depends very little on polarization. Therefore the polarization splitting is controlled by the mismatch between the center of the stop band ω_s and the Fabry–Pérot frequency ω_c. We can exploit the fact that $\omega_s(\theta)$ varies roughly as $1/\cos\theta_{\mathrm{eff}}$, just like $\omega_c(\theta)$, and obtain the approximate form

$$\omega_m^{\mathrm{TM}}(\theta) - \omega_m^{\mathrm{TE}}(\theta) \simeq \frac{L_c(L_{\mathrm{DBR}}^{\mathrm{TM}}(\theta) - L_{\mathrm{DBR}}^{\mathrm{TE}}(\theta))}{L_{\mathrm{eff}}(0)^2} \times \frac{(\omega_s(0)-\omega_c(0))}{\cos\theta_{\mathrm{eff}}}. \tag{16}$$

The penetration depths can be evaluated by means of the equations in Appendix A. In the limit $n_1 \simeq n_2 \simeq n_c \equiv n_{\mathrm{eff}}$ the following approximate equation is obtained:

$$\omega_m^{\mathrm{TM}}(\theta) - \omega_m^{\mathrm{TE}}(\theta) \simeq \frac{L_c L_{\mathrm{DBR}}(0)}{L_{\mathrm{eff}}(0)^2} \frac{2\cos\theta_{\mathrm{eff}}\sin^2\theta_{\mathrm{eff}}}{1-2\sin^2\theta_{\mathrm{eff}}} \times (\omega_s(0)-\omega_c(0)). \tag{17}$$

This equation (which is valid for both cases $n_1<n_2$ and $n_1>n_2$) is somewhat less accurate compared to Eq. (16), but it displays more clearly the angular dependence: basically, the polarization splitting is proportional to $\omega_s(0)-\omega_c(0)$, and it increases with angle like $\sin^2\theta_{\mathrm{eff}}$. We emphasize that the TM mode can be at higher or lower energy, according to which of $\omega_s(0)$ or $\omega_c(0)$ is higher: the first case is realized when the DBR period $a+b<\lambda/2$, while the second case (TE higher) occurs when $a+b>\lambda/2$.

4.2. Single cavity with quantum wells

We now consider a cavity of width L_c with one QW at the center (see Fig. 3a). The dispersion equations for TE and TM polarized polariton modes can be written in the form of Eq. (11), where r_c and t_c are now the amplitude reflection and transmission coefficients of light from the QW, Eqs. (6) and (7). For the heavy-hole exciton $t_{\mathrm{QW}}=1+r_{\mathrm{QW}}$, thus in

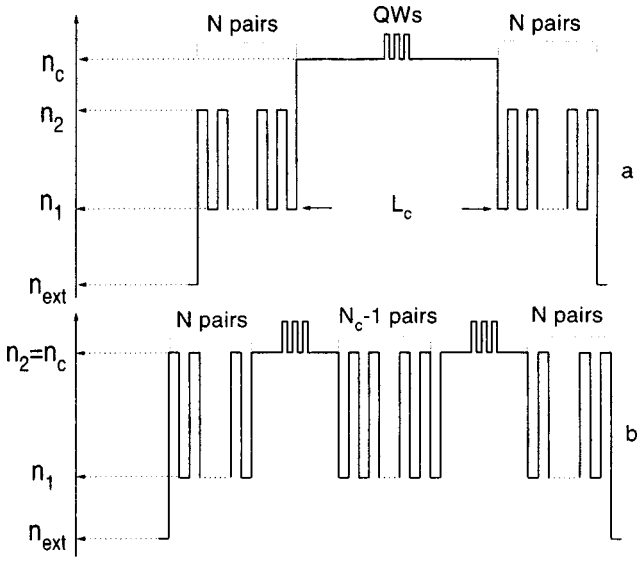

FIG. 3. Refractive index profile of (a) the single-cavity structure, and (b) the coupled-cavity structure. A set of three QWs at the center of each cavity is indicated.

Eq. (11) the vanishing of the second bracket gives simply $r_{\mathrm{DBR}}\exp(ik_zL_c)=-1$: this is equivalent to saying that the QW exciton state (which is symmetric w.r.t. the center of the QW) is not coupled to an antisymmetric cavity mode. The mixed exciton-cavity modes correspond to the symmetric solutions and are described by zeros of the first bracket in Eq. (11), which in the case of the heavy hole exciton resonance reduces to[38]

$$\frac{\Gamma^{\alpha}}{\omega-\omega_{\mathrm{ex}}+i\gamma_{\mathrm{ex}}}=i\frac{1-r^{\alpha}_{\mathrm{DBR}}e^{ik_zL_c}}{1+r^{\alpha}_{\mathrm{DBR}}e^{ik_zL_c}},\quad \alpha=\mathrm{TE,TM}. \tag{18}$$

Far from the frequency of a cavity mode the r.h.s. of (18) is always finite, and the dressed exciton energy can be found by perturbation theory as $\omega=\omega_{\mathrm{ex}}-i\gamma_{\mathrm{ex}}+\Delta\omega_{\mathrm{ex}}$, where the radiative shift $\Delta\omega_{\mathrm{ex}}$ is of the order of the radiative broadening Γ. On the other hand the r.h.s. of (18) vanishes at the frequency of a symmetric cavity mode, and in this case the radiative shift of the exciton cannot be found by perturbation theory: rather, the vanishing of the r.h.s. marks the crossover to a nonperturbative regime of exciton-radiation coupling. The proper way to proceed is to expand the r.h.s. for frequencies close to resonance. We use again the parametrization (10): since the factor $r_{\mathrm{DBR}}\exp(ik_zL_c)$ equals unity at the complex frequency of the cavity mode $\omega_m-i\gamma_m$ (see the discussion leading to Eqs. (12)–(14)), it can be written as $\exp(i(n_cL_{\mathrm{eff}}/c(\omega-\omega_m+i\gamma_m)\cos\theta_c)$ and the r.h.s. of (18) can be expressed in terms of the (small) difference $\omega-\omega_m+i\gamma_m$. Expanding up to first order in $(\omega-\omega_m+i\gamma_m)$, the exciton and the cavity mode are found to behave like two coupled, damped oscillators:

$$(\omega-\omega_{\mathrm{ex}}+i\gamma_{\mathrm{ex}})(\omega-\omega_m+i\gamma_m)=V^2, \tag{19}$$

where

$$V^{\alpha}(\theta)=\left(\frac{2c\Gamma^{\alpha}(\theta)}{n_cL^{\alpha}_{\mathrm{eff}}(\theta)\cos\theta_c}\right)^{1/2},\quad \alpha=\mathrm{TE,TM} \tag{20}$$

is the exciton–cavity coupling depending on angle and polarization. Using the expressions for the angle-dependent radiative widths given in Sec. 1 we have

$$V^{\mathrm{TE}}(\theta)=\left(\frac{1}{4\pi\varepsilon_0}\frac{2\pi e^2f_{xy}}{n_c^2mL^{\mathrm{TE}}_{\mathrm{eff}}(\theta)}\right)^{1/2}\frac{1}{\cos\theta_c}, \tag{21}$$

$$V^{\mathrm{TM}}(\theta)=\left(\frac{1}{4\pi\varepsilon_0}\frac{2\pi e^2f_{xy}}{n_c^2mL^{\mathrm{TM}}_{\mathrm{eff}}(\theta)}\right)^{1/2}. \tag{22}$$

Equation (19) is often derived by diagonalizing a 2×2 Hamiltonian, in which two oscillators of frequencies $\omega_{\mathrm{ex}}-i\gamma_{\mathrm{ex}}$ and $\omega_m-i\gamma_m$ are coupled by a matrix element V. The present treatment yields a rigorous derivation of this two-oscillator model, together with microscopic expressions for the various parameters, with their angle- and polarization-dependence.

The occurrence of two distinct regimes is clearly evident when Eq. (19) is solved in the resonant case ($\omega_0=\omega_m$):

$$\omega=\omega_{\mathrm{ex}}-i\frac{(\gamma_{\mathrm{ex}}+\gamma_m)}{2}\pm\sqrt{V^2-\frac{1}{4}(\gamma_{\mathrm{ex}}-\gamma_m)^2}. \tag{23}$$

For the purely homogeneous broadening assumed here, the linewidth in the strong-coupling regime is the average of γ_{ex} and γ_m. The weak-coupling regime corresponds to an imaginary square root in (23) (i.e., $2V<|\gamma_{\mathrm{ex}}-\gamma_m|$); the exciton decay is still an irreversible process like in an isolated QW, but the emission rate in the direction of the cavity mode may be increased by orders of magnitude.[56] Instead, the strong-coupling regime occurs for $2V>|\gamma_{\mathrm{ex}}-\gamma_m|$, and corresponds to a real square root in (23). In this case optical confinement leads not only to a quantitative, but also to a qualitative modification of the emission properties of the system. The eigenmodes are mixed exciton–radiation states and exhibit a splitting in the frequency domain (Rabi splitting) given by

$$\Omega=2\sqrt{V^2-\frac{1}{4}(\gamma_{\mathrm{ex}}-\gamma_m)^2}. \tag{24}$$

The maximum value of the splitting occurs when the two linewidths γ_{ex} and γ_m are equal. The frequency splitting corresponds to energy oscillations in the time domain between the exciton and cavity modes.

When N identical QWs are placed in the microcavity, cooperative effects arise. Radiative coupling rearranges the N exciton states into a single, ''bright'' state which is maximallly coupled to light, and $N-1$ ''dark'' states which have little interaction with the radiation field.[57–60] The dark states come into play when considering scattering and thermalization of cavity polaritons;[14] also, they can be mixed up with the bright state when disorder is present.[60] Apart from these cases the dark states do not play a role for the optical response of cavity-embedded QW excitons, which is determined only by the degree of cooperation in the bright state. This is measured by an effective number of wells, which can be calculated by summing the squared electric field at the QW positions, and is given by[54,38,40]

$$N_{\mathrm{eff}}=\frac{N}{2}\pm\frac{1}{2}\frac{\sin Nkl}{\sin kl}, \tag{25}$$

where the upper (lower) sign is appropriate for a symmetric (antisymmetric) electric field inside the microcavity, and l indicates the period of the multiple QW. By working to linear order in Γ_0 (which amounts to neglecting multiple interferences between the wells) all the previous formulas remain valid, provided Γ_0 is replaced with $N_{\rm eff}\Gamma_0$. An exact formalism considering additional polariton modes arising due to the radiative coupling between different wells is developed in Ref. 40, and the case of two non-identical QWs in a microcavity including radiative coupling is studied in Refs. 35 and 61.

In principle, all quantities appearing in the previous equations depend on angle and/or polarization: exciton frequency $\omega_{\rm ex}$, cavity–mode frequency ω_m^α, cavity mode linewidth γ_m, exciton–photon matrix element V. However, in practice, the angle and polarization dependence of ω_m is by far the dominant effect. In fact $\omega_{\rm ex}$ may be taken as independent of angle, since spatial dispersion of the exciton is negligible at the small internal angles accessible to optical experiments. Also, V and γ_m can be seen to change only by a few percent even at large external angles; since both quantities are usually of the order of a few meV or smaller, their variation with angle is a small fraction of a meV and can be neglected.

4.3. Experiments

The experiments were carried out on a sample[62] consisting of a one-wavelength (λ) GaAs cavity sandwiched by 20 period $\lambda/4$ $Al_{0.13}Ga_{0.87}As$/AlAs DBRs. The top and bottom DBR were p- and n-doped, respectively. The cavity contains a set of centrally placed 10 nm wide $In_{0.13}Ga_{0.87}As$ QWs with 10 nm barriers. The structure was grown by metal-organic vapor phase epitaxy (MOVPE) on a GaAs substrate. The sample was placed in a cryostat with angular access of $\sim 130°$, permitting values up to $\theta = 60°$ to be achieved. White light illumination from a projector lamp with angular spread $< 1°$ was employed. The reflected light was dispersed by a grating spectrometer, and detected by a Ge photodiode.

The real structure differs from the one assumed in the theoretical treatment (Fig. 3a) due to the presence of the GaAs substrate. Thus the cavity structure is slightly unbalanced: the incident beam impinges on the top mirror (air side) with a calculated reflectivity $R_1 = 0.9964$, whereas the bottom mirror (substrate side) has a reflectivity $R_2 = 0.9874$ (Ref. 63). As already remarked, the main effect of unbalancing is that reflectivity dips are much less pronounced and do not reach zero; the previous expressions for mode energies in the high-reflectivity limit remain unchanged, however.

A series of polarization-resolved reflectivity spectra at different angles was shown in Fig. 1 of Ref. 41. We just recall the main features: at low angles the cavity mode (C) is at lower energy compared to the exciton (X), which appears weakly in reflectivity. On increasing the angle the cavity mode shifts to higher energy and an anticrossing behavior typical of the strong-coupling regime is seen. The two reflectivity dips have equal intensities at an angle $\theta = 30°$; at this angle mixed cavity polaritons with equal exciton and photon amplitudes are realized. For larger angles the cavity mode rapidly shifts to higher energy and the exciton is again barely visible.

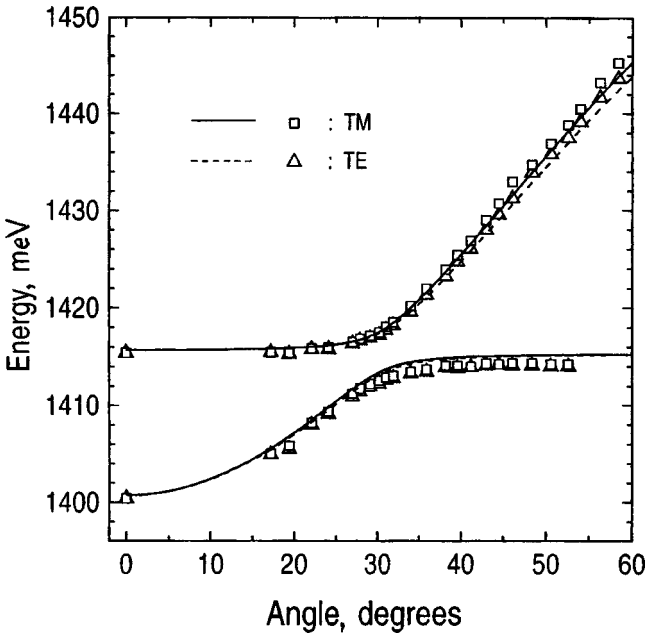

FIG. 4. Dispersion of cavity polaritons in a GaAs cavity with three $In_{0.13}Ga_{0.87}As$ QWs and $AlAs/Al_{0.13}Ga_{0.87}As$ mirrors. Continuous and dashed lines are the theoretical curves for TM and TE polarizations respectively; squares and triangles are the experimental data from positions of reflectivity dips.

With increasing angle the reflectivity dips become more pronounced for TM and less pronounced for TE polarization. This can be understood from Eqs. (A2) and (A5), since the reflectivity R_1 of the top mirror increases with angle for TE and decreases for TM polarization (while R_2 has a smaller variation with angle due to the presence of the substrate): thus the cavity becomes more unbalanced for TE and less unbalanced for TM, thereby explaining the trend of reflectivity dips.[64] This also implies that, in an unpolarized experiment, the TM component dominates in determining the position of reflectivity structures (see Sec. 5.3). An analysis of linewidths and their angular dependence and a numerical transfer matrix fit to the dip intensities are presented in Ref. 41.

In Fig. 4 we show the measured and calculated dispersion of cavity polaritons for both polarizations. The calculations were made using the analytic relations of the previous Sections and of Appendix A, for a symmetric structure with $N = 20$ quarter-wave pairs in each DBR. The cavity and DBR layer thicknesses were adjusted slightly in order to account for the observed mode energies and polarization splitting: we used $L_c = 257$ nm, $a = 73$ nm, $b = 63.8$ nm. These values are consistent with wide-band reflectivity spectra, as discussed below. The energy-dependent refractive indices are taken from the 300 K data of Ref. 65, decreased by 1.3% for use at 10 K. At 8650 Å the values are 3.5467 for GaAs and 3.0108 for AlAs; the refractive index of GaAs increases by about 0.9% from 1.40 to 1.45 eV (Ref. 65). For the QW exciton $\omega_{\rm ex} = 1415.4$ meV, $f_{xy} = 4.2 \times 10^{12}\ {\rm cm}^{-2}$ (Ref. 66), leading to $\Gamma_0 = 0.052$ meV, with three QWs and $N_{\rm eff} = 2.52$. We also

take $\gamma_{ex}=0.9$ meV from the experimental linewidth of the exciton (FWHM$\sim$1.8 meV).

The first feature to be noticed is the anticrossing at $\theta\simeq 30°$, with a Rabi splitting of $\sim$5 meV. The penetration depth is calculated to be $L_{DBR}=780$ nm and the effective length $L_{eff}\simeq 1.04\,\mu$m, yielding a Rabi splitting $2\hbar V=4.7$ meV, in good agreement with the experimental value. The Rabi splitting for QW excitons in microcavities yields an accurate measurement of the oscillator strength through formulas (21)–(22), provided the penetration depth in the dielectric mirrors is properly taken into account.

Next we consider the polariton dispersion at high angles (where it almost concides with the cavity-mode dispersion). The energy dependence of the index of refraction, although weak, is crucial for obtaining good agreement with the experimental results. This can be understood from Eq. (15) (neglecting the TM–TE difference for the moment). If the refractive index is taken to be independent of energy, the effective index is $n_{eff}\simeq 3.25$ and the cavity-mode frequency at $\theta=60°$ would be 1454 meV, which is about 10 meV higher than the experimental result. A similar discrepancy was noticed before[54] and could not be explained. However, since the effective index increases by 0.7% from 1.4 to 1.45 eV, the use of Eq. (15) leads to a cavity-mode energy of 1444 meV at $\theta=60°$, in agreement with the experimental value. Thus including the energy-dependence of the index of refraction fully solves the problem of mode dispersion at high angles. We also note that the strong sensitivity of the cavity-mode energy to the refractive index in the DBR layers through $\omega_s(0)$ implies that a weak nonlinearity in one of the DBR layers might be amplified and give rise to a strong nonlinear response of the microcavity system.[67]

Finally we turn to the polarization splitting. Experimentally the TM mode is higher in energy; the TM–TE splitting of the upper cavity polariton is $\sim$1.7 meV at the largest angle $\theta=60°$. From the discussion of Sec. 4.1, and in particular Eq. (16), this implies that the frequency of the center of the stop band ω_s is greater than the Fabry–Pérot frequency ω_c. This expectation is confirmed by wide-band reflectivity spectra where the cavity dips are found to be displaced to lower energy relative to the center of the stop band by $\sim$10 meV, implying $\omega_c<\omega_s$. Furthermore the parameters we employ for our calculations give $\omega_c=1.358$ eV and $\omega_s=1.409$ eV at $\theta=0$, consistent with both the experimental deduction of $\omega_c<\omega_s$ from the wide band spectra, and with the observed sign of the TM–TE splitting. The angular dependence of the splitting is then controlled by the penetration depths (see inset of Fig. 2). Using the same set of parameters as before, in Fig. 5 we compare the calculated TM–TE splitting of upper and lower cavity polaritons with the experimental results. The formation of mixed exciton-cavity modes around $\theta=30°$ is also reflected in the TM–TE splitting, which has a peculiar behavior in the anticrossing region. The polarization splitting of the bare cavity mode increases like $\sin^2\theta_{eff}$ [see Eq. (17)]: this behavior appears outside the anticrossing region for the lower polariton at low angles, and for the upper polariton at large angles. Although the experimental results show some unavoidable spread (note the scale on the energy axis), agreement between experiment and theory is very satisfactory. Thus the comparison of calculated and measured polarization splitting confirms the accuracy of the analytic treatment.

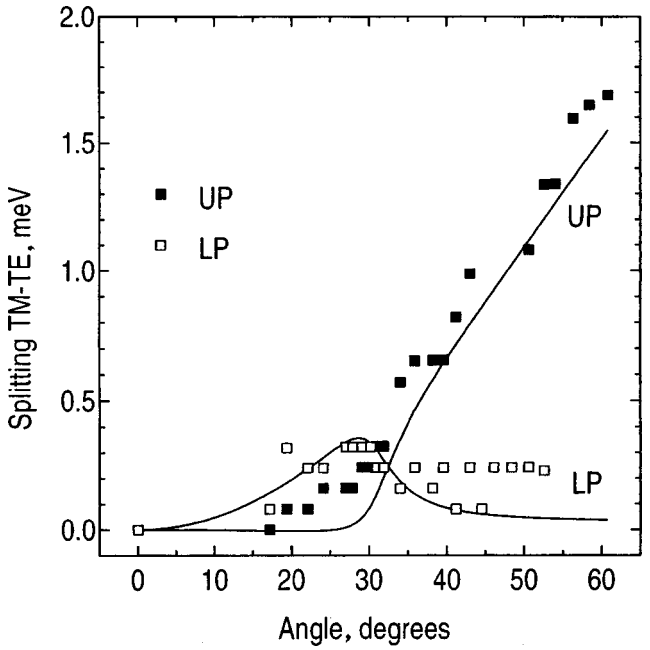

FIG. 5. TM–TE polarization splitting of upper and lower polaritons in the GaAs cavity of Fig. 4, with the same parameters. Continuous lines — theoretical curves; closed and open squares — experimental data.

5. COUPLED MICROCAVITIES

5.1. Empty, coupled cavities

We shall now derive relations for the energies and widths of the cavity-modes for two empty coupled microcavities. We first consider a symmetric structure (see Fig. 3b): this requires that the left and right DBRs are the mirror image of each other, and that the two cavities have the same length L_c, so that both photon eigenmodes have the same frequency ω_m and width (HWHM) γ_m in the absence of coupling. The number of quarter-wave pairs in the symmetric central mirror is half-integer: we denote it by $N_c-1/2$ (cf. Fig. 3b).

The central mirror couples the two degenerate modes at ω_m of the isolated cavities and breaks their degeneracy. Due to the symmetry of the system, the cavity modes may be classified as symmetric (S) and antisymmetric (A). Their complex energies are given in the limit $R,R_c\to 1$ by (see Appendix B for a derivation)

$$\omega=\omega_j-i\tilde{\gamma}_m=\omega_m+(-1)^j V_{opt}-i\tilde{\gamma}_m,\quad j=1,2, \tag{26}$$

with

$$V_{opt}=\frac{c\sqrt{1-R_c}}{2n_c L_{eff}\cos\theta_c} \tag{27}$$

representing the coupling constant between the two cavities, and

$$\tilde{\gamma}_m=\frac{c(1-R)}{4n_c L_{eff}\cos\theta_c}. \tag{28}$$

R and R_c are the reflectivities of the external and central mirrors, respectively, dependent on both angle and polarization. For even N_c the symmetric mode lies at higher energy than the antisymmetric one, while for odd N_c the reverse is true (we are now specifying to the case $n_1 < n_2$, otherwise the identification of S and A mode is interchanged). Equation (26) follows from diagonalizing a 2×2 Hamiltonian, which describes two identical cavity modes coupled by a matrix element $V_{\rm opt}$. The angular dependence of R_c for the two polarizations (see Appendix A) is such that $V_{\rm opt}$ increases with angle for TM, and decreases for TE polarization.

Comparison with the single cavity case shows that the mode widths in the coupled cavity structure are *reduced* by a factor of two: the physical interpretation of this result (which is rigorously derived in Appendix B) is that the decay rate of the coupled cavity mode is the average of that of left and right cavities, but each cavity mode can now decay on one side only of the coupled structure. The predicted reduction in coupled-cavity linewidth is however difficult to observe, since it requires comparing the optical behavior of two different samples.

When the two cavities have different lengths, it is no longer possible to speak of a symmetric and an antisymmetric mode: the thicker (thinner) cavity has a larger weight in the low (high) energy mode. We show here that the combined effects of cavity mismatch and absorption give rise to differing intensities of the reflectivity dips. The dip intensities can be calculated analytically[68] also when the refractive index is assumed to have an imaginary part, and the results are as follows. Since in the presence of absorption it is the top (outer) cavity which gives the largest contribution to the reflectivity spectrum, the corresponding peak is stronger. On the other hand the relative intensities in the transmission spectrum do not depend on which cavity is thicker. These conclusions confirm the results obtained by numerical simulations in Ref. 31.

This behavior is illustrated in Fig. 6, which displays the normal incidence reflectivity of two coupled GaAs microcavities with AlAs/GaAs mirrors. Fig. 6a is calculated for a real refractive index, while Fig. 6b includes absorption through an imaginary part $\kappa = 0.005$ of the refractive index in the GaAs layers. Figure 6a demonstrates that the cavity mismatch alone yields reflectivity dips which are much less pronounced, since the structure is now unbalanced, but produces only a small asymmetry (unless the cavity mismatch is very large). Furthermore, the reflectivity spectra are the same from both sides, irrespective of which cavity is thicker (this is implied by the general form (3) of the transfer matrix for a non-absorbing structure). In Fig. 6b the cavity mismatch is taken to be much smaller than in Fig. 6a (thus the dip positions are almost unchanged), but nevertheless the two dips are much broader and have different intensities: thus even a small cavity unbalancing produces a sizeable peak broadening and asymmetry when combined with a finite imaginary part of the refractive index. Moreover, the reflectivity spectra change when the order of the cavities is changed: when the top cavity is thinner (dashed line) the dip at higher energy is stronger than the dip at lower energy, while for a thicker top cavity (solid line) the lower dip is stronger. These conclusions will be important for interpreting the experimental results of Sec. 5.3.

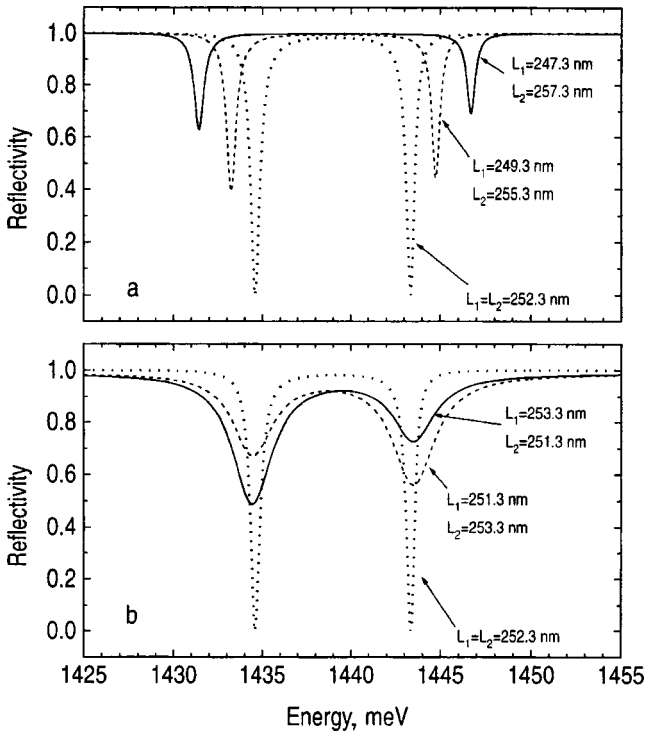

FIG. 6. Calculated normal incidence reflectivity for two empty coupled GaAs microcavities. (a) Each layer in the structure is described by a real refractive index. (b) The GaAs layers are described by a complex refractive index with an imaginary part $\kappa = 0.005$.

5.2. Coupled cavities with quantum wells

We now consider two identical microcavities of length $L_c = \lambda$, each containing a QW at the antinode of the electric field (see Fig. 3b). Because of the symmetry of the system, the dispersion equations for exciton–polaritons in two coupled microcavities can be written again as two independent equations for symmetric and antisymmetric polariton modes:

$$\frac{\Gamma}{\Delta} = \frac{-i(\sqrt{RR_c} - \sqrt{R_c}e^{-i\chi} + \sqrt{R}e^{i\chi} - e^{-2i\chi})}{\pm\sqrt{1-R_c}(e^{-i\chi} + \sqrt{R})} \Big/ (1+\sqrt{R}e^{i\chi})(1+e^{-2i\chi}+2\sqrt{R_c}e^{-i\chi}), \tag{29}$$

with $\chi = (n_c/c)\, L_{\rm eff}(\omega - \omega_m)\cos\theta_c$. Expanding the r.h.s in (29) up to first order in $(\omega - \omega_m)$, we find that the two equations reduce to

$$(\omega - \omega_{\rm ex} + i\gamma_{\rm ex})(\omega - \omega_m + V_{\rm opt} + i\tilde{\gamma}_m) = V^2, \tag{30}$$

$$(\omega - \omega_{\rm ex} + i\gamma_{\rm ex})(\omega - \omega_m - V_{\rm opt} + i\tilde{\gamma}_m) = V^2, \tag{31}$$

with the coupling $V_{\rm opt}$ between the two cavities and the linewidth $\tilde{\gamma}_m$ given by (27) and (28), respectively. The effective coupling V represents the exciton–cavity mode interaction and is calculated to be

$$V^2 = \frac{2\Gamma c}{n_c L_{\rm eff}\cos\theta_c} \frac{(1+\sqrt{R})^2(1+\sqrt{R_c})}{(R+1+4\sqrt{R}+2\sqrt{RR_c})}. \tag{32}$$

In the limit $R, R_c \to 1$, V reduces to (21) for TE or to (22) for TM polarization, i.e., it coincides with the coupling constant for the single QW embedded in a microcavity.

It is interesting and useful to interpret the results in terms of an oscillator model. The twofold-degenerate lowest exciton state in two identical and uncoupled QWs has the symmetric and antisymmetric eigenfunctions

$$|S\rangle = (|\mathrm{QW1}\rangle + |\mathrm{QW2}\rangle)/\sqrt{2}, \tag{33}$$

$$|A\rangle = (|\mathrm{QW1}\rangle - |\mathrm{QW2}\rangle)/\sqrt{2}, \tag{34}$$

where $|\mathrm{QW1}\rangle$ and $|\mathrm{QW2}\rangle$ are the single exciton wave functions in the two QWs. On the other hand, as already stated, coupling between the two photon modes at equal frequency ω_m leads to the formation of symmetric and antisymmetric coupled cavity modes, with complex frequencies given by Eq. (26). The symmetric exciton state only interacts with the symmetric photon mode, and the antisymmetric exciton only interacts with the antisymmetric photon mode: since the coupled cavity frequencies do not coincide, there are four distinct exciton-polariton states which may be observed in reflection.

The two coupled cavities with QWs are therefore described by a four–oscillator model, whose Hamiltonian can be written as

$$\begin{bmatrix} \omega_m - i\tilde{\gamma}_m & V_{\mathrm{opt}} & V & 0 \\ V_{\mathrm{opt}} & \omega_m - i\tilde{\gamma}_m & 0 & V \\ V & 0 & \omega_{\mathrm{ex}} - i\gamma_{\mathrm{ex}} & 0 \\ 0 & V & 0 & \omega_{\mathrm{ex}} - i\gamma_{\mathrm{ex}} \end{bmatrix} \tag{35}$$

in the basis of localized cavity and exciton states. Equation (35) includes all the couplings between the four oscillators present in the system. It also allows for generalizations, like having different cavity parameters (in which case ω_m differs for the two cavities) or different QW excitons (in this latter case ω_{ex} would have two different values). By changing basis to the states (33)–(34) for the exciton and the analogous ones for the cavity states, the Hamiltonian (35) takes a 2×2 block form in which symmetric or antisymmetric exciton states of energy $\omega_{\mathrm{ex}} - i\gamma_{\mathrm{ex}}$ are coupled by a matrix element V to symmetric or antisymmetric cavity modes of energy $\omega_m \pm V_{\mathrm{opt}} - i\tilde{\gamma}_m$, leading again to Eqs. (39)–(31). The simple physical model used in the first of Ref. 33 is therefore recovered.

5.3. Experiments

The coupled cavity structure was grown by MOVPE and consists of two λ-thick GaAs cavities (nominal thickness $L_c = 250$ nm) and three GaAs/AlAs dielectric mirrors. The top DBR contains 12 periods, the central one 14.5 (thus $N_c = 15$) and the bottom DBR 17.5 periods, ending on a GaAs substrate. Each cavity contains three 10 nm wide $In_{0.06}Ga_{0.94}As$ QWs separated by 10 nm GaAs barriers. The number of periods in the central mirror was chosen in order to achieve an optical splitting between symmetric and antisymmetric cavity modes of the order of the Rabi splitting: this maximizes the effect of coupling between the four oscillators present in the system, and allows the removal of degeneracy of exciton states to be achieved, as is shown below. The different number of periods in the top and bottom DBRs partially compensates for the presence of the substrate. The main effect of asymmetry in the real structure is again in determining the absolute values of reflectivity dips, which is not the main issue here. We also note that, in these high-finesse microcavities, absorption is rather strong so that transmission, although measurable, is usually only a few per cent; therefore in order to make a detailed and reliable comparison between experiment and theory we chose to concentrate on reflectivity results.

In Fig. 7a we show the measured unpolarized reflectivity spectra at different angles. At the lowest angle $\theta = 10°$ the symmetric and antisymmetric cavity modes are clearly seen, together with a weak exciton feature. The unsplit exciton peak indicates that the two sets of QWs have nearly the same exciton energies; on the other hand the different intensities of the two cavity peaks point to slightly different values for the cavity lengths, with the top cavity being thicker. On increasing the angle the two cavity modes shift to higher energies and gradually mix with the exciton states. At $\theta = 20°$ the exciton states appear as two peaks split by about 2 meV: the removal of degeneracy of spatially separated exciton states has been achieved. For angles around $\theta = 30°$, the four states are strongly mixed and can no longer be attributed to distinct exciton and cavity states. It is interesting to observe that the third peak becomes narrower in the resonance region: this feature will be discussed in more detail below. For $\theta > 40°$ the cavity modes are at higher energies than the excitonic states, which again become degenerate. The relative intensity of the cavity modes is similar to that at low angles; however the dips are broader, since the cavity modes are now degenerate with the excitonic continuum in the QWs.[7]

We notice that the two energetically split excitonic states are both observed in reflectivity spectra, i.e., they are both ''bright.'' This is a new situation compared to the single cavity case, where if the QW excitons are identical only one state is bright and the remaining ones are dark and unobservable (see discussion of Sec. 4.2). Thus the double cavity configuration allows a qualitatively new phenomenon to be obtained, namely a sizeable radiative splitting between bright excitonic states, which cannot be observed either for free QWs nor for QWs in a single cavity.

Fig. 7b shows the calculated reflectivity curves at the same angles for TM polarization (which dominates the unpolarized spectra, as for the single cavity case). Parameters are chosen as follows: cavity lengths $L_1 = 253.6$ nm, $L_2 = 251$ nm, DBR layers $a = 70.34$ nm, $b = 59.52$ nm (close to nominal values, and again adjusted to reproduce mode energies and polarization splittings). The penetration depth and effective length at $\theta = 0$ are $L_{\mathrm{DBR}} = 670$ nm and $L_{\mathrm{eff}} = 922$ nm. The reflectivity of the central mirror is $R_c = 0.97$ (note that Eqs. (A2) and (A5) apply also to a symmetric mirror, taking $N = N_c$, provided the number of quarter-wave pairs is $N_c - 1/2$ as in Fig. 3b), leading to an optical matrix element $V_{\mathrm{opt}} = 5.2$ meV. An imaginary part $\kappa = 0.005$ has been added to the index of refraction for the GaAs layers.

The choice of the excitonic parameters is important. The

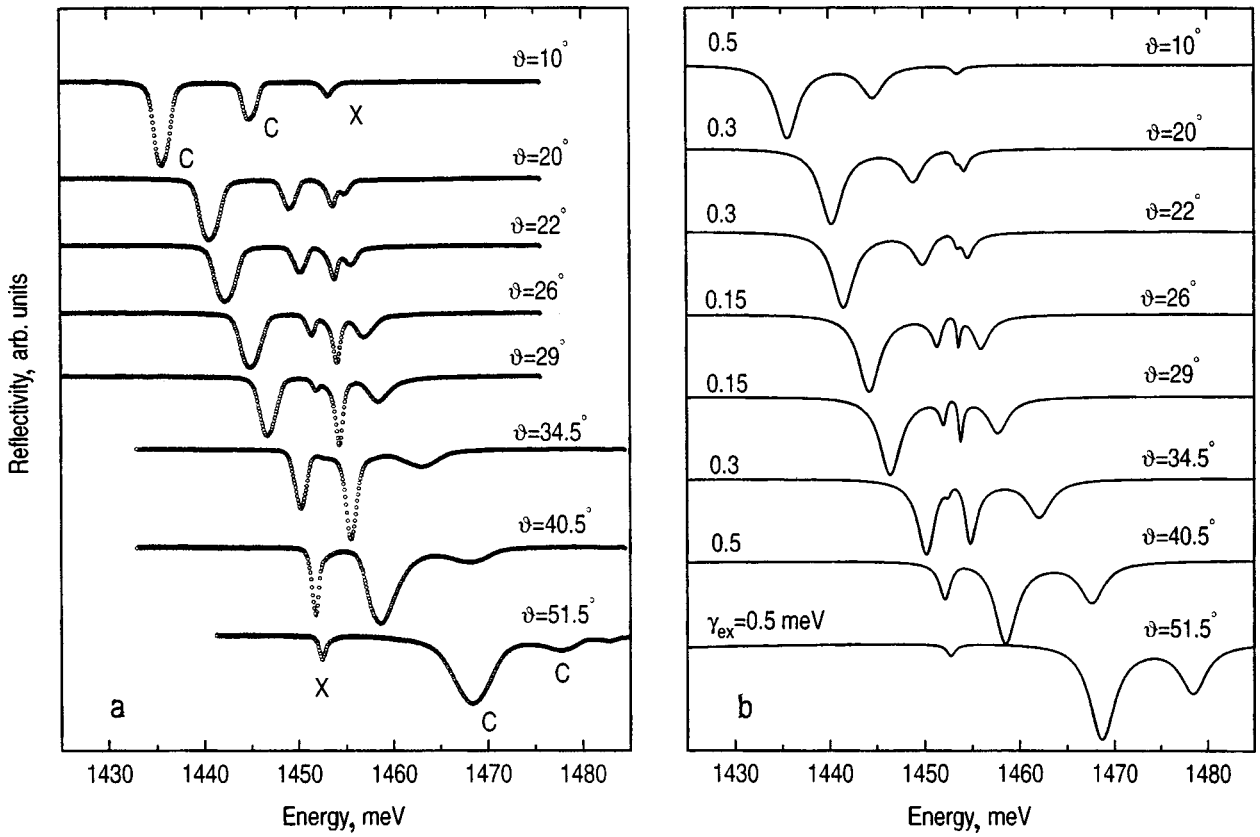

FIG. 7. Measured (a) and calculated (b) reflectivity spectra as a function of angle for two coupled GaAs cavities each containing three $In_{0.06}Ga_{0.94}As$ QWs. Parameters are given in the text and above the curves.

exciton frequency is $\omega_{ex}=1453$ meV. The exciton halfwidth is taken to be different for each curve, in order to account for the effect of resonance narrowing; starting from the experimental value $\gamma_{ex}=0.5$ meV (HWHM) at low and high angles, reproducing the width of the third peak requires values of γ_{ex} down to 0.3 or 0.15 meV at resonance (the values of γ_{ex} are indicated on each curve). The oscillator strength per unit area is $f_{xy}=4.2\times10^{12}\,\mathrm{cm}^{-2}$ leading again to a radiative width $\Gamma_0=0.052$ meV for the sets of three QWs. Note that the oscillator strength of excitons in $In_xGa_{1-x}As/GaAs$ QWs of ~10 nm width is almost independent of In concentration.[66] The exciton-cavity matrix element for each QW is calculated to be $V=2.5$ meV. We also account for absorption in the excitonic continuum by adding a further contribution to the imaginary part of the refractive index in the QW regions, for energies $E_b\sim8$ meV above the excitonic transition energy.[66] From the known absorption probability for interband transitions, which is $w\simeq0.7\%$ for the heavy-hole to conduction band transition,[69,70] we obtain an absorption coefficient $\alpha=7\times10^3\,\mathrm{cm}^{-1}$ and a value $\kappa=0.05$.

The calculated reflectivity curves reproduce the important features of the experimental spectra of Fig. 7a. The relative intensities of the cavity modes at low or high angles is explained by the combination of cavity mismatch and absorption in the GaAs layers, following the theoretical discussion of Sec. 5.1: the most pronounced dip is the lowest energy one, corresponding to the top cavity being thicker. The observed increase of linewidth of the cavity dips at high angle is reproduced by the calculation when absorption of the excitonic continuum is included. Furthermore, in the resonance region the anticrossing behavior and the change of relative intensities of the various peaks is reproduced very well; the linewidth of the third peak agrees with the observed one, but only when a very narrow excitonic homogeneous broadening is assumed. Thus the present results give further evidence for the occurrence of line narrowing of cavity polaritons at resonance. This was first attributed to ''motional'' narrowing due to the very light in-plane mass of cavity polaritons;[16,17] recently it has been shown[18–21] that a resonance narrowing occurs also for any mechanism of inhomogeneous broadening of the exciton line, although the ''motional'' effect is necessary to eliminate scattering between low-k polariton states.

It can be noticed from Fig. 7 that the relative intensities of the various dips are well reproduced by the calculation, but the intensity of the third dip is not large enough when compared to that of the fourth dip. In order to examine this question and the resonance narrowing in more detail, we show an enlarged view of the reflectivity in the resonance region in Fig. 8 for $\theta=26°$. The experimental result is compared to three different calculations. In the first one (curve (a)) the off-resonance excitonic linewidth $\gamma_{ex}=0.5$ meV is taken: this is seen to be inadequate as the third peak is too weak and its linewidth is too large. In the second calculation (curve (b)) the narrower halfwidth $\gamma_{ex}=0.15$ meV is assumed: now the width of the third peak is close to the ex-

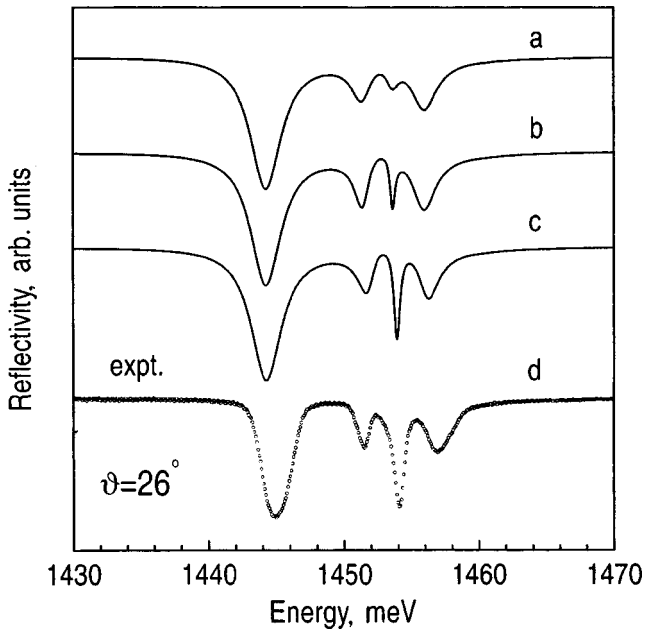

FIG. 8. Reflectivity lineshape in the resonance region at an angle $\theta=26°$ for the two coupled GaAs cavities. Curve (a): theory, $\gamma_{ex}=0.5$ meV, identical QWs ($\hbar\omega_{ex}=1453$ meV). Curve (b): theory, $\gamma_{ex}=0.15$ meV, identical QWs. Curve (c): theory, $\gamma_{ex}=0.15$ meV, $\hbar\omega_{ex}=1453$ meV for the QWs of the top cavity, $\hbar\omega_{ex}=1454$ meV for the QWs of the bottom cavity. Curve (d): experimental results.

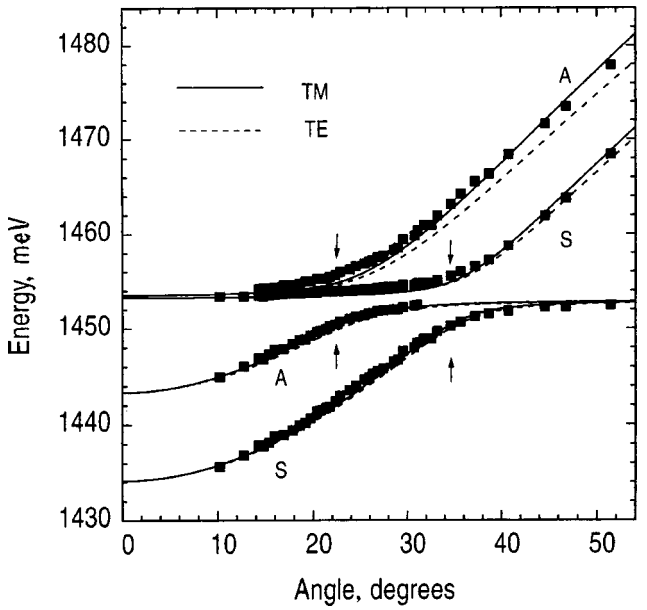

FIG. 9. Dispersion of cavity polaritons for the two coupled GaAs cavities of Figs. 7 and 8 each containing three InGaAs QWs. Parameters are given in the text. Continuous and dashed lines — theoretical curves (solid = TM, dashed = TE); squares — experimental data. The arrows denote the separate anticrossings of A and S modes.

perimental one, and its intensity is increased, but still being a bit weaker than in the experiment. As a possible explanation for the intensity of the third peak we introduce a small energy difference of 1 meV for the two QW excitons (curve (c)), with the QW of the inner cavity being at higher energy. In this case the third peak moves closer in energy to the fourth one and gains part of its oscillator strength, thereby leading to an intensity ratio which is very similar to the experimental one. We should also note that other explanations cannot be ruled out; reproducing the observed intensities at resonance in all details would probably require a more realistic model of excitonic broadening, including, e.g., an inhomogeneous distribution of excitonic levels[18,29,71] which goes beyond our simple Lorentzian model.

In Fig. 9 the cavity polariton dispersion measured from the position of unpolarized reflectivity dips is compared to the one calculated for both TE and TM polarizations. Here, in order to use the analytic equations, we have assumed the symmetric structure shown in Fig. 3b, with a thickness $L_c=252.3$ nm and $N=12$ pairs in the external DBRs. Several features can be seen. At $\theta=10°$ the symmetric and antisymmetric coupled-cavity modes are well separated from the exciton resonance and have an energy of 1435.5 and 1445 meV, respectively, close to the values at normal incidence; the optical splitting of cavity modes is thus $2V_{opt}=9.3$ meV. The same value for the optical splitting is also obtained at an angle $\theta=50°$, when the two cavity modes are outside the anticrossing region and at much higher energy than the exciton. At intermediate angles strong interaction between the four oscillators occurs. The antisymmetric cavity mode interacts with the antisymmetric linear combination of exciton states and anticrossing occurs at $\theta\simeq22°$, with a Rabi splitting of ~5 meV: this is reproduced well by the calculation using the known exciton oscillator strength, as in the single cavity case. Anticrossing between the symmetric cavity- and exciton modes occurs at $\theta=35°$ with the same Rabi splitting ~5 meV. The two anticrossings are indicated by arrows on the plot. Thus both the optical matrix element V_{opt} and the exciton-cavity matrix element V can be read directly from the dispersion curves and are close to the calculated values. The experimental dispersion at high angles agrees well with the calculated one and is closer to that for TM polarization, as discussed in Sec. 4 and in Ref. 64. This corresponds to the previous considerations, that the position of reflectivity dips in unpolarized spectra is mostly determined by TM polarization. Finally, we remark that good agreement at high angles depends critically on inclusion of the energy dependence of the index of refraction, as in the single-cavity case: when this is neglected, the calculated dispersion turns out to be much steeper than the experimental one.

In Fig. 10 we present an example of polarization-resolved reflectivity spectra at the largest measured external angle $\theta=51.5°$. The exciton peak is seen to be unsplit, since the interaction between exciton and cavity modes is weak. The peaks labeled ''C'' represent optically coupled modes of the two cavities. We first remark that the lower-energy cavity dips are much more intense for both polarizations: this is due to a slightly larger thickness of the top cavity combined with the presence of absorption, as already discussed. Both the lower (symmetric) and upper (antisymmetric) coupled cavity modes have a polarization splitting, the TM mode being higher in energy than the TE one; the splitting is larger for the upper cavity peak. These features, as well as the relative intensities, are reproduced well by the calculation. The en-

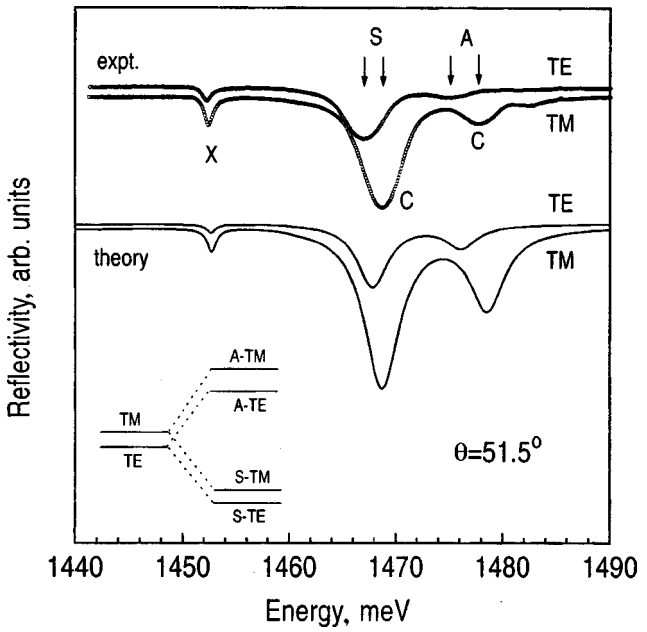

FIG. 10. Experimental and theoretical reflectivity curves for the GaAs coupled cavities at $\theta = 51.5°$, for TE and TM polarizations. Inset — schematic illustration of polarization splitting of the optical modes in a single cavity (left) and in coupled cavities.

ergy positions of the structures depend on polarization through the isolated cavity mode $\omega_m^\alpha(\theta)$ as well as the optical coupling $V_{\rm opt}^\alpha$ (Eq. (27)); the inset in Fig. 10 illustrates the evolution of the polarization splitting from the single to the coupled cavity for the present case of odd N_c. The polarization splittings of the upper and lower doublet are calculated as

$$\Delta\omega_A = \Delta\omega_m + V_{\rm opt}^{\rm TM} - V_{\rm opt}^{\rm TE} = 2.2\ {\rm meV}, \tag{36}$$

$$\Delta\omega_S = \Delta\omega_m - V_{\rm opt}^{\rm TM} + V_{\rm opt}^{\rm TE} = 0.8\ {\rm meV}, \tag{37}$$

respectively. The predicted order of levels is the same as in the experimental result, namely S–TE, S–TM, A–TE, A–TM on increasing energy. Note that this is not a general property, since it depends on the polarization splitting for the single cavity (which can have either sign) as well as on the size of $V_{\rm opt}^\alpha$. The splitting of the antisymmetric mode is larger because the optical matrix element $V_{\rm opt}$ is larger for TM polarization (see also the inset). The experimental values of the polarization splittings are $\Delta\omega_A = 2.5$ meV for the upper doublet and $\Delta\omega_S = 1.7$ meV for the lower doublet, in fair agreement with the values given in (36)–(37). Thus we can conclude that a good understanding of polarization splitting of coupled cavities has been achieved.

6. CONCLUSIONS

Angle- and polarization-resolved spectroscopy on microcavities with QWs yields very detailed information about exciton-light coupling in the strong-coupling regime. Interpreting cavity-polariton spectroscopy at meV or sub-meV level requires the inclusion of several effects: reflection phase delay in the dielectric mirrors, angle- and polarization dependence of mode frequency and of exciton-cavity coupling, energy dependence of the refractive index, and optical coupling between the cavities, which are analyzed in the present paper mainly on the basis of analytic results. The theoretical formulation based on semiclassical theory can be easily extended or applied to other related situations.

The energy of single-cavity modes is determined by the Fabry–Pérot frequency ω_c and by the center of the stop band ω_s, weighted by their characteristic lengths: the penetration depth in the dielectric mirrors carries a nontrivial angle- and polarization dependence. The polarization splitting of single-cavity mode depends on the mismatch between ω_c and ω_s, and increases with internal angle like $\sin^2\theta_{\rm eff}$. When QWs are embedded in the microcavity at an antinode of the electric field, the exciton and cavity mode are described at each angle by a two-oscillator model, whose parameters are expressed in terms of microscopic properties of the exciton and structural parameters. Weak- and strong-coupling regimes and the formation of cavity polaritons are described. Comparison with experimental results on a GaAs-based cavity with $In_{0.13}Ga_{0.87}As$ QWs shows that a good understanding of the exciton-cavity mode interaction, polariton dispersion and polarization properties has been achieved. For the polariton dispersion it is important to include the energy dependence of the index of refraction, which makes the cavity mode considerably less steep at high angles.

Coupling of two identical cavities through a central mirror induces an optical splitting between symmetric and antisymmetric modes, which also depends on angle and polarization. A mismatch of cavity lengths combined with absorption in the structure leads to different intensities of reflectivity dips. When QW excitons are embedded in both cavities at antinode positions, the system behaves as four coupled oscillators, leading to a removal of degeneracy of exciton states separated by a macroscopic distance. The energetically split excitonic oscillators are both bright and observable, unlike the situation for two identical QWs in free space or in a single cavity. If the two cavities (and the two QWs) are identical, separate anticrossing of symmetric and antisymmetric modes occurs. These features are confirmed by experimental results on a coupled GaAs cavity with $In_{0.06}Ga_{0.94}As$ QWs. The polariton dispersion for coupled cavities is well described by theory; a lineshape analysis allows an effect of line narrowing of cavity polariton linewidths in the resonance region to be revealed. Finally, the polarization splitting of coupled-cavity system has been analyzed in detail and is shown to depend both on single-cavity factors and on angle- and polarization-dependence of the optical coupling. Inclusion of all these effects provides a good description of the experimental results.

The authors are indebted to D.M. Whittaker for many helpful discussions and for pointing out the importance of inclusion of the energy dependence of the refractive indices to fit the cavity-mode dispersion. The work at Sheffield was supported by EPSRC grant GL/L32187.

APPENDIX A: PARAMETRIZATION OF DBR REFLECTION COEFFICIENT

Evaluation of the quantities appearing in the parametrization of the DBR reflectivity, Eq. (10), requires expanding

the elements of the transfer matrix up to linear order in terms of two small parameters ε_1 and ε_2 defined as follows:

$$\varepsilon_1=\frac{n_1}{c}a(\omega\cos\theta_1-\omega_{1s}),$$

$$\varepsilon_2=\frac{n_2}{c}b(\omega\cos\theta_2-\omega_{2s}), \tag{A1}$$

where a,b are the thicknesses of DBR layers (see Fig. 1), and θ_1 and θ_2 are the angles in the layers with refractive indexes n_1 and n_2 respectively. The frequencies ω_{1s} and ω_{2s} are defined by $n_1\omega_{1s}a/c=n_2\omega_{2s}b/c=\pi/2$. Note that, as far as ω_{1s} may differ from ω_{2s}, our expressions can be used also when the $\lambda/4$ condition is not exactly satisfied. For the case $n_1<n_2$, lengthy but straightforward calculations lead — for a large number N of periods — to the following expressions:

TE polarization:

$$R(\theta)=1-4\frac{n_{\rm ext}}{n_c}\frac{\cos\theta}{\cos\theta_c}\left(\frac{n_1\cos\theta_1}{n_2\cos\theta_2}\right)^{2N}, \tag{A2}$$

$$\omega_s(\theta)=\frac{\pi c}{2(a+b)}\frac{n_1\cos\theta_1+n_2\cos\theta_2}{n_1n_2\cos\theta_1\cos\theta_2}, \tag{A3}$$

$$L_{\rm DBR}(\theta)=\frac{2n_1^2n_2^2(a+b)}{n_c^2(n_2^2-n_1^2)}\frac{\cos^2\theta_1\cos^2\theta_2}{\cos^2\theta_c}. \tag{A4}$$

TM polarization:

$$R(\theta)=1-4\frac{n_{\rm ext}}{n_c}\frac{\cos\theta_c}{\cos\theta}\left(\frac{n_1\cos\theta_2}{n_2\cos\theta_1}\right)^{2N}, \tag{A5}$$

$$\omega_s(\theta)=\frac{\pi c}{2}\frac{n_1\cos\theta_2+n_2\cos\theta_1}{n_1n_2(a\cos^2\theta_1+b\cos^2\theta_2)}, \tag{A6}$$

$$L_{\rm DBR}(\theta)=\frac{2n_1^2n_2^2}{n_c^2}\frac{a\cos^2\theta_1+b\cos^2\theta_2}{n_2^2\cos^2\theta_1-n_1^2\cos^2\theta_2}. \tag{A7}$$

At normal incidence, and if the $\lambda/4$ condition is exactly satisfied, we have

$$a=\frac{1}{4}\frac{\lambda_s}{n_1}\quad b=\frac{1}{4}\frac{\lambda_s}{n_2}, \tag{A8}$$

where λ_s is the operating wavelength *in vacuum*; then the above formulas reduce to

$$R(0)=1-4\frac{n_{\rm ext}}{n_c}\left(\frac{n_1}{n_2}\right)^{2N}, \tag{A9}$$

$$\omega_s(0)=\frac{\pi c}{2(a+b)}\frac{n_1+n_2}{n_1n_2}=\frac{2\pi c}{\lambda_s}, \tag{A10}$$

$$L_{\rm DBR}(0)=\frac{2n_1^2n_2^2(a+b)}{n_c^2(n_2^2-n_1^2)}=\frac{\lambda_s}{2}\frac{n_1n_2}{n_c^2(n_2-n_1)}, \tag{A11}$$

and coincide with those given in Ref. 37 and 38.

The reflection coefficient for $n_1>n_2$ may be similarly evaluated. In this case it is parametrized according to the lower sign in Eq. (10) of the text, and we obtain:

TE polarization:

$$R(\theta)=1-4\frac{n_c}{n_{\rm ext}}\frac{\cos\theta_c}{\cos\theta}\left(\frac{n_2\cos\theta_2}{n_1\cos\theta_1}\right)^{2N}, \tag{A12}$$

$$\omega_s(\theta)=\frac{\pi c}{2}\frac{n_1\cos\theta_1+n_2\cos\theta_2}{n_1^2a\cos^2\theta_1+n_2^2b\cos^2\theta_2}, \tag{A13}$$

$$L_{\rm DBR}(\theta)=\frac{2}{n_1^2-n_2^2}(n_1^2a\cos^2\theta_1+n_2^2b\cos^2\theta_2). \tag{A14}$$

TM polarization:

$$R(\theta)=1-4\frac{n_c}{n_{\rm ext}}\frac{\cos\theta}{\cos\theta_c}\left(\frac{n_2\cos\theta_1}{n_1\cos\theta_2}\right)^{2N}, \tag{A15}$$

$$\omega_s(\theta)=\frac{\pi c}{2(n_1^2a+n_2^2b)}\frac{n_1\cos\theta_2+n_2\cos\theta_1}{\cos\theta_1\cos\theta_2}, \tag{A16}$$

$$L_{\rm DBR}(\theta)=\frac{2\cos^2\theta_1\cos^2\theta_2(n_1^2a+n_2^2b)}{\cos^2\theta_c(n_1^2\cos^2\theta_2-n_2^2\cos^2\theta_1)}. \tag{A17}$$

APPENDIX B: ASYMMETRIC CAVITY, COUPLED CAVITY LINEWIDTH

In this Appendix, we extend the treatment of Sec. 4.1 by deriving formulas for mode frequency and width of an asymmetric cavity, and also prove the results reported in Sec. 5.1 for a coupled cavity.

The dispersion relation for an asymmetric cavity of width L_c surrounded by mirrors with reflection coefficients r and r_c is

$$rr_c e^{2ik_zL_c}=1. \tag{B1}$$

This formula can be derived either by working out the transfer matrix of the structure using parametrizations (3) and (4) for right and left mirrors, or by taking Eq. (11) for a cavity of width $2L_c$ in the limit $t_c\to 0$ for the central object. Introducing the usual parametrization (10) for the DBR reflection coefficient, this equation for ω can be solved in the complex plane yielding $\omega=\omega_m(\theta)-i\gamma_m(\theta)$, with the mode frequency given by

$$\omega_m=\frac{L_c\omega_c+\frac{1}{2}(L_{\rm DBR}\omega_s+L_{{\rm DBR},c}\omega_{s,c})}{L_c+\frac{1}{2}(L_{\rm DBR}+L_{{\rm DBR},c})} \tag{B2}$$

and the mode halfwidth

$$\gamma_m=-\frac{c\ln\sqrt{RR_c}}{2n_cL_{\rm eff}\cos\theta_c}, \tag{B3}$$

where $L_{\rm eff}=L_c+(1/2)(L_{\rm DBR}+L_{{\rm DBR},c})$, with obvious notations for the centers of stop bands and penetration depths. For $R,R_c\to 1$, formula (B2) reduces to Eq. (14) for the mode halfwidth of a symmetric cavity.

We now consider a symmetric structure with two cavities of width L_c coupled by a central mirror; the dispersion equation is (11) of the main text. Since the central mirror is assumed to be symmetric, its reflection and transmission coefficients satisy $t_c/t_c^*=-r_c/r_c^*$ (see Sec. 3). This implies

that the phase of t_c differs from the phase of r_c by $\pm\pi/2$, or $t_c = \pm i r_c \sqrt{(1-R_c)/R_c}$. The $\pm$ sign corresponds to an even or odd number of periods in the central mirror. The dispersion equation (11) can be written, therefore, as

$$r r_c e^{2ik_z L_c} = \frac{1}{1 \pm i\sqrt{\dfrac{1-R_c}{R_c}}}, \tag{B4}$$

where the l.h.s. equals unity at the eigenfrequency of each isolated cavity (see Eq. (B1)). By expressing the l.h.s. in terms of the isolated cavity frequency (B2) and (B3), the complex solutions for the coupled cavity are found as

$$\omega = \omega_m - i\gamma_m + \frac{ic \ln\left(1 \pm i\sqrt{\dfrac{1-R_c}{R_c}}\right)}{2n_c L_{\text{eff}} \cos\theta_c}. \tag{B5}$$

The imaginary part of the logarithm yields the optical splitting between S and A modes, while the real part gives a correction to the single cavity linewidth. We obtain:

$$\omega = \omega_m \pm V_{\text{opt}} - i\tilde{\gamma}_m, \tag{B6}$$

where

$$V_{\text{opt}} = \frac{c}{2n_c L_{\text{eff}} \cos\theta_c} \arcsin\sqrt{1-R_c}, \tag{B7}$$

$$\tilde{\gamma}_m = -\frac{c}{2n_c L_{\text{eff}} \cos\theta_c} \ln\sqrt{R}. \tag{B8}$$

The expression for the optical coupling reduces for $R_c \to 1$ to Eq. (27) of the main text. The halfwidth is reduced compared to Eq. (B3) for a single cavity: the effect of optical coupling between the two cavities is to suppress the contribution to the linewidth coming from decay through the mirror of reflectivity R_c, and to leave only the decay rate through the external mirror of reflectivity R.

This conclusion can also be derived using the concept of *quasi-modes*,[28] which are formed by the stationary states of a closed cavity weakly coupled to the external electromagnetic field. For a single cavity, the linewidth can be expressed by $\gamma_m = \gamma_{\text{left}} + \gamma_{\text{right}}$ in terms of the decay rates from either side; for a coupled cavity, since the eigenmodes S and A are linear combinations of single cavity modes, the matrix elements to left and right outer states are reduced by a factor $1/\sqrt{2}$, and the whole width is reduced by a factor of two.

[1] J. J. Hopfield, Phys. Rev. **112**, 1555 (1958); V. M. Agranovich, J. Exp. Theor. Phys. **37**, 430 (1959); [Sov. Phys. JETP **37**, 307 (1960)].

[2] C. Weisbuch, M. Nishioka, A. Ishikawa, and Y. Arakawa, Phys. Rev. Lett. **69**, 3314 (1992).

[3] R. Houdré, C. Weisbuch, R. P. Stanley, U. Oesterle, P. Pellandini, and M. Ilegems, Phys. Rev. Lett. **73**, 2043 (1994).

[4] R. Houdré, R. P. Stanley, U. Oesterle, M. Ilegems, and C. Weisbuch, Phys. Rev. B **49**, 16761 (1994); T. R. Nelson, Jr., J. P. Prineas, G. Khitrova, H. M. Gibbs, J. D. Berger, E. K. Lindmark, J.-H. Shin, H.-E. Shin, Y.-H. Lee, P. Tayebati, and L. Javniskis, Appl. Phys. Lett. **69**, 3031 (1996); L. A. Graham, Q. Deng, D. G. Deppe, and D. L. Huffaker, Appl. Phys. Lett. **70**, 814 (1997).

[5] T. B. Norris, J. K. Rhee, C. Y. Sung, Y. Arakawa, M. Nishioka, and C. Weisbuch, Phys. Rev. B **50**, 14 663 (1994); H. Wang, J. Shah, T. C. Damen, W. Y. Jan, J. E. Cunningham, M. Hong, and J. P. Mannaerts, Phys. Rev. B **51**, 14713 (1995); G. Bongiovanni, A. Mura, F. Quochi, S. Gürtler, G. L. Staehli, F. Tassone, R.P. Stanley, U. Oesterle, and R. Houdré, Phys. Rev. B **5**, 7084 (1997).

[6] T. A. Fisher, A. M. Afshar, D. M. Whittaker, M. S. Skolnick, J. S. Roberts, G. Hill, and A. Pate, Phys. Rev. B **51**, 2600 (1995).

[7] J. Tignon, P. Voisin, C. Delalande, M. Voos, R. Houdré, U. Oesterle, and R. P. Stanley, Phys. Rev. Lett. **74**, 3967 (1995); J. Tignon, R. Ferreira, J. Wainstain, C. Delalande, P. Voisin, M. Voos, R. Houdré, U. Oesterle, and R. P. Stanley, Phys. Rev. B **56**, 4068 (1997).

[8] T. A. Fisher, A. M. Afshar, M. S. Skolnick, D. M. Whittaker, and J. S. Roberts, Phys. Rev. B **53**, R10469 (1996).

[9] J. D. Berger, O. Lyngnes, H. M. Gibbs, G. Khitrova, T. R. Nelson, E. K. Lindmark, A. V. Kavokin, M. A. Kaliteevski, and V. V. Zapasskii, Phys. Rev. B **54**, 1975 (1996).

[10] A. Armitage, T. A. Fisher, M. S. Skolnick, D. M. Whittaker, P. Kinsler, and J. S. Roberts, Phys. Rev. B **55**, 16395 (1997).

[11] J.-K. Rhee, D. S. Citrin, T. B. Norris, Y. Arakawa, and M. Nishioka, Solid State Commun. **97**, 941 (1996); R. Houdré, J. L. Gibernon, P. Pellandini, R. P. Stanley, U. Oesterle, C. Weisbuch, J. O'Gorman, B. Roycroft, and M. Ilegems, Phys. Rev. B **52**, 7810 (1995); F. Jahnke, M. Kira, S. W. Koch, G. Khitrova, E. K. Lindmark, T. R. Nelson, Jr., D. V. Wick, J. D. Berger, O. Lyngnes, H. M. Gibbs, and K. Tai, Phys. Rev. Lett. **77**, 5257 (1996); O. Lyngnes, J. D. Berger, J. P. Prineas, S. Park, G. Khitrova, H. M. Gibbs, F. Jahnke, M. Kira, and S. W. Koch, Solid State Commun. **104**, 297 (1997).

[12] R. P. Stanley, R. Houdré, C. Weisbuch, U. Oesterle, and M. Ilegems, Phys. Rev. B **53**, 10 995 (1996); R. P. Stanley, S. Pau, U. Oesterle, R. Houdré, and M. Ilegems, Phys. Rev. B **55**, 4867 (1997).

[13] V. Savona and C. Weisbuch, Phys. Rev. B **54**, 10835 (1996).

[14] F. Tassone, C. Piermarocchi, V. Savona, A. Quattropani, and P. Schwendimann, Phys. Rev. B **53**, R7642 (1996).

[15] S. Pau, G. Björk, J. Jacobson, H. Cao, and Y. Yamamoto, Phys. Rev. B **51**, 7090 (1995); S. Pau, G. Björk, H. Cao, F. Tassone, R. Huang, Y. Yamamoto, and R. P. Stanley, Phys. Rev. B **55**, 1942 (1997).

[16] D. M. Whittaker, P. Kinsler, T. A. Fisher, M. S. Skolnick, A. Armitage, A. M. Afshar, M. D. Sturge, and J. S. Roberts, Phys. Rev. Lett. **77**, 4792 (1996); P. Kinsler, and D.M. Whittaker, Phys. Rev. B **54**, 4988 (1996).

[17] V. Savona, C. Piermarocchi, A. Quattropani, F. Tassone, and P. Schwendimann, Phys. Rev. Lett. **78**, 4470 (1997).

[18] A. V. Kavokin, Phys. Rev. B **57**, 3757 (1998).

[19] D. M. Whittaker, Phys. Rev. Lett. **80**, 4791 (1998).

[20] C. Ell, J. Prineas, T. R. Nelson, Jr., S. Park, H. M. Gibbs, G. Khitrova, S. W. Koch, and R. Houdré, Phys. Rev. Lett. **80**, 4795 (1998).

[21] J. J. Baumberg, A. Armitage, M. S. Skolnick, and J. S. Roberts, Phys. Rev. Lett. **81**, 661 (1998).

[22] G. R. Hayes, S. Haacke, M. Kauer, R. P. Stanley, R. Houdré, U. Oesterle, and B. Deveaud, Phys. Rev. B **58**, 10 175 (1998).

[23] F. Quochi, G. Bongiovanni, A. Mura, J. L. Staehli, B. Deveaud, R. P. Stanley, U. Oesterle, and R. Houdré, Phys. Rev. Lett. **80**, 4733 (1998).

[24] P. Kelkar, V. Kozlov, H. Leon, A. Nurmikko, C. Chu, D. Grillo, J. Han, C. Hua, and R. Gunshor, Phys. Rev. B **52**, 5491 (1995).

[25] L. S. Dang, D. Heger, R. André, F. Boeuf, and A. Romestain, Phys. Rev. Lett. **81**, 3920 (1998).

[26] T. Ishihara, T. Kuitani, Y. Sato, T. Fujita, M. Yamanishi, in *Physics of Semiconductors*, edited by M. Scheffler and R. Zimmermann (World Scientific, Singapore, 1996), p. 3087; T. Fujita, Y. Sato, T. Kuitani, and T. Ishihara, Phys. Rev. B **57**, 12428 (1998).

[27] D. G. Lidzey, D. D. C. Bradley, M. S. Skolnick, T. Virgili, S. Walker, D. M. Whittaker, Nature (London) **395**, 53 (1998).

[28] V. Savona, C. Piermarocchi, A. Quattropani, P. Schwendimann, and F. Tassone, in *New Aspects in Optical Properties of Nanostructures*, Special issue of Phase Transitions, Vol. 68 (Gordon and Breach, 1999).

[29] G. Khitrova, H.M. Gibbs, F. Jahnke, M. Kira, and S.W. Koch (to be published).

[30] M. S. Skolnick, T. A. Fisher, and D. M. Whittaker, Semicond. Sci. Technol. **13**, 645 (1998).

[31] R. P. Stanley, R. Houdré, U. Oesterle, M. Ilegems, and C. Weisbuch, Appl. Phys. Lett. **65**, 2093 (1994).

[32] P. Pellandini, R. P. Stanley, R. Houdré, U. Oesterle, M. Ilegems, and C. Weisbuch, Appl. Phys. Lett. **71**, 864 (1997).

[33] A. Armitage, M. S. Skolnick, V. N. Astratov, D. M. Whittaker, G. Panzarini, L. C. Andreani, T. A. Fisher, J. S. Roberts, A. V. Kavokin, M. A. Kaliteevski, and M. R. Vladimirova, Phys. Rev. B **57**, 14877 (1998); G. Panzarini, L. C. Andreani, A. Armitage, D. Baxter, M. S. Skolnick, V. N. Astratov, J. S. Roberts, A. V. Kavokin, M. R. Vladimirova, and M. A. Kaliteevski, Phys. Rev. B **59** (1999) (to be published).
[34] D. S. Citrin, Phys. Rev. B **49**, 1943 (1994); L. C. Andreani, Phys. Rev. B **188**, 29 (1995).
[35] G. Panzarini, and L. C. Andreani, Phys. Rev. B **52**, 10780 (1995).
[36] L. Pavesi, G. Panzarini, and L. C. Andreani, Phys. Rev. B **58**, 15 798 (1998).
[37] D. I. Babic, and S. W. Corzine, IEEE J. Quantum Electron. **28**, 514 (1992).
[38] V. Savona, L. C. Andreani, P. Schwendimann, and A. Quattropani, Solid State Commun. **93**, 733 (1995).
[39] A. V. Kavokin, and M. A. Kaliteevski, Solid State Commun. **95**, 859 (1995).
[40] E. L. Ivchenko, M. A. Kaliteevski, A. V. Kavokin, and A. I. Nesvizhskii, J. Opt. Soc. Am. B **13**, 1061 (1996).
[41] D. Baxter, M. S. Skolnick, A. Armitage, V. N. Astratov, D. M. Whittaker, T. A. Fisher, J. S. Roberts, D. J. Mowbray, and M. A. Kaliteevski, Phys. Rev. B **56**, R10032 (1997).
[42] For a review see, e.g., L. C. Andreani, in *Confined Excitons and Photons: New Physics and Devices*, edited by E. Burstein and C. Weisbuch (Plenum, New York, 1995), p. 57.
[43] E. L. Ivchenko, S. Jorda, and A. I. Nesvizhskii, Fiz. Tekh. Poluprovodn. **27**, 977 (1993) [Sov. Phys. Semicond. **27**, 530 (1993)].
[44] D. S. Citrin, Phys. Rev. B **50**, 5497 (1994).
[45] L. C. Andreani, Phys. Lett. A **192**, 99 (1994).
[46] F. Tassone, F. Bassani, and L. C. Andreani, Nuovo Cimento D **12**, 1673 (1990); F. Tassone, L. C. Andreani, and F. Bassani, Phys. Rev. B **45**, 6023 (1992).
[47] L. C. Andreani, F. Tassone, and F. Bassani, Solid State Commun. **77**, 641 (1991).
[48] E. L. Ivchenko, Fiz. Tverd. Tela (Leningrad) **33**, 2388 (1991) [Sov. Phys. Solid State **33**, 1344 (1991)].
[49] D. S. Citrin, Phys. Rev. B **47**, 3832 (1993).
[50] M. Born and E. Wolf, *Principles of Optics*, 4th ed. (Pergamon, N. Y., 1970).
[51] H. A. McLeod, *Thin-Film Optical Filters*, 2nd ed. (Hilger, 1986).
[52] A. Yariv and P. Yeh, *Optical Waves in Crystals* (Wiley, New York, 1984).
[53] C. R. Pidgeon and S. D. Smith, J. Opt. Soc. Am. **54**, 1459 (1964).
[54] S. Jorda, Phys. Rev. B **51**, 10 185 (1995).
[55] This approximate formula for the dispersion is usually derived from the relation $\omega_m=(c/n_{\text{eff}})\sqrt{k_z^2+k_\parallel^2}$, considering that the wavevector along the cavity axis is quantized, leading to $\omega_m(\theta)=\omega_m(0)(1-\sin^2\theta/n_{\text{eff}}^2)^{-1/2}$.
[56] H. Yokoyama, Y. Nambu, and T. Kawakami, in *Confined Excitons and Photons: New Physics and Devices*, edited by E. Burstein and C. Weisbuch (Plenum, New York, 1995), p. 427; G. Björk, Y. Yamamoto, and H. Heitmann, *ibid.*, p. 467.
[57] D. S. Citrin, Solid State Commun. **89**, 139 (1994).
[58] L. C. Andreani, Phys. Status Solidi B **188**, 29 (1995).
[59] G. Björk, S. Pau, J. M. Jacobson, H. Cao, and Y. Yamamoto, Phys. Rev. B **52**, 17310 (1995).
[60] V. M. Agranovich, G. C. La Rocca, and F. Bassani, Phys. Status Solidi A **164**, 39 (1997); G. C. La Rocca, F. Bassani, and V. M. Agranovich, J. Opt. Soc. Am. B **15**, 652 (1998).
[61] V. M. Agranovich, H. Benisty, and C. Weisbuch, Solid State Commun. **102**, 631 (1997).
[62] This sample was first reported in T. A. Fisher, A. M. Afshar, M. S. Skolnick, D. M. Whittaker, and J. S. Roberts, Solid-State Electron. **40**, 493 (1996) and in Ref. 8.
[63] The more precise values quoted in Ref. 41 include absorption, as well as oxidation of the top 50 Å of the top AlGaAs layer.
[64] Experimentally, another reason for the dominant TM polarization is that the reflection coefficient of the cryostat window is greater for TE than for TM, therefore the intensity of light falling on the sample is larger for TM than for TE.
[65] J. T. Boyd, IEEE J. Quantum Electron. **8**, 788 (1972).
[66] R. Atanasov, F. Bassani, A. D'Andrea, and N. Tomassini, Phys. Rev. B **50**, 14381 (1994); R. C. Iotti and L. C. Andreani, Phys. Rev. B **56**, 3922 (1997).
[67] I. Carusotto, G. C. La Rocca, Phys. Status Solidi A **164**, 377 (1997).
[68] G. Panzarini (unpublished).
[69] W. T. Masselink, P.J. Pearah, J. Klem, C. K. Peng, H. Morkoç, G. D. Sanders, and Y.-C. Chang, Phys. Rev. B **32**, 8027 (1985).
[70] S. Frisk, J.-L. Staehli, L.C. Andreani, A. Bosacchi, S. Franchi, in *Optics of Excitons in Confined Systems*, edited by A. D'Andrea, R. Del Sole, R. Girlanda, and A. Quattropani (IOP Conference Series **123**), p. 183 (1992).
[71] L. C. Andreani, G. Panzarini, A. V. Kavokin, and M. R. Vladimirova, Phys. Rev. B **57**, 4670 (1998).

Published in English in the original Russian journal. Reproduced here with stylistic changes by the Translation Editor.

METALS. SUPERCONDUCTORS

Quantum waves in noble metals

S. N. Savel'eva, V. G. Skobov, and A. S. Chernov

A. F. Ioffe Physicotechnical Institute, Russian Academy of Sciences, 194021 St. Petersburg, Russia
(Submitted November 18, 1998)
Fiz. Tverd. Tela (St. Petersburg) **41**, 1354–1360 (August 1999)

A theoretical study is presented of the effect of hole energy quantization in a dc magnetic field on microwave penetration through a noble-metal plate. It is shown that quantization results in strong oscillations of cyclotron absorption. Between the absorption peaks, the damping decreases sufficiently to enable propagation of unique quantum waves. Excitation of such waves in a metallic plate gives rise to sharp oscillations of its surface resistance with magnetic field. The shape of these oscillations is also very unusual. © *1999 American Institute of Physics.* [S1063-7834(99)00208-7]

It is known that metals with unequal electron and hole concentrations placed in a dc magnetic field are capable of supporting propagation of helicons, i.e., electromagnetic waves with a quadratic spectrum. The region of their existence is bounded by a threshold on the weak magnetic-field side. Below the threshold there exists collisionless cyclotron absorption, which makes wave propagation impossible. This condition holds for small amplitudes of the rf field. The magnetic field of a large-amplitude wave ''traps'' the carriers responsible for the cyclotron absorption, thus resulting in its substantial weakening.[1] This suppression of the cyclotron damping may be sufficiently strong to make the dissipative part of nonlocal conductivity in the region of magnetic fields much lower than the helicon threshold field which turns out to be small compared to the nondissipative part. As a result, propagation of nonlinear waves with frequencies proportional to the fourth power of the wave vector becomes possible in metals with unequal concentrations of electrons and holes.[2]

Besides carrier trapping by the magnetic field of a wave, one can conceive of another mechanism for suppressing collisionless damping in metals. This mechanism is quantization of electronic states in a magnetic field. Indeed, cyclotron absorption of a wave is due to carriers having a fixed value of the momentum component along the dc magnetic field, $p_z = p_{z0}$, whose average displacement during the cyclotron period is equal to the rf wavelength in the metal. On the other hand, as a result of quantization of carrier transverse energy in a dc magnetic field **H**, the longitudinal momentum of the carriers on the Fermi surface takes on discrete values p_n, which depend on the magnitude of H. If one of the p_n coincides with p_{z0}, carriers absorbing efficiently the wave energy will exist on the Fermi surface, and the cyclotron absorption will exceed by far the level typical of the absence of quantization. If, however, p_{z0} falls between two adjacent p_n, no carriers satisfying the condition of cyclotron absorption will exist at the Fermi surface, and the absorption will be much weaker than that in the classical case (this is similar to the situation prevailing in the case of giant oscillations of ultrasound damping in metals[3]). As a result, absorption considered as a function of H represents a series of narrow and high quantum peaks separated by broad and deep minima. It is essential that the absorption in these minima is suppressed strongly compared to its classical level. Therefore the dissipative part of nonlocal conductivity may turn out to be small compared to the nondissipative one within the corresponding intervals of H. In this case, quantum waves with a spectrum similar to that in the nonlinear regime will exist in the metal. It is the theory of such waves in metals with unequal concentrations of electrons and holes that is considered in this paper. Section 1 will present the theory for the simplest case of alkali metals having a spherical Fermi surface, and Section 2, that for noble metals, where the conditions for existence of quantum waves are substantially more favorable.

1. WAVES IN AN ALKALI METAL

1.1. Classical case

Consider wave propagation in an alkali metal with a spherical Fermi surface for $\mathbf{H} \| \mathbf{k} \| z$, where $\mathbf{k}$ is the wave vector. In this case the Fourier transform of nonlocal conductivity in the absence of quantum effects will be written (see, e.g., Ref. 4)

$$\sigma_{\pm}(k,\omega,H) = \frac{4\pi e^2}{(2\pi\hbar)^3} \int_0^{\infty} d\varepsilon \frac{df(\varepsilon)}{d\varepsilon_F} \times \int \frac{(\varepsilon - p_z^2/2m)\,dp_z}{\nu - i(\omega \pm \omega_c - k v_z(p_z))}, \qquad (1)$$

where ω is the wave angular frequency, $-e$ is the electronic charge, m the electron mass, $v_z = \partial\varepsilon/\partial p_z$ is the velocity component along the z axis, ε_F is the Fermi energy, $\omega_c = eH/mc$ is the cyclotron frequency, c is the velocity of light, $f(\varepsilon) = [\exp((\varepsilon - \varepsilon_F)/k_0 T) + 1]^{-1}$ is the Fermi function, T is the temperature, k_0 is the Boltzmann constant, ν is the

electron collisional frequency with the scatterers, and the $\pm$ indices refer to the right- and left-hand circular polarizations of the wave field.

Equation (1) has a simple physical meaning. Indeed, in the case of a uniform static electric field and in the absence of a magnetic field, the expression in parentheses in the denominator of the integrand vanishes, reducing (1) to the static conductivity $\sigma_0 = n_e e^2/m\nu$, where n_e is the electron concentration. In the case of a uniform hf field, where $\omega \gg \nu$, and $k=0$ and $H=0$, the conductivity does no longer depend on ν, $\sigma = n_e e^2/m(-i\omega)$, the current lags behind in phase by $\pi/2$ with respect to the electric field, and there are no Joule losses. In the case of a monochromatic wave with frequency ω and wave vector $\mathbf{k}$, an electron moving along the z axis with a velocity v_z will feel the electric field with a frequency $\omega' = \omega - kv_z$ because of the Doppler effect. Finally, in the presence of a dc magnetic field $\mathbf{H} \| \mathbf{k}$ the frequency of the field acting upon the electron increases by ω_c if this field rotates towards the electron (the plus polarization), and decreases by ω_c if it rotates in the same sense as the electron (the minus polarization).

Replacing $df(\varepsilon)/d\varepsilon$ by $-\delta(\varepsilon - \varepsilon_F)$, we integrate Eq. (1) over p_z and ε to obtain

$$\sigma_\pm(q) \equiv \sigma_{xx} \pm \sigma_{yx} = \frac{ne^2}{m[\nu - i(\omega \pm \omega_c)]} F_\pm(q), \tag{2}$$

$$F_\pm(q) = \frac{3}{2}\left(\frac{1}{q^2} - \frac{1-q^2}{2q^3} \ln \frac{1+q}{1-q} \right), \tag{3}$$

where $q = kv_F/(\mp\omega_c - \omega - i\nu)$, and $v_F = (2\varepsilon_F/m)^{1/2}$ is the Fermi velocity. Equations (2) and (3) are a generalization of the expression of Reuter and Sondheimer,[5] who considered the $H=0$ case. We shall be interested in the case where $\omega_c \gg \omega, \nu$ and the quantity $q = kv_F/\omega_c$ is the ratio of the electron displacement at the reference point on the Fermi sphere during the cyclotron period to the wavelength of the electromagnetic wave.

The wave dispersion equation

$$k^2c^2 = 4\pi i \omega \sigma_\pm \tag{4}$$

can be presented in the form

$$q^2 = \mp \frac{2}{3} \xi F_\pm(q), \quad \xi = \frac{6\pi\omega n m^2 v_F^2 c}{eH^3}. \tag{5}$$

In the region of strong magnetic fields, where $\xi < 1$, the roots of Eq. (5) are less than one. In these conditions, the logarithm in (3) and, hence, the root of the dispersion equation for the minus polarization are real. This is just the helicon root, and it exists within the field domain $H > H_L$, where H_L is the field corresponding to the $\xi = 1$ condition. For $H < H_L$, the quantity $q^2 > 1$, and the logarithm in (3) has an imaginary part $-i\pi \operatorname{sgn} q$, which describes cyclotron absorption. In the region of weak fields, where $\xi \gg 1$, the quantity $q^2 \gg 1$, and

$$F_-(q) \simeq \frac{3\pi i}{4|q|} + \frac{3}{q^2}. \tag{6}$$

The imaginary part of (6) exceeds the real one, and for $\xi \gg 1$ an anomalous skin effect takes place. This is the situation in the classical case.

1.2 Quantum case

In the case of strong magnetic fields and low temperatures, where $\hbar\omega_c \gg k_0 T$, one should take into account quantization of transverse electron motion; the energy of this motion takes on discrete values $\hbar\omega_c(n+1/2)$, where $n = 0,1,2,\ldots$. The expression for the conductivity $\sigma_\pm$ in the quantum case can be obtained from Eq. (1) if ε is replaced by $\varepsilon_{np_z} = \hbar\omega_c(n+1/2) + p_z^2/2m$, and integration over ε, by summation over n with simultaneous multiplication by $\hbar\omega_c$, As a result of this replacement, the expression for the real part of conductivity $\sigma'_\pm \equiv \operatorname{Re}\sigma_\pm$ assumes the form

$$\sigma'_\pm = \frac{4\pi e^2(\hbar\omega_c)^2}{(2\pi\hbar)^3} \sum_{n=0}^{\infty} \int_{-\infty}^{\infty} dp_z \frac{df(\varepsilon_{np_z})}{d\varepsilon_F} \times \frac{\nu(n+1/2)}{\nu^2 + (\omega \mp \omega_c - kv_z)^2}. \tag{7}$$

Equation (7) was derived under the assumption that $\hbar\omega \ll k_0 T$. In the opposite case one should make one more replacement

$$\frac{df(\varepsilon_{np_z})}{d\varepsilon_F} \to \frac{1}{\hbar\omega}[f(\varepsilon_{np_z}) - f(\varepsilon_{np_z} + \hbar\omega)].$$

Expressing the derivative of the Fermi function through the hyperbolic cosine and introducing the notation

$$\Phi(p_z) \equiv \sum_{n=0}^{\infty} \left(n + \frac{1}{2}\right) \frac{df(\varepsilon_{np_z})}{d\varepsilon_F} = \frac{1}{4k_0 T} \sum_{n=0}^{\infty} \left(n + \frac{1}{2}\right) \times \cosh^{-2}\left[\frac{\varepsilon_F - \hbar\omega_c(n+1/2) - p_z^2/2m}{2k_0 T} \right], \tag{8}$$

$$D(p_z) = \frac{\nu/\pi}{\nu^2 + (\omega_c - kv_z)^2}, \tag{9}$$

we can present the expression for σ' in the form

$$\sigma' = \frac{e^2 {\omega_c}^2}{2\pi\hbar} \int_{-\infty}^{\infty} \Phi(p_z) D(p_z) dp_z. \tag{10}$$

The function $\Phi(p_z)$ represents a series of narrow and high peaks located at

$$p_z = p_n \equiv [2m(\varepsilon_F - \hbar\omega_c(n+1/2))]^{1/2}, \quad n = 0,1,2,\ldots n_F, \tag{11}$$

where n_F is the largest value of n at which the radicand in (11) is positive.

The distance between adjacent peaks

$$\Delta_n \equiv p_n - p_{n+1} \simeq m\hbar\omega_c/p_n. \tag{12}$$

The function $D(p_z)$ has a maximum at

$$p_z = p_c \equiv \frac{m\omega_c}{k} = \frac{p_F}{q} \tag{13}$$

with a width

$$\Delta p = p_c \nu/\omega_c \ll p_c \quad . \tag{14}$$

The quantity p_c is the longitudinal momentum component of the electrons which are responsible for cyclotron absorption in classical conditions. The product $\Phi(p_z)D(p_z)$ and, hence, the nonlocal conductivity σ' associated with cyclotron absorption are very sensitive to the relation between Δp and the distance between the values of p_n closest to p_c. The most interesting is the case where the width of the maximum in the D function, Δp, is much smaller than Δ_n (the distance between the adjacent minima in the Φ function). Taking into account Eqs. (12) and (14), this condition reduces to the inequality

$$\eta \equiv \frac{\nu\varepsilon_F}{\hbar\omega_c{}^2} \ll q^2 \quad . \tag{15}$$

If the latter is satisfied, the magnitude of cyclotron absorption determined by integral (10) depends very strongly on the overlap of the Φ and D functions, i.e. on the distance between p_c and the p_n value closest to it. If p_c coincides with one of the p_n, σ' is maximal. If, however, p_c is at midgap between p_n and p_{n+1}, σ' is minimal. The values of p_n depend on H. Therefore as H varies, the values of the electron longitudinal momentum corresponding to the various Landau levels at the Fermi sphere shift along the p_z axis and pass in turn through the p_c value. As a result, the σ' *vs* H plot becomes a sequence of narrow and high quantum peaks separated by broad, deep minima. This quantum structure of cyclotron absorption is similar to the giant quantum oscillations in ultrasound damping.[3] We are interested in the situation where quantization results in suppression of cyclotron absorption. Therefore, rather than discussing the height and width of the quantum maxima, we shall instead consider the minima. In doing this, we choose the case of temperatures low enough that the inequalities

$$k_0 T \ll \hbar\omega_c \eta/q^2 \ll \hbar\omega_c \tag{16}$$

are met, and the shape of the quantum oscillations of σ' is determined by electron scattering. Let H be such that p_c falls in the middle of the interval between p_N and p_{N+1}, i.e. $p_c = (p_N + p_{N+1})/2$. Then it is sufficient to retain in sum (8) terms with $n=N$ and $n=N+1$, and replace function $D(p_z)$ in (10) by its values at the points $p_z = p_N$ and $p_z = p_{N+1}$, which are equal to $4\nu m^2/\pi k^2 \Delta_N^2 \simeq 16\eta^2/\pi\nu q^4$. We obtain

$$\sigma'_{\min} = \frac{2\eta}{q^2}\sigma_a \quad , \tag{17}$$

where

$$\sigma_a = \frac{3\pi n_e e c}{4H|q|} = \frac{3\pi n_e e^2}{4m v_F |k|}, \tag{18}$$

and σ_a is the conductivity determining the anomalous skin effect. Because we are considering case (15), the conductivity at the minima of quantum oscillations is indeed much smaller than its classical value. Thus quantization is capable of strongly suppressing collisionless wave damping in a metal. In principle, quantization affects the imaginary part of conductivity, $\sigma'' = \mathrm{Im}\,\sigma$, as well. An analysis shows, however, that quantum deviations of σ'' become noticeable only in the immediate vicinity of the quantum absorption peaks and are practically absent at the absorption minima. In other words, function $F_-(q)$ at the minima of absorption is given by the expression

$$F^{(-)}_{\min}(q) = \frac{3}{q^2} + i\frac{3\pi\eta}{2|q|^3} \quad . \tag{19}$$

Within the region of ω and H, where $\xi \gg 1$, the roots of the dispersion relation (5) are large: $q^2 \gg 1$. Therefore, in the $\xi \gg 1$ and $\eta < 1$ case, the solution of the dispersion equation for the minus polarization can be written roughly in the form

$$q_- \equiv q' + iq'' = (2\xi)^{1/4} + i\frac{\pi\eta}{8} \quad . \tag{20}$$

We readily see that $q'' \ll q'$ in the case under consideration, i.e., this solution relates to a propagating mode. Thus suppression of cyclotron absorption at the minima of giant oscillations leads, in principle, to a possibility of propagating unique quantum waves. These waves exist in the region of magnetic fields much lower than the helicon threshold field, and their field rotates in the same sense as the helicon field.

Let us discuss now the possibility of observing quantum waves in an alkali metal. For a Na crystal with an electron mean free path of 0.2 mm ($\nu = 5\times10^9\ \mathrm{s}^{-1}$), in a field $H = 200$ kOe, the parameter $\eta \simeq 1$. For a wave frequency $\omega/2\pi = 80$ GHz, $\xi \simeq 20$. It can be added that the real part of the wave vector k exceeds by only a factor six its imaginary part, i.e., the wave is damped. Thus, for realizable values of ν and H, alkali metals turn out to be inappropriate for observing of quantum waves.

2. WAVES IN NOBLE METALS

2.1 Classical limit

Noble metals are much more suitable for observation of quantum waves than the alkali ones. Two reasons account for this. First of all, the carrier mean free path in them can be two orders of magnitude larger than that in the alkali metals. The parameter η defined by (15) decreases accordingly. Besides, due to specific features of the Fermi surface in noble metals, the threshold of the region of cyclotron absorption by electrons in the $\mathbf{H}\|\mathbf{k}\|$ [110] geometry lies on the short-wavelength side rather than on the long-wavelength one as is the case usually.[4] As a result, only holes, whose concentration is nearly an order of magnitude lower than that of electrons, contribute to collisionless damping of short-wavelength modes. This likewise causes a decrease in damping and improves the conditions for observing quantum waves. It appears to be, therefore, of interest to develop a theory of such waves in noble metals.

Consider propagation of a wave in a copper crystal in the $\mathbf{H}\|\mathbf{k}\|$ [110] geometry. The electronic part of nonlocal conductivity in this case can be written[4]

$$\sigma_{\pm}^{(e)}(k,\omega,H)=i\frac{n_e ec}{HI_{\pm}}s(q)\,, \tag{21}$$

$$s(q)=1-\frac{q^2}{\sqrt{q^2-1}}\arctan\frac{1}{\sqrt{q^2-1}}\ , \tag{22}$$

$$q=\frac{kcp_0}{eHI_{\pm}},\quad I_{\pm}=\pm 1+\frac{\omega+i\nu}{\omega_{ce}}\ , \tag{23}$$

where the ''*e*'' index refers to the quantities relating to electrons, $p_0=0.6\,\hbar\text{Å}^{-1}$ is the momentum dimensionality parameter determining the minimum displacement in the cyclotron period, $u_e=2\pi cp_0/eH$. Because we are interested in the $\omega_{ce}\gg\omega,\nu$ case, we shall assume in what follows $I_{\pm}=\pm 1$.

In the vicinity of the central Fermi cross section there are dog-bone-type hole orbits, whose concentration n_h is one fifth the n_e. We shall describe the holes in terms of the model where their dispersion law has the form

$$\varepsilon(\mathbf{p})=\frac{1}{2m}\left[\frac{1}{4p^2}(p_x^2+p_y^2-p_a^2)^2+p_z^2\right]\ , \tag{24}$$

where m is the mass dimensionality constant, and p and p_a are the momentum dimensionality constants. The cross sectional area of the constant-energy surface by the $p_z=$ const plane in this model can be written

$$S(\varepsilon,p_z)\equiv\pi(p_x^2+p_y^2)=\pi(p_a^2-2p\sqrt{2m\varepsilon-p_z^2})\ . \tag{25}$$

The cyclotron mass of the holes m_c and their displacement in one cyclotron period are given by the expressions

$$m_c(\varepsilon,p_z)=\frac{1}{2\pi}\left|\frac{\partial S}{\partial\varepsilon}\right|=\frac{mp}{\sqrt{2m\varepsilon-p_z^2}}\ , \tag{26}$$

$$u_h(\varepsilon,p_z)=\frac{c}{eH}\frac{\partial S}{\partial p_z}=2\pi\frac{cp}{eH}\frac{p_z}{\sqrt{2m\varepsilon-p_z^2}}\ . \tag{27}$$

We accept the following values for the parameters

$$m=10^{-28}g,\quad p=1.0\ \hbar\text{Å}^{-1},\quad p_a=0.9\ \hbar\text{Å}^{-1},$$
$$p_F=\sqrt{2m\varepsilon_F}=0.3\ \hbar\text{Å}^{-1}. \tag{28}$$

Although the hole orbits in copper are essentially different from circular, the dependence of S and u_h on p_z in this model is in good agreement with Powell's calculations.[6] In particular, it is seen from Eqs. (26) and (27) that the cyclotron mass and displacement tend to infinity at the edge of the hole-orbit layer ($p_z\to\sqrt{2m\varepsilon}$). Therefore there are grounds to assume that nonlocal conductivity in the form

$$\sigma_{\pm}^{(h)}(k,\omega,H)=\frac{2e^2}{(2\pi\hbar)^3}\int_0^{\infty}d\varepsilon\frac{df(\varepsilon)}{d\varepsilon_F}\int_{-\infty}^{\infty}\times\frac{S(\varepsilon,p_z)\,dp_z}{m_c(\varepsilon,p_z)[\nu-i(\omega\mp\omega_c-kv_z)]} \tag{29}$$

will describe correctly the cyclotron absorption by holes. After insertion of Eqs. (25) and (26) in Eq. (29) and a change from $df(\varepsilon)/d\varepsilon_F$ to $\delta(\varepsilon-\varepsilon_F)$, calculation of $\sigma_{\pm}^{(h)}$ will not meet with difficulties. We shall be interested in what follows in the limiting case $q^2\gg 1$, where the dissipative conductivity associated with cyclotron absorption can be presented in the form

$$\sigma_0(q)\equiv Re\,\sigma_{\pm}^{(h)}=\frac{\pi}{2}\frac{p_a^2-2pp_F}{p_a^2-\pi pp_F/2}\frac{p_0}{p}\frac{n_h ec}{H|q|}=\alpha\frac{n_e ec}{H|q|},$$
$$n_h=\frac{p_F(p_a^2-\pi pp_F/2)}{2\pi^2\hbar^3},\quad \alpha\simeq 0{,}1\ . \tag{30}$$

In this region, the electronic function $s(q)$ defined by Eq. (22) assumes the form

$$s(q)\simeq-\frac{2}{3q^2}\ . \tag{31}$$

Neglecting the contribution of holes to the nondissipative part of conductivity, the dispersion equation (4) for the plus-polarization wave can be recast to

$$q^2=\left(\frac{1}{q^2}+i\frac{3\alpha}{2|q|}\right)\xi,\quad \xi=\frac{8\pi\omega n_e p_0^2 c}{3eH^3}. \tag{32}$$

A comparison of Eqs. (32) and (6) shows the ratio of the dissipative to nondissipative term for copper to be one fifth that for an alkali metal.

In the region of H satisfying the conditions

$$1\ll\xi\ll\frac{1}{\alpha^4}=10^4\ , \tag{33}$$

Eq. (32) has the solution

$$q=\xi^{1/4}+i\frac{3}{8}\alpha\xi^{1/2}\ . \tag{34}$$

Although within region (33) the quantity q'' is small compared to q', it is nevertheless too large to allow penetration of this mode through a copper plate; indeed, for a plate thickness $d=0.1$ mm, $\xi=10$, and $H=20$ kOe, the product $k''d=eHq''d/(p_0c)$ is 5.5, i.e. the signal is attenuated by 250 times.

2.2 Quantum waves in copper

Since for $q^2>1$ there is no cyclotron absorption by electrons, we shall have to consider the effect of quantization only for the hole part of nonlocal conductivity. To do this, we use the quasi-classical quantization rule, by which the area of hole orbits can assume only discrete values

$$S(\varepsilon,p_z)\equiv\pi(p_x^2+p_y^2)=2\pi\frac{\hbar eH}{c}n\ , \tag{35}$$

where n is an integer. Inserting (35) in Eq. (24), we obtain the hole eigenenergy spectrum

$$\varepsilon_{np_z}=\frac{1}{2m}\left[\left(\frac{\hbar eH}{cp}\right)^2(N-n)^2+p_z^2\right],\quad N=\frac{cp_a^2}{2\hbar eH}. \quad (36)$$

Note that the hole transverse energy in this model is proportional to the square of H and $(N-n)^2$ rather than their first power, as this is the case with the Fermi sphere.

The quantum expression for nonlocal hole conductivity can be derived from Eq. (29) by substituting in it Eqs. (35) and (36) and replacing integration over ε by summation over n and multiplication by $\hbar\omega_c$. We finally come to the expression

$$\sigma'=\frac{e^2}{2\pi^2\hbar}\left(\frac{eH}{c}\right)^2\sum_n\int_{-\infty}^{\infty}dp_z\frac{df(\varepsilon_{np_z})}{d\varepsilon_F}\times\frac{n\nu}{m_c^2[\nu^2+(\omega_c-kp_z/m)^2]}, \quad (37)$$

which differs from (7) in the eigenenergy spectrum (36) and the fact that the cyclotron mass m_c in Eq. (37) depends substantially on p_z.

The integrand in (37) can be conveniently analyzed by introducing functions Φ and D similar to functions (8) and (9). The peaks of function Φ are located at

$$p_z=p_n\equiv\left[p_F^2-\left(\frac{\hbar eH}{pc}\right)^2(N-n)^2\right]^{1/2}, \quad (38)$$

and the maximum in $D(p_z)$, at the value $p_z=p_c$, which is the solution to equation $kp_z/m=eH/cm_c(\varepsilon_F,p_z)$ and has the form

$$p_c=\frac{p_F}{\sqrt{1+(qp/p_0)^2}}. \quad (39)$$

We readily see that $p_c<p_F$ for any q, i.e. that cyclotron absorption by holes exists for any wavelengths. The width of the maximum in the D function can be written

$$\Delta p=\frac{p_0}{q}\frac{\nu mc}{eH}. \quad (40)$$

The distance between adjacent peaks in $\Phi(p_z)$

$$\Delta_n\equiv p_{n+1}-p_n=\left(\frac{\hbar eH}{pc}\right)^2\frac{N-n}{p_n} \quad (41)$$

for $p_n=p_c$ is

$$\Delta_c=q\frac{\hbar eH}{p_0c}, \quad (42)$$

and for the corresponding quantum number n one obtains

$$n_c=\left[\frac{c}{\hbar eH}\left(\frac{p_a^2}{2}-\frac{q}{\sqrt{1+(qp/p_0)^2}}\frac{p_Fp^2}{p_0}\right)\right], \quad (43)$$

where the brackets denote the integer part of the number. The distance between the quantum levels close to the resonant hole cross section

$$\hbar\omega_{c0}\equiv\varepsilon_{n_c}-\varepsilon_{n_c+1}\simeq\frac{1}{m}\left(\frac{\hbar eH}{pc}\right)^2(N-n_c)=\frac{\hbar eH}{mc}\frac{p_F}{p_0}\frac{q}{\sqrt{1+(qp/p_0)^2}}. \quad (44)$$

For $q^2\gg1$, we have $\hbar\omega_{c0}=\hbar eHp_F/(mcp_0)$, i.e. the cyclotron mass of these holes $m_c=mp/p_F$.

The mean free path of carriers in noble metals can exceed by two orders of magnitude that in the alkali metals. Therefore, in contrast to the latter, copper is characterized by the situation where the first of the inequalities (16) is reversed, and the conditions

$$\left(\frac{p_0}{qp}\right)^2\frac{\varepsilon_F\nu}{\hbar\omega_{c0}^2}\ll\frac{k_0T}{\hbar\omega_{c0}}\ll1 \quad (45)$$

are satisfied. The first of these inequalities means that the width of the maximum of the $D(p_z)$ function is less than that of the $\Phi(p_z)$ peaks. This is essential when one calculates cyclotron absorption in the region of the maxima appearing when the D maximum coincides with the consecutive maxima in the Φ function. We are not interested in the intervals around these absorption maxima, because quantum waves cannot propagate in the corresponding magnetic-field regions. By contrast, we shall investigate the neighborhood of the absorption minima, where the wave damping is substantially smaller than that in the classical case. Because far from the peaks the Φ function falls off exponentially, within these intervals the derivative of the Fermi function can be approximated with a delta function

$$df(\varepsilon_{np_z})/d\varepsilon_F\to\delta(\varepsilon_{np_z}-\varepsilon_F). \quad (46)$$

To validate this replacement, the second inequality of (46) is sufficient. On inserting (46) in Eq. (37) and integrating over p_z we can present σ' in the form

$$\sigma'=\sigma_0(q)Q(q,H), \quad (47)$$

$$Q(q,H)=\frac{\hbar\nu q^2p_c}{2\pi\varepsilon_Fn_c}\sum_n\frac{n}{p_n}\left[\left(\frac{\nu}{\omega_c}\right)^2+\left(1-q\frac{pp_n}{p_0\sqrt{p_F^2-p_n^2}}\right)^2\right]^{-1}, \quad (48)$$

where σ_0, p_c, and n_c are given by expressions (30), (39), and (43), respectively. Equation (48) was derived under the assumption that $q^2\gg1$. The Q function characterizes the difference of the quantum conductivity associated with cyclotron absorption from its asymptotic form in the limit of anomalous skin effect for $H\to0$.

The difference in the parentheses in Eq. (48) passes through a minimum at $n=n_c$ to increase afterwards rapidly with increasing $|n-n_c|$. As for the n/p_n factor, in the region of $n\sim n_c$ it is a smooth function of n. Therefore it can be replaced with acceptable accuracy with n_c/p_c, after which Q assumes the form

$$Q \simeq \frac{\hbar \nu q^2}{2\pi\varepsilon_F} \sum_n \left[\left(\frac{\nu}{\omega_c} \right)^2 + \left(1 - q \frac{pp_n}{p_0 \sqrt{p_F^2 - p_n^2}} \right)^2 \right]^{-1} . \tag{49}$$

The minima in Q lie at the values of H at which the maximum of D lies exactly at the center between two consecutive peaks in the Φ function, where $p_c = (p_n + p_{n+1})/2$. In these conditions, the difference in the parentheses in Eq. (49) is equal to $qp\Delta_c/(2pp_F)$, and the summation over n results in multiplication by $\pi^2/4$. We finally come to

$$Q_{\min} = \frac{2\pi}{q^2} \left(\frac{p_0}{p} \right)^2 \frac{\varepsilon_F \nu}{\hbar \omega_{c0}^2} . \tag{50}$$

For $\omega_{c0}^2 \gg \nu\varepsilon_F/\hbar$ this quantity is seen to be small, i.e. cyclotron absorption is strongly suppressed.

Thus quantization of the hole transverse energy results in the imaginary term on the right-hand side of Eq. (32) becoming multiplied by function $Q(q,H)$. Because within the intervals of H of interest here the imaginary term in the dispersion equation is small compared to the real one, this equation can be solved by replacing q in the imaginary term with $q' = \xi^{1/4}$, which is the root of the dispersion equation for $Q = 0$. We come finally to

$$q_1 \simeq \xi^{1/4} \left[1 + \frac{3i}{2} \alpha \xi^{1/4} Q(\xi^{1/4}, H) \right], \qquad q_2 \simeq i\xi^{1/4}. \tag{51}$$

The root q_2 relates to the decaying field component, and the q_1 root, to the quantum wave, whose spectrum can be written

$$\omega = \frac{3p_0^2 c^3}{8\pi n_e e^3 H} k^4 . \tag{52}$$

Let us turn now to an analysis of the surface impedance of a copper plate with the surface normal parallel to the [110] axis and excited antisymmetrically by the electric field. The expression for the plate impedance for the case where carrier reflection from the sample surface is diffuse, and the field in it is a superposition of two exponential components is given in Ref. 4 [Eq. (3.11)]. In the case under study here, $\xi \gg 1$, this expression transforms to

$$Z \simeq \frac{4\pi\omega}{c^2} \left(\frac{1}{k_1'} \frac{1 - \exp(ik_1 d)}{1 + \exp(ik_1 d)} + \frac{1}{k_2'} \right) , \tag{53}$$

where

$$k_1 \equiv k_1' + \quad ik_2' = \frac{eH}{cp_0} q_1(H), \quad k_2 = ik_1' , \tag{54}$$

and d is the plate thickness. The first term in Eq. (53) is due to excitation of a standing quantum wave in the plate, and the second, to that of the damped component.

Now to the results of a calculation carried out for the model parameters (28), frequency $\omega = 2 \times 10^{10}$ s^{-1}, $\nu = 4 \times 10^8$ s^{-1} (carrier mean free path 4 mm), and $d = 0.1$ mm. Note that the resonant-hole cyclotron mass is approximately two and a half times smaller than the free-electron mass. Therefore for $H = 20$ kOe and $T = 1.4$ K, the $\hbar\omega_{c0}/k_0 T$ ratio is of the order of ten, so that for $H > 20$ kOe and $T = 1.4$ K the quantization condition is fully met.

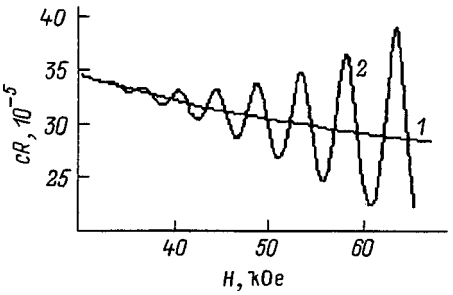

FIG. 1. Envelopes of the quantum oscillations in the surface resistance of a plate.

Quantum oscillations in copper in the geometry considered here have a very small period in magnetic field, of the order of 10 Oe. They cannot be displayed graphically over a broad magnetic-field range; indeed, within an H interval of 30 kOe the number of oscillations is about two thousand. Therefore we shall present a quantum-oscillation envelope over a broad region of magnetic fields, with fragments of the $R(H)$ oscillating curve shown within narrow intervals of H. Curve *1* in Fig. 1 shows the surface resistance of the plate, $R_0(H)$, in the classical limit. For the values of H at which the cyclotron absorption is large and wave propagation cannot take place, the plate surface resistance $R = \mathrm{Re}\, Z$ coincides with R_0. At the same time, for the values of H corresponding to the quantum minima in absorption, the wave field penetrates through the plate, making R substantially different from R_0. Curve *2* in Fig. 1 was constructed assuming the cyclotron absorption for all H to be the same as at the minima. The oscillations in curve *2* are due to variation of the wave field phase $k_1' d$; as follows from Eq. (53), the minima correspond to the values of H at which $k_1'(H)d = 2\pi s$, where s is an integer, and the maxima, to those of H at which $k_1'(H)d = \pi(2s+1)$. As the damping increases with variation of H, the R plot transforms abruptly from curve *2* to curve *1*. Conversely, as the damping decreases and approaches its minimum, curve *1* in the plot of R becomes replaced by curve *2*. Figures 2–4 present fragments of the true $R(H)$ curve drawn within narrow intervals of magnetic-field variation. Figure 2 relates to the neighborhood of one of the minima of curve *2* in Fig. 1 (here an even number of halfwaves fit into the plate thickness), and Fig. 3, to that of

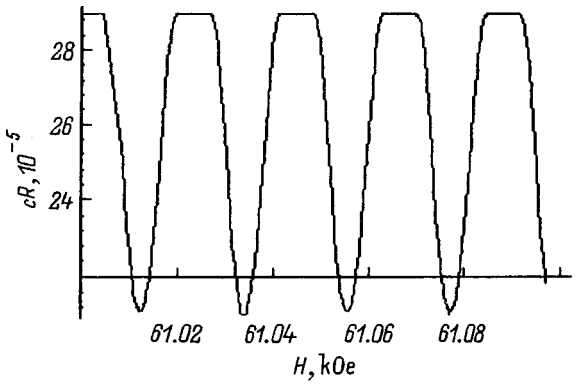

FIG. 2. A fragment of the $R(H)$ plot in the neighborhood of the magnetic field for which an integral number of waves fit into the plate thickness.

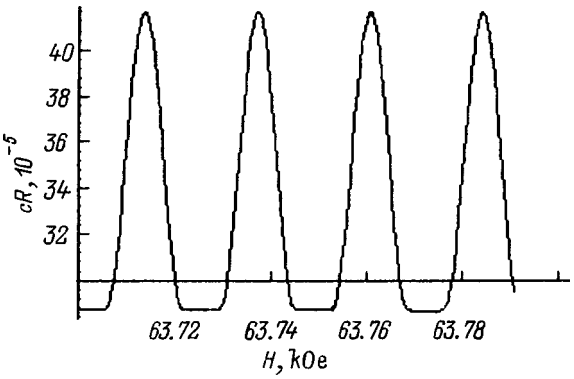

FIG. 3. A fragment of the $R(H)$ plot in the neighborhood of the magnetic field for which an odd number of halfwaves fit into the plate thickness.

one of the maxima (with an odd number of halfwaves fitting into the plate thickness). Figure 4 corresponds to a region around the value of H at which curves *1* and *2* in Fig. 1 cross. We readily see a cross-over from an oscillatory pattern

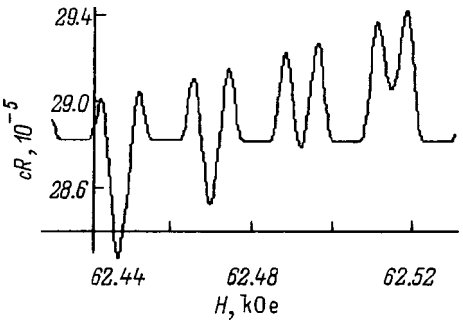

FIG. 4. A fragment of the $R(H)$ plot in the neighborhood of the magnetic field for which the oscillation amplitude is minimal.

with minima to that with maxima. The oscillation amplitude in Fig. 4 is many times smaller than that in Figs. 2 and 3, and they exhibit a more complex structure.

In conclusion, the following note appears to be appropriate. The Fermi-surface model considered here describes adequately the variation of $S(p_z)$ in noble metals in the $\mathbf{H}\|[110]$ geometry. However besides the electronic and hole orbits this geometry also allows a narrow layer of open orbits, which were disregarded by us. Carriers with open orbits do not contribute to cyclotron absorption, but make possible collisionless absorption of the Landau damping type. Quantization practically does not affect the magnitude of this absorption. Therefore the wave damping k_1'' at the minima of cyclotron-absorption quantum oscillations may turn out to be substantially larger than that without open orbits. To eliminate this complication, one should deflect the **H** vector by a few degrees from the strict [110] orientation. Because the open-orbit layer is very narrow, there will be no open orbits for **H** tilt angles from the [110] axis greater than 2°. In these conditions, the behavior of the Fermi-surface cross-sectional area $S(p_z)$ practically does not vary, the model considered by us will adequately describe the real situation in noble metals, and all the results obtained here will remain valid.

Support of the Russian Fund for Fundamental Research (Grant 98-02-18393) is gratefully acknowledged.

[1] I. F. Voloshin, G. A. Vugal'ter, V. Ya. Demikhovskiĭ, L. M. Fisher, and V. A. Yudin, Zh. Éksp. Teor. Fiz. **73**, 1503 (1977) [Sov. Phys. JETP **46**, 790 (1977)].
[2] V. G. Skobov and A. S. Chernov, Zh. Éksp. Teor. Fiz. **109**, 992 (1996) [JETP **82**, 535 (1996)].
[3] V. L. Gurevich, V. G. Skobov, and Yu. A. Firsov, Zh. Éksp. Teor. Fiz. **40**, 786 (1961) [Sov. Phys. JETP **13**, 552 (1961)].
[4] A. S. Chernov and V. G. Skobov, Phys. Rep. **244**, 1 (1994).
[5] G. E. Reuter and E. H. Sondheimer, Proc. R. Soc. London, Ser. A **195**, 336 (1946).
[6] B. Perrin, G. Weisbuch, and A. Libchaber, Phys. Rev. B **1**, 1501 (1970).

Translated by G. Skrebtsov

Evolution of the population of outer 6*s* and 5*d* shells in rare-earth metals

V. A. Shaburov, A. E. Sovestnov, Yu. P. Smirnov, and A. V. Tyunis

B. P. Konstantinov St. Petersburg Nuclear Physics Institute, Russian Academy of Sciences, 188350 Gatchina, Leningrad District, Russia

(Submitted December 25, 1998)
Fiz. Tverd. Tela (St. Petersburg) **41**, 1361–1362 (August 1999)

The shifts of the $K\alpha_1$ and $K\beta_1$ lines of all rare-earth (RE) metals (from La to Lu) have been measured experimentally by the x-ray shift method. The population of the RE-metal 6*s* and 5*d* shells has been determined by comparing the experimental and theoretical shifts obtained within the Dirac–Fock (Koopmans) model. Trivalent metals exhibit a monotonic cross-over from the $6s^{\approx 2}5d^{\approx 1}$ to $6s^{\approx 1}5d^{\approx 2}$ configuration with increasing atomic number. © *1999 American Institute of Physics.* [S1063-7834(99)00308-1]

It is known that all rare-earth (RE) metals, except Eu and Yb, are trivalent under normal external conditions, i.e. they have the same outer (or valence) 6*s* and 5*d* shell and are chemically similar. At the same time they differ strongly in physical properties. Indeed, the melting point and Debye temperature increase monotonically with atomic number *Z* in the La–Lu series by about a factor two. One observes also substantial differences in the thermal expansion coefficient, resistance to oxidation, mechanical characteristics, etc. (see, e.g., Ref. 1). Their magnetic properties are strongly dissimilar as well, particularly in the low-temperature domain. The monotonic variation of physicochemical properties is attributed to the increase in the number of 4*f* electrons in the RE metal series. However, alongside the localized 4*f* electrons, one cannot rule out the importance of the outer *s* and *d* electrons, which are responsible for many physical properties, among them electrical conductivity, exchange $f-s,d$ interaction, valence-bond formation in compounds, etc. In particular, when studying RE-metal-based systems having specific physical properties (mixed valence, heavy fermions, isomorphous phase transitions, Kondo lattices, etc.), one should know not only the 4*f*-shell population and its variation with external conditions but also the electron distribution among the 6*s* and 5*d* valence levels, which govern the density of states at the Fermi level, a fundamental characteristic of these systems.

It is usually assumed (c.f., monograph Ref. 1) that the electronic outer-shell configuration of trivalent RE metals is $5d^16s^2$, and that of the divalent Eu and Yb, $6s^2$, although experimental evidence for this at the microscopic level is practically lacking. Moreover, some authors believe the electronic configuration of trivalent RE metals to be $5d^26s^1$ rather than $5d^16s^2$ (Ref. 2). The electronic structure of RE metals is sometimes presented as $(5d6s)^3$.

This paper reports determination of the 5*d* and 6*s* populations of metallic La, Ce, Pr, Nd, Sm, Eu, Gd, Tb, Dy, Ho, Er, Tm, Yb, and Lu by the x-ray shift method (see, e.g., Refs. 3 and 4). Compounds with a known electronic structure, MF_3 or M_2O_3, served as references. The scheme of the experiment and the measurement procedure used were described elsewhere.[4,5] The metals to be studied (≈99.9%) were in the form of either foils (≈0.2 mm thick) or finely dispersed filings. The samples were enclosed in sealed aluminum containers to prevent their oxidation.

The population of the RE-metal 5*d* and 6*s* states was determined from a comparison of the experimental with theoretical shifts obtained within the relativistic Dirac–Fock (Koopmans) model. One solved coupled equations

$$\Delta E_{\mathrm{calc}}(n_d,n_s,n_d^i,n_s^i)^{\alpha(\beta)}=\Delta E^{\alpha(\beta)},$$

$$n_d+n_s=n,$$

$$n_d^i+n_s^i=3(1-i),$$

where $\Delta E_{\mathrm{calc}}(n_d,n_s,n_d^i,n_s^i)^{\alpha(\beta)}$ is the calculated $K\alpha(\beta)$ line shift approximated by a second-order polynomial, $\Delta E^{\alpha(\beta)}$ are the experimental RE-metal shifts, n_d and n_s are the 5*d* and 6*s* populations of the metals, and n_d^i and n_s^i are those of the references, *i* is the ionicity of the reference by Pauling, which is 0.9 for the fluorides and 0.8 for the oxides, and $n=2$ for Eu and Yb and $n=3$ in the remaining cases. The experimental and calculated shifts of the $K\alpha_1$ and $K\beta_1$ lines (ΔE) are listed in Table I, and the corresponding 5*d*

TABLE I. Experimental and calculated shifts of the $K\alpha_1$ and $K\beta_1$ lines in RE metals (relative to MF_3 and M_2O_3).

		$\Delta E(K\alpha_1)$, meV		$\Delta E(K\beta_1)$, meV	
RE metal	Lattice type	Exp.	Calc.	Exp	Calc.
La	dhcp	60±6	46	−16±9	13
Ce	fcc	50±4	33	−40±5	−15
Pr	dhcp	42±5	37	−34±9	−20
Nd	dhcp	41±3	36	−34±7	−12
Sm	α Sm	50±6	46	−7±8	−1
Eu	hcp	−50±3	−47	−80±7	−95
Gd	hcp	19±4	19	−38±8	−37
Tb	hcp	24±5	23	−57±9	−53
Dy	hcp	15±6	30	6±10	−26
Ho	hcp	20±5	25	−24±8	−34
Er	hcp	18±4	25	−23±6	−35
Tm	hcp	−14±6	0	−16±12	−65
Yb	hcp	14±3	14	—	—
Lu	hcp	11±6	23	5±13	−35

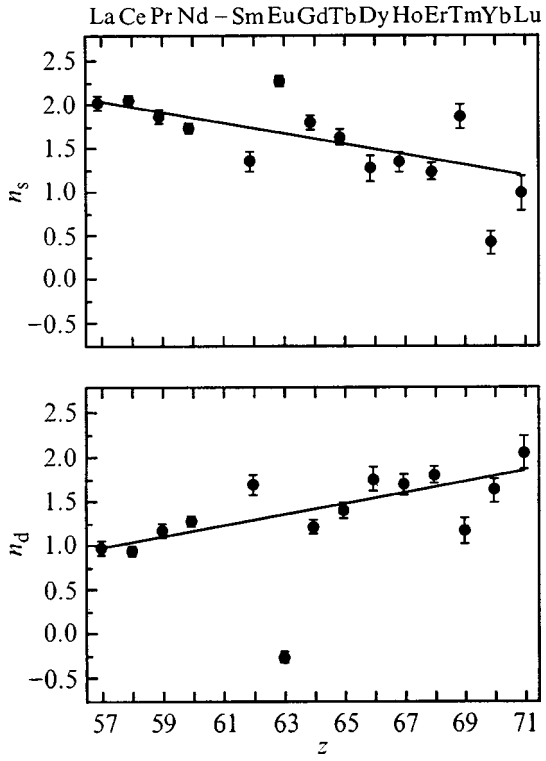

FIG. 1. RE-metal $5d$ and $6s$ shell population (n_d and n_s) vs atomic number Z.

and $6s$ electronic populations (n_d and n_s,) in Fig. 1.

The difference in the physical properties of RE metals is explained, as a rule, by the difference in the number of $4f$ electrons. Incomplete screening of the nuclear charge by the $4f$ electrons becoming pronounced with increasing Z gives rise to an increase in the effective charge whose field is felt by the outer electrons. This causes, in its turn, contraction of both the $4f$ and the valence shells, a phenomenon called the lanthanide contraction. Because the internal screening of the $5d$ electrons is weaker than that of the $6s$ (the radial distance from the maximum in the $5d$-electron charge density to the nucleus is about one half that for $6s$ electrons[6]), electrons of the $5d$ shells are attracted more strongly to the nucleus. This results in a faster (compared to the $6s$) lowering of the $5d$ levels with increasing Z,[1] and, accordingly, in an increased the $5d$ population. The cross-over from the $6s^{\approx 2}5d^{\approx 1}$ to $6s^{\approx 1}5d^{\approx 2}$ configuration observed by us is shown in Fig. 1. For trivalent RE metals, one observes a monotonic decrease in the number of $6s$ electrons accompanied by a simultaneous increase in the $5d$ population. Linear least-squares fitting yields the following dependences of the $6s$ and $5d$ orbital populations of trivalent RE metals on the number of their $4f$ electrons (n_{4f}):

$$n_{6s}=(2.02\pm 0.04)-(0.06\pm 0.01)n_{4f},$$

$$n_{5d}=(0.98\pm 0.04)+(0.06\pm 0.01)n_{4f}.$$

Our data show that the increase of n_{4f} with Z may bring about not only the well known differences in the macroscopic properties of RE metals but changes on the microscopic scale as well (the monotonic cross-over from the $6s^{\approx 2}5d^{\approx 1}$ configuration in the beginning of the RE-metal series to $6s^{\approx 1}5d^{\approx 2}$ at the end of the series).

The redistribution of the outer $6s$ and $5d$ electrons can, in its turn, distort (in second order, as it were) the monotonic behavior of the physical properties of RE metals with increasing Z. For instance, the electrical resistivity, the Hall coefficient, work function, etc.,[1] whose mechanism is governed by the s and d electrons of the conduction band, exhibit no correlation with the atomic number.

The authors thank O. I. Sumbaev for fruitful discussions and comments.

Support of the Russian Fund for Fundamental Research (Project 96-02-17811) under Grant No. 95-02-06327a is gratefully acknowledged.

[1] K. A. Gschneidner, Jr., *Rare-Earth Alloys* (Van Nostrand, Princeton, 1961; IIL, Moscow, 1965).
[2] A. M. Begley, R. G. Jordan, W. M. Temmerman, and P. J. Durham, Phys. Rev. B **41**, 11780 (1990).
[3] O. I. Sumbaev, in *Modern Physics in Chemistry* (Academic, New York, 1977), Vol. 1, No. 4, p. 33.
[4] O. I. Sumbaev, Usp. Fiz. Nauk **124**, No. 2, 281 (1978) [Sov. Phys. Usp. **21**, 141 (1978)].
[5] V. A. Shaburov, I. M. Band, A. I. Grushko, T. B. Mezentseva, E. V. Petrovich, A. E. Sovestnov, Yu. P. Smirnov, O. I. Sumbaev, M. B. Trzhaskovskaya, and I. A. Markova, Zh. Éksp. Teor. Fiz. **65**, 1157 (1973) [Sov. Phys. JETP **38**, 573 (1973)].
[6] F. Herman and S. Skillman, *Atomic Structure Calculations* (Prentice Hall, Englewood Cliffs, 1963).

Translated by G. Skrebtsov

Superconductivity, Seebeck coefficient, and band structure transformation in $Y_{1-x}Ca_xBa_2Cu_{3-x}Co_xO_y$ ($x=0-0.3$)

M. V. Elizarova and V. É. Gasumyants

St. Petersburg State Technical University, 195251 St. Petersburg, Russia
(Submitted November 24, 1998)
Fiz. Tverd. Tela (St. Petersburg) **41**, 1363–1371 (August 1999)

The temperature dependences of the resistivity and of the Seebeck coefficient S is studied in three series of $Y_{1-x}Ca_xBa_2Cu_{3-x}Co_xO_y$ samples ($x=0-0.3$) differing in oxygen content. It was found that the critical temperature decreases for $y\approx 7.0$, and $S(T=300\,\mathrm{K})$ increases with doping, whereas oxygen deficiency results in a nonmonotonic variation of these quantities with increasing x. The band structure parameters have been determined from an analysis of the $S(T)$ relations using a phenomenological theory of electron transport. It was found that an increase in x results in a gradual increase in band asymmetry, which is caused by calcium-induced creation of additional states in the band responsible for conduction in the normal phase. An analysis has shown that high impurity concentrations in oxygen-deficient $Y_{1-x}Ca_xBa_2Cu_{3-x}Co_xO_y$ samples bring about an additional ordering of the structure, which may be caused by formation of a cobalt superlattice. It has also been shown that, in the case of Ca and Co codoping, the dependence of critical temperature on effective conduction-band width coincides with the universal correlation relation observed in the $YBa_2Cu_3O_y$ system with single substitutions in various lattice sites.
[S1063-7834(99)00408-6]

Although substitutions in various cation sublattices in $YBa_2Cu_3O_y$ have been attracting considerable interest, the mechanism by which some impurities act on superconductivity and electron transport in the normal phase still remains unclear. It is well known presently that all nonisovalent impurities have a strong influence on the state of the oxygen subsystem, because the disruption of charge balance caused by incorporation of an impurity cation into the lattice is compensated by an increase or deficiency in oxygen content, depending on the valences of the impurity and substituted element.[1–8] Thus when studying the effect of a nonisovalent impurity on the properties of a compound one has to take into account simultaneous action of two factors, namely, of the impurity itself and of the change in the properties of this compound resulting from a deviation from oxygen stoichiometry.

In this connection it appears of interest to study systems codoped in different cation sublattices by impurities of different valence states relative to the cations they substitute for. In this case the impurities compensate their effects by the charge balance in the lattice and, accordingly, the state of the oxygen subsystem. As a result, if the two impurities are introduced in equal amounts [$Y_{1-x}Ca_xBa_2Cu_{3-x}M_xO_y$ (where M=Fe, Co, or Al) and $Y_{1-x}Ca_xBa_{2-x}La_xCu_3O_4$], the oxygen content in the system remains practically constant with increasing doping level,[9–11] which offers a possibility of investigating the influence of the impurities themselves on the properties of $YBa_2Cu_3O_y$.

While the effect of double doping on the properties of $YBa_2Cu_3O_y$ is dealt with in a large number of publications studying various combinations of impurities, the available experimental data on transport coefficients in such systems are anything but systematic. Most of the works study only the resistivity, whereas information on the Seebeck coefficient in doubly-doped systems is practically absent. In our work we decided to choose as a subject for the study the $Y_{1-x}Ca_xBa_2Cu_{3-x}Co_xO_y$ compound, because the Ca+Co impurity combination appears to us particularly interesting. This stems from the fact that, first, our earlier data[12] indicate a specific action of calcium on the band structure of $YBa_2Cu_3O_y$, whose manifestation should be more pronounced for a fixed oxygen content, and, second, using cobalt as a codopant is most preferable, because it occupies only chain sites at not too-high doping levels, thus simplifying greatly the analysis of the data obtained. The Ca→Y+Co→Cu doping was investigated previously by a number of authors, but most of these works deal with a study of the variation in the superconducting[9,13,14] and crystallochemical[15–17] properties of $YBa_2Cu_3O_y$ induced by these impurities. No systematic investigation of the transport properties in this compound has been carried out thus far.

As shown by our previous studies, investigation of transport coefficients in the normal phase provides rich information on band structure and properties of the carrier system in $YBa_2Cu_3O_y$. The electron transport model[18] used by us (the narrow-band model) permits studies of samples with a deliberately varied composition to reveal specific features in the influence of various impurities on band structure parameters and to draw conclusions about the mechanism of impurity effects by comparing these data to the variation of superconducting properties in the compound under study. Therefore the objective of the present work was to investigate the be-

TABLE I. Unit cell parameters and oxygen content for the starting series of $Y_{1-x}Ca_xBa_2Cu_{3-x}Co_xO_y$ samples.

x	a, Å	b, Å	$a-b$, Å	c, Å	y
0.00	3.818	3.890	0.072	11.666	6.95
0.05	3.830	3.890	0.060	11.668	6.96
0.10	3.862	3.870	0.008	11.673	6.95
0.15	3.864	3.868	0.004	11.676	6.97
0.20	3.865	3.865	0	11.695	6.98
0.25	3.867	3.867	0	11.689	7.00
0.30	3.866	3.866	0	11.698	7.02

havior of the resistivity and Seebeck coefficient in $YBa_2Cu_3O_y$ under Ca→Y+Co→Cu doping for various oxygen contents, to analyze the results obtained in terms of the narrow-band model, and to reveal the specific features in the effect of this impurity combination on band structure parameters and characteristics of the carrier system in $Y_{1-x}Ca_xBa_2Cu_{3-x}Co_xO_y$.

1. CHARACTERISTICS OF THE SAMPLES STUDIED AND MEASUREMENT METHOD

The studies were carried out on three series of $Y_{1-x}Ca_xBa_2Cu_{3-x}Co_xO_y$ samples ($x=0.0-0.3$) with different oxygen contents. The samples were prepared at the Institute of Silicate Chemistry, Russian Academy of Sciences, by standard solid-phase synthesis from starting oxides and carbonates of the corresponding metal components. The final oxidation of the samples performed to saturate them with oxygen was performed in an oxygen flow at 450 °C for 6 h, followed thereafter by the same procedure at 400 °C for 10 h. The oxygen content in the second and third series was reduced by additional annealing in an oxygen-deficient atmosphere for 2 h at 450 and 475 °C, respectively.

X-ray diffraction measurements showed all samples to be single phase to within 1%. The oxygen content was determined by iodometric titration to within $\pm 0.01-0.02$. The oxygen index and unit-cell parameters derived from x-ray diffraction analysis with an accuracy of ± 0.002 are presented in Tables I–III for all samples. One readily sees that, in all the three series, the oxygen index y increases insignificantly with doping level (the starting series) or remains practically constant. In the samples with a close-to-stoichiometric oxygen composition, the transition from orthorhombic to tetragonal symmetry occurs at $x\approx 0.2$ and, as the oxygen content is lowered, orthorhombic distortions disappear at an impurity concentration $x\approx 0.1$.

TABLE II. Unit cell parameters and oxygen content for the $Y_{1-x}Ca_xBa_2Cu_{3-x}Co_xO_y$ series after annealing at 450 °C.

x	a, Å	b, Å	$a-b$, Å	c, Å	y
0.00	3.826	3.890	0.064	11.702	6.82
0.05	3.837	3.880	0.043	11.711	6.84
0.10	3.863	3.863	0	11.711	6.84
0.15	3.864	3.864	0	11.716	6.83
0.20	3.868	3.868	0	11.720	6.83
0.25	3.868	3.868	0	11.715	6.82
0.30	3.868	3.868	0	11.714	6.84

TABLE III. Unit cell parameters and oxygen content for the $Y_{1-x}Ca_xBa_2Cu_{3-x}Co_xO_y$ series after annealing at 475 °C.

x	a, Å	b, Å	$a-b$, Å	c, Å	y
0.00	3.824	3.896	0.072	11.704	6.74
0.05	3.836	3.886	0.050	11.710	6.75
0.10	3.864	3.864	0	11.713	6.76
0.15	3.865	3.865	0	11.717	6.78
0.20	3.866	3.866	0	11.730	6.78
0.25	3.868	3.868	0	11.730	6.80
0.30	3.870	3.870	0	11.725	6.78

The temperature dependences of the resistivity and Seebeck coefficient were obtained for all samples in the range $T=T_c-300$K. The resistivity was measured by the standard ac four-probe technique (20 Hz) in the frequency and phase selection regimes. The absolute magnitude of the Seebeck coefficient was determined relative to copper electrodes, with a subsequent correction for the absolute values of the Seebeck coefficient of copper introduced. The temperature drop across the sample was maintained during the measurement within 1–2 K.

2. EXPERIMENTAL RESULTS

The temperature dependences of the resistivity exhibit for all series a pattern typical of HTSC materials, namely, a linear decline from room temperature down to the superconducting transition. The slope of the $\rho(T)$ relations varies only weakly with increasing doping level. The dependence of T_c on impurity concentration determined for the three series of $Y_{1-x}Ca_xBa_2Cu_{3-x}Co_xO_y$ samples with different oxygen compositions is displayed in Fig. 1. Deviation from oxygen stoichiometry results in a degradation of the superconducting properties from one series to another, in accordance with the general pattern of the effect of oxygen deficiency on the superconducting properties of the $YBa_2Cu_3O_y$ system. The pattern of the $T_c(x)$ dependence is, however,

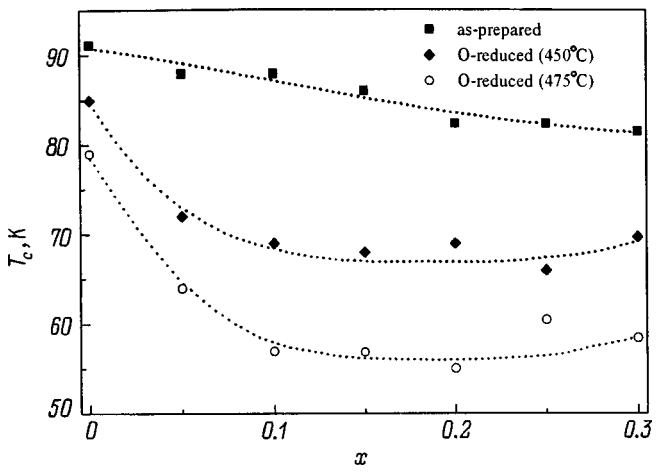

FIG. 1. Critical temperature vs doping level in the $Y_{1-x}Ca_xBa_2Cu_{3-x}Co_xO_y$ system with different oxygen contents.

different for the starting and annealed samples. For close to stoichiometric oxygen contents, an increase in the Ca and Co content results in a monotonic suppression of superconductivity, which is weaker than that observed[12,18] with separate Ca and Co substitutions. At the same time, for low impurity concentrations ($x \leqslant 0.1$) in oxygen-deficient samples, T_c decreases appreciably (by 15 and 20 K in the series annealed at 450 and 475 °C, respectively), whereas when the doping level is increased still more ($x \geqslant 0.1$), T_c remains practically unaffected. It should be pointed out that such a behavior of the critical temperature is fairly unusual, and has been observed for the first time in a study of double substitutions. One can present for illustration the data on the effect of double substitutions Ca+Fe and Ca+Al,[10,19] as well as our results[20] obtained in simultaneous substitution of Ca at the Y site and of La at the Ba site. We note specifically that Ref. 20, which also studied the effect of the variation of oxygen content on the properties of $Y_{1-x}Ca_xBa_{2-x}La_xCu_3O_y$, revealed that an increase in Ca and La content results in successive suppression of superconductivity both in the series with a close-to-stoichiometric oxygen content and in oxygen-deficient samples. Hence substitution of cobalt at chain-copper sites accompanied by calcium doping exhibits certain features which are seen particularly clearly when extra oxygen deficiency is produced and are not characteristic of the other double substitutions. We shall consider below some possible physical reasons for the nontrivial dependence of the critical temperature.

Figure 2 presents graphically three families of temperature dependences of the Seebeck coefficient in the $Y_{1-x}Ca_xBa_2Cu_{3-x}Co_xO_y$ system for various states of the oxygen subsystem, and Fig. 3, concentration dependences of the Seebeck coefficient obtained at $T=300$ K (S_{300}). Deviation from oxygen stoichiometry is seen to result, on the whole, in an increase in the Seebeck coefficient in absolute magnitude in the annealed series compared to the starting samples. In the starting $Y_{1-x}Ca_xBa_2Cu_{3-x}Co_xO_y$ series, S_{300} grows with increasing doping level very weakly, within 5 μV/K (see Fig. 3), and practically does not vary at all for impurity concentrations $x \geqslant 0.15$. As for the oxygen-deficient series, the $S_{300}(x)$ relations are seen (Fig. 3) to become nonmonotonic, with the maximum in S_{300} reached at different Ca and Co concentrations, namely, at $x \approx 0.20-0.25$ and $x \approx 0.15$ for the samples annealed at 450 and 475 °C, respectively. As seen from Fig. 3, for small x in the annealed series, S_{300} increases with doping level considerably faster than in the starting one and $S_{300}(x)$ grows the faster the larger is the extent of reduction in the series. For $x > 0.15$, the difference in the values of S_{300} between the annealed series practically disappears. Another significant observation is that, in all the series studied, the $S(T)$ relations acquire additional features with increasing x which are not typical of yttrium-based high-T_c superconductors, namely, they exhibit an extended region of linear growth, with the slope of $S(T)$ increasing with doping level. These unusual features are seen particularly clearly in the starting series, i.e., in samples with close to stoichiometric oxygen content (Fig. 2a). The small absolute magnitude of the Seebeck coefficient and a very weak growth of S_{300} with doping level make more prominent the above-mentioned progressive increase of this coefficient for $x \geqslant 0.15$ samples at $T=120$ K [near the maximum in the $S(T)$ relation]. As shown in our earlier publications,[12,21] the appearance of such features in $S(T)$ relations is connected with the specific effect the Ca impurity exerts on the band spectrum of $YBa_2Cu_3O_y$. In the annealed series, viewed against the general oxygen deficiency, the Ca-induced characteristic transformation of the shape of the $S(T)$ relations is not so clearly pronounced and becomes evident only in heavily doped samples.

Note that the variation with increasing doping level of T_c correlates with the variation of S_{300} for all the series studied. The weak monotonic decrease of the critical temperature in samples with a close-to-stoichiometric oxygen composition reflects the weak monotonic growth of S_{300}, and, in oxygen-deficient series, S_{300} exhibits a noticeable growth for low impurity concentrations ($x \leqslant 0.1$), i.e. in the same region where one observes a comparatively strong decrease of T_c. At the same time at high doping levels one does not see suppression of superconductivity, and S_{300} varies not as strongly.

Summing up, note the following points. The mutual compensation by impurities of their effects on the lattice charge balance accounts for the weak variation of the Seebeck coefficient in absolute magnitude with increasing doping level, which makes the specific Ca-induced features in the $S(T)$ relations more revealing. One has also observed an unusual effect of annealing in an oxygen-deficient atmosphere on the concentration dependences of the critical temperature and S_{300}, which is apparently associated with the specific influence of the Ca+Co impurity combination on the properties of the $YBa_2Cu_3O_y$ system.

3. ANALYSIS OF THE RESULTS AND CONCLUSIONS

All the experimental data obtained have been analyzed in terms of the phenomenological theory of electron transport described in detail in Ref. 18. As shown earlier,[12,21] calcium impurity affects in a specific way the band structure of $YBa_2Cu_3O_y$, namely, a conduction-band asymmetry sets in and grows with increasing calcium content. Our previous conclusions suggest that the reason for this lies in that Ca introduces additional states into the band responsible for conduction. Taking into account the asymmetry, whose degree is characterized by the asymmetry parameter b, one can write analytic expressions for the chemical potential and the Seebeck coefficient in the following form[12]

$$\mu^* = \ln \frac{\sinh(FW_D^*)}{\sinh[(1-F)W_D^*]} - bW_D/k_0T, \tag{1}$$

$$S = -\frac{k_B}{e}\left\{\frac{W_\sigma^*}{\sinh W_\sigma^*}\left[\exp(-\mu^*) + \cosh W_\sigma^* - \frac{1}{W_\sigma^*}(\cosh\mu^* + \cosh W_\sigma^*) \times \ln\frac{\exp(\mu^*)+\exp(W_\sigma^*)}{\exp(\mu^*)+\exp(-W_\sigma^*)}\right] - \mu^*\right\}, \tag{2}$$

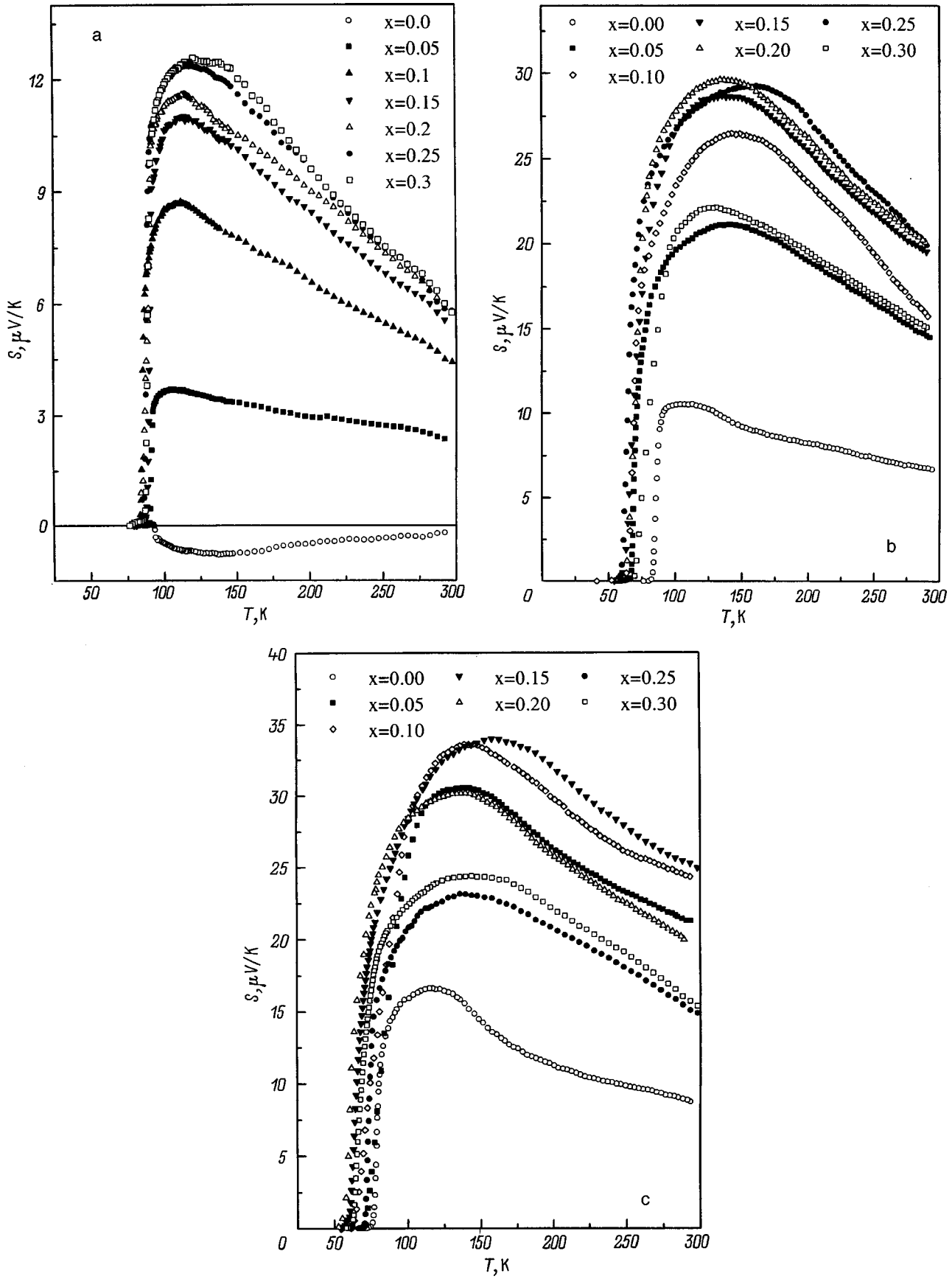

FIG. 2. Temperature dependences of the Seebeck coefficient in the $Y_{1-x}Ca_xBa_2Cu_{3-x}Co_xO_y$ compound. a—Starting series of samples, b—series annealed at 450 °C, c—series annealed at 475 °C.

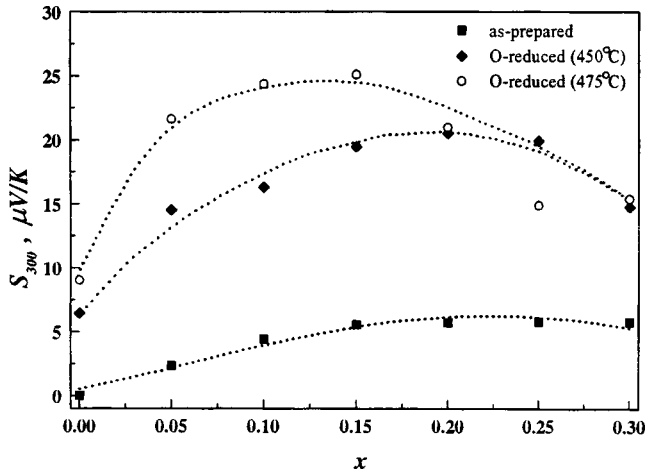

FIG. 3. Dependence of the room-temperature Seebeck coefficient, S_{300}, on doping level in the $Y_{1-x}Ca_xBa_2Cu_{3-x}Co_xO_y$ compound with different oxygen contents.

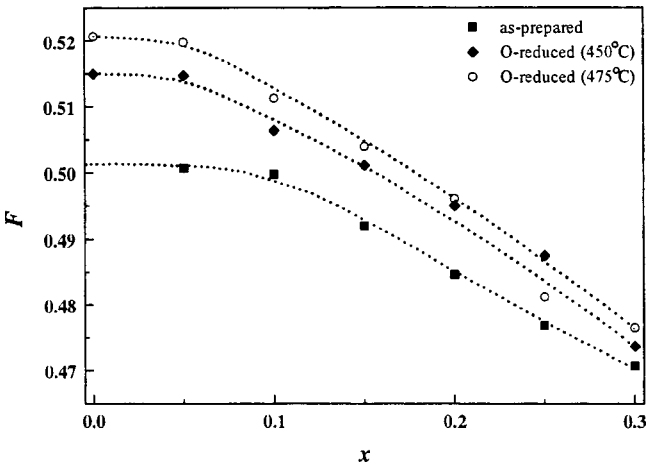

FIG. 4. Dependence of band filling by electrons on doping level in the $Y_{1-x}Ca_xBa_2Cu_{3-x}Co_xO_y$ compound with different oxygen contents.

where k_B is the Boltzmann constant, e is the electronic charge, $W_D^* \equiv W_D/2k_BT$, and $W_\sigma^* \equiv W_\sigma/2k_BT$. There are three main model parameters in Eqs. (1) and (2), namely, F, the band filling by electrons; W_D, the total conduction-band effective width; and W_σ, the effective band width in conduction. By analyzing the temperature dependences of the Seebeck coefficient and by fitting the theoretical to experimental $S(T)$ curves, one can estimate the band structure parameters and follow their transformation as the sample composition is varied.

A good quantitative fit of the experimental to calculated $S(T)$ curves was achieved, which permitted unambiguous determination of the model parameters. The only exception was the undoped sample in the series with a close-to-stoichiometric oxygen content. The absolute values of the Seebeck coefficient for this sample are very small. In this case, the form of the $S(T)$ relationship can be strongly affected by fine features in the conduction-band structure, whose inclusion into the approximation used here would be difficult. This may increase substantially the error in band-structure-parameter calculation. For this reason the experimental data obtained on the first sample were used only in a qualitative analysis.

Figure 4 presents the band filling by electrons F as a function of doping level for all the series studied. F is seen to increase in the oxygen-deficient series with respect to the starting series depending on the extent of reduction, which can be accounted for by the general nature of the effect of oxygen deficiency on this parameter.[18] The growth in F (decrease of the hole concentration) reflects the donor action of the oxygen vacancies, as this follows from the crystallochemical considerations as well. As for the doping-induced variation of F, the pattern of the $F(x)$ relationship, as evident from Fig. 4, is the same for the three series. For low impurity concentrations ($x<0.10$), F varies insignificantly, and as the doping level continues to increase, it falls off by a close to linear law. This behavior cannot be explained by simple crystallochemical considerations, which suggest that, in the case of impurities compensating the effects of one another on the lattice charge balance, the degree of band filling by electrons should vary very weakly, in accordance with the weak growth in the oxygen content (see Tables I–III). The linear decrease of the F quantity can be explained in the following way. Our calculations show that the degree of band asymmetry increases linearly with doping level as $b \approx -0.07x$. This means that the number of additional states in the band grows directly proportional to calcium content. In this case the filling F (equal to the ratio of the total number of electrons in the band, which practically does not vary, to the total number of states, which grows linearly with x) falls off linearly with increasing doping level. Note another point. In the case of a symmetric band, the Seebeck coefficient reverses its sign at exactly half filling,[18] while if an asymmetry is present, there is no such unambiguous relationship. As shown in our previous study[22] dealing with a bismuth-based HTSC system, positive Seebeck coefficients for an asymmetric band can occur also at less than half band filling by electrons as well. The values $F<0.5$, presented in Fig. 4 and corresponding to positive Seebeck coefficients for the compositions studied in our work for the case where one of the codopants is calcium, originate from the band asymmetry resulting from additional states in the band formed by the Ca impurity.

It appears of interest, therefore, to discuss the behavior of the S_{300} quantity, since it reflects directly the Fermi level dynamics in the band responsible for conduction in the normal phase. As seen from Fig. 3, S_{300} in the starting samples increases from one series to another, corresponding to the number of free electrons increasing with oxygen deficiency (the Fermi level shifts upward from the midgap position). The variation of S_{300} with increasing impurity concentration in each series, in its turn, cannot be explained by simple crystallochemical considerations. In the case of single substitutions,[18] a slight increase in the doping level gives rise to a substantial shift of the Fermi level and, accordingly, to a strong change in the absolute values of the Seebeck coefficient, against which fine features in the band structure do not affect noticeably the temperature and concentration dependences of S. For instance, in the case of the single Co→Cu

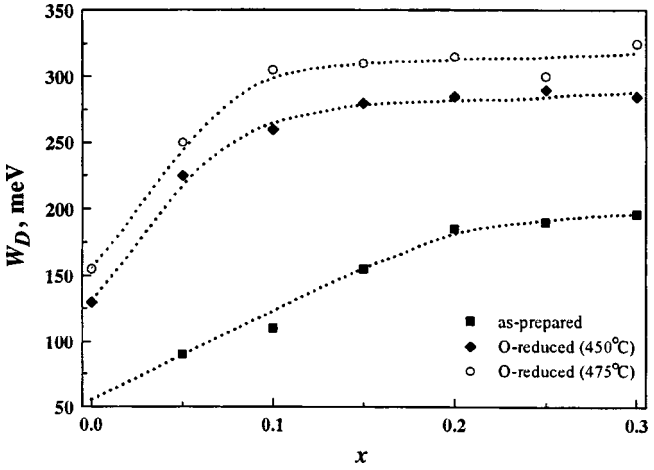

FIG. 5. Dependence of the total effective conduction-band width in the $Y_{1-x}Ca_xBa_2Cu_{3-x}Co_xO_y$ compound with different oxygen contents.

substitution, S_{300} of $YBa_2Cu_{3-x}Co_xO_y$ samples increases from close to zero in an undoped sample to 60 μV/K in the sample with a $x=0.30$ Co content.[18] In the $Y_{1-x}Ca_xBa_2Cu_{3-x}Co_xO_y$ system, successive growth of the doping level results, due to the charge-compensation effect, in a very slow E_F shift and, accordingly, in a comparatively weak variation, on the whole, of the Seebeck coefficient in absolute magnitude. In this case the pattern of the $S(T)$ relation and, in particular, the S_{300} quantity is affected not only by variation of the number of carriers in the band but by fine features in the band structure near the Fermi level, which cannot be described quantitatively in the frame of the simplest approximation. Thus the $S_{300}(x)$ relations can obviously follow a more complex pattern, because the Fermi-level dynamics is governed by an interplay between the number of carriers and that of band states, which likewise varies with calcium content (which is evidenced by the gradual growth of the band asymmetry). It should be stressed that single doping with Ca, unlike the Co impurity (as well as the other nonisovalent substitutions studied thus far[18]), also exhibits some features,[12] which permits one to assign with certainty the onset of band asymmetry to the calcium impurity. Thus the nontrivial variation of S_{300} and of the shape of $S(T)$ relations with increasing doping level provides additional evidence for a specific effect of Ca on the band structure.

The dependence of the total effective band width W_D on doping level for all the series studied is displayed in Fig. 5. As shown in detail earlier,[18] the general consequence of an increase in the number of oxygen vacancies (which gives rise to increasing lattice disorder) is, in full agreement with the Anderson model, an increase in bandwidth (i.e. a growth of the W_D parameter) and a relative decrease of the interval of delocalized states in width (i.e. a decrease of the W_σ/W_D quantity). Hence the increase of W_D observed to occur from one series to another is caused by disorder in the oxygen subsystem of the $Y_{1-x}Ca_xBa_2Cu_{3-x}Co_xO_y$ samples subjected to annealing in reducing conditions. We are turning now to an analysis of the dynamics of W_D variation with impurity concentration in each series.

As seen from Fig. 5, the conduction-band width in the sample series with close-to-stoichiometric oxygen content increases monotonically with doping level, and this growth slows down substantially for impurity concentrations $x \geqslant 0.20$. At the same time the oxygen parameter y in the starting series of samples (Table I) varies extremely weakly for $x \leqslant 0.15$, and increases practically to the stoichiometric value as x continues to increase. This means that, in the heavily doped region, the Ca and Co impurities do not fully compensate their effects in the lattice, which is obviously a consequence of the fact that the Co impurity, unlike Ca, perturbs directly the CuO chains, i.e., affects directly the oxygen subsystem. The compensation of the effect of cobalt by calcium turns out to be insufficiently strong to maintain the charge balance in the system, and this is what accounts for the weak growth of oxygen content. As a result, in the region of low impurity concentrations in starting $Y_{1-x}Ca_xBa_2Cu_{3-x}Co_xO_y$ samples, the increase of bandwidth with increasing x is caused by a general lattice disordering induced by the impurity cations. The presence of a smooth section in the $W_D(x)$ relationship is associated, in its turn, with the oxygen content approaching stoichiometry in the heavy-doping region, which brings about increasing order on the oxygen subsystem. Thus the broadening of the band caused by the dopants, on the one hand, and its narrowing due to some ordering in the oxygen subsystem, on the other, result in the effective bandwidth remaining practically constant in the heavy-doping region. Note that, as shown in our work,[23] a similar narrowing of the band as one approaches oxygen stoichiometry is observed to occur also in the case of single La and Co doping in $Y(Ba_{1-x}La_x)_2Cu_3O_y$ and $YBa_2Cu_{3-x}Co_xO_y$ samples at an impurity concentration $x=0.05$, which corresponds to the maximum critical temperature.

As for the series with a reduced oxygen content, their $W_D(x)$ relations follow the same pattern (see Fig. 5), and one observes only a quantitative difference between the effective widths of the conduction band, which is associated with different extents of reduction in each series. In both cases the band widens considerably in the region of low impurity concentrations ($x \leqslant 0.10$), whereas the value of W_D for heavily doped samples remains practically constant. An inspection of the dynamics of the oxygen subsystems in the two oxygen-deficient series shows that in both cases the oxygen content increases weakly at low x and practically does not vary in the region of heavy doping. This means that the $W_D(x)$ relation observed for both oxygen-deficient series is not a direct consequence of the variation of oxygen content in the samples. Note that, in the similar system $Y_{1-x}Ca_xBa_{2-x}La_xCu_3O_y$ studied by us,[20] the bandwidth grows monotonically with the degree of doping, both with a close-to-stoichiometric oxygen content and in the case of oxygen deficiency. Hence one may conclude that the smooth section in the $W_D(x)$ relation is due to a specific effect of the Ca→Co impurity combination studied.

Considered in terms of our concepts, the constant bandwidth with increasing doping level is an indication of the presence of some additional lattice ordering at high Ca and Co concentrations. In this connection, the data obtained in

Ref. 16 appear of interest. It was found[16] that the Co→Cu substitution in the $YBa_2Cu_3O_y$ system makes the Co distribution nonuniform for $x \geqslant 0.10$, namely, the cobalt atoms form clusters. The size of these clusters increases substantially after annealing the samples in an oxygen-deficient atmosphere or when the samples are additionally doped with calcium. Hence formation of large cobalt clusters is most probable in $Y_{1-x}Ca_xBa_2Cu_{3-x}Co_xO_y$ samples annealed in an oxygen-deficient atmosphere. On the other hand, Ref. 16 suggests that Co atoms form clusters through sharing chain-oxygen atoms, because cobalt ions are more stable when the oxygen coordination number is five. It is this that accounts for the weak variation of the oxygen index y for high impurity concentrations in oxygen-deficient series (see Tables II and III), because the formation of cobalt clusters involving oxygen atoms assumes that compensation of the lattice perturbations induced by impurity cations requires a substantially smaller amount of excess oxygen than in the case of statistically distributed cobalt atoms. Formation of a cobalt and oxygen superlattice may lead to a certain ordering in the chain subsystem and, hence, to a relative narrowing of the conduction band. This assumption may provide an explanation for the constancy of the effective bandwidth with increasing impurity concentration in heavily doped samples.

In conclusion one should point out the following consideration. All series studied here exhibit a correlation between the variation of the critical temperature T_c and the effective bandwidth W_D (compare Figs. 1 and 5). We observed earlier that the $T_c(W_D)$ relation is universal for the $YBa_2Cu_3O_y$ system in the case of single nonisovalent substitutions which do not involve directly the copper sites in the sheets.[24] This relation is plotted in Fig. 6 together with the results obtained in this work. One readily sees that the data obtained for the systems studied here also coincide with the universal correlation dependence $T_c(W_D)$, which suggests the following considerations concerning the nature of the effect of calcium on the conduction-band structure. Calculations show that the band asymmetry is small, so that two different cases are possible, namely, either the additional peak of calcium states is fairly small compared to the overall value of the DOS function, or it lies close to midgap, i.e., in the immediate vicinity of the Fermi level. In the latter case, the presence of this peak should affect considerably the density of states at Fermi level $D(E_F)$ by increasing it and thus resulting in higher values of T_c in the $Y_{1-x}Ca_xBa_2Cu_{3-x}Co_xO_y$ system compared to the single-substitution cases. However taking into account the method of model approximation of the $D(E)$ function used, the correlation dependence $T_c(W_D)$ for the $Y_{1-x}Ca_xBa_2Cu_{3-x}Co_xO_y$ system should differ appreciably from that for the single-substitution cases, and the magnitude of T_c in samples containing calcium should be higher. The fact that the critical temperature as a function of effective bandwidth in the system under study is in agreement with the universal correlation dependence for the $YBa_2Cu_3O_y$ system means that the appearance of additional states in the $Y_{1-x}Ca_xBa_2Cu_{3-x}Co_xO_y$ system does not exert a dominant effect on the superconducting properties of this compound. Hence the additional peak is small, lies most probably not in the immediate vicinity of the Fermi level,

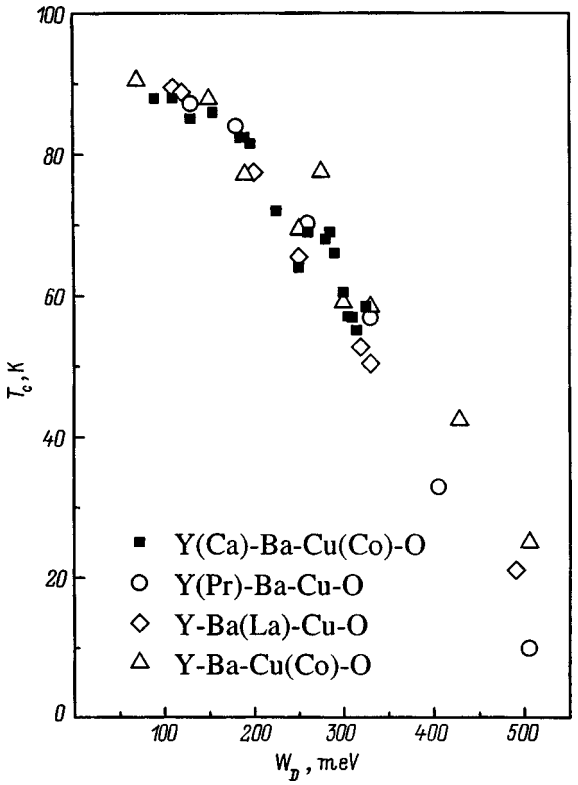

FIG. 6. Universal correlation dependence relating critical temperature to effective conduction-band width in the $YBa_2Cu_3O_y$ system for different substitutions. The data for single-substitution samples were taken from Ref. 24.

and is not more than an insignificant feature in the DOS function, which turns out to be inessential when calculating the effective conduction-band width within the $D(E)$ approximation used, and results only in the band becoming asymmetric. Thus the existence of a universal correlation between T_c and W_D in the $YBa_2Cu_3O_y$ system for various deviations from stoichiometry implies that the superconducting properties of the compound are dominated not by the small features in the band structure but rather by the small width of the conduction band as a general property of the $YBa_2Cu_3O_y$ band spectrum.

Thus an analysis of data on the specific features of the effect of double doping on the properties of the normal phase and T_c in the $Y_{1-x}Ca_xBa_2Cu_{3-x}Co_xO_y$ system permits the following conclusions:

(1) Ca→Y+Co→Cu doping results in a weak monotonic decrease of T_c for a close-to-stoichiometric oxygen content. The pattern of the $T_c(x)$ dependence changes with deviation from oxygen stoichiometry, namely, for low impurity concentrations ($x \leqslant 0.10$) one observes a strong drop of T_c, which remains practically constant with further increase of the doping level;

(2) The $S(T)$ dependences transform with increasing doping level in the $Y_{1-x}Ca_xBa_2Cu_{3-x}Co_xO_y$ system, namely, one observes the appearance of an extended region with a linear growth of the Seebeck coefficient accompanied by an increase in the slope of the relations;

(3) Band structure calculations made within the narrow-band model showed that Ca doping gives rise to a monotonic

growth of the degree of conduction-band asymmetry as a result of the Ca impurity introducing additional states in the band responsible for conduction in the normal phase. It is the onset of this asymmetry and its increase that account for the transformation of the $S(T)$ relations and the appearance of the features nontypical of the $YBa_2Cu_3O_y$ system;

(4) An analysis of the concentration dependences of the band-structure parameters shows the onset of additional ordering in the oxygen-deficient $Y_{1-x}Ca_xBa_2Cu_{3-x}Co_xO_y$ system at high impurity concentrations, which can be induced by formation of a cobalt-ion superlattice. This results in a relative narrowing of the conduction band and in a weak change of T_c;

(5) The observed correlation between T_c and the effective conduction-band width is in agreement with the universal correlation dependence for the $YBa_2Cu_3O_y$ system for different single nonisovalent substitutions. The existence of a universal $T_c(W_D)$ correlation under substitution in different cation sublattices, including the case of double doping, permits a conclusion that the small width of the DOS peak has a dominant effect on the superconducting properties of the $YBa_2Cu_3O_y$ system.

The authors express their thanks to I. B. Patrina (Institute of Silicate Chemistry, Russian Academy of Sciences) for providing samples for the study and for their characterization. One of the authors (V.É.G.) expresses his gratitude to the St. Petersburg Administration, Russian Academy of Sciences, and the Ministry of General and Professional Education of Russia for individual financial support (Grant for Young Scientists, 1998).

[1] J. M. Tarascon, P. Barboux, P. F. Miceli, L. H. Greene, G. W. Hull, M. Eibschutz, and S. A. Sunshine, Phys. Rev. B **37**, 7458 (1988).
[2] K. Westerholt, H. J. Wüller, H. Bach, and P. Stauche, Phys. Rev. B **39**, 11680 (1989).
[3] Y. Xu, R. Sabatini, A. R. Moodenbaugh, Y. Zhu, S.-G. Shyu, M. Suenaga, K. W. Dennis, and R. W. McCallum, Physica C **169**, 205 (1990).
[4] R. Liang, M. Itoh, T. Nakamura, and R. Aoki, Physica C **157**, 83 (1989).
[5] A. Manthiram and J. B. Goodenough, Physica C **159**, 760 (1989).
[6] A. Tokiwa, Y. Syono, M. Kikuchi, R. Suzuki, T. Kajatani, N. Kobayashi, T. Sasaki, O. Nakatsu, and Y. Muto, Jpn. J. Appl. Phys., Part 2 **27**, L1009 (1988).
[7] Z. Jirak, J. Hejtmanek, E. Pollert, A. Triska, and P. Vasek, Physica C **156**, 750 (1988).
[8] M. R. Chandrachood, I. S. Mulla, S. M. Gorwadkar, and A. P. Sinha, Appl. Phys. Lett. **56**, 183 (1990).
[9] E. Suard, A. Maignan, V. Caignaert, and B. Raveau, Physica C **200**, 43 (1992).
[10] Y. Zhao, H. K. Liu, and S. X. Dou, Physica C **179**, 207 (1991).
[11] P. R. Slater and C. Greaves, Supercond. Sci. Technol. **5**, 205 (1992).
[12] V. É. Gasumyants, E. V. Vladimirskaya, M. V. Elizarova, and N. V. Ageev, Fiz. Tverd. Tela (St. Petersburg) **40**, 2145 (1998) [Phys. Solid State **40**, 1943 (1998)].
[13] B. Raveau, C. Michel, M. Hervieu, D. Groult, A. Maignan, and J. Provost, J. Supercond. **5**, 203 (1992).
[14] Y. Zhao, H. K. Liu, X. B. Zhuge, G. Yang, J. A. Xia, Y. Y. He, and S. X. Dou, Physica B **194–196**, 1957 (1994).
[15] Y. Zhao, Y. He, H. Zhang, X. Zuge, and X. Tang, J. Phys.: Condens. Matter **4**, 2263 (1992).
[16] M. G. Smith, J. B. Goodenough, A. Manthiram, R. D. Taylor, and H. Oesterreicher, Phys. Rev. B **46**, 3041 (1992).
[17] R. Sharma, R. Ganguly, H. Rajagopal, A. Sequeira, J. V. Yakhmi, and M. Dasannacharya, J. Supercond. **8**, 271 (1995).
[18] V. E. Gasumyants, V. I. Kaidanov, and E. V. Vladimirskaya, Physica C **248**, 255 (1995).
[19] Z. Xu, S. Ouyang, J. Wang, X. Tang, and Q. Zhang, Chin. Sci. Bull. **37**, 1520 (1992).
[20] V. E. Gasumyants, M. E. Elizarova, and I. B. Patrina, Phys. Rev. B **59**, 6550 (1999).
[21] E. V. Vladimirskaya, V. É. Gasumyants, and I. P. Patrina, Fiz. Tverd. Tela (St. Petersburg) **37**, 1990 (1995) [Phys. Solid State **37**, 1084 (1995)].
[22] V. E. Gasumyants, N. V. Ageev, E. V. Vladimirskaya, V. I. Smirnov, A. V. Kazanskiy, and V. I. Kaydanov, Phys. Rev. B **53**, 905 (1996).
[23] V. É. Gasumyants, E. V. Vladimirskaya, M. V. Elizarova, and I. B. Patrina, Fiz. Tverd. Tela (St. Petersburg) **41**, 389 (1999) [Phys. Solid State **41**, 350 (1999)].
[24] V. É. Gasumyants, E. V. Vladimirskays, and I. B. Patrina, Fiz. Tverd. Tela (St. Petersburg) **39**, 1520 (1997) [Phys. Solid State **39**, 1352 (1997)].

Translated by G. Skrebtsov

Anomaly in the upper critical magnetic field common to $YBa_2Cu_3O_{7-\delta}$, $HoBa_2Cu_3O_{7-\delta}$, and $Nd_{1.85}Ce_{0.15}CuO_{4-\delta}$ irradiated by helium ions

S. I. Krasnosvobodtsev, N. P. Shabanova,*) V. S. Nozdrin, and A. I. Golovashkin

P. N. Lebedev Physics Institute, Russian Academy of Sciences, 117924 Moscow, Russia
(Submitted August 24, 1998; resubmitted February 1, 1999)
Fiz. Tverd. Tela (St. Petersburg) **41**, 1372–1376 (August 1999)

The high-temperature superconductors $YBa_2Cu_3O_{7-\delta}$, $HoBa_2Cu_3O_{7-\delta}$, and $Nd_{1.85}Ce_{0.15}CuO_{4-\delta}$ are found to possess a common anomaly in the variation of the upper critical magnetic field owing to irradiation by helium ions. While the resistivity ρ increases by many times, the increase in H_{c2} from scattering by radiation defects typical of ordinary superconductors does not occur. In terms of the ordinary mechanism, the anomaly may be explained by a significant reduction in the conduction electron density resulting from a loss of oxygen, which causes a significant rise in ρ with a small change in the scattering. © *1999 American Institute of Physics.* [S1063-7834(99)00508-0]

The upper critical magnetic field H_{c2} is one of the most important characteristics of superconductors of the second kind and, classically, is determined by the fundamental parameters of the electronic structure and by the parameters characterizing the scattering of conduction electrons.[1–6] The scattering raises the upper critical magnetic field H_{c2}, thereby inhibiting the Larmor orbits of the electrons in a magnetic field, which causes Cooper pair decay in the condensate.[5,7] The standard concepts have been reliably confirmed for ordinary phonon superconductors (Nb_3Sn [8–10] and NbC [8,11,12]).

How H_{c2} varies in the high-temperature superconductors (HTSCs) with electron scattering has not been studied. Research in this area is of interest for clarifying the mechanism of high-temperature superconductivity.

Our systematic experimental studies of the critical parameters of the cuprates $YBa_2Cu_3O_{7-\delta}$ (YBCO), $HoBa_2Cu_3O_{7-\delta}$ (HBCO),[8,13] and $Nd_{1.85}Ce_{0.15}CuO_{4-\delta}$ (NCCO)[14,15] with gradual changes in the defect concentrations by means of irradiation by energetic helium ions have yielded an unexpected result.[16] A sharp difference has been observed in the way H_{c2} varies in the high-temperature superconductors and ordinary superconductors. In this paper we present new experimental data and discuss the possible reasons for the observed anomaly.

1. EXPERIMENT

We have studied epitaxial HTSC films of YBCO, HBCO and NCCO with their *c* axis oriented perpendicular to the surface of the single-crystal substrates. The technical details of the method for *in situ* synthesis of films with optimum parameters by laser sputtering have been discussed elsewhere.[17,18]

The defect concentration was varied by bombarding the films with energetic ions. In order to attain greater uniformity of the distribution of radiation defects, the lightest ions, He^+ and He^{++}, were used and their energy was chosen to ensure that their mean free path in the crystal lattice exceeded the sample thickness ($\sim$200 keV and 3.6 MeV depending on the film thickness). Irradiation was done at room temperature.

In the experiment, the temperature dependence of the upper critical magnetic field $H_{c2}(T)$ was determined from the temperature shift in the superconducting transition induced by a magnetic field perpendicular to the film.[8] The superconducting transition was measured in terms of the resistance.

In NCCO the magnetic field produced a temperature shift in the rather sharp resistive transition with little temperature broadening, so it was possible to determine the phase curve $H_{c2}(T)$ with sufficient accuracy.[14,15] The temperature of the phase transition in a magnetic field corresponding to $H_{c2}(T)$ is, evidently, somewhat closer to the onset of the resistive $\rho-\rho_n$ transition.[19] In fact, we have shown[15] that the $H_{c2}(T)$ curve for this compound determined from the temperature shift in the onset of the transition is essentially linear (Fig. 1a), in accordance with the Ginzburg–Landau theory for superconductors of the second kind near T_c.

For YBCO and HBCO, it is difficult to determine $H_{c2}(T)$ in this fashion, because of the rapidly increasing broadening of the transition with rising the magnetic field.[20] Nevertheless, for this group of HTSCs we took the point at which the resistivity ρ_n of the normal state near the transition fell by a factor of two (the middle of the transition) to be the temperature of the superconducting transition in a magnetic field when determining the temperature variation of the upper critical field. This result is used for qualitative comparison with the results for ordinary and HTSC materials in which the broadening is negligible.

The temperature dependences of the upper critical field for NCCO for initial and irradiated samples are shown in Fig. 1a. Also shown there for comparison (Fig. 1b) is $H_{c2}(T)$ for irradiated NbC. In NbC the slope of the plot of H_{c2} as a function of temperature increases when the concentration of radiation defects is raised, as is typical of classical

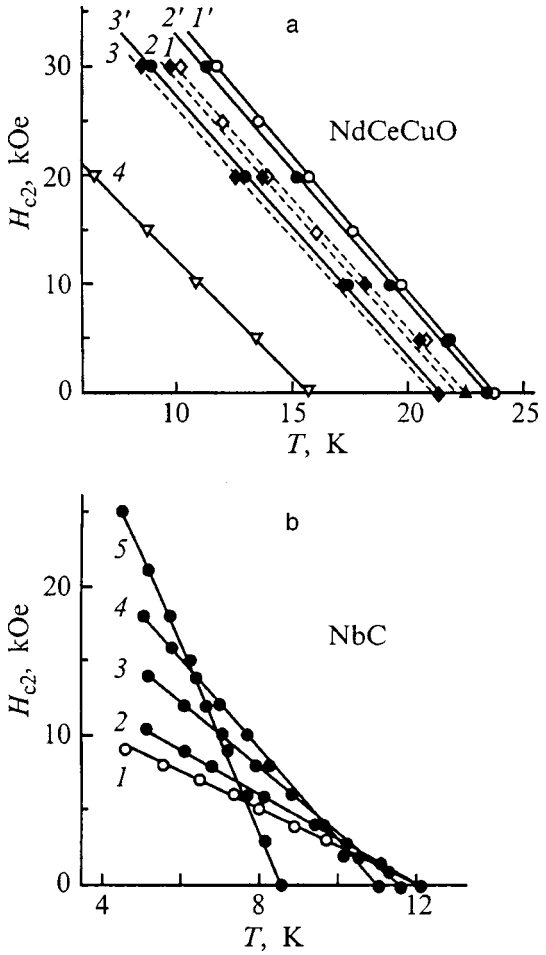

FIG. 1. Temperature dependences of the upper critical magnetic field $H_{c2}(T)$ for films irradiated by different fluences F of He^+ ions. a — $Nd_{1.85}Ce_{0.15}CuO_{4-\delta}$, F (cm^{-2}): *1,1′* — 0, *2,2′* — 1×10^{13}, *3,3′* — 1×10^{14}, *4* — a film with deficient oxygen[19]; b — NbC, F (cm^{-2}): *1* — 0, *2* — 3×10^{14}, *3* — 1.4×10^{15}, *4* — 5×10^{15}, *5* — 3×10^{16}.

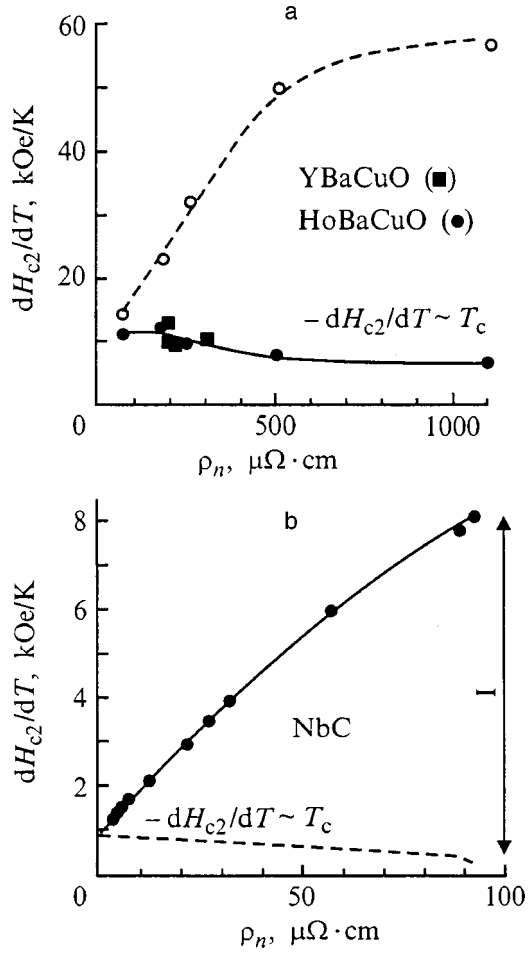

FIG. 2. The change in the slope $-dH_{c2}/dT$ of the upper critical magnetic field as a function of temperature, $H_{c2}(T)$ with increasing resistivity ρ_n produced by irradiation in HTSC compounds $YBa_2Cu_3O_{7-\delta}$ and $HoBa_2Cu_3O_{7-\delta}$ (a) and the superconductor NbC (b). The smooth curve is experimental and the dashed curve is estimated using the GLAG theory. I represents the contribution of scattering according to GLAG.

superconductors.[8,12] For the high-temperature superconductor NCCO, $-dH_{c2}/dT\,T_c$ is constant, even though the critical temperature T_c falls substantially. In the case of YBCO and HBCO, the slope of the upper critical magnetic field as a function of temperature was even found to decrease as a result of irradiation (Fig. 2a).

2. ANOMALOUS VARIATION OF H_{c2} IN THE HTSC COMPOUNDS $YBa_2Cu_3O_{7-\delta}$, $HoBa_2Cu_3O_{7-\delta}$ AND $Nd_{1.85}Ce_{0.15}CuO_{4-\delta}$ OWING TO IRRADIATION

The upper critical field of a superconductor of the second kind in the absence of scattering is determined by the electronic structure parameters: $-dH^0_{c2}/dT \sim T_c/\langle \nu^{*2}\rangle \sim T_c m/E_F$.[3,6,8] Here $\langle \nu^2\rangle$ is the square of the component of the Fermi velocity ν perpendicular to the direction of the magnetic field averaged over the Fermi surface, ν^* corresponds to the renormalized Fermi velocity of a material with a strong electron-phonon interaction, m is the effective mass, and E_F is the Fermi energy.

In ordinary superconductors the scattering of conduction electrons by radiation defects increases the upper critical magnetic field. According to the classical Ginzburg–Landau–Abrikosov–Gorkov (GLAG) theory, near T_c the contribution of scattering to H_{c2} for superconductors of the second kind increases in proportion to $N^*(0)\rho_n$,[5] where $N^*(0)$ is the renormalized density of electronic states at the Fermi level and ρ_n is a measure of the scattering.

Therefore, in a real superconductor the slope of the upper critical field H_{c2} as a function of temperature is given by $-dH_{c2}/dT \sim -dH^0_{c2}/dT + N^*(0)\rho_n$.[11]

The pure term, $-dH^0_{c2}/dT$, which is determined by $T_c/\langle \nu^{*2}\rangle$ is invariant, as long as the electronic structure of the material is maintained. T_c does not change because of scattering on normal impurities and defects (according to Anderson's theorem[21]). When the defect concentration is high enough, the pure term can vary relatively slowly because of spreading of the Fermi surface and a drop in the critical temperature.

The scattering term, which is proportional to $N^*(0)\rho_n$, causes H_{c2} to rise as the number of scattering centers increases when their number does not lead to a significant change in the electronic structure. Otherwise, a sharp reduction in $N^*(0)$ can be observed, which leads to a drop in H_{c2}.[8,10]

Figure 2 shows the results of a study of the upper critical magnetic field of the high-temperature superconductors YBCO and HBCO irradiated by helium ions. (Near T_c the critical field for a given temperature is determined by the slope $-dH_{c2}/dT$.) Data for the classical superconductor NbC are shown in this figure for comparison.

In the case of the superconducting compound NbC, scattering by radiation defects leads to a rise in H_{c2} in accordance with GLAG (Fig. 2b). The classical ideas predict a similar picture for the HTSCs (Fig. 2a). The change in H_{c2} for YBCO and HBCO owing to scattering (the dashed curve) was calculated from the change in the mean-free-path l of the conduction electrons which we estimated for irradiated films of these compounds.[8]

For the HTSC compounds the experimentally observed behavior of the upper critical magnetic field differed sharply from that predicted classically. In particular, when the concentration of radiation defects is increased in the region where Anderson's theorem holds ($T_c \approx$ const) and there is no reason to expect significant changes in $N^*(0)$, H_{c2} should rise by at least a factor of 2–3 in these HTSC compounds because of scattering.[8,13–16] However, this was not observed experimentally (Figs. 1a and 2a).

3. POSSIBLE REASONS FOR THE ANOMALOUS VARIATION OF H_{c2} IN SUPERCONDUCTING CUPRATES

If the rise in the resistivity is caused by scattering of conduction electrons by radiation defects, then the observations are in conflict with conventional ideas, according to which scattering makes the critical field increase. The observed change in H_{c2} of the HTSC compounds caused by ion bombardment is close to the change in the pure term (Fig. 3). Nevertheless, we have attempted to find an explanation for this effect within the framework of the ordinary mechanism.

(1) In the case of YBCO and HBCO we have assumed that the critical field determined from the middle of the resistive transitions does not correspond to H_{c2}. Here it was necessary to assume that the resistive transition differs substantially from the phase transition owing to dissipative vortex motion and fluctuations in the order parameter.[13,20]

However, a study of H_{c2} for NCCO revealed the existence of a similar anomaly following irradiation. The superconducting transition of this cuprate in a magnetic field is sharp enough for a reliable experimental determination of $H_{c2}(T)$. Thus, on the whole, explaining this anomaly in terms of some significant difference between the resistive and phase transitions is unconvincing.

(2) The observations cannot be explained by assuming that the upper critical field of the HTSC materials is determined by the paramagnetic limit H_p or by the destruction of Cooper pairs through Larmor precession of the electrons (H_{c2}). According to Ref. 22, scattering should weaken the paramagnetic limit, i.e., inhibit the orientation of the spins along the magnetic field. Thus, we might expect H_p to increase upon irradiation, but this is not confirmed by experiment. In addition, an estimate of the paramagnetic limit gives a value much higher than the observed value.[16]

(3) This result can be regarded as the absence of the usual relationship between H_{c2} and the resistivity ρ_n caused by current flow effects when the damage is nonuniform.

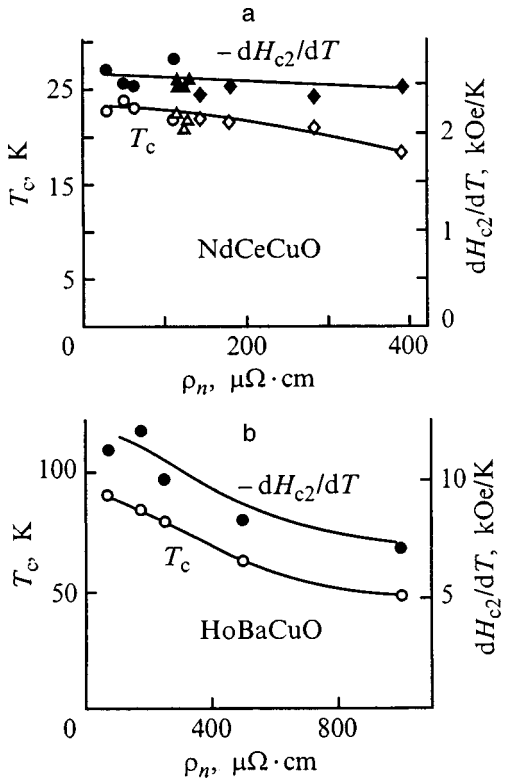

FIG. 3. Experimental dependences of the critical temperature (*1*) and upper critical magnetic field (*2*) on the resistivity of films of $Nd_{1.85}Ce_{0.15}CuO_{4-\delta}$ (a) and $HoBa_2Cu_3O_{7-\delta}$ (b) irradiated by helium ions.

In the case of thin films of the conventional superconductor NbC, irradiation did not produce an inhomogeneity for doses up to the maximum, when the defect concentration had been increased by more than an order of magnitude.[12] This is indicated by the sharp superconducting transition in terms of the dynamic magnetic susceptibility (inductive transition) in the irradiated samples.

In NCCO, smearing of the inductive superconducting transition produced by irradiation was observed, and this is evidence of the development of some inhomogeneity. A possible reason for this may be the weak atomic bonds of chain and apical oxygen typical of the cuprates. We assumed that the impact of an energetic particle causes formation of an oxygen depleted region whose size is comparable to the coherence length. Because of the redistribution of the current in an inhomogeneous superconductor in a magnetic field, the resistivity of the normal state, ρ_n, may not correspond to that of the material for which H_{c2} has been measured.

However, some of the experimental facts are hard to explain by the inhomogeneity. In terms of the conventional mechanism it is reasonable to assume that, in an inhomogeneous system, the field is also nonuniform. Because of the complex current flow in a magnetic field, a superconductor of this sort should resemble a polycrystalline anisotropic superconductor of the type discussed in Refs. 23 and 24. The width of the resistive transition in such a material increases as the applied magnetic field is raised. Here the low-temperature part of the transition (end) corresponds to a re-

gion with minimal H_{c2}, while the temperature for the onset of the transition is determined by the values of the maximum and minimum critical fields. We, however, did not find any growth in the field broadening of the transition in NCCO in a magnetic field when a radiation inhomogeneity developed.

(4) It should be noted that when HTSC materials are irradiated, significant changes in the critical and transport properties take place for fluences 1–2 orders of magnitude lower than for ordinary materials.[25,26] At these fluences ($10^{13}-10^{15}\,\mathrm{cm}^{-2}$) changes of these kinds are only beginning in ordinary superconductors. The sensitivity of HTSC materials to irradiation can be explained by the release of weakly bound oxygen. The level of radiation defects among the metallic atoms is low because of the low doses, while that among oxygen atoms (δ) is low in principle (a few percent, even with release of oxygen leading to loss of superconductivity). Thus, the scattering changes little. Thus the effect of irradiation is analogous to the effect of changing the oxygen content of the films.

In this case it may be assumed that the change in the parameters of an HTSC material is caused mainly by a change in the concentration n of conduction electrons. In particular, the observed growth in the resistivity, $\rho \sim m\nu/nl$, is attributable to an drop in n, rather than to rise in the concentration of scattering centers. In the pure limit, the slight change in the critical field is explained by the similar rate of fall of T_c and the Fermi level: $-dH_{c2}/dT \sim T_c m/E_F$.

Therefore, for the two types of HTSCs, $YBa_2Cu_3O_{7-\delta}$, $HoBa_2Cu_3O_{7-\delta}$, and $Nd_{1.85}Ce_{0.15}CuO_{4-\delta}$, while the resistivity rose by many times as a result of bombardment by energetic helium ions, the upper critical magnetic field determined from resistivity measurements was observed to undergo an anomalously small change similar to the variation in H_{c2} of the pure material without electron scattering.

Based on conventional concepts, the observed anomaly cannot be explained by a sharp difference in the measured critical field from the $H_{c2}(T)$ phase curve resulting from the broadening of the transition (1) or paramagnetic unpairing (2). Proposition (3), according to which the anomaly is caused by inhomogeneity of the radiation damage also does not explain all the facts. We believe the most probable explanation (4) in terms of an ordinary mechanism is the escape of oxygen during irradiation, which causes a significant change in the concentration of conduction electrons. Here we have shown that the change in the concentration of crystal lattice defects acting as scattering centers is small.

We postulate that the anomalous behavior of H_{c2} during irradiation of high-temperature superconducting materials may also be caused by an unusual mechanism for superconductivity in which the coherence length of the condensate is slightly sensitive to changes in the conduction electron system. A nonphonon mechanism for unpairing of electrons, such as an exciton mechanism,[27,28] may explain the high T_c of the superconducting cuprates. However, in terms of the concept of coherent unpairing in the system of conduction electrons, it remains unclear why scattering of these electrons does not affect the coherence length and H_{c2}. The hypothesis of superconductivity by another carrier group becomes interesting in such a situation.

This work was supported by the Scientific Council of the RNTP on Current approaches in the physics of condensed media in the area of ''Superconductivity'' (Grant No. 98027) and by the Russian Fund for Fundamental Research (Grant No. 96-02-19696).

*)E-mail: natalia@shab.akzo.msk.ru

[1] V. L. Ginzburg, Zh. Éksp. Teor. Fiz. **23**, 236 (1952).
[2] L. P. Gor'kov, Zh. Éksp. Teor. Fiz. **37**, 1407 (1960) [Sov. Phys. JETP **10**, 998 (1960)].
[3] L. P. Gor'kov and T. K. Melik-Barkhudarov, Zh. Éksp. Teor. Fiz. **45**, 1493 (1963) [Sov. Phys. JETP **18**, 1035 (1963)].
[4] E. Helfand and N. R. Werthamer, Phys. Rev. **147**, 288 (1966).
[5] N. R. Werthamer, in *Superconductivity*, edited by R. D. Parks (Marcel Dekker, N. Y., 1969), Vol. 1, p. 321.
[6] W. H. Butler, Phys. Rev. Lett. **44**, 1516 (1980).
[7] E. Z. Meilikhov and V. G. Shapiro, Sverkhprovodimost: Fiz., Khim., Tekh. **4**, 1437 (1991).
[8] N. P. Shabanova, S. I. Krasnosvobodtsev, V. S. Nozdrin, and A. I. Golovashkin, Fiz. Tverd. Tela (St. Petersburg) **38**, 1969 (1996) [Phys. Solid State **38**, 1085 (1996)].
[9] A. I. Golovashkin, E. V. Pechen', and N. P. Shabanova, Tr. Fiz. Inst. Akad. Nauk SSSR **190**, 128 (1988).
[10] A. I. Golovashkin and N. P. Shabanova, Physica C **185–189**, 2709 (1991).
[11] S. I. Krasnosvobodtsev, N. P. Shabanova, E. V. Ekimov, V. S. Nozdrin, and E. V. Pechen', Zh. Éksp. Teor. Fiz. **108**, 970 (1995) [JETP **81**, 534 (1995)].
[12] N. P. Shabanova, S. I. Krasnosvobodtsev, V. S. Nozdrin, E. V. Pechen, A. V. Varlashkin, S. V. Antonenko, G. I. Zhabrev, and A. I. Golovashkin, Czech. J. Phys. **46**, 853 (1996).
[13] N. P. Shabanova, A. I. Golovashkin, E. V. Pechen, S. V. Antoneko, V. F. Elesin, and V. E. Zhuchkov, Physica C **235–240**, 1355 (1994).
[14] S. I. Krasnosvobodtsev, N. P. Shabanova, V. S. Nozdrin, E. V. Pechen', and A. I. Golovashkin, Kratk. Soobshch. Fiz. No. 1–2, 20 (1998).
[15] S. I. Krasnosvobodtsev, N. P. Shabanova, V. S. Nozdrin, E. V. Pechen, S. V. Antonenko, G. I. Zhabrev, and A. I. Golovashkin, Physica C **282–287**, 1291 (1997).
[16] V. S. Nozdrin, N. P. Shabanova, V. A. Dravin, and S. I. Krasnosvobodtsev, Kratk. Soobshch. Fiz. No. 5, 3 (1998).
[17] A. I. Golovashkin, E. V. Ekimov, S. I. Krasnosvobodtsev, V. P. Martovitsky, and E. V. Pechen, Physica C **162–164**, 715 (1989).
[18] V. S. Nozdrin, S. I. Krasnosvobodtsev, O. M. Ivanenko, P. V. Bratukhin, and K. V. Mitsen, Pis'ma Zh. Tekh. Fiz. **22**(24), 1 (1996) [Tech. Phys. Lett. **22**, 996 (1996)].
[19] J. Herrmann, M. C. Andrade, C. C. Almasan, R. P. Dickey, M. B. Maple, Wu Jiang, S. N. Mao, and R. L. Greene, Phys. Rev. B **54**, 3610 (1996).
[20] N. P. Shabanova, E. V. Pechen, S. V. Antonenko, V. F. Elesin, and V. E. Zhuchkov, Physica C **235–240**, 1341 (1994).
[21] P. W. Anderson, J. Phys. Chem. Solids **11**, 26 (1959).
[22] N. R. Werthamer, E. Helfand, and P. C. Hohenberg, Phys. Rev. **147**, 295 (1966).
[23] L. I. Glazman, A. E. Koshelev, and A. G. Lebed', JETP Lett. **46**, S123 (1988).
[24] L. I. Glazman, A. E. Koshelev, and A. G. Lebed', Zh. Éksp. Teor. Fiz. **94**, 259 (1988) [Sov. Phys. JETP **67**, 362 (1988)].
[25] S. V. Antonenko, A. I. Golovashkin, V. F. Elesin, I. A. Esin, V. E. Zhuchkov, S. I. Krasnosvobodtsev, E. V. Pechen', and I. A. Rudnev, JETP Lett. **47**, 314 (1988).
[26] V. F. Elesin and I. A. Rudnev, Sverkhprovodimost: Fiz., Khim., Tekh. **4**, 2055 (1991).
[27] V. L. Ginzburg, Zh. Éksp. Teor. Fiz. **47**, 2318 (1964) [Sov. Phys. JETP **20**, 1549 (1964)].
[28] W. A. Little, Phys. Rev. A **134**, 1416 (1964).

Translated by D. H. McNeill

Diagnostics of thermal kinetic coefficients in $YBa_2Cu_3O_{7-\delta}/LaAlO_3$ thin-film bolometers

A. M. Grishin

Royal Institute of Technology, S-100 44 Stockholm, Sweden

Yu. V. Medvedev and Yu. M. Nikolaenko

Donetsk Physicotechnical Institute, Academy of Sciences of Ukraine, 340114 Donetsk, Ukraine

(Submitted February 4, 1999)
Fiz. Tverd. Tela (St. Petersburg) **41**, 1377–1384 (August 1999)

An experimental method is developed for studying the film temperature as a function of time in a film–substrate–thermostat system irradiated by pulsed microwaves which yields numerical values for the thermodynamic coefficients of the film and substrate, as well as the thermal resistance of the film–substrate and substrate–thermostat interfaces. © *1999 American Institute of Physics.* [S1063-7834(99)00608-5]

The design of thin-film bolometers is based on optimization of the electrical and thermal characteristics of the film structure and all the structural features affecting power absorption and heat transfer. Solving this kind of problem requires an appropriate set of diagnostics for the film structure (in particular, for its thermodynamic coefficients). For a particular substrate material, if it is not a sufficiently perfect single crystal, this is important, since, for example, the thermal conductivity can depend substantially on the microscopic structure. In addition, modern bolometer designs often include an intermediate sublayer between the film and the dielectric substrate for the purpose of improving the film quality or, specially, of creating an additional thermal barrier.[1] A theoretical estimate of the thermal resistance at the interface between a film and substrate can be extremely approximate, even without such a sublayer.[2–5]

In this paper we develop a nonsteady-state method for monitoring the thermal resistance of film–substrate (R_{fs}) and substrate–thermostat (R_{st}) interfaces. The proposed method can also be used for determining the specific heat of the film (C_f) and substrate (C_s) in a single experiment.

This method is based on deducing the film temperature T_f as a function of time from experimental data on the time and temperature dependences of the film resistance during the evolution of a stationary nonequilibrium state in the film–substrate–thermostat system as the film is heated by microwaves or a dc current.

When a Joule heating power P_j is delivered to the film, the film is heated relative to the surrounding medium by $\Delta T = T_f - T_0$, where T_0 is the temperature of the thermostat. The heat generated in the film passes through the thermal resistance R_{fs} of the film–substrate interface, the internal thermal resistance $R_s = D/S\lambda_s$ of the substrate (D is the substrate thickness, S is the junction area, and λ_s is the thermal conductivity of the substrate material), and the thermal resistance R_{st}. Thus, three time constants are involved in establishing a thermal equilibrium in a film–substrate–thermostat system: $\tau_1 = C_f R_{fs}$ for establishing equilibrium at the boundary between the film and the substrate, $\tau_2 = C_s R_s$ for establishing equilibrium in the substrate, and $\tau_3 = C_s R_{st}$ for establishing equilibrium between the lower boundary of the substrate and the thermostat. After determining these characteristic time constants experimentally, along with the amplitude of the temperature drops at the substrate and at the substrate–thermostat interface, we can investigate the thermodynamic coefficients of the structure.

The advantage of the proposed modification of the time dependent method for determining the thermodynamic characteristics is the possibility of obtaining numerical values for the specific heats and thermal conductivities of the materials in the film structure. This is attainable because the Joule heating power released in the film by microwave radiation is normalized in a special way. Microwaves are used for technical convenience of channeling, time manipulation, and precise control of the power. In addition, microwaves are a relatively low-energy radiation, so its use eliminates the physical mechanisms by which superconductivity is directly suppressed when optical and infrared radiation are employed.[1]

1. EXPERIMENT

The design of the measurement cell we have used in the experimental studies of the function $T_f(t)$ is shown in Fig. 1. It is made of copper and consists of a circular waveguide flange. A cover is attached to the flange by a demountable junction and the film structure is glued to its inner surface. The structure is irradiated with microwaves from the film side. Microwave power is introduced into the measurement cell through a $7.2\times3.6\,\mathrm{mm}^2$ German silver waveguide that was copper coated on the inside. The measurement cell is placed in a nitrogen cryostat to cool it and is separated from the liquid nitrogen by an airtight can. Heat is exchanged between the measurement cell and the nitrogen through several copper conductors with a total thermal resistance of 10–100 K/W. The temperature of the measurement cell is controlled within the range 77–300 K by an electrical heater and is stabilized by an electronic device with a resolution of

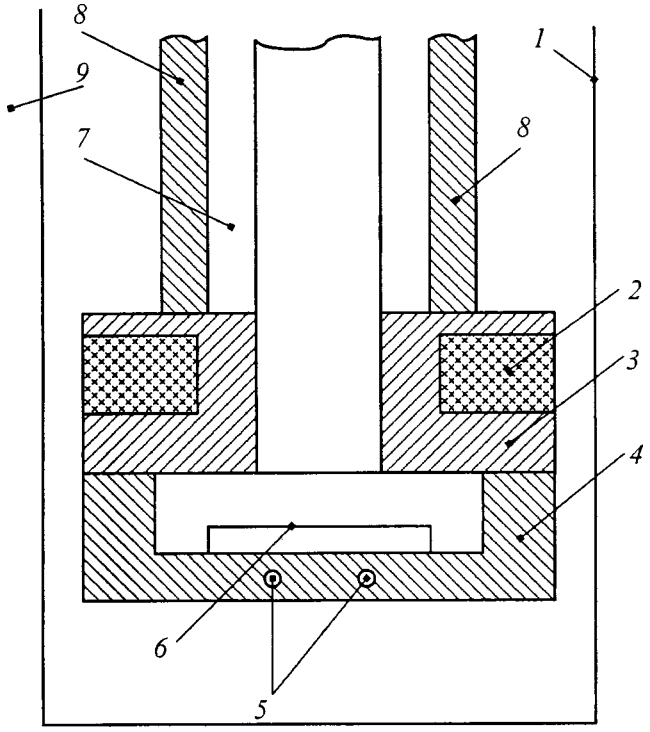

FIG. 1. Design of the measurement cell: (*1*) airtight ''can,'' (*2*) heater, (*3*) waveguide flange, (*4*) flange cover, (*5*) temperature probes, (*6*) film structure, (*7*) waveguide, (*8*) copper heat-transfer leads, (*9*) liquid nitrogen.

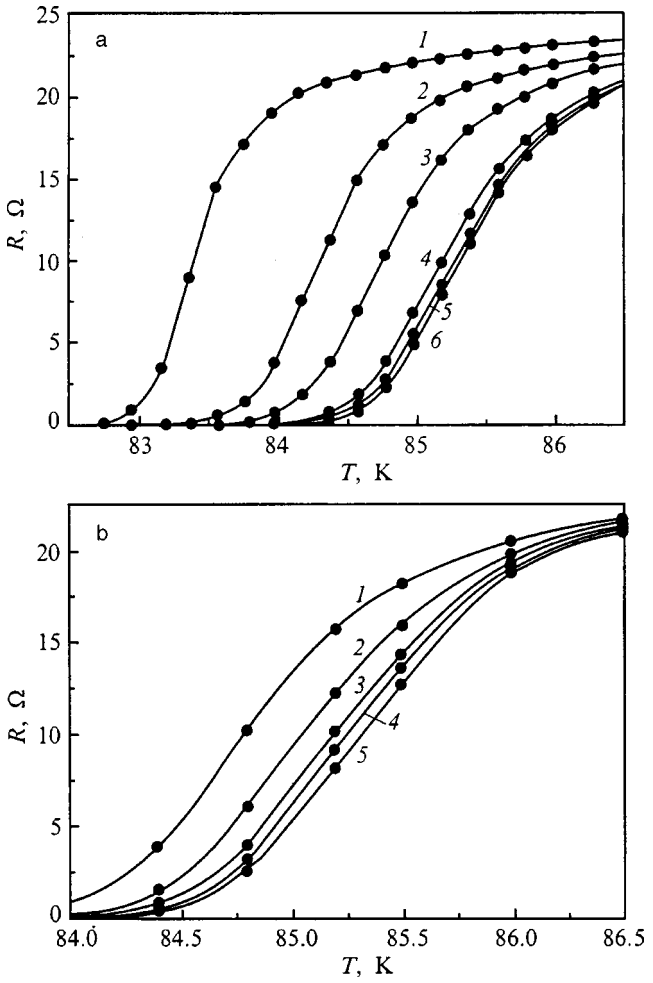

FIG. 2. Electrical resistance of $YBa_2Cu_3O_{7-\delta}/LaAlO_3$ films as a function of temperature. a — Constant measurement current (mA): *1* — 10; *2* — 7; *3* — 5; *4* — 2; *5* — 1; *6* — 0.1. b — Measurement current— 0.1 mA, microwave power attenuation (dB): *1* — 0; *2* — 3; *3* — 6; *4* — 9; *5* — ∞.

10^{-2} K.[6] The galvanic contacts are attached to the film in a four-probe circuit. Both dc and pulsed currents can be excited in the film through the resistive coupling. The pulsed current source and a two-conductor coaxial feed provide a rectangular current pulse with a risetime of less than 10^{-7} s in the superconducting films.

We have used a $Y_1Ba_2Cu_3O_{7-\delta}$ film with a thickness of 0.2 μm on a high quality single-crystal $LaAlO_3$ substrate with dimensions $9\times3\times0.5\,mm^3$ as a model structure. The distance between the contacts is 6.5 mm. The film was obtained by magnetron rf sputtering of a stoichiometric YBCO target in a mixed atmosphere of argon and oxygen on a substrate that was temperature controlled at $T=800$ °C and then annealed at 800 °C (for 1.5 min.) and 450 °C (30 min).[7]

The film is characterized by a superconducting transition onset temperature of about 87.5 K and a resistance of 10.08 Ω/□ at this temperature. The high nonohmic region, which is usually associated with a Kosterlitz–Thouless transition in a vortex system[8] or with the formation of a vortex glass state,[9] begins when the temperature is reduced below $T=83.75$ K. For $T>84$ K and transport currents that are not too high, the current–voltage characteristics are linear.

In the ohmic region, because a temperature difference develops between the film and the thermostat, the $R(T)$ curve undergoes a transition depending on the magnitude of the transport current (Fig. 2a). In our experiment, the magnitude of this effect is determined by the thermal resistance of the substrate–thermostat interface, which was deliberately chosen to be quite high. The change in the $R(T)$ curve, besides including a simple shift, develops because of a strong nonlinearity in $R(T)$ as the transport current increases and because of an additional heat release at the current contacts, whose resistance has a nonlinear temperature dependence similar to $R(T)$.

Depending on the microwave power (Fig. 2b), the change in the shape of the $R(T)$ curves for a low dc measurement current is also mainly caused by Joule heating in the film. The nonbolometric effect of the microwave power on the shape of the curves owing to the fast resistive response can be significant only for very low film resistances. As can be seen from Fig. 3a, at the microwave power levels used here, $\Delta V/I$ is on the order of $10^{-3}\,\Omega$ (ΔV is the voltage amplitude of the fast nonequilibrium response and I is the constant measurement current). The main reason for the change in the shape of the $R(T)$ curve (besides the shift) is the strong temperature dependence of the film impedance $Z(T)$ in the neighborhood of the superconducting transition[10] and, therefore, the variable amount of Joule heat released in the film at different temperatures. This prevents universal use of the $R(P_{\mu w},T)$ curve for normalizing the Joule heating power P_j.

The method for studying the time variation in $R(T)$ when microwave power is applied to a film is based on using

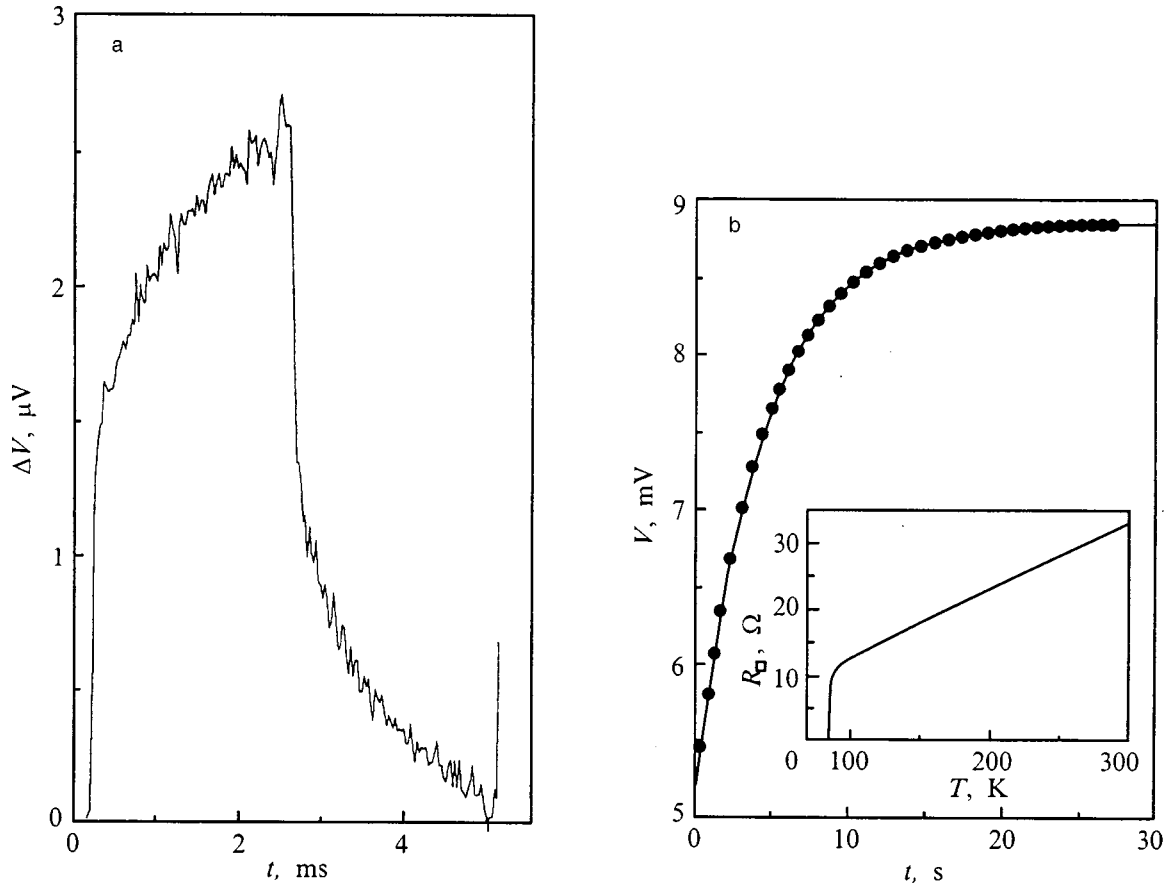

FIG. 3. Electrical resistance of a $YBa_2Cu_3O_{7-\delta}/LaAlO_3$ film as a function of time: a — with a sequence of rectangular microwave pulses with a reciprocal duty factor of 2 and duration 2.38 ms (experiment); b — (solid circles) — single (long) power pulse (experiment), smooth curve — calculation according to Eq. (10). Inset: temperature dependence of the electrical resistance of the film $R_\square(T)$.

an analog-to-digital converter with a maximum sampling rate of 10^6 Hz as a recording device. The voltages at the contacts on the film are stored in the computer memory in a linear time scale with different orders of magnitude for the time scales. We have used rather small measurement currents $I = 0.1-1$ mA so that the resulting power dissipation could be neglected compared to the Joule heating from the microwaves. The slowest processes with a time scale of the order of 1–10 s were recorded when the microwaves were turned on once. For smaller time scales, we used a sequence of microwave pulses with a reciprocal duty factor of 2. Figures 3a and 3b show the most informative portions of the $R(t)$ curve recorded in the periodic and single (long) pulse microwave power regimes.

The nature of the transition process characterized by the largest amplitude ΔR_3, a time constant $\tau_3 = 4.6$ s, and the emergence of the system into a stationary regime is easily established by varying the thermal resistance at the substrate–thermostat interface (R_{st}). When the substrate is attached to the surface of thermostat by a nondense point contact, R_{st} depends strongly on the pressure of the heat exchange gas. Thus, as the pressure of gaseous helium is increased, ΔR_3 and τ_3 both decrease.

The resistive response of the film shown in Fig. 3a is independent of the pressure of the heat transfer gas, i.e., it may be related to either the electrodynamics of the film or to heat transfer processes inside the film–substrate system. In terms of its structure, the resistive response contains at least two components with roughly equal amplitudes and highly different relaxation times. The fast component of the resistive response actually reproduces the shape of the original rectangular microwave pulse. The temperature dependence of its amplitude is shown in Fig. 4a. The maximum in this curve is shifted toward lower temperatures compared to the maximum of the derivative $R(T)$, which indicates that the effect is nonbolometric in nature. Our upper bound estimate for the relaxation time is 10^{-7} s on the basis of the risetime of the resistive response on the oscilloscope trace, and the lower bound is 2.5×10^{-12} s. This latter estimate was based on the observed exponential dependence of the amplitude of the fast resistive response compared to the amplitude of the temperature drop at the substrate– thermostat interface, ΔT_3, as the microwave frequency is raised over the range 38-78 GHz (Fig. 4b). A unique determination of the nature of the fast resistive response lies beyond the scope of this article, and a discussion of the possible physical mechanisms for this phenomenon can be found elsewhere.[11] The second component of the resistive response in Fig. 3a with a characteristic time scale τ_2 of order 10^{-3} s is caused by propagation of the heat flux within the substrate. This is easily confirmed, for example, by varying its thickness.

In order to analyze the temporal response of the bolom-

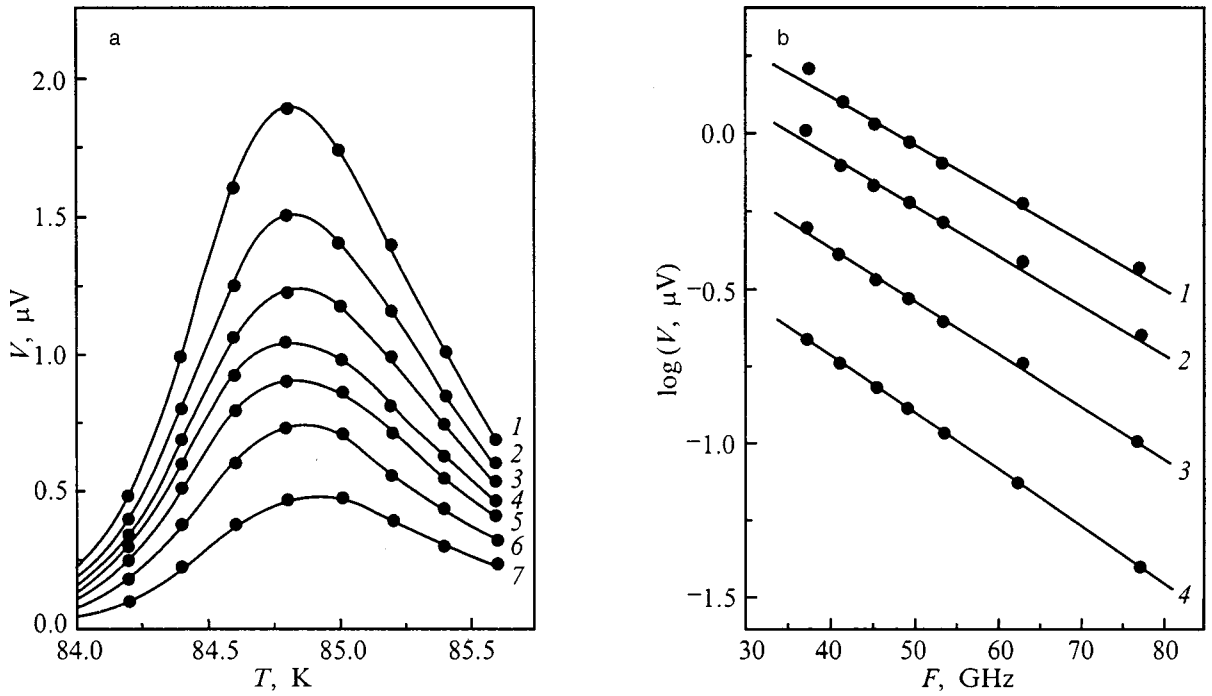

FIG. 4. Dependence of the amplitude of the fast resistive response of a $YBa_2Cu_3O_{7-\delta}/LaAlO_3$ film to microwave power on temperature (a) and on the microwave frequency (b). a — microwave frequency (GHz): *1* — 37.5; *2* — 41.5; *3* — 45.5; *4* — 49.5; *5* — 53.5; *6* — 63; *7* — 77. Measurement current $I=1$ mA. The attenuation of the power by the attenuator at $F-37.5$ GHz is -9 dB. For the other frequencies the power level is set so that the bolometric part of the resistive response (Fig. 3) is unchanged. b — film temperature (K): *1* — 84.6; *2* — 84.4; *3* — 84.2; *4* — 84.0.

etric resistivity curve, we shall analyze the time-temperature function of the film theoretically.

2. THE FUNCTION $T_f(t)$. THEORY

We now write down a system of equations for the propagation of a parallel heat flux in a film–substrate–thermostat system with an internal heat source in the film and a constant thermostat temperature T_0:

$$c_f\rho_f V_f(\partial T_f/\partial t)=-S\lambda_{fs}(T_f-T_s(x=0,t))+P_j(T), \quad (1)$$

and

$$c_s\rho_s(\partial T_s/\partial t)=\lambda_s\partial^2 T_s/\partial x^2. \quad (2)$$

Here c_f and c_s are the specific heat of the film and substrate materials, respectively, ρ_f and ρ_s are the densities of the film and substrate materials, respectively, and V_f is the volume of the film, and the thermal conductivity of the film–substrate interface is $\lambda_{fs}=(R_{fs}S)^{-1}$.

The initial and boundary conditions are

$$T_f=T_s=T_0, \quad t=0, \quad (3)$$

$$\lambda_s(\partial T_s/\partial x)=\lambda_{fs}(T_f-T_s(0)), \quad x=0, \quad (4)$$

and

$$\lambda_s(\partial T_s/\partial x)=\lambda_{st}(T_s(D)-T_0), \quad x=D. \quad (5)$$

We have assumed that the x axis is directed perpendicular to the plane of the film. The point $x=0$ is chosen to be at the film–substrate boundary. The point $x=D$ corresponds to the substrate–thermostat boundary. We neglect the temperature gradient in the film and take the thermal conductivities at the interfaces, $\lambda_{fs}=(R_{fs}S)^{-1}$ at $x=0$ and $\lambda_{st}=(R_{st}S)^{-1}$ at $x=D$, to be constant with respect to T for the given T_0. (We assume small temperature changes, i.e., $(T_f-T_0)\ll T_0$.) We also ignore instability effects owing to self heating of the film structure, which can occur because of the strong dependence $P_j(T)=\alpha(T)P_{\mu w}+I^2R$ (α is the microwave absorption coefficient).[12]

For a weak dependence, linearized over a small segment ΔT,

$$P_j(T)=I^2[R(T_0)+(\partial R/\partial T)\Delta T]+P_{\mu w}[\alpha(T_0)+(\partial\alpha/\partial T)\Delta T],$$

when there is no qualitative change in the temperature evolution, leading to a quantitative correction for the thermal conductivity of the form[1]

$$\lambda_{fs}^*=\lambda_{fs}(T)-\frac{1}{S}(I^2\partial R/\partial T+P_{\mu w}\partial\alpha/\partial T). \quad (6)$$

Figure 5 is a log-log plot of the film temperature as a function of time obtained by numerical solution of the system of Eqs. (1)–(5). These results are for a film of $Y_1Ba_2Cu_3O_{7-\delta}$ on a substrate of $LaAlO_3$ at $T=90$ K.[1,3,12–14] The film and substrate thicknesses are $l=1.7\times10^{-7}$ and $D=4\times10^{-4}$ m. The thermal conductivity of the film–substrate and substrate–thermostat boundaries are $\lambda_{fs}=10^7$ and $\lambda_{st}=130$ W/m^{2}K and the specific thermal conductivity of the substrate is $\lambda_s=18.14$ W/m K. The specific heat and density of the film and substrate materials are: $c_f=181.3$ J/kgK, $\rho_f=6.3\times10^3$ kg/m^3 and $c_s=163.4$ J/kgK, $\rho_s=6.51\times10^3$ kg/m^3.

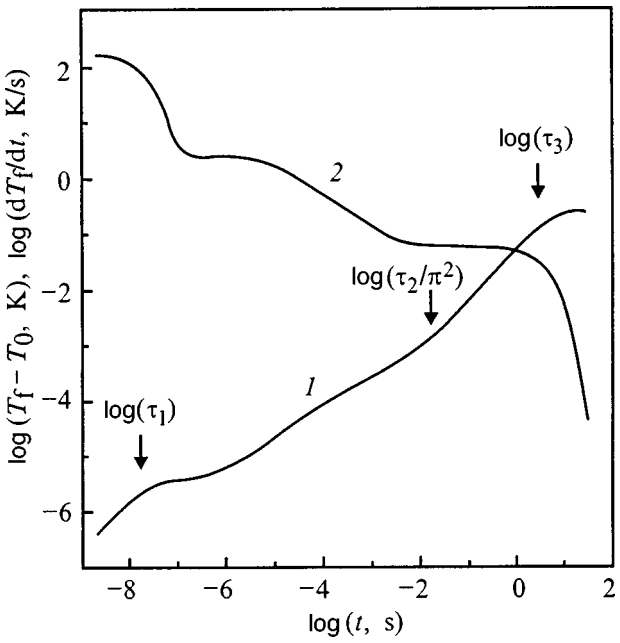

FIG. 5. Log-log plots of the time-temperature function of a film, $(T_f(t) - T_0)$ (*1*) and its derivative with respect to time (*2*) obtained by numerical solution of Eqs. (1) and (2) with the initial and boundary conditions (*3–5*) and parameters corresponding to a $YBa_2Cu_3O_{7-\delta}/LaAlO_3$ structure at $T = 90$ K.

The process of establishing a steady-state nonequilibrium state in which the film temperature is independent of time takes place in several stages, which are characterized by substantially different rates of change of the function $T_f(t) - T_0$ (Fig. 5).

At the time the heat source is turned on $(t=0)$, the film is heated at a maximum rate $\partial T_f/\partial t = P_j/C_f$ determined by the Joule heating power P_f and the specific heat $C_f = c_f \rho_f V_f$ of the film.

As the film temperature increases, a thermal flux into the substrate develops and the rate of heating of the film decreases sharply. In the idealized case where the substrate has an infinite heat capacity, over a characteristic time of $5\tau_1$ $(\tau_1 = R_{fs}C_f)$ a temperature difference of $\Delta T_1 = P_j \times R_{fs}$ is established at the film–substrate interface to within about 0.6%. The corresponding functional dependence

$$T_f(t) - T_0 = \Delta T_1(1 - \exp(-t/\tau_1)) \qquad (7)$$

is plotted on a linear time scale as curve *2* of Fig. 6a. Curve *1* of this figure was constructed taking the finite heat capacity of the substrate into account, i.e., it is part of the $T_f(t)$ curve in Fig. 5. Clearly, for times $t < 2\tau_1$, curves *1* and *2* coincide with great accuracy. For $t = 5\tau_1$, because curve *1* does not reach a steady state, a difference develops, which is about 6% in this case. The rate of heating of the film in the time from $t = 5\tau_1$ to roughly $50\tau_1$ is constant. This is quite evident from the behavior of $\partial T_f/\partial t$ (curve *2* of Fig. 5).

The next stage in the reduction in the rate at which the film is heated is associated with the propagation of heat into the depth of the substrate. In the case of a thermally isolated substrate-thermostat boundary, the time scale for reaching a steady-state heat flux in the substrate is given by τ_2/π^2,

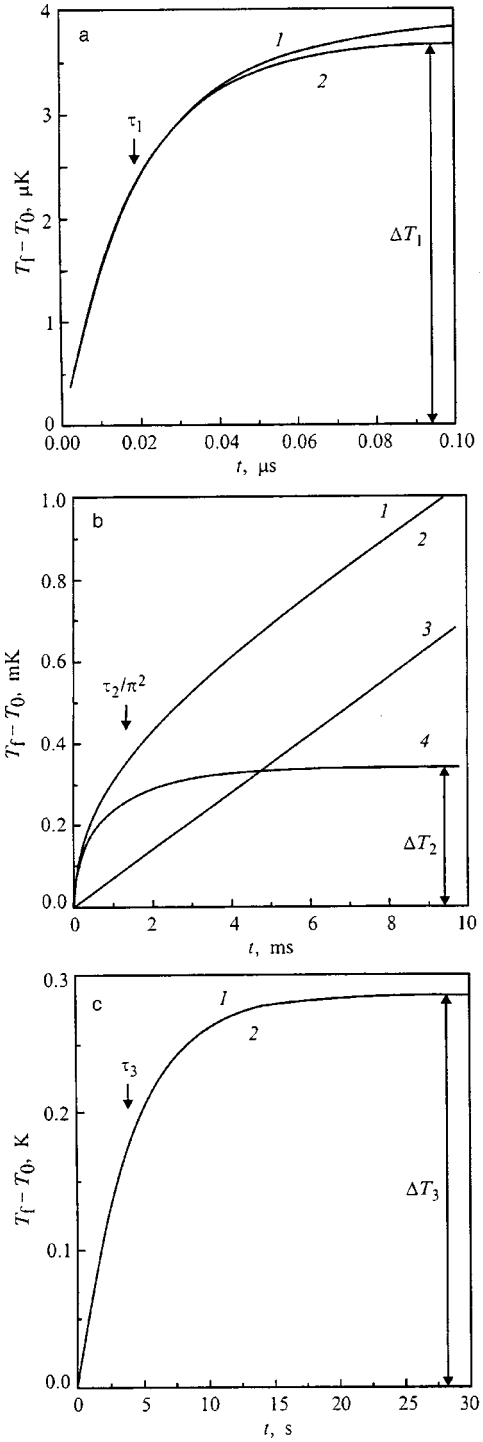

FIG. 6. Time-temperature function $(T_f(t) - T_0)$ on a linear time scale with scales of the order of the relaxation times for the thermal flux: at the film–substrate interface (τ_1) (a); over the substrate thickness (τ_2) (b); at the substrate–thermostat interface (τ_3) (c). *1* — numerical solution of Eqs. (1) and (2); *2* — calculated using the equations for the idealized processes: a — Eq. (7); b — Eq. (8); c — Eq. (9). *3* and *4* in Fig. 6b correspond to the linear and saturating parts of Eq. (8).

while the amplitude of the temperature difference that develops over the thickness of the substrate is $\Delta T_2 = P_j D/3S\lambda_s = P_j R_s/3$.[15] $T_f(t)$ is plotted in Fig. 6b on a linear time scale for two cases corresponding to a thermally isolated boundary[15]

TABLE I. Time constants τ_1 and temperature amplitudes $T_i (i=1-3)$, calculated for YBCO-film structures with thicknesses of 1.7×10^{-7} m on substrates with sizes of $9\times3\times0.5\,\mathrm{mm}^3$.

Substrate material (T_0)	c_s J/kg·K	ρ_s kg/m^3	λ_s W/m^2·K	λ_{fs} W/m·K	λ_{st} W/m·K	τ_1 ns	τ_3 ms	τ_3 s	ΔT_1 μK	ΔT_2 mK	ΔT_3 K
$LaAlO_3$	163.4	6520	18.14	10^7	130	19.4	14.7	4.10	3.70	1.02	0.29
(90 K)	–	–	–	10^6	–	194	–	–	37	–	–
	–	–	–	10^5	–	1940	–	–	370	–	–
Al_2O_3 (90 K)	94.4	3980	700	10^7	–	19.4	0.13	1.45	3.70	0.03	–
$SrTiO_3$ (90 K)	212	6400	4.50	–	–	–	75.4	0.29	3.70	4.12	–
MgO (300 K)	1160	3580	58.6	–	–	21.5	5.39	4.86	3.70	0.32	–

Note: The following parameter values were used in the calculations: $c_f=181.3$ J/kgK for $T=90$ K[16] and $c_f=352.9$ J/kgK for $T=300$ K.[17] The data for c_s and λ_s were taken from Ref. 16, for λ_{fs} — from Ref. 5.

$$T_s(0,t)=T_0+\frac{P_j t}{c_s\rho_s V_s}+\Delta T_2\left(1-\frac{6}{\pi^2}\sum_{n=1}^{\infty}\frac{1}{n^2}\times\exp\left(-n^2\pi^2\frac{t}{\tau_2}\right)\right) \tag{8}$$

and to a thermally conducting substrate–thermostat interface. In this case, the two curves coincide entirely. On a time scale of order τ_2/π^2, the function $T_s(t)-T_0$ is the sum of two functions corresponding to (1) the establishment of a temperature difference ΔT_2 over the substrate thickness as the heat flux reaches the substrate–thermostat boundary and (2) a rise in the average substrate temperature. The first function saturates, while the second increases linearly with slope $\partial T/\partial t=P_j/(C_s+C_f)$. The duration of the linear segment is determined by the thermal conductivity of the substrate–thermostat boundary, which, in turn, determines the time scale τ_3 for the system to reach a steady state. When the thermal resistance of the substrate–thermostat interface is much greater than that of the substrate (always possible in an experiment) and the temperature gradient in the substrate can be neglected compared to the difference between the average substrate temperature and the thermostat temperature when the thermal flux is attained (i.e., heating of the structure is being considered), the time constant $\tau_3=R_{st}(C_s+C_f)$, while the amplitude of the temperature difference at the substrate-thermostat interface is $\Delta T_3=P_j P_{st}$. The corresponding function

$$T_f(t)-T_0=\Delta T_3(1-\exp(t/\tau_3)) \tag{9}$$

is plotted on a linear scale in Fig. 6c. For a time scale on the order of τ_3, it is entirely the same as $T_f(t)-T_0$ calculated using Eqs. (1) and (2). This happens because for the given YBCO/$LaAlO_3$ structure, as for many others, the rigid inequalities $\tau_1\ll\tau_2\ll\tau_3$ and $\Delta T_1\ll\Delta T_2\ll\Delta T_3$ are satisfied, while for the accuracy of the figure with its linear axes cannot resolve ΔT_2 at the level of ΔT_3. Data on ΔT_1 and τ_1 calculated for YBCO-film structures on certain widely used substrates are listed in Table I.

If τ_3 greatly exceeds the transverse and longitudinal thermal relaxation times in the substrate, then the formula $\Delta T_3=P_j R_{st}$ can be used for normalizing the Joule heating power. Here we are speaking of normalizing $P_j=\alpha P_{\mu w}$ with respect to equivalent heating of the film structure in an amount ΔT_3 by a dc current, taking into account the heat release at the current contacts, $P_j=I^2(R+R_c)$, where R and R_c are the electrical resistances of the film and the current contacts.

Here we note some features of using rectangular pulses of duration t_0 with a period of $2t_0$. In this case, the film is periodically heated and cooled and, by varying the duration, it is possible to study any portion of the $T_f(t)$ curve. However, there will be no direct correspondence with the curves obtained by turning on the power once. If the pulse duration is chosen to be equal to $5\tau_1$, then, as noted above, over this time interval the film will heat up to within about 0.6% of its peak temperature, adequate for ordinary experimental measurements, provided the substrate is an ideal thermostat. Over the time the pulse is off, the film will cool to the substrate temperature with the same accuracy in accordance with $\Delta T_1\exp(-t_0/\tau_1)$. Since a real substrate has a finite heat capacity, the amplitude of the change in the film temperature will be somewhat greater, but the same as when the power is turned on once. The minimum film temperature against the background of which a periodic change takes place will differ from the thermostat temperature and will be greater by an amount $(\Delta T_2+\Delta T_3)/2$. The factor 1/2 appears because of the renormalization of the time averaged power taking the pulse duty cycle into account. Naturally, it is assumed that the variable component of the temperature is recorded after the pulsed power has been acting the film for long enough $(t\gg\tau_3)$.

In a similar fashion, by choosing a pulse duration t_0 equal to $5\tau_2$, we obtain a time-dependent regime which is convenient for recording the change in the film temperature caused by setting up a temperature difference across the substrate thickness. Here the amplitude of the periodic change in the film temperature will be the same as in the case of single

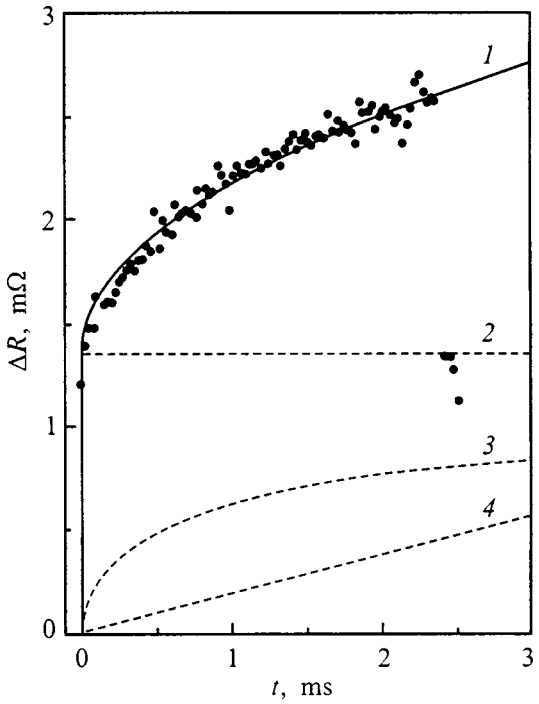

FIG. 7. The approximation (*1*) for the experimental $R(t)$ curve (points) as the sum of three functions: constant — *2*, saturating — *3* and linear — *4*. *3* — corresponds to calculating the saturating part of $R(t)=T_f(t)\partial R/\partial T$, with $T_f(t)$ given by the third term in Eq. (8) with the following parameters: $\tau_2=13.6$ ms, $\partial R/\partial T=2.68\ \Omega$/K, and $\Delta T_2(\partial R/\partial T)=2.7$ mΩ.

heating pulse, but the minimum temperature will be $T_0+\Delta T_3/2$.

3. ANALYSIS OF THE EXPERIMENTAL CURVES

The points in Fig. 3b represent the time dependence of the electrical resistance of the film for a thermostat temperature $T_0=85$ K recorded for a single pulse of microwave power at time $t=0$. The smooth curve in this figure corresponds to the formula

$$R(t,T_0)=R(0,T_0)+(\partial R/\partial T)\Delta T_3(1-\exp(-t/\tau_3)), \tag{10}$$

where $R(0,T_0)=5.15\ \Omega$, $\partial R/\partial T=9.81\ \Omega$/K, $\Delta T_3=0.376$ K, and $\tau_3=4.6$ s. The value of $\partial R/\partial T$ was obtained by taking the simplest linear approximation of the corresponding segment of the $R(T)$ curve. Taking a Joule heating power during microwave irradiation, normalized to the current dissipation $P_j=I^2(R+R_c)$, equal to 1.09×10^{-3} W, we obtain a value for the thermal resistance of the substrate–thermostat interface of $R_{st}=\Delta T_3/P_j=338$ K/W and a total heat capacity of the film and substrate of $C_f+C_s=\tau_3/R_{st}=1.36\times10^{-2}$ J/K. Note that here R is the resistance of the entire film and not just the part between the contacts.

The bolometric portion of the resistive response in Fig. 3a (see Fig. 7) is approximated by the sum of a linear function with slope $\partial R/\partial t=0.19\ \Omega$/s and a function which goes to saturation that corresponds to Eq. (8), $\Delta T_2^*\partial R/\partial T=0.9\ \Omega$, with $\tau_2=13.6$ ms. Taking $\partial R/\partial T=2.68\ \Omega$/K for $T_0=84.1$ K, we find: $\partial T/\partial t=7.08\times10^{-2}$ K/s and $\Delta T_2=3.37\times10^{-4}$ K. Note that the time scale for the saturating function in Eq. (8) is determined by τ_2/π^2 and it is, in fact, of the order of magnitude of the power pulse duration, while the minimum film temperature for $T_0=84.1$ K is $T_f=T_0+\Delta T_3/2=84.29$ K. Normalizing the Joule heating power at $T_0=84.1$ K ($P_j=0.96\times10^{-3}$ W), we obtain: $R_s=3\Delta T_2/P_j=1.06$ K/W and $C_s=P_j/(\partial T/\partial t)=1.34\times10^{-2}$ J/K. This implies that the thermal conductivity and specific heat of the substrate are $\lambda_s=17.47$ W/m K and $c_s=152.2$ J/kgK, respectively. They are in good order-of-magnitude agreement with the data of Ref. 13.

The time dependences corresponding to the establishment of thermal equilibrium throughout the thickness of the substrate and in the system as a whole are, therefore, easily recorded using standard experimental equipment and can be reliably identified. Note that, since only two experimental parameters are being determined here from a large number of experimental points (a curve), thorough optimization of the detector channel to eliminate noise is actually not required.

Faster equipment is required to measure the thermal resistance at the film–substrate interface by the method proposed here. This applies to the detection system, which must record data on a time scale of the order of 10^{-8} s, and to the microwave generator, which must provide a pulse risetime of 10^{-9} s as the power is manipulated. A study of R_{fs} using a pulsed optical technique has been published.[18]

The method developed here, together with a computer data analysis program, is suitable for making rapid measurements and may be useful for the systematic analysis of film structures. On the whole, this method can be used to separate the contribution of direct thermal effects during studies of electrodynamic effects in semiconductor and metal films, as well as of vortex dynamics phenomena in superconducting films.

[1] Z. M. Zhang and A. Frenkel, J. Supercond. **7**, 871 (1994).
[2] C. G. Levey, S. Etemad, and A. Inam, Appl. Phys. Lett. **60**, 126 (1992).
[3] M. Nahum, S. Verghese, P. L. Richards, and K. Char, Appl. Phys. Lett. **59**, 2034 (1991).
[4] C. D. Marshall, A. Tokmakoff, I. M. Fishman, C. B. Eom, J. M. Phillips, and M. P. Fayer, J. Appl. Phys. **73**, 850 (1993).
[5] O. V. Matyunina and A. V. Pogrebnyakov, Pis'ma Zh. Tekh. Fiz. **23**, 56 (1997) [Tech. Phys. Lett. **23**, 478 (1997)].
[6] V. M. Prozorovskiĭ and Yu. M. Nikolaenko, USSR Inventor's Certificate No. SU 1319000 MKI[3] G 05 D 23/19. Published June 23, 1987, Bulletin No. 23.
[7] J. H. Xu, B. M. Moon, I. L. Zhou, K. V. Rao, and G. G. Zhang, Proc. ICMAS-92, Paris (1992), p. 117.
[8] S. N. Artemenko and Yu. I. Latyshev, Mod. Phys. Lett. B **6**, 367 (1992).
[9] C. Dekker, R. H. Koch, B. Oh, and A. Gupta, Physica C **185–189**, 1799 (1991).
[10] E. K. Moser, W. J. Towasch, M. J. McClorey, J. K. Furdyna, and M. W. Coffey, Phys. Rev. B **49**, 4199 (1994).
[11] E. M. Gershenzon, M. E. Gershenzon, G. N. Gol'tsman, A. D. Semenov, and A. V. Sergeev, IEEE Trans. Magn. **27**, 2 (1991).
[12] Yu. D. Varlamov, A. N. Volkov, M. R. Predtechenksiĭ, A. N. Smal', and A. V. Turbin, Sverkhprovodimost' **5**, 1736 (1992).
[13] Peter C. Michael, John U. Trefny, and Baki Yarar, J. Appl. Phys. **72**(1), 107 (1992).

[14] I. G. Kozhevnikov and L. A. Novitskiĭ, *Thermophysical Properties of Materials at Low Temperatures* (Mashinostroenie, Moscow, 1982), 328 pp.
[15] H. Carslaw and G. Jaeger, *The Conduction of Heat in Solids*, (GIFML-Nauka, Moscow, 1964), 487 pp.
[16] M. B. Salamon, S. E. Inderhees, J. P. Rice, B. C. Pazol, D. M. Ginsberg, and N. Goldenfeld, Phys. Rev. B **83**, 885 (1988).
[17] A. Jung, A. Bezingem, D. Cattani, M. Decroux, D. Eckert, M. Francois, A. Hewat, J. Muller, and K. Yvon, Helv. Phys. Acta **61**, 460 (1988).
[18] A. Yu. Klokov, T. I. Galkina, and A. F. Plotnikov, Fiz. Tverd. Tela (St. Petersburg) **40**, 191 (1998) [Phys. Solid State **40**, 169 (1998)].

Translated by D. H. McNeill

SEMICONDUCTORS. DIELECTRICS

Free electronic states of UO_2: analysis of x-ray absorption by total multiple scattering

G. É. Yalovega and A. V. Soldatov*)

Rostov State University, 344090 Rostov-on-Don, Russia
(Submitted October 20, 1998)
Fiz. Tverd. Tela (St. Petersburg) **41**, 1385–1388 (August 1999)

The experimentally observed x-ray absorption spectrum of oxygen in UO_2 is analyzed theoretically. The experimental absorption spectrum of oxygen is shown to agree well with details of the density of free *p* states of oxygen in the conduction band. It is found that a minimum cluster of atoms surrounding an absorbing oxygen ion required to reproduce all the details of the fine structure of the density of states at the bottom of the conduction band is of the order of 40 atoms. An analysis of the densities of the electronic states reveals the existence of hybridization of free *p* states of oxygen with *s* states of uranium in the conduction band of UO_2, as well as the exclusion of *p* states of oxygen by *d* states of uranium beyond the confines of the energy interval where they are localized.
[S1063-7834(99)00708-X]

The subtle details of the electronic structure of strongly correlated electronic systems and, in particular, of UO_2 are still a matter of discussion.[1] Most of the unique properties of these compounds are determined by the interaction of the $5f$ states of uranium among themselves and with other electronic states of the compound. The effects of the localization and delocalization of the $5f$ electronic states of uranium have very recently been studied experimentally[2] and theoretically.[3] X-ray absorption spectroscopy at the $L_{2,3}$, $M_{2,3}$ and $M_{4,5}$ edges of uranium has been invoked in studies of the electronic subsystem of UO_2.[4–6] Without a theoretical interpretation of the experimental x-ray spectra, it is impossible to determine the electronic structure of a given material. However, because the photoelectrons are excited from highly localized regions when the above x-ray spectra are formed, theoretical interpretation of the experimentally observed spectra is extremely difficult. It should also be noted that not only the $5f$ state of uranium, but also the other states with which the $5f$ states interact, must be studied in order to clarify the behavior of the electronic system of the uranium oxides. Thus, x-ray absorption has been measured in the region of the characteristic absorption jump of the ligand atoms (the oxygen *K* edge).[7] The theoretical analysis of these data, however, was not very successful. In this paper we present a theoretical analysis of the experimentally absorption spectrum of oxygen[7] by the complete-multiple-scattering method, which yields new information on the details of the electronic structure in the conduction band of UO_2.

1. COMPUTATIONAL METHOD

The algorithm for the complete-multiple-scattering method used in the present calculations has been described in detail elsewhere.[8] In the calculations, a fluorite unit cell with a lattice constant of $a = 5.47$ Å was employed.[9] The cluster formed by nearest-neighbor atoms of a central oxygen atom is divided into spheres as shown in Table I. A crystal muffin–tin (MT) potential with adjoining MT spheres was derived for calculating the phase shifts. The MT radii and MT constants which we obtained by this procedure for constructing the MT potential[8] are listed in Table II. In calculating the crystal potential we used a Mattheis approximation with Slater exchange. The atomic charge densities were obtained by a self-consistent field method taking relativistic effects into account with the Dirac equations. The calculations included phase shifts with orbital angular momenta up to four for all the atomic species. The only remaining parameter is the set of MT radii.

Various methods have been proposed before for choosing the MT radii. Some authors recommend using MT spheres which are tangent at the point where the potentials intersect along directions joining nearest atoms or which minimize the potential jump in the case of polyatomic compounds. In other cases, the best results have been obtained using values averaged between the ionic and atomic (covalent) radii. Another criterion using tangent MT spheres minimizes the total electronic charge contained in the intersphere region. There is also the Normal criterion, which is now widely used. In the present group of programs, the average of the discrepancies of the potentials, averaged in the region between an MT sphere and a Wigner–Seitz sphere, are minimized. (A Wigner–Seitz sphere is taken to be a sphere whose volume equals that of a Wigner–Seitz cell.) Usually it is possible to find a set of tangent or almost tangent MT spheres, but in some special cases (for example, to reproduce a covalent bond, as some authors recommend) MT spheres that overlap to 10-20% can be used. This choice of MT spheres is done automatically using the algorithm for minimizing the function. The Fermi distribution function was included for comparing the theoretical spectrum, obtained from the partial density of states and the dipole matrix element of the transition, with the experimental spectrum.

TABLE I. Structure of clusters of atoms surrounding a central absorbing oxygen atom in a UO_2 crystal.

Sphere number	Atom	Number of atoms in sphere	Radius of sphere (Å)
1	U	4	2.367
2	O	6	2.734
3	O	12	3.866
4	U	12	4.534
5	O	8	4.735

The theoretical spectra in all the figures are given in a normalized form (i.e., the absorption coefficient relative to the atomic coefficient at high energies). In order to obtain absolute units for the absorption coefficient these normalized values are multiplied by the corresponding value of the atomic absorption coefficient.

2. RESULTS AND DISCUSSION

The first stage of a theoretical analysis of the x-ray absorption spectrum of oxygen in UO_2 is to choose the minimum cluster size surrounding an atomic oxygen absorber which describes all the details of the absorption spectrum. Figure 1 compares the theoretically calculated *K*-absorption edge of oxygen in UO_2 for different cluster sizes. The partition of the cluster of atoms into spheres is listed in Table I. An analysis of the data shown in Fig. 1 shows that the three major structural details of the absorption spectrum (*A*, *B*, and *C*) show up only when at least four spheres are included in the surroundings of the absorber atom. This indicates that the x-ray absorption spectrum of the oxygen in UO_2 is the result of multiple scattering of photoelectron waves in large atomic clusters (at least 35 atoms). The need to include a large number of surrounding atoms is typical for materials with a high degree of crystal lattice symmetry.[10]

The data shown in Fig. 1 were obtained for the ground-state potential of the electronic subsystem of UO_2. During absorption of x rays, a photoelectron moves in the field of an absorbing oxygen atom with a vacancy in the inner 1*s* level, on which external electrons relax. Thus, for comparison with the experimental spectrum we have done the calculation for the relaxation potential in the Z_1-st approximation.[11] Figures 2a and 2b show a comparison of the theoretical and experimental spectra. The spectra are in good agreement in terms of the energies of the major details in the spectrum. Some differences in the shape of the spectra occur because, in calculating the theoretical spectrum, we have neglected some

TABLE II. Muffin-tin radii R_{mt} and muffin-tin constants V_0 (the zero in energy is at the vacuum level).

Atom	R_{mt} (Å)	V_0 (eV)
O	0.77	−22.24
U	1.40	−21.62

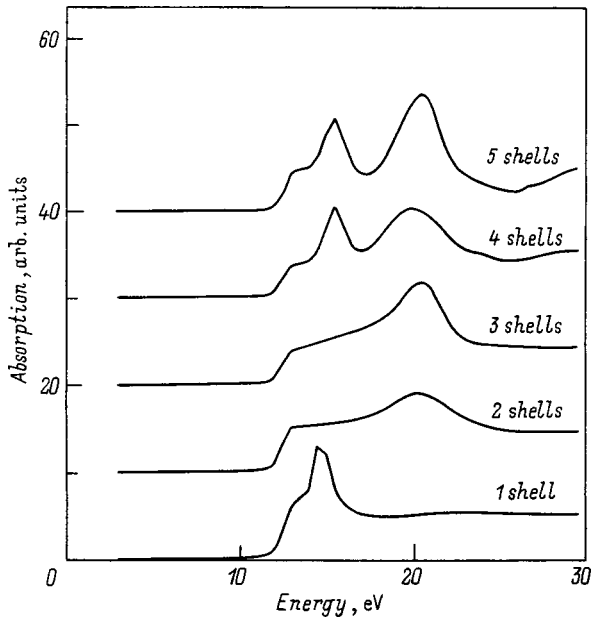

FIG. 1. Transition probability in the region of the x-ray absorption *K* edge of oxygen in UO_2 calculated for clusters of different sizes.

factors leading to broadening of the spectrum, specifically: the finite ''hole'' lifetime, the photoelectron mean free path, and the experimental resolution.

In the dipole approximation the x-ray absorption coefficient $a(E)$ for the *K* edge absorption of oxygen is proportional to the product of the square of the dipole transition probability matrix element and the density of free *p* states of the oxygen,[11] i.e.,

$$a(E) \sim |m_L(E)|^2 N_p^0(E).$$

Here $N_p^0(E)$ is the partial density of the free *p* states of oxygen and

$$m_L(E) = \frac{\int dr\, \Phi_1(r,E)\Delta(r)\Psi_c(r)}{\left[\int dr\, \Phi_1^2(r,E)\right]^{1/2}}$$

is the normalized dipole transition matrix element, where $\Phi_1(r,E)$ is the solution of the radial Schrödinger equation for the energy *E* for the MT potential ($l=1$ for the *K* edge), $\Delta(r)$ is the electron- photon interaction operator, and $\Psi_c(r)$ is the wave function of the core *K* level.

Figure 2c shows the transition probability matrix element as a function of the energy of the x-ray photon. Its weak dependence on the photon energy shows that the experimental absorption spectrum should agree fairly well with the density of the free *p* states of oxygen as a function of energy in the conduction band of UO_2. Therefore, this analysis of the absorption coefficient of oxygen as a function of the atomic cluster size (Fig. 1) indicates that such a specific characteristic of the electronic subsystem of a solid as the free-electron density of states in the conduction band of UO_2 also acquires its major details in a cluster of similar size (of the order of 40 atoms).

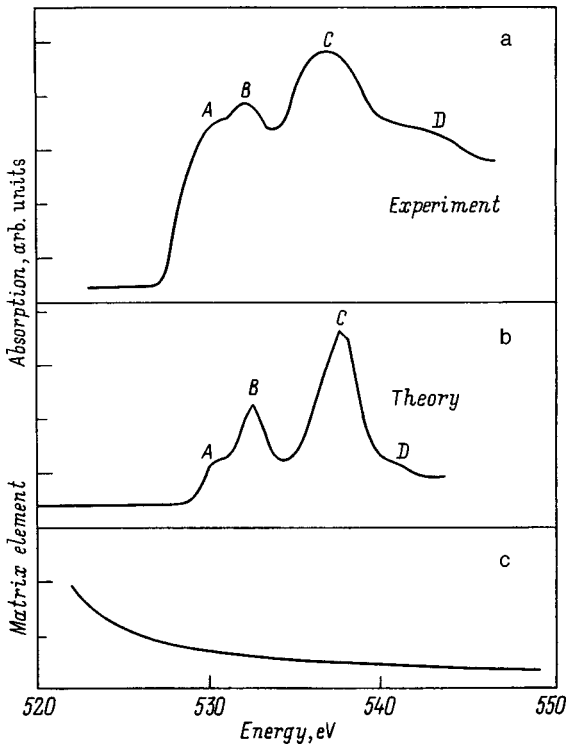

FIG. 2. Comparison of an experimental x-ray absorption spectrum in the neighborhood of the oxygen K edge[7] (a) with a theoretical calculation by the total multiple scattering method for a cluster of five spheres (b) (see Table I). (c) The square of the transition probability matrix element as a function of x-ray photon energy. All the spectra are in relative units.

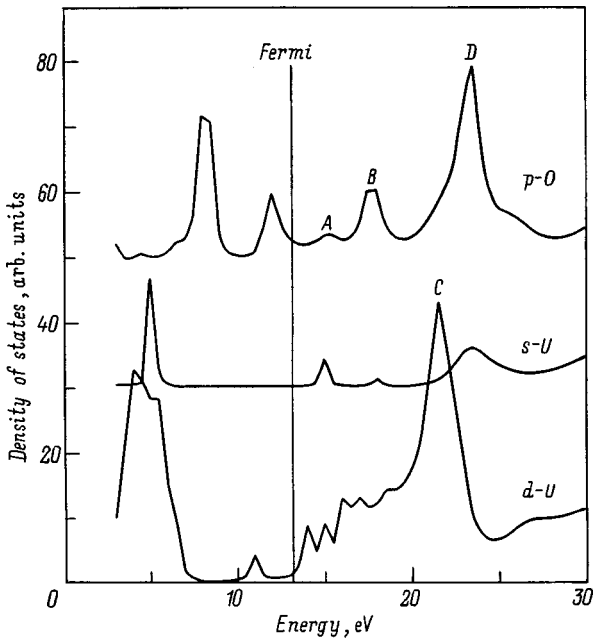

FIG. 3. Partial densities of the electronic states of UO_2. The vertical line approximates the location of the Fermi level.

The observed agreement between the theoretical and experimental spectra evidences adequacy of the scheme used to construct the crystal potential for describing the electronic structure of UO_2. The same potential was used to calculate the s and d states of uranium. A combined analysis of the shapes of the calculated densities of electronic states is shown in Fig. 3. Is can be seen that states below the Fermi level (the top of the valence band) mainly have the p symmetry of oxygen while, in the lower part of the conduction band, the states have a mixed character. In regions A and B, the oxygen p states are hybridized with uranium states, and in region C, a unique resonant interaction of the localized d states of uranium with delocalized p states of oxygen and s states of uranium is observed, specifically, uranium d states squeeze the oxygen p and uranium s states out of this region. In the region of the free states, we have observed this effect before in studies of the x-ray absorption spectra of $LaFeO_3$[12] and the orthoferrites.[13] An analogous effect has been observed for the region of filled electron states in a whole series of compounds[14] and is referred to as an $s(p)-d$ resonance.

These results yield the following conclusions.

(1) The fine structure of the x-ray K absorption edge of oxygen is extremely sensitive to the distribution of the electron density of the free states in the conduction band of UO_2. Thus, the method described here is exceedingly promising for studying the electronic structure of oxygen-containing compounds of the actinides.

(2) The electron density of the free states in the conduction band of UO_2 can be described by complete multiple scattering of a photoelectron wave within a large atomic cluster (in this case on the order of 40 atoms).

(3) Free p states of oxygen are hybridized with s states of uranium at the bottom of the conduction band of UO_2, while the d states of uranium interact with the p states of oxygen in a particular way, such that the localized d states exclude delocalized p states of oxygen beyond the energy interval in which they are located.

*)E-mail: soldatov@phys.rnd.runnet.ru

[1] *Actinides-93 Conference Proceedings*, edited by D. Clark, D. E. Hobart, and J. Fuger (Elsevier, 1994).
[2] M. Koga, W. Liu, M. Dolg, and P. Fulde, Phys. Rev. B **57**, 10 648 (1998).
[3] S. L. Molodtsov, J. Boysen, and M. Richter, Phys. Rev. B **57**, 13 241 (1998).
[4] J. Petiau, G. Calas, D. Petitmaire, and A. Bianconi, Phys. Rev. B **34**, 7350 (1986).
[5] J. Guo, D. E. Ellis, E. Apl, L. Soderholm, and G. K. Shenoy, Phys. Rev. B **39**, 6125 (1989).
[6] G. Kalkowski, G. Kaindl, W. D. Brewer, and W. Krone. Phys. Rev. B **35**, 2667 (1987).
[7] F. Jollet, T. Petit, S. Gota, N. Thromat, and M. Gautier-Soyer, J. Phys.: Condens. Matter **9**, 9 393 (1997).
[8] S. Della Long, A. V. Soldatov, M. Pompa, and A. Bianconi, Comput. Mater. Sci. **4**, 199 (1995).
[9] R. W. Wyckoff, *Crystal Structure* (Interscience, N. Y., 1963).
[10] A. V. Soldatov and T. S. Ivanchenco, AIP Press, N. Y. (1997), p. 737.
[11] A. Bianconi, in *X-ray Absorption: Principles, Applications and Techniques of EXAFS, SEXAFS and XANES*, edited by R. Prinz and D. Koningsberger (Wiley, N. Y., 1989).
[12] A. V. Soldatov, N. A. Povahzynaja, and G. E. Yalovega, J. Phys. (France) **7**, C2–517 (1997).
[13] A. V. Soldatov, Solid State Commun. **97**, 53 (1996).
[14] E. P. Domashevskaya and V. A. Terechov, Phys. Status Solidi B **105**, 121 (1981).

Translated by D. H. McNeill

Selective laser spectroscopy of localized excitons in GaSe–GaTe solid solutions in a magnetic field

A. N. Starukhin, B. S. Razbirin, and A. V. Chugreev

A. F. Ioffe Physicotechnical Institute, Russian Academy of Sciences, 194021 St. Petersburg, Russia

M. Happ and F. Henneberger

Universität Humboldt, Berlin, Germany
(Submitted December 29, 1998)
Fiz. Tverd. Tela (St. Petersburg) **41**, 1389–1393 (August 1999)

The Zeeman effect in the emission spectra of localized excitons in semiconductor solid solutions has been studied by selective laser spectroscopy. It was shown that the fine structure appearing in the emission spectra of $GaSe_{1-x}Te_x$ crystals under resonant monochromatic excitation in a magnetic field originates from spin relaxation of the light-induced localized excitons between their Zeeman sublevels. The localized-exciton g factor and its dependence on the energy of localized-exciton formation and solid-solution composition has been measured. © *1999 American Institute of Physics.* [S1063-7834(99)00808-4]

Many features in the electron energy spectrum of semiconductor solid solutions can be described successfully in terms of band theory in the effective, or virtual ideal-crystal approximation.[1,2] In contrast to an ideal crystal, however, fluctuations in the solid-solution composition generate a fluctuating electronic potential, which is responsible for the existence of mobility edges for electrons and holes and for the formation of tails in the density of localized states.[3] Coulomb interaction of localized electrons (or holes) with carriers of opposite sign gives rise to formation of stable two-particle states, i.e., localized excitons.[4–6] Emission and absorption of light by localized excitons (LE) at low temperatures accounts to a considerable extent for the near-band-edge features in the optical spectra of semiconductor solid solutions.

Depending on the angular momentum states of the electron and the hole in the exciton, the excitonic states are characterized by different magnitude and orientation of the total angular momentum (total spin) of the exciton. Studies of the Zeeman effect at excitons may provide important information on the spin structure and properties of excitonic states. The Zeeman splitting of the exciton ground state is usually about ~ 0.1 meV/T, and therefore the possibility of such studies is restricted to a large extent by the width of the exciton emission (absorption) lines. The energy levels of localized excitons form a quasicontinuum, so that optical transitions involving LEs manifest themselves in optical emission and absorption spectra as broad bands even at helium temperatures, which precludes application of efficient high-resolution spectroscopy to the investigation of the LE energy structure. A similar situation existing in molecular spectroscopy suggested the use of laser-induced narrowing of the inhomogeneously broadened molecular emission bands, which is based on selective population by monochromatic (laser) light of excited molecular states in a very narrow energy interval within the broad band of their resonant emission.[7] This method permitted one to perform first-time studies of complex molecules in disordered media.[8]

This paper reports a direct observation of the Zeeman effect on localized excitons in semiconductor solid solutions made under selective laser excitation. This permitted us to determine for the first time in an optical experiment the effective LE g factor and to study its dependence on the exciton localization energy and the solid-solution composition. GaSe–GaTe solid solutions were chosen as model objects for the investigation.

1. EXPERIMENTAL

Gallium selenide and telluride crystals belong to the group III–VI layered crystals. The $GaSe_{1-x}Te_x$ solid solutions ($x=0.15$ and 0.22) were grown by the Bridgman method and were not doped deliberately. The samples for the study were cleaved from ingots along the crystal-layer plane perpendicular to the crystal optic axis c. The luminescence in the solid solutions was excited by a tunable dye laser pumped by an argon laser. The excitation power was about 50 mW. The pump beam impinged on the sample surface at a small angle to the normal and the radiation was measured along the normal. The samples were placed in a transparent cryostat cooled with liquid helium. The magnetic fields were generated by a superconducting solenoid. The spectra were measured with a diffraction spectrometer.

2. EXPERIMENTAL RESULTS AND THEIR DISCUSSION

Figure 1 presents an LE luminescence spectrum of $GaSe_{0.78}Te_{0.22}$ excited by light with photon energy in excess of the energy of formation of direct free excitons, $E_{n=1} \approx 1.985$ eV in the mixed crystal. The spectrum represents an asymmetric band of width $\Delta(h\nu)=23$ meV located in the energy region $h\nu \leqslant E_{n=1}$. The band shape reflects the LE distribution in states with different localization energies,[9,10] the position of the short-wavelength edge corresponding to the LE formation energy at the mobility edge E^m (Ref. 9).

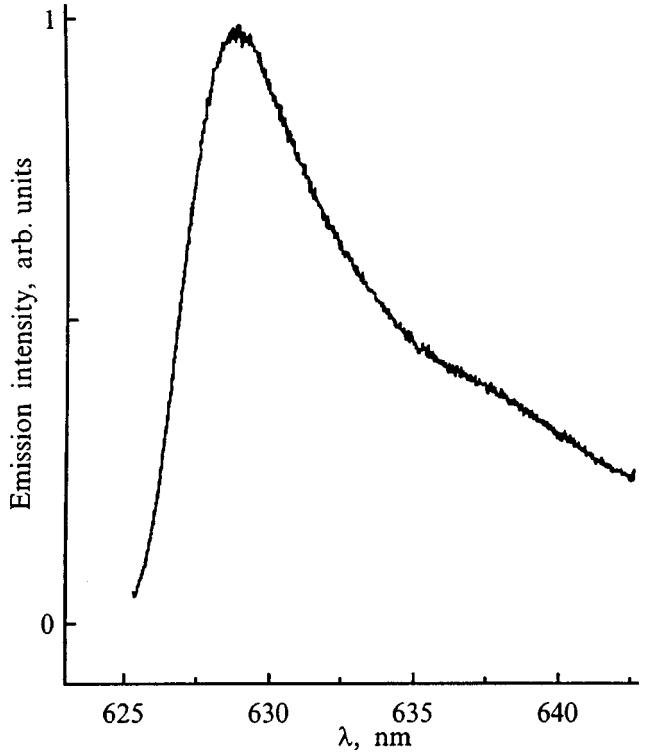

FIG. 1. Luminescence spectrum of a $GaSe_{0.78}Te_{0.22}$ solid solution under interband excitation. $T=6$ K, $B=0$.

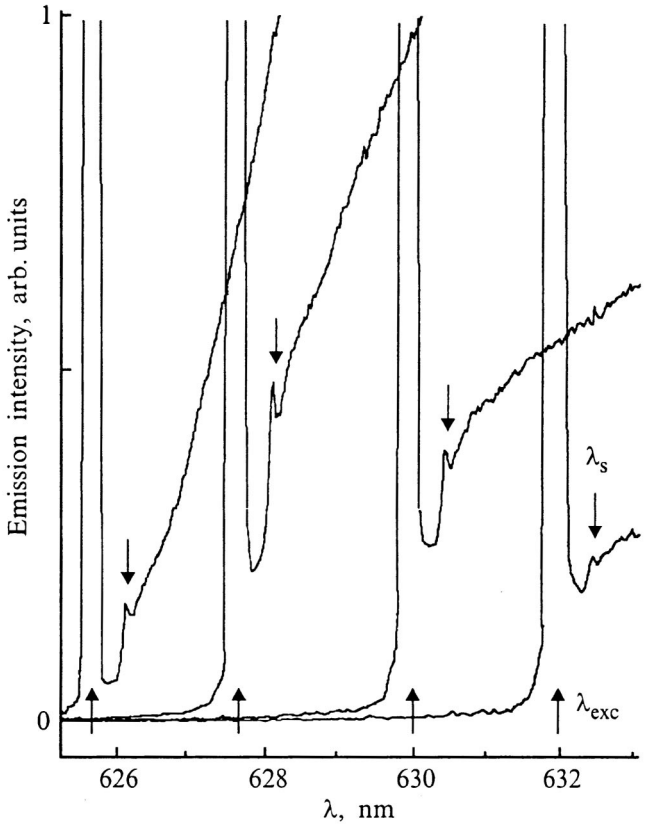

FIG. 2. Fragments of emission spectra of a $GaSe_{0.78}Te_{0.22}$ solid solution excited by light of different wavelengths λ_{exc} in a magnetic field $B=7.5$ T. Faraday geometry. $T=6$ K. The spectra relate to the radiation component polarized orthogonally to the pump polarization.

The luminescence intensity decreases rapidly with increasing crystal temperature. The shape of the luminescence band, its spectral position, and the temperature dependence are typical of localized excitons.

Exciting the solid solution with photons $h\nu_{exc}<E^m$ (with the pump frequency swept within the LE emission band) changes the band shape. This change in shape is due to the fact that, out of the LE spectrum presented in Fig. 1, only LE states with the formation energy $E_{LE}=h\nu_{exc}$ are populated (resonantly) in these conditions. At low temperatures, the photogenerated LEs can tunnel subsequently only to states having lower energies, $E_{LE}<h\nu_{exc}$, whereas states with $E_{LE}>h\nu_{exc}$ (which correspond to the part of the emission band in Fig. 1 lying short of the pump line) cannot be populated.

2.1. Magneto-optic effect

Application of an external magnetic field $\mathbf{B}\|\mathbf{c}$, $\mathbf{B}\|\mathbf{k}_{light}$ (Faraday geometry) in the conditions of resonant LE excitation by monochromatic laser light produces a striking effect, namely, starting from fields $B\geqslant 3$ T, a narrow emission line *S*, about 0.2 meV wide, appears at top of the broad emission band on the long-wavelength side of the pump line (Fig. 2). (The *S* line is seen most clearly when detecting the radiation in the polarization orthogonal to that of the pump light.) As the energy of the exciting photons approaches the mobility edge in the exciton system ($h\nu_{exc}\rightarrow E^m$), the line drops steeply in intensity. The *S* line shifts toward longer wavelengths with increasing magnetic field (but at a fixed $h\nu_{exc}$) (Fig. 3), with the energy distance $\Delta E=h\nu_{exc}-h\nu_S$ between the pump line and the *S* line varying proportional to *B*:

$$\Delta E=g\mu_B B\,, \tag{1}$$

where μ_B is the Bohr magneton, and coefficient $g=3.4\pm 0.2$. The LE luminescence spectra obtained from $GaSe_{0.85}Te_{0.15}$ mixed crystals exhibit a similar magneto-optic effect under selective laser excitation (Fig. 4), but for $GaSe_{0.85}Te_{0.15}$ g is different: $g=3.8\pm 0.2$.

2.2. Analysis of the results

Let us analyze the specific features in resonant LE excitation by monochromatic light. For $x\leqslant 0.35$, $GaSe_{1-x}Te_x$ direct-gap solid solutions retain the symmetry of the GaSe crystals (D^1_{3h}), which, by analogy with the $GaSe_{1-x}S_x$ solid solutions,[2] suggests a similarity between the band structures of GaSe and $GaSe_{1-x}Te_x$ within the above compositional range. In GaSe crystals, the ground state of the direct free exciton, with the exchange interaction taken into account, splits into two states, a singlet and a triplet (the splitting Δ_1 between these states is 2 meV).[11] The total spin of the electron and the hole in the singlet exciton is zero. The state of singlet excitons in a magnetic field should exhibit only a weak diamagnetic shift.[11] Singlet excitons are optically active only in the $\mathbf{E}\|\mathbf{c}$ polarization and are not seen in our experimental conditions.

Triplet excitons are characterized by a total spin $S=1$ and spin projections on the $\mathbf{c}$ axis $S_z=0,\pm 1$. Transitions to the $S_z=\pm 1$ states are allowed in the $\mathbf{E}\perp\mathbf{c}$ polarization, and

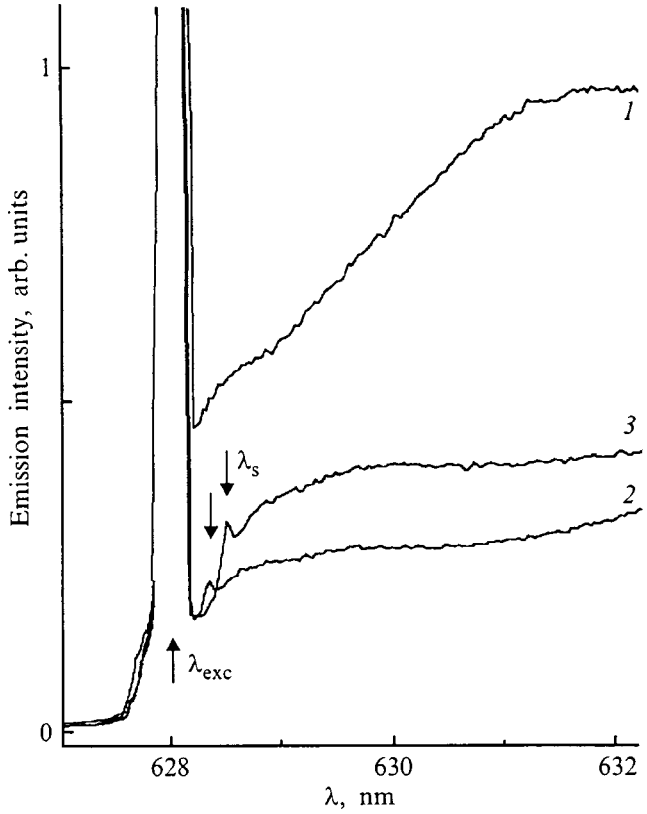

FIG. 3. Emission spectra of a $GaSe_{0.78}Te_{0.22}$ solid solution obtained under selective excitation vs magnetic field. $\lambda_{exc}=628.0$ nm. Faraday geometry, $T=6$ K. B(T): *1* — 0, *2* — 5, *3* — 7.5.

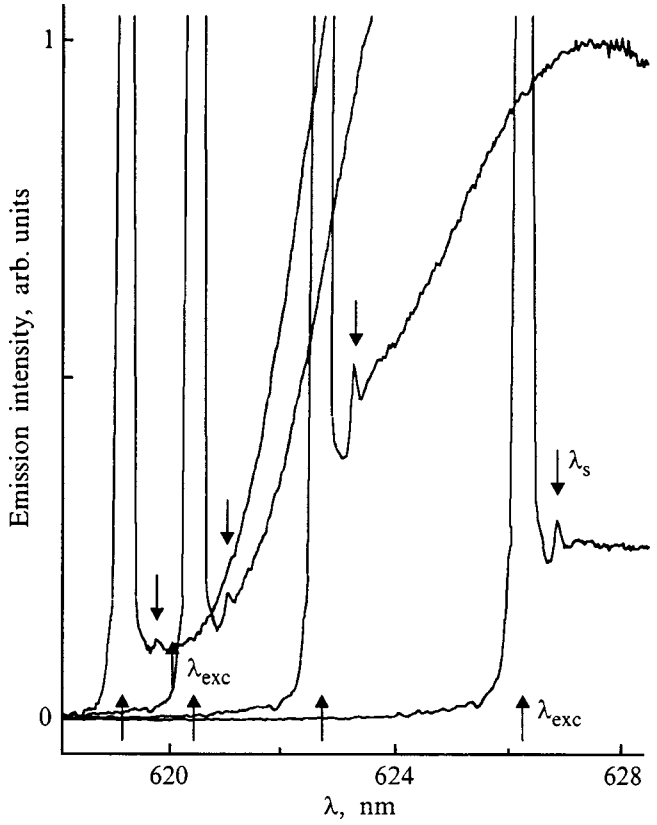

FIG. 4. Fragments of emission spectra of a $GaSe_{0.85}Te_{0.15}$ solid solution excited by light of different wavelengths λ_{exc} in a magnetic field $B=7.5$ T. Faraday geometry. $T=6$ K. The spectra relate to the radiation component polarized orthogonally to the pump polarization.

the $S_z=0$ state is optically inactive. Because the crystal is anisotropic, the $S_z=0$ state is split from the $S_z=\pm 1$ states by an amount $\Delta \ll \Delta_1$. Longitudinal magnetic field $\mathbf{B}\|\mathbf{c}$ splits the exciton states with $S_z=\pm 1$ into two states with $S_z=+1$ and $S_z=-1$, with the corresponding radiations right- and left-hand polarized. The splitting

$$\Delta E = g_{\|}\mu_B B\,, \tag{2}$$

where $g_{\|}$ is the longitudinal component of the exciton g factor.[11]

Consider now a system of localized excitons in an external magnetic field. Unlike free excitons, the LE spin structure in a solid solution feels, generally speaking, a perturbation from the fluctuation potential, whose parameters are different for different LEs. However if the external magnetic field is strong enough, so that the perturbation of the LE spin states induced by the magnetic field is considerably in excess of that due to the fluctuation potential, the levels of all LEs in the solid solution will exhibit the same Zeeman splitting pattern.

Under these conditions, linearly polarized monochromatic laser light will select out of the whole LE ensemble in the chosen geometry only two groups of centers, each of them being resonantly excited by light to one of its Zeeman sublevels. The condition for the center excitation can be written

$$h\nu_{exc} = E^{(1)} - 0.5\, g_{\|}^{(1)}\mu_B B = E^{(2)} + 0.5\, g_{\|}^{(2)}\mu_B B\,, \tag{3}$$

where $E^{(1)}$ and $E^{(2)}$ are the energies of LE formation in the above groups in the absence of magnetic field (and neglecting the effect of the fluctuation potential on the LE spin structure), and $g_{\|}^{(1,2)}$ are the longitudinal components of the g factors of LEs with the formation energies $E^{(1,2)}$, respectively. Note that even for $h\nu_{exc}=$ const, magnetic field variation gives rise to successive excitation of various groups of LEs differing in the $E^{(i,k)}$ set. In accordance with the proposed scheme, pump light with a photon energy $h\nu_{exc}$ populates the lower Zeeman sublevel (with $S_z=+1$) in the first LE group, and simultaneously the upper Zeeman sublevel (with $S_z=-1$) in the second group of LEs. Rather than dwelling on the radiative and nonradiative processes characteristic of all LEs, we note that photocreated LEs of the first group can undergo energy relaxation only by tunneling to lower-lying states of other LEs, while the LEs of the second group can make also intracenter transitions to lower-lying spin sublevels with $S_z=0$ and $S_z=+1$ with energies $E_0^{(2)}=E^{(2)}$ and $E_{+1}^{(2)}=E^{(2)}-0.5g_{\|}^{(2)}\mu_B B$, respectively. If the probability of these intracenter transitions associated with a change in the exciton spin state exceeds that of LE tunneling from the upper Zeeman sublevel to any state in the continuum of LE states with energies in the vicinity of the $E_0^{(2)}$ and $E_{+1}^{(2)}$ sublevels, the population of the LE states with energies $E_0^{(2)}$ and $E_{+1}^{(2)}$ will exhibit relative maxima. This will

be reflected in the LE radiation spectrum in the appearance in a magnetic field of an additional emission peak at the frequency

$$h\nu_S = E_{+1}^{(2)} = h\nu_{\text{exc}} - g_{\parallel}^{(2)}\mu_B B \tag{4}$$

(we may recall that the $S_z = 0$ state is optically inactive). This peak should shift toward longer wavelengths with increasing field. It is this situation that is observed in the experiment. An analysis shows that the quantity $g_{\parallel}^{(2)}$ practically does not depend, within the accuracy of its determination ($\sim 5\%$), on the position of the pump line, i.e., the g factor in the solid solution under consideration is the same for all LEs exhibiting the Zeeman effect (Figs. 2 and 4) (therefore the upper index in the $g_{\parallel}^{(i)}$ notation can be dropped, $g_{\parallel}^{(i)} \equiv g_{\parallel}$). On the other hand, the LE g factor depends clearly on the solid-solution composition. A comparison of the experimental relationship (1) with (4) yields $g_{\parallel} = 3.4 \pm 0.2$ for the $GaSe_{0.78}Te_{0.22}$ solid solution and $g_{\parallel} = 3.8 \pm 0.2$ for $GaSe_{0.85}Te_{0.15}$.

It is of interest to compare the values of $g_{\parallel}$ obtained for the solid solutions with the excitonic g factor in pure GaSe. The longitudinal component of the g factor of direct free excitons in GaSe is $g_{\parallel} = 2.7$,[11] which is substantially smaller than the LE g factors in the solid solutions studied here. On the other hand, the values of the LE g factors found are close to those of the effective g factors of excitons bound to ionized centers or isoelectronic impurities in GaSe: $g_{\parallel} = 3.3 - 3.6$ (Refs. 12 and 13). A possible reason for the difference between the g factors of bound and free excitons in GaSe is the contribution of electronic states of the indirect conduction-band minimum to the wave functions of bound excitons (the direct and indirect minima are close in energy); note also that the magnetic-field-induced splitting of the levels of excitons bound to the above defects and of those of direct free excitons has the same nature. It may be conjectured that a similar situation is valid for LEs in $GaSe_{1-x}Te_x$ direct-gap solid solutions with $x \leqslant 0.35$. There are grounds to assume that the difference between the energies of the indirect and direct conduction-band minima in $GaSe_{1-x}Te_x$ increases with increasing tellurium content.[1)] This is what may account for the decrease in the LE g factor observed to occur as one goes from the $x = 0.15$ composition to $x = 0.22$. Besides, an increase in the concentration of tellurium, an element with a higher atomic number than that of selenium, should amplify the effects associated with spin-orbit interaction. The wave function of triplet excitons in GaSe contains a small fraction of the singlet state, whose admixture to the triplet-exciton wave function is due to the spin-orbit interaction of valence electrons in the crystal.[11] In this case an increase of tellurium content in the solid solution should result in an increase of the admixture of the singlet state to the triplet-exciton wave function and, as a consequence, in a decrease of the effective g factor of these states.

We note in conclusion that the width of the S line permits one to estimate the lifetime τ_{LE} of the localized-exciton states exhibiting the Zeeman effect. The width of the S line is $\delta E \approx 0.2$ meV (this value corresponds to the limiting resolution of the measuring system, so that the true linewidth $\delta E \leqslant 0.2$ meV). The uncertainty relation yields $\tau_{\text{LE}} \geqslant \hbar/\delta E = 300$ ps.

Support of the Russian Fund for Fundamental Research (Grant 97-02-18139) is gratefully acknowledged.

[1)] Replacement of sulfur in $GaSe_{1-x}S_x$ by the heavier selenium results in a decrease of the gap width, which at zone center is substantially larger than that at the edge corresponding in position to the indirect conduction-band minimum.[2] This relationship possibly holds for the $GaSe_{1-x}Te_x$ system with tellurium substituted for selenium.

[1] S.-H. Wei, L. G. Ferreira, J. E. Bernard, and A. Zunger, Phys. Rev. B **42**, 9622 (1990).
[2] M. Schlüter, J. Camassel, S. Kohn, J. P. Voitchovsky, Y. R. Shen, and M. L. Cohen, Phys. Rev. B **13**, 3534 (1976).
[3] Zh. I. Alferov, E. L. Portnoĭ, and A. A. Rogachev, Fiz. Tekh. Poluprovodn. **2**, 1194 (1968) [Sov. Phys. Semicond. **2**, 1001 (1968)].
[4] S. Lai and M. V. Klein, Phys. Rev. Lett. **44**, 1087 (1980).
[5] M. Oueslati, C. Benoit à la Guillaume, and M. Zouaghi, Phys. Rev. B **37**, 3037 (1988).
[6] S. Permogorov and A. Reznitsky, J. Lumin. **52**, 201 (1992).
[7] R. I. Personov, J. Photochem. Photobiol., A **62**, 321 (1992).
[8] B. M. Kharlamov, E. I. Al'shits, and R. I. Personov, Zh. Éksp. Teor. Fiz. **87**, 750 (1984) [Sov. Phys. JETP **60**, 428 (1984)].
[9] A. G. Abdukadyrov, S. D. Baranovskiĭ, S. Yu. Verbin, E. L. Ivchenko, A. Yu. Naumov, and A. N. Reznitskiĭ, Zh. Éksp. Teor. Fiz. **98**, 2056 (1990) [Sov. Phys. JETP **71**, 1155 (1990)].
[10] E. L. Ivchenko, M. I. Karaman, D. K. Nel'son, B. S. Razbirin, and A. N. Starukhin, Fiz. Tverd. Tela (St. Petersburg) **36**, 400 (1994) [Phys. Solid State **36**, 218 (1994)].
[11] E. Mooser and M. Schlüter, Nuovo Cimento B **18**, 164 (1973).
[12] E. M. Gamarts, E. L. Ivchenko, G. E. Pikus, B. S. Razbirin, and A. N. Starukhin, Fiz. Tverd. Tela (Leningrad) **22**, 3620 (1980) [Sov. Phys. Solid State **22**, 2119 (1980)].
[13] E. M. Gamarts, E. L. Ivchenko, G. E. Pikus, B. S. Razbirin, V. I. Safarov, and A. N. Starukhin, Fiz. Tverd. Tela (Leningrad) **24**, 2325 (1982) [Sov. Phys. Solid State **24**, 1320 (1982)].

Translated by G. Skrebtsov

EXAFS studies of the local environment of lead and selenium atoms in $PbTe_{1-x}Se_x$ solid solutions

A. I. Lebedev, I. A. Sluchinskaya, and V. N. Demin

M. V. Lomonosov Moscow State University, 119899 Moscow, Russia

I. Munro

Daresbury Laboratory, Warrington WA4 4AD, UK

(Submitted December 11, 1998; resubmitted January 20, 1999)
Fiz. Tverd. Tela (St. Petersburg) **41**, 1394–1402 (August 1999)

EXAFS spectroscopy is used to study the local environment of lead and selenium atoms in $PbTe_{1-x}Se_x$ solid solutions. In addition to a bimodal distribution of the bond lengths in the first-coordination sphere, an unusually large value of the Debye–Waller factors for the Pb–Pb interatomic distances (second-coordination sphere) and a substantial deviation of this value from Vegard's law are observed. Monte Carlo calculations show that these observations are related to the complicated structure of the distribution function for Pb–Pb distances. It is found that the number of Se–Se pairs in the second-coordination sphere exceeds the statistical value, which indicates that chemical factors play an important role in the structure of the solid solutions. The contribution of chemical factors to the enthalpy of mixing of the solid solution is estimated ($\approx$0.5 kcal/mole) and this value is shown to be comparable to the deformation contribution. © *1999 American Institute of Physics.* [S1063-7834(99)00908-9]

Knowledge of the true structure of solid solutions, i.e., the local displacements of atoms from their ideal lattice sites and the deviations in the distributions of the atoms from statistical distributions, is needed to understand the physical properties of these crystals. EXAFS spectroscopy is now widely used for studying the structure of solid solutions.

EXAFS studies of solid solutions of III-V and II-VI semiconductors having the sphalerite structure[1–6] have revealed a bimodal distribution of the bond lengths in the first-coordination sphere. This implied that the local structure of the solid solutions should, most likely, be described in the approximation of fixed chemical bond lengths proposed by Bragg and Pauling, rather than in the approximation of a virtual crystal. Up to now, solid solutions of IV-VI semiconductors having the rock salt (NaCl) structure have been studied by EXAFS only to examine the locations of the noncentral impurities;[7–10] no systematic investigations of the local structure have been made for these solid solutions that contain no noncentral impurities.

In this paper we present results from a study of the local structure of $PbTe_{1-x}Se_x$ solid solutions by EXAFS spectroscopy. These solid solutions are of great interest in connection with their use for creating IR optoelectronic devices based on heterostructures with matching crystal-lattice parameter. PbTe and PbSe form a continuous series of solid solutions over the entire range of compositions. The periods of the crystal lattices in the initial binary compounds are 6.460 and 6.126 Å at 300 K, i.e., this solid solution is characterized by a rather large relative difference (slightly larger than 5%) in the interatomic distances. In addition, this solid solution was of interest to us because, in it, for $x \approx 0.25$, the lattice was found to be ''softest'' with respect to the appearance of a ferroelectric phase when tin atoms are introduced.[11]

1. EXPERIMENTAL TECHNIQUE

Samples of $PbTe_{1-x}Se_x$ solid solution with $x = 0.1$, 0.25, 0.5, and 0.75 were obtained by melting stoichiometric compositions of the binary compounds PbTe and PbSe together in evacuated quartz vials with subsequent homogenizing annealing at 720 °C for 170 h. According to x-ray measurements, the samples were single-phase. Immediately before the EXAFS measurements, the alloys were ground to a powder, sifted through a mesh, and deposited on a scotch tape. An optimum thickness of the absorbing layer for taking spectra was obtained by multiple layering (usually 8 layers) of the type.

The EXAFS spectra were studied at station 7.1 of the synchrotron radiation source at the Daresbury Laboratory (Great Britain) with an electron energy of 2 GeV and a maximum beam current of 230 mA. Measurements were made at the K absorption edge of Se (12658 eV) and the L absorption edge of Pb (13055 eV) at 80 K in transmission geometry. The synchrotron radiation was monochromatized by a two- crystal Si(111) monochromator. The intensities of the radiation incident on (I_0) and transmitted through (I_t) the sample were recorded by ionization chambers filled with He + Ar mixtures with compositions such that 20 and 80% of the x radiation, respectively, was absorbed. Contamination of the radiation output from the monochromator by higher harmonics could be neglected for the energy range employed in these experiments.

The resulting spectra were analyzed in the usual way.[12] After subtraction of the background absorption of the radiation by other atoms, the monotonic part $\mu x_0(E)$ of the ab-

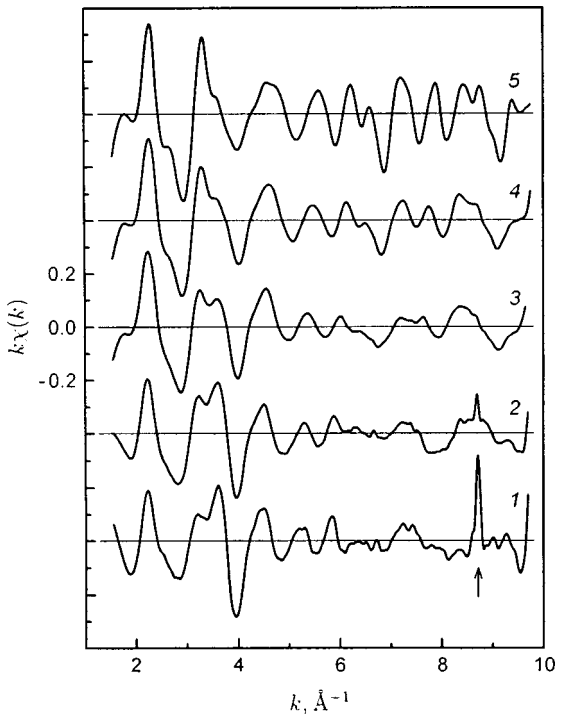

FIG. 1. $k\chi(k)$ for samples of $PbTe_{1-x}Se_x$ at the K absorption edge of Se. x: *1* — 0.1, *2* — 0.25, *3* — 0.5, *4* — 0.75, *5* — 1. The arrow denotes the location of the glitches.

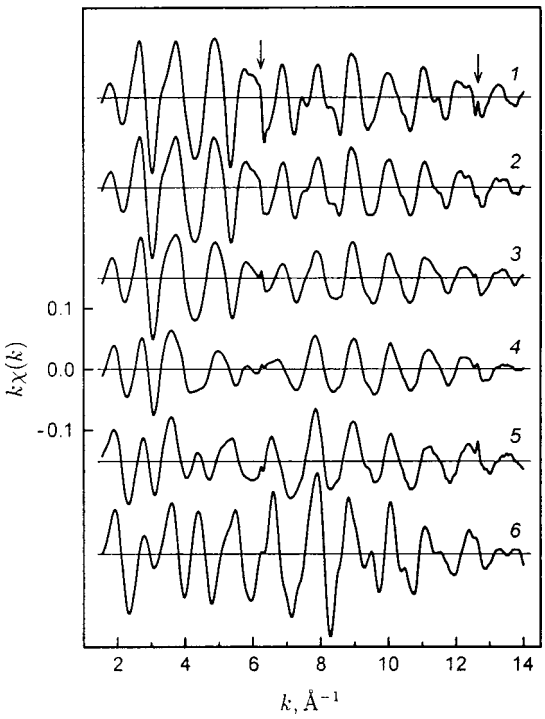

FIG. 2. $k\chi(k)$ for samples of $PbTe_{1-x}Se_x$ at the L_{III} absorption edge of Pb. x: *1* — 0, *2* — 0.1, *3* — 0.25, *4* — 0.5, *5* — 0.75, *6* — 1. The arrows indicate the locations of glitches.

sorption was separated from the transmission curves $\mu x(E) = \ln(I_0/I_t)$ (here E is the energy of the radiation) by curve fitting and the EXAFS function $\chi = (\mu x - \mu x_0)/\mu x_0$ was calculated as a function of the photoelectron wave vector $k = [2m(E-E_0)/\hbar^2]^{1/2}$. The origin for the photoelectron energy E_0 was taken to be the energy corresponding to the inflection point in the absorption edge. The jump μx at the absorption edge varied over 0.08–1.4. At least two spectra were taken for each sample.

When multiple scattering effects are neglected, information on the local environment of the central atom, i.e., the distances R_j, coordination numbers N_j, and Debye-Waller factors σ_j^2, for each jth coordination sphere enters the EXAFS function as follows:[12]

$$\chi(k) = \frac{1}{k}\sum_j \frac{N_j S_0^2}{R_j^2} f(k)\exp[-2R_j/\lambda(k) - 2k^2\sigma_j^2]\sin[2kR_j + \psi(k)].$$

Besides the structural parameters characterizing the local environment, this equation includes the amplitude $f(k)$, the sum of the backscatter phase and the phase of the central atom $\psi(k)$, the photoelectron mean-free-path $\lambda(k)$, and a parameter S_0^2, which accounts for many-electron and inelastic effects in the central and scattering atoms. The functions $f(k)$, $\psi(k)$, and $\lambda(k)$ were calculated using the FEFF5 program.[13]

The information of interest to us for the first-coordination spheres was extracted from the experimental $\chi(k)$ curves with the aid of the forward and inverse Fourier transforms using Hemming windows. Quantitative values of the parameters R_j, N_j, and σ_j^2 were found by minimizing the root- mean-square deviation between the experimental and calculated $k\chi(k)$ curves using a modified Levenberg–Marquardt algorithm. Besides these parameters, the shift in the zero on the energy scale dE_0 was varied simultaneously. The number of varied parameters (8–9) was usually half the number of independent parameters in the data ($2\Delta k\Delta R/\pi = 12$–$20$, where Δk and ΔR are the regions for discrimination of the data under Fourier filtration in k and R space[12]). The accuracy with which the parameters was determined was established from the covariant matrix. The errors reported here correspond to the standard deviation. In order to enhance the accuracy, it was assumed that the correction energy dE_0 is the same for all the coordination spheres, while the coordination numbers correspond to the known coordination numbers in an fcc lattice.

2. EXPERIMENTAL RESULTS

Figure 1 shows typical experimental $k\chi(k)$ curves obtained at the K absorption edge of Se for samples of $PbTe_{1-x}Se_x$ and PbSe. The range of wave numbers for these data is bounded above by $k \approx 9.7$ Å^{-1} because of the closeness of the L_{III} absorption edge of lead. Figure 2 shows plots of $k\chi(k)$ for samples of $PbTe_{1-x}Se_x$, PbTe, and PbSe at the L_{III} absorption edge of Pb. The sharp jumps in the curves indicated by arrows in Figs. 1 ($k \approx 8.7$ Å) and 2 ($k \approx 6.2$ and 12.7 Å), the so-called glitches, are not related to properties of the samples, but to those of the monochromator. After the glitches were removed, the data were analyzed by the method described in the previous section.

TABLE I. Experimentally determined local concentrations of Se atoms surrounding Se.

x	0.1	0.25	0.5	0.75	1.0
$N_{Se-Se}/12$	0.34 ± 0.04	0.45 ± 0.03	0.60 ± 0.02	0.78 ± 0.01	0.96 ± 0.02

In processing the data, we have restricted ourselves to finding the parameters for the first two coordination spheres. In analyzing the data at the absorption edge of Pb, it was noted that the lead atoms in the first-coordination sphere are surrounded by six atoms of two kinds (Se and Te). Here each pair (Pb–Te, Pb–Se) is described by its own set of structural parameters (R_j, N_j, σ_j^2). The second-coordination sphere consists of 12 lead atoms which, we have assumed lie at the same distance.[a)] In order to reduce the number of variable parameters, the relative contributions of the Pb–Te and Pb–Se pairs in the $\chi(k)$ curves were calculated using the known chemical compositions of the samples and the relative contributions of the first- and second-coordination spheres, in accordance with their coordination numbers. The complete set of parameters characterizing the nearest neighbors of the lead atoms was characterized by 8 parameters.

In analyzing the data taken at the Se absorption edge, we assumed that the first-coordination sphere of the selenium always consists of 6 lead atoms, while the second-coordination sphere can contain either Se or Te atoms. Here the number of Se and Te atoms in the second-coordination sphere can differ from the statistical number because of short-range order in the solid solution. Thus, the analysis was done both in the approximation of a statistical distribution of chalcogenide atoms in the lattice and taking the possibility of short-range order into account.

In the case of a statistical distribution of chalcogenide atoms, the problem was limited to finding a set of 8 parameters characterizing the short-range order of the Se atoms in the solid solution.[b)]

In order to account for the possible deviation from a statistical distribution of the chalcogenide atoms in the second-coordination sphere of Se, yet another variational parameter was introduced, N_{Se-Se}, the number of Se atoms in the second-coordination sphere of an Se atom. Here it was assumed that the total number of atoms in the second-coordination sphere was always equal to 12.

Taking the possibility of short-range order into account when processing the data ensured a considerably better agreement between the experimental and theoretical $k\chi(k)$ curves than for a random distribution of atoms in the lattice. The values of N_{Se-Se} which we obtained (see Table I) indicate a distinct short-range order, specifically, Se atoms being surrounded in the second-coordination sphere by atoms of the same type. This is consistent with a study of the thermodynamic properties of the PbTe–PbSe system.[14]

Figures 3 and 4 contain plots the interatomic distances and Debye-Waller factors as functions of the composition x for Pb–Te and Pb–Se bonds obtained by analyzing data from both absorption edges.[c)] Despite the rather large errors in determining the Pb–Se distances in samples with a low selenium content, the distances obtained at both absorption edges are in agreement. As Fig. 3 implies, the distribution of the interatomic bond lengths in $PbTe_{1-x}Se_x$ solid solutions has a distinct bimodal character. The Debye-Waller factor depends on x differently for the Pb–Te and Pb–Se bonds (Fig. 4): while σ^2_{Pb-Te} is essentially independent of the composition, σ^2_{Pb-Se} has a maximum near $x=0.5$. Nevertheless, σ^2 is less than $0.01\ Å^2$ for both bonds.

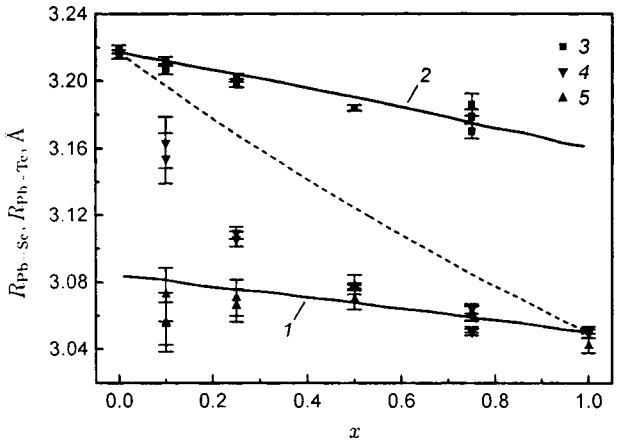

FIG. 3. Average interatomic Pb–Se (*1*) and Pb–Te (*2*) distances as functions of the composition x of $PbTe_{1-x}Se_x$ solid solutions. The points indicate the bond lengths of: *3* — Pb–Te, *4* — Pb–Se, *5* — Se–Pb. The smooth curves are from a Monte Carlo model calculation and the dashed curve is the average interatomic distance (half the lattice parameter).

Figures 5 and 6 contain plots of the interatomic distances and Debye–Waller factors as functions of the composition parameter for Pb–Pb atom pairs located in the second-coordination sphere with respect to one another, and Figs. 7 and 8, similar curves for Se–chalcogen atom pairs assuming short-range order. These figures imply that the experimental dependence of the Pb–Pb distance deviates significantly from a Vegard law, while the Se–chalcogen pairs follow Vegard's law much better.

The dependences of the Debye–Waller factors for Pb–Pb and Se–chalcogen atom pairs on x are qualitatively analogous, although they differ quantitatively. In these data, it is

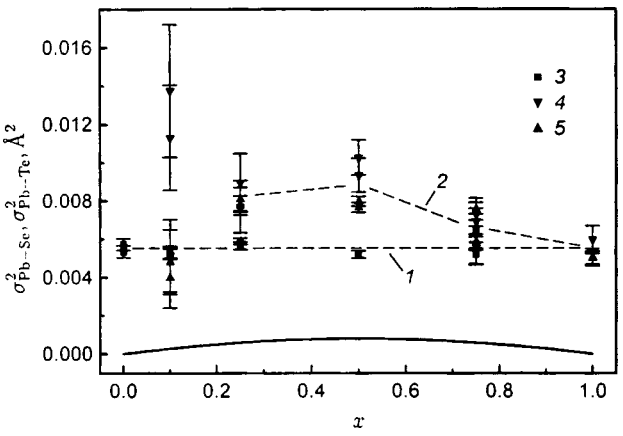

FIG. 4. The Debye–Waller factors for Pb–Te (*1*) and Pb–Se (*2*) bonds as functions of the composition x of $PbTe_{1-x}Se_x$ solid solutions. The points denote data for the bonds: *3* — Pb–Te, *4* — Se–Pb, *5* — Pb–Se. The smooth curve is the static contribution to the Debye–Waller factor calculated by a Monte Carlo method. (The curves for both bonds essentially overlap.)

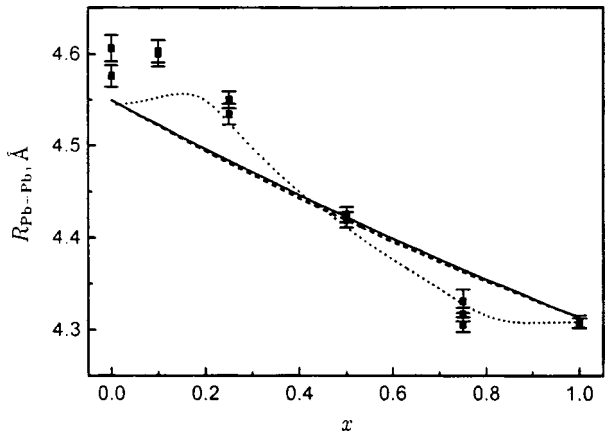

FIG. 5. The Pb–Pb interatomic distance as a function of the composition x of $PbTe_{1-x}Se_x$ solid solutions. The points are experimental data. The smooth curve was calculated by a Monte Carlo method, the dashed curve is the average interatomic distance, and the dotted curve is the result of an analysis for the model $\chi(k)$ curves.

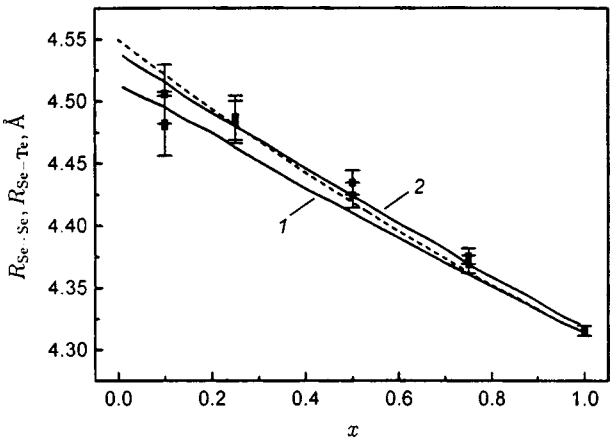

FIG. 7. The Se–Se (*1*) and Se–Te (*2*) interatomic distances as functions of the composition x of $PbTe_{1-x}Se_x$ solid solutions. The points are experimental data. The smooth curves were calculated by a Monte Carlo method and the dashed curve is the average interatomic distance calculated from the lattice parameter.

noteworthy that the Debye–Waller factors for Pb–Pb pairs reach a maximum near $x \approx 0.25$, while these values are unexpectedly large (up to 0.05 Å^2) and significantly exceed those for the Se–chalcogen pairs.

In order to explain the anomalously large Debye–Waller factors for Pb–Pb pairs, we initially assumed that the solid solutions can undergo a transition to a microcoherent state, for example, due to mechanical effects when the powders were ground or because the solid solution decomposes when the alloys are not cooled fast enough after annealing. In order to verify this proposition, a second series of samples was prepared with compositions identical to those in the first series. The alloys in this series were ground before annealing and all the annealed powders were quenched from 720 °C in water. Data from these samples taken at the L_{III} absorption edge of Pb did not reveal any changes in the behavior of the Debye–Waller factor for the Pb–Pb pairs as a function of x compared to the first series of samples. Moreover, additional low-temperature annealing at 100–400 °C was done on a number of samples from the second series with $x = 0.25$ in order to observe any changes caused by possible decomposition of the solid solution. No significant changes were observed in the Debye–Waller factor for the Pb–Pb pairs.

In order to understand the reason for the unusual behavior of the interatomic distances and Debye–Waller factor as functions of composition for the Pb–Pb pairs (Figs. 5 and 6), we decided to model the static distortions in the $PbTe_{1-x}Se_x$ solid solutions by a Monte Carlo method. This method has been used previously[3,15] to model distortions in semiconductor solid solutions with a sphalerite structure.

3. MONTE CARLO MODEL

The static distortions in $PbTe_{1-x}Se_x$ solid solutions were modelled in the approximation of elastically deformed bonds. For a given random distribution of Se and Te atoms in one of the fcc sublattices, a set of atomic coordinates $\{\mathbf{r}_i\}$

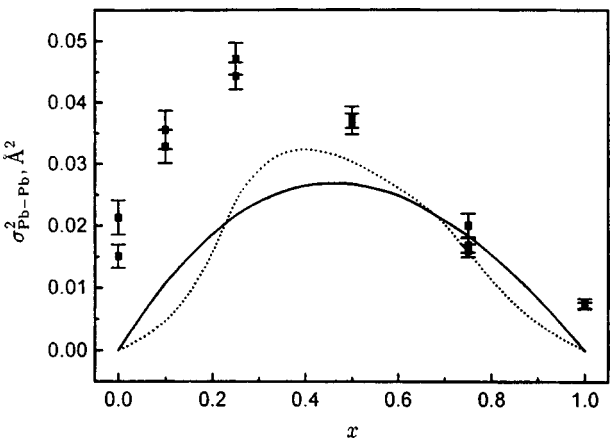

FIG. 6. The Debye–Waller factor for Pb–Pb atom pairs as a function of the composition x of $PbTe_{1-x}Se_x$ solid solutions. The points are experimental data. The smooth curve was calculated by a Monte Carlo method and the dotted curve is the result of an analysis for the model $\chi(k)$ curves.

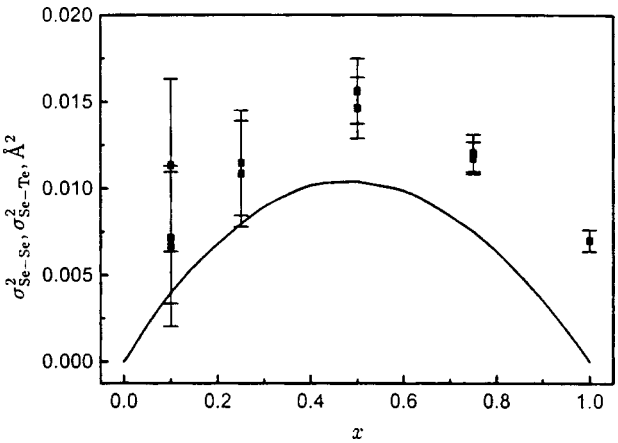

FIG. 8. The Debye–Waller factors for Se–Se and Se–Te atom pairs as functions of the composition x of $PbTe_{1-x}Se_x$ solid solutions. The points are experimental data. The smooth curve was calculated by a Monte Carlo method.

was found for which the total strain energy from the change in the bond lengths and deviation of the angles between them from 90°,

$$U=\frac{1}{2}\sum_i\left[\sum_{j=1}^{6}A_{s(i,j)}\left(\frac{|\mathbf{r}_i-\mathbf{r}_j|-d_{s(i,j)}}{d_{s(i,j)}}\right)^2+B\sum_{(j,k)=1}^{12}\left(\frac{(\mathbf{r}_i-\mathbf{r}_j)(\mathbf{r}_i-\mathbf{r}_k)}{|\mathbf{r}_i-\mathbf{r}_j|\mathbf{r}_i-\mathbf{r}_k|}\right)^2\right],$$

was minimized. In the first term the sum is taken over the six nearest neighbors for each of the lattice sites. The indices $s(i,j)=1,2$ correspond to Pb–Se and Pb–Te atom pairs at sites i and j, A_s is the stiffness coefficient for the corresponding bond, and d_s is its equilibrium length in the binary compound ($d_1=3.050$, $d_2=3.217$ Å at 80 K). In the second term the sum is taken over all 12 different angles between bond pairs for each of the lattice sites. The stiffness constants with respect to lengthening of the Pb–Se (A_1) and Pb–Te (A_2) bonds were calculated from published[16] values of the elastic moduli for PbSe and PbTe according to the relation $A=(C_{11}+2C_{12})/4$, and the stiffness constants with respect to bending, according to $B=C_{44}/32$, where C_{44} is the average of the corresponding moduli for PbSe and PbTe.

The model calculations were done on $m\times m\times m$ lattices with $m=10-30$ nodes and periodic boundary conditions for several random distributions of the Se and Te atoms in the chalcogenide sublattice. Starting at a position among the nodes of an ideal fcc lattice, each of the atoms could undergo a shift in a direction for which the strain energy of the lattice decreased for a fixed position of the remaining atoms. The step size for a single displacement was adaptively reduced from 0.01 to 0.0002 Å. After roughly 1000 iteration steps per atom, the strain energy U ceased to vary and the resulting configuration of displacements was assumed to be in equilibrium. The set of coordinates for all the pairs of atoms located in the first- and second-coordination spheres found in this way was used to calculate the distribution function for the interatomic distances. Since the periodic boundary conditions required that the lattice parameter be fixed, the calculations were done for an entire set of these lattice parameters. In the following, we shall take the lattice parameter to be the value for which a minimum energy U was obtained.

Model calculations on lattices of different sizes showed that the excess energy owing to the finite lattice size varies roughly as m^{-3} and that for $m>16$, finite lattice effects can be neglected.

The Monte Carlo calculations of the average Pb–Se and Pb–Te bond lengths and their dispersions (static Debye–Waller factors) as functions of x are plotted as the smooth curves in Figs. 3 and 4. As is to be expected, the distribution of the distances in the first-coordination sphere has a distinct bimodal character. We shall define the relaxation parameter ε' for the $A-C$ bond as the change in the bond length for the extreme compositions of the solid solution $AB_{1-x}C_x$ relative to the change in the average interatomic distance,

$$\varepsilon'=\frac{R^0_{Ac}-R_{Ac}[AB]}{R^0_{AB}-R^0_{AC}},$$

where R^0_{AB} and R^0_{AC} are the bond lengths in the binary compounds AB and AC, and $R_{AC}[AB]$ is the length of the A–C bond for impurity C in compound AB (in the limit of infinite dilution). For the Pb–Te and Pb–Se bonds, this quantity was 0.35 and 0.21, respectively. The difference between the two values of ε' is a consequence of the substantial difference between the stiffness coefficients A_1 and A_2 (roughly a factor of 1.5). The value of ε' calculated for the Pb–Te bond is in fair agreement with experiment ($\varepsilon'\approx 0.36$). A comparison for the Pb–Se bond is difficult because of the large experimental errors. It is interesting that the calculations of the average interatomic distance as a function of composition (the dashed curve in Fig. 3) deviate significantly (by roughly 0.009 Å) and negatively from Vegard's law.

Figures 5–8 contain plots of the average interatomic distances and their dispersions for Pb–Pb, Se–Se, and Se–Te atom pairs in the second-coordination sphere with respect to one another. The substantially larger static Debye–Waller factors for the second-coordination sphere compared to the first mean that the lattice adapts to the existence of different chemical bond lengths through local rotation. The model results for Se–chalcogen atom pairs are in fairly good agreement with experimental data, while the results for Pb–Pb pairs are in poor agreement with experiment. The reasons for this discrepancy will be discussed in detail in the next section.

According to our model calculations, the average Se–Se distance in the solid solution is 0.01–0.02 Å shorter than the Se–Te distance (Fig. 7) and their Debye–Waller factors are roughly equal ($\sigma^2_{\mathrm{Se-Se}}\approx\sigma^2_{\mathrm{Se-Te}}$). This justifies treating the chalcogenide atoms as a single second-coordination sphere during the analysis of the surroundings of the selenium atoms.

Therefore, Monte Carlo modelling of the distortions in $PbTe_{1-x}Se_x$ solid solutions has made it possible to establish the inevitability of strong static distortions in the Pb–Pb distance and to demonstrate qualitative agreement between the calculations and experiment for the first-coordination sphere and for the Se–chalcogenide atom pairs. The model calculations, however, have not provided an explanation for the discrepancy between the experimentally determined and calculated Pb–Pb distances, which may be related to an the inadequacy of the one-dimensional approximation employed to analyze the experimental data for the Pb–Pb distances.

4. DISCUSSION

We now discuss the validity of a single-mode approximation for the interatomic distances in the second-coordination sphere of $PbTe_{1-x}Se_x$ solid solutions.

It has been proposed[1,17] that the number of ''modes'' in the distribution of the A–A distances in an $AB_{1-x}C_x$ solid solution is determined by the number of different combinations through which a pair of A atoms are bound, i.e., the distribution must be bimodal for lattices having a sphalerite structure and trimodal for NaCl-type lattices.

Thus, in processing our experimental data, we have begun with an attempt to find a set of parameters with which the distribution of the Pb–Pb distances could be represented

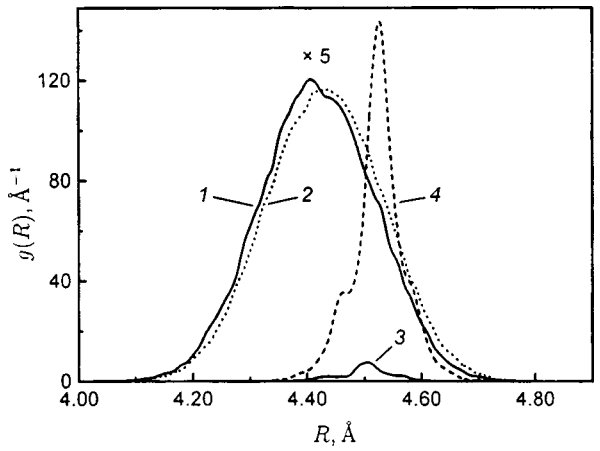

FIG. 9. Distributions of the Se–Se (*1, 3*) and Se–Te (*2, 4*) interatomic distances for $PbTe_{1-x}Se_x$ samples with $x=0.5$ (*1, 2*) and $x=0.05$ (*3, 4*), calculated by a Monte Carlo method.

in the form of a sum of several Gaussians. Unfortunately, because of the large Debye–Waller factor for Pb–Pb pairs, the range of data in k space within which the EXAFS oscillations were observed was limited and did not allow us to determine the parameters for a trimodal model (the solution was unstable). In the bimodal approximation, physically reasonable values of the distances could be obtained only for compositions close to the binary compounds; near $x=0.5$ the distance to one of the components of the coordination sphere became unphysically large (~ 4.7 Å). Since neither the trimodal nor the bimodal description could be used for processing the data from all the samples, we were forced to limit the analysis to the single-mode approximation.

Let us consider the distribution functions $g(R)$ for Se–Se, Se–Te and Pb–Pb atom pairs calculated by a Monte Carlo method (Figs. 9 and 10). It is clear that for $x \approx 0$ and $x \approx 1$, the distribution functions have a fine structure, which is smeared out as $x \to 0.5$. The difference between the distribution functions for Se–chalcogenide and Pb–Pb atom pairs is the following: for the surroundings of selenium (Fig. 9), the average Se–Se and Se–Te interatomic distances are close

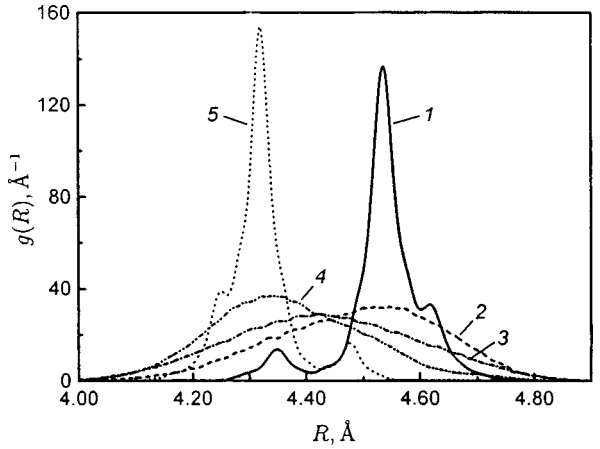

FIG. 10. Distributions of the Pb–Pb interatomic distances for $PbTe_{1-x}Se_x$ samples with different compositions calculated by a Monte-Carlo method. x: *1* — 0.05, *2* — 0.25, *3* — 0.5, *4* — 0.75, *5* — 0.95.

and the fine structure components are relatively close to one another, at distances of the order of the amplitude of the thermal vibrations at 80 K. For the surroundings of lead (Fig. 10), on the other hand, a rather sharply expressed structure is typical, with distances between the components that greatly exceed the amplitude of the thermal vibrations. These results confirm the general phenomenon[1,6] that the distribution of the distances between the atoms which undergo substitution in the solid solution $AB_{1-x}C_x$ can be regarded as having a single mode, while for atom pairs A–A, it is more complicated.

Figure 10 implies that the distribution function for atom pairs A–A in our solid solution with an NaCl structure cannot be described in the trimodal approximation. Nevertheless, the fine structure components can be divided arbitrarily into two groups whose centers of gravity differ significantly. Therefore, it appears that, when the smearing of the curves is not too great, it is possible to approximate the distribution function by a sum of two Gaussians.

In order to check how well the Monte Carlo calculations of the distribution functions agree with the experimental data, we have used the functions $g(R)$ found here to compute $\chi(k)$ according to

$$\chi(k)=\frac{S_0^2}{k}f(k)\int\frac{g(R)}{R^2}\exp[-2R/\lambda(k)]\sin[2kR+\psi(k)]dR.$$

Then the synthesized curves were processed by the same method employed for the experimental data (one distance in the second-coordination sphere). The interatomic distances and static Debye–Waller factors found in this way are plotted as dotted curves in Figs. 5 and 6. The resulting curves are in good agreement with the experimental data, i.e., the Monte Carlo calculations of the distribution function provide a qualitatively accurate description of the actual structure of the solid solution.

Our results, therefore, show that the distortions in the second-coordination sphere of atoms in the chalcogenide sublattice in $PbTe_{1-x}Se_x$ solid solutions (where substitution takes place) can be described with sufficient accuracy in a single-mode approximation while, for the atoms in the lead sublattice (not subject to substitution), it is difficult to find a good working approximation and the best way out is to use distribution functions calculated by a Monte Carlo method.

The experimentally measured Debye–Waller factors are known to consist of static and dynamic terms which correspond to static distortions of the structure and thermal lattice vibrations. A Monte Carlo calculation only gives the static part of the Debye–Waller factor. Thus, the observed discrepancy between the experimental and calculated Debye–Waller factors can be attributed to thermal vibrations. In the first coordination sphere (Fig. 4), the dynamic contribution to the Debye–Waller factor is an order of magnitude greater than the static contribution, even at 80 K. The difference in the factors for Pb–Te and Pb–Se bonds appears to be related to the substantial mass difference between tellurium and selenium atoms. A more detailed analysis of these data becomes difficult because the phonon spectrum in $PbTe_{1-x}Se_x$ is

bimodal.[18] The contribution of thermal vibrations to the Debye–Waller factor for Se–chalcogenide atom pairs (Fig. 8) turns out to be slightly greater for the atoms in the first-coordination sphere (the movements of the atoms in the second-coordination sphere are more weakly correlated) and the measurements are independent of x to within the measurement error. However, as Fig. 6 implies, for Pb–Pb atom pairs, the thermal contribution depends on x. The maximum amplitude of the thermal vibrations is observed at $x \approx 0.25$. This results is qualitatively consistent with our earlier data,[11] and this implies that the lattice of the $PbTe_{1-x}Se_x$ solid solution with $x \approx 0.25$ is ''softer,'' so that a phase transition can be observed when part of the lead atoms are replaced by tin.

We now consider the features of the local structure of $PbTe_{1-x}Se_x$ solid solutions. As shown above, the parameter ε' was ≈ 0.36 for this solid solution, i.e., it is intermediate between the values observed previously in III-V and II-VI semiconductors with a sphalerite structure[5] (0.05–0.24) and in alkali halide crystals with an NaCl structure[17] (≈ 0.5).

It is obvious that one of the main factors leading to changes in the bond length around an impurity atom is the appearance of elastic deformations caused by the difference in size of the substituted atoms B and C. As simple arguments show,[19] ε' is determined by the crystal structure (mutual position of the atoms in the lattice), so that it is only meaningful to compare data obtained for identical structures. Neglecting bond bending and displacement of atoms in the second- and further-coordination spheres with the same stiffness for A–B and A–C bonds, $\varepsilon' = 0.25$ was found for a sphalerite structure and $\varepsilon' = 0.5$ for an NaCl structure. The more realistic Monte Carlo calculation done here, which took the influence of all the factors listed above into account, yielded $\varepsilon' = 0.35$ and 0.21 for the two bonds in a $PbTe_{1-x}Se_x$ solid solution with an NaCl structure, which is in fair agreement with experiment.

However, the strain contribution, alone, appears to be insufficient to explain all the experimental data. An attempt[17] to calculate ε' by a Monte Carlo method for the alkali halide $RbBr_{1-x}I_x$ and $K_{1-x}Rb_xBr$ crystals with an NaCl structure yielded values close to those found for $PbTe_{1-x}Se_x$, but differing substantially from experiment. A large difference between experimental values of ε' for III-V and II-VI semiconductors with a sphalerite structure and those predicted by the deformation model has also been noticed.[5] We believe that these discrepancies are associated with another group of factors which can affect the local structure, namely, the so-called chemical factors, which take into account the individual properties of the interacting atoms (their valence, electronegativity) and chemical bond type.

These factors also show up in the thermodynamic properties; thus, the enthalpy of mixing a solid solution, ΔH_m, is known to consist of two components, strain and chemical. The total deformation energy U calculated by a Monte Carlo method is just the strain contribution to ΔH_m. In III-V and II-VI semiconductors with a sphalerite structure, the strain energy is in good agreement with the experimentally determined enthalpy of mixing.[20] Unfortunately, the available published data on the enthalpy of mixing of $PbTe_{1-x}Se_x$ solid solutions ($\Delta H_m \lesssim 0.2$ kcal/mole) are not very exact. And, although this quantity is positive, which is indicative a potential tendency for the solid solution to decompose, the difference between the calculated strain term ($U = 0.38$ kcal/mole) and the measured ΔH_m may be evidence of the presence of chemical factors.

Individual members of this group of factors may either increase or reduce ε' (the chemical bond length). Let us assume that in the solid solution under study here, their effects are compensated and the agreement between the calculated and experimental ε' is good.

The local concentrations of Se–Se (short-term order) found in our experiments can be used to estimate the contribution of chemical factors to the enthalpy of mixing. We shall take the temperature T_f at which the diffusion of the chalcogenide atoms freezes out to be the temperature at which two nearest chalcogenide atoms undergo exchange in one second, which corresponds to a diffusion coefficient of $D = 2 \cdot 10^{-15}$ cm^2/s. The known[21] temperature variations of the diffusion coefficients yield an estimate of $T_f \approx 540$ K and, in the approximation of a pairwise interatomic interaction, we have calculated how much greater the energy of an Se–Te pair is than the average energy of the Se–Se and Te–Te pairs: $\Delta E \approx 0.5$ kcal/mole (0.02 eV) for a sample with $x = 0.5$. This value gives an idea of the magnitude of the chemical contribution to the enthalpy of mixing, since atoms in the second-coordination sphere do not interact through deformations, so there is no strain contribution to this quantity. A comparison of the values of ΔE and U obtained here shows that in the $PbTe_{1-x}$ Se_x solid solutions the strain and chemical contributions to the enthalpy of mixing are of the same order of magnitude.

The use of a pairwise interatomic-interaction approximation is not, however, entirely correct, since the atoms in the second-coordination sphere do not interact directly (either chemically or deformationally). The development of short-range order is apparently associated with some sort of more complicated interactions involving three or more atoms. In our experiments, the largest deviations from a statistical distribution of the chalcogenide atoms were observed at low Se concentrations and showed up as an elevated number of Se–Pb–Se configurations with 90° Pb–Se bonds. This suggests that there is a significant difference in the energies of the configurations in which atoms of given species lie in the same and in different p orbitals. These configurations can be represented schematically in the following way:

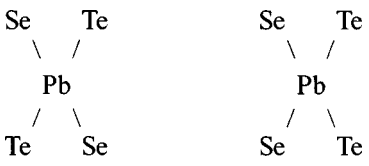

It is not impossible that this behavior originates in peculiarities of the chemical bond in IV-VI semiconductors, specifically its unsaturated character.

Using the strain approximation for calculating the bond lengths and pairwise distribution functions in the first- and second-coordination spheres, therefore, provides a qualitatively accurate description of the distortion in the structure of

$PbTe_{1-x}Se_x$ solid solutions. However, this model cannot explain the differences in the experimentally observed ε' in systems for which the model predicts close values of that parameter as well as the development of short-range order. This indicates that chemical factors must be taken into account, along with the deformation interaction, when describing the properties of solid solutions.

This work was supported by the Russian Fund for Fundamental Research (Grant No. 95-02-04644).

[a)] Studies of solid solutions with a sphalerite structure[1–3] have shown that the atoms in the second-coordination sphere can also be at different distances. Our assumption will be justified below.

[b)] To determine the parameters more accurately the additional assumptions $R_{Se-Te}=R_{Se-Se}$ and $\sigma^2_{Se-Te}=\sigma^2_{Se-Se}$ were introduced, and the Te and Se atoms were treated as a single-coordination sphere. These restrictions are justified by earlier studies of solid solutions which revealed a single-mode distribution of the bond lengths in the solid solution sublattice, within which isoelectronic substitution takes place,[1,6] and by our Monte Carlo modelling of the structure of the $PbTe_{1-x}Se_x$ solid solution. (See the next section.)

[c)] In analyzing the data we have included the systematic errors in calculating the theoretical scattering amplitudes and phases using the FEFF program. The distances obtained at the Pb edge were corrected by 0.025 Å,[10] and in analyzing the data obtained at the Se edge, a statistical correction of 0.5 rad was added to the scattering phase. These corrections ensured good agreement between the distances obtained by processing the EXAFS spectra and from x-ray data for standard PbTe and PbSe compounds.

[1] J. C. Mikkelsen, Jr. and J. B. Boice, Phys. Rev. B **28**, 7130 (1983).
[2] A. Balzarotti, N. Motta, A. Kisiel, M. Zimnal-Starnawska, M. T. Czyżyk, and M. Podgórny, Phys. Rev. B **31**, 7526 (1985).
[3] N. Motta, A. Balzarotti, P. Letardi, A. Kisiel, M. T. Czyżyk, M. Zimnal-Starnawska, and M. Podgórny, Solid State Commun. **53**, 509 (1985).
[4] W.-E. Pong, R. A. Mayanovic, B. A. Bunker, J. K. Furdyna, and U. Debska, Phys. Rev. B **41**, 8440 (1990).
[5] R. A. Mayanovic, W.-E. Pong, and B. A. Bunker, Phys. Rev. B **42**, 11174 (1990).
[6] Z. H. Wu, K. Q. Lu, Y. R. Wang, J. Dong, H. F. Li, C. X. Li, and Z. Z. Fang, Phys. Rev. B **48**, 8694 (1993).
[7] Q. Islam and B. A. Bunker, Phys. Rev. Lett. **59**, 2701 (1987).
[8] B. A. Bunker, Q. T. Islam, and W. F. Pong, Physica B **158**, 578 (1989).
[9] Z. Wang and B. A. Bunker, Phys. Rev. B **46**, 11277 (1992).
[10] A. I. Lebedev, I. A. Sluchinskaya, V. N. Demin, and I. H. Munro, Phys. Rev. B **55**, 14770 (1997).
[11] A. I. Lebedev and I. A. Sluchinskaya, Fiz. Tverd. Tela (Leningrad) **32**, 1780 (1990) [Sov. Phys. Solid State **32**, 1036 (1990)].
[12] P. A. Lee, P. H. Citrin, P. Eisenberger, and B. M. Kincaid, Rev. Mod. Phys. **53**, 769 (1981).
[13] J. Mustre de Leon, J. J. Rehr, S. I. Zabinsky, and R. C. Albers, Phys. Rev. B **44**, 4146 (1991).
[14] Shamsuddin and S. Misra, Z. Metallkd. **70**, 541 (1979).
[15] M. Podgórny, M. T. Czyżyk, A. Balzarotti, P. Letardi, N. Motta, A. Kisiel, and M. Zimnal-Starnawska, Solid State Commun. **55**, 413 (1985).
[16] *Numerical Data and Functional Relationships in Science and Technology*, Landolt-Börnstein New Series, Group 3, Vol. 17f (Springer-Verlag, Berlin, 1983).
[17] J. B. Boyce and J. C. Mikkelsen, Jr., Phys. Rev. B **31**, 6903 (1985).
[18] H. Finkenrath, G. Franz, and N. Uhle, Phys. Status Solidi B **95**, 179 (1979).
[19] C. K. Shih, W. E. Spicer, W. A. Harrison, and A. Sher, Phys. Rev. B **31**, 1139 (1985).
[20] Z. H. Wu and K. Q. Lu, J. Phys.: Condens. Matter **6**, 4437 (1994).
[21] *Numerical Data and Functional Relationships in Science and Technology*, Landolt-Börnstein New Series, Group 3, Vol. 17d (Springer-Verlag, Berlin, 1984).

Translated by D. H. McNeill

Using the $^{57m}Fe^{3+}$ Mössbauer probe to determine the EFG tensor parameters at CuO cation sites

V. F. Masterov,*) F. S. Nasredinov, N. P. Seregin, and P. P. Seregin

St. Petersburg State Technical University, 195251 St. Petersburg, Russia
(Submitted December 16, 1998; resubmitted February 2, 1999)
Fiz. Tverd. Tela (St. Petersburg) **41**, 1403–1406 (August 1999)

Mössbauer emission spectroscopy of the $^{57}Co(^{57m}Fe)$ isotope has shown that the impurity iron atoms appearing at the CuO-lattice cation sites after the decay of $^{57}Co^{2+}$ are donors and can become stabilized in two charge states, $^{57m}Fe^{3+}$ and $^{57m}Fe^{2+}$, and that the population ratio of these states depends on the Fermi level, whose position is governed by native CuO-lattice defects. A satisfactory agreement between the calculated and experimental values of the quadrupole splitting in Mössbauer spectra has been obtained for the $^{57m}Fe^{3+}$ centers. This permits one to consider the results obtained in the $^{57}Co(^{57m}Fe)$ Mössbauer emission spectroscopy study of cuprates as reliable experimental data on the crystal-field EFG tensor parameters at copper sites. © *1999 American Institute of Physics.* [S1063-7834(99)01008-4]

Mössbauer spectroscopy is widely employed in studies of cuprate HTSCs.[1] Because copper does not have Mössbauer isotopes, Mössbauer spectroscopy of ^{57}Fe impurity atoms is extensively used in investigations of the copper sublattices;[2] it is assumed that the ^{57}Fe probe stabilizes at the copper sites of the HTSC sublattices, so that, by comparing the measured with calculated quadrupole splittings in Mössbauer spectra, one can draw conclusions on the nature of the local copper-atom environment.

The quadrupole splitting can be calculated reliably only for the Fe^{3+} probe having a spherically symmetric $3d^5$ outer electronic shell, where the electric-field gradient (EFG) at the iron nuclei is generated primarily by lattice ions (the crystal-field EFG). However stabilization of Fe^{3+} at the sites of divalent copper Cu^{2+} (which is the most probable copper state in most HTSCs) should give rise to the formation of centers compensating the difference in charge between the substituting and replaced atoms. The compensating centers can be located near the impurity probe and in this way affect the EFG in a non-obvious way. The validity of the above considerations was buttressed by our study of the state of ^{57}Fe impurity atoms in CuO made by Mössbauer absorption spectroscopy;[3] the Fe^{3+} impurity atoms were found to substitute for Cu^{2+} ions in the CuO lattice to form associations of the type $Fe^{3+}-V-Fe^{3+}$ (V is the cation vacancy), and calculation of the EFG tensor parameters at ^{57}Fe nuclei in such associations turns out to be a difficult problem because of the creation of additional sources of EFG which change appreciably the total EFG.

As will be shown later, however, these problems can be eliminated by using the emission version of Mössbauer spectroscopy. We have carried out a comparison of experimental and theoretical quadrupole splittings in $^{57}Co(^{57m}Fe)$ Mössbauer emission spectra of $^{57m}Fe^{3+}$ impurity ions at copper sites in the CuO lattice. While data on CuO:^{57}Co Mössbauer emission spectra are available in the literature,[4–6] an analysis of all these data from a common standpoint is lacking.

1. EXPERIMENTAL TECHNIQUE AND RESULTS

Copper oxide was obtained by precipitating copper hydroxide from a $CuSO_4$ water solution with an alkali, with subsequent annealing of the sediment in an oxygen ambient. Cobalt in the form of $^{57}CoSO_4$ was added to a water solution of blue vitriol, with the cobalt concentration in CuO not exceeding $10^{17}\,cm^{-3}$.

The Mössbauer spectra were measured on a CM-2201 spectrometer at temperatures varied from 295 to 5 K. The absorber was $K_4Fe(CN)_6\cdot 3H_2O$ with a ^{57}Fe surface density of $0.1\,mg/cm^2$.

If the copper hydroxide was annealed within the 830–920 °C interval (the anneal time was 2 h), the Mössbauer spectra of CuO:^{57}Co samples taken at 295 K were a superposition of two quadrupole doublets (Fig. 1) with isomer shifts corresponding to the ions $^{57m}Fe^{3+}$ (spectrum *1*) and $^{57m}Fe^{2+}$ (spectrum *2*), with the fraction of the $^{57m}Fe^{3+}$ ions being 0.79 (0.02) for the anneal temperature of 920 °C, and 0.19 (0.02) for 830 °C. The parameters of spectra *1* and *2* are listed in Table I. A decrease of the spectrum measurement temperature below the Néel point is accompanied by a broadening of the spectra, with a gradual onset of the allowed hyperfine structure (spectrum *3* in Fig. 2). It is significant that, even for a sample containing Fe^{3+} and Fe^{2+} in a ratio ~1:1, the spectrum taken at 5 K was a magnetic sextet corresponding to one iron-atom state only (Fig. 2). The characteristics of this spectrum are given in Table I. The magnitude of the isomer shift and magnetic field at the nucleus are typical of divalent iron.

2. DISCUSSION OF RESULTS

The presence of a correlation between the transition of CuO to the antiferromagnetic state and the creation of mag-

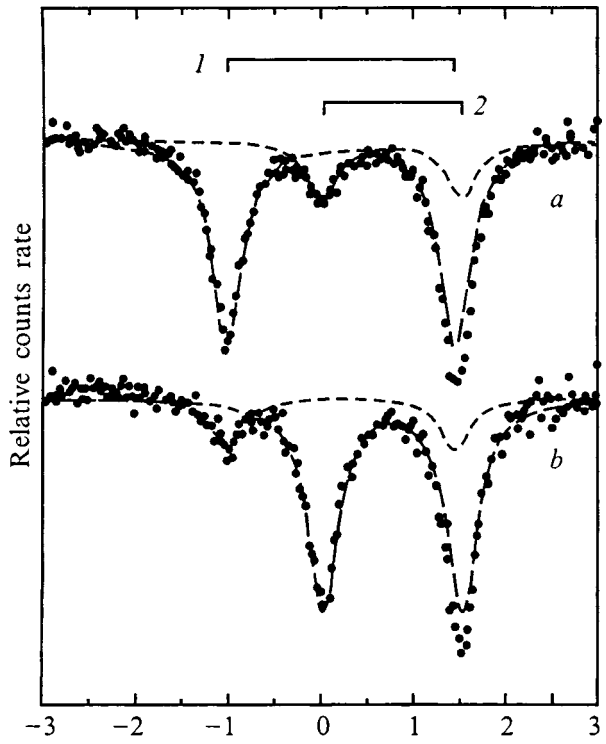

FIG. 1. Mössbauer emission spectra of CuO:^{57}Co measured at 295 K samples annealed at (a) 920 °C and (b) 860 °C. The experimental spectra are unfolded into quadrupole doublets (dashed lines), and the positions of these doublets corresponding to (*1*) $^{57m}Fe^{3+}$ and (*2*) $^{57m}Fe^{2+}$ centers are shown.

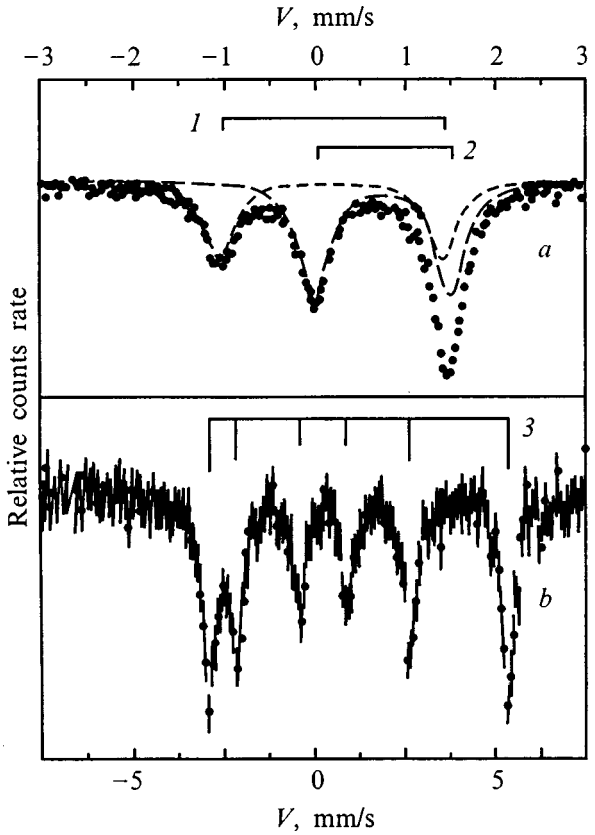

FIG. 2. Mössbauer emission spectra of CuO:^{57}Co measured at (a) 295 K and (b) 5 K for a sample annealed at 870 °C (the ratio of the areas bounded by spectra 1 and 2 at 295 K ~0.4:0.6). The 295 K spectrum is deconvolved into two quadrupole doublets (dashed lines), and the positions of these doublets corresponding to (*1*) $^{57m}Fe^{3+}$ and (*2*) $^{57m}Fe^{2+}$ centers are shown. (*3*) The position of the components of the Zeeman sextet corresponding to the $^{57m}Fe^{2+}$ centers at 5 K.

netic fields at the ^{57m}Fe nuclei permits a conclusion that the impurity cobalt atoms enter copper sites in the CuO lattice, and that the daughter ^{57m}Fe iron atoms produced in the cobalt radioactive decay may reside in different charge states, at least at room temperature.

The chemical properties of cobalt and the conditions of sample preparation used suggest that cobalt impurity atoms should form Co^{2+} isovalent substitutional centers in the CuO lattice, so that the ^{57m}Fe daughter atoms should occupy substitutional sites.

It should be pointed out that electron capture in ^{57}Co is accompanied by Auger-electron emission leaving the daughter atom in a multiply ionized state $^{57m}Fe^{n+}$ ($n \sim 7$). Such an ion is an effective trapping center for Auger electrons, and the $^{57m}Fe^{n+}$ ion becomes neutralized to one of its valence-stable states in a time $\sim 10^{-12}$ s. The final stabilized state of the daughter atom ($^{57m}Fe^{2+}$ or $^{57m}Fe^{3+}$) depends, however, both on the nature of the electrical activity of the iron center and on the nature and concentration of electrically active native defects in the CuO lattice.

The cupric oxide CuO is a semiconductor with a band gap of 1.35 eV.[7] EPR data[8] show undoped CuO samples to be oxygen deficient, this deficiency being the larger, the higher is the anneal temperature. Oxygen deficiency can be reduced by annealing in an oxygen ambient.[8] Thus it could be expected that spectrum 1 is due to single $^{57m}Fe^{3+}$ impurity ions produced by radioactive decay of $^{57}Co^{2+}$ in the CuO copper sites. In other words, one of the Auger electrons is

TABLE I. Parameters of the Mössbauer emission spectra of ^{57m}Fe impurity atoms in CuO.

Type of spectrum	*T*, *K*	Ion	Δ, mm/s	I.S., mm/s	Γ, mm/s	*B*, T
1	295	Fe^{3+}	2.50(2)	−0.25(1)	0.40(2)	
2	295	Fe^{2+}	1.52(2)	−0.80(1)	0.42(2)	
3	5	Fe^{2+}	1.30(4)	−0.81(2)	0.45(3)	25.5(2)

Note. Δ—Quadrupole splitting, I.S.—isomer shift, Γ—spectral linewidth, B—magnetic-field induction at the Fe^{3+} nuclei.

captured during the $^{57m}Fe^{n+}$ neutralization by a native lattice defect.

We calculated the crystal-field EFG tensor for the cation site in the CuO lattice in the point-charge approximation (the lattice was presented in the $Cu^{2+}O^{2-}$ form). The unit cell parameters were taken from Ref. 9. The crystal-field EFG tensor was off-diagonal in the crystallographic axes, and its diagonalization yields $V_{zz}=0.738\,e/\text{Å}^3$ and $\eta=0.29$, where $\eta=(V_{yy}-V_{xx})/V_{zz}$ is the asymmetry parameter of the crystal-field EFG tensor, and V_{xx}, V_{yy}, and V_{zz} are components of the crystal-field EFG tensor, with $|V_{zz}|>|V_{yy}|>|V_{xx}|$.

The quadrupole splitting of a $^{57m}Fe^{3+}$ Mössbauer spectrum was calculated from $\Delta_c=(1/2)eQV_{zz}(1-\gamma)(1+\eta^2/3)^{1/2}$, where γ is the Sternheimer coefficient [for the Fe^{3+} ion, $\gamma=-(7.97-9.14)$, Refs. 10 and 11], and the expected value of Δ_c lies from 2.14 to 2.42 mm/s.

Thus one observes a satisfactory agreement between the experimental Δ and calculated Δ_c quadrupole splittings of Mössbauer spectrum *1*, if we assume it to originate from single $^{57m}Fe^{3+}$ ions occupying copper sites in the CuO lattice.

The nature of the $^{57m}Fe^{2+}$ state presented by spectrum *2* can be understood if one takes into account the experimental observation that the only state left in the emission spectra taken below the Nëel temperature of samples containing comparable amounts of $^{57m}Fe^{2+}$ and $^{57m}Fe^{3+}$ is $^{57m}Fe^{2+}$. Obviously enough, the transition of $^{57m}Fe^{3+}$ to $^{57m}Fe^{2+}$ entails electronic processes. In other words, the $^{57m}Fe^{2+}$ ion should be considered as a neutral donor center, whereas $^{57m}Fe^{3+}$ is a singly ionized state of this center. The fine structure of a Mössbauer emission spectrum depends on the relative length of the time required for a thermodynamic equilibrium to set in between the neutral and ionized iron centers, τ, and the lifetime τ_0 of the ^{57}Fe Mössbauer level,[12] namely, if $\tau \ll \tau_0$, the experimental spectrum will reflect an averaged state of iron atoms produced in a fast electron exchange between the $^{57m}Fe^{2+}$ and $^{57m}Fe^{3+}$ centers, while if $\tau \ll \tau_0$, the experimental spectrum will be a superposition of the $^{57m}Fe^{2+}$ and $^{57m}Fe^{3+}$ spectra, and the $^{57m}Fe^{3+}$ contribution to the spectrum will correspond to the fraction of the ^{57}Co atoms having electron trapping centers within the mean free path λ_0 of the Auger electrons.

Taking into account the presence of both iron states in room-temperature spectra of CuO:^{57}Co samples, one should conclude that the emission spectra of CuO:^{57}Co reflect a nonequilibrium situation ($\tau \gg \tau_0$) arising in the course of neutralization of highly-charged $^{57m}Fe^{n+}$ states in the CuO lattice, and that the fraction of $^{57m}Fe^{3+}$ ions contributing to the spectra corresponds to that of the $^{57}Co^{2+}$ atoms having electron trapping centers within their close environment (within λ_0).

Decreasing the temperature of spectral measurements from 295 to 5 K brings about stabilization of all daughter iron atoms in the $^{57m}Fe^{2+}$ neutral state only. To interpret this observation, one should recall that undoped cupric oxide CuO is oxygen deficient and *n* type. The isovalent $^{57}Co^{2+}$ impurity in the CuO lattice is electrically inactive, and its presence does not affect the Fermi level position. The concentration of electrically active ^{57m}Fe iron centers in CuO is so low that the presence of iron likewise does not influence the Fermi level. Thus the position of the Fermi level is controlled only by native defects in the CuO structure. At low temperatures, the Fermi level lies close to the conduction-band bottom, and all native-defect levels are occupied by electrons. Therefore the Auger electrons formed in the course of radioactive transformation of the parent $^{57}Co^{2+}$ atoms become trapped by the daughter iron atoms, so that all iron atoms end up by being stabilized in the $^{57m}Fe^{2+}$ state (with no free-electron-capture centers present within a distance of λ). An increase of temperature shifts, as a rule, the Fermi level towards the midgap and, therefore, part of the native-defect levels turn out to be free and can act as Auger-electron trapping centers. As a result, iron atoms stabilize in the form of both $^{57m}Fe^{2+}$ and $^{57m}Fe^{3+}$, with the concentration ratio of these forms depending on both the spectrum measurement temperature (the higher the temperature, the larger is the fraction of the $^{57m}Fe^{3+}$ canters) and the concentration of native defects (other conditions being equal, the native-defect concentration is the higher, the higher is the anneal temperature and, hence, the higher is the $^{57m}Fe^{3+}$ center concentration). Prolonged storage of samples at room temperature results in a decrease of native-defect concentration and an increase of the $^{57m}Fe^{2+}$ contribution to the emission spectra. It is this phenomenon that was observed in Refs. 4 and 6.

Support of the Russian Fund for Fundamental Research (Grant 97-02-16216) is gratefully acknowledged.

*)Deceased.

[1] V. F. Masterov, F. S. Nasredinov, and P. P. Seregin, Fiz. Tverd. Tela (St. Petersburg) **37**, 1265 (1995) [Phys. Solid State **37**, 687 (1995)].
[2] P. Boolchand and D. McDaniel, Hyperfine Interact. **72**, 125 (1992).
[3] V. F. Masterov, F. S. Nasredinov, G. T. Daribaeva, V. F. Kobelev, P. P. Seregin, and N. N. Troitskaya, Fiz. Tverd. Tela (Leningrad) **33**, 2699 (1991) [Sov. Phys. Solid State **33**, 1525 (1991)].
[4] C. Niedermayer, A. Golnik, E. Recknagel, M. Rossmanith, A. Weidinger, X. S. Chang, A. Kleinhammes, N. Rosov, J. Saylor, R. Schuhmann, L. Takacs, A. Teh, G. Zhang, C. Hohenemser, and J. I. Budnick, Phys. Rev. B **38**, 2836 (1988).
[5] M. G. Smith, R. D. Taylor, M. P. Pasternak, and H. Oesterreicher, Phys. Rev. B **42**, 2188 (1990).
[6] A. Barcs, L. Bottyan, B. Molnar, D. L. Nagy, N. S. Ovanesyan, and H. Spiering, Hyperfine Interact. **55**, 1187 (1990).
[7] F. P. Koffyberg and F. A. Benko, J. Appl. Phys. **53**, 1173 (1982).
[8] A. Gupta and P. Shah, Phys. Rev. B **50**, 13706 (1994).
[9] S. Asbrink and L.-J. Norrby, Acta Crystallogr., Sect. B: Struct. Crystallogr. Cryst. Chem. **26**, 8 (1970).
[10] R. P. Gupta and S. K. Sen, Phys. Rev. A **8**, 1169 (1973).
[11] R. M. Sternheimer, Phys. Rev. **146**, 140 (1966).
[12] V. F. Masterov, F. S. Nasredinov, S. A. Nemov, and P. P. Seregin, Fiz. Tekh. Poluprovodn. **30**, 884 (1996) [Semiconductors **30**, 472 (1996)].

Translated by G. Skrebtsov

Local characteristics of crystal electronic structure in the Hartree–Fock method

V. A. Veryazov, A. V. Leko, and R. A. Évarestov

Institute of Chemistry, St. Petersburg State University, 198904 St. Petersburg, Russia
(Submitted December 29, 1998)
Fiz. Tverd. Tela (St. Petersburg) **41**, 1407–1411 (August 1999)

The formalism developed in molecular theory for calculation of local electronic-structure characteristics in a nonorthogonal atomic basis is generalized to systems with translational symmetry. Expressions have been derived to describe the bond orders, covalency, and valence in a crystal for restricted and unrestricted Hartree–Fock methods. Nonempirical electronic-structure calculations and an analysis of chemical bonding in the TiO_2, Ti_2O_3, and TiO titanium oxide crystals have been performed. © *1999 American Institute of Physics.* [S1063-7834(99)01108-9]

The band theory of solids is usually employed to consider characteristics of the electronic structure of a crystal which are associated with the potential periodicity and the corresponding electronic-state delocalization over the crystal, namely, the electronic energy bands, effective masses, etc. At the same time crystals, like molecules, are made up of atoms interacting with one another, which gives rise to electronic density localization along bonds (covalent crystals), around atomic nuclei (ionic crystals), or to the more complex and most widespread pattern of electronic density distribution.

In the recent decade, the Hartree–Fock (HF) method in the LCAO approximation, which had been already successfully employed for a long time in molecular theory, has gained wide acceptance in calculations of the electronic structure of crystals.[1] The HF method compares well in accuracy with other approaches while being, at the same time, the best starting approximation to take into account electronic correlations.[2] This method enables nonempirical calculations of both band and local characteristics of the electronic structure of a crystal and can be extend readily to cover systems with lower-order periodicity (polymers and crystal surfaces in the plate model).[1)]

The density matrix obtained in the calculation permits one to derive the characteristics employed usually when describing chemical bonding in molecules or crystals (the electronic configuration of an atom, atomic charges Q_A, atomic-bond orders W_{AB} and covalency C_A, and the total and free atomic valences V_A).

In molecular theory, the local electronic-structure characteristics were defined for the orthogonalized atomic basis used in approximate calculations, with subsequent generalization to the case of a nonorthogonal basis employed in HF calculations.[3,4]

The first attempts at a theoretical determination of local electronic-structure characteristics of crystals have been made only quite recently, and then only for the orthogonal basis[5–7] used in semiempirical versions of the HF method.

Note that determination of local characteristics by traditional methods of band theory for solids, which make use, as a rule, of the plane-wave basis (OPW, APW, density functional), involves additional approximations to calculate electronic-density-matrix elements in an atomic basis.[8]

The present work generalizes the existing methods of determination of local electronic-structure characteristics to crystalline systems, which are calculated in terms of the band model in the LCAO approximation using a nonorthogonal atomic basis. An analysis is made of the one-determinant approximation for a multi-electron wave function of a crystal within the restricted (RHF) and unrestricted (UHF) HF approaches.

Section 1 considers the electronic-density operator and matrix in the atomic-orbital basis and derives an expression which relates the density-matrix elements in the atomic basis and the Bloch basis taking into account the translational symmetry of a crystal.

Section 2 introduces definitions of local electronic-structure characteristics in a nonorthogonal atomic basis for different versions of the HF method.

Section 3 discusses the results of nonempirical HF calculations of the local electronic-structure characteristics of crystalline titanium oxides for various degrees of oxidation.

1. CRYSTAL ELECTRONIC-DENSITY OPERATOR AND MATRIX IN THE LCAO APPROXIMATION

Consider the most widespread version of the HF method, where, for the multi-electron wave function of a molecule or crystal, one takes a determinant constructed from single-electron wave functions, i.e., spin orbitals $\psi_i^\sigma(\mathbf{r})$, where $\sigma=\alpha,\beta$ are spin functions.

The single-electron functions are calculated by solving the HF equations[2]

$$\left(-\frac{1}{2}\Delta+V(\mathbf{r})+\int\frac{\rho_{\mathbf{r}\mathbf{r}'}}{|\mathbf{r}-\mathbf{r}'|}d^3\mathbf{r}'\right)\psi_i^\sigma(\mathbf{r})$$
$$-\frac{1}{2}\int\frac{\rho_{\mathbf{r}\mathbf{r}'}}{|\mathbf{r}-\mathbf{r}'|}\psi_i^\sigma(\mathbf{r}')d^3\mathbf{r}'=E_i^\sigma\psi_i^\sigma(\mathbf{r}). \quad (1)$$

The two-electron part of the Fock operator depends on the density matrix, which for a one-determinant wave function can be expressed through spin orbitals

$$\rho_{\mathbf{rr}'}=\rho^{\alpha}_{\mathbf{rr}'}+\rho^{\beta}_{\mathbf{rr}'}=\sum_{\sigma}\sum_{i}^{\mathrm{occ}}\psi_i^{\sigma}(\mathbf{r})\psi_i^{\sigma *}(\mathbf{r}'). \tag{2}$$

The summation in Eq. (2) is carried out over the spin orbitals corresponding to occupied single-electron states.

Closed-shell systems are analyzed using the RHF method, which requires coincidence of the spatial orbitals corresponding to spins α and β [$\psi_i^{\alpha}(\mathbf{r})=\psi_i^{\beta}(\mathbf{r})$]. In the RHF method, the spinless density operator $\hat{\rho}=2\Sigma_i^{\mathrm{occ}}|\psi_i\rangle\langle\psi_i|$ satisfies the conditions of duodempotency

$$\hat{\rho}^2=2\sum_{i}^{\mathrm{occ}}|\psi_i\rangle\langle\psi_i|2\sum_{j}^{\mathrm{occ}}|\psi_j\rangle\langle\psi_j|$$

$$=4\sum_{ij}^{\mathrm{occ}}|\psi_i\rangle\delta_{ij}\langle\psi_j|=2\hat{\rho}. \tag{3}$$

In the UHF method, the orbitals for spins α and β are considered independently, i.e., one takes into account spin polarization for electrons with opposite spins. The density operators $\hat{\rho}_{\alpha}$ and $\hat{\rho}_{\beta}$ for electrons with spins α and β and the total-density operator $\hat{\rho}$ satisfy the relations

$$\hat{\rho}=\hat{\rho}_{\alpha}+\hat{\rho}_{\beta};\quad \hat{\rho}_{\alpha}^2=\hat{\rho}_{\alpha};$$

$$\hat{\rho}_{\beta}^2=\hat{\rho}_{\beta};\quad \hat{\rho}^2=(\hat{\rho}_{\alpha}+\hat{\rho}_{\beta})^2=2\hat{\rho}-\hat{\rho}_s^2, \tag{4}$$

where $\hat{\rho}_s=\hat{\rho}_{\alpha}-\hat{\rho}_{\beta}$ is the spin-density operator.

The single-electron functions ψ_i^{σ} used in the LCAO approximation for molecules are presented in the form of a linear combination of basis atomic otbitals

$$\psi_i^{\sigma}=\sum_{\lambda}C_{i\lambda}^{\sigma}\varphi_{\lambda}. \tag{5}$$

By applying the density operator $\hat{\rho}_{\sigma}$ to the atomic orbital φ_{μ} one obtains

$$\hat{\rho}_{\sigma}|\varphi_{\mu}\rangle=\sum_{i}^{\mathrm{occ}}|\psi_i^{\sigma}\rangle\langle\psi_i^{\sigma}|\varphi_{\mu}\rangle=\sum_{i}^{\mathrm{occ}}\sum_{\nu}\sum_{\lambda}C_{i\nu}^{\sigma *}C_{i\lambda}^{\sigma}S_{\lambda\mu}\varphi_{\nu}$$

$$=\sum_{\nu}(P^{\sigma}S)_{\nu\mu}\varphi_{\nu}, \tag{6}$$

where $S_{\mu\nu}=\int\varphi_{\mu}^{*}(\mathbf{r})\varphi_{\nu}(\mathbf{r})d\mathbf{r}$ are elements of the overlap matrix S, and $P_{\nu\lambda}^{\sigma}=\Sigma_i^{\mathrm{occ}}C_{i\nu}^{\sigma *}C_{i\lambda}^{\sigma}$. Equation (6) means that the density operator $\hat{\rho}_{\sigma}$ in the LCAO basis is presented by the $(P^{\sigma}S)$ matrix.[4]

The operator relations (3) and (4) can be used to derive matrix relations

$$(PS)^2=2(PS), \tag{7}$$

$$(PS)^2=2(PS)-(P^sS)^2, \tag{8}$$

for the RHF and UHF methods, respectively, with $P=P^{\alpha}+P^{\beta}$ and $P^s=P^{\alpha}-P^{\beta}$.

The crystal orbitals $\Psi_i^{\sigma}(\mathbf{k},\mathbf{r})$ for systems with translational symmetry are presented in the LCAO approximation in the form of a linear combination of Bloch sums of the $\Phi_i(\mathbf{k},\mathbf{r})$ atomic functions

$$\Psi_i^{\sigma}(\mathbf{k},\mathbf{r})=\sum_{\mu}C_{i\mu}^{\sigma}(\mathbf{k})\Phi_{\mu}(\mathbf{k},\mathbf{r}), \tag{9}$$

$$\Phi_{\mu}(\mathbf{k},\mathbf{r})=\sum_{n}\exp(i\mathbf{k}\mathbf{R}_n)\varphi_{\mu}(\mathbf{r}-\mathbf{R}_A-\mathbf{R}_n). \tag{10}$$

The $\varphi_{\mu}^{An}(\mathbf{r})=\varphi_{\mu}(\mathbf{r}-\mathbf{R}_A-\mathbf{R}_n)$ atomic orbital is centered on atom A in the unit cell with a translation vector $\mathbf{R}_n$. The density operator for the crystal can be written

$$\hat{\rho}_{\sigma}=\frac{2}{V_{BZ}}\int_{BZ}\sum_{i}^{\mathrm{occ}}|\Psi_i^{\sigma}(\mathbf{k},\mathbf{r})\rangle\langle\Psi_i^{\sigma}(\mathbf{k},\mathbf{r})|d\mathbf{k}. \tag{11}$$

Integration in Eq. (11) is performed over the vectors $\mathbf{k}$ in the first Brillouin zone.

Taking into account Eq. (9), we obtain

$$\hat{\rho}_{\sigma}\varphi_{\mu}^{A0}(\mathbf{r})=\sum_{\lambda n}(P^{\sigma}S)_{\lambda\mu}^{Bn,A0}\varphi_{\lambda}^{Bn}(\mathbf{r}), \tag{12}$$

where

$$(P^{\sigma}S)_{\lambda\mu}^{Bn,A0}=\frac{1}{V_{BZ}}\int_{BZ}(P^{\sigma}(\mathbf{k})S(\mathbf{k}))_{\lambda\mu}\exp(i\mathbf{k}\mathbf{R}_n)d\mathbf{k}. \tag{13}$$

The matrix elements $S_{\mu\nu}(\mathbf{k})$ and $P_{\mu\nu}^{\sigma}(\mathbf{k})$ in the basis of Bloch sums $\Phi_{\mu}(\mathbf{k},\mathbf{r})$ are calculated by the expressions

$$S_{\mu\nu}(\mathbf{k})=\sum_{n}\exp(-i\mathbf{k}\mathbf{R}_n)$$

$$\times\int\varphi_{\mu}^{*}(\mathbf{r}-\mathbf{R}_A)\varphi_{\nu}(\mathbf{r}-\mathbf{R}_B-\mathbf{R}_n)d\mathbf{r}, \tag{14}$$

$$P_{\mu\nu}^{\sigma}(\mathbf{k})=\sum_{i}^{\mathrm{occ}}C_{i\mu}^{\sigma *}(\mathbf{k})C_{i\nu}^{\sigma}(\mathbf{k}). \tag{15}$$

The expansion coefficients $C_{i\mu}^{\sigma}(\mathbf{k})$ are calculated by solving matrix equations of the CO LCAO method for the crystal

$$F^{\sigma}(\mathbf{k})C^{\sigma}(\mathbf{k})=S(\mathbf{k})C^{\sigma}(\mathbf{k})E^{\sigma}(\mathbf{k}), \tag{16}$$

where $F^{\sigma}(\mathbf{k})$ is the Fock operator matrix, and $E^{\sigma}(\mathbf{k})$ is the single-electron energy vector. Self-consistent solution of Eqs. (16) involves calculation of the $F^{\sigma}(\mathbf{k})$ and $S(\mathbf{k})$ matrices over a finite special-point set in the Brillouin zone, and integration over the zone required to calculate the elements of the $F^{\sigma}(\mathbf{k})$ matrix is replaced by summation over the point set.[9]

2. LOCAL CHARACTERISTICS OF THE CRYSTAL ELECTRONIC STRUCTURE

Because of the normalization of the multi-electron wave function, $\mathrm{Sp}(\hat{\rho})=N^{\mathrm{tot}}$ (N^{tot} is the total number of electrons in the system, $\hat{\rho}=\hat{\rho}_{\alpha}+\hat{\rho}_{\beta}$). In view of the translational symmetry of the crystal, one can introduce density normalization per unit cell. Denoting by N the number of electrons per cell, we write in the matrix form

$$\mathrm{Sp}(PS)=\frac{1}{V_{BZ}}\int_{BZ}\sum_{\mu}(PS)_{\mu\mu}(\mathbf{k})d\mathbf{k}$$

$$=\sum_{\mu}(PS)_{\mu,\mu}^{A0,A0}=N. \tag{17}$$

This relation permits one to use the diagonal elements of matrix (PS) to describe the electronic-density distribution among the atoms in the system. In accordance with the definition of Mulliken,[10] the electronic population of an atom is a sum of the elements of matrix (PS) over the basis orbitals of this atom

$$N_{An}=N_{A0}=\sum_{\mu\in A}(PS)^{A0,A0}_{\mu\mu}$$
$$=\sum_{\mu\in A}\left(\sum_{n}\sum_{\lambda}P^{A0,Bn}_{\mu\lambda}S^{Bn,A0}_{\lambda\mu}\right)$$
$$=\sum_{\mu\in A}P^{A0,A0}_{\mu\mu}+\sum_{B\neq A}R_{A0,B0}+\sum_{n\neq 0}\sum_{B}R_{A0,Bn}, \quad (18)$$

where the quantities

$$R_{A0,Bn}=\sum_{\mu\in A}\sum_{\lambda\in B}P^{A0,Bn}_{\mu\lambda}S^{Bn,A0}_{\lambda\mu} \quad (19)$$

are called overlap populations. The charge on the atom is given by

$$Q_{A0}=Z_{A0}-N_{A0}, \quad (20)$$

where Z_{A0} is the nuclear charge for an all-electron calculation or the core charge if the pseudopotential approximation is used. The absolute value $|Q_{A0}|$ is called also the electrovalence of an atom.

Recalling relation (8), the expression for atomic populations within the unresticted HF method can be recast in the form

$$N_{A0}=\frac{1}{2}\sum_{\mu\in A}(((PS)^2)^{A0,A0}_{\mu\mu}+((P^sS)^2)^{A0,A0}_{\mu\mu})$$
$$=\frac{1}{2}\sum_{\mu\in A}\left(\sum_{n}\sum_{\lambda}(PS)^{A0,Bn}_{\mu\lambda}(PS)^{Bn,A0}_{\lambda\mu}\right.$$
$$\left.+(P^sS)^{A0,Bn}_{\mu\lambda}(P^sS)^{Bn,A0}_{\lambda\mu}\right)$$
$$=\frac{1}{2}\left(B_{A0,A0}+\sum_{B\neq A}B_{A0,B0}+\sum_{n\neq 0}\sum_{B}B_{A0,Bn}\right), \quad (21)$$

where the quantities

$$B_{A0,Bn}=\sum_{\mu\in A}\sum_{\lambda\in B}((PS)^{A0,Bn}_{\mu\lambda}(PS)^{Bn,A0}_{\lambda\mu}$$
$$+(P^sS)^{A0,Bn}_{\mu\lambda}(P^sS)^{Bn,A0}_{\lambda\mu}) \quad (22)$$

are actually a generalization to crystals of the definition of bond order in a nonorthogonal atomic basis introduced[4] earlier for molecules.

When using an orthonormalized set of basis functions, the overlap matrix S is an identity matrix, which simplifies considerably Eqs. (20)–(22). The method most widely used to obtain an orthonormalized basis is symmetric orthogonalization of atomic basis functions by Löwdin.[11] The density matrix $\tilde{P}$ in the Löwdin basis can be obtained from the P matrix using the relation $\tilde{P}=S^{1/2}PS^{1/2}$. In this case, Eqs. (20) and (22) are actually a definition of charge when analyzing populations by Löwdin[11] or of the bond order by Wiberg.[12]

It appears natural to define the covalency C_{A0} of atom A in a crystal as a sum of the orders of all bonds of this atom

$$C_{A0}=\sum_{B\neq A}B_{A0,B0}+\sum_{n\neq 0}\sum_{B}B_{A0,Bn}. \quad (23)$$

Using Eq. (21), one can readily express the covalency only through the elements of matrix (PS) in the basis of orbitals of atoms A:

$$C_{A0}=2N_A-B_{A0,A0}=2\sum_{\mu\in A0}(PS)^{A0,A0}_{\mu\mu}$$
$$-\sum_{\mu\in A0}\sum_{\mu'\in A0}(PS)^{A0,A0}_{\mu\mu'}(PS)^{A0,A0}_{\mu'\mu}$$
$$-\sum_{\mu\in A0}\sum_{\mu'\in A0}(P^sS)^{A0,A0}_{\mu\mu'}(P^sS)^{A0,A0}_{\mu'\mu}. \quad (24)$$

The restricted HF method may be considered as a particular case of the unrestricted one, for which the spin density P^s in Eqs. (22) and (24) is zero.

An expression for the total valence of an atom taking into account both the ionic and covalent components of chemical bonding was proposed[13]

$$V_{A0}=\frac{1}{2}(C_{A0}+\sqrt{C^2_{A0}+4Q^2_{A0}}). \quad (25)$$

An analysis of a large number of compounds with ionic-covalent bonding showed that this relation permits obtaining reasonable values of the valence.[5] The validity of the definition introduced was buttressed, however, by semiempirical calculations made on an orthogonalized atomic basis. This work is a first systematic investigation of the validity of this relation for nonempirical calculations on a nonorthogonal atomic basis made with the use of Eqs. (20) and (24) for atomic charges and covalencies.

3. ELECTRONIC STRUCTURE AND CHEMICAL BONDING IN CRYSTALLINE TITANIUM OXIDES

The above formalism for calculation of local electronic-structure characteristics of crystals was applied by us to a number of titanium oxides with the metal atom oxidized to various degrees. Although the quadrivalent state of the titanium atom is the most stable, the existence of oxygen com-

TABLE I. Crystal structure of titanium oxides: space group, number of formula units per cell Z, and nearest interatomic distances.

Structural characteristics	TiO(hex)	Ti_2O_3	TiO_2(r)	TiO_2(a)	TiO_2(b)
Group	$P\bar{6}m2$	$R\bar{3}c$	$P4_2/mnm$	$I4_1/amd$	$Pbca$
Z	2	2	2	2	8
R_{Ti-Ti}, Å	3.03	2.58	3.00	3.10	2.95
	3.24	2.99	3.55	3.76	3.06
R_{Ti-O}, Å	2.38	2.02	1.95	1.94	1.86
	3.86	2.07	1.97	1.99	1.92

TABLE II. Local electronic-structure characteristics of titanium oxides in the Hartree–Fock method.

Crystal	Mulliken				Löwdin			
	P_d	Q_{Ti}	V_{Ti}	V_{O}	P_d	Q_{Ti}	V_{Ti}	V_{O}
TiO(hex)	2.38	1.62	2.14	2.04	2.70	1.27	2.30	2.15
Ti_2O_3	1.82	2.26	3.61	2.05	2.50	1.43	3.98	2.30
TiO_2(r)	1.46	2.66	3.94	2.08	2.18	1.73	4.18	2.36
TiO_2(a)	1.47	2.65	3.98	2.08	2.19	1.72	4.23	2.36
TiO_2(b)	1.49	2.63	3.97	2.09	2.21	1.70	4.23	2.38

pounds of titanium in formal oxidation states of III and II, as well as of a series of nonstoichiometric compounds was established.

Table I presents the space-group symbol, the number of formula units in the cell, and the shortest Ti–Ti and Ti–O distances for TiO,[14] Ti_2O_3,[15] and TiO_2 in the rutile (r), anatase (a), and brookite (b) modifications.

For the TiO_2 and Ti_2O_3 crystals, band structure calculations were carried out earlier both in the Hartree–Fock[16,17] and local exchange[18] approximations. We are not aware of the existence of any electronic structure calculations for TiO. The available publications focus attention primarily on description of the band structure of titanium oxides and restrict the discussion of the nature of chemical bonding in these compounds to an analysis of atomic charges.

We have used in this work both the restricted and unrestricted HF treatments implemented in the CRYSTAL-95 program.[19] The core states were described in the calculations by the pseudopotentials and on the atomic bases proposed in Ref. 16. A self-consistent electronic-density calculation was done over a grid of 216 BZ points. Self-consistent solutions obtained with different starting density matrices were considered for each compound by the scheme proposed in Ref. 20. Tables II and III list the values corresponding to insulator solutions with the lowest total crystal energy.

Table II presents local electronic-structure characteristics of the titanium oxides obtained by the RHF method, namely, the Ti d-orbital populations P_d and atom charges Q_{Ti}, as well as the atomic valences V_A. Also given are the local characteristics calculated using Eqs. (20)–(22) in a nonorthogonal atomic basis and a basis orthogonalized according to Löwdin. As follows from a comparison of the results obtained from population analyses by Mulliken and Löwdin, the Löwdin analysis shows the chemical bonding in the crystals under study to be largely covalent, with the total valences of the titanium and oxygen atoms differing substantially from the expected stoichiometric values. It was shown[21] that the calculations made using a valence atomic basis (without polarizing functions) in the Löwdin population analysis agree better with the expected values. The population analysis by Mulliken made in a nonorthogonal basis was found to be less sensitive to the inclusion of polarizing functions into the calculation.

TABLE III. Local properties of chemicla bonding in titanium oxide crystals in the restricted and unrestricted HF methods: titanium d-orbital populations P_d, atomic charges Q_A, covalencies C_A, atomic valences V_A, and bond orders B_{AB} for nearest-neighbor atoms.

Local electronic-structure	TiO(hex)		Ti_2O_3		TiO_2(r)
	RHF	UHF	RHF	UHF	RHF
P_d	2.38	2.34	1.82	1.77	1.46
Q_{Ti}	1.63	1.67	2.26	2.32	2.66
C_{Ti}	0.90	0.69	2.19	1.23	2.15
V_{Ti}	2.14	2.05	3.61	3.01	3.94
Q_{O}	−1.63	−1.67	−1.51	−1.55	−1.33
C_{O}	0.74	0.66	0.94	0.88	1.24
V_{O}	2.04	2.03	2.05	2.05	2.08
$B_{\mathrm{Ti-Ti}}$	0.03	0.01	0.89	0.03	0.01
	0.00	0.00	0.00	0.01	0.01
$B_{\mathrm{Ti-O}}$	0.11	0.10	0.20	0.19	0.36
	0.00	0.00	0.21	0.19	0.30

Note. For the TiO_2 crystal, the RHF and UHF results coincide.

As seen from Table III, the results obtained with the restricted and unrestricted HF methods for TiO_2 (with a formal titanium configuration d^0) do not differ practically from one another. The results of a calculation of the local properties of the TiO_2 modifications shows them to be only weakly sensitive to structural changes.

The largest difference between the calculations made in the RHF and UHF approximations was found for Ti_2O_3 with a formal titanium atom configuration d^1, where one can expect substantial spin polarization effects.

As seen from Table III, the RHF method predicts a high bond order between titanium atoms, which, in its turn, results in an overestimated titanium valence. This pattern of chemical bonding is not borne out by experiments.

As follows from Table III, an increase in the degree of Ti oxidation from II to IV gives rise to an increase in the charge on the titanium atom, but the relative ionicity and the absolute value of the charge on the oxygen atom decrease. UHF calculations show that, in all the above insulator oxygen compounds of titanium, there is no strong covalent interaction among the metal atoms.

The valences of titanium and oxygen calculated with Eqs. (20)–(25) practically coincide with the expected stoichiometric values. This gives one grounds to hope that the above relations will prove to be applicable to an analysis of the valence states of atoms in nonstoichiometric titanium compounds.

Thus our study of titanium oxides shows that the scheme proposed here for the analysis of chemical bonding permits description of the local electronic-structure characteristics in accordance with the common chemical concepts. The above consideration suggests that, when used in describing the electronic structure of poorly studied compounds, the local characteristics of chemical bonding may be treated as addi-

tional quantities, whose analysis may provide an evaluation of the validity of the approach employed.

An appreciable role in transition-metal compounds is played by electron-correlation effects, which may be considered within the framework of multi-configurational methods employing the cluster model of the crystal. In this case, local characteristics can be calculated using the approach developed in Ref. 22.

Support of the Russian Fund for Fundamental Research (Grant 96-03-33796a) is gratefully acknowledged.

[1)] In the literature dealing with the theory of solids, the LCAO approximation for crystal-field orbitals is sometimes erroneously identified with the tight-binding method, which is conventionally used as an interpolation scheme in calculations made with more rigorous methods.

[1] *Quantum-Mechanical* ab initio *Calculations of the Properties of Crystalline Materials*, edited by C. Pisani, Lecture Notes in Chemistry, Vol. 67 (Springer, Berlin, 1996).
[2] M. I. Petrashen', N. N. Kristoffel, and I. V. Abarenkov, Vestnik LGU No. 10, 5 (1963).
[3] S. G. Semenov, Vestnik LGU No. 16, 119 (1973).
[4] I. Mayer, Int. J. Quantum Chem. **29**, 73 (1986).
[5] R. A. Evarestov and V. A. Veryazov, Rev. Solid State Sci. **5**, 415 (1991).
[6] R. C. Bochicchio and H. F. Reale, J. Phys. B **26**, 4871 (1993).
[7] R. A. Evarestov and V. P. Smirnov, J. Phys.: Condens. Matter **9**, 3023 (1997).
[8] M. D. Segall, R. Shah, C. J. Pickard, and M. C. Payne, Phys. Rev. B **54**, 16317 (1996).
[9] R. A. Evarestov and V. P. Smirnov, Phys. Status Solidi B **119**, 9 (1983).
[10] R. S. Mulliken, J. Chem. Phys. **23**, 1833 (1955).
[11] P. Löwdin, Adv. Quantum Chem. **5**, 185 (1970).
[12] K. B. Wiberg, Tetrahedron **24**, 1083 (1968).
[13] R. A. Evarestov and V. A. Veryazov, Theor. Chim. Acta **81**, 95 (1991).
[14] S. Moehr and H. Müller-Buschbaum, Z. Anorg. Allg. Chem. **620**, 1175 (1994).
[15] C. E. Rice and W. R. Robinson, J. Solid State Chem. **21**, 145 (1977).
[16] B. Silvi, N. Fowati, N. Noda, and C. R. A. Cotton, J. Phys. Chem. Solids **52**, 1005 (1991).
[17] M. Catti, G. Sandrone, and R. Dovesi, Phys. Rev. B **55**, 16122 (1997).
[18] L. F. Mattheiss, J. Phys.: Condens. Matter **8**, 5987 (1996).
[19] R. Dovesi, V. R. Saunders, C. Roetti, M. Causà, N. M. Harrison, R. Orlando, and E. Aprà, *Crystal-95 Manual* (Torino, 1996).
[20] R. A. Evarestov, A. V. Leko, and V. A. Veryazov, Phys. Status Solidi B **210**, R3 (1998).
[21] R. A. Evarestov, A. V. Leko, and V. A. Veryazov, Phys. Status Solidi B **203**, R3 (1997).
[22] R. Ponec, M. Krack, and K. Jug, Theor. Chim. Acta **93**, 165 (1996).

Translated by G. Skrebtsov

Specific structural features and thermal resistance of shungite carbon to graphitization

S. V. Kholodkevich*) and V. I. Berezkin

Scientific Research Center for Ecological Safety, Russian Academy of Sciences, 197110 St. Petersburg, Russia

V. Yu. Davydov

A. F. Ioffe Physicotechnical Institute, Russian Academy of Sciences, 194021 St. Petersburg, Russia
(Submitted February 6, 1999)
Fiz. Tverd. Tela (St. Petersburg) **41**, 1412–1415 (August 1999)

A Raman scattering study is reported of the structural changes in natural glassy carbon in shungite I induced by a thermal treatment within the 500–2700 °C range in an inert atmosphere. It has been found that thermal treatment results in an insignificant increase of the graphite phase content in the bulk of the samples, whereas in the near-surface regions graphitization of the shungite glassy carbon can be more pronounced. The observed resistance of the shungite to graphitization can be explained within a structural model in which the shungite glassy carbon consists of closely packed nanostructures representing hollow multi-layered globules enveloped in random-network carbon. © *1999 American Institute of Physics.* [S1063-7834(99)01208-3]

The shungites represent silicate formations containing natural glassy carbon in amounts from a few per cent to 99.6% in some samples. These disordered structures exhibit diverse compositions and, besides carbon, contain quartz, mica, metal oxides, alumosilicates, etc. All these components are mixed in a remarkably uniform way.[1–3]

X-ray structural data show the regions of coherent x-ray scattering to be microcrystallites containing three to six distorted and heavily defected graphite-like atomic layers with an order-of-magnitude larger number of aromatic rings per layer. Electron diffraction measurements[1] and Raman spectra[4] yield practically the same size for the graphite-like carbon microcrystallites in shungite-I (with the highest carbon content of up to 98%), ~25 Å.

A distinctive feature of the natural glassy carbon in the shungites is its resistance to graphitization up to temperatures of about 3000 °C. In shungites of different types the process of partial graphitization terminates at different temperatures ranging from 2200 to 2800 °C,[2] but one cannot conduct it to completion. Some authors[2] attribute this to the presence of chain carbon characterized by stable –C≡C– and =C=C= bonds, which present the main obstacle to the graphitization of shungites. Other authors[5] believe the presence of heteroatoms in the shungite material to be the main reason for the resistance to graphitization.

This paper reports a Raman scattering (RS) study of the structural changes in the shungite carbon induced by a thermal treatment.

1. EXPERIMENTAL TECHNIQUE

The samples of shungite-I taken from one lot were typically a few mm in size and had a specific weight of 1.85 g/cm^3. The measurements were carried out in the backscattering geometry. The spectra were excited by the 5145-Å line of an Ar^+ laser at incident power levels of 5 to 30 mW. The size of the excitation region varied from 20 to 50 μm. A micrometer attachment with a step of ~50 μm was used for scanning the surface. One measured both the starting samples and the samples thermally treated at 500, 1000, 2000, and 2700 °C. To prevent the samples from oxidation, the treatment was performed in an argon ambient in a special microwave furnace. After heating the furnace to the desired temperature, the sample was maintained at it for 5–10 min, then the furnace was turned off, and the sample was slowly cooled without removal to room temperature, at which the measurements were made. The microcrystallite size was calculated by comparing the integrated scattered intensities of the corresponding bands,[6] which were isolated using a special computer code.

2. EXPERIMENTAL RESULTS

Figure 1 presents RS spectra of the starting samples (curve *1*) and of the samples subjected to a thermal treatment (curves *2–5*). The spectra of the shungite samples are similar to those typical of most disordered carbon structures. The two strongest bands peak at 1355 and 1580–1590 cm^{-1} and correspond to the A_{1g} and E_{2g2} vibrational modes of crystalline graphite, respectively. The first band is forbidden by selection rules and appears only in the amorphous phase of carbon. The position, halfwidths, and intensity ratio of these bands obtained from curve *1* practically coincide both with the data of Ref. 4 and with the similar RS features characteristic of the so-called onion-like carbon modification.[7]

Thermal treatment of the samples gives rise to certain changes in the spectra, the most characteristic of them being a change in the intensity ratio of the main scattering bands. As the annealing temperature is increased, this ratio changes

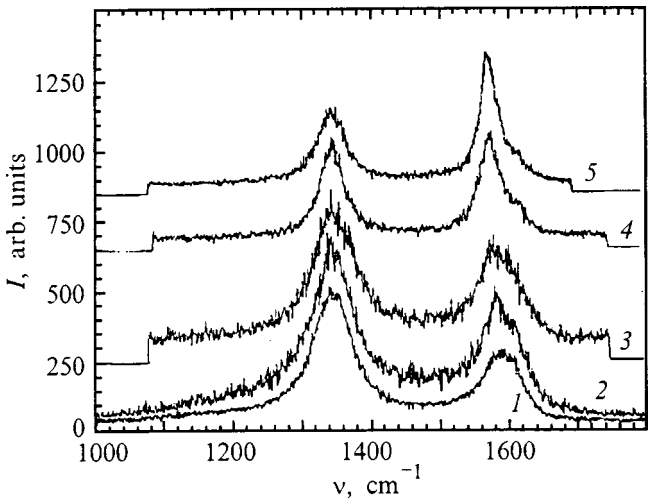

FIG. 1. RS spectra of shungite-I after annealing in an inert atmosphere at various temperatures, T(°C): *1* — 20, *2* — 500, *3* — 1000, *4* — 2000, *5* — 2700. For convenience, the curves are shifted along the vertical scale.

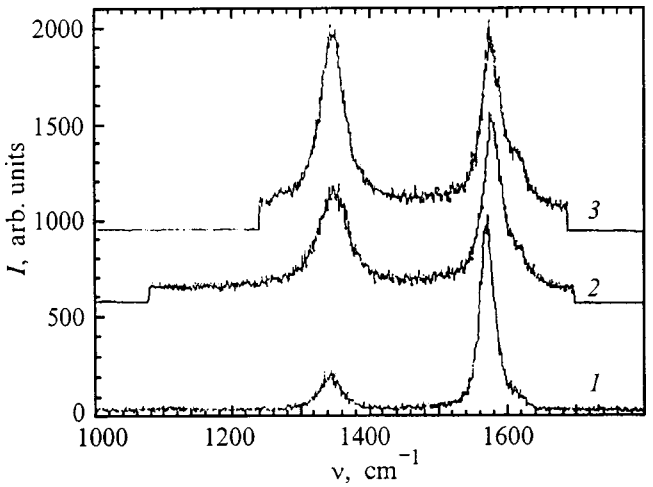

FIG. 2. RS spectra of shungite-I after annealing at 2700 °C in an inert atmosphere. *1* — from the near-surface region, *2* and *3* — from different points on the cleaved surface in the bulk of the sample.

slightly in favor of the higher-frequency band (curves *2* and *3*), to make the bands about equal in amplitude at 2000 °C (curve *4*). The strongest changes are observed in the samples heated to 2700 °C (curve *5*); indeed, the high-frequency band exceeds now considerably in intensity the low-frequency one, which indicates the carbon to have acquired a slightly more ordered structure, i.e. its partial graphitization.

To check whether this effect relates to the bulk of the sample or only to its near-surface region, additional measurements were carried out on cleaved surfaces. It was found that up to 2000 °C inclusive, Raman spectra taken from the surface and from the bulk practically do not differ. At 2700 °C, the degree of graphitization of the surface (curve *1* in Fig. 2) is substantially larger than that of the bulk (curves *2* and *3*). In connection with this, Fig. 1 shows also a bulk Raman spectrum (curve *5*).

3. DISCUSSION OF RESULTS

Graphitization in carbon materials proceeds usually by the following scheme. At temperatures ~1000–2000 °C the diameter of the layers L_a increases through merging of neighboring frameworks and attachment of disordered carbon atoms. The interplanar distances d practically do not change. Above 2000 °C, the framework growth slows down, and d decreases noticeably, which is accompanied by azimuthal ordering of layers with respect to one another. After this, the hexagonal frameworks become packed to form parallel layers with packets of different thickness.[8]

Figure 3 shows graphically the dependence of the microcrystallite size L_a on annealing temperature based on the data of Fig. 1. One readily sees a monotonic growth, and while in the starting sample $L_a \sim 24$ Å, after the thermal treatment L_a increases more than twofold. For the sample corresponding to curve *1* in Fig. 2, $L_a \sim 162$ Å. The interlayer separation d in shungites decreases only slightly, and at 2800 °C it may become, for instance, $d = 3.436$ Å, to be compared with the starting value $d = 3.497$ Å.[2] The latter figure is close to the mean value for the shungites. We may recall that for crystalline graphite $d = 3.355$ Å.

The above experimental data do indeed show that graphitization in high-carbon shungites subjected to a high-temperature treatment comes to an end neither in the bulk nor on the surface, otherwise the band at 1355 cm^{-1} would have disappeared completely. The reasons for this should be sought in the specific features of the shungite structure and composition.

The shungites have a complex mineralogical composition. Even the high-carbon shungites-I may contain a variety of impurities in amounts as high as a few per cent. In our opinion, however, impurity atoms not only cannot interfere with graphitization in shungites but should rather favor it. The point is that a number of metals, as well as silicon, are known[9] to act as catalysts in the graphitization of carbon materials. The process is intensified through the formation of carbides and of eutectic alloys of the type of Me–MeC or MeC–C (where Me is a metal or silicon atom), where alternating events of carbide synthesis-decomposition lead to the formation of graphite. The impurities which are not involved in the carbide formation, i.e., which do not act as catalysts, do not exert any noticeable influence on the process.[8,9] By far the majority of non-carbon components in the shungites exhibit catalytic action.

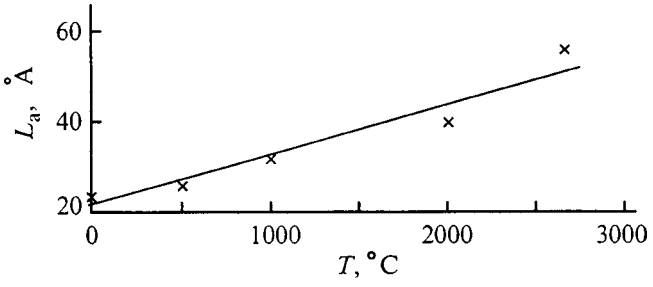

FIG. 3. Dependence of the size of shungite-I microcrystallites on sample annealing temperature.

As for the chain carbon, it can exist both in basal planes and provide strong bonding between them. It is believed that for each five-six atoms in a layer in the shungites-I there may be one to two carbon atoms bound strongly to the adjacent plane.[1,2] For such a high concentration of chain-carbon atoms, their presence in the shungite structure could be, in our opinion, detected by such direct methods as, e.g., IR absorption or RS in the 2100–2300 cm^{-1} region, which is characteristic of linear carbon chains.[10] No such features have been observed thus far, however, in the shungites. On the other hand, if we take into account that adjacent carbon layers in both the transverse and longitudinal directions can be joined through structural defects, for instance, screw and edge dislocations, there appears no need for invoking the assumption of the presence of linear carbon molecules.[8]

Judged from the standpoint of its disordering, the shungite occupies probably one of the extreme places in the solid-carbon series, because the absence of three-dimensional (hkl)-type reflections in its diffractograms does not give any grounds for presenting the shungite carbon as finely dispersed or poorly crystallized graphite. The shungites-I should differ substantially in structure from synthetic glassy carbon as well (which is characterized by rigid crossing multiple carbon bonds, graphite-diamond-type bonds, and bridging oxygen[9]), because, for approximately equal L_a, carbon content, and porosity, the specific weight of the latter is 1.4–1.5 g/cm^3, whereas that of the former is typically 1.79–1.85 g/cm^3 (Ref. 1), which is at the level of high-quality single-crystal industrial graphites and is in excess of that of the other known forms of natural amorphous carbon.

Electron microscopy shows the fundamental building block in the shungite structure to be the globule, which represents supposedly a hollow, close to spherical, particle surrounded by a multi-layer shell and ~ 100 Å in size.[11] The regions of x-ray coherent scattering are the most extended plane walls of the globule, i.e., regions of similar carbon-layer arrangement. The carbon located between the globules provides their bonding to one another.[12] It is apparently the least organized form and represents the random-framework carbon. This structure is similar to the onion-like carbon, which forms at $\sim 1000\,^{\circ}C$ in a structural diamond-graphite phase transition on the surface of 40-Å diamond clusters, which are obtained in the course of detonation synthesis from the carbon of explosive substances.[7] Here the globule is not hollow but contains a diamond nanocluster. As for the shungites, thermal treatment reduces the layer curvature as a result of globule coalescence and formation of comparatively larger hollow particles.[12] An increase in ellipticity may also account for the observed growth of microcrystallites in visible size.

It is known that the structure of nongraphitizing carbon materials remains imperfect even after prolonged treatment at very high temperatures and, if there are globules there, they do not change their morphology up to the carbon sublimation temperatures.[13] If the graphitization process is considered as a transformation of a two- to three-dimensional structure, one can say that, while the microcrystallites are seen to become larger, their mutual orientation remains chaotic. It is appropriate to point out here that the efficiency of graphitization, for instance, of industrial soot, decreases with decreasing size of the spherical soot particles because of the influence of the increasing curvature of their surface and the most finely dispersed, channel-type soots, with particles 100–400 Å in size, do not graphitize at all.[14] Thus the shungite microcrystallites merged in globules are not capable of complete coalescence as a result of their small size and the absence of mutual orientation. In other words, the lack of tendency to graphitization is inherent in the structure of the shungite substance itself.

The above reasoning makes it clear why the graphitization process on the surface of a sample proceeds to a considerably greater extent. In the bulk, by far the majority of the globules remain intact as a result of their being closely packed, and microcrystallites have no possibility of mutual alignment. By contrast, on the surface, the additional surface energy can facilitate breaking the bonds which are stable in the bulk of the sample, and the globules, being no longer closed, can break into microcrystalline fragments more extensively than in the bulk, thus producing favorable conditions for the carbon layers to pack into a regular crystal lattice. However graphitization does not come to completion on the surface as well, because the original structure places a constraint on the growth of microcrystallites and globule destruction, i.e., the shungite itself represents a highly disordered material even after thermal treatment.

An analysis of the results obtained in this work permits the following conclusions.

Within the 500–2700 °C temperature range, the graphite-like microcrystallites of the shungite glassy carbon in the bulk increase in size by a factor of two to three, and on the surface of a sample, these structural elements can increase by nearly an order of magnitude. No complete graphitization is reached in either case, which is connected, in our opinion, neither with impurity atoms nor with a possible presence of chain-carbon atoms.

Only complete destruction of globules can apparently provide favorable conditions for transformation of the shungite glassy carbon to ultradisperse graphite.

The shape of the RS spectra obtained from onion-like carbon is affected more by the size of globular nanostructures than by the degree and character of filling of their internal space. Therefore the assumption of the globules in the shungites being hollow requires additional confirmation.

Support of the Russian Fund for Fundamental Research (Grant 98-03-32684) is gratefully acknowledged.

*)E-mail: Kholod@ip.nwpi.ru

[1] *Shungites — a New Carbon Raw Material* [in Russian], edited by V. A. Sokolov, Yu. K. Kalinin, and E. F. Dyukkiev (Karelia, Petrozavodsk, 1984).
[2] *The Shungites of Karelia and Ways of Their Integrated Use* [in Russian], edited by V. A. Sokolov and Yu. K. Kalinin (Karelia, Petrozavodsk, 1975).
[3] *The Shungite Rocks of Karelia* [in Russian], edited by A. M. Shlyamin (Karelia, Petrozavodsk, 1981).
[4] S. V. Kholodkevich and V. V. Poborchiĭ, Pis'ma Zh. Tekh. Fiz. **20**, No. 3, 22 (1994) [Tech. Phys. Lett. **20**, 184 (1994)].

[5] *Organic Substance of the Shungite Rocks of Karelia* [in Russian], edited by M. M. Filippov (Karelian Scientific Center, Russian Academy of Sciences, Petrozavodsk, 1994).
[6] F. Tuinstra and J. L. Koenig, J. Chem. Phys. **53**, 1126 (1970).
[7] A. E. Aleksenskiĭ, M. V. Baĭdakova, A. Ya. Vul', V. Yu. Davydov, and Yu. A. Pevtsova, Fiz. Tverd. Tela (St. Petersburg) **39**, 1125 (1997) [Phys. Solid State **39**, 1007 (1997)].
[8] V. P. Sosedov and E. F. Chalykh, *Graphitization of Carbon-Containing Materials* [in Russian] (Metallurgiya, Moscow, 1987).
[9] V. I. Kostikov, N. N. Shipkov, Ya. A. Kalashnikov, B. K. Dymov, V. P. Shevyakov, and I. A. Bubnenkov, *Graphitization and Diamond Formation* [in Russian] (Metallurgiya, Moscow, 1991)
[10] M. B. Guseva, V. G. Babaev, V. M. Babina, N. D. Novikov, and V. V. Khvostov, *Abstract of the All-Union Symposium Amorphous and Microcrystalline Semiconductors* (St. Petersburg, 1998), p. 55.
[11] V. V. Kovalevski, N. N. Rozhkova, A. Z. Zaidenberg, and A. N. Yermolin, Mol. Mater. **4**, 77 (1994).
[12] V. V. Kovalevskiĭ, Zh. Neorg. Khim. **39**, 31 (1994).
[13] A. S. Fialkov, *Carbon and Graphite Materials* [in Russian] (Énergiya, Moscow, 1979).
[14] V. B. Fenelonov, *Porous Carbon* [in Russian] (Institute of Catalysis, Novosibirsk, 1995).

Translated by G. Skrebtsov

DEFECTS. DISLOCATIONS. PHYSICS OF STRENGTH

Instability of an elastically compressed silicon surface under etching

Yu. G. Shreter, D. V. Tarkhin, S. A. Khorev, and Yu. T. Rebane

A. F. Ioffe Physicotechnical Institute, Russian Academy of Sciences, 194021 St. Petersburg, Russia
(Submitted July 17, 1998; resubmitted November 30, 1998)
Fiz. Tverd. Tela (St. Petersburg) **41**, 1416–1418 (August 1999)

An unusual relief in the form of linear defects resembling quasicracks or grooves was observed on a compressionally stressed surface of a bent silicon surface subjected to chemical etching. The average distance between the forming defects was determined by the magnitude of the surface mechanical strain. The reason for this is assumed to be an Asaro–Tiller–Srolovitz instability in the compressed-surface–etching-agent system. A simple technique is proposed for producing considerable mechanical strains, up to 0.5%, in a silicon surface at room temperature. © *1999 American Institute of Physics*. [S1063-7834(99)01308-8]

More than two decades ago, Asaro and Tiller predicted the onset of thermodynamic instability in a flat, compressionally stressed surface of a solid, and pointed out its possible relation to the formation and growth of microcracks on the surface of mechanically stressed solids.[1] These ideas were further developed theoretically by Grinfel'd[2] and Srolovitz.[3] This instability was recently observed to set in in stressed He[4] crystals[4] and polymer films.[5]

The instability of a stressed surface consists essentially in that, if atoms on the surface of a solid can diffuse freely or transfer to a melt, this surface will undergo rearrangement (corrugation) under mechanical loading and tend to a minimum of elastic and surface energy.[3]

Unusual patterns in the distribution of cracklike defects were observed recently around scratches on Si samples following their etching.[6,7] The nature of these defects and their distribution over the sample surface remained unclear because of the complexity of the phenomena occurring on a scratched surface, such as residual mechanical strain,[8] creation and healing of microcracks and dislocations,[9–11] and formation on the Si surface of an amorphous[12] or metallic[13] phase.

This work investigates the effect of the magnitude and sign of mechanical strains on the distribution pattern of the defects observed to appear under etching of elastically stressed Si single crystals. The experiments were carried out on samples of dislocation-free Si bent elastically at room temperature. This permitted one to avoid creation of dislocations, cracks, or any phase transformations, as well as to study the effect of compression and tension on defect formation when atoms on the sample surface are activated by a chemical etching agent.

The results obtained are explained in terms of the Asaro–Tiller–Grinfel'd (ATG) theory.[1–3]

1. EXPERIMENTAL

The samples were cut from a (111)-oriented *p*-Si single-crystal wafer ($\rho = 10\,\Omega\cdot$cm) grown by the Chochralski technique. Dislocation-free silicon whose surface was thoroughly polished chemically was chosen to reduce the influence of sample defects. The samples were given a special shape (Fig. 1) that measured $18\times 3\times 0.3$ mm. The central (thin) part of the samples, $d_2 = 0.1-0.175$ mm thick and $l_2 = 2$ mm long, was etched with an HNO_3:CH_3COOH:HF (5:3:3) agent. The left-hand, thick part of the sample was fixed in a special teflon holder. A calibrated screw (*3*) applied a load from below (Fig. 1). Thus the upper surface of the sample was subjected to compression, and the lower one, to tension. The loading could be varied with the screw. Such a geometry of the sample, its fixing, and the point of load application permitted one to obtain a linear variation of the stress over the length in the thin section of the sample, with the maximum of mechanical stress at the fixing point. The maximum strain obtained by us in this arrangement was $\sim 0.5\%$ at 300 K.

The structure was fabricated of teflon and could be immersed directly with the sample into the etch. A Secco selective etch[14] was used to study corrosive phenomena occurring on the stressed surface of silicon. The etch time was 15 s, and the temperature, 300 K.

2. RESULTS AND DISCUSSION

The unusual surface relief was observed on the compressed side of the sample after the etching. The lower, extended side remained specular. Figure 2 presents typical SEM images. In these images obtained at different distances from the fixing point the strain increases from *a* to *c*. One

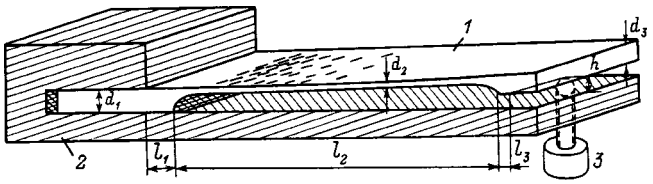

FIG. 1. Arrangement for sample straining and geometry of the sample. *1* — Sample, *2* — teflon holder, *3* — screw for loading the sample.

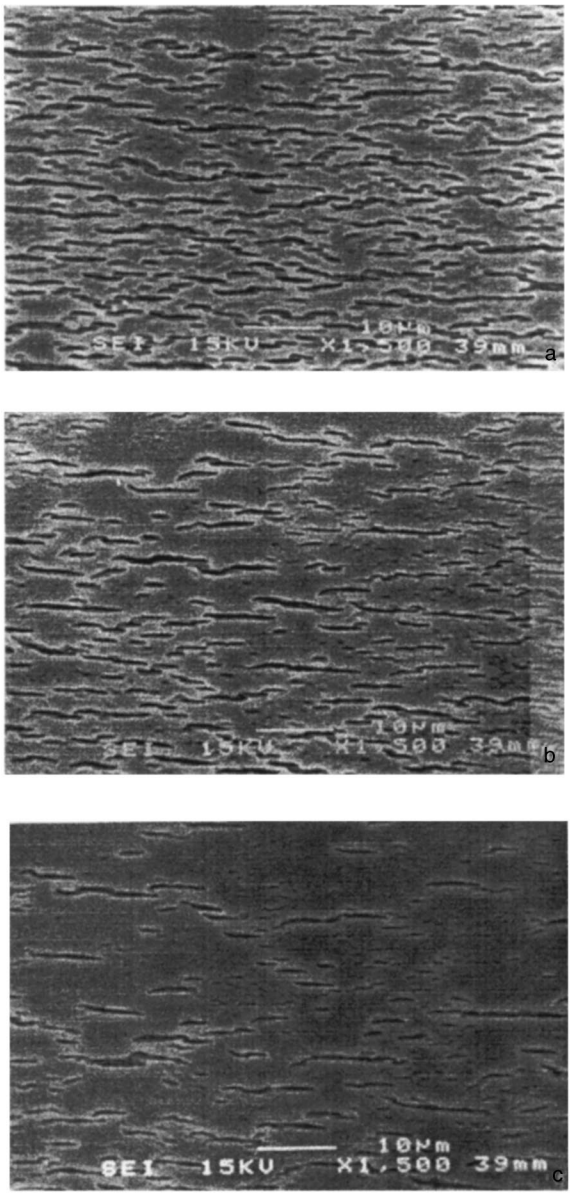

FIG. 2. SEM image of the etched silicon surface for various loads/distances from the fixing point. The distance from the fixing point increases (the load decreases) from (a) to (c).

readily sees that the average distance between the deep grooves increases as one moves away from the fixing point and as the strain decreases.

Uniaxial surface strain u_{xx} is related to the distance x from the sample edge [(*1*) in Fig. 1] through

$$u_{xx}=\frac{h(a-x)}{2bd^2(x)}, \tag{1}$$

where

$$a=l_1+l_2+l_3 \tag{2}$$

and

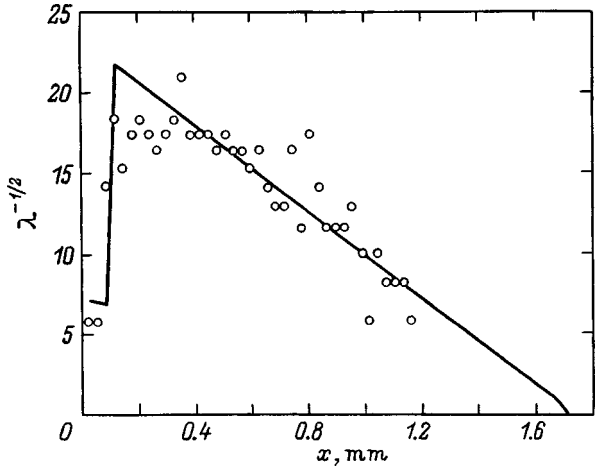

FIG. 3. Plot of $\lambda^{-1/2}$ as a function of distance from the fixing point. Points — experimental data, line — theory.

$$b=-\frac{1}{6}\left(\frac{l_1^3}{d_1^3}+\frac{l_2^3}{d_2^3}+\frac{l_3^3}{d_3^3}\right)-\frac{1}{2}\left(\frac{l_1^2l_2}{d_1^3}+\frac{l_1^2l_3}{d_1^3}+\frac{l_2^2l_3}{d_2^3}\right)$$
$$+\frac{1}{2}(l_1+l_2+l_3)\left(\frac{l_1^2}{d_1^3}+\frac{l_2^2}{d_2^3}+\frac{l_3^2}{d_3^3}\right)+(l_1+l_2+l_3)$$
$$\times\left(\frac{l_1l_2}{d_1^3}+\frac{l_1l_3}{d_1^3}+\frac{l_2l_3}{d_2^3}\right). \tag{3}$$

This relation holds only for a thin sample, where $d_1 \ll l_1$, $d_2 \ll l_2$, and $d_3 \ll l_3$. For our samples, $d_1=d_3$. As evident from Eq. (3), the strain in the thick part of the sample is substantially smaller than that in its thin part. Therefore when describing the strain in the thin part of the sample, one may neglect, in a first approximation, the bending of the thick part (provided the lengths l_1 and l_3 are not much larger than l_2). Thus setting $l_1=l_3=0$, we obtain an expression for the thin part of the sample:

$$u_{xx}=\frac{3dh}{l^2}\left(1-\frac{x}{l}\right), \tag{4}$$

where $d=d_2$, $l=l_2$.

For the parameters of our samples $l=1.7$ mm, $d=0.1$ mm, and $h=0.1$ mm, Eq. (4) permits estimation of the maximum strain $u_{xx}^{\max}\sim 0.5\%$. As seen from Eqs. (1) and (3), the strain decreases linearly with decreasing x in the thin part of the sample, to vanish at the load application point.

Figure 3 displays the reciprocal square root of the average distance between the observed grooves plotted vs x. The average distance between deep grooves λ was determined by dividing the microscope field of view of 30 μm by the number of grooves in the latter. This relation is seen to be close to linear in the thin part of the sample. This means that $\lambda \sim 1/u_{xx}^2$, which permits one to relate the phenomenon observed to an instability of the compressed surface. The main driving force of this instability is the tendency of the system toward a minimum of total energy, which includes the elastic and surface tension energies. This gives rise to development

of surface corrugation under uniaxial compression. The characteristic wavelength of this surface modulation λ is given by the expression[3,5]

$$\lambda(x) = \pi\gamma(1-\sigma^2)/E\,u_{xx}(x)^2, \tag{5}$$

where E, $u_{xx}(x)$, σ, and γ are Young's modulus, uniaxial stress, the Poisson ratio, and surface tension, respectively.

Figure 3 plots the experimental and theoretical dependences $\lambda^{-1/2}(x)$ against distance from the fixing point. The theoretical curve was obtained from Eqs. (1)–(5) using the following parameters: $l_1 = 0.1$ mm, $l_2 = 1.6$ mm, $l_3 = 0.1$ mm, $d_1 = 0.225$ mm, $d_2 = 0.125$ mm, $d_3 = 0.225$ mm, $h = 0.1$ mm, $E = 1.629 \times 10^{11}$ N·m^{-2} (Ref. 15), $\sigma = 0.223$ (Ref. 15), and γ was taken equal to 1 eV·Å^{-2}.

The satisfactory agreement between the theoretical curve and experimental data gives us grounds to assign tentatively the observed phenomenon to a manifestation of the Asaro–Tiller–Grinfel'd instability under corrosion-induced cracking of material. In this case, surface rearrangement occurs by chemical removal of atoms rather than through surface diffusion or evaporation–condensation processes.[16] However the absence of instability on the extended Si surface remains unclear within this model.

Support of the Russian Fund for Fundamental Research (Grants 98-01-01084 and 96-15-96392) is gratefully acknowledged.

[1] R. J. Asaro and W. A. Tiller, Metall. Trans. A **3**, 1789 (1972).
[2] M. A. Grinfel'd, Dokl. Akad. Nauk SSSR **290**, 1358 (1986) [Sov. Phys. Dokl. **31**, 831 (1986)].
[3] D. J. Srolovitz, Acta Metall. **37**, 621 (1988).
[4] R. H. Torii and S. Balibar, J. Low Temp. Phys. **89**, 391 (1992).
[5] J. Berréhar, C. Caroli, C. Lapersonne-Meyer, and M. Schott, Phys. Rev. B **46**, 3487 (1992).
[6] Y. G. Shreter, Y. T. Rebane, D. V. Tarkhin, S. A. Khorev, D. Cherns, and J. W. Steeds, in *Microscopy of Semiconducting Materials-1995*, edited by A. G. Cullis and A. E. Staton-Bevan, Inst. Phys. Conf. Ser., No. 146 (1995), p. 499.
[7] Y. G. Shreter, Y. T. Rebane, D. V. Tarkhin, D. Cherns, and J. W. Steeds, Mater. Sci. Forum **196-201**, 1231 (1995).
[8] M. Renninger, J. Appl. Crystallogr. **5**, 163 (1972).
[9] A. S. T. Badrick, F. Eldeghaidy, K. E. Puttick, and M. A. Shahid, J. Phys. D **10**, 195 (1977).
[10] J. Sunada, Jpn. J. Appl. Phys. **13**, 1944 (1974).
[11] K. E. Puttick and M. M. Hosseini, J. Phys. D **13**, 875 (1980).
[12] K. Minowa and K. Sumino, Phys. Rev. Lett. **69**, 320 (1992).
[13] I. V. Gridneva, Yu. V. Milman, and V. I. Trefilov, Phys. Status Solidi A **14**, 177 (1972).
[14] F. Secco d'Aragona, J. Electrochem. Soc. **119**, 948 (1972).
[15] A. L. Ruoff, in *High Pressure Science and Technology*, Vol. 2, edited by K. D. Timmerhaus and M. S. Baker (Plenum Press, New York, 1979), p. 525.
[16] W. H. Yang and D. J. Srolovitz, Phys. Rev. Lett. **71**, 1593 (1993).

Translated by G. Skrebtsov

Quantum chemical modelling of the structure and properties of hypervalent defects in vitreous SiO_2 and GeO_2

A. S. Zyubin

Institute of Novel Chemical Problems, Russian Academy of Sciences, 142432 Chernogolovka, Russia

S. A. Dembovskiĭ*)

Institute of General and Inorganic Chemistry, Russian Academy of Sciences, 117907 Moscow, Russia
(Submitted January 10, 1999)
Fiz. Tverd. Tela (St. Petersburg) **41**, 1419–1423 (August 1999)

A cluster approximation using a semiempirical MNDO-PM3 scheme is used to study the structure and properties of the defect structures which develop in vitreous SiO_2 and GeO_2 during the interaction of the previously discovered most probable defects (two-member cycles, fragments with double bonds $O=A<(A=Si, Ge)$ and open chains) with valence-saturated segments of a fracture surface. During the interaction of open chains with such a surface, defects with a large dipole moment (up to 15–20 D) are formed, which may create anisotropic highly polarized regions in the glass. The bonds around hypervalent centers are weakened, and the characteristics of the newly formed and already existing bonds approach one another; that is, in a grouping of this sort, other decay paths may exist that change the direction of fracture. In structures formed by the interaction of $O=A<$ defects and two-member cycles with the surface, hypervalent bonds are easily broken; that is, the hypervalent configuration is transformed into an ordinary one. In a number of cases, the potential surface contains two or three minima with similar energies, separated by low or moderate potential barriers. © *1999 American Institute of Physics.* [S1063-7834(99)01408-2]

In some earlier papers[1,2] we have used quantum-chemical-cluster calculations based on an MNDO-PM3 scheme to study the properties of the cyclical fragments Cn which form a continuous disordered lattice in vitreous SiO_2 and GeO_2. It turned out that the resistance to fracture in links of various sizes can differ by a factor of 2–3, despite their similar relative stabilities and the similarity of the structural characteristics of the polyhedra which form them. Four-member rings are the ''weakest'' in these glasses, since when they are destroyed the bonds may be shifted to form two-member cycles. This implies that the breakup of the continuous disordered lattice during softening should begin along surfaces having a maximum concentration of these ''weak'' links. Since they are not sufficiently numerous to form a continuous surface, even the more durable structural units which exist in the fracture zone will break up. On the granule surfaces, which come apart and stick together continuously as the glass softens,[1,2] the most probable defects should include two-member cycles, as well as fragments with double $O=A<$ bonds and open chains with broken bonds. These defects interact with one another without a barrier or with low barriers and this leads to recovery of the cells of the initial continuous disordered lattice. In this paper we examine other possibilities which arise during the interaction of defects with valence-saturated fragments of the fracture surface of continuous disordered lattice, in which the coordination number of the A atoms is 4 and that of the oxygen atoms is 2. In such cases, hypervalent configurations should develop in the initial stage. These configurations[3] are specific microscopic centers that correspond to the ''soft atomic configurations'' in the Klinger–Karpov model.[4–6] The purpose of this paper is to study the structure and properties of these configurations and the possibility of their further transformation.

1. COMPUTATIONAL TECHNIQUE

As in Refs. 1 and 2, the defect regions of the continuous disordered lattice are modelled by clusters in which the active region is surrounded by at least two layers of A–O bonds, the boundary of the cluster passes through A atoms, which are fixed more rigidly than oxygen atoms in the continuous disordered lattice, and broken bonds at the cluster boundary are closed by H atoms. As an initial element for modelling the valence-saturated fragments of the fracture surface of the continuous disordered lattice, we have used a six-member C6 cycle, since it is the most stable structural element of the AO_2 glasses on a medium order scale length[1,2] and has the highest concentration.[7] It should be noted that because of the similarity of the electronic and structural characteristics of the continuous disordered lattice fragments, on a near ordering scale replacing a C6 cycle by its nearest neighbors (C5 or C7) should not lead to significant changes in the results.

In the C6 cycle shown in Fig. 1, the inner A atoms form a crown structure in which one triplet of A atoms lies above the plane of the figure and another, below it. Here the ''outer'' A–O–A bridges are positioned so that three of them are directed below this plane and another three lie

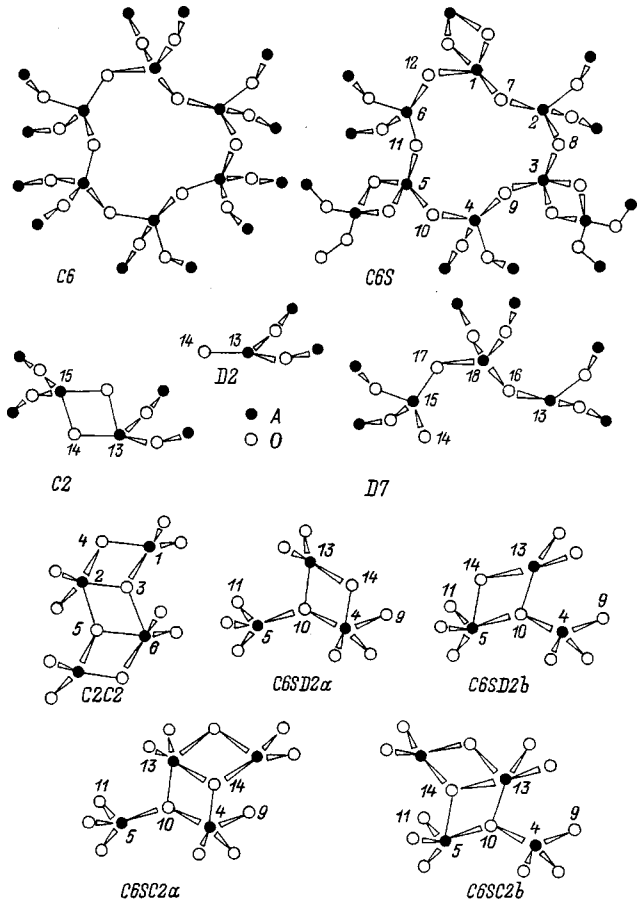

FIG. 1. Schematic representation of part of a fracture surface, initial defects, and fragments of hypervalent configurations in glassy SiO_2 and GeO_2.

above the plane, while the remaining six do not deviate significantly from lines parallel to the plane of the figure. In modelling a fragment of the fracture surface, the part of the continuous disordered lattice lying above the plane is ''cut.'' Here the broken bonds which appear above a C6 and in its nearest surroundings are closed on one another to form more energetically stable defects, C2 cycles, around the C6. The result is a C6S cluster (see the figure) which contains no broken bonds; all of its atoms have conventional coordination numbers: 4 for A and 2 for O. To construct it, the boundary A atoms are fixed at the same positions as in the initial defect-free cluster, while the positions of the remaining atoms are optimized with respect to a minimum total energy.

There is a substantial number of atoms ($\sim 50-60$) in the clusters which model the interaction of the most probable defects, C2, D2, and D7 (see the Fig. 1), with a surface fragment of this sort and the calculations for these systems can be carried out only through semiempirical methods. According to Ref. 2, for SiO_2 and GeO_2 entirely satisfactory results are obtained with the MNDO-PM3 approximation,[8] at least for structures with ''normal'' valances. In order to verify the feasibility of this approximation for hypervalent configurations, we have done some nonempirical calculations of C2C2 systems (see the figure) formed by the interaction of two C2 cycles and those examined in Ref. 2 with PM3. In these calculations, clusters with only one layer of

TABLE I. Bond lengths and orders [$R(i,j)$ Å, $Q(i,j)$] in a hypervalent C2C2 complex and the energy DE (kcal/mole) required to break it up into to isolated two-member cycles.

PM3	i,j	1, 3	1, 4	2, 3	2, 4	2, 5	3, 6	DE	
SiO_2	$R(i,j)$	1.70	1.66	1.81	1.73	1.73	1.74	48	
	$Q(i,j)$	0.77	0.94	0.50	0.72	0.64	0.62		
GeO_2	$R(i,j)$	1.81	1.77	1.89	1.82	1.87	1.86	29	
	$Q(i,j)$	0.77	0.98	0.54	0.77	0.54	0.54		
SCF / SBKp								SCF	MP2
SiO_2	$R(i,j)$	1.70	1.62	1.79	1.75	1.84	1.84	15	31
	$Q(i,j)$	0.85	1.22	0.66	0.95	0.71	0.71		
GeO_2	$R(i,j)$	1.78	1.70	1.87	1.83	1.92	1.93	24	38
	$Q(i,j)$	0.75	1.14	0.61	0.83	0.58	0.58		

A–O bonds surrounding the active region were used, but with complete optimization of the geometric parameters. ''Agglomeration'' of C2 cycles leads to a drop in the total energy, which is more significant for SiO_2. In the C2C2 configuration, the bonds formed by atoms with elevated coordination numbers are weakest; they are longest and have the lowest orders. (See Table I.) In the PM3 approximation, this kind of complex is a local minimum of the potential surface and can be transformed into a four-member C4 cycle after a low (~ 10 kcal/mol) barrier is overcome. Here the hypervalent 2–3 and 5–6 bonds break, while 2–5 and 3–6 are strengthened. In order to verify these results, we have performed nonempirical calculations of similar systems using the GAMESS code[9] at an SCF level using an SBK pseudopotential[10] with a corresponding two-exponent basis supplemented by polarizing d AO at the atoms of the active region (in the following, SCF/SBKp). The energy DE required to break the complex into two C2 cycles was also determined more accurately by taking the correlation of the electrons into account in a second order Meller-Plesset (MP2) scheme. Despite a quantitative difference (up to 0.07–0.1 Å for the interatomic distances), the qualitative relationships between the lengths and orders of the bonds in the PM3 and nonempirical approaches are the same (see Table I). DE is more sensitive to the level of approximation. A correct estimate of this quantity requires both a more flexible basis and taking the electron correlations into account. The values of DE for SiO_2 and GeO_2 do equilibrate, but for GeO_2 it is somewhat higher; that is, for SiO_2, PM3 overestimates and for GeO_2, it underestimates the stability of the hypervalent structures. It should be noted that in nonempirical calculations neglecting the polarizing AO, the C2C2 configuration is not a local minimum and when the geometric parameters are optimized, it transforms to C4. Evidently, in the nonempirical approach the barrier in the way of the C2C2– C4 transition is still lower than in PM3. Thus, the semiempirical PM3 approximation correctly implies the possible existence of and the features of the geometric structure and electronic structure for the hypervalent configurations in SiO_2 and GeO_2, but it distorts the relationship of their energy stabilities.

2. RESULTS AND DISCUSSION

In a model C6S cluster after optimization of the coordinates of its interior atoms, the cycle of six A atoms becomes almost flat; the oxygen atoms are slightly raised above it. Here the lengths and orders of the A–O bonds remain almost the same as in the original C6 cycle: 1.63–1.66 Å, 0.84–0.90 for SiO_2 and 1.77–1.78 Å, 0.88–0.92 for GeO_2. The interaction of the defects with the two-member cycles of the cluster modelling the fracture surface was not considered, since they have already been studied in Refs. 1 and 2. Only those configurations which can develop when defects join with fragments of the relatively weakly stressed six-member cycle and here two possibilities were considered: the configuration is formed with the participation of an A atom from the weakly distorted tetrahedron (variant *a*) or of an atom from a two-member cycle, where the AO_4 tetrahedron is more significantly distorted (variant *b*).

Interactions of this sort lead to formation of metastable structures with elevated coordination numbers for atoms in the contact region. The bonds in which such atoms participate are substantially weakened; they are 0.10–0.12 Å shorter and their orders are 20–30% shorter than the bonds in the initial structure. The characteristics of the bonds in the nearest surroundings change little. For these configurations, further transformation is possible, with their conversion into structures with ordinary coordination numbers.

For an open D7 chain (see Fig. 1), the ground state[1,2] is a triplet corresponding to two broken A–O bonds [the unpaired electrons are localized at the incompletely coordinated atoms A(13) and O(14)]. The singlet lies 30–40 kcal/mol higher and is characterized by a strong alternation of bond lengths and order and a high polarity. (The dipole moment is as high as 15–20D.) When they interact with the surface, the relationship of the stabilities of the single and triple change: the singlet state becomes the ground state and the triplet lies 30–50 kcal/mol higher. The reduction in the energy when the C6S cluster used to model the surface joins with a D7 chain in the singlet state is ~130 kcal/mol for SiO_2 and 50–55 kcal/mol for GeO_2, but given the results described in the section on method, it should be expected that, in the first case, this values is significantly overestimated and, in the second, underestimated. The alternation of bonds within a chain is lessened, but an analogous alternation shows up in the fragments of the C6 cycle with which the D7 fragments interact. (Variant *a* corresponds to formation of 6–14 and 9–13 bonds and variant *b*, to 5–14 and 8–13; see Fig. 1). Here the bonds around the hypervalent centers 6, 9 or 5, 8 are weakened; the characteristics of the newly formed and already existing bonds become almost the same (see Tables II and III). This means that the other breakup variants in this grouping, which change the direction of fracture, require essentially the same energy expenditures as the recovery of the initial state. The high polarity of the defect when D7 and C6S merge is retained; in the configurations considered here the dipole moment is 17–18D, i.e., interactions of this sort are capable of creating anisotropic, highly polarized regions in glass.

Type D2 and C2 fragments are also capable of ''sticking'' to a valence-saturated fragment of a C6S surface to form the C6SD2a, C6SD2b, C6SC2a, and C6SC2b hypervalent regions shown in the figure. The corresponding energy drop for a D2 fragment is substantial: 59 and 71 kcal/mol (for variants *a* and *b*) in SiO_2 and 35 and 43 kcal/mol in GeO_2, respectively. When C2 and C6S interact, there is less stabilization: 43 and 53 kcal/mol for SiO_2 and 0 and 9 kcal/mol for GeO_2. Given the results in the section on methods, it should be expected that these values are high for SiO_2 and low for GeO_2, and, in terms of a more accurate approach, the energy reduction on forming these structures in GeO_2 may be larger than in SiO_2.

Qualitatively, the following behavior is easily identified during the formation of the hypervalent structures: the energy reduction is larger, when the defect contained more valence-unsaturated atoms. For identical defects, those configurations in which an A atom contained in a two-member cycle acts as a hypervalent center are more stable; this is a consequence of the greater distortion of the AO_4 tetrahedron in the initial structure. Evidently, in the valence-saturated portions of the fracture surface, centers of this sort must play

TABLE II. Bond lengths and orders [$R(i,j)$, Å, $Q(i,j)$] in open chains interacting with a fragment of a valence-saturated surface.

	i,j	13,9	13,16	16,18	18,17	17,15	15,14	14,6
a	$R(i,j)$	1.75	1.62	1.66	1.63	1.68	1.64	1.73
SiO_2	$Q(i,j)$	0.64	0.94	0.75	0.97	0.73	1.01	0.62
a	$R(i,j)$	1.86	1.74	1.79	1.75	1.80	1.76	1.84
GeO_2	$Q(i,j)$	0.70	1.01	0.76	1.02	0.75	1.07	0.62
	i,j	13,8	13,16	16,18	18,17	17,15	15,14	14,5
b	$R(i,j)$	1.75	1.62	1.66	1.63	1.68	1.62	1.69
SiO_2	$Q(i,j)$	0.63	0.93	0.77	0.94	0.76	1.04	0.67
b	$R(i,j)$	1.86	1.76	1.80	1.76	1.80	1.75	1.81
GeO_2	$Q(i,j)$	0.68	1.01	0.80	1.00	0.76	1.06	0.67

TABLE III. Bond lengths and orders [$R(i,j)$, Å, $Q(i,j)$] in cyclic surface fragments interacting with an open chain.

	i,j	1,12	1,7	2,7	2,8	3,8	3,9
a	$R(i,j)$	1.64	1.66	1.64	1.65	1.61	1.73
SiO_2	$Q(i,j)$	0.95	0.80	0.92	0.77	0.96	0.66
a	$R(i,j)$	1.75	1.78	1.76	1.78	1.75	1.86
GeO_2	$Q(i,j)$	1.05	0.84	0.95	0.81	0.92	0.68
b	$R(i,j)$	1.63	1.64	1.61	1.73	1.73	1.60
SiO_2	$Q(i,j)$	0.99	0.79	0.92	0.65	0.63	1.02
b	$R(i,j)$	1.76	1.77	1.76	1.86	1.85	1.74
GeO_2	$Q(i,j)$	0.85	0.75	0.94	0.68	0.65	1.09
	i,j	4,9	4,10	5,10	5,11	6,11	6,12
a	$R(i,j)$	1.75	1.61	1.68	1.62	1.70	1.69
SiO_2	$Q(i,j)$	0.62	0.97	0.73	1.01	0.69	0.70
a	$R(i,j)$	1.88	1.75	1.80	1.74	1.82	1.82
GeO_2	$Q(i,j)$	0.62	1.02	0.76	1.08	0.69	0.71
b	$R(i,j)$	1.67	1.61	1.69	1.69	1.61	1.67
SiO_2	$Q(i,j)$	0.71	1.02	0.67	0.70	1.02	0.75
b	$R(i,j)$	1.80	1.74	1.81	1.81	1.75	1.80
GeO_2	$Q(i,j)$	0.72	1.07	0.69	0.73	1.03	0.77

TABLE IV. Potential curves for regroupings of the hypervalent C6SD2a, C6SD2b, C6SC2a, and C6SC2b configurations into ordinary configurations. E_r is the relative energy (kcal/mol), $R(i;j)$ (Å) is the variable distance.

$R(i;j)$		1.8	1.9	2.0	2.1	2.2	2.3	2.4	2.6	2.8	3.0	3.2
SiO_2,	$i;j$						E_r					
C6SD2a	4;10	0.0	–	4.5	–	8.0	8.3	8.1	7.5	8.0	–	–
C6SD2b	5;10	0.0	–	2.3	3.8	4.2	3.5	–	0.6	0.3	0.9	–
C6SC2a	13;14	–	0.0	–	6.1	8.0	7.9	–	6.5	5.7	5.7	–
C6SC2a*	4;10	–	–	11.4	–	16.3	–	16.4	15.5	15.3	15.1	14.9
C6SC2b	13;14	0.0	–	7.3	–	13.0	–	13.9	13.3	13.5	–	–
C6SC2b*	5;10	–	–	19.2	–	24.4	–	24.3	21.7	21.1	20.9	21.4
$R(i;j)$		1.9	2.0	2.1	2.2	2.3	2.4	2.5	2.6	2.7	2.8	3.2
GeO_2,	$i;j$						E_r					
C6SD2a	4;10	0.0	–	2.7	3.4	3.2	2.9	3.5	–	–	–	–
C6SD2b	5;10	0.2	0.0	1.1	1.5	1.0	−0.4	−0.5	0.4	–	–	–
C6SC2a	13;14	0.0	–	7.0	–	12.1	–	15.8	18.0	20.3	19.7	–
C6SC2a*	4;10	18.1	19.1	–	22.6	–	22.3	–	21.0	–	23.8	–
C6SC2b	13;14	0.0	–	7.6	–	13.0	–	16.1	18.1	18.5	17.0	17.0

Note: In the configurations indicated with an asterisk, $R(13;14)$ corresponds to the second minimum (~ 3 Å).

a more active role in the process of transforming the continuous disordered lattice of the AO_2 oxide glasses.

The interaction of a type D2 defect with an ordinary A–O bond, when the geometric parameters of the system have been fully optimized, leads to a barrierless entry of this defect into a bond and the transformation of the hypervalent configuration into an ordinary one, both in the nonempirical approach and in the PM3 approximation. In the hypervalent C6SD2a and C6SD2b defects, the rigid surroundings inhibit their spontaneous transformation into structures with ordinary coordination numbers for the A and O atoms. In order to examine the possibility of such a transition, in the model clusters the potential surface was scanned with respect to stretching the hypervalent bonds. It was found that increasing the length of a hypervalent bond leads to a monotonic reduction in its order. For example, the order of the ''double'' 13–14 bond is reduced and its length is increased, while for bonds adjacent to a hypervalent defect, the characteristics change in the opposite way; that is, the hypervalent structure transforms into an ordinary one. On the potential surface there are two minima which are close in energy and separated by a low (less than 10 kcal/mol) potential barrier (see Table IV); that is, a structure of this type is nonrigid and has a two-well potential. The characteristics of the potential surfaces of these defects correspond to the properties of the ''soft atomic configurations'' postulated by Klinger and Karpov[4–6] for explaining many features of vitreous systems. It is entirely possible that such structures of one of the possible prototypes for these hypothetical objects, as suggested in Ref. 3. Strongly stretched (almost to complete breaking) tricentered Si–O–Si bridges have similar properties,[11] but the concentration of this kind of defect should be very low.

For the C6SC2a and C6SC2b defects constructed with the participation of a two-member cycle, the picture is more complicated. The stretching of the 4–10 or 5–10 bond (see the figure) leads to a monotonic energy increase, i.e., the second minimum does not develop. As the length of bond 13–14 increases, a very shallow local minimum appears which lies above the initial structure for both SiO_2 and GeO_2 (see Table IV). The resulting configuration has a hypervalent bond; thus, it can under go further transformation. Stretching this bond leads to the appearance of an additional minimum, still less favorable than the previous one, except for C6SC2b (GeO_2, where it does not develop. It should be noted that for GeO_2 the relative stability of the hypervalent configuration compared to the ordinary configuration, is greater than for SiO_2. As in the case of the C6SD2a and C6SD2b configurations, destruction of the hypervalent interactions makes the characteristics of the bonds in the nearest surroundings equilibrate and become almost the same as those for the ordinary bonds in defect-free structures; that is, the hypervalent configurations transform into ordinary ones. The energy difference between them reaches 15–20 kcal/mol, so that, although the potential surfaces of these structures have two or three local minima, it is hardly legitimate to compare them with the ''soft atomic configurations'' of Klinger-Karpov. The most like role for these defects is bond switching during transformation of the continuous disordered lattice. In structures of the type C6SC2, the transition from hypervalent to ordinary configurations makes it possible for the cluster boundaries to shift by distances equal to three-four O–A bond lengths through straightening of the 10–13–15–14–4 or 5–14–15– 13–10 loops (see Fig. 1) without great expenditure of energy and makes the transformation of the continuous disordered lattice easier in this region.

It should be noted that the relative stabilities of the hypervalent and ordinary configurations in C6SD2 and C6SC2 type structures should vary significantly, depending on the position of the boundary atoms in the cluster: stretching the C6S cycle, which leads to an increase in the 4–5 distance, will facilitate stabilization of the ordinary configuration, and compression, that of the hypervalent configuration. Since the

structure of a glass is irregular and is determined to a substantial extent by random factors, these defects should have a rather broad energy spectrum, in one part of which a hypervalent configuration may be primary, and in another part, an ordinary configuration. This, however, does not change the main result, namely that, for the defects considered in this section, when hypervalent configurations are involved, bond switching can take place easily and causes substantial changes in the local structure of the continuous disordered lattice without a large energy expenditure.

These results indicate that the hypervalent structures having a higher packing density considered here can develop from ordinary structures, if, for some reason, part of the bonds in the continuous disordered lattice have been destroyed so that isolated segments of it become mobile. It is extremely probable that the rate for a mechanism of this sort in structural transformations increases in glass under UV irradiation, which causes an increase in its refractive index.[12] Since the relative stability of the hypervalent structures is higher when Ge is involved, doping quartz glass with germanium should enhance this effect.

In sum, when the most probable defects resulting from fracture of vitreous SiO_2 and GeO_2 interact with valence-saturated fragments of a fracture surface, metastable hypervalent structures may develop which are capable of participating in further transformation of the continuous disordered lattice. In individual cases, the transformation of hypervalent into ordinary configurations involves overcoming a low (less than 10 kcal/mol) barrier; that is, a nonrigid system develops with a two-well potential of the type in the Klinger–Karpov ''soft atomic configuration.'' For the defects formed from open chains, the singlet electronic state, which has a large dipole moment (up to 15-20D), stabilizes. When a hypervalent configuration develops the high polarity of the defect is retained, and this may create anisotropic high polarity regions in the glass.

This work was supported by the Russian Fund for Fundamental Research (Grants No. 97-03-33188a and 96-02-17575).

*)E-mail: sergdemb.@ionchran.msk.ru

[1] A. S. Zyubin and S. A. Dembovskiĭ, Zh. Neorg. Khim. **41**, 679 (1996).
[2] A. S. Zyubin, O. A. Kondakova, and S. A. Dembovskiĭ, Fiz. Khim. Stekla **23**, 85 (1997).
[3] S. A. Dembovskiĭ and E. A. Chechetkina, *Vitrification* [in Russian] (Nauka, Moscow 1990).
[4] M. I. Klinger and V. G. Karpov Zh. Éksp. Teor. Fiz. **82**, 1687 (1982) [Sov. Phys. JETP **55**, 976 (1982)].
[5] M. I. Klinger, Phys. Rep. **165**, 1809 (1988).
[6] D. A. Parshin, Fiz. Tverd. Tela (St. Petersburg) **36**, 1809 (1994) [Phys. Solid State **36**, 991 (1994)].
[7] B. P. Feuston and S. H. Garofalini, J. Chem. Phys. **89**, 5818 (1988).
[8] J. J. P. Stewart, J. Comput. Chem. **10**, 209 (1989).
[9] M. W. Schmidt, K. K. Baldridge, J. A. Boatz *et al.*, ''General atomic and molecular electronic structure system,'' J. Comput. Chem. **14**, 1347 (1993).
[10] W. J. Stewens, H. Basch, and M. Krauss, J. Chem. Phys. **81**, 6026 (1984).
[11] E. M. Dianov, V. O. Sokolov, and V. B. Sulimov, J. Non-Cryst. Solids **211**, 197 (1997).
[12] V. B. Sulimov, V. O. Sokolov, E. M. Dianov, and B. Pumellek, Kvant. Élektron. (Moscow) **23**, 1013 (1996).

Translated by D. H. McNeill

EPR of a non-Kramers iron ion in $KTaO_3$

D. V. Azamat, S. A. Basun, V. É. Bursian, A. G. Razdobarin, and L. S. Sochava

A. F. Ioffe Physicotechnical Institute, Russian Academy of Sciences, 194021 St. Petersburg, Russia

H. Hesse and S. Kapphan

FB Physik, Universität Osnabrück, 49069 Osnabrück, Germany
(Submitted March 11, 1999)
Fiz. Tverd. Tela (St. Petersburg) **41**, 1424–1427 (August 1999)

The EPR spectrum of the non-Kramers iron ion Fe^{4+} ($S=2$) in a $KTaO_3$:Fe crystal appearing after illumination of the sample in the visible has been detected and studied. Because of the large initial splitting ($|D|=4.15\ cm^{-1}$), only transitions within the $|\pm 1\rangle$ and $|\pm 2\rangle$ doublets are seen experimentally. Superhyperfine structure in the spectrum of a non-Kramers ion in perovskites has been detected for the first time. A structure is proposed for the center responsible for the new EPR spectrum, which represents a complex of a Fe^{4+} ion substituting for Ta with an oxygen vacancy at the nearest anion site. © *1999 American Institute of Physics.* [S1063-7834(99)01508-7]

EPR is widely used in studies of photoinduced charge transfer between defect centers and the lattice. The amount of information this method can provide increases substantially if one can measure the EPR spectrum of a variable-charge center not in one but in both of its charge states, i.e. in states with both a half-integer and an integer spin.

This work reports a study of the EPR spectrum of a new tetragonal iron center with the spin $S=2$ in the cubic crystal of a $KTaO_3$ incipient ferroelectric (a brief communication about this center was given in Ref. 1). The center is photosensitive, and an analysis of its presence or absence before and after illumination of samples with different Fermi level positions has permitted us to draw a conclusion regarding its microscopic structure.

Our interest in these centers stems, among other things, from the discovery of their alignment under illumination with polarized light, a phenomenon which is the subject of a separate paper.[2]

1. EPR SPECTRUM OF A NON-KRAMERS IRON ION

We studied $KTaO_3$:Fe single crystals grown at the Physics Department, Osnabrück University (Germany), with a batch iron content of 2000–10000 ppm. The crystals were grown in air on a seed with an excess of K_2O. Rectangular samples measuring typically $1.5\times 2\times 4$ mm were cut from a single-crystal boule and studied primarily in the as-grown state. Several samples were annealed in an oxidizing or reducing atmosphere.

The EPR spectra were measured on a standard Radiopan SE/X 2544 3-cm range spectrometer.

The EPR spectra of the samples obtained at nitrogen temperature consist of a large number of lines, the strongest of them corresponding to the known iron centers in $KTaO_3$, namely, a rhombic, Fe^{3+} (Ref. 3), and two tetragonal, $Fe_K^{3+}-O_i$,[4] and the so-called Fe-4/2 (Ref. 5) (the explanation of the notation and a discussion are presented below). Illumination of as-grown samples at $T=78$ K by visible light gives rise to a new spectrum, which is much weaker than the three above-mentioned ones and has a clearly resolved superhyperfine (ligand hyperfine) structure (Fig. 1).

1.1. Angular dependence of the fine-structure lines

The angular dependences of the fine-structure line positions (Fig. 2) attest to a tetragonal symmetry of the center and have a shape characteristic of a center with spin $S=2$ and a large initial splitting $|D|\gg g\beta H$.[6] It is the large magnitude of $|D|$ that accounts for the presence in the spectrum only of the lines corresponding to ΔM-forbidden transitions $|+1\rangle\leftrightarrow|-1\rangle$ and $|+2\rangle\leftrightarrow|-2\rangle$. The spin Hamiltonian (written without inclusion of the superhyperfine structure)[7]

$$\mathbf{H}=g\beta\mathbf{HS}+D\left[S_z^2-\frac{1}{3}S(S+1)\right]+\frac{1}{48}a(S_+^4+S_-^4) \qquad (1)$$

with the parameters found by us

$$S=2;$$
$$g=1.982\pm 0.005;$$
$$|D|=(4.15\pm 0.02)\,cm^{-1};$$
$$a=(0.147\pm 0.002)\,cm^{-1} \qquad (2)$$

allows a fairly accurate description of the angular dependences of the resonant fields for all the spectral lines (Fig. 2). The calculations were performed using a program[8] developed by Grachev.

All main measurements were carried out at $T=78$ K. The strongest line in the spectrum (the $|+1\rangle\leftrightarrow|-1\rangle$ transition, $\theta=90°$) is seen clearly at room temperature as well, at which its width (about 30 Oe) determined by superhyperfine interaction does not increase.

Note that a recent ODMR study[9] of $KTaO_3$ reveals the presence of a tetragonal iron center with $S=2$ and $g=2.02$,

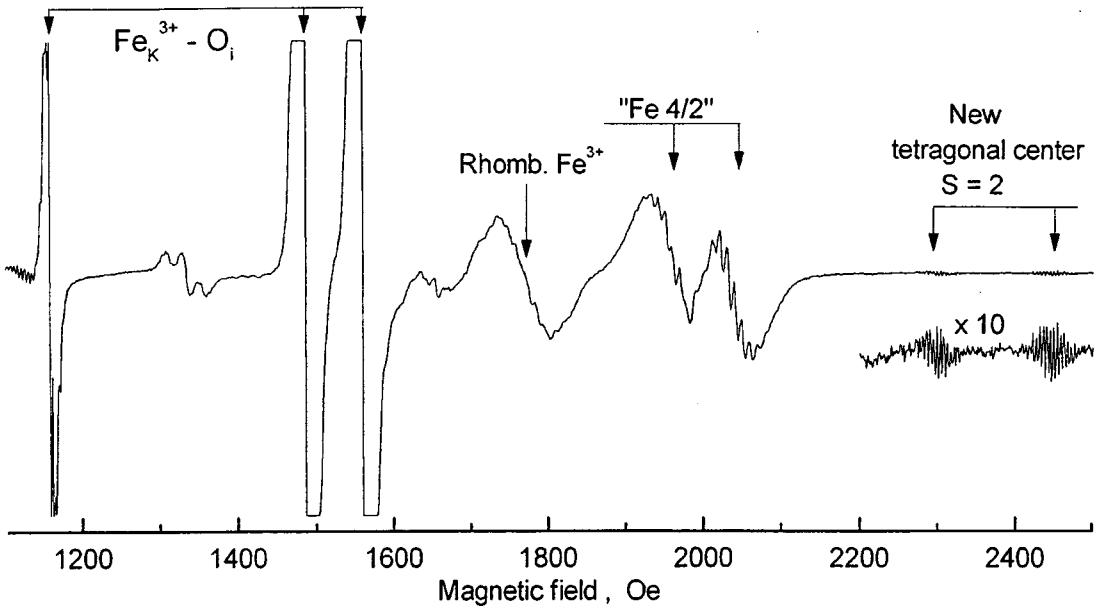

FIG. 1. Typical EPR spectrum of a $KTaO_3$:Fe sample (10,000 ppm) illuminated by blue light. $T=78$ K. 9.34 GHz. **H** oriented close to the [110] direction ($\theta=43°$).

which was assigned to Fe_K^{4+}–O_i. One observed only the $|+2\rangle\leftrightarrow|-2\rangle$ transition within the angular range $\theta=0-64°$, which did not permit determination of the other spectral parameters (only the upper bounds on D and a were estimated, $D<-5$ and $a<0.1$ cm^{-1}). Although the difference between the g factors found in Ref. 9 and this work is quite substantial, the same initial (oxidized) state of the samples and a similar method of center generation used in both studies argue for these centers being identical. Nevertheless, we propose another interpretation for the center observed by us (see below).

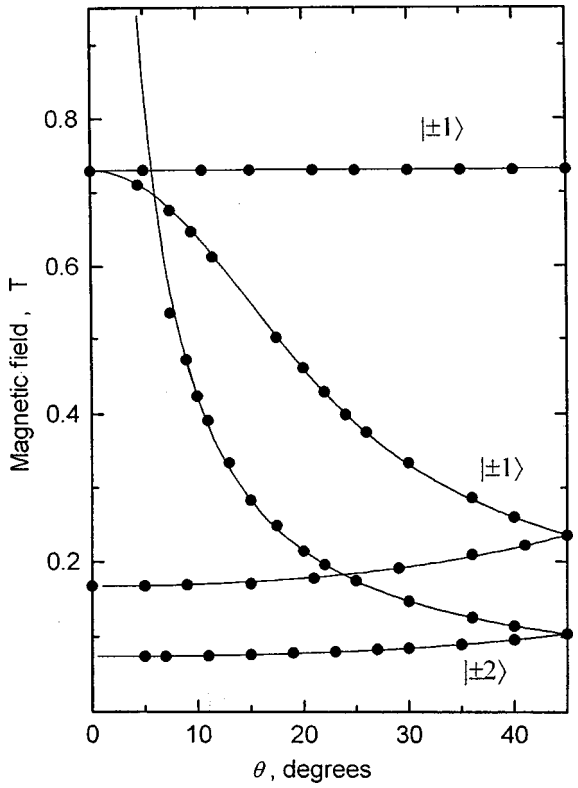

FIG. 2. Angular dependences of the EPR lines (without shf structure) obtained in the (100) plane for an $S=2$ tetragonal iron center in $KTaO_3$:Fe. θ — angle between the $\langle 100\rangle$ direction and the magnetic field, $\nu=9.29$ GHz, $T=78$ K. Points — experiment, curves — calculation.

1.2. Superhyperfine structure

All the lines of the spectrum under consideration exhibit a clearly resolved superhyperfine (shf) structure, in which one reliably resolves more than 30 components (Fig. 3b). Such a large number of components indicates that this struc-

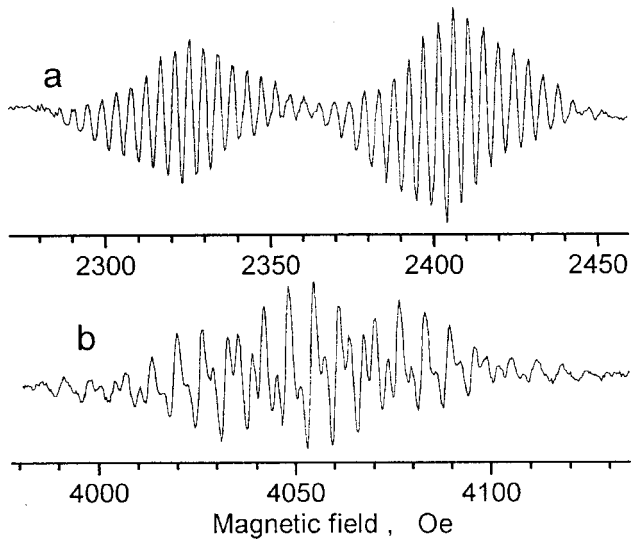

FIG. 3. Superhyperfine structure in the spectrum of tetragonal iron, $|+1\rangle\leftrightarrow|-1\rangle$ transition. $T=78$ K. θ: (a) 44°, (b) 23.5°.

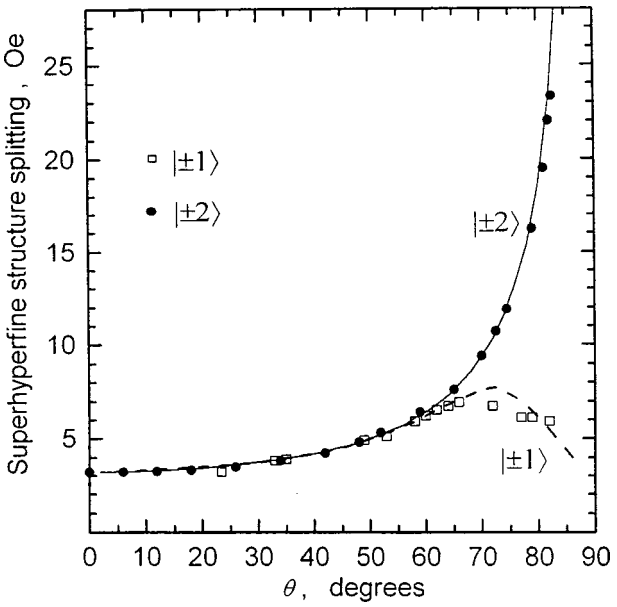

FIG. 4. Angular dependence of the superhyperfine splitting. {100} plane. $T=78$ K. Points — experiment, curves — calculation.

ture is due most likely to nuclei not of potassium (eight K nuclei would have yielded only 25 components) but rather of tantalum (100%, $I=7/2$).

The shf splitting at $\theta=0°$ is $A=(3.0\pm0.1)\times10^{-4}$ cm^{-1}. The magnitude of A increases strongly for the $|+2\rangle\leftrightarrow|-2\rangle$ line as **H** approaches the perpendicular orientation (Fig. 4). The angular dependence of A for the $|+1\rangle\leftrightarrow|-1\rangle$ transition is substantially smoother. Note that the experimental angular dependences $A(\theta)$ for the lines of both transitions are well fitted by the theoretical curves obtained using parameters (2) under the assumption of isotropic superhyperfine interaction (Fig. 4).

1.3. Specific observational features of EPR in an incipient ferroelectric

Note that the considerable difference in the intensity of the two groups of lines corresponding to the X and Y centers (see Fig. 3a) might seem strange at first glance (if one takes into account the insignificant deviation of **H** from the [110] direction, at which both groups merge). This phenomenon is accounted for by the noticeable distortion of the microwave field in the resonator[7] appearing as one places into the latter a $KTaO_3$ sample, for which the static dielectric constant ε is about 800 at $T=78$ K. Obviously enough, the $KTaO_3$ sample acts here as a second resonator, because its dimensions are considerably in excess of one half of the microwave wavelength in this material (which is about 0.5 mm).

This gives rise to a set of microwave modes, each being a linear combination of two coupled modes, namely, of the spectrometer resonator mode and of the sample resonator mode. The microwave field vector $\mathbf{H}_1$ for such a mixed mode deviates to a certain extent from the initial (vertical) orientation, which results in a partial lifting of forbiddenness[6] from the $\Delta M=\pm2,\pm4$ electronic transitions measured experimentally. Obviously, the extent to which the forbiddenness is lifted may be different for the X and Y centers, and this is what results in different intensities of the corresponding line groups (Fig. 3a). The above reasoning is buttressed convincingly by the appreciable variation of the X to Y amplitude ratio observed when one tunes the spectrometer to different vibrational modes in the resonator (the dips in the klystron generation zone curve).

The same factors make determination of the absolute concentrations of the observed centers impossible.

2. STRUCTURE OF THE $S=2$ IRON CENTER

The problem of the microscopic structure of the $S=2$ tetragonal iron center under study here is fairly complex. First, the $S=2$ spin corresponds to two charge states of the iron ion, Fe^{2+} (d^6) and Fe^{4+} (d^4) [Ref. 6]. Second, it is known that the iron ion can occupy the sites of both Ta (Fe_{Ta}) and K (Fe_K). Finally, there are a number of factors which account for this center being tetragonal, namely, the presence near the Fe ion of a compensating defect (an oxygen vacancy V_O in the case of Fe_{Ta} or an interstitial oxygen O_i for Fe_K), Jahn–Teller distortion of the FeO_6 complex, and off-central displacement of the iron ion from the site.

Note that the most typical defects in the $KTaO_3$ lattice are those associated with the oxygen sublattice, namely, an oxygen vacancy and an interstitial oxygen ion. It is known also that these defects act as local charge compensators for the iron impurity by forming complexes of tetragonal symmetry, Fe_K–O_i and Fe_{Ta}–V_O. Their EPR spectra corresponding to Fe in the $+3$ state are well known.[4,10] Both complexes are photochromic.[11] At the same time there is no reliable identification of other charge states of these centers. Two other spectra of the tetragonal iron, the so-called ''Fe-4/2'' and a new spectrum presented in this work, have been obtained. It appears reasonable to attempt their assignment in terms of the two reliably established complexes, Fe_K–O_i and Fe_{Ta}–V_O.

2.1. On a possible structure of the Fe-4/2 center

This spectrum, named after the values $g_\perp^{\rm eff}\approx4$ and $g_\parallel^{\rm eff}\approx2$, was assigned[5] to either Fe_K^+ or Fe_{Ta}^{5+}. Based on a comparison of the superhyperfine splittings, we were inclined to the Fe_{Ta}^{5+} assignment.[12] Because this is essential for understanding the structure of the $S=2$ center as well, we feel it appropriate to present here two more arguments for the latter interpretation, which are based on the presence or absence of the spectra under consideration in the samples subjected to annealing in a reducing or oxidizing atmosphere.

By keeping a sample in the dark at a sufficiently high temperature (300 K in our case) and cooling it subsequently to 78 K, one can reach thermodynamically equilibrium populations of defects in different charge states. Obviously enough, they may turn out not to be the same in crystals having differing Fermi level positions. However, in each given sample, a given defect can exist either in one or two adjacent charge states. Because the Fe_K–O_i complexes in an oxidized sample reside in two charge states, Fe_K^{3+}–O_i and Fe_K^{2+}–O_i,[11] no Fe_K^{5+}–O_i or Fe_K^{+}–O_i complexes can be present there. Hence the Fe-4/2 spectrum observed in the

same sample cannot be assigned to $Fe_K{-}O_i$. After the reduction of the sample in hydrogen the Fe-4/2 spectrum disappears, to be replaced by the spectrum of the $Fe_{Ta}^{3+}{-}V_O$ center.

These results provide supportive evidence for the Fe-4/2 spectrum belonging to the $Fe_{Ta}^{5+}{-}V_O$ complex.

2.2. Structure of the $S=2$ iron center

We start consideration of the possible structures of the $S=2$ center under study with the potassium site. The observed spectrum can originate from light-induced recharging of the $Fe_K^{3+}{-}O_i$ centers present in as-grown samples in the form of either $Fe_K^{2+}{-}O_i$ or $Fe_K^{4+}{-}O_i$. In this case it should appear also in the reduced sample after illumination with visible light, which produces[11] a noticeable concentration of the $Fe_K^{3+}{-}O_i$ centers. Part of these newly created centers should, in their turn, undergo recharging to the $S=2$ state under consideration in exactly the way this occurs in as-grown samples. This is, however, at odds with the result of a special, carefully performed experiment, which showed that the spectrum of the $S=2$ center is observed in reduced samples neither in the equilibrium state nor following illumination.

As for the tantalum site, the $Fe_{Ta}^{5+}{-}V_O$ center present originally in oxidized and as-grown samples (see Sect. 2.1) can capture an electron liberated in the light-induced ionization of other defects. The $S=2$ $Fe_{Ta}^{4+}{-}V_O$ center thus created is, in our opinion, the most likely source for the new EPR spectrum.

Obviously enough, the above reasoning does not give us grounds to assume the model of the observed $S=2$ iron center proposed here to be the only possible one. This model has received, however, a number of weighty arguments from a detailed study of the alignment of these tetragonal iron centers, which takes place under sample illumination with polarized light in the course of both creation and annihilation of such centers. These arguments will be discussed at length in another paper.[2]

Thus the totality of the experimental data obtained to date permits one to consider the $Fe_{Ta}^{4+}{-}V_O$ complex as the most probable source of the new EPR spectrum of iron-doped potassium tantalate crystals reported in this work.

The authors owe their gratitude to P. G. Baranov for fruitful discussions and consultations on the relevant calculations, and to A. A. Kaplyanskiĭ, for interest in the work and support.

Partial support of the Russian Fund for Fundamental Research (Grant 99-02-18319) and RFBR-DFG (Grants 96-02-00138 and 436RUS113/341/0) is gratefully acknowledged.

[1] D. V. Azamat, S. A. Basun, V. É. Bursian, A. G. Razdobarin, and L. S. Sochava, in *Current Problems in Magnetic Resonance and Its Applications* [in Russian] (Kazan' University, Kazan', 1998), p. 35.
[2] S. A. Basun, V. E. Bursian, H. Hesse, S. Kapphan, A. G. Razdobarin, and L. S. Sochava, Phys. Rev. B (in press).
[3] A. P. Pechenyi, M. D. Glinchuk, T. V. Antimirova, and W. Kleemann, Phys. Status Solidi B **174**, 325 (1992).
[4] I. P. Bykov, M. D. Glinchuk, A. A. Karmazin, and V. V. Laguta, Fiz. Tverd. Tela (Leningrad) **25**, 3586 (1983) [Sov. Phys. Solid State **25**, 2063 (1983)].
[5] H.-J. Reyher, B. Faust, M. Maiwald, and H. Hesse, Appl. Phys. B: Lasers Opt. **64**, 331 (1996).
[6] A. Abragam and B. Bleaney, *Electron Paramagnetic Resonance of Transition Ions* (Clarendon Press, Oxford, 1970), Vol. 1, Ch. 3.
[7] R. L. Berney and D. L. Cowan, Phys. Rev. B **23**, 37 (1981).
[8] http://www.physik.uni-osnabrueck.de/resonanz/Grachev/
[9] B. Faust, H.-J. Reyher, and O. F. Schirmer, Solid State Commun. **98**, 445 (1996).
[10] D. M. Hannon, Phys. Rev. **164**, 366 (1967).
[11] S. A. Basun, V. E. Bursian, H. Hesse, S. Kapphan, L. S. Sochava, and V. S. Vikhnin, *Proceedings of the XIII International Conference on Defects in Insulating Materials* (Wake Forest University, 1996), publ. in: Mater. Sci. Forum **239-241**, 345 (1997).
[12] V. É. Bursian, V. S. Vikhnin, and L. S. Sochava, Fiz. Tverd. Tela (St. Petersburg) **39**, 626 (1997) [Phys. Solid State **39**, 547 (1997)].

Translated by G. Skrebtsov

MAGNETISM AND FERROELECTRICITY

State of iron atoms in $SiO_2 \cdot xFe_2O_3$ gels

V. S. Rusakov

M. V. Lomonosov Moscow State University, 119899 Moscow, Russia

V. M. Cherepanov

Russian Scientific Center Kurchatov Institute, 123182 Moscow, Russia

A. M. Bychkov

V. I. Vernadskii GEOKhI Institute, Russian Academy of Sciences, 117975 Moscow, Russia

(Submitted November 30, 1998)
Fiz. Tverd. Tela (St. Petersburg) **41**, 1428–1431 (August 1999)

Mössbauer studies are made of ^{57}Fe nuclei in dry $SiO_2 \cdot xFe_2O_3$ gels at low temperatures in external magnetic fields. It is shown that the state of the iron atoms in the gels depends significantly on their concentration. In dry gels with an iron content exceeding $0.01Fe_2O_3$, the Fe atoms belong to finely dispersed particles of the oxide with maximum sizes of ~ 80 Å in a superparamagnetic state. For lower iron contents, the Fe atoms are in the form of a highly diluted paramagnetic impurity of trivalent ions in a diamagnetic matrix. It is assumed that clusters develop from a small number of iron and oxygen ions dispersed in the gel matrix. Here spin-lattice relaxation of the magnetic moments of the iron atoms is observed. [S1063-7834(99)01608-1]

We have recently carried out Mössbauer studies of the crystallization of quartz and cristobalite under low-temperature hydrothermal conditions in the presence of impurity oxides of trivalent iron oxide for the first time.[1,2] The initial material for synthesis of polymorphic silica was a dried $SiO_2 \cdot 0.001^{57}Fe_2O_3$ gel. These studies were done in order to determine the structural, charge, and spin states of the iron atoms during the crystallization process. It was established that under alkaline hydrothermal conditions a stable quartz+aegirine association is formed, while crystallization of cristobalite under neutral conditions takes place in two stages. The structural, charge, and spin states of the iron atoms were determined in all stages of synthesis. At the same time, at room temperature in the initial material, we observed relaxation behavior characteristic of the magnetic moments of iron atoms, of which ^{57}Fe is one.

In this paper we conduct Mössbauer studies on ^{57}Fe nuclei at low temperatures in external magnetic fields in order to clarify the character of this relaxation of the magnetic moments and determine the states of the iron atoms in dry $SiO_2 \cdot xFe_2O_3$ gels.

1. EXPERIMENTAL TECHNIQUE

$SiO_2 \cdot xFe_2O_3$ gels were prepared from mixtures of equivalent amounts of a saturated solution of trivalent iron nitrate $^{57}Fe(NO_3)_3$ and silicon-ethyl ether $Si(OC_2H_5)_4$ with added ethyl alcohol. These mixtures were evaporated from a water bath with continuous mixing and pulverization until a dry state was reached. Then the gels were annealed in alundum crucibles at 500 °C and carefully ground in a jasper mortar.[1,2]

Mössbauer measurements were made at room temperature on an MS1101E spectrometer manufactured by MOSTÉK (Russia) in an absorption geometry with constant acceleration. The γ-ray source was the isotope ^{57}Co in an Rh matrix. The Mössbauer spectra were processed and analyzed using the MSTools code.[3,4]

2. RESULTS AND DISCUSSION

A Mössbauer spectrum of an $SiO_2 \cdot 0.001^{57}Fe_2O_3$ gel measured at room temperature (Fig. 1) in the residual magnetic field of ~ 1 Oe of the electromagnetic vibrator of the Mössbauer spectrometer consisted of a very broad resonance line in the center of the range of Doppler velocities v. This is typical of the relaxation of the magnetic moment of iron atoms, of which ^{57}Fe is one. In order to clarify the nature of this relaxation we made some additional measurements at the boiling point of liquid nitrogen, T_N (Fig. 1). This yielded a hyperfine magnetic structure in the spectrum, which consisted of visible portions of three partial spectra—an asymmetric sextet, triplet, and quadrupole doublet. The intensity of the sextet was twice that of the triplet.

The hyperfine parameters of the quadrupole doublet (the shift $\delta = 0.36(2)$ and quadrupole displacement $\varepsilon = 0.53(4)$, as well as the width $\Gamma = 1.1(3)$ of the components) indicate that this partial spectrum belongs to iron atoms, which together with oxygen atoms form particles with sizes up to

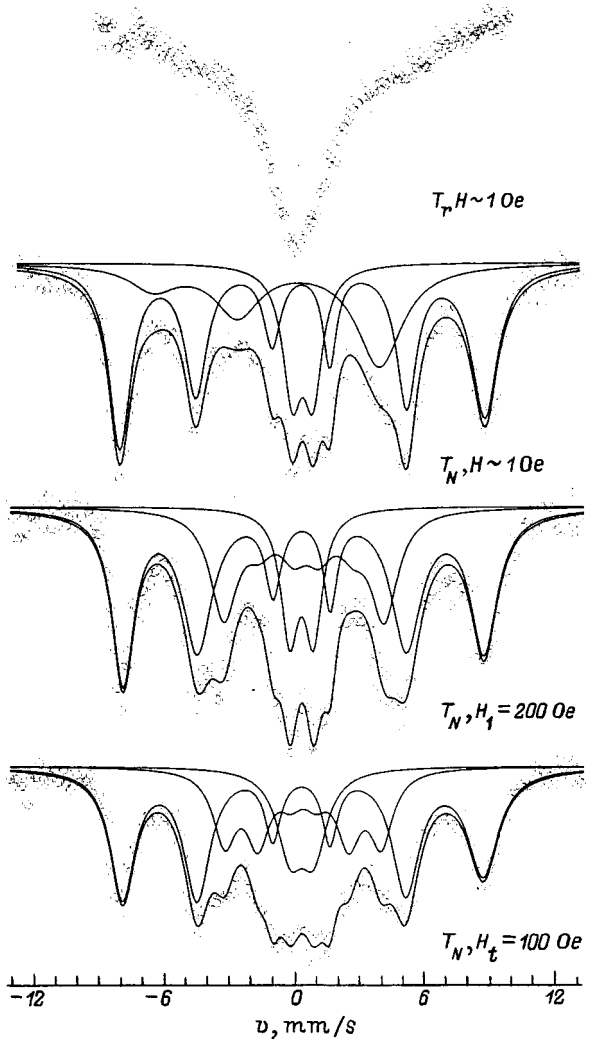

FIG. 1. Mössbauer spectra of ^{57}Fe nuclei in an $SiO_2 \cdot 0.001^{57}Fe_2O_3$ gel at room T_r and liquid nitrogen T_N temperatures without an external magnetic field and in longitudinal H_l and transverse H_t fields.

~ 80 Å and are in a superparamagnetic state[5–7] (as occurs for the gels we have used to crystallize ferrisilicate feldspars and acmite[8,9]). These iron atoms were $\sim 16\%$. As for the remaining two partial spectra, their interpretation (especially of the triplet, which does not usually appear in Mössbauer spectra of ^{57}Fe) requires a more detailed examination of the behavior of the isolated paramagnetic ion Fe^{3+} during resonant absorption (emission, scattering) of γ-rays by ^{57}Fe nuclei in the solid state.

For the isolated paramagnetic ion[10,11] the magnetic structure of the Mössbauer spectrum is determined by the hyperfine interaction of the nucleus with the electron shell and the Zeeman interaction of the magnetic moment of the electron shell with the magnetic field **H**. We shall consider only weak magnetic fields ($H \ll \sim 100$ kOe), for which the direct interaction of the nucleus with the field **H** can be neglected. In the case of Fe^{3+} ions, the ground state $^6S_{5/2}$ term is split into three doubly degenerate Stark levels (Kramers doublets). If the energy of the ground state Stark splitting is high compared to the hyperfine interaction energy, then for each level (i), separately, one can introduce its own hyperfine interaction tensor $\hat{A}^{(i)}$ and the g-tensor proportional to it, $\hat{g}^{(i)}$, and the spin Hamiltonian can be written in the form[10,11]

$$H^{(i)} = H_{hf}^{(i)} + H_Z = \mathbf{I}\hat{A}^{(i)} + \mu_B \mathbf{H}\hat{g}^{(i)}\mathbf{S}'. \quad (1)$$

Here $H_{hf}^{(i)}$ and H_Z are the Hamiltonians for the hyperfine and Zeeman interactions, respectively, **I** is the nuclear spin, $S' = 1/2$ is the effective spin of the electron shell, whose value is determined by the degree of degeneracy of the levels, i is the number of the Kramers doublet, μ_B is the Bohr magneton, and **H** is the resultant magnetic field at the ion, which equals the sum of the weak random magnetic field $\mathbf{H}_r$ ($\sim 1 - 10$ Oe) and the external field $\mathbf{H}_0$.

Equation (1) implies that the location of the energy levels of the electronic-nuclear system of the Fe^{3+} ion is determined, not only by the magnitude and direction of the field **H**, but also by the magnitudes of the components of the anisotropic, generally speaking, tensors $\hat{A}^{(i)}$ and $\hat{g}^{(i)}$. This means that the locations of the hyperfine structure components of the partial spectra for different Kramers doublets will react differently to a change in the magnitude and orientation of **H**.

In the absence of an external magnetic field, the weak random intracrystalline magnetic fields $\mathbf{H}_r$, which originate in the magnetic moments of neighboring nuclei and ions, will act on a paramagnetic ion. In this case, if for a given Kramers doublet the energy of the Zeeman interaction of the magnetic moment of the electron shell with the magnetic field is significantly less than the energy of the hyperfine interaction of the ions with the electron shell, $g\mu_B H \ll A$, then the energy levels will be determined by the total magnetic moment of the system, $F = I + S$, and the projections m_F of this moment in the direction of the field **H**.[10] As the electronic-nuclear level schemes and the associated allowed Mössbauer transitions ($\Delta m_F = 0, \pm 1$) of Fig. 2 show, for this Kramers doublet the partial spectrum will consist of a set of three broadened resonance lines.

If, however, the external field is sufficiently high for the Zeeman energy of the electron shell to be much greater than the hyperfine interaction of the nucleus with the electron shell, $g\mu_B H \gg A$, then the coupling between **I** and **S** is broken and the energy levels will be determined by the projections of the spins I_Z and S_Z in the field direction **H**. In this case, as the scheme of Fig. 2 shows, in the spectrum taken in an external field $\mathbf{H}_0$, for this Kramers doublet the partial spectrum will consist of a Zeeman sextet (a set of six resonance lines). The so-called ''stabilization of the hyperfine structure'' in a low external magnetic field will be observed.

If we consider a rhombic crystal field for the Fe^{3+} ion, as has been done[12,13] for impurity Fe^{3+} ions in aluminum nitrate $Al(NO_3)_3 9H_2O : {}^{57}Fe^{3+}$, then it turns out that the hyperfine interaction tensor $\hat{A}$ and the g tensor $\hat{g}$ for one of the Kramers doublet ($i = 2$) are symmetric, while for the other two doublets ($i = 1,3$) they are strongly anisotropic with the same components (with different notation for the axes):

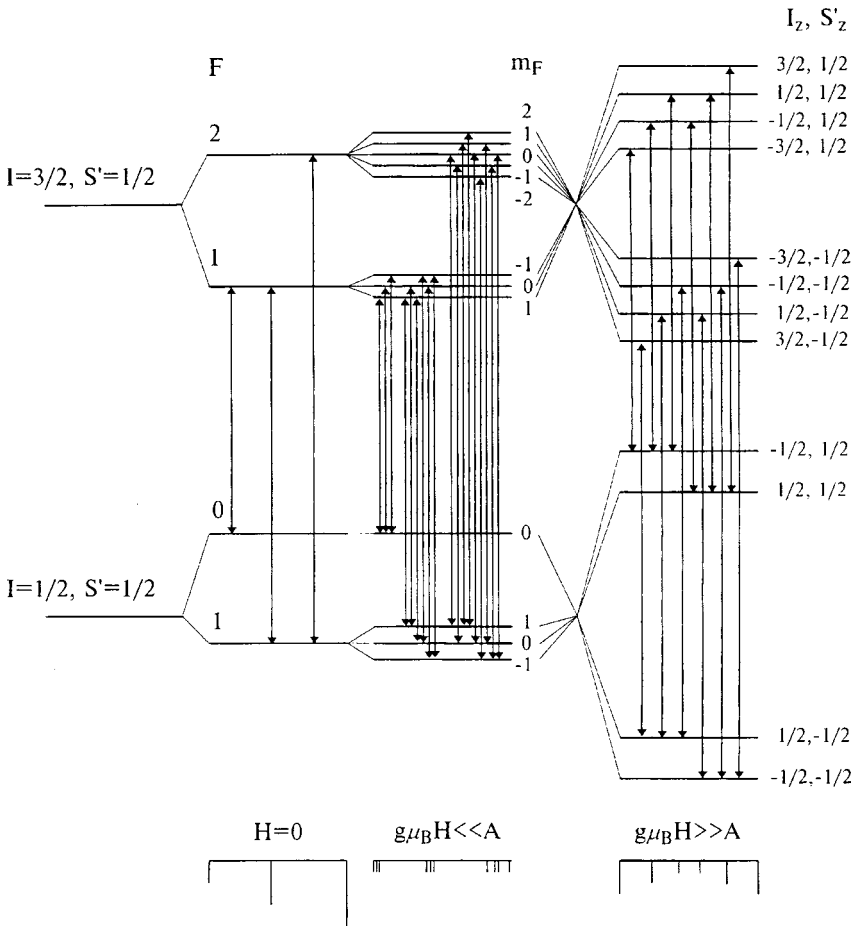

FIG. 2. Level scheme and Mössbauer transitions, together with line diagrams of Mössbauer spectra, for the electron-nuclear $^{57}Fe^{3+}$ system.

$$\begin{cases} g_{xx}^{(2)}=g_{yy}^{(2)}=g_{zz}^{(2)}=\dfrac{30}{7}\approx 4.29; \\ g_{xx}^{(1)}=g_{xx}^{(3)}=\dfrac{6}{7}\approx 0.86; \\ g_{yy}^{(1)}=g_{zz}^{(3)}=\dfrac{12(3+\sqrt{7})}{7}\approx 9.68; \\ g_{zz}^{(1)}=g_{yy}^{(3)}=\dfrac{12(3-\sqrt{7})}{7}\approx 0.61; \\ A_{jk}^{(i)}=\dfrac{A_0}{2}g_{jk}^{(i)}. \end{cases} \tag{2}$$

The existence of strongly anisotropic tensors $\hat{A}$ and $\hat{g}$ for a Kramers doublet stabilizes[10] the hyperfine structure of the corresponding partial structure in the weak random magnetic field $\mathbf{H}_r$, even in a polycrystalline sample. For a doublet with isotropic $\hat{A}$ and $\hat{g}$ tensors, an additional external magnetic field $\mathbf{H}_0 \sim 100-200$ Oe is required to stabilize the hyperfine magnetic structure.[10]

Now it can be understood that the triplet observed in the experimental spectrum (Fig. 1) corresponds to a Kramers doublet with isotropic $\hat{A}$ and $\hat{g}$ tensors, while the intense sextet, to two doublets with highly anisotropic components. Here some asymmetry in the intense components of the sextet may be explained both by a local inhomogeneity (the sample material is a dried x-ray amorphous gel) and by some departure in the local symmetry of the surroundings of the Fe^{3+} ion from rhombic. An applied external magnetic field [both along ($H_l = 200$ Oe) and perpendicular to ($H_t = 100$ Oe) the direction of the γ-rays] actually stabilized the corresponding partial spectrum, converting it from a triplet into a Zeeman sextet (see Fig. 1), finally confirming the proposed interpretation.

A significant broadening (up to 12 mm/s) of the resonance lines in the spectrum can be attributed both to a local inhomogeneity for the iron atoms in the gel matrix and to the ''residual'' effect of spin-lattice relaxation.

Therefore, the iron atoms in the initial gel exist in the form of a highly dilute paramagnetic impurity of trivalent ions in the diamagnetic matrix of the gel. Clusters probably develop from a very small number of iron and oxygen atoms dispersed in the gel matrix.

The observed state of the Fe atoms is not typical of gels with more than $0.1Fe_2O_3$ iron content.[8,9] For comparison, Fig. 3 shows Mössbauer spectra of ^{57}Fe nuclei in an $SiO_2 \cdot 0.1Fe_2O_3$ gel at room and liquid-nitrogen temperatures without an external magnetic field and in longitudinal and transverse fields. The spectra are a superposition of two partial spectra: a Zeeman sextet corresponding to rather large particles of a magnetically ordered α-Fe_2O_3 phase and a quadrupole doublet corresponding to finely dispersed oxide particles with dimensions no large than ~ 80 Å.[5–7] Evi-

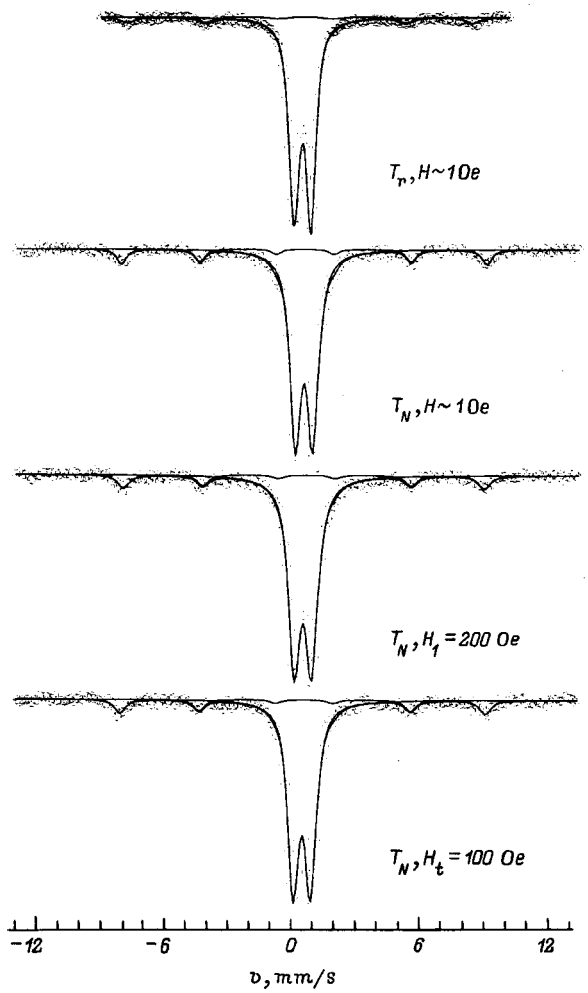

FIG. 3. Mössbauer spectra of ^{57}Fe nuclei in an $SiO_2 \cdot 0.1Fe_2O_3$ gel at room T_r and liquid-nitrogen T_N temperatures without an external magnetic field and in longitudinal H_l and transverse H_t fields.

dently, on going from room to liquid-nitrogen temperature, the hyperfine structure of the spectrum does not change significantly. Only a slight increase in the ''hyperfine'' magnetic field H_n is observed, along with an increase in the relative intensity of the Zeeman sextet, which confirms the supermagnetic behavior of the small iron oxide particles. Applying low ($\sim 100-200$ Oe) magnetic fields did not cause any significant changes in the spectrum.

Studies on ^{57}Fe nuclei in $SiO_2 \cdot 0.1Fe_2O_3$ gels showed that the Mössbauer spectra at room temperature, as for the $SiO_2 \cdot 0.1Fe_2O_3$ gels, consist of a paramagnetic line and, at liquid nitrogen temperature, manifest signs of spin-lattice relaxation of the magnetic moments of the impurity paramagnetic iron atoms.

Therefore, the Fe atoms in dried gels containing iron in amounts exceeding $0.01Fe_2O_3$ belong to finely dispersed oxide particles with maximum sizes of ~ 80 Å which are in a superparamagnetic state.

These studies have shown that the state of the iron atoms in dry $SiO_2 \cdot xFe_2O_3$ gels depends significantly on their concentration. Thus, in $SiO_2 \cdot 0.001Fe_2O_3$ gels, the Fe atoms exist in the form of a highly diluted paramagnetic impurity of trivalent ions in a diamagnetic matrix. Clusters probably develop from a very small number of iron and oxygen atoms which are dispersed in the gel matrix. Here spin-lattice relaxation of the magnetic moments of the iron atoms is observed. In dried gels with iron contents exceeding $0.01Fe_2O_3$, the Fe atoms belong to finely dispersed oxide particles with maximum sizes of ~ 80 Å which are in a superparamagnetic state.

[1] A. M. Bychkov, V. S. Rusakov, and G. A. Sukhadol'skiĭ, Geokhimiya, No. 10, 1019 (1996).
[2] V. S. Rusakov, A. M. Bychkov, and G. A. Sukhadol'skiĭ, Vestn. LGU. Ser 3, Fiz. Astron., No. 5, 66 (1996).
[3] V. S. Rusakov, N. I. Chistyakova, and D. A. Khramov, in *The Third International Symposium on the Industrial Applications of the Mössbauer Effect. ISIAME'92*, Otsu, Japan (1992).
[4] V. S. Rusakov and N. I. Chistyakova, in *Latin American Conference on Applications of the Mössbauer Effect. LACAME'92*, Buenos Aires, Argentina (1992), N 7–3.
[5] W. Künding, H. Bemmel, D. Konstabaris, and R. H. Lindquist, in *The Mössbauer Effect* (Atomizdat, Moscow, 1969), pp. 222–238.
[6] I. P. Suzdalev, Fiz. Tverd. Tela (Leningrad) **12**, 998 (1970) [Sov. Phys. Solid State **12**, 781 (1970)].
[7] Yu. F. Krupyanskiĭ and I. P. Suzdalev, Zh. Éksp. Teor. Fiz. **65**, 1715 (1973) [Sov. Phys. JETP **38**, 859 (1973)].
[8] V. S. Rusakov, A. M. Bychkov, N. I. Chistyakova, N. A. Kuz'mina, and V. S. Urusov, Geokhimiya No. 1, 73 (1996).
[9] O. E. Yagova, V. S. Rusakov, N. A. Kuzmina, and A. M. Bychkov, Experiment in Geosciences **6**, No. 2, 45 (1997).
[10] A. M. Afanas'ev and Yu. M. Kagan, JETP Lett. **8**, 382 (1968).
[11] S. S. Yakimov, Izv. Akad. Nauk SSSR, Ser. Fiz. **50**, 2449 (1986).
[12] A. M. Afanas'ev, E. Yu. Tsymbal, S. S. Yakimov, V. M. Cherepanov, M. A. Chuev, W. Zinn, K. Sauer, and A. Holtzwart, Fiz. Tverd. Tela (Leningrad) **29**, 2102 (1987) [Sov. Phys. Solid State **29**, 1208 (1987)].
[13] V. M. Cherepanov, M. A. Chuev, and S. S. Yakimov, Fiz. Tverd. Tela (Leningrad) **30**, 1076 (1988) [Sov. Phys. Solid State **30**, 624 (1988)].

Translated by D. H. McNeill

Correlation properties of the stochastic magnetic structure of ultradispersed ferromagnetic materials

A. A. Ivanov, V. A. Orlov, and G. O. Patrushev

Krasnoyarsk State Pedagogical University, 660049 Krasnoyarsk, Russia
(Submitted December 18, 1998)
Fiz. Tverd. Tela (St. Petersburg) **41**, 1432–1436 (August 1999)

The properties of the stochastic magnetic structure of ultradispersed ferromagnetic materials are studied. The correlation coefficients of the magnetization of a magnetic material are calculated for various types of chaos in the anisotropy field. The effects of different types of disorder on the parameters of a stochastic magnetic structure are compared. Numerical simulations by various methods confirm the theoretical results. © *1999 American Institute of Physics.* [S1063-7834(99)01708-6]

The motifs of the intense research on ultradispersed magnetic materials and multilayer structures have general physical and practical aspects. In particular, these materials open up wide prospects for the creation of high-capacity information carriers. There are a variety of methods for theoretical study of magnetic materials with inhomogeneities in the anisotropy field: micromagnetism methods, spectral analysis, spin-wave theory, etc. Each of these approaches has its advantages and disadvantages. For example, the micromagnetism method is problematical for studies of the dynamic properties of magnetic materials, significant difficulties arise in examining nonsteady-state processes by spectral analysis, and the spin-wave theory often leads to computational problems. The choice of one or another method as an instrument by researchers is dictated by the specifics of the problems to be solved. In addition, for some problems a preference is given to the approaches natural for a given class of tasks, as they say, on the basis of the ''first principles'' of the phenomenon being studied. In particular, micromagnetism techniques[1–4] and spectral analysis methods[5,6] are fruitful for examining the properties of a stochastic magnetic structure. Numerical simulation is often used to verify analytic results.[1,2] In this paper we propose a study of the properties of a stochastic magnetic structure from the standpoint of the correlation theory of random processes.

1. CORRELATION PROPERTIES OF MAGNETIZATION

Let us consider a one dimensional layered model of a ferromagnetic material (Fig. 1). The magnetic properties of the layers are the same and characterized by the anisotropy constant K and the exchange constant A. In the approximation of large exchange (compared to the energy of the crystallographic anisotropy), a system of nonlinear equations has been obtained[2] for the equilibrium position of the magnetization of a multilayer sample of finite size:

$$\frac{\vartheta_2-\vartheta_1}{x_2-x_1}=\frac{1}{2\delta_0^2}(x_2-x_1)\sin(\vartheta_2+\vartheta_1-2\alpha_1),$$

$$\frac{\vartheta_3-\vartheta_2}{x_3-x_2}-\frac{\vartheta_2-\vartheta_1}{x_2-x_1}=\frac{1}{4\delta_0^2}(x_3-x_2)\sin(\vartheta_3+\vartheta_2-2\alpha_2)+\frac{1}{4\delta_0^2}(x_2-x_1)\sin(\vartheta_2+\vartheta_1-2\alpha_1),$$

$$\frac{\vartheta_{n+1}-\vartheta_n}{x_{n+1}-x_n}-\frac{\vartheta_n-\vartheta_{n-1}}{x_n-x_{n-1}}=\frac{1}{4\delta_0^2}(x_{n+1}-x_n)\sin(\vartheta_{n+1}+\vartheta_n-2\alpha_n)+\frac{1}{4\delta_0^2}(x_n-x_{n-1})\sin(\vartheta_n+\vartheta_{n-1}-2\alpha_{n-1}),$$

$$-\frac{\vartheta_{N+1}-\vartheta_N}{x_{N+1}-x_N}=\frac{1}{2\delta_0^2}(x_{N+1}-x_N)\sin(\vartheta_{N+1}+\vartheta_N-2\alpha_N), \quad (1)$$

where N is the number of layers in the sample, x_n are the coordinates of the interlayer boundaries, ϑ_n are the polar angles of the magnetization at the layer boundaries, α_n are the polar angles of the direction of the local anisotropy axes (see Fig. 1), and $\delta_0=\sqrt{A/K}$ is the characteristic correlation radius of action of the exchange forces.

A detailed study of the stochastic magnetic structure of magnetic materials of this type[7] has shown that the magnetization has a block structure, i.e., breaks up into weakly interacting regions of quasiuniform magnetization. The effective parameters of the blocks, such as their width, effective anisotropy constants, directions of the effective anisotropy axes, etc., have been studied in detail in our earlier papers. In addition, it should be emphasized that the previous analysis of nonuniform models of this sort was conducted under the assumption that the magnetization turning processes are stationary and ergodic. In fact, as will be shown below, the random process of aligning the magnetization under the influence of an inhomogeneity in the anisotropy field can, in general, also be spatially nonstationary.

In analyzing the correlation properties of the stochastic magnetic structure of the multilayer magnetic material being examined here, it is convenient to use a representation of

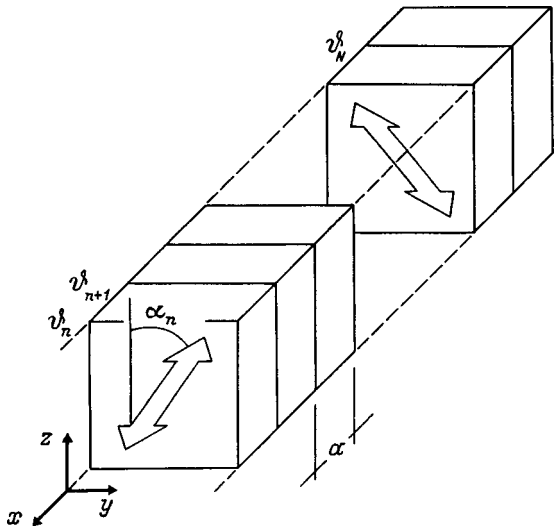

FIG. 1. Model of a layered magnetic material. ϑ and α are the polar angles of the magnetization and of the local anisotropy axis, respectively.

Eqs. (1) in the form of a stochastic differential equation. In fact, the system of Eqs. (1) is nothing other than a difference form of the equation

$$\frac{d^2\vartheta(x)}{dx^2}=\frac{1}{2\delta_0^2}\sin(2\vartheta(x)-2\alpha(x)). \tag{2}$$

In the case $\langle a\rangle \ll \delta_0$, where $\langle a\rangle$ is the average layer width, the correlation between the direction of the local anisotropy axis and the magnetization can be neglected. The distribution of the magnetization is described by a smooth function $\vartheta(x)$: at large distances compared to the layer width it varies slowly. Given the above remarks, Eq. (2) can be simplified and rewritten in the following form:

$$\frac{d^2\vartheta(x)}{dx^2}=-\frac{1}{2\delta_0^2}\sin(2\alpha(x)). \tag{3}$$

The general solution of the Cauchy problem for Eq. (3) with zero initial conditions is the function

$$\vartheta(x)=\frac{1}{2\delta_0^2}\int_0^x t\sin(2\alpha(t))dt-\frac{1}{2\delta_0^2}x\int_0^x \sin(2\alpha(t))dt. \tag{4}$$

Since Eq. (3) describes a nonsteady-state random process,[8] the correlation function, often used in spectral analysis,[9] is not an adequate characteristic of the coupling of the magnetization in different parts of a magnetic material. In our case, it is convenient to use the correlation coefficient given by

$$r(x,\xi)=\frac{\langle\vartheta(x)\vartheta(x+\xi)\rangle}{\sqrt{\langle(x)^2\langle\vartheta(x+\xi)^2\rangle}}. \tag{5}$$

The correlation coefficient (5) is easily calculated[10] if the inhomogeneity correlation function

$$\psi(x,x+\xi)=\langle\sin(2\alpha(x))\sin(2\alpha(x+\xi))\rangle \tag{6}$$

is specified. Table I lists the inhomogeneity correlation functions for models of layered magnetic materials with different kinds of chaos in the anisotropy field. The first row lists the results for a layered magnetic material with a fixed layer thickness and a random symmetric distribution of the polar angles of the local anisotropy axes about a given direction. The second row lists the results for a layered magnetic material with alternating directions of the local anisotropy axis in neighboring layers ($\pm\alpha_0$) and with random layer widths with a binomial distribution. Finally, the third row lists the parameters of a layered magnetic material with random directions of the local anisotropy axis and random layer thicknesses.

The function ψ characterizes stationary ergodic processes,[12] so the inhomogeneity correlation function depends only on the difference ξ in the coordinates, but not on x. Although $\psi(\xi)$ differs significantly for the different types of disorder, a numerical simulation showed that the functional dependences of the magnetization correlation function

TABLE I. Inhomogeneity correlation functions $\psi(\xi)$ and magnetization structure functions $Q(\xi)$ of magnetic materials with different types of disorder in an anisotropy field.

Type of chaos in the anisotropy field	Statistical characteristics $\psi(\xi)$, $Q(\xi)$ for $\xi>0$
1. Magnetic material with orientational chaos in an anisotropy field (no spatial disorder).	$\psi(\xi)=\langle\sin^2(2\alpha)\rangle\left[1-\frac{\xi}{a}\right]$ for $\xi<a$ and $\psi(\xi)=0$ for $\xi>a$, $Q(\xi)=\frac{a}{4\delta_0^4}\langle\sin^2(2\alpha)\rangle[x\xi^2+\frac{1}{3}\xi^3]$
2. Magnetic material with alternating directions of the local anisotropy axis with alternating directions of the local anisotropy axes of neighboring layers and spatial disorder in an anisotropy field.	$\psi(\xi)=\sin^2(2\alpha_0)\exp\left(-\frac{\xi}{\langle a\rangle/2}\right)$, $Q(\xi)=\frac{\langle a\rangle}{2\delta_0^4}\sin^2(2\alpha_0)[x\xi^2+\frac{1}{3}\xi^3]$
3. Magnetic material with orientational and spatial disorder in the anisotropy field.	$\psi(\xi)=\langle\sin^2(2\alpha)\rangle\exp\left(-\frac{\xi}{\langle a\rangle}\right)$ $Q(\xi)=\frac{\langle a\rangle}{4\delta_0^4}\langle\sin^2(2\alpha)\rangle[x\xi^2+\frac{1}{3}\xi^3]$

for the three models are indistinguishable (with differences only in the numerical coefficients).[11] In fact, even for nonstatic aligning of the magnetization, in all three cases the correlation coefficient (5) takes the same form

$$r(x,\xi)=\frac{1+(3/2)(\xi/x)}{[1+(\xi/x)]^{3/2}}, \tag{7}$$

for x and ξ containing more than one layer.

In the case of a nonstatic alignment of the magnetization under the influence of the inhomogeneity of the anisotropy field, the question arises of defining a block as a region of magnetization which behaves independently of similar neighboring regions during magnetic reversal by a rotating field.[1] In fact, a numerical simulation of a nonsteady-state process (see below) showed that blocks, in this sense, are not observed. Even in this case, however, there is a characteristic correlation length for the quasiuniformity, δ_s, which should correspond to the earlier estimates under the assumption of steady-state processes.[1,2] We determine the dependence of δ_s on $\langle a\rangle$ from the equation

$$Q(x,\xi)=f(\mu). \tag{8}$$

Here $f(\mu)$ is a function which depends on the degree of texturing of the magnetic material, $\mu=\langle\cos(2\alpha)\rangle$, and $Q(x,\xi)=\langle(\vartheta(x+\xi)-\vartheta(x))^2\rangle$ is a magnetization structure function, which is listed in the table for the cases considered here (calculated simply by substituting the solution (4) in Q). In order to estimate the quasiuniform magnetization width it is logical to set $f(\mu)$ equal to the dispersion in the directions of the local anisotropy axes. In other words, we choose a distance ξ over which the dispersion of the turning in the magnetization is comparable to the dispersion in the fluctuations in the polar angles of the local anisotropy axis. On the other hand, the distance δ_s should equal the characteristic decay length of the correlation coefficient to within a numerical factor.

As an example let us consider the first case in the table. Here Eq. (8) transforms to

$$\frac{\langle a\rangle}{4\delta_0^4}\left[x\delta_s^2+\frac{1}{3}\delta_s^3\right]=\frac{\langle\alpha^2\rangle}{\langle\sin^2(2\alpha)\rangle}. \tag{9}$$

The undetermined parameter x in Eq. (9) is nothing other than the shift in the asymptotes of the power law dependence of Q on ξ.

For estimates, we can set $x=0$, i.e., consider the turn in the magnetization from the sample surface. Then, from Eq. (9) we have

$$\delta_s\approx\sqrt[3]{[2\pi^2\delta_0^4/\langle a\rangle}. \tag{10}$$

A similar calculation was carried out for the second and third models.

It should be emphasized separately that the functional dependence of δ_s on $\langle a\rangle$ determined by Eq. (9) is independent of the degree of texturing of the magnetic material. Despite the presence of texture in the distribution of the local asymmetry axes,[1] the magnetization, nevertheless, has the characteristic decay length of the correlation coefficient, which has a power law dependence on $\langle a\rangle$ with an exponent of $-1/3$.

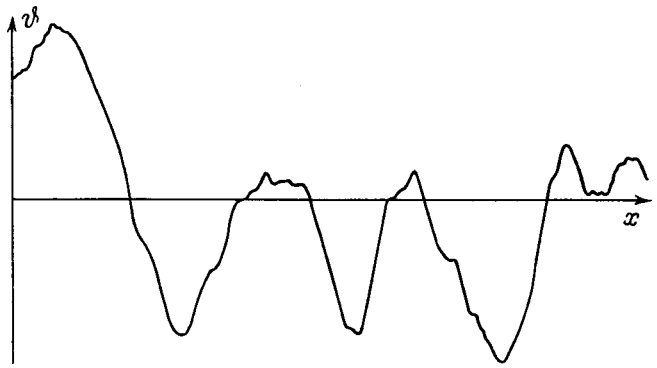

FIG. 2. Typical distribution of the magnetization obtained by simple iteration from uniform seeding.

The resulting δ_s coincides, to within a numerical coefficient, with estimates by other methods in Ref. 2.

The calculated block widths can be used to rewrite Eq. (7) for the correlation coefficient (7) as

$$r(\delta_s,\xi)=\frac{1+(3/2)(\xi/\delta_s)}{[1+(\xi/\delta_s)]^{3/2}}. \tag{11}$$

The form of r for the three models studied here will differ only in the rate of decay of the correlation coupling, which corresponds to the characteristic correlation length (10).

Note the remarkable catastrophic change in the functional dependence of r on ξ on going from a nonstationary to a stationary random process. In fact, it is evident[11] that for large ξ, r falls off asymptotically as $\frac{3}{2}\sqrt{\delta_s/\xi}$, and not exponentially at all.[9,11] What is involved in the physics of the change from nonsteady- to steady-state behavior will be discussed later.

2. COMPUTER SIMULATION

A stochastic magnetic material was modelled by synchronous dynamics, which reduces in our case to numerically solving a system of nonlinear equations (1) by simple iteration. The stability of the resulting distributions of the magnetization was tested by a method described in detail elsewhere.[13] Figure 2 shows a typical distribution of the magnetization obtained for uniform initial seeding: $\vartheta_1^{(0)}=\vartheta_2^{(0)}=\ldots=\vartheta_n^{(0)}=\ldots=\vartheta_{N+1}^{(0)}$. It is already obvious from visual observation that the process $\vartheta(x)$ is stationary and ergodic. In fact, the values of the dispersion of the magnetization, correlation functions, and other statistical characteristics, calculated by ensemble averaging the resulting realizations and by averaging over the coordinate x were the same.

In addition, Eq. (1) was solved numerically as a Cauchy problem, i.e., a rigorous solution of the nonlinear equations with subsequent verification that the last equation in the system was satisfied. Typical distributions of the magnetization obtained by this method are shown in Fig. 3. It is important to note that this method can be used to obtain nonsteady-

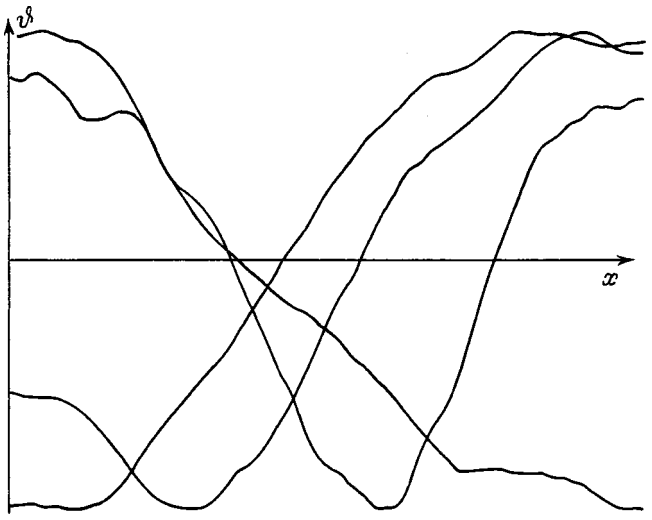

FIG. 3. Typical distributions of the magnetization obtained by the shooting method.

state solutions. The existence of a characteristic quasiuniformity length and of a nonexponential asymptotic dependence for the correlation coefficient in the nonsteady-state process was confirmed by simulating a magnetic material by just this method. (See Fig. 4.)

The results of the two methods considered here, simple iteration (''descent along the field''[1]) and the Cauchy problem, are realized in actual magnetic materials. Both approaches are based on real physical processes. The solution of the nonlinear system of Eqs. (1) by iteration or by ''descent along the field'' models the actual magnetization of a magnetic material prior to saturation with subsequent shutoff of the external field and free decay of the magnetization to the equilibrium state. Numerical solution of Eqs. (1) as a Cauchy problem resembles the aligning of the magnetization under the influence of nonuniformities in the anisotropy during sequential deposition of layers (during fabrication of films without an external magnetic field). Evidently, magnetization aligning under the influence of an inhomogeneity in the anisotropy field changes from a nonsteady-state into a steady-state process if the magnetic material was in a strong external magnetic field after it was prepared. Here the correlation properties of the stochastic magnetic structure of the multilayer sample have changed fundamentally. In particular, the functional dependence of the correlation coefficient on position has changed. The dispersion in the magnetization turning for $x \to \infty$ approached a definite final value (as opposed to a nonstationary process). Blocks developed which undergo magnetic reversal independent of one another, and so on.

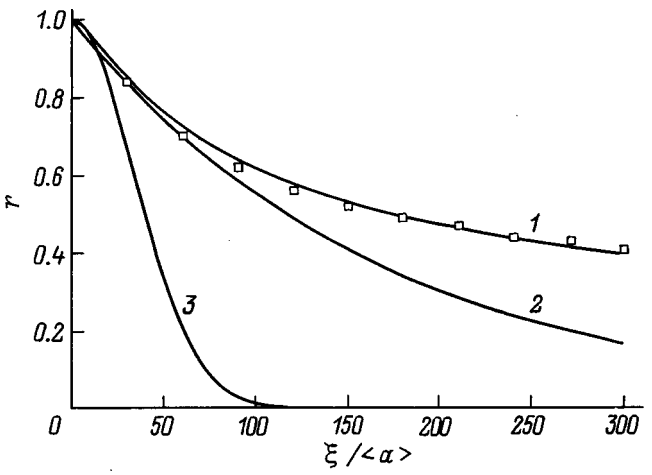

FIG. 4. Functional dependence of the correlation function on the number of layers. Curve *1* — Eq. (11), curve *2* — exponential dependence $r=\exp(-\xi/\delta_s)$, curve *3* — Gaussian dependence $r=\exp(-\xi^2/\delta_s^2)$. The individual points represent the numerical simulations of $r(\xi)$.

A one-dimensional layered model of a ferromagnetic material, therefore, yields the following results:

(1) It has been shown analytically that the functional dependence of the correlation coefficient of the stochastic magnetic structure of ferromagnetic materials is the same for different types of chaos in the anisotropy field (spatial or orientational).

(2) The characteristic correlation radius of the stochastic magnetic structure has been calculated for a nonsteady-state process of aligning the magnetization under the influence of the nonuniformity in the anisotropy field.

(3) A computer simulation has illustrated the possibility of realizing both steady-state and nonsteady-state processes for the alignment of the magnetization under the influence of an inhomogeneity in the anisotropy field. In addition, a physical interpretation of the change from a one to the other process has been provided in terms of magnetization processes that actually take place.

[1] A. A. Ivanov and G. O. Patrushev, Fiz. Met. Metalloved. **84**(4), 35 (1997).
[2] A. A. Ivanov, V. A. Orlov, and G. O. Patrushev, Fiz. Met. Metalloved. **84**(2), 47 (1997).
[3] E. V. Sinitsyn and I. G. Bostrem, Zh. Éksp. Teor. Fiz. **85**, 661 (1983) [Sov. Phys. JETP **58**, 385 (1983)].
[4] S. Nieber and H. Kronmuller, Phys. Status Solidi B **153**, 367 (1989).
[5] V. A. Ignatchenko, Zh. Éksp. Teor. Fiz. **54**, 303 (1968) [Sov. Phys. JETP **27**, 162 (1968)].
[6] V. A. Ignatchenko and R. S. Iskhakov, Fiz. Met. Metalloved. No. 6, 75 (1992).
[7] A. A. Ivanov and G. O. Patrushev, *Abstract of the 14th All-Union Coordination Meeting on the Physics of Magnetic Phenomena* [in Russian], Irkutsk (1991), 28 pp.
[8] V. N. Tutubalin, *Theory of Probability and Random Processes* [in Russian], Izd-vo. MGU, Moscow (1992), 400 pp.
[9] V. A. Ignatchenko and Y. I. Man'kov, Phys. Rev. B **56**, 194 (1997).
[10] S. M. Rytov, *Introduction to Statistical Radiophysics. Random Processes* [in Russian] (Nauka, Moscow, 1976), Part I, 496 pp.
[11] A. A. Ivanov, V. A. Orlov, and G. O. Patrushev, Fiz. Met. Metalloved. **85**(6), 138 (1998).
[12] A. G. Goryainov and V. I. Tikhonov, *Statistical Electronics. Examples and Problems* [in Russian] (Sov. Radio, Moscow, 1980), 544 pp.
[13] M. A. Pochernin, Dep. in VINITI reg. No. 04.04.90, 1830-B90 (Irkutski Ped. Inst., Irkutsk, 1990), 16 pp.

Translated by D. H. McNeill

Nonlinear magnetic susceptibility and microwave spin dynamics of R_2CuO_4 quasi-2D antiferromagnets (R=Eu, Pr, Gd)

E. I. Golovenchits*) and V. A. Sanina

A. F. Ioffe Physicotechnical Institute, Russian Academy of Sciences, 194021 St. Petersburg, Russia
(Submitted December 25, 1998)
Fiz. Tverd. Tela (St. Petersburg) **41**, 1437–1444 (August 1999)

An experimental study of nonlinear ac magnetic susceptibility and microwave spin dynamics of R_2CuO_4 quasi-2D Heisenberg antiferromagnets (R=Eu, Pr, Gd) has been carried out. The data obtained can be accounted for if one assumes the existence of a random-field (RF) state in the Eu_2CuO_4 and Pr_2CuO_4 tetragonal crystals within the $77 \leqslant T \leqslant 350$ K range covered. If this is so, 3D antiferromagnetic order persists only within limited regions, while in CuO_2 layers there are 2D Heisenberg antiferromagnetic spin fluctuations with large correlation lengths. In the Gd_2CuO_4 crystal there exists, besides uniform 3D antiferromagnetic long-range order with weak ferromagnetism, an admixture of an RF-type state.
 [S1063-7834(99)01808-0]

Crystals of the R_2CuO_4 family, where R=Pr, Nd, Gd, Sm, and Eu, belong to the class of quasi-2D Heisenberg antiferromagnets. All crystals of the family, except Gd_2CuO_4, possess tetragonal symmetry T' $(I4/mmm)$.[1] At $T \sim 660$ K, Gd_2CuO_4 undergoes a structural phase transition from the high-temperature tetragonal, T', to a low-temperature orthorhombic phase with space group $Acam$.[2]

The R_2CuO_4 crystals have recently been studied intensely, primarily as model objects for HTSC compounds, which, like R_2CuO_4, are constructed of square lattices of Cu^{2+} ions with spin $S=1/2$ in CuO_2 layers. Besides, these crystals may serve as an illustration of low-dimensional magnets with a fairly simple lattice and a ratio of the exchange integrals within the CuO_2 planes and between them of $\sim 10^{-5}$.

A series of studies of magnetic, as well as of dielectric and structural properties of Eu_2CuO_4, were reported in a number of publications.[3–8] It was shown that Eu_2CuO_4 undergoes a phase transition at $T \simeq 150-160$ K involving a change in both magnetic and structural properties.[3,4,8] At $T \simeq 150$ K, one observed a jump in static magnetic susceptibility in the (ab) plane perpendicular to the tetragonal axis c.[3] Local orthorhombic distortions were found to occur at temperatures $T \leqslant 150-160$ K in the CuO_2 layers.[8] As the temperature increases, a low-frequency dispersion in dielectric susceptibility and an anomalous microwave dynamic magnetic susceptibility set in starting from $T \simeq 120$ K.[4,5] The latter features were observed to persist up to $T \sim 450$ K, the highest temperatures studied.

We analyzed the experimental data on dielectric properties in terms of the 2D Ising orbital-glass model.[4] As for the anomalous microwave spin dynamics, it was induced by the presence of 2D uniform (with $q=0$), well-defined (with a damping much weaker than the natural frequency, $\gamma \ll \omega_0$) spin-wave excitations of the type of spin waves.[5]

In accordance with neutron diffraction data of the R_2CuO_4 quasi-2D Heisenberg antiferromagnets (R=Nd, Pr, Gd, Sm, and Eu), their Néel temperature is usually $T_N \simeq 250-300$ K. It is assumed that below T_N, 3D uniform long-range magnetic order persists in the Cu subsystem.

Neutron studies of Bragg scattering attest to the persistence of 3D antiferromagnetic ordering in Eu_2CuO_4 up to $T \simeq 270$ K.[9] If one assumes the existence of a uniform 3D long-range antiferromagnetic order in the Eu_2CuO_4 crystal at temperatures $T \leqslant T_N \simeq 270$ K, then 2D uniform, well-defined spin-wave excitations could set in only for $T \geqslant T_N \simeq 270$ K. At the same time, experiment reveals their existence starting at a temperature $T \simeq 120$ K, which is substantially lower than T_N.

In an attempt to explain all available experimental data on the Eu_2CuO_4 crystal, one assumed[6] the existence in it of a quasi-2D antiferromagnetic state of the random-field (RF) type similar to that considered in Ref. 10. It was also assumed that 3D antiferromagnetic order persists only within regions of a limited spatial extent, and that there are also 2D Heisenberg antiferromagnetic fluctuations with large correlation lengths $\xi \gg a$.

The purpose of this work was a continuation of the experimental investigation of Eu_2CuO_4 crystals, as well as studying Pr_2CuO_4 and Gd_2CuO_4, by nonlinear ac magnetic susceptibility and microwave dynamic magnetic and dielectric susceptibility techniques within a temperature range of 77–300 K. We were interested primarily in the extent to which the physical situation observed in Eu_2CuO_4 is common for the whole class of R_2CuO_4 compounds.

The paper is organized as follows. First, one considers and analyzes the experimental data available on the nonlinear ac magnetic susceptibility for all the three above crystals and, second, one presents data on the microwave magnetic and dielectric susceptibilities together with their analysis for the same crystals, and, finally, a possible scheme of the phase states of the crystals based on the totality of data collected is considered.

1. NONLINEAR MAGNETIC SUSCEPTIBILITY

1.1. Formulation of the problem

As already mentioned, an RF state is assumed to exist in the crystals under study here. This state is nonlinear, and it is investigated by studying nonlinear ac magnetic susceptibility. Studies of the nonlinear susceptibility in the critical region near second-order phase transitions showed this method to be efficient.[11–14]

In nonlinear magnetic-susceptibility experiments one usually studies the response at multiple frequencies $n\omega$ ($n \geqslant 1$) to an ac magnetic field applied to a sample at a frequency ω [$h = h_0 \sin(\omega t)$].

The magnetic moment of a nonlinear system can be presented as a sum of moments[12]

$$M = M_0 + M_1 + M_2 + M_3 + \cdots = M_0 + \chi_1 h_0 + \chi_2 h_0^2 + \chi_3 h_0^3 + \cdots, \quad (1)$$

where the quantities χ_n are nth-order susceptibilities, and M_0 is spontaneous magnetization. For $M_0 = 0$, expansion (1) contains only odd terms.

In the case where the contribution due to higher-order moments falls off rapidly enough, one can limit oneself to retaining only a few low-order terms in (1), after which the expansion can be recast in a harmonic form. The coefficients of this expansion are experimentally measured harmonic amplitudes A_n, which permit calculation of the corresponding nonlinear susceptibilities. For instance, leaving terms up to the seventh order inclusive in Eq. (1), we obtain

$$A_3 = (1/4)\chi_3 h_0^3 + (5/16)\chi_5 h_0^5 + (21/64)\chi_7 h_0^7. \quad (2)$$

The first harmonic characterizes primarily the linear susceptibility due to pair correlations, which are always dominant. The $A_{3,5,\ldots}$ harmonics originate from higher-order correlations. The presence of spontaneous (or induced by a dc field $H_0 \neq 0$) magnetization gives rise to even harmonics as well.

When studying low-frequency susceptibility (at frequencies considerably lower than those of spin-wave excitations), one is interested in the quasistatic response of a uniform ($q = 0$) magnetic moment of the crystal to an applied ac magnetic field. It is known that static susceptibilities of ferromagnets exceed by far those of antiferromagnets. However the static susceptibilities of weakly ferromagnetic antiferromagnets approach in magnitude those of ferromagnets. In this connection, one may expect that, in weakly ferromagnetic antiferromagnets residing in a nonlinear state, the nonlinear harmonics should likewise be close in amplitude to those of ferromagnets.

It is known that, in order for a weak ferromagnetism to exist in antiferromagnets, the crystal symmetry should allow the presence of the Dzyaloshinsky–Moriya interaction.[15] For a weak ferromagnetism to appear in R_2CuO_4 quasi-2D antiferromagnets, the tetragonal T' structure should be rhombically distorted.

Antiferromagnets with a weak ferromagnetic moment are characterized by two order parameters: a ferromagnetic (with $q = 0$) and an antiferromagnetic [with $q = Q(\pi/a)$, where $Q(\pi/a)$ is the antiferromagnetic vector] one. The ferromagnetic order parameter has singularities near T_N at $q = 0$, and the antiferromagnetic one becomes critical in the vicinity of T_N for $q \simeq Q(\pi/a)$. Thus the presence of a weak ferromagnetism in antiferromagnets permits observation of low-frequency nonlinear harmonics in the critical region.

For temperatures $T \ll T_N$, weak ferromagnets can exhibit also a nonlinearity due either to a domain structure or to the existence of a cooperative but disordered state (random field, or spin glass).

1.2. Experimental results

This study dealt with the behavior of the second (A_2) and third (A_3) harmonics for the R_2CuO_4 crystals (R=Eu, Pr, Gd). The technique of the measurements was similar to that used by us earlier in studies[16] of nonlinear dielectric susceptibility. In contrast to the case of dielectric measurements, one naturally had to place here the sample in an ac magnetic field. The induction method used is based on measuring the emf induced by a sample at the double or triple frequency with respect to that of the applied field. One measured the temperature dependences $A_2(T)$ and $A_3(T)$ within the range of 77–350 K. The measurements were carried out at a number of exciting magnetic-field frequencies ω in the 1–30 kHz interval. The magnetic-field amplitude h_0 was varied from 0.5 to 5 Oe. The $A_2(h_0^2)$ and $A_3(h_0^3)$ relationships were found to be close to linear within the above h_0 limits. Measurements were also performed under a dc external magnetic field $H_0 \leqslant 1$ kOe. As in Ref. 16, the sensitivity of the setup was determined by the amplitude of the parasitic harmonics, which was of the order of 10^{-6} of that of the exciting field h_0. In these conditions, the ratio of the parasitic to useful signal amplitudes for $A_{3,\max}$ was $10^{-3} - 10^{-4}$.

Temperature dependences of the nonlinear-harmonic amplitudes were recorded each time by heating the sample, which was preliminarily cooled from room temperature to $T \sim 77$ K both in the zero-field cooling (ZFC) regime ($H_0 = 0$) and with a dc magnetic field applied (the FC regime). When FC cooled, the H_0 field was turned off at a low temperature, and the measurements were carried out during heating at $H_0 = 0$.

(*a*) Gd_2CuO_4. The $A_3(T)$ relations measured on Gd_2CuO_4 crystals are plotted in Fig. 1. Similar dependences were observed also for the second harmonic, but the A_2 amplitude was 30–50 times smaller than A_3. As seen from Fig. 1, Gd_2CuO_4 exhibits $A_3 \neq 0$ harmonics both in the ZFC and FC regimes. One notices also a strong peak in the A_3 amplitude near $T \simeq 290$ K $\simeq T_N$ and substantially weaker signals at temperatures below T_N.

When a $H_0 \neq 0$ field was again applied, the low-temperature A_2 signals measured under heating first increased substantially in amplitude, after which, as the field was increased still more ($H_0 > 200$ Oe), both the A_3 and A_2 signals were suppressed.

(*b*) Eu_2CuO_4. Figure 2 presents amplitudes of the A_3 harmonics for Eu_2CuO_4 crystals. Note that in Eu_2CuO_4, unlike Gd_2CuO_4, one did not observe A_2 and A_3 signals in the ZFC regime throughout the temperature range covered. However, when working in the FC regime with the dc field

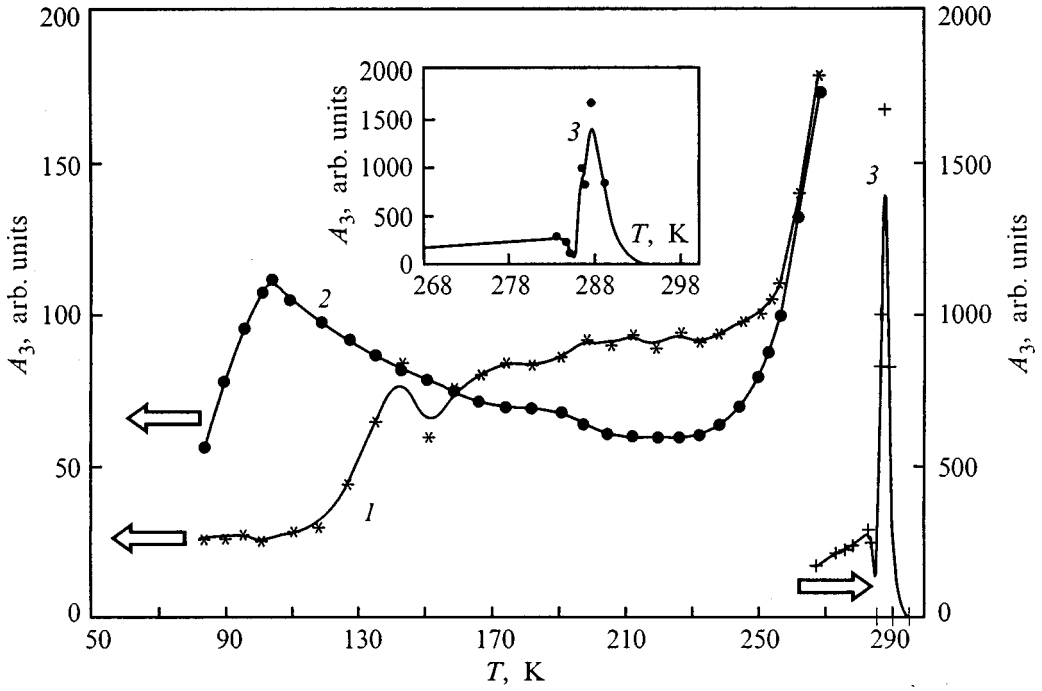

FIG. 1. Temperature dependence of the third-harmonic amplitude in Gd_2CuO_4. *1* — ZFC regime, *2* — FC regime, *3* — temperature dependence of A_3 for the critical region (the ZFC and FC regimes practically coincide). Inset: Curve *3* shown on a larger vertical but a finer temperature scale.

turned off at the lowest temperature, a third harmonic signal was seen to appear, and it was likewise considerably in excess of the second-harmonic signal, as in the case of Gd_2CuO_4. As evident from Figs. 1 and 2, the A_3 amplitude for Eu_2CuO_4 is comparable in magnitude with that for Gd_2CuO_4 measured at low temperatures. In contrast to Gd_2CuO_4, the Eu_2CuO_4 crystal does not exhibit a maximum in the temperature dependence $A_3(T)$ near $T \simeq T_N$. Besides, $A_3 \neq 0$ only below 150–160 K.

If an external dc magnetic field $H_0 \simeq 20$ Oe was again applied during measurements under a warmup, the A_3 signal was completely suppressed (but reversibly, i.e. the signal recovered if the field was switched off).

(*c*) Pr_2CuO_4. The A_2 and A_3 harmonics did not appear in Pr_2CuO_4 crystals under any of the above conditions.

It should be pointed out that in all the above cases the A_2 and A_3 signals were observed in the three crystals only when the vectors of the ac field h and of the dc field H_0 were in the (ab) crystal plane. No nonlinear effects were observed with the fields oriented along the (c) axis.

1.3. Analysis of experimental data

(*a*) Gd_2CuO_4. Crystals of Gd_2CuO_4 are known to exhibit rhombic distortions of the T' structure below $T < 660$ K and a weak ferromagnetic moment in the ab plane for $T < T_N$.[2] It appears only natural to relate the strong peak of the A_3 amplitude observed at 290 K (Fig. 1) to the critical region around T_N. As evident from Fig. 1, however, Gd_2CuO_4 produces also weaker, but distinct signals due to the nonlinear

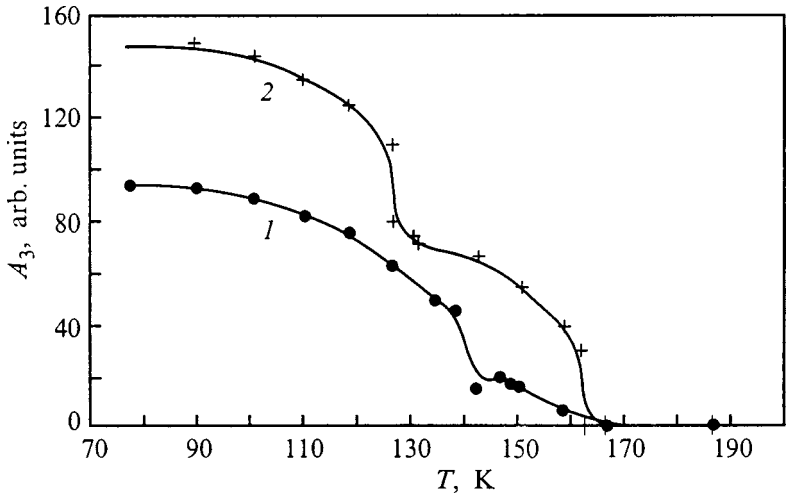

FIG. 2. Temperature dependence of the third-harmonic amplitude in Eu_2CuO_4. Measurement frequency 3ω(kHz): *1* — 6, *2* — 30.

A_3 harmonics at lower temperatures, outside the critical region. As already mentioned, this low-temperature nonlinearity may originate from either a domain structure, if a uniform 3D long-range magnetic order prevails in the crystal, or an admixture of a disordered phase to the uniform magnetic state.

(b) Eu_2CuO_4. The above method of formation of the A_3 signal in Eu_2CuO_4 for $T \leqslant 150-160$ K indicates the existence in the ab plane of the crystal of a residual, nonequilibrium magnetic moment induced by the external dc magnetic field.

We believe that the crystal may contain local-scale weak ferromagnetic moments in the ab plane (the RF state) for $T \leqslant 150-160$ K.

The temperature dependence $A_3(T)$ in the $T \leqslant 160$ K region (see Fig. 2) is close to the temperature dependence of the magnetic order parameter, although it exhibits some features near 120 and 150 K. On the other hand, the temperature dependence of the intensity of the superstructure reflection, revealed[8] at $T \leqslant 150-160$ K in Eu_2CuO_4, behaves in a similar way. This reflection vanishes at the same temperature as the A_3 signal (see Fig. 5 in Ref. 8). Thus the structural phase transition at $T \simeq 150-160$ K is accompanied by a change in the magnetic properties as well.

According to Ref. 8, one observes in Eu_2CuO_4 near $T \simeq 150-160$ K local-scale rhombic distortions at the structural phase transition caused by oxygen ion displacements around Cu^{2+} ions in the CuO_2 layers. The existence of such distortions within limited regions at temperatures $T \leqslant 150-160$ K accounts for the possibility of occurrence on the same local scales of weak ferromagnetic moments [oriented in the (ab) planes] producing $A_3 \neq 0$ signals. For $T \geqslant 160$ K, rhombic distortions vanish. This is accompanied by vanishing of the weak ferromagnetic moments and, accordingly, of the third harmonic signals as well.

One may thus maintain that there exists a quasi-2D antiferromagnetic state with a weak ferromagnetic moment on a local scale and nonlinear properties in Eu_2CuO_4 at low temperatures ($T \leqslant 150-160$ K), in other words, there exists an RF state in the crystal at low temperatures, as for $T \geqslant 150-160$ K (see Ref. 6).

(c) Pr_2CuO_4. As already mentioned, no $A_3, A_2 \neq 0$ signals were observed in Pr_2CuO_4 in the conditions in which such signals are produced in Eu_2CuO_4 and Gd_2CuO_4. This implies that this crystal does not support weakly ferromagnetic states throughout the temperature range studied, even on a local scale. It may be conjectured that the local structural distortions observed to exist in the Pr_2CuO_4 crystals do not break its tetragonal symmetry.

2. MICROWAVE DYNAMIC MAGNETIC AND DIELECTRIC SUSCEPTIBILITIES

This Section will deal with the results obtained in a study of microwave dynamic magnetic and dielectric susceptibilities in Pr_2CuO_4 and Gd_2CuO_4 and compare them with earlier data[5] for Eu_2CuO_4. The methods of measurement and calculation of the susceptibilities were similar to those employed in Ref. 5.

2.1. Formulation of the problem. Eu_2CuO_4 crystal

The Eu_2CuO_4 crystal revealed[5] uniform (with $q=0$), well-defined (with damping $\gamma \ll \omega_0$) spin-wave excitations of the type of spin waves in CuO_2 layers. These excitations were found to exist starting from $T > 120$ K up to $T \simeq 450$ K, the temperature up to which the measurements were carried out. Thus spin-wave excitations set in for $T \ll T_N$ and persisted up to $T \gg T_N$ without changing with increasing temperature and without any features appearing at $T \simeq T_N$. This implies a 2D nature of the observed spin-wave excitations.

We also observed the existence of the above spin-wave excitations by microwave dynamic magnetic susceptibility. The following features were found:

(1) The dynamic magnetic susceptibility considerably exceeded of the static one;

(2) The real part of the dynamic magnetic susceptibility exceeded by far the imaginary one (i.e. one had here low-damping excitations);

(3) When the ac magnetic field was oriented along the c axis of the crystal, the real part of the dynamic magnetic susceptibility became negative at $T \simeq 120$ K. In our case of a dielectric crystal, the latter may be caused by dispersion of the real part of the magnetic susceptibility near resonant absorption, if the frequency of the measurements is slightly exceeds of the resonant frequency and weak losses are taken into account (see Ref. 5).

Thus one observed in Eu_2CuO_4 a gap in the spectrum of 2D spin-wave excitations within a broad temperature range, in addition to $T < T_N$, also temperatures both below and substantially in excess of T_N. The gap was found to be $\omega_0 \sim 0.1$ meV.[5]

An analysis was made of the conditions favoring the existence of uniform, well-defined spin-wave excitations in 2D Heisenberg antiferromagnets.[5] In such antiferromagnets, spin-wave excitations with a wave vector q considered in an exchange approximation are well defined if the correlation length of the 2D Heisenberg antiferromagnetic spin fluctuations $\xi \gg a$, and the condition $q\xi \gg 1$ are upheld. The natural frequency ω_0 and damping γ of such excitations can be written[17]

$$\omega_0 = cq, \quad \gamma = c\kappa. \tag{3}$$

Here c is the spin-wave velocity, and $\kappa = 1/\xi$. Clearly enough, uniform ($q=0$) spin-wave excitations considered in the exchange approximation can be only damped.

The situation changes if one takes into account a strong anisotropy with a spin-nonconserving symmetry, for instance, uniaxial. In this case, besides the correlation length of 2D Heisenberg antiferromagnetic spin fluctuations $\xi = a \exp(2\pi\rho_s/k_BT)$,[17] there appears also a spin correlation scale in the layers because of the anisotropy, $\xi_a = a \exp(2\pi\rho_s/k_BT_a)$, where T_a is the effective temperature characterizing the anisotropy energy. It was shown[5] that for a strong enough uniaxial anisotropy and if the conditions $\xi \gg a$ and $q_a\xi \gg 1$ are upheld, where $q_a = 1/\xi_a$, the frequency and damping of spin excitations with wave vectors $0 \leqslant q \ll q_a$ can be written

$$\omega_0 = cq_a, \quad \gamma = c\kappa. \tag{4}$$

Such spin-wave excitations, including uniform ones, are well defined.

It was shown that the strong uniaxial anisotropy necessary for the scales $q_a \gg \kappa$ to form in Eu_2CuO_4 crystals originates from the Ising random molecular field of 2D orbital glass.[4,5]

Thus the existence of 2D uniform, well-defined spin-wave excitations indicates the existence in Eu_2CuO_4, within the temperature range where such excitations are observed, of 2D Heisenberg antiferromagnetic spin fluctuations with large correlation lengths $\xi \gg a$, and of a strong uniaxial anisotropy, such that $q_a \xi \gg 1$. Note that, if an RF state is present in a crystal for temperatures $T < T_N$, then 2D uniform, well-defined spin-wave excitations can exist for $T < T_N$ as well. In our experiments such spin-wave excitations set in for $T \geqslant 120$ K. The data on the nonlinear ac susceptibility in Eu_2CuO_4 presented in Sec. 1 argue for the persistence of the RF state in the crystal for $T < 120$ K (down to the lowest measurement limit of 77 K) as well.

Summing up the results obtained on microwave spin dynamics and the nonlinear susceptibility, we come to a conclusion that Eu_2CuO_4 supports an RF-type quasi-2D state throughout the temperature range covered. There are two phase transitions, at $T \sim 150-160$ and $\sim 250-270$ K. Near $T \sim 150-160$ K, the Eu_2CuO_4 crystal changes its structural state and the character of magnetic anisotropy. For $T \leqslant 150$ K, CuO_2 layers exhibit rhombic distortions on a local scale and a weak ferromagnetism in the (ab) plane on the same local scale. For $T \geqslant 150$ K, the crystal symmetry is tetragonal (the local rhombic distortions generating a weak in-plane ferromagnetism vanish), but there appear the orbital-glass state and uniform, well-defined spin-wave excitations in the CuO_2 layers.

Neutron diffraction measurements suggest that $T \sim 250-270$ K is the Néel temperature for the Eu_2CuO_4 crystal. In our microwave spin-dynamics experiments the frequency of uniform spin-wave excitations becomes equal at $T \sim 250-270$ K to their damping ($\omega_0 \simeq \gamma$). As a result, the spin-wave regime persisting at lower temperatures transfers to damping spin excitations for $T > 250-270$ K. The phase transition is, however, strongly diffuse because of the presence of the RF state.

If the state of the CuO_2 layers, as well as the anisotropy mechanisms are common for R_2CuO_4 crystals with different RE ions, one may expect observation of uniform, well-defined spin-wave excitations in crystals with other RE ions as well. In this connection we performed a study of R_2CuO_4 crystals (R = Pr, Gd). As in the case of Eu_2CuO_4, in order to obtain information on the structural state of the crystal we measured also the temperature dependences of the microwave dielectric susceptibility.

2.2. Microwave magnetic and dielectric susceptibilities of R_2CuO_4 crystals (R = Pr, Gd) and their analysis

(a) Pr_2CuO_4. Figure 3 presents data obtained on the dynamic magnetic susceptibility of Pr_2CuO_4 crystals. Figure 4 compares the data for the real parts of the dynamic magnetic susceptibility of Pr_2CuO_4 and Eu_2CuO_4. As seen from

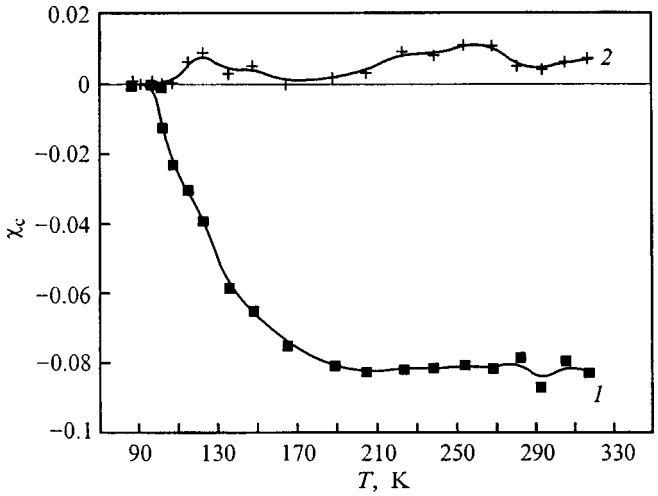

FIG. 3. Temperature dependence of dynamic magnetic susceptibility for Pr_2CuO_4. *1* — real part of susceptibility along the *c* axis, $\mathrm{Re}\chi_c$, *2* — imaginary part of this susceptibility, $\mathrm{Im}\chi_c$. Frequency — 36 GHz. The dynamic magnetic susceptibility is given in the Gaussian system.

Fig. 3, Pr_2CuO_4 exhibits the same features in the dynamic magnetic susceptibility as the ones discussed above for Eu_2CuO_4 (Ref. 5). The only difference consists in the magnitude of the susceptibilities and a shift of the characteristic temperature at which $\mathrm{Re}(\chi_c)$ reverses its sign to lower temperatures (see Figs. 3 and 4). Thus Pr_2CuO_4 also exhibits within a broad temperature region, from $T \sim 90-100$ K up to the maximum point of measurements ($T \sim 350$ K), 2D uniform, well-defined spin-wave excitations similar to those observed[5] in Eu_2CuO_4. This suggests that Pr_2CuO_4 also supports in the above temperature region 2D Heisenberg antiferromagnetic spin fluctuations with large correlation lengths (in other words, a quasi-2D RF state exists in the crystal). Note also that the uniaxial anisotropy is close in magnitude to the anisotropy in Eu_2CuO_4.

The experimental data on microwave spin dynamics permit estimation of the characteristic magnitude of the wave vectors q_a and of the effective uniaxial-anisotropy temperatures for both crystals. Using Eq. (4), the spin-wave velocity

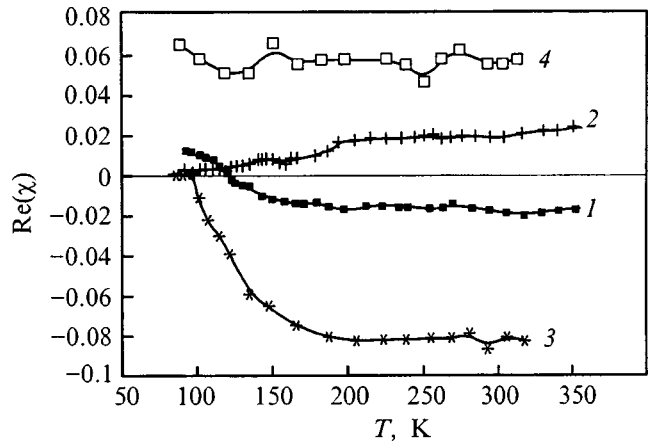

FIG. 4. Temperature dependences of the real parts of the dynamic magnetic susceptibility of (*1,2*) Eu_2CuO_4 and (*3,4*) Pr_2CuO_4 measured (*1,3*) along the *c* axis and (*2,4*) along the *a* axis. Frequency — 36 GHz.

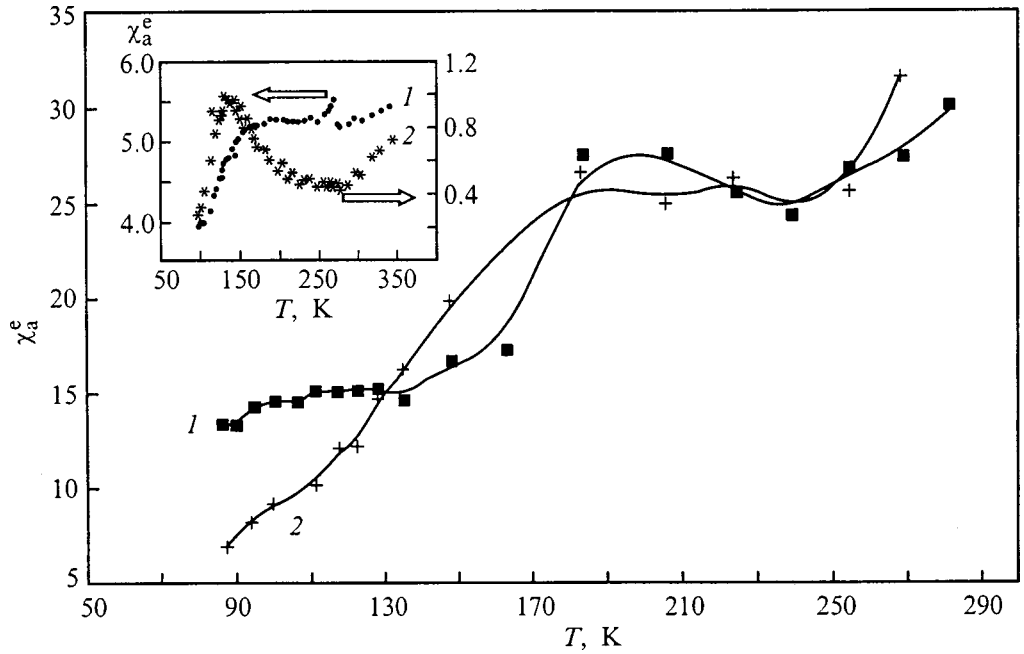

FIG. 5. Temperature dependences of the dielectric susceptibility of Pr_2CuO_4. *1* — real part of the susceptibility in the (ab) plane, $\mathrm{Re}\chi_a^e$, *2* — imaginary part of this susceptibility, $\mathrm{Im}\chi_a^e$. Frequency — 33 GHz. The inset shows a similar plot for Eu_2CuO_4 from Ref. 5.

derived from inelastic neutron scattering measurements on La_2CuO_4 ($c=0.4\times10^6$ cm/s),[18] and the value $\omega_0\sim30$ GHz measured by us (the natural frequencies ω_0 for Pr_2CuO_4 and Eu_2CuO_4 are close in magnitude), we obtain $q_a\simeq5\times10^5$ cm^{-1}. For $T=200$ K and, taking into account that $a\simeq4\times10^{-8}$ cm, we come to $k\simeq5\times10^4$ cm^{-1}, i.e., the condition $q_a\gg k$ is indeed upheld. The value of $\xi_a=1/q_a$ yields $T_a\sim250$ K. Note that the value $T_a\sim250$ K obtained for Eu_2CuO_4 coincides with the temperature of the maximum density of states for orbital glass.[4–6]

The reversal in sign of the real part of the dynamic magnetic susceptibility along the *c* axis, observed to occur in the Pr_2CuO_4 and Eu_2CuO_4 crystals at $T\simeq90$ and $\simeq120$ K, respectively, implies a change in the frequency ω_0 with respect to the fixed operating frequency at these temperatures. Indeed, in order for $\mathrm{Re}(\chi_c)$ to be positive, the operating frequency should be somewhat lower than ω_0.[5] $\mathrm{Re}(\chi_c)$ becomes negative in the reverse case, where the operating frequency is slightly in excess of ω_0. As follows from Eq. (4), the change in the magnitude of ω_0 may be due to a change in the magnetic anisotropy.

Figure 5 displays data on the real and imaginary parts of the dielectric susceptibility for Pr_2CuO_4 crystals when the ac electric field lies in the (ab) plane. Similar to Eu_2CuO_4, features in the temperature dependences of dielectric susceptibility are observed here only in this orientation. As evident from Fig. 5, there is a region of anomalous variation of the real and imaginary parts of dielectric susceptibility χ_a^e, which is extended in temperature and is characteristic of diffuse structural phase transitions. A comparison with similar dependences for Eu_2CuO_4 (see the inset to Fig. 5) shows that the structural phase transition in Pr_2CuO_4 occurs at approximately the same temperatures, but is still more diffuse.

Summing up the experimental data on the nonlinear ac magnetic susceptibility and microwave dynamics, we believe that Pr_2CuO_4 undergoes a structural phase transition accompanied by a change in the magnetic anisotropy of the crystal. The transition is similar to that observed in Eu_2CuO_4 at $T\simeq150-160$ K. In Pr_2CuO_4, however, this transition takes place at a lower temperature and is still more diffuse. Local structural distortions in Pr_2CuO_4 do not break the tetragonal symmetry and no weak ferromagnetism appears.

(b) Gd_2CuO_4. Figure 6 presents data on the dynamic magnetic susceptibility of Gd_2CuO_4 crystals. The pattern here is seen to be somewhat different than that for Pr_2CuO_4 and Eu_2CuO_4. The dynamic magnetic susceptibility is again considerably the static one and, therefore exceeds uniform, well-defined modes do exist in this crystal as well. However the values of $\mathrm{Re}(\chi_c)$ and $\mathrm{Im}(\chi_c)$ are practically equal within

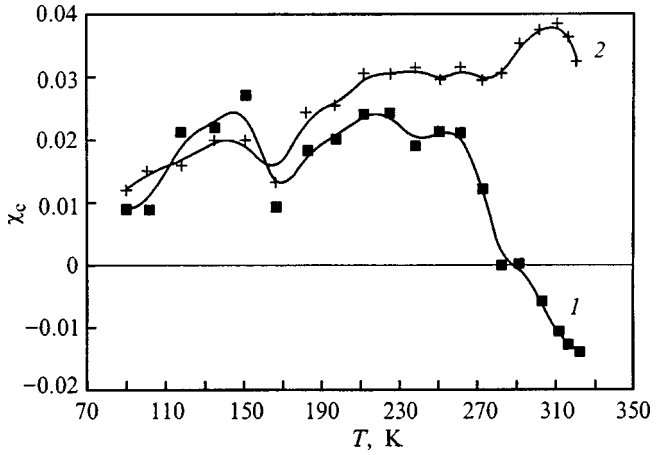

FIG. 6. Temperature dependence of the dynamic magnetic susceptibility of Gd_2CuO_4. *1* — real part of the susceptibility along the *c* axis, $\mathrm{Re}\chi_c$, *2* — imaginary part of this susceptibility, $\mathrm{Im}\chi_c$. Frequency — 36 GHz.

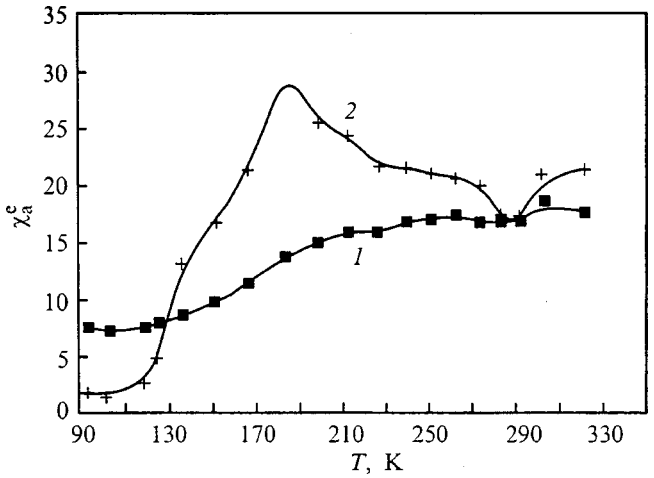

FIG. 7. Same as in Fig. 5 but for Gd_2CuO_4.

a broad temperature range, which implies that the spin-wave excitations are not of the same quality as those in Pr_2CuO_4 and Eu_2CuO_4. Also, $\mathrm{Re}(\chi_c)$ becomes negative only close to $T \simeq 290-300$ K, i.e., the change of the magnetic anisotropy in Gd_2CuO_4 occurs at a substantially higher temperature than it does in Pr_2CuO_4 and Eu_2CuO_4 (practically in the critical region around T_N).

Figure 7 plots the real and imaginary parts of dielectric susceptibility for the Gd_2CuO_4 crystal obtained with an ac electric field in the (ab) plane. The features seen in the temperature dependences of dielectric susceptibility of Gd_2CuO_4 are observed also only in this orientation, which likewise conforms to the results of direct studies[2] of the nature of structural distortions. Gd_2CuO_4 crystals are also seen to undergo a diffuse structural phase transition, although at somewhat higher temperatures than is the case with Pr_2CuO_4 and Eu_2CuO_4 crystals, and have a more pronounced maximum in the imaginary part of dielectric susceptibility at $T \simeq 180-190$ K.

A combined analysis of data on microwave spin dynamics and nonlinear susceptibility permits a conclusion that the Gd_2CuO_4 crystal exhibits, besides uniform 3D antiferromagnetic long-range order and a weak ferromagnetism in the (ab) plane, an admixture of the RF phase for $T<T_N$ as well. Indeed, only in this case are 2D antiferromagnetic spin fluctuations with large correlation lengths, providing a possibility for the existence of 2D uniform well-defined spin-wave excitations, capable of persisting at temperatures $T<T_N \simeq 290$ K. These spin-wave excitations possess higher damping constants than those in the Pr_2CuO_4 and Eu_2CuO_4 crystals, which may be due to the larger nonuniformity of the crystal state.

Thus all the three crystals studied exhibit an RF-type nonuniform magnetic and structural state for $T<T_N$. In Gd_2CuO_4, this nonuniform state is admixed to the main 3D uniform state with long-range magnetic order. Possible reasons for the onset of an RF state in R_2CuO_4 crystals are discussed in Ref. 19. Note that the assumption of the existence in the crystals studied by us of an RF-type state and the proposed physical explanation do not contradict the available experimental data, and in some cases permit interpretation of these data. Among them are, for instance, the presence of a small jump in the Bragg neutron-scattering peak for Eu_2CuO_4 at $T \simeq 150$ K followed by its practically linear falloff in intensity with increasing temperature,[9] the repulsion of the acoustic-phonon branch by a spin-wave mode possessing a temperature-independent gap in $Pr(Nd)_2CuO_4$,[20] and an EPR observation[21] of a glass-like state in Eu_2CuO_4.

Support of the Russian Fund for Fundamental Research (Grant 97-02-18061) is gratefully acknowledged.

*)E-mail: golovenchits@shurpop.ioffe.rssi.ru

[1] H. Müller-Buschbaum and W. Wollschläger, Z. Anorg. Allg. Chem. **414**, 76 (1975).
[2] M. Braden, W. Paulus, A. Cousson, P. Vigoureux, G. Heger, A. Goukassov, P. Bourges, and D. Petitgrand, Europhys. Lett. **25**, 625 (1994).
[3] A. V. Babinskiĭ, E. I. Golovenchits, N. V. Morozov, V. A. Sanina, and L. M. Sapozhnikova, Fiz. Tverd. Tela (Leningrad) **34**, 60 (1992) [Sov. Phys. Solid State **34**, 31 (1992)].
[4] A. V. Babinskiĭ, S. L. Ginzburg, E. I. Golovenchits, and V. A. Sanina, JETP Lett. **57**, 299 (1993).
[5] E. I. Golovenchits, S. L. Ginzburg, V. A. Sanina, and A. V. Babinskiĭ, Zh. Éksp. Teor. Fiz. **107**, 1641 (1995) [JETP **80**, 915 (1995)].
[6] E. I. Golovenchits, V. A. Sanina, and A. V. Babinskiĭ, Zh. Éksp. Teor. Fiz. **110**, 714 (1996) [JETP **83**, 386 (1996)].
[7] E. I. Golovenchits, V. A. Sanina, A. A. Levin, Yu. I. Smolin, and Yu. F. Shepelev, Fiz. Tverd. Tela (St. Petersburg) **39**, 1600 (1997) [Phys. Solid State **39**, 1425 (1997)].
[8] V. P. Plakhty, A. B. Stratilatov, and S. Beloglazov, Solid State Commun. **103**, 683 (1997).
[9] T. Chattopadhyay, J. W. Lynn, N. Rosov, T. E. Grigereit, S. N. Barilo, and D. I. Zhigunov, Phys. Rev. B **49**, 9944 (1994).
[10] R. J. Birgeneau, R. A. Cowley, G. Shirane, and H. Yoshizawa, J. Stat. Phys. **34**, 817 (1984).
[11] A. Z. Patashinskiĭ and V. L. Pokrovskiĭ, Zh. Éksp. Teor. Fiz. **46**, 994 (1964) [Sov. Phys. JETP **19**, 677 (1964)].
[12] S. V. Maleev, Soc. Sci. Rev. A, Phys. **8**, 323 (1987).
[13] I. D. Luzyanin and V. P. Khavronin, Zh. Éksp. Teor. Fiz. **87**, 2129 (1984) [Sov. Phys. JETP **60**, 1229 (1984)].
[14] I. D. Luzyanin and V. P. Khavronin, Zh. Éksp. Teor. Fiz. **92**, 1798 (1987) [Sov. Phys. JETP **65**, 1008 (1987)].
[15] D. Dzyaloshinski, J. Phys. Chem. Solids **4**, 241 (1958); T. Moriya, Phys. Rev. **120**, 91 (1960).
[16] E. I. Golovenchits, V. A. Sanina, and A. V. Babinskiĭ, JETP Lett. **63**, 674 (1996).
[17] S. Chakravarty, B. Halperin, and D. Nelson, Phys. Rev. B **39**, 2344 (1989).
[18] T. Thio, T. R. Thurston, N. W. Preyer, P. J. Picone, M. A. Kastner, H. P. Jenssen, D. R. Gabbe, C. Y. Chen, R. J. Birgeneau, and A. Aharony, Phys. Rev. B **38**, 905 (1988); T. Thio, C. Y. Chen, B. S. Freer, D. R. Gabbe, H. P. Jenssen, M. A. Kastner, P. J. Picone, N. W. Preyer, and R. J. Birgeneau, *ibid.* **41**, 231 (1990).
[19] E. I. Golovenchits and V. A. Sanina, Fiz. Tverd. Tela (St. Petersburg) **41**, 1259 (1999) [Phys. Solid State **41**, 1149 (1999)].
[20] D. V. Fil', I. G. Kolobov, I. D. Fil', S. N. Barilo, and D. I. Zhigunov, Fiz. Nizk. Temp. **21**, 1225 (1995) [Low Temp. Phys. **21**, 937 (1995)].
[21] R. D. Zysler, M. Tovar, C. Rettori, D. Rao, H. Shore, S. B. Oseroff, D. C. Vier, S. Schultz, Z. Fisk, and S.-W. Cheong, Phys. Rev. B **44**, 9467 (1991).

Translated by G. Skrebtsov

Evolution of the optical properties of single-crystal $La_{1-x}Sr_xMnO_3$

L. V. Nomerovannaya, A. A. Makhnëv, and A. Yu. Rumyantsev

Institute of Metal Physics, Urals Branch of the Russian Academy of Sciences, 620219 Ekaterinburg, Russia
(Submitted December 28, 1998)
Fiz. Tverd. Tela (St. Petersburg) **41**, 1445–1449 (August 1999)

An ellipsometric method is used to study the dispersion of the real $\varepsilon_1(\omega)$ and imaginary $\varepsilon_2(\omega)$ parts of the complex dielectric permittivity of single-crystal $La_{1-x}Sr_xMnO_3$ ($x=0.1$, 0.2, and 0.3) for energies from 100 meV to 5 eV at room temperature. It is found that, when lanthanum is replaced by strontium, the optical spectrum changes fundamentally. A shift in the main features of the spectrum of initial $LaMnO_3$ at 1.9 and 4.7 eV to lower energies takes place, as well as a partial redistribution of the optical-conductivity spectral weight in the band gap region $E<1.7$ eV. For compositions with $x=0.2$ and 0.3, a fine structure of the interband absorption is observed against a background of non-Drude optical conductivity at low energies. © *1999 American Institute of Physics.* [S1063-7834(99)01908-5]

When the rare earth element is replaced by a divalent metal in the family of oxides with a perovskite structure $Re_{1-x}A_xMnO_3$ (Re=La, Nd and A=Ca, Sr, Ba), extremely large changes in the physical parameters result: a metal–insulator transition, an antiferromagnetic–ferromagnetic transition, a paramagnetic–ferromagnetic transition with unusual transport properties, giant negative magnetostriction, and structural phase transitions. For $0.2\leqslant x\leqslant 0.5$, materials that are ferromagnetic at low temperatures transform with increasing temperature to a paramagnetic state that has a Curie temperature $T_C=200-350$ K.[1]

Unusual changes in the electronic structure with varying temperature have been observed by spectroscopic (including optical) methods. In single-crystal $La_{1-x}Sr_xMnO_3$ ($x=0.175$, $T_C=273$ K) near the metal–insulator boundary[2] and in polycrystalline film $Nd_{0.7}Sr_{0.3}MnO_3$ ($T_C=180$ K),[3] a redistribution in the spectral weight of the optical conductivity over a wide range of the spectrum $0-3$ eV has been observed during transitions into the metallic state. A gap-like feature has been observed in the optical-conductivity spectrum for $T>T_C$. As the temperature is reduced for $T<T_C$ or the magnetic field is increased, the gap region is filled and the intensity of the low energy absorption rises. As opposed to the ferromagnetic metals (Fe, Co, Ni), the charge carriers in these compounds turned out to be fully spin polarized below T_C. This absorption has been interpreted[2] in terms of transitions with charge transfer between occupied $Mn^{3+}e_g$ levels and unoccupied $Mn^{4+}e_g$ levels split by Jahn–Teller distortions.

The optical properties of these manganite compositions have been studied only with varying temperature,[2,3] and not at all with varying composition of the divalent metal. At the same time, it is known that, for example, when the rare earth element is replaced or there is an oxygen nonstoichiometry in high temperature superconductors (copper oxide compounds), the optical properties and, therefore, the electronic structure change fundamentally.[4,5] In addition, spectroscopic methods for studying the readjustment of the electronic spectrum during the metal–insulator transition with changing stoichiometry in highly correlated systems, such as the manganites, are of independent interest. This is so, first of all, because it is still not clear which factors cause the metal–insulator transition as the concentration is varied.[6] In addition, difficulties arise in choosing an approximation for calculating the electronic structure of the perovskites in the framework of one- electron band calculations.[7]

In order to better understand the readjustment of the electronic spectrum when lanthanum is replaced by strontium in the antiferromagnetic insulator $LaMnO_3$, in this paper we conduct an ellipsometric study of the optical properties of single crystal $La_{1-x}Sr_xMnO_3$.

1. SAMPLES, TECHNIQUE

The single crystal samples of lanthanum manganite $La_{1-x}Sr_xMnO_3$ ($x=0.1$, 0.2 and 0.3) were grown by crucible-less zone melting with radiation heating of the zone. The preparations for obtaining the single crystals were made of a mixture of powdered Mn_2O_3, $SrCO_3$, and La_2O_3 in accordance with standard ceramic technology. The temperature dependences of the electrical resistance of these samples are given elsewhere.[8] The temperatures of the transition to the magnetically ordered state, T_C, were 160 ($x=0.1$), 320 ($x=0.2$), and 353 K ($x=0.3$).[9] The samples for the optical measurements had dimensions of $5\times2\times2$ mm^3. Mirror surfaces were prepared by mechanical polishing with diamond powder of grain size $d<0.5\,\mu$m.

The refractive index n and absorption constant k were measured by the Beatty method on an automatic ellipsometer mounted on a KSVU-12 base with angles of incidence for the light of 67° and 71° over the spectral interval from 100 meV to 5 eV at room temperature with errors of 2–4%. The values of n and k were used to calculate the real $\varepsilon_1=n^2-k^2$ and imaginary $\varepsilon_2=2nk$ parts of the complex dielectric permittivity and the optical conductivity $\sigma=nk\omega/2\pi$ (ω is the angular frequency of the light wave).

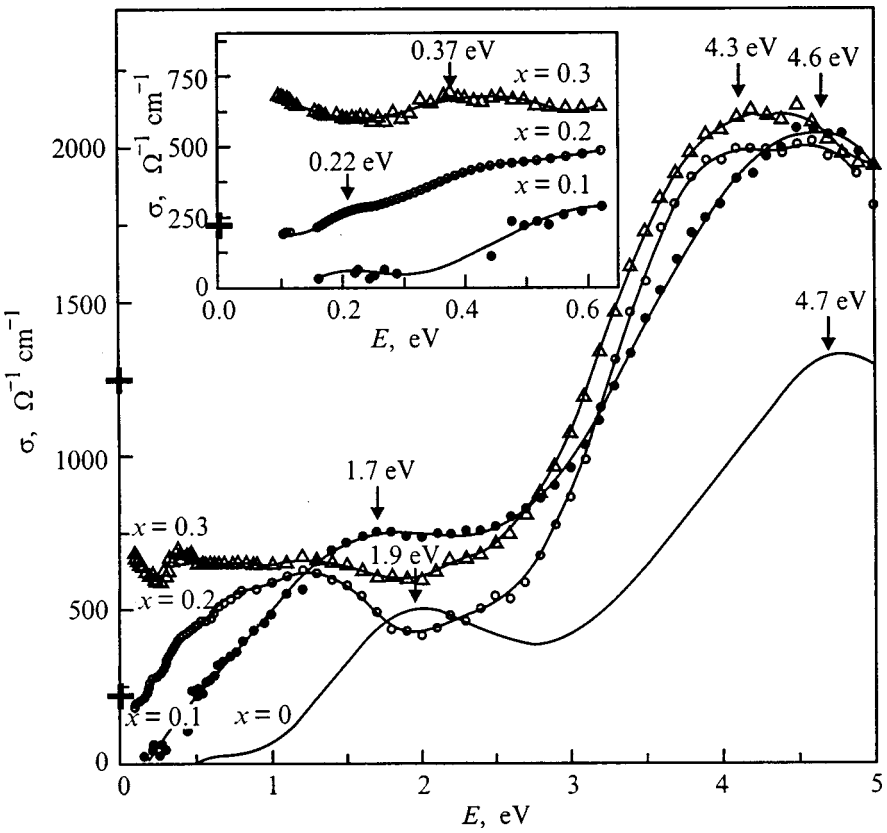

FIG. 1. Optical conductivity spectrum $\sigma(\omega)$ of single crystal $La_{1-x}Sr_xMnO_3$ ($x=0.1$, 0.2, and 0.3). The spectrum $\sigma(\omega)$ of polycrystalline $LaMnO_3$ is taken from Ref. 10. The inset shows the low-energy part of $\sigma(\omega)$. The arrows denote the positions of the peaks in $\sigma(\omega)$. The + signs on the axis indicate the static conductivities for $x=0.2$ and 0.3.

2. RESULTS AND DISCUSSION

Figure 1 shows the optical conductivity spectra $\sigma(\omega)$ of single crystals of $La_{1-x}Sr_xMnO_3$ with strontium contents $x=0.1$, 0.2, and 0.3. Also shown there is a plot of $\sigma(\omega)$ for a polycrystalline sample of $LaMnO_3$.[10] Plots of the real $\varepsilon_1(\omega)$ and imaginary $\varepsilon_2(\omega)$ parts of the complex dielectric permittivity are shown in Figs. 2a and 2b, respectively.

It can be seen that the change in the optical absorption spectrum as lanthanum is replaced by strontium is complicated. The $\sigma(\omega)$ curve for the crystal with a minimum strontium content ($x=0.1$) contains two distinct broad absorption bands: a steplike band centered at 1.7 eV and an intense band at 4.6 eV. Compared to pure $LaMnO_3$, the two absorption bands were shifted to lower energies. Peaks can be seen at 1.9 and 4.7 eV in the pure compound. The $\sigma(\omega)$ spectrum of $LaMnO_3$ has a gap-like feature at $E\sim 1.1$ eV. As the impurity strontium is increased further ($x=0.2$ and 0.3), the band with a peak at 4.6 eV continues to shift toward lower energies by 0.3–0.4 eV, while the first band at 1.7 eV is veiled by the appearance of a contribution from free-charge carriers. This is unambiguously and more clearly indicated by the behavior of the functions $\varepsilon_1(\omega)$ and $\varepsilon_2(\omega)$ (Fig. 2). The spectrum of $\varepsilon_2(\omega)$ for $x=0.1$ illustrates the smearing out of the low energy wing of the first band. The sharp rise in $\varepsilon_2(\omega)$ and the simultaneous fall in the absolute magnitude of $\varepsilon_1(\omega)$ for crystals with $x=0.2$ and 0.3 are caused by the onset of the free-carrier contribution. The passage through zero of $\varepsilon_1(\omega)$ for $x=0.3$ is an indication of a dominant contribution from free carriers, beginning at 0.2 eV. It is known that the negative contribution to $\varepsilon_1(\omega)$ originates in the mechanism of intraband (Drude) carrier acceleration, while the positive contribution is associated with interband quantum-mechanical transitions.

In addition, against the background of the non-Drude behavior of $\sigma(\omega)$ for energies below 1 eV, absorption peaks are observed at 0.22 eV for a sample with $x=0.2$ and at 0.37 eV for one with $x=0.3$. The broad band with a maximum at 0.37 eV has a fine structure (inset in Fig. 2a), which shows up better in $\varepsilon_1(\omega)$. Therefore, introducing strontium (as does[2] reducing the temperature $T<T_C$ for fixed x) causes additional absorption at energies $E<1.1$ eV.

Another feature of the optical conduction of $La_{1-x}Sr_xMnO_3$, which is most noticeable for $x=0.2$, is a redistribution of the spectral weight from high energies to lower energies.

The redistribution of the spectral weight with varying strontium concentration shows up most clearly on calculating the spectral density function of the electrons according to

$$N_{eff}=\frac{2m}{\pi e^2}\int_0^{\infty}\sigma(\omega')d\omega', \tag{1}$$

where m and e are the mass and charge of the electron. N_{eff} is proportional to the number of electrons involved in optical transitions up to energy $\hbar\omega$ (in our case up to 5 eV), regardless of the mechanism by which they are excited. The values of N_{eff} calculated from $\sigma(\omega)$ (Fig. 1) are shown in Fig. 3. For $x=0.1$, N_{eff} becomes significant near the absorption edge (see the inset to Fig. 1), beginning at 0.5 eV. The plots of N_{eff} for samples with $x=0.1$ and 0.2 have two characteristics energies, $E=1.7$ and 5.0 eV, where N_{eff} is independent

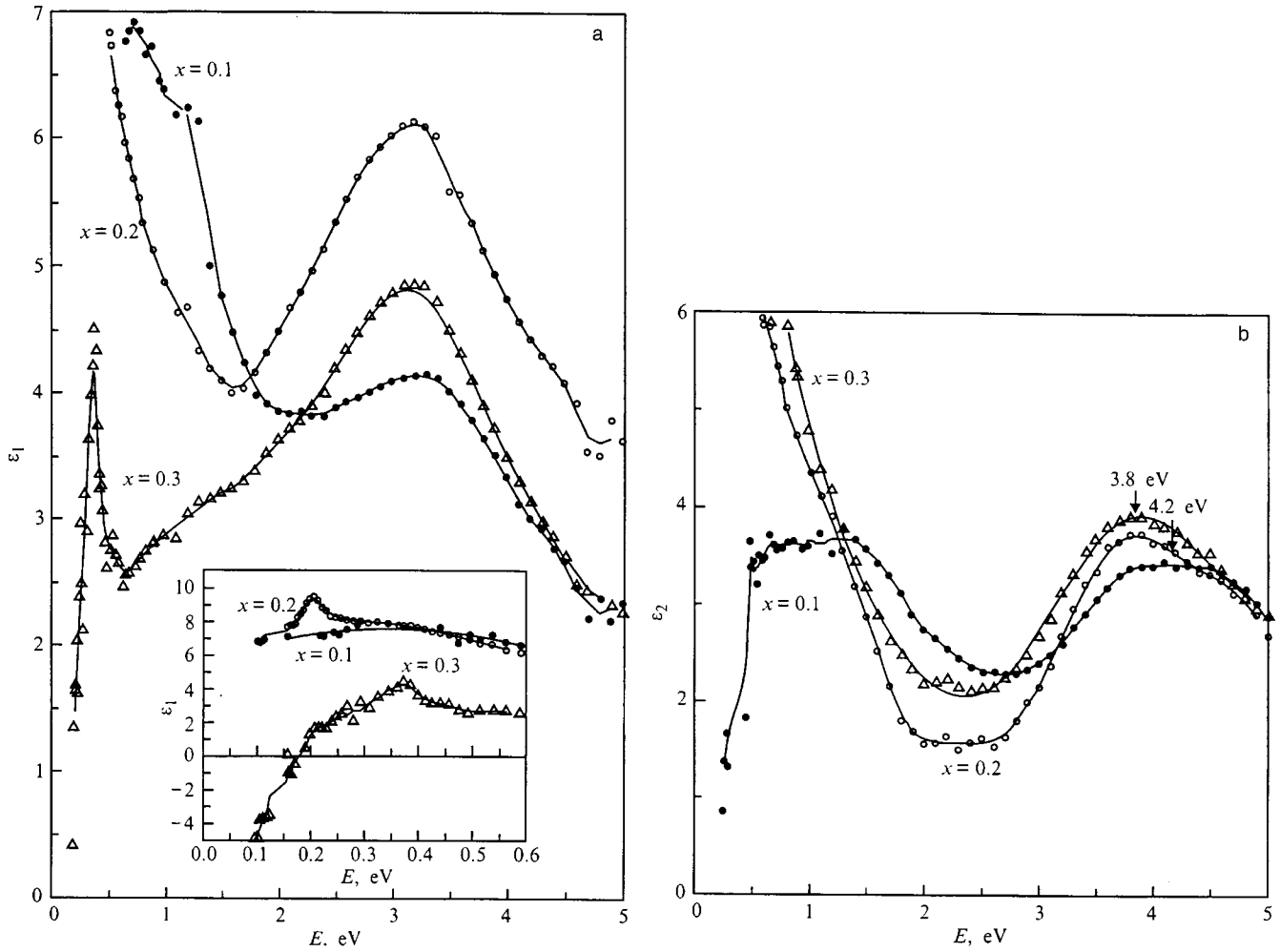

FIG. 2. The real ε_1 (a) and imaginary ε_2 (b) parts of the complex dielectric permittivity of single crystal $La_{1-x}Sr_xMnO_3$ ($x=0.1$, 0.2 and 0.3). The inset shows the low-energy part of $\varepsilon_1(\omega)$. The arrows denote the location of the peaks.

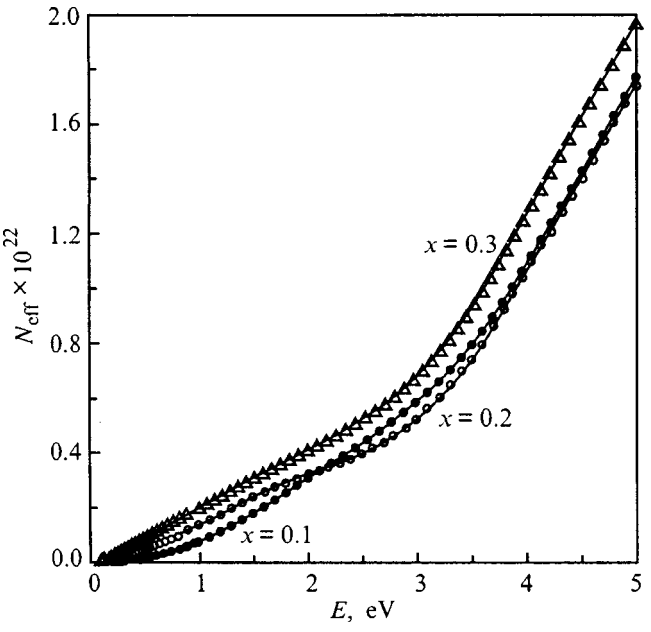

FIG. 3. Spectral electron density N_{eff}, determined from the sum rule for the conductivity $\sigma(\omega)$ for single crystal $La_{1-x}Sr_xMnO_3$ ($x=0.1$, 0.2 and 0.3).

of x. The first value lies near the peak of the fundamental absorption band. The crystal with $x=0.2$ shows a distinct redistribution of the electron density from energies of 2.0–5.0 eV into the region $E<1.7$ eV. For $x=0.3$, N_{eff} increases smoothly over the entire spectral range. Similar behavior has been observed in the copper HTSC oxides, although one significant difference should be noted. In $La_{2-x}Sr_xCuO_4$, for example, introducing Sr did not reduce the energy of the fundamental gap formed by transitions $Cu(3d)\rightarrow O(2p)$ with charge transport. Only a redistribution of the spectral weight from high energies into the gap region was observed.[11] In $La_{1-x}Sr_xMnO_3$ we observed, not only a redistribution of the spectral weight, but also a shift in the band peak from 1.9 in $LaMnO_3$ to 1.7 eV in $La_{0.9}Sr_{0.1}MnO_3$. Thus, doping $LaMnO_3$ with strontium led to a more radical change in the electronic structure than in HTSC or ordinary semiconductors, where impurity states develop in the gap without changing its energy.

Similar behavior has been observed in a study of the electronic structure of $La_{1-x}Sr_xMnO_3$ by photoemission and x-ray spectroscopy.[12] When La was inserted into $SrMnO_3$, absorption ($e_g\uparrow$ symmetry) appeared below E_F by $1-2$ eV with an intensity that rose with increasing lanthanum concentration, while the intensity of absorption ($e_g\uparrow$ symmetry)

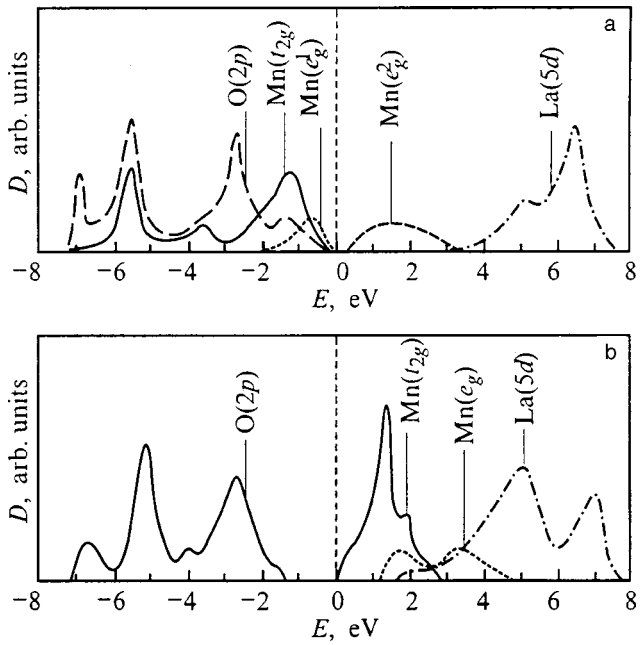

FIG. 4. Density of states D (schematic) of $LaMnO_3$ for spin along ($\uparrow$) (a) and opposite to ($\downarrow$) (b) the magnetization.

above E_F decreased, indicating transfer of spectral weight from unoccupied to occupied $e_g\uparrow$ states with n doping. This sort of change in the spectrum was inconsistent with the behavior of a rigid-band model.

A schematic arrangement of the bands in the initial $LaMnO_3$ proposed[10] on the basis of analyzing optical, photoemission, and x-ray data, as well as data from theoretical band calculations,[7,13,14] imply that the electronic band structure of this compound is very complicated. Figure 4 is a schematic illustration of the energies of the bands in the band structure of $LaMnO_3$ for spins directed along and opposite to the magnetization. The splitting of the Mn($3d$) bands in $LaMnO_3$ is caused by the combined effect of the crystal-field, exchange, and Jahn–Teller distortions. The Mn $(3d)t_{2g}\uparrow$ and $e_g\uparrow$ bands (with spin direction along the magnetization) are filled, while the $t_{2g}\downarrow$ and $e_g\downarrow$ bands (with spin directed opposite to the magnetization) are not filled. The half filled $e_g\uparrow$ band is split owing to Jahn–Teller distortions of the MnO_6 octahedron into $e_g^1\uparrow$ and $e_g^2\uparrow$ bands. This splitting may be responsible for opening the band gap and the insulating behavior of $LaMnO_3$. The Mn($3d$)$\uparrow$ bands overlap the O($2p$) band and are strongly hybridized in the interval 0–7 eV below the Fermi level E_F, while the Mn($3d$)$\downarrow$ bands are separated from the O($2p$) bands. The $5d$ band of lanthanum lies 2–4 eV above the Fermi level. Replacing the lanthanum with a divalent metal leads to coexistence of Mn^{3+} and Mn^{4+} ions.

The absorption band in the $\sigma(\omega)$ band of the original $LaMnO_3$ at 1.9 eV has been interpreted[10] as formed by transitions from occupied O($2p$)-$e_g^1\uparrow$ states into free $e_g^2\uparrow$ states, and the Jahn–Teller splitting was estimated to be $\sim$0.5 eV. The second band at 4.6 eV was attributed to transitions from O($2p$) to free $e_g^2\uparrow$ states.

Given the above remarks, the experimentally observed evolution of the optical spectrum of $LaMnO_3$, as lanthanum is replaced by strontium, can be understood as follows. The high densities of states of the O($2p$)$\downarrow$ band below E_F and the Mn($3d$)$t_{2g}\downarrow$ band above E_F in $LaMnO_3$ indicate that the main contribution to $\sigma(\omega)$ for $E>2$ eV is from dipole $p-d$-transitions in the band system, as opposed to the magnetization. The energy of the edge of the band with a peak at 1.9 eV in $LaMnO_3$ is then related to the onset of transitions from O($2p$) to Mn($3d$)$t_{2g}\downarrow$, while the edge of the intense band with a peak at 4.6 eV is related to O($2p$)$\rightarrow$La($5d$) transitions. The shift in the band from 1.9 to 1.7 eV with minimal strontium ($x=0.1$) may have several causes: first, a reduction in the Jahn–Teller splitting of the $e_g\uparrow$ band, second, a shift of the O($2p$) band closer to the Fermi level, and, third, a shift of the Mn($3d$)$t_{2g}\downarrow$ band. The second and third causes can also explain the monotonic shift in the low-energy wing of the band at 4.6 eV as the strontium content is increased further. Undoubtedly, transitions between the $3d$-electronic states of Mn^{3+} and Mn^{4+} make a contribution to the broad band at 1.7 eV.

Because of the reduction in E_F and the shifts of the O($2p$) and Mn($3d$)$t_{2g}\downarrow$ bands, even for minimal Sr concentrations ($x=0.1$), a low-energy absorption shows up in the gap region of the initial $LaMnO_3$, which leads to a visible shift in the band peak to 1.7 eV and extends its low-energy wing. The optical absorption for the composition with $x=0.1$ at $E<0.6$ eV has been attributed[9] to the interaction of the light with low mobility charge carriers (polarons). As the Sr concentration is raised further, the low energy absorption against a non-Drude background contains a fine structure with peaks at 0.22 ($x=0.2$)and 0.37 eV ($x=0.3$), which is associated with interband transitions between electronic states within the e_g^1 band of manganese hybridized with the O($2p$) band. It should be emphasized that the intensity of the low-energy absorption increases as T_C rises in the samples from 160 ($x=0.1$) to 353 K ($x=0.3$).

The results from a study of the optical properties of the manganites $La_{1-x}Sr_xMnO_3$ presented here indicate that their electronic structure varies substantially. As the Sr concentration is raised, the spectral features of the optical conductivity shift toward lower energies. In the band gap of the initial insulating $LaMnO_3$, a fine structure is observed in the interband absorption against a non-Drude optical conductivity whose intensity depends on T_C. For $x=0.2$, a partial redistribution of the optical-conductivity spectral weight from higher energies into the region of the band gap of $LaMnO_3$ occurs; this has been observed in other oxides during metal-insulator transitions. It is clear that further systematic studies are required both to distinguish the contributions to $\sigma(\omega)$, and to determine the electronic structure parameters responsible for the compositional metal-insulator transition in $La_{1-x}Sr_xMnO_3$.

[1] É. L. Nagaev, Usp. Fiz. Nauk **166**, 833 (1996).
[2] Y. Okimoto, T. Katsufuji, T. Ishikawa, A. Urushibaru, T. Arima, and T. Tokura, Phys. Rev. Lett. **75**, 109 (1995).
[3] S. G. Kaplan, M. Quijada, H. D. Drew, D. B. Tanner, G. C. Xiong, R. Ramesh, C. Kwon, and T. Venkatesan, Phys. Rev. Lett. **77**, 2081 (1996).
[4] L. V. Nomerovannaya, A. A. Makhnev, and M. M. Kirillova, Thin Solid Films **234**, 531 (1993).

[5] L. V. Nomerovannaya, A. A. Makhnev, S. V. Naumov, and O. N. Kiseleva, Fiz. Met. Metalloved. **83**, 53 (1997).
[6] A. Fujimori, J. Hase, H. Namatame, Y. Fujishima, Y. Tokura, H. Eisuki, S. Uchida, K. Takegahara, and F. M. F. De Groot, Phys. Rev. Lett. **69**, 1796 (1992).
[7] J. Solovyev, N. Hamada, and K. Terakura, Phys. Rev. B **53**, 7158 (1996).
[8] V. E. Arkhipov, V. P. Dyakina, S. G. Karabashev, V. V. Marchenkov, Ya. M. Mukovskiĭ, V. E. Naĭsh, V. E. Startsev, E. P. Khlybov, and A. Chopnik, Fiz. Met. Metalloved. **84**(6), 93 (1997).
[9] N. N. Loshkareva, Yu. P. Sukhorukov, B. A. Gizhevskii, A. A. Samokhvalov, V. E. Arkhipov, V. E. Naish, S. G. Karabashev, and Ya. M. Mukovskii, Phys. Status Solidi A **164**, 863 (1997).
[10] J. H. Jung, K. H. Kim, D. J. Eom, T. W. Noh, E. J. Choi, J. Yu, Y. S. Kwon, and Y. Chung, Phys. Rev. B **55**, 15489 (1997).
[11] S. Uchida, T. Ido, H. Takagi, T. Arima, Y. Tokura, and S. Tajima, Phys. Rev. B **43**, 7942 (1991).
[12] T. Satpathy, A. E. Boquet, T. Mizokava, H. Namatame, A. Fujimori, M. Abbate, Y. Takeda, and M. Takano, Phys. Rev. B **51**, 13942 (1995).
[13] W. E. Pickett and D. J. Singh, Phys. Rev. B **53**, 1146 (1996).
[14] D. A. Papaconstantopoulos and W. E. Pickett, Phys. Rev. B **57**, 12751 (1998).

Translated by D. H. McNeill

Magnetic and transport properties of $CuCr_{1-x}V_xS_2$ compounds

R. F. Al'mukhametov, R. A. Yakshibaev, and É. V. Gabitov

Bashkir State University, 450074 Ufa, Russia
(Submitted December 28, 1998)
Fiz. Tverd. Tela (St. Petersburg) **41**, 1450-1451 (August 1999)

A comparison of experimental and calculated effective magnetic moments shows that the sulfur in $CuCr_{1-x}V_xS_2$ compounds has two different oxidation states, S^{1-} and S^{2-}, while the vanadium has a higher degree of oxidation (V^{3+}) than the chromium (Cr^{2+}). A model is proposed to explain the reduction in the activation energy for defect formation in the Cu-sublattice and the rise in the Cu^+-cation conductivity when chromium is replaced by vanadium. © *1999 American Institute of Physics.* [S1063-7834(99)02008-0]

The chromium dichalcogenides $MCrX_2$ (M=Ag, Cu; X=S, Se) have mixed ionic-electronic conductivity and belong to the hexagonal system. The structure of these compounds consists of alternating $X-Cr-X$ triple-atomic layers perpendicular to the hexagonal c axis, between which the copper and silver atoms lie.[1–3] The atoms inside the triple layers of CrX_2 are bound to one another by strong ionic-covalent bonds, while the neighboring triple layers are bound to one another by weak van-der-Waals forces. However, the nature of fast ion transport in these systems has not been studied adequately as a function of the nature of the atomic bonds. In this paper we report some data from a study of the magnetic susceptibility and discuss the influence of the bonds among the atoms in $CuCr_{1-x}V_xS_2$ on the Cu^+-cation conductivity.

Samples were synthesized by solid-phase reaction from the original elements at 700 °C. Structural studies were conducted with a DRON-3 diffractometer with a high-temperature UVD-2000 attachment using Co $K\alpha$-radiation at temperatures ranging from room temperature to 600 °C. The magnetic susceptibility was studied over 20–400 °C by the Faraday method.

X-ray phase studies of compositions having x=0, 0.05, 0.1, and 0.15 showed that the samples were a single phase while the x-ray diffraction patterns of compositions with x=0.2, 0.25, and 0.3 contained weak lines belonging to Cu_3VS_4. The amount of this compound in the test samples did not change over 20–600 °C as the V content was changed.

The temperature dependences of the unit-cell parameters a and c are linear. Around 400 °C these curves have a break with a discontinuous change in the coefficient of thermal expansion. Our structural studies show that this is related to a redistribution of the mobile Cu atoms among the different crystallographic sites. a and c barely change with the vanadium content, which is explained by the similarity of the atomic numbers and atomic sizes of Cr and V (R_V=1.34, R_{Cr}=1.27 Å).[4] Given the linear dependence of the unit-cell parameters on the composition and an analysis of the integrated intensities of the lines, we found that the substitution of chromium by vanadium in $CuCr_{1-x}V_xS_2$ is isomorphic.

The reciprocal susceptibility $1/\chi(T)$ has a linear temperature dependence and obeys the Curie-Weiss law. For compositions with x=0, 0.15, 0.2, and 0.25, the Curie temperature is negative, which indicates the existence of antiferromagnetic interactions in these compounds. For x=0.1 and 0.3 the Curie temperature takes small positive values, which points to the existence of a weak ferromagnetic interaction. Our results for $CuCrS_2$ are consistent with the data of Refs. 1–3.

The calculated and experimental effective magnetic moments are plotted in Fig. 1 as functions of the composition. In the calculations it was assumed that the orbital angular momentum is completely ''frozen'' by the crystal field, which is true for the atoms in $CuCr_{1-x}V_xS_2$.[5] Calculations were made for different models. The best agreement with experiment is observed when the chromium atoms in the $CuCr_{1-x}V_xS_2$ are bound to sulfur atoms with a double bond and the vanadium atoms, with a triple bond. This is consistent with the higher electronegativity of vanadium. The Cu atoms are bound to S atoms by a single bond.

The sizes of the S in the compounds $CuCrS_2$ (1.74 Å), $AgCrS_2$ (1.748 Å), and $NaCrS_2$ (1.774 Å) are closer to the size of the S^{2-} ion (1.82 Å) than to that of the S atom (1.04 Å).[1] The sizes of the Cr in $CuCrS_2$ (0.64 and 0.705 Å) and in $AgCrS_2$ (0.612 and 0.652 Å) are closer to those of Cr^{3+} (0.64 Å) and Cr^{2+} (0.83 Å), than to that of the Cr atom (1.27 Å). Thus, we assume that the bonds of the atoms in $CuCr_{1-x}V_xS_2$ are predominantly ionic.

These results make it possible to explain qualitatively the rise in the Cu^+-cation conductivity as the V content is increased in the samples studied here (Fig. 2). To do this, let us consider a fragment of the $CuCrS_2$ structure[1,2] (Fig. 3). The coordination of the Cr atoms within the triple layers is octahedral. The chalcogen atoms of the neighboring triple layers are densely packed and form two nonequivalent tetrahedral sites (α and β). For $CuCrS_2$ at room temperature, the Cu atoms occupy α sites with a probability of 0.95 and β sites with a probability of 0.05.[6] It is assumed that Cu^+ ion transport in structure of this type occurs in the basal planes through successive jumps between α and β sites.[7] As our studies of the magnetic susceptibility show, the sulfur atoms

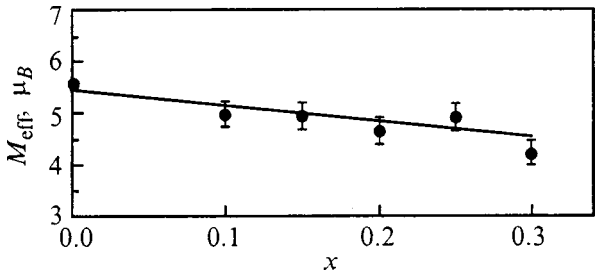

FIG. 1. Effective magnetic moment of $CuCr_{1-x}V_xS_2$ compounds as a function of the V content. (Points are experimental data, the curve is calculated.)

in the triple layers are nonequivalent: S atoms lying above the van-der-Waals gap have an effective charge of $-e$, while those lying below it have a charge of $-2e$. (e is the unit charge.) When Cr is replaced by vanadium, the effective charge of the sulfur atoms lying above the van-der-Waals gap increases to $-2e$. An elementary calculation including only the Coulomb interaction of the Cu^+ ions with their nearest neighbors shows that replacing Cr by vanadium leads to a reduction in the energy of defect formation in the Cu-sublattice and to increased ionic conductivity.

Therefore, we have shown that, in the $CuCr_{1-x}V_xS_2$ system, isomorphic substitution of chromium by vanadium takes place. The bonds between the atoms are predominantly ionic. Depending on the composition, a ferromagnetic or antiferromagnetic interaction is observed. Replacing the chromium leads to a growth in the Cu^+-cation conductivity. A model has been proposed for explaining this phenomenon.

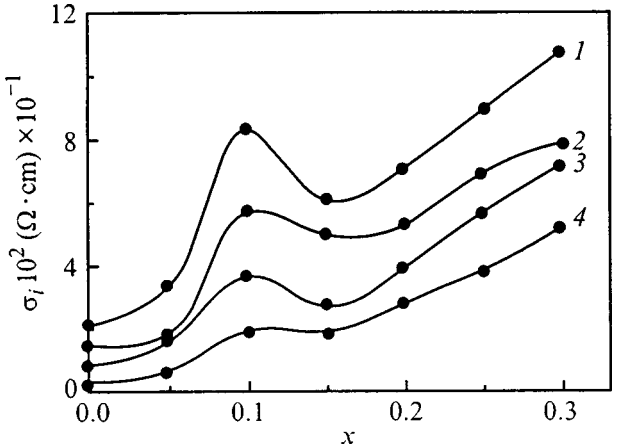

FIG. 2. The Cu^+-cation conductivity as a function of the V content of $CuCr_{1-x}V_xS_2$ at different temperatures T (°C): *1* — 415, *2* — 375, *3* — 360, *4* — 345.

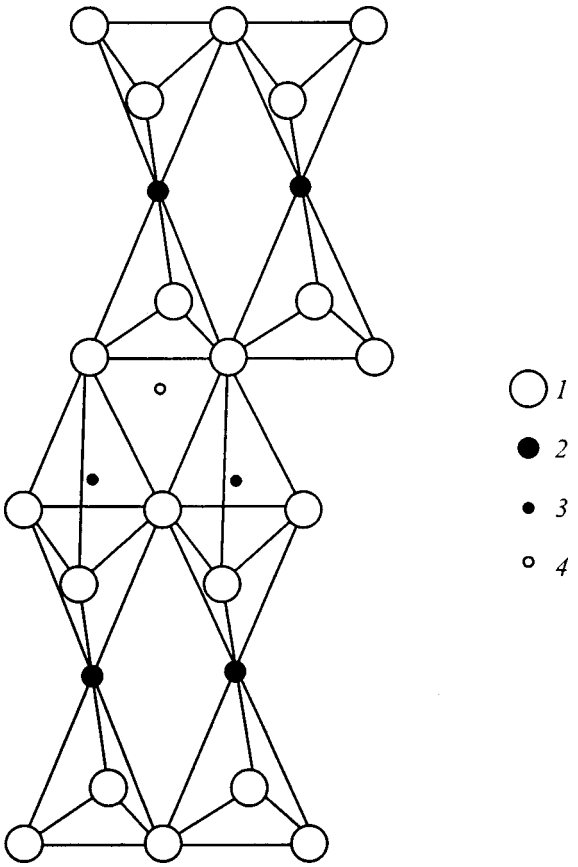

FIG. 3. A fragment of the $CuCrS_2$ structure. *1* — S, *2* — Cr, *3*, *4* — Cu in α and β sites, respectively.

[1] P. F. Bongers, C. F. van Bruggen, J. Koopstra, W. P. A. Omloo, G. A. Wiegers, and F. Jellinek, J. Phys. Chem. Solids **29**, 977 (1968).
[2] F. M. R. Engelsman, G. A. Wiegers, F. Jellinek, and B. van Laar, J. Solid State Chem. **6**, 574 (1973).
[3] N. Le. Nagard, G. Collin, and O. Gorochov, Mater. Res. Bull. **14**, 1411 (1979).
[4] I. T. Goronovskiĭ, Yu. P. Nazarenko, and E. F. Nekrich, *A Brief Handbook of Chemistry* [in Russian] (Nauk. Dumka, Kiev, 1987).
[5] Ya. G. Dorfman, *Magnetic Properties and Structure of Material* [in Russian] (GITTL, Moscow, 1955).
[6] R. A. Yakshibayev, G. R. Akmanova, R. F. Almukhametov, and V. N. Konev, Phys. Status Solidi A **124**, 417 (1991).
[7] P. Druesch, T. Hibma, and W. Buhrer, Phys. Rev. B **27**, 5052 (1983).

Translated by D. H. McNeill

Spin-wave resonances in a nonuniform bilayer iron-garnet film

N. K. Dan'shin,*) V. S. Dellalov, A. I. Linnik, and V. F. Shkar'

Donetsk Physicotechnical Institute, Ukrainian Academy of Sciences, 340114 Donetsk, Ukraine
(Submitted September 18, 1998; resubmitted February 1, 1999)
Fiz. Tverd. Tela (St. Petersburg) **41**, 1452–1455 (August 1999)

Magnetic resonances are investigated in bilayer Bi-substituted iron garnet films, one layer of which possesses easy-axis and the other easy-plane anisotropy. The behavior of resonances as a function of film thickness, temperature, and annealing is studied. It is shown experimentally that the resonance absorption lines observed in such a nonuniform structure in an external magnetic field oriented perpendicular to the film plane correspond to ferromagnetic (FMR) and spin-wave (SWR) resonances. In addition, the SWR series is excited in the most nonuniform part of the film. A qualitative model explaining the experimental data and making it possible to obtain experimentally the profile of the effective-magnetic-anisotropy field throughout the thickness of the film is proposed. [S1063-7834(99)02108-5]

Investigations of FMR spectra in layered iron-garnet film structures yield important information about the excitation, propagation, and interaction of various types of magnetic waves. There is a series of works devoted to this subject.[1–5] It is shown in these works, for example, that, aside from uniform FMR, nonuniform SWR or a unique resonance, called an FMR doublet,[4] can be observed in bilayer films. The interpretation of the results obtained in Refs. 1 and 2 was facilitated by the fact that the corresponding films actually were or were considered to be close to model films. It was kept in mind that in such structures two films with uniform magnetic properties but with substantially different parameters are separated by a relatively thin boundary layer where these parameters undergo a sharp jump. However, the uniformity of the parameters of the layers and of the interface depend on the composition of the material and the film growth conditions. For this reason, an interesting problem, in our view, is to establish a definite relation between the FMR and SWR spectra and the magnitude and nature of the nonuniformity of the material throughout the thickness. To this end it was suggested that the materials presented in Ref. 3 be investigated in a different experimental geometry, frequency, temperature, and so on.

A bilayer film, grown by liquid-phase epitaxy, using a double-crucible technology,[6] on a gallium-gadolinium garnet substrate with the normal to the substrate plane oriented along the [111] axis, was chosen as the object of investigation. The first layer deposited on the film was a 0.1-μm-thick layer with the composition $(YGdLa)_3(FeGa)_5O_{12}$. This layer was characterized by an easy-magnetization plane. The second layer, grown on top of the first one, had the composition $(YBiLu)_3(FeGa)_5O_{12}$ and was characterized by an easy-magnetization axis (normal to the film plane). Together with the nonuniform boundary layer, it was about 2.0 μm thick. All other parameters of the layers, determined by standard methods,[7] are presented in Table I.

The measurements were performed on a reflection direct-amplification radiospectrometer with magnetic-field modulation. The magnetic field derivative of the imaginary part of the magnetic susceptibility was recorded in the experiments. A strip line, on whose plane 6-mm-in-diameter disk-shaped samples were glued face down, served as the measuring cell.

Traces of the absorption lines, associated with magnetic oscillations in such a structure for a normally magnetized film measured at 295 K, are shown in Fig. 1. Here and below, an absorption line is actually the magnetic field derivative of the imaginary part of the magnetic susceptibility. The numbers at the end of each trace are the total thickness of all magnetic layers, in μm. Oscillation No. *1* corresponds to uniform FMR in the first layer, oscillation No. *6* corresponds to uniform FMR in the second layer, and the lines *2*, *3*, *4*, and *5* are ordinarily identified as SWR in the first layer. Spectra of this kind are studied in Ref. 2, where it is shown, specifically, that excitation of SWR between two uniform FMR lines from different layers of the film is explained by the skin effect (similarly to the rotation plane of a spin wave[8]) at the interface. This means that, if the second layer is removed (for example, by successive etching), then the pinning of the spins at the interface, which in such an explanation is a necessary condition for the excitation of SWR, will vanish. In addition, if the second layer is completely etched off, all SWR modes of the first layer should vanish simultaneously.[1] This fundamental property of SWR was not observed in our experiments on the above-indicated film structures. As is evident from Fig. 1a, as the second layer is etched off, the lines *6*, *5*, *4*, *3*, and *2* vanish in succession. This means that the observed spectrum of oscillations cannot be explained on the basis of pinning of spins on a sharp interface between films.

To verify that we are indeed dealing with SWR and not uniform FMR from individual layers of a multilayer structure (Bi-containing films can indeed by multilayered, if special measures in growing such films are not taken[7]), the sample was subjected to 10-h high-temperature (1320 K) anneal. It is known that such treatment changes the parameters

TABLE I. The parameters of the film layers.

Layer No.	$4\pi M$	A, 10^{-7} ergs/cm	$\gamma\cdot 10^{-7}$ Oe·s	ΔH, Oe	H_0^*, Oe
1	400	2.6	1.69	10	−330
2	171	2.6	1.5	20	1470

Note. $4\pi M$ — Saturation magnetization; A — exchange interaction constant; γ — gyromagnetic ratio; ΔH — FMR linewidth; $H_0^* = 2K/M - 4\pi M$ — effective anistropy field of uniform layers of the initial film (K —uniaxial anisotropy constant).

of the film material, including decreasing the uniaxial magnetic anisotropy induced during growth.[7] Annealing did indeed decrease the effective uniaxial anistropy of the film. As expected,[7] the lines *6* and *1* (Figs. 2a and 2b) of uniform FMR in each layer shifted to high fields. At the same time, the lines *2*, *3*, *4*, and *5* shifted to low fields. In addition, the resonance field of line 5 became less than the resonance field of line *6* (FMR of the second layer), so that in accordance with Ref. 2 this SWR mode is not excited.

The series of absorption peaks appearing in the annealed sample near line *6* on the low-field side is apparently due to the fact that the effective anisotropy in the surface layer became greater than in the interior layers (as a result of the direct contact with air during annealing). This could lead to pinning of spins in this layer and excitation of a series of new SWRs in the uniform part of the second layer. As one can see from Fig. 3a, the indicated series of resonances also vanishes when this near-surface layer is etched off.

Therefore it can be regarded as established that the lines *2*, *3*, *4*, and *5* are SWRs and not FMRs from different layers of a multilayer structure. However, their unusual behavior on etching of the sample — successive vanishing as film thickness decreases — suggests that a nonuniform region into

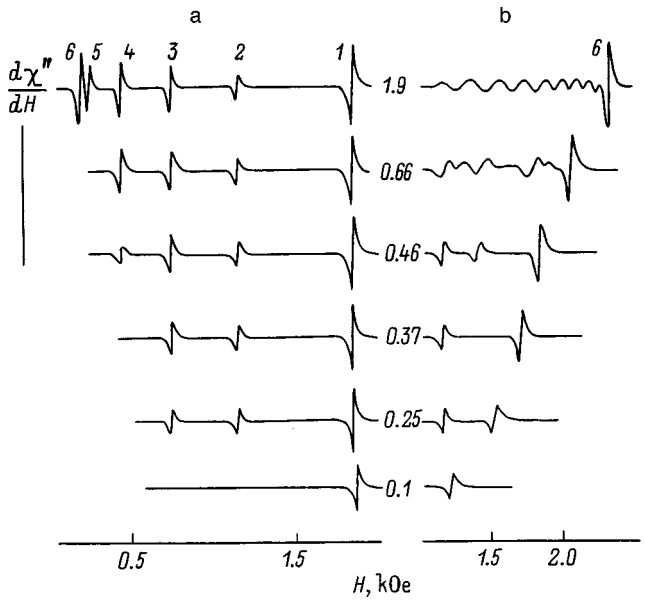

FIG. 1. Resonance absorption line in the initial sample when the second layer of the film is etched off to the thickness indicated on each trace (in μm) in a magnetic field perpendicular (a) and parallel (b) to the film plane at frequency ν=4.07 GHz and temperature T=295 K. Absorption lines: *1* — FMR in the first layer; *2*, *3*, *4*, *5* — SWRs with n=1, 2,3,4; *6* — FMR from the uniform part of the second layer.

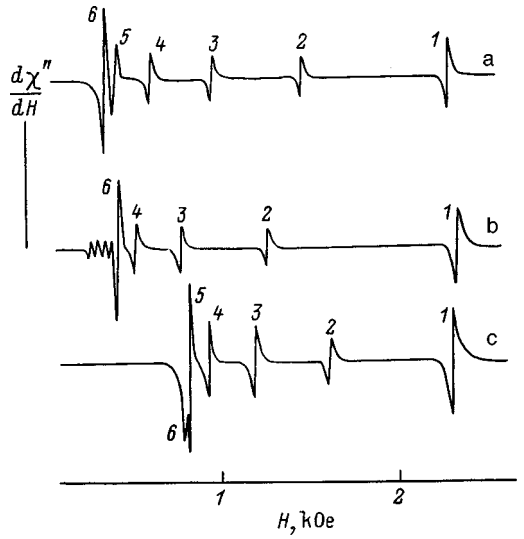

FIG. 2. Traces of resonance absorption lines in a magnetic field perpendicular to the film plane for the initial (a), annealed (b), and initial at 305 K (c) samples at frequency ν=4.99 GHz. Absorption lines: *1* — FMR in the first layer; *2*, *3*, *4*, *5*, — SWRs with n=1,2,3; *6* — FMR from the uniform part of the second layer.

which a spin wave can penetrate exists between the virtually uniform first and second layers of the initial film. We shall model the physical picture of the appearance of the series of SWRs for such a layer. For this, we employ the following expression[5] for the resonance field of the n-th SWR:

$$H_n = \omega/\gamma_1 - H_0^* - 2A(\pi n/h)^2/M, \tag{1}$$

where γ_1 is the gyromagnetic ratio for layer 1, $\omega = 2\pi\nu$ is the angular frequency of oscillations of the magnetization vector M, h is the thickness of the layer where the SWR series is resolved, and H_0^* is the effective anisotropy field in layer *1*. As is well known,[1] in a two-layer film, a series of the SWRs can be excited in either layer depending on the direction of the external magnetic field. In addition, the field positions of the series of SWR lines is always bounded by the uniform FMR film of the neighboring layer, where the spin wave does not propagate — the wave decays over the depth of the skin layer; this corresponds formally to the case $k^2 < 0$ (where k is the wave number). If the films were uniform over the thickness and possessed a sharp interface between layers, then, in the first place, the experimentally observed series of the SWRs would be described by the expression (1) for H_n, i.e., the quadratic law (1) would be satisfied. In the second place, the entire series of SWR lines would be preserved upon successive etching until the interface between the indicated layers vanishes. In our case neither situation occurs. Moreover, the resonant fields of uniform FMR in the second layer with an in-plane external field start to decrease as the layer is etched (Fig. 1b). An especially sharp decrease of the resonant field starts at thickness $\approx$0.6 μm and continues down to $\approx$0.1 μm. This means that the second layer contains an approximately 0.5-μm-thick transitional region where the effective anisotropy field decreases smoothly as the thickness of this layer decreases.

Let us assume that the position of the absorption lines *1*, *2*, *3*, *4*, and *5* is described by the expression (1) for a series of

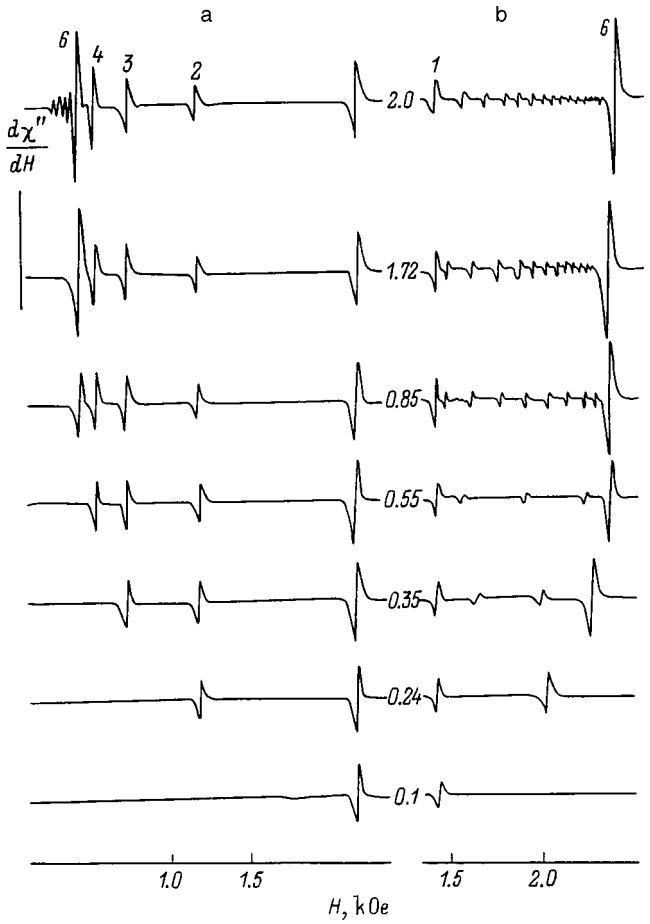

FIG. 3. Resonance absorption lines in an annealed sample with the second layer of the film etched off to the thickness indicated on each trace (in μm) in a magnetic field perpendicular (a) and parallel (b) to the film plane at frequency ν=4.99 GHz and temperature T=295 K. Absorption lines: *1* — FMR in the first layer; *2, 3, 4* — SWRs with n=*1,2,3*; *6* — FMR from the uniform part of the second layer.

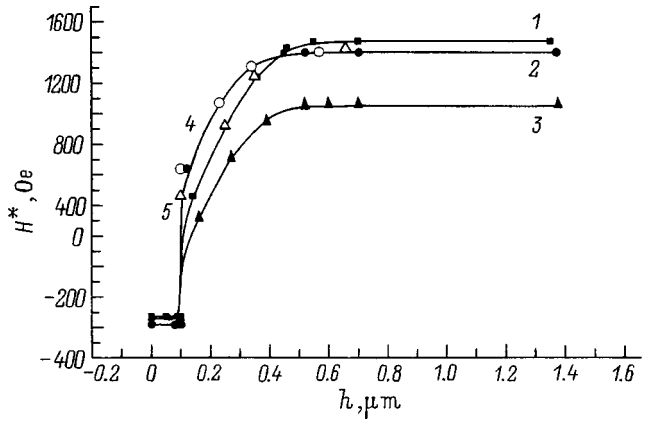

FIG. 4. Effective anisotropy field measured at T=295 K versus the thickness for the initial (*1*), annealed (*2*), and initial heated-to-T=305-K (*3*) samples; *4, 5* — points at which the SWR peaks vanish on etching of the annealed and initial samples, respectively.

oscillations with the numbers $n=0,1,2,3,4$. In addition, the $n=0$ mode corresponds to excitation of nearly uniform FMR. Then all other absorption lines can be attributed to nonuniform oscillations arising as a result of the reflection of a spin wave from the plane of rotation (where $k=0$). As the external magnetic field decreases, this plane of rotation, which starts at the interface between the first and second layers, advances into the transitional region of the second layer. As soon as the plane of rotation reaches a thickness into which the $n=1$ mode can fit, the first SWR peak arises, and as the spin wave penetrates further into the transitional region, SWR modes with increasingly higher numbers will be observed until this region terminates. If a uniform part of the film exists beyond the transitional region, then uniform FMR is observed in it. As is well known, the wave number k for uniform FMR is likewise zero. Therefore the resonant fields in which the corresponding SWR lines are observed have the same intensities as the fields H_{FMR} of uniform FMR in the plane of rotation. Therefore $H_n=H^n_{\mathrm{FMR}}$, and $H^n_{\mathrm{FMR}}=\omega/\gamma_2-H^*_n$, where γ_2 is the gyromagnetic ratio for layer *2* and H^*_n is the effective anisotropy field of the film in the plane of rotation of the spin wave for the n-th SWR mode. We note that the indicated plane of rotation of a spin wave in the transitional layer corresponds only functionally to a classic plane of pinning of spins, for example, on a sharp interface between two uniform films. In reality, it is virtual, and the corresponding thickness h, which varies with the field, is nothing more than an adjustable parameter satisfying expression (1).

Thus, the thickness corresponding to the excitation of the corresponding spin-wave mode can be calculated from the magnitude of the SWR field, and the effective anisotropy field of the film[8] at a given thickness can be determined from the uniform FMR field (which, as we can see, is exactly the value of the SWR field of this mode). This makes it possible to construct the thickness dependence of the anisotropy field of the film. It should be kept in mind that the calculation based on Eq. (1) should be performed taking account of the changes in the film parameters, when the spin wave starts to advance into the nonuniform layer. Figure 4 shows the dependences of the anisotropy fields for the initial and annealed samples, and the film thicknesses at which the corresponding SWR modes vanish (during layer-by-layer etching) are also shown. It is evident that the points corresponding to the computed value of H^* and the thickness at which the corresponding SWR modes vanish fall quite well on the general curves. This figure also shows, as an argument confirming the correctness of the adopted model, the thickness dependence of the anisotropy in the initial (unannealed) film, heated to 305 K. It was calculated according to the absorption traces and is presented in Fig. 2c. As is well known,[7] the uniaxial-anisotropy constant of a film decreases quite rapidly with increasing temperature, so that such a temperature variation of the anisotropy profile is not surprising. It can also be concluded from Fig. 4 that the thickness of the transitional region of the film decreased after annealing. This can be explained by an increase in the uniformity of the layers of the film, which is consistent with existing ideas about processes occurring during annealing.

It is now understandable why the quadratic law (1) of the SWR mode distribution is not satisfied and why these modes vanish not all at once but in succession. The reason is the existence of a nonuniform transitional region between the

uniform layers of the film. The penetration depth of spin waves into this region depends on the intensity of the external magnetic field. This means that the film thickness required for excitation of SWR can be fixed by the field. Standing spin waves (SWRs) with different values of n, which are seen on the traces of the absorption presented in Figs. 1–3, arise precisely at this thickness. As soon as not only the uniform but also the transitional (nonuniform) part of the second layer of the film is removed by successive etching, the conditions for the appearance of planes of rotation of the spin waves and, therefore, excitation of the corresponding SWR modes, vanish immediately. The finale of this evolution, as one can see from Figs. 1 and 3, occurs when the film is etched to thickness $h \simeq 0.1$ μm, at which point only the FMR line from the first uniform layer remains in the absorption traces.

In summary, our investigations show that, in the two-layer film structure studied (and in general, apparently, in any other structure), the unusual properties of the FMR spectra are due to the existsnce of, together with layers which are uniform with respect to anisotropy, a transitional region where the effective anisotropy varies monotonically. An external indicator of the fact that SWR has a classical nature is the satisfaction of the quadratic dispersion law (1) in the arrangement of the absorption peaks of SWRs with respect to the field. It is supposed that the observed SWR is due to interference of spin waves in an anisotropy-uniform film accompanying the pinning of spins at the sharp boundaries of the film. In the general case, however, when a nonuniform transitional layer whose anisotropy varies according to an arbitrary law (which can depend on the film composition and the technology used to produce the film) is present, there are no grounds for expecting Eq. (1) to hold. When this law does not hold, an alternative explanation of experimental data, one explanation being presented in the present paper, must always be sought. The main assertion is that the conditions for excitation of SWRs can be realized not only in the uniform but also in the nonuniform part of a film structure. The penetration depth of a spin wave in the nonuniform region of the film (position of the plane of rotation of the wave) depends on the external magnetic field — the penetration depth of the wave increases as the field decreases.

This work was supported by the Fund for Fundamental Research of the Ukrainian Ministry of Science.

*)E-mail: danshin@host.dipt.donetsk.ua

[1] A. M. Grishin, V. S. Dellalov, V. F. Shkar, E. I. Nikolayev, and A. I. Linnik, Phys. Lett. A **140**, 133 (1989).
[2] A. M. Grishin, V. S. Dellalov, V. F. Shkar', and S. V. Yampol'skiĭ, Fiz. Nizk. Temp. **22**, 1056 (1996) [Low Temp. Phys. **22**, 805 (1996)].
[3] V. S. Dellalov, A. I. Linnik, V. F. Shkar, and S. V. Yampolskii, J. Magn. Magn. Mater. **172**, 74 (1997).
[4] A. M. Grishin, V. S. Dellalov, E. I. Nikolaev, V. F. Shkar', and S. V. Yampol'skiĭ, Zh. Éksp. Teor. Fiz. **104**, 3450 (1993) [JETP **77**, 636 (1993)].
[5] B. Hoekstra, R. P. van Stapele, and J. M. Robertson, J. Appl. Phys. **48**, 382 (1977).
[6] E. I. Nikolaev and I. A. Krasin, Kristallografiya **33**, 478 (1988) [Sov. Phys. Crystallogr. **33**, 282 (1988)].
[7] A. M. Balbashov, V. F. Lisovskiĭ, V. K. Raev *et al.*, *Magnetic Bubble Components and Systems* [in Russian] (Radio i svyaz', Moscow, 1987).
[8] A. G. Gurevich and G. A. Melkov, *Magnetic Oscillations and Waves* [in Russian] (Nauka, Moscow, 1994).

Translated by M. E. Alferieff

Dielectric properties of $Sn_2P_2S_6$ crystals as a function of their growth conditions

M. M. Maĭor

Uzhgorod State University, 294000 Uzhgorod, Ukraine
(Submitted January 21, 1999)
Fiz. Tverd. Tela (St. Petersburg) **41**, 1456–1461 (August 1999)

The behavior of the permittivity near a phase transition in $Sn_2P_2S_6$ crystals of different technological quality is studied. It is established that, in high-resistance crystals, where an internal electric field is formed by the screening of spontaneous polarization in the polar phase, long-time relaxation of ε is observed in a temperature range $\sim$2 K above T_{max}. This relaxation and change in the form of the maximum of $\varepsilon'(T)$ at a phase transition are attributed to an internal electric field induced by the volume space charge formed in regions near the surface. It is established that the existing differences in the properties of $Sn_2P_2S_6$ crystals are due to deviations from stoichiometry, arising during growth and synthesis of the crystals. © *1999 American Institute of Physics.* [S1063-7834(99)02208-X]

Crystals of the ferroelectric–semiconductor $Sn_2P_2S_6$ possess high pyroelectric[1] and piezoelectric[2] parameters, making them interesting objects for practical applications. However, variations in the dielectric and electrophysical parameters from one crystal to another seriously limits applications of these crystals. Thus elevated values of the electric conductivity and dielectric losses, due to both through conduction and volume-charge polarization, are very undesirable for pyro- and piezoelectric materials. For this reason, a very pressing problem is to understand the nature of the uncontrollable variance of the parameters and mechanisms of dielectric losses in this ferroelectric semiconductor and to learn how to control them. In addition, the nature of the long-time relaxation of ε observed[3] in a narrow temperature interval above T_{max} is not completely understood.

1. EXPERIMENT

$Sn_2P_2S_6$ crystals are grown by the gas-transport reaction and Bridgman methods. However, the above-mentioned variations in the dielectric and electrophysical parameters occur among crystals obtained by both methods. For this reason, for definiteness, crystals grown only by the Bridgman method were investigated. Two types of crystals with very high values of $\tan\delta$ ($\tan\delta = 0.05$ at $T = 290$ K) (type I) and with very low values of $\tan\delta$ ($\tan\delta = 0.002$) (type II) were selected. Both types of crystals were obtained from initial materials with identical quality. This enables us to suppose that the existing uncontrollable difference in the properties is due to a deviation from stoichiometry that occurs during synthesis of the crystals. To check this supposition crystals with deviation from stoichiometry with respect to Sn and S were grown and investigated. An experimental sample consisted of a $5\times5(1-0.5)$ mm wafer with electrodes on the large faces. An indium–gallium amalgam, as well as bismuth and gold, deposited by vacuum sputtering, were used as electrodes. The temperature–frequency dependences of the permittivity and the temperature dependences of ac and dc electric conductivity were measured. The dc electric conductivity was measured with a U5-7 electrometric amplifier. The measurements of the thermally stimulated depolarization currents were performed with 1 K/min rate of temperature variation. The low-frequency dielectric measurements (80 Hz–20 Hz) were performed with an E8-2 bridge.

2. EXPERIMENTAL RESULTS

The temperature dependences of ε' near a phase transition in both types of crystals for the polar direction [100] are presented in Figs. 1 and 2. The measurements were performed with cooling of the samples after a 1-h anneal at $T = 370-380$ K. This measurement regime makes it possible to avoid the internal electric field, due to the screening of the spontaneous polarization, from influencing the temperature behavior of ε'. The existence of temperature hysteresis of the peak in $\varepsilon'(T)$ is due to the formation of an internal electric field.[4] It should be noted that this internal field and, in consequence, the temperature hysteresis of the maximum of $\varepsilon'(T)$ are observed only in type-II crystals.

As follows from Figs. 1 and 2, $\varepsilon'(T)$ in the paraelectric phase, with the exception of a narrow temperature range adjoining T_{max} ($\sim$2 K), follows the Curie–Weiss law with the constant $C = 9.1\times10^4$ and 4.5×10^4 K^{-1} for type-I and -II crystals, respectively. The deviation of the function $1/(\varepsilon' - \varepsilon'_0)(T)$ from linearity near T_{max} for the type-I crystal is very small. At the same time, for the type-II crystal the amplitude of this deviation is much larger. It should be underscored that, as the frequency of the measuring field increases (Fig. 2), the relative amplitude of this effect increases. Moreover, as one can see clearly from Figs. 1 and 2, there is a correlation between the amplitude effect and the degree of smearing of the peak in $\varepsilon'(T)$: In type-II crystals, where the peak in $\varepsilon'(T)$ is more diffuse, the amplitude of the deviation of $1/\varepsilon'(T)$ from linearity is greater than in type-I crystals, where the peak in $\varepsilon'(T)$ is sharp.

A characteristic feature of type-I crystals is an increase in dielectric losses at low frequencies with increasing tem-

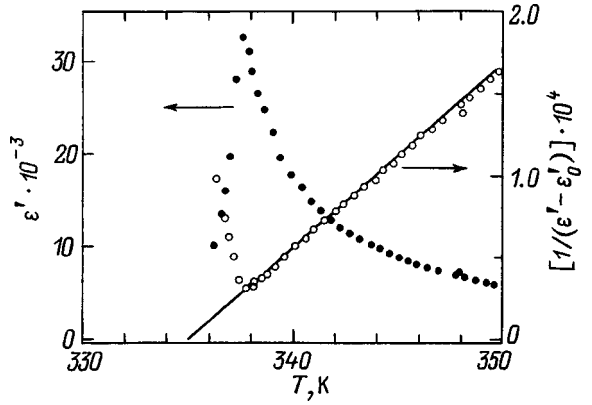

FIG. 1. Temperature dependences of ε' (filled circles) and $1/(\varepsilon'-\varepsilon'_0)$ (open circles) for a type-I $Sn_2P_2S_6$ crystal ($\varepsilon'_0=40$). The solid line shows the extrapolation of the linear section of the function $1/(\varepsilon'-\varepsilon'_0)(T)$ to zero.

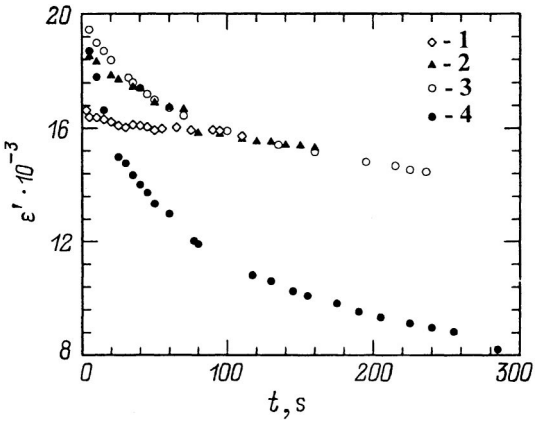

FIG. 3. Time relaxation of ε' in type–II $Sn_2P_2S_6$ crystals near a phase transition: *1* — $T_{max}+1.1$ K; *2* — $T_{max}+0.6$ K; *3* — $T_{max}+0.3$ K; *4* — $T_{max}-0.3$ K ($T_{max}=356.5$ K).

perature in the paraelectric phase, followed by an increase in the real part of ε at $T>350$ K. This effect is more clearly seen in the temperature dependences of ε' for the nonpolar [010] cut. A negligible increase of ε' at low frequencies is also noted in type-II crystals. The contribution to ε', responsible for an increase in this quantity in the measured temperature interval, is completely suppressed at measuring-field frequencies above 10 kHz.

Long-time relaxation of ε' (Fig. 3) is observed in type-II crystals at temperatures where the function $1/(\varepsilon'-\varepsilon'_0)(T)$ deviates from linearity (~2 K above T_{max}). The degree of this relaxation increases as temperature approaches T_{max} from above. Relaxation becomes more intense below T_{max}.

Figure 4 shows the temperature dependences of ε' after the sample was held at stable temperatures in a range where relaxation of ε' occurs. It is clearly seen that the peak in $\varepsilon'(T)$ becomes smeared after relaxation. Moreover, after the sample is held at T very close to T_{max}, another anomaly in the form of a shoulder appears at $T\approx T_{max}+1.5$ K in the temperature dependence of $\varepsilon'(T)$, in addition to the peak at temperature corresponding to the peak in the annealed sample. After the sample remains in the ferroelectric phase for a definite period of time, only one diffuse peak, shifted upwards in temperature, appears in the dependence $\varepsilon'(T)$ (curves *5* and *6* in Fig. 4).

Investigations of ε' as a function of the amplitude of the measuring field showed that there is an appreciable dielectric nonlinearity in the noted temperature interval above T_{max}. The field-dependence of ε' increases smoothly at a transition into the ferroelectric phase (Fig. 5). A remarkable feature of the reverse dependences of ε' in type-II crystals is the presence of hysteresis: The zero-field value of ε' after the sample was exposed to a field is less than at the start of the cycle. This testifies that the crystal acquires the capability of being polarized in this temperature interval.

The thermally stimulated depolarization current of a prepolarized type-I crystal contains an intense peak at $T\approx 380$ K in the polar direction together with a peak in the pyroelectric

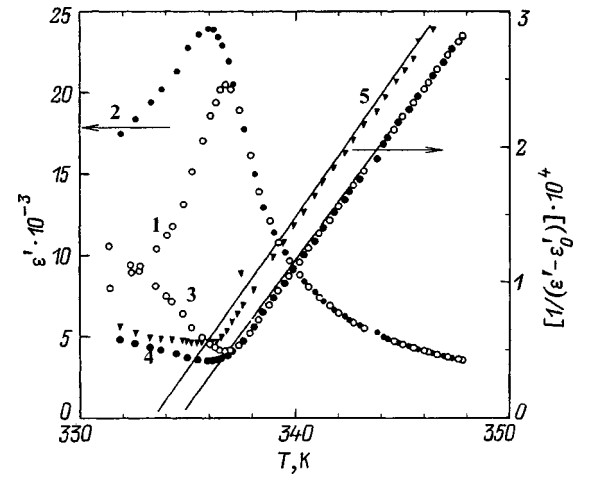

FIG. 2. Temperature dependences of ε' (*1*, *2*) and $1/(\varepsilon'-\varepsilon'_0)$ (3, 4) with measuring field strength 0.2 (*1*, *3*) and 2 V/cm (*2*, *4*) for a type-II $Sn_2P_2S_6$ crystal ($f=10$ kHz). Curve *5* corresponds to the temperature dependence of $1/(\varepsilon'-\varepsilon'_0)$ with a 700 kHz measuring field ($E_m\approx 1$ V/cm). The solid line shows the extrapolation of the linear section of $1/(\varepsilon'-\varepsilon'_0)(T)$ to zero.

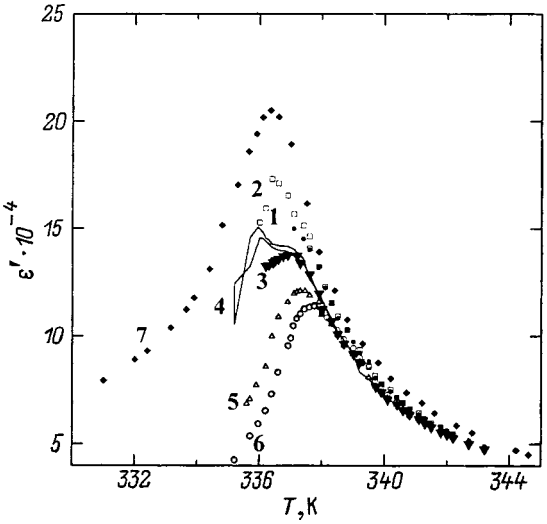

FIG. 4. Temperature dependence of ε' in type-II $Sn_2P_2S_6$ after the sample is held for 3 h at: *1* — 336.9 (heating); *2* — cooling; *3* — 336.2 K (heating); *4* — 336.3 K (heating and cooling); *5* — 335.6 K (heating); *6* — 328.1 K (heating) ($T_{max}=336.5$ K); *7* — cooling after annealing of a sample at $T=370$ K for 1 h.

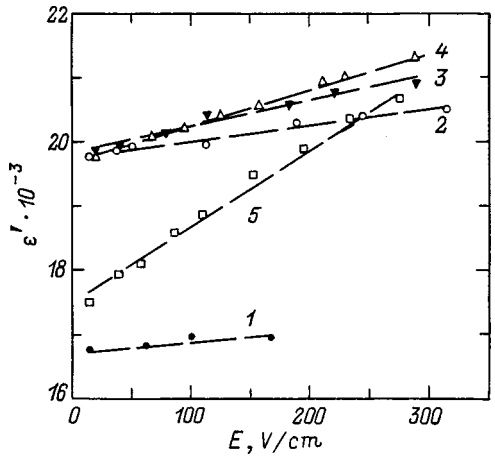

FIG. 5. Permittivity versus the amplitude of the measuring field in a type–II $Sn_2P_2S_6$ crystal near the peak. *T*, K: *1* — 338.5 K; *2* — 336.6 K; *3* — 336.4 K; *4* — 336.2 K; *5* — 335.7 K.

current at T_c. Near this peak the current is comparable in magnitude to the pyroelectric current near a phase transition. It should be underscored that the observed depolarization current at temperatures above T_c is clearly not of pyroelectric nature. The charge freed in the relaxation process is much greater than the charge that can be stored in a geometric capacitance. A charge of the same order of magnitude is freed during polarization of (010)-cut samples. These facts testify that the observed relaxation current is not related to the change in the charge state within the interior volume, but rather it is due to a change in the space charge in regions near the electrodes. For type–II crystals, lines of thermally stimulated depolarization current were not observed in this temperature range.

3. DISCUSSION

It is well known[5] that the existence of near-electrode layers, which can greatly influence the dielectric and ferroelectric properties, is characteristic for ferroelectric semiconductors.[5] In $Sn_2P_2S_6$ crystals, an effect due to surface layers was observed in the dependence of the permittivity of a sample near a phase transition on the sample thickness[6] as well as in pyroelectric measurements.[7] The strong thickness dependence of ε' occurs even for thicknesses of the order of several millimeters. Therefore, the fact that the temperature corresponding to extrapolation of $1/\varepsilon'(T)$ to zero is different from the temperature of the peak in $\varepsilon'(T)$ (Figs. 1 and 2) cannot be explained except by the influence of the near-electrode layers. We note that in individual samples ε' at the peak reaches values of $(70-100)\times 10^3$. The difference between $T_{\max}$ and T_0 is minimal.

The essence of the influence of the near-electrode layers on ε' is as follows. A space charge is formed in the near-electrode region at the metal–ferroelectric-semiconductor boundary as a result of the difference of the work functions. This space charge induces a strong electric field in a thin near-electrode region. This field decreases the permittivity in the near-surface layer. However, because of the small thickness, the capacitance of the near-surface layers can reach high values. Consequently, the ''surface capacitances'' attached to the volume of the sample greatly renormalize the total capacitance of the sample only near the peak, where the capacitance of the sample becomes comparable to the capacitances of the near-surface layers.

The existence of a low-frequency dielectric dispersion (at $f<10$ kHz), extending over a wide frequency range, and an increase in the low-frequency permittivity with decreasing temperature, observed in both the polar and nonpolar (010) cuts in the paraelectric phase, can be explained by a superposition of effects due to the impedance of the near-surface layers and the presence of a series resistance associated with the electrodes.

The deviation from the Curie–Weiss law in the temperature dependence of ε', specifically, the presence of a contribution on top of the contribution following the dependence $1/(\varepsilon-\varepsilon_0'(T))$, observed near $T_{\max}$ in the paraelectric phase in type-II crystals, could be due to two factors. The first one is fluctuations of the order parameter, whose contribution to ε' in uniaxial ferroelectrics is expected to be very small because of suppression of the fluctuations by long-range Coulomb forces.[8] The other reason for the observed effect could be the appearance of small polar regions in the region of localization of defects at temperatures even higher than T_c. The dynamics of these defect-induced clusters could be responsible for the observed additional contribution to ε'. The fact that this effect occurs in crystals where greater smearing of the peak in $\varepsilon'(T)$ is natural, supports the latter supposition. Moreover, the strong dependence of ε' on the amplitude of the measuring field (Fig. 5) and the character of the reverse ε' curves indicate that high-polarizability polar regions are present in this temperature range. The presence of a piezoelectric resonance of the dispersion of the permittivity in annealed samples in this temperature range and the sharp increase in the dielectric losses, starting at $T\approx T_{\max}+3$ K, likewise support to this supposition.

The behavior of both the real and imaginary parts of ε' near T_c, as a function of the amplitude of the measuring field, is qualitatively similar to ferroelectrics having a diffuse phase transition:[9] the peaks in $\varepsilon'(T)$ and $\varepsilon''(T)$ increase and shift to lower temperatures (Fig. 2). Modern concepts of relaxational phase transitions are based on the idea that a transition to a macroscopically polar state occurs via a state which is characterized by the presence of microscopic polar regions. The dielectric response of such a system is similar to the response of a polydomain ferroelectric, and its characteristics features are a wide spectrum of relaxation times and strong nonlinearity. The microscopic nature of polar microregions existing in $Sn_2P_2S_6$ at $T>T_{\max}$ is such that apparently such regions can be induced by charged defects.

The long-time relaxation of ε' observed in the ferroelectric phaser in type-II crystals results from suppression of the domain dielectric contribution under the influence of an internal electric field due to screening of the spontaneous polarization. The mechanism leading to the formation of an internal electric field in a ferroelectric semiconductor is as follows. The depolarization field due to the existence of a

spontaneous polarization leads to a spatial redistribution of the charge carriers in deep centers. The establishment of a steady-state density of charge carriers throughout the volume of the ferroelectric semiconductor is determined by two processes: the change in density as a result of breakdown of the generation–recombination equilibrium and the motion of charge carriers in coordinate space, i.e., as a result of diffusion and drift in an electric field.[10]

The thermal or photoelectric charge carriers excited from deep centers are carried off by the depolarizing field in the direction of the field, and there is not enough time for them to be retrapped. The generation process becomes dominant. For one end of the sample the depolarization field will be depleting for majority carriers. The carrier distribution on deep centers will continue until the internal electric depolarization field is compensated. Since diffusion–drift equilibrium is established rapidly, the formation time of the charge compensating spontaneous polarization will be determined by the rate of change of the density of ionized centers.

The following question arises: Why is there no internal field (no volume-nonuniform distribution of charge carriers on deep centers) in type-I crystals (i.e., in lower-resistance crystals)? One reason is that, as a result of the higher charge-carrier density, the depolarizing field is screened by charge in surface traps. This is supported by the fact that the total depolarization charge near a phase transition in type-I crystals is much larger than the charge associated with spontaneous polarization. This testifies that, together with pyroelectric current, leakage of near-electrode space charge contributes to the depolarization current.

Figure 6 shows on a semilogarithmic scale the time dependence of $\Delta\varepsilon' = \varepsilon' - \varepsilon'_t$ at various temperatures. As one can see, the relaxation of ε' can be described by the exponential function $\Delta\varepsilon' \sim e^{-t/\tau}$ with one characteristic time τ. Closer to the peak in $\varepsilon'(T)$ (curve *1* in Fig. 6b), another exponential section with a much shorter characteristic relaxation time appears in the temperature dependence of ε' just as for a polar phase (curves *2* Figs. 6b and 6c). Thus it clear from the results results presented that the character of the relaxation in the polar phase is generally the same for $T < T_{\max}$ and $T > T_{\max}$. Such a time relaxation of ε' has recently been observed near a second-order phase transition in TGS crystals.[11] This effect was attributed to the evolution of domain structure. Thus, it follows from the experimental facts presented above that the long-time relaxation in a narrow temperature range above $T_{\max}$ (Fig. 4) followed by the appearance of an additional shoulder in $\varepsilon'(T)$ (curve *4* in Fig. 5) occurs only in crystals where an internal electric field arises from screening of the spontaneous polarization. Therefore it is logical to conclude that the effects noted above — the time relaxation of ε' at temperatures above $T_{\max}$ [similarly to relaxation of ε' in the polar phase (Fig. 6)] and the appearance of an additional shoulder in $\varepsilon'(T)$ in type-II crystals — are also due to the influence of an internal electric field on the sample.

However, the absence of a macroscopic ferroelectric polarization at temperatures above $T_{\max}$, evidently rules out the mechanism leading to the formation of an internal electric field due to the screening of spontaneous polarization. An exception is the case where microscopic polar regions exist even for $T > T_{\max}$ as a result of the nonuniformity of the sample.

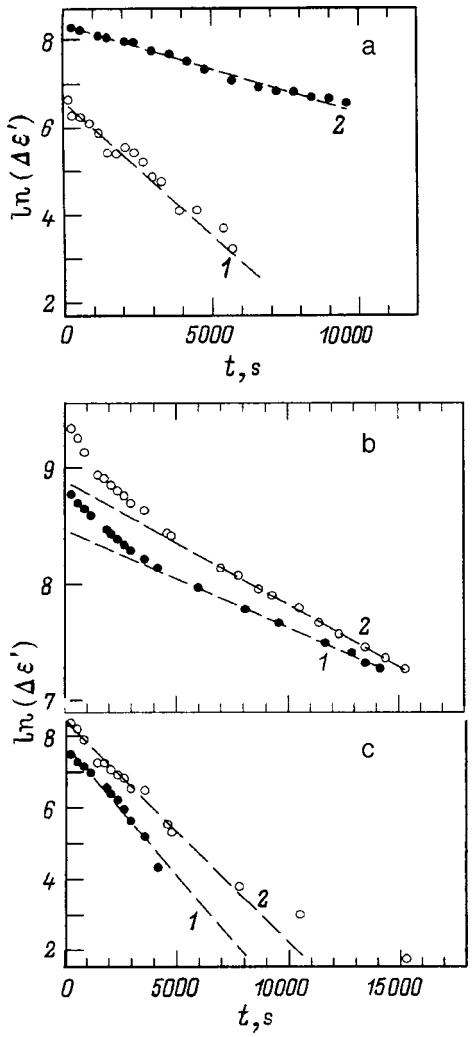

FIG. 6. Time dependence of $\Delta\varepsilon' = \varepsilon' - \varepsilon'_t$, where ε'_t is the parameter used to fit the function $\varepsilon'_t = \varepsilon'_b + \varepsilon'_0 e^{-t/\tau}$ to the experimental curves *1* — $T_{\max}+1.1$ K; *2* — $T_{\max}+0.6$ K (a); *1* — $T_{\max}+0.3$ *K; 2* — $T_{\max}-0.3$ K (b). The dashed lines in the figures correspond to fitting the function indicated above to the experimental results. Adjustable parameters: curve *1* — $\varepsilon'_0 = 15876$ and $\tau = 1632$ s; curve *2* — $\varepsilon'_0 = 14611$ and $\tau = 4945$ s (a); curve *1* — $\varepsilon'_0 = 13033$ and $\tau = 11850$ s; curve *2* — $\varepsilon'_0 = 7410$ and $\tau = 9360$ s (b); c — curves of $\Delta\varepsilon'$ versus time, obtained by subtracting from the experimental curves the fitting functions extrapolated to short times (shown in Fig. 6b).

However, it should be noted that in ferroelectrics–semiconductors, besides an internal electric field which is of a volume character (when a substantial field exists in the volume of the sample), fields exist near the surface.[5] These fields can influence greatly the distribution of the polarization over the sample (i.e., the domain structure) as well as repolarization processes. The fact that even after a long anneal of a prepolarized sample at high temperatures ($T > 370$ K), when the internal electric field in the volume of the sample (associated with screening of spontaneous polarization) vanishes, the degree of polarizability (or relative fraction of single–domain material), determined according to the total paraelectric charge, remains at 70–80% attests to the

presence of such near-electrode regions in type-2 $Sn_2P_2S_6$ crystals. Therefore this near-electrode field greatly influences the distribution of the spontaneous polarization when the sample is cooled to the ferroelectric phase.

The nature of this field is due to the charge in the surface levels. However, unfortunately, the penetration depth of this field cannot be estimated because the required parameters are unknown for $Sn_2P_2S_6$ crystals.

In summary, the observed relaxation of the permittivity at temperatures above T_{max}, evidently, can be attributed to the polarizing action of the near-surface electric fields: These fields induce a polar state near the surface. As is well known,[5] this same mechanism is the basis for the formation of oppositely oriented domains.

The additional maximum in $\varepsilon'(T)$, after a sample is held for a definite time near T_c above T_{max}, is probably due to the behavior of ε' in the near-surface regions of a sample which are subjected to an internal electric field.

The answer to the question of why these effects are absent in type-I crystals is that, as a result of the higher density of free charge carriers (the conductivity in these crystals is much higher than in type-II crystals), the penetration depth of the near-surface field is much smaller.

Crystals were grown from $Sn_{1.9}P_2S_{5.9}$ and $Sn_{2.1}P_2S_{6.1}$ charges to establish the technological reason for the differences in the properties of $Sn_2P_2S_6$ crystals. It was determined that the properties of the former crystals are to those of type-I crystals and the properties of the latter crystals are similar to those of type-II crystals. The high values of the electric conductivity in type-I crystals are most likely due to sulfur vacancies, since a deviation from stoichiometry in crystals grown from a $Sn_{1.9}P_2S_{5.9}$ charge will correspond to a deficiency of sulfur.

I thank M. I. Gurzan for kindly providing the samples for these studies.

This work was performed as part of the International Program INCO/COPERNICUS (ERBIC 15CT970712).

[1] M. M. Maĭor, Yu. M. Vysochanskiĭ, I. P. Prits, Sh. B. Molnar, and L. A. Seĭkovskaya, Kristallografiya **35**, 1300 (1990) [Sov. Phys. Crystallogr. **33**, 767 (1990)].
[2] M. M. Maĭor, Yu. M. Vysochanskiĭ, I. P. Prits, Sh. B. Molnar, V. Yu. Slivka, E. D. Rogach, F. I. Savenko, and A. P. Kudinov, Izv. Akad. Nauk SSSR, Neorg. Mater. **27**, 655 (1991).
[3] A. A. Molnar, Yu. M. Vysochanskiĭ, A. A. Gorvat, and Yu. S. Nakonechnyĭ, Zh. Éksp. Teor. Fiz. **106**, 1747 (1994) [JETP **79**, 945 (1994)].
[4] V. M. Rizak, M. M. Maĭor, M. I. Gurzan, and Yu. Slivka, Ukr. Fiz. Zh. **33**, 1740 (1988).
[5] V. M. Fridkin, *Ferroelectrics–Semiconductors* [in Russian] (Nauka, Moscow, 1976).
[6] Yu. M. Vysochanskiĭ, M. I. Gurzan, M. M. Maĭor, V. M. Rizak, and V. Yu. Slivka, Ukr. Fiz. Zh. **35**(4), 448 (1990).
[7] O. V. Malyshkina, A. A. Bogomolov, and M. M. Major, Ferroelectrics **182**(4), 11 (1996).
[8] B. A. Strukov and A. P. Levanyuk, *The Physical Principles of Ferroelectric Phenomena in Crystals* [in Russian] (Nauka, Moscow, 1983).
[9] A. E. Glazounov, A. K. Tagantsev, and A. J. Bell, Ferroelectrics **184**(1–4), 217 (1996).
[10] F. I. Savenko, *Dielectric Aging and Screening Phenomena in Modified Antimony Sulphiodate*, Candidate's Dissertation, Rostov-on-Don, 1987.
[11] J. Przeslawski del Castillo Fernander, T. Iglesias, and J. A. Gonzalo, Ferroelectrics **186**(1–4), 329 (1996).

Translated by M. E. Alferieff

LATTICE DYNAMICS. PHASE TRANSITIONS

Ultrafast vibronic phase transitions induced in semiconductors by femtosecond laser pulses

V. I. Emel'yanov and D. V. Babak

International Laser Center, M. V. Lomonosov Moscow State University, 119899 Moscow, Russia
(Submitted September 4, 1998; resubmitted December 24, 1998)
Fiz. Tverd. Tela (St. Petersburg) **41**, 1462–1466 (August 1999)

The intermode anharmonic interaction in the theory of ultrafast ($t \sim 10^{-13}$ s) vibronic phase transitions induced on semiconductor surfaces (Si, GaAs) by femtosecond laser pulses is calculated. The conditions for plasma-induced transitions either to a state of chaotic disorder in the positions of the atoms (''cold liquid'') or into a state with crystal symmetry different from the initial symmetry (a new crystalline phase) are determined. It is shown that a NaCl-type structure is realized in GaAs for a transition of the second type, the transition being due to the instability of the longitudinal optical phonon branch. The corresponding numerical estimates are made for Si and GaAs. © *1999 American Institute of Physics.* [S1063-7834(99)02308-4]

Since the 1980s various groups have been studying the ultrafast (times of the order of 10^{-13} s, shorter than the energy transfer times τ_{e-ph} from the electronic subsystem to the lattice) change in symmetry of semiconductor crystal surfaces by femtosecond laser pulses, generating a dense electron–hole (e–h) plasma. Such ultrafast laser-induced phase transitions (LIPTs) have been studied experimentally by the structure-sensitive method of detecting the reflected first and second harmonics (SHs) in Si,[1–3] in GaAs,[4–10] and in InSb.[7] Recent experiments[9] in GaAs testify to ultrafast collapse of the band gap and a transition into a metallic phase; in the process, the SH signal vanishes at times of the order of hundreds of femtoseconds, attesting to a transition of GaAs into a centrosymmetric state.[10]

There exist two basic points of view concerning the mechanism of ultrafast structural LIPTs. In the cold-liquid (CL) model the ultrafast change in symmetry of a crystal in a near-surface layer is attributed to the appearance of disorder in atomic positions,[1–3] which can be attributed to an instability of the phonon-mode continuum. In the new-crystal-phase (NCP) model the experimental results of Ref. 4 on femtosecond LIPTs in GaAs are interpreted from the standpoint of plasma-induced instability of a single phonon mode, leading to a transition to a new crystal (centrosymmetric) state.[11–13]

In theoretical works,[14–17] an instability of transverse acoustic phonon modes is considered as a mechanism of ultrafast LIPTs in semiconductors. In the present paper it will be shown that ultrafast structural LIPTs in semiconductors could be due to an instability of optical phonon modes. This is explained as follows.

Calculations of the free energy as a function of the deformation and the density of the e–h plasma[18] have shown that laser excitation is most likely to induce in GaAs a transition to a centrosymmetric metallic NaCl-type structure, as the structure closest in energy to the initial zinc-blende phase. A phase transition from the zinc-blende structure of GaAs to a NaCl-type structure occurs as a result of a shift of the Ga and As sublattices relative to one another along the vector $\boldsymbol{\tau} = 0.25s[111]b$ ($\boldsymbol{\tau}$ is a vector directed along the diagonal of the face-centered cubic cell, b is the length of the diagonal,[19] and s is a parameter). A noncentrosymmetric GaAs structure is obtained for $s=1$ and a NaCl-type centrosymmetric structures for $s=2$.

The relative displacements of the two sublattices of the atomic planes of Ga and As in the direction of the vector $\boldsymbol{\tau}$ correspond to the branch of longitudinal optical (LO) phonons with $\mathbf{q}=0$. Therefore the phase transition of GaAs to a NaCl-type structure should be attributed to a plasma-induced instability of a single LO phonon mode with $q=0$, $\Omega_0 = 5.3\times 10^{13}\,\mathrm{s}^{-1}$, at the center of the Brillouin zone. A similar conclusion can also be drawn for Si.

In the present paper a theory of plasma-induced instability of the LO branch is constructed. The intermode phonon–phonon interaction, leading to ultrafast transformation of the crystal structure, described by the time evolution of the spectral function of the relative atomic displacements, is taken into account. It is shown that, depending on the irradiation conditions and the characteristics of the crystal, a transition is possible either to the CL state or to an NCP state. The conditions for each of these states to occur are determined, and an interpretation is given for experiments on the induction of ultrafast structural LIPTs in Si[1–3] and GaAs.[4,8–10]

In the absence of laser pumping, the results of this theory agree with the results of equilibrium vibronic theory of ferroelectricity.[20]

1. CLOSED SYSTEM OF EQUATIONS OF THE VIBRONIC MODEL OF A CRYSTAL IN A LASER FIELD

We shall use the vibronic model, proposed in the equilibrium theory of ferroelectricity[20] and used in the theory of laser-induced phase transitions,[21] to study the plasma-induced instability of LO modes in GaAs and Si.

In the simplest (''molecular'') model, a covalent crystal is represented as a system of diatomic molecules in unit cells.[22] The electronic spectrum in such a model consists of two (degenerate) levels with an upper level a, corresponding to the conduction band, and a lower level b, corresponding to the valence band. The transition frequency between the levels is $\omega_{ab}=E_g/\hbar$, where E_g is the band gap.

The equation for the Fourier amplitude $u_0\equiv u_{q=0}$ of the LO phonon mode is,[21] taking account of the interaction with the electronic subsystem,

$$\frac{\partial^2 u_0}{\partial t^2}+\tilde{\omega}_0^2 u_0=\frac{1}{\mu}|\theta|\Delta\rho_{aa}-\frac{1}{\mu}(\theta_{ab}\rho_{ba}+\theta_{ba}\rho_{ab}), \qquad (1)$$

where $\tilde{\omega}_0$ is the frequency of the limiting optical phonon neglecting the electron–phonon anharmonicity, μ is the reduced mass of the cell, $\theta_{ab}=\theta_{ba}$ are the off-diagonal matrix elements of the optical deformation potential, $|\theta|=|\theta_{aa}-\theta_{bb}|$, $\theta_{bb}>\theta_{aa}>0$, ρ_{aa} and ρ_{ab} are the diagonal and off-diagonal elements of the electron density matrix ($\rho_{ab}=\rho_{ba}$), $\Delta\rho_{aa}=\rho_{aa}-\rho_{aa}^0\approx\rho_{aa}$ is the laser-induced change in the diagonal element of the density matrix (ρ_{aa}^0 — equilibrium value of the diagonal element). It follows from Eq. (1) that in equilibrium ($\partial^2 u_0/\partial t^2=0$) with no laser pumping ($\rho_{ab}=\rho_{ba}=0$, $\Delta\rho_{aa}=0$) $u_0=0$, which corresponds to the initial, noncentrosymmetric, dielectric phase of GaAs.

The equation for the low-frequency off-diagonal element of the electronic density matrix $\rho_{aa}\sim\exp(-i\tilde{\omega}_0 t)$ has the form[21]

$$\frac{\partial\rho_{ab}}{\partial t}+i\omega_{ab}\rho_{ab}=\frac{i|\theta|u_0\rho_{ab}}{\hbar}+\frac{i\theta_{ab}u_0 D_{ab}}{\hbar}-\frac{iC\xi_L\rho_{ab}}{\hbar}. \qquad (2)$$

Here $D_{ab}=\rho_{aa}-\rho_{bb}<0$, $C=C_{aa}-C_{bb}$, where C_{aa} and C_{bb} are matrix elements of the acoustic deformation potential, $\xi_L=\nabla\cdot\mathbf{u}_L$ is the laser-induced deformation of the medium, and $\mathbf{u}_L$ is the vector of laser-induced displacement of the medium.

The equation for the conduction electron density n_e has the form

$$\frac{\partial n_e}{\partial t}=-\frac{n_e}{\tau}-\gamma_A n_e^3+D_e\frac{\partial^2 n_e}{\partial z^2}+\frac{\alpha cE^2(1-R)}{2\pi\hbar\omega}\exp(-\alpha z), \qquad (3)$$

where a (cm^{-1}) and R are, respectively, the optical absorption and reflection coefficients; ω and E are the frequency and amplitude of the laser field at the surface $z=0$, γ_A is the Auger recombination constant, c is the speed of light in vacuum, τ is the linear recombination time, and D_e is the ambipolar diffusion coefficient of the carriers in a direction normal to the surface.

To obtain α as a function of u_0 we write the equation for the high-frequency part of the off-diagonal density matrix element $\rho_{ab}^{(\omega)}\sim\exp(i\omega t)$

$$\frac{\partial\rho_{ab}^{\omega}}{\partial t}+i\left(\omega_{ab}-\frac{|\theta|u_0}{\hbar}+\frac{C\xi_L}{\hbar}\right)\rho_{ab}^{\omega}+\gamma_{ab}\rho_{ab}^{\omega}=-\frac{id_{ab}D_{ab}}{\hbar}E\exp\left(-\frac{\alpha z}{2}\right), \qquad (4)$$

where d_{ab} is the off-diagonal dipole-moment matrix element and γ_{ab} is the relaxation constant of the off-diagonal element of the density matrix. Taking account of the electron density matrix depends on the quasimomentum, an expression can be obtained from Eq. (4) for the optical absorption coefficient of a two-band semiconductor in the general form

$$\alpha=\alpha(\hbar\omega-E_{g0}-C\xi_L+|\theta|u_0)\approx\alpha_0+\alpha'\frac{|\theta|u_0}{\hbar}+\frac{1}{2}\alpha''\left(\frac{\theta u_0}{\hbar}\right)^2. \qquad (5)$$

For a direct-gap semiconductor, considered here,

$$\alpha_0=\mathrm{const}\cdot\sqrt{\hbar\omega-E_g},\quad \alpha'=\frac{\partial\alpha}{\partial\omega},\quad \alpha''=\frac{\partial^2\alpha}{\partial\omega^2}. \qquad (6)$$

The equations (1)–(3) and (5) form a closed system of vibronic equations for a crystal in a laser field.

2. LASER-INDUCED SOFTENING OF THE LONGITUDINAL OPTICAL PHONON BRANCH AND A VIBRONIC PHASE TRANSITION

It is evident from Eq. (5) that for a PT with the appearance of a static displacement $u_0>0$, neglecting the laser-induced deformation,

$$E_{g\,eff}=E_{g0}-|\theta|u_0, \qquad (7)$$

where in the nonstationary conventional regime $u_0\sim\exp(\gamma_0 t)$ (see Ref. 17).

It follows from Eq. (7) that $u_0=E_g/|\theta|=b/4$ corresponds to a centrosymmetric metallic phase with NaCl structure ($E_{g\,eff}=0$).

Neglecting in Eq. (3) diffusion and linear combination ($\gamma_A n_e^2\gg\tau_p^{-1}$), we obtain for the plasma density at the surface $z=0$, taking account of Eq. (5),

$$n_e=\sqrt[3]{\frac{\alpha cE^2(1-R)}{2\pi\hbar\omega\gamma_A}}\approx n_{e0}\left[1+\frac{1}{3}\frac{\alpha'}{\alpha_0}\frac{|\theta|u_0}{\hbar}+\left(\frac{1}{6}\frac{\alpha''}{\alpha_0}-\frac{2}{9}\frac{(\alpha')^2}{(\alpha_0)^2}\right)\left(\frac{|\theta|u_0}{\hbar}\right)^2\right], \qquad (8)$$

where

$$n_{e0}=\sqrt[3]{\frac{\alpha_0 cE^2(1-R)}{2\pi\hbar\omega\gamma_A}}. \qquad (9)$$

Using Eqs. (3), (8), and (6), we express the increment to the diagonal density-matrix element $\rho_{aa}=n_e/n$ in terms of u_0, and we obtain ρ_{ab} from Eq. (2). Substituting the expres-

sions obtained into Eq. (1), we obtain a closed nonlinear equation for the Fourier amplitude of the limiting optical mode with $q=0$

$$\frac{\partial^2 u_0}{\partial t^2}+\omega_0^2 u_0=-|\Gamma_A|u_0^2. \tag{10}$$

Here the renormalized frequency of a soft LO phonon is

$$\omega_0^2=\tilde{\omega}_0^2\left(1-\frac{2|D_{ab}|\theta_{ab}^2}{E_{g0}\mu\tilde{\omega}_0^2}-k_1\xi_L-k_2 n_{e0}\right), \tag{11}$$

where

$$k_1=\frac{2\theta_{ab}^2 C|D_{ab}|}{E_{g0}^2\mu\tilde{\omega}_0^2},\quad k_2=\frac{|\theta|^2}{6\mu n\tilde{\omega}_0^2(\hbar\omega-E_{g0})}.$$

The electron–lattice anharmonicity constant is

$$\Gamma_A=-\left\{\frac{2\theta_{ab}^2|\theta||D_{ab}|}{\mu E_{g0}^2}+\frac{7|\theta|^3 n_{e0}}{72\mu n(\hbar\omega-E_g)^2}\right\}.$$

In the absence of laser pumping ($n_{e0}=0$, $\xi_L=0$) the expression (11) is identical to the well-known formula obtained for the frequency of a soft optical phonon in the equilibrium vibronic theory of ferroelectricity.[20] An equilibrium phase transition to a crystal phase with a new symmetry results from the vanishing of the effective optical phonon frequency at the critical temperature T_{cr}, determined by the equation $\tanh(E_{g0}/2k_BT_{cr})=E_{g0}\mu\tilde{\omega}_0^2/2\theta_{ab}^2$, which follows from Eq. (11) with $\omega_0^2=0$ and is identical to the corresponding equation in Ref. 20. The two additional terms in Eq. (11) take account of the effect of the density n_{e0} of the nonequilibrium e–h plasma and the laser-induced deformation ξ_L. For the region where the deformation softens the phonon frequency ($C\xi_L>0$), we have from Eq. (11) for the squared frequency of the soft optical phonon

$$\omega_0^2=\Omega_0^2(1-|\sigma\xi_L|)\left(1-\frac{n_{e0}}{n_{cr}}\right). \tag{12}$$

Here the squared frequency of the limiting optical phonon in the electronic ground state is, taking account of e–p anharmonicity,

$$\Omega_0^2=\tilde{\omega}_0^2\left(1-\frac{2\theta_{ab}^2|D_{ab}|}{E_{g0}\mu\tilde{\omega}_0^2}\right),\quad \sigma=\frac{2\theta_{ab}^2 C|D_{ab}|}{E_{g0}^2\mu\Omega_0^2} \tag{13}$$

and the critical density of the e–h plasma at which the optical phonon frequency vanishes is

$$n_{cr}=(1-|\sigma\xi_L|)n_{cr1}, \tag{14}$$

where the critical density of the e–h plasma in the absence of deformation ($\xi_L=0$) is $n_{cr1}=6n\mu\Omega_0^2(\hbar\omega-E_{g0})|\theta|^{-2}$.

The softening of the frequency of the limiting optical phonon ($\omega_0\to 0$) results in softening of the entire LO phonon branch near $q=0$, where the phonon frequencies w_q are given by

$$\omega_q=\omega_0(1-\beta q^2), \tag{15}$$

where ω_0 is given by Eq. (12) and $\beta>0$ is a constant that can be determined from the phonon dispersion curve for LO phonons as

$$\beta=-\frac{1}{2\omega_0}\frac{\partial^2\omega_q}{\partial q^2}\Big|_{q=0}. \tag{16}$$

The expression (15) is obtained from a very simple lattice model in the form of a one-dimensional system of elastically coupled atomic Au and Ga planes.

As follows from Eqs. (15) and (12), for $n_{e0}>n_{cr}$ the frequencies of optical phonons near $q=0$ become imaginary

$$\omega_q=\pm i\gamma_q,\quad \omega_0=\pm i\gamma_0,\quad \text{and}\quad \gamma_q=\gamma_0-\beta\gamma_0 q^2, \tag{17}$$

where γ_q and γ_0 are real quantities, and the phonon modes convert into unstable modes of relative atomic displacements in the direction of the vector $\boldsymbol{\tau}$.

We shall now find the spectral function of the atomic displacements.

3. KINETIC EQUATION FOR THE SPECTRAL FUNCTION OF THE RELATIVE ATOMIC DISPLACEMENTS

The Hamiltonian of the system of phonons taking account of the anharmonic interaction of optical and acoustic phonons is

$$H=H_0+H_{unh}=\sum_q \hbar\omega_q\left(b_q^+ b_q+\frac{1}{2}\right)$$
$$+\sum_{q_1q_2} V_{q_1q_2}(b_{q_1}a_{q_2}b_{q_1+q_2}^+ + b_{-q_1-q_2}a_{-q_2}^+ b_{-q_1}^+). \tag{18}$$

Here

$$V_{q_1q_2}=\frac{1}{6}\sqrt{\frac{\hbar^3}{8M\mu^2N^3}}N^{-1/2}$$
$$\times\frac{\sum_{n_1,n_2}\mathbf{f}_{n_1n_2}\exp\{i(\mathbf{q}_1\cdot\mathbf{r}_{n_1}+\mathbf{q}_2\cdot\mathbf{r}_{n_2})\}}{\sqrt{\omega_{q_1}\Omega_{q_2}\omega_{-q_1-q_2}}}, \tag{19}$$

N is the number of atoms in the crystal, M is the cell mass, $\Omega_e=qs$ is the acoustic phonon frequency, s is the sound speed, a_q, a_{-q}^+ and b_q, b_{-q}^+ are, respectively, the annihilation and creation operators for acoustic and optic phonons, and $\mathbf{r}_k$ is the equilibrium radius vector of the k-th cell

$$\mathbf{f}_{k,l,m}=\left[\frac{\partial^3\Phi}{\partial\mathbf{r}_k\partial\mathbf{r}_l\partial\mathbf{r}_m}\right]_{U_i=0},\quad i=k,l,m,$$

where Φ is the interatomic interaction energy of the entire crystal.

We shall now determine the spectral function of the relative atomic displacements as

$$S(q)=\frac{\hbar}{\mu\omega_q}n_q,\quad n_q=\langle b_q^+ b_q\rangle. \tag{20}$$

Using the Heisenberg equations, following from Eq. (18), for the operators of stable acoustic and unstable optical modes we obtain for $n(q)$ the equation

$$\frac{\partial n_q}{\partial t}=2\gamma_q n_q-\frac{i}{\hbar}\sum_{q_1}\{V_{q_1,q-q_1}\langle b_q^+ b_{q_1}a_{q-q_1}\rangle - V_{-q_1,-q+q_1}\langle b_q b_{q_1}^+ a_{q-q_1}^+\rangle\}. \quad (21)$$

From the equations for b_q, b_q^+, and a_q^+, introducing into the latter the decay constant δ_q of stable acoustic modes and taking account of the fact that acoustic phonons are strongly damped ($\delta_q \gg \Omega_q, \gamma_q$), we obtain for the correlation function $\langle b_q^+ b_{q_1}a_{q-q_1}\rangle$ the expression

$$\langle b_q^+ b_{q_1}a_{q-q_1}\rangle=\frac{i}{\hbar}\sum_{q_1}\frac{V_{-q_1,-q+q_1}}{\delta_{q-q_1}}n_{q1}N_{q-q_1},$$

where $N_{q-q_1}=(\exp(\hbar\Omega_{q-q_1}/k_BT)-1)^{-1}$ is the filling number of the acoustic phonon mode $q-q_1$. A similar expression is also obtained for the correlation function $\langle b_q b_{q_1}^+ a_{q-q_1}^+\rangle$.

Then, using the definition (20), we have from Eq. (21) the desired kinetic equation for the spectral function of the atomic displacements

$$\frac{\partial S(q)}{\partial t}=(\gamma_q+\gamma_{q_1})S(q)+\frac{2}{\hbar^2}\times\sum_{q_1}\frac{V^2}{\delta_{q-q_1}}\frac{\omega_{q_1}}{\omega_q}N_{q-q_q}S(q_1). \quad (22)$$

The expression following from Eq. (19) for $n_{e0}>n_{cr}$ for the anharmonic interaction constant V^2 is

$$V^2\equiv V_{q_1,q-q_1}V_{-q_1,-q+q_1}=-\frac{1}{288}\frac{\hbar^3}{NM\mu^2}\frac{|f^2|}{\Omega_{q-q_1}\gamma_q^2}<0,\quad |f|^2\approx g^2\left(\frac{W}{a^3}\right)^2, \quad (23)$$

where $g>1$ is the number of nearest neighbors and W is the interatomic interaction energy per cell. The derivation of Eq. (23) employed the fact that for $n_{e0}>n_{cr}$, taking account of Eq. (17), $(\omega_{q_1}\omega_{-q_1}\omega_q\omega_{-q})^{-1/2}\approx-\gamma_q^{-2}$.

4. DIFFUSION COLLAPSE OF THE SPECTRAL FUNCTION OF THE RELATIVE ATOMIC DISPLACEMENTS

The decay constant of stable acoustic phonon modes in Eq. (22) can be expressed by

$$\delta_{q-q_1}=|q-q_1|b, \quad (24)$$

where $b=\dfrac{2\pi\theta C_{ab}^2 n_e^*}{\hbar\gamma_{ab}Ms}\dfrac{n_e^*}{n}$ and n_e^* is the effective conduction-electron density in a degenerate semiconductor that participate in phonon absorption.

Setting $\gamma_{q_1}\approx\gamma_q$ in Eq. (22), switching from summation to integration, and using Eqs. (23) and (24) we obtain a linear integral equation for the spectral function

$$\frac{\partial S(q)}{\partial t}=2\gamma_q S(q)-|A|\int_{-\infty}^{+\infty}dq_1K(|q-q_1|)S(q_1), \quad (25)$$

where

$$|A|=\frac{1}{576\pi^2}\frac{n}{n_e^*}\frac{\gamma_{ab}}{\gamma_0^2}\frac{\hbar^2|f|^2}{\mu^2\theta_{ab}^2}a,\quad K(|q-q_1|)=\frac{N_{q-q_1}}{|q-q_1|^2}.$$

Making the substitution of variables $q_1=q-\xi$ and expanding the function $S(q_1)$ in the integrand in Eq. (25) in a Taylor series in ξ, we obtain from Eq. (25) a diffusion equation for the spectral function of atomic displacements in q space with a negative diffusion coefficient D

$$\frac{\partial S(q)}{\partial t}=2\gamma_q S(q)-|D|\frac{\partial^2 S}{\partial q^2}, \quad (26)$$

where the modulus of the spectral diffusion coefficient is

$$|D|=\frac{|A|}{2}\int_{-\infty}^{+\infty}d\xi K(|\xi|)\xi^2\equiv\frac{A}{2}\frac{2kT}{\hbar s}\int_{x_m}^{\infty}\frac{dx}{e^x-1}.$$

Here the lower limit of integration is determined by the uncertainty of $|\boldsymbol{\xi}|=|\mathbf{q}-\mathbf{q}_1|$ (the vectors $\mathbf{q}$ and $\mathbf{q}_1$ are directed along [111]): $x_m=(\hbar s/kT)\min|\xi|=(\hbar s/kT)2\pi\alpha$, where α is the optical absorption coefficient.

Then the spectral diffusion coefficient is

$$|D|=\frac{\hbar}{576\pi^2}\frac{n}{n_e^*}\frac{\gamma_{ab}}{\Omega_0^2}\frac{k_BT}{a^5\mu^2 s}g^2\left(\frac{W}{C_{ab}}\right)^2\left(\frac{n_{e0}}{n_{cr}}-1\right)^{-1}\times\ln\left(\frac{2\pi\alpha\hbar s}{kT}\right). \quad (27)$$

We shall assume that initially (at $t=0$) $S(q,0)=S_0=$ const. Then the solution of Eq. (26) for the nonequilibrium spectral function of the relative atomic displacements is

$$S(q,t)=S_0\frac{\exp(2\gamma_0 t)}{\sqrt{1-8\beta\gamma_0|D|t^2}}\exp\left(-\frac{q^2}{\dfrac{1}{4\beta\gamma_0 t}-2|D|t}\right). \quad (28)$$

We introduce the characteristic collapse time of the spectrum as

$$t_m=\frac{1}{\sqrt{8|D|\beta\gamma_0}}. \quad (29)$$

As one can see from Eq. (28), for times $0<t<t_m$ the spectral function $S(q,t)$ evolves from a uniform initial distribution to a Gaussian distribution with a maximum, which increases in time, at the center $q=0$ of the Brillouin zone and a width which decreases in time. At $t=t_m$ the spectral function of the optical atomic displacements collapses into a δ function: $S(q,t_m)\sim\delta(q)$.

For

$$t_m<(2\gamma_0)^{-1}<\tau_{cr}\sim\tau_P, \quad (30)$$

where τ_{cr} is the time during which the plasma density n_{e0} exceeds the critical value n_{cr} and over the time τ_P there is enough time for the amplitudes of the modes to grow and the mode spectrum collapses into a δ function at $q=0$. Thus in the case (30) the lattice passes in a time τ_P into a state with completely correlated coherent relative displacement of atoms in all cells of the crystal, i.e., into an NCP phase.

On the other hand, for

$$(2\gamma_0)^{-1} \ll t_m, \quad (2\gamma_0)^{-1} < \tau_{cr} \sim \tau_P \tag{31}$$

a wide mode spectrum builds up over the time τ_P, and on account of the nonlinearity this spectrum stabilizes and becomes flat. Therefore in the case (31) a transition into the CL state occurs.

We shall make some numerical estimates for LIPTs in GaAs and Si. From Eqs. (14) and (13) for GaAs with $\mu=6\times10^{-23}$ g, $\Omega_0=5.3\times10^{13}\,\mathrm{s}^{-1}$, $\omega=3\times10^{15}\,\mathrm{s}^{-1}$, $E_{g0}=1.44$ eV, $|\theta|\sim10^{-3}$ erg/cm, $n=2\times10^{22}\,\mathrm{cm}^{-3}$, $\theta_{ab}=2.1\times10^{-4}\,\mathrm{erg\cdot cm}^{-1}$, and $|C|=20$ eV (Ref. 23) and the approximate value $\xi_L=0.25$,[24] we have for the critical plasma density $n_{cr}=3\times10^{21}\,\mathrm{cm}^{-3}$. Under the experimental conditions of Ref. 4, $E^2=4\times10^9\,\mathrm{erg\cdot cm}^{-3}$, $R=0.35$, $\gamma_A=4\times10^{-28}\,\mathrm{cm}^6\,\mathrm{s}^{-1}$,[23] taking account of the nonlinear increase in the optical absorption coefficient $\alpha_0\sim10^2\overline{\alpha_0}=4.3\times10^6\,\mathrm{cm}^{-1}$, from Eq. (29) we estimate the plasma density as $n_{e0}\sim3.5\times10^{21}\,\mathrm{cm}^{-3}>n_{cr}$.

From Eqs. (12) and (17) we find $\gamma_0=10^{13}\,\mathrm{s}^{-1}$. Using the data from Ref. 23, we have taking account of Eq. (16) $\beta\gamma_0\sim10^{-1}\,\mathrm{cm}^2\,\mathrm{s}^{-1}$. Using in Eqs. (27) and (29) $W=3.1\times10^{-11}$ erg, $g=4$, $T=300$ K, $s=5\times10^5$ cm/s, $a=3.6\times10^{-8}$ cm, $n/n_e^*\sim2\times10^2$, $\gamma_{ab}\sim10\cdot\Omega_0$, $C_{ab}\sim1$ eV[23] and the values obtained above for n_{e0} and n_{cr}, we estimate the spectral diffusion coefficient in GaAs as $|D|=5\times10^{26}\,\mathrm{cm}^{-2}\mathrm{s}^{-1}$ and the spectrum collapse time as $t_m=48\,\mathrm{fs}<(2\gamma_0)^{-1}\sim50\,\mathrm{fs}<\tau_{cr}\sim\tau_P$. Therefore the conditions (30) for a transition into an NCP state are satisfied.

We shall now make similar estimates for Si. For the same values of ω, E^2, and T and $\alpha_0\sim10^2\overline{\alpha_0}=4.5\times10^5\,\mathrm{cm}^{-1}$, $R=0.35$, $\gamma_A=4\times10^{-31}\,\mathrm{cm}^6\mathrm{s}^{-1}$, $C_{ab}\sim1$ eV (Ref. 23) we obtain from Eq. (9) $n_{e0}\sim1.7\times10^{22}\,\mathrm{cm}^{-3}$. Substituting into Eqs. (27) and (29) $n_{cr}=9\times10^{21}\,\mathrm{cm}^{-3}$ (Ref. 16), $\mu=2.4\times10^{-23}$ g, $W=2.88\times10^{-12}$ erg, $g=4$, $\Omega_0=1.1\times10^{14}\,\mathrm{s}^{-1}$, $s=10^6$ cm/s, $a=3.4\times10^{-8}$ cm, $n/n_e^*\sim2\times10^2$, $\gamma_{ab}\sim10\times\Omega_0$,[23] $\gamma_0=5\times10^{13}\,\mathrm{s}^{-1}$, and $\beta\gamma_0\sim10^{-1}\,\mathrm{cm}^2\mathrm{s}^{-1}$, we estimate the spectral diffusion coefficient in Si as $|D|=2.2\times10^{24}\,\mathrm{cm}^{-2}\mathrm{s}^{-1}$ and the spectrum collapse time as $t_m=756\,\mathrm{fs}\gg(2\gamma_0)^{-1}=10$ fs, $\tau_{cr}\sim\tau_P\gg(2\gamma_0)^{-1}$. Therefore, for Si, the conditions (31) for a transition into the CL state are satisfied with a large margin.

In summary, the analysis performed in the present paper shows that, during LIPTs in GaAs a transition to an NCP state is most likely to occur in GaAs, while a transition to a CL state occurs in Si.

[1] C. V. Shank, R. Yen, and C. Hirlimann, Phys. Rev. Lett. **50**, 454 (1983).
[2] C. V. Shank, R. Yen, and C. Hirlimann, Phys. Rev. Lett. **54**, 2151 (1985).
[3] H. W. K. Tom, G. D. Aumiller, and C. H. Brito-Cruz, Phys. Rev. Lett. **60**, 1438 (1988).
[4] S. V. Govorkov, I. L. Shumaĭ, W. Rudolph, and J. Shröder, JETP Lett. **52**, 117 (1990).
[5] K. Sokolovski-Tinten, H. Schulz, J. Bialkowski, and D. von der Linde, Appl. Phys. **53**, 227 (1991).
[6] K. Sokolovski-Tinten, J. Bialkowski, and D. von der Linde, Phys. Rev. B **51**, 14 186 (1995).
[7] I. L. Shumay and V. Hofer, Phys. Rev. B **53**, 15 878 (1996).
[8] Y. Siegal, E. N. Glezer, and E. Mazur, Phys. Rev. B **49**, 16 403 (1994).
[9] E. N. Glezer, Y. Siegal, L. Huang, and E. Mazur, Phys. Rev. B **51**, 6959 (1995).
[10] E. N. Glezer, Y. Siegal, L. Huang, and E. Mazur, Phys. Rev. B **51**, 9589 (1995).
[11] S. V. Govorkov, V. I. Emel'yznov, N. I. Koroteev, and I. L. Shumay, J. Lumin. **53**, 153 (1992).
[12] S. V. Govorkov, V. I. Emel'yanov, I. L. Shumaĭ, W. Rudolph, and T. Shröder, Izv. Ross. Akad. Nauk, Ser. Fiz. **56**(6), 64 (1992).
[13] S. V. Govorkov, V. I. Emel'yanov, and I. L. Shumay, Laser Phys. **2**, 77 (1992).
[14] V. Heine and J. A. Van Vechten, Phys. Rev. B **13**, 1622 (1976).
[15] R. Biswas and V. Ambegaokar, Phys. Rev. B **26**, 1982 (1982).
[16] P. Stampfli and K. H. Bennemann, Phys. Rev. B **42**, 7163 (1990); Phys. Rev. B **49**, 7299 (1994).
[17] V. I. Emel'yanov and D. V. Babak, Laser Phys. **7**, 514 (1997).
[18] Yu. V. Kopaev, V. V. Menyaĭlenko, and S. N. Molotkov, Fiz. Tverd. Tela (Leningrad) **27**, 3288 (1985) [Sov. Phys. Solid State **27**, 1979 (1985)].
[19] Toshinobu Soma, J. Phys. C **11**, 2681 (1978).
[20] N. Kristoffel and P. Konsin, Phys. Status Solidi **21**, 39 (1967); **28**, 731 (1968).
[21] A. V. Andreev, V. I. Emel'yanov, and Yu. A. Il'inskii, *Cooperative Effects in Optics: Superradiance and Phase Transitions* (Adam Hilger, Bristol, 1993).
[22] M. Lannoo and J. Bourgoin, *Point Defects in Semiconductors I* (Springer-Verlag, Berlin, 1981).
[23] Landolt-Bornstein, *Numerical Data and Functional Relationships in Science and Technology. New Series. Group III. Vol. 17. Semiconductors. Subvolume a. Physics of Group IV Elements and III–V Compounds.*
[24] V. I. Emel'yanov and I. F. Uvarova, Zh. Éksp. Teor. Fiz. **94**, 255 (1988) [Sov. Phys. JETP **67**, 1662 (1988)]; Laser Phys. **2**, 389 (1992).

Translated by M. E. Alferieff

Sound propagation anomalies and phase diagram of chromium alloys

A. I. Mitsek and T. V. Golub*)

Institute of Metal Physics, Ukrainian Academy of Sciences, 252680 Kiev, Ukraine
(Submitted February 1, 1999)
Fiz. Tverd. Tela (St. Petersburg) **41**, 1467–1472 (August 1999)

Calculations of the complex elastic moduli $\hat{C}(T)$ in dilute Cr alloys are compared to measurements of the velocity and damping of sound near T_N and at high temperatures $T>T_N$ (T_N — Néel temperature). The thermodynamic calculation is based on the covalent bond model of $3d$ ions in a state with different numbers n of covalent electrons. The parameters $A_{ij}^{(n)}$ of indirect exchange between the ions of the i and j sublattices are expressed in terms of the covalent bond energy $\Gamma_{ij}^{(n)}$. The stability of the charge and spin density waves (CDWs and SDWs) is found by a variational method and is determined by the dispersion of $\Gamma_{ij}^{(n)}$ and by the Coulomb parameters U_n. For a small structural vector $\mathbf{Q}$ the phase diagram contains a superantiferromagnetic phase (SAFM) at temperatures $T_N<T\leq 2T_N$. The peak of the defect $|\Delta E(T)|$ of the modulus and of the sound damping $\Delta_h(T_N)$ near the first-order SDW–SAFM transition is determined by the structure of the transitional domain. Measurements of the anomalous growth of $E(T)$ at temperatures $T>T_N$ make it possible to determine the magnetostriction constants $\lambda(T)$ of Ce alloys in the SAFM phase on the basis of the SAFM theory.
 [S1063-7834(99)02408-9]

1. NONUNIFORMITY OF THE SPIN STRUCTURE OF Cr AND ITS ALLOYS

Metallic Cr is distinguished by its properties from metals of the heavy half of the $3d$ group (Mn, Fe, Co, Ni). Its brittleness, corrosion resistance, and so on could be determined by the variable valence of the Cr atom ($3d^5 4s^1$). The discovery of spin density waves (SDWs) in Cr and of a complicated domain structure of Cr (see Ref. 1) explained the existence of special temperature points $T=T_{SF}\simeq 120$ K and $T_N\simeq 310$ K in the phase diagram of Cr. Since there are two spin-order parameters in the SDW state (the SDW amplitude S_w ($S_w\simeq 1/2$) and the structure vector $\mathbf{Q}$ ($|q|\sim 0.1$)), whose directions along [100]-type axes are identical for $T<T_{SF}$ or orthogonal for $T_N>T>T_{SF}$, the parameters of different types of domain walls (energy and thickness) differ in order of magnitude.[2] The additional of small concentrations of impurities X ($c_x\leqslant 10^{-2}$) suppresses SDWs and transfers the alloy Cr–X to a commensurate (Néel) state on the line $c_x(T_{1C})$. The Néel temperature T_N increases sharply (sometimes by a factor of 2) as a result of this concentration transition (see Ref. 3). The type of transition also changes (in pure Cr and its alloys with SDWs it is a first-order transition near T_N).

This suggested that the suppression of SDWs at $T>T_N$ is accompanied by local ''homogenization'' of the spin density, which forms clusters with antiferromagnetic (AFM) Néel structure (see Refs. 2 and 4). This nonuniform, superantiferromagnetic (SAFM) state exists at temperatures $T_N<T\leqslant 2T_N$.

The most striking anomalies are a deep minimum $\sim 10^{-1}$ of the sound speed (elastic modulus $C_{11}(T)$) and growth of $C_{11}(T)$ in the region $T_N<T\leqslant 2T_N$ as well as an absorption peak near T_N (just as near other transitions: T_{SF} and T_{1C}[1,2]). We assume that these anomalies are due to the nonuniform spin structure, specifically, the transitional domain structure and SAFM clusters.

The unusual (for typical metals) mechanical and other properties of Cr (with good metallic electric conductivity, though much lower (by a factor of 2 or 3 at 300 K) than in Co or Fe) indicate that the metal bond (itinerant electrons) plays a lesser role. The role of covalent bonds increases correspondingly. This decreases the likelihood that a simple band model of SDWs will be applicable (Overhauser et al.; see Ref. 1) to Cr alloys. Periodicity due to the nonuniformity of the distribution of covalent $3d$ electrons seems more likely.

It is also necessary to discuss the use of a ''Grüneisen parameter'' by Fawcett et al.[5] to describe the magnetic state of Cr. Grüneisen's initial theory[6] for an ideal (Debye) phonon gas has been extended to a gas of ferromagnons.[7] An attempt in Ref. 5 to obtain a ''Grüneisen rule'' in the form of a relation between the elastic moduli, the specific heat, and other (sometimes arbitrarily chosen) characteristics led to different (even with respect to sign) ''Grüeisen parameters'' for Cr at $T\ll T_N$ and $T\simeq T_N$. It is evident from the results obtained in Refs. 6 and 7 that in order for a Grüneisen constant to exist (elastic and magnetic) the model of a gas of elementary elastic (phonons) or spin (magnon) excitations must be applicable. For Cr this condition[6,7] does not hold, so that there is no justification for introducing a ''Grüneisen parameter.'' The use of such a parameter for interpreting the experimental data in Cr alloys leads to inconsistencies.

To construct the phase diagrams of metals, specifically, the magnetic details of the phase diagrams, the role of localized (magnetic and covalent) electrons must be taken into account carefully. The zone electrons are manifested in their

TABLE I. Values of the changes in Young's modulus, $(\Delta E/E)_{T_N}$, and the sound damping, $(\Delta_h)_{T_N}$, in chromium and its alloys (at $T=T_N$).

No.	Composition, wt. %	T_N, K	f, 10^3 Hz	E, GPa	$(\Delta E/E)_{T_N}$	$(\Delta_h)_{T_N}$, 10^{-4}
1	Cr–0.5 N	311	2.8	282.7	−0.059	45
2	Cr–0.5 N–0.4 Zr	311	2.7	287	−0.061	5.4
3	Cr–0.5 Nb	270	3.0	293	−0.048	1.8
4	Cr–0.9 Fe	290	2.8	290	−0.06	4
5	Cr–5 MgO	311	2.7	265	−0.019	0.8
6	Cr, quenched single crystal	311	3.7	285.5	−0.056	100
7	Cr, annealed single crystal	311	3.7	284.6	−0.057	99
8	Cr, polycrystal	311	2.9	269	−0.08	90
9	Cr, nonreduced La and Y polycrystal	311	2.8	287	−0.049	3.6

interaction with local electrons (hybridization, scattering, and so on).

The anomalies in the mechanical properties of AFM crystals, especially cubic crystals, are often greater than the magnetic susceptibility anomalies. For this reason, measurements of the sound velocity and absorption make it possible to estimate more accurately the characteristics of the AFM state and to find the boundaries of the magnetic phases.

2. SAMPLES AND MEASUREMENT PROCEDURE

In the present work the temperature dependences of the modulus of normal elasticity on T_N in Cr and its alloys are measured up to 1000 K. Polycrystalline chromium contains interstitial impurities: C (to 10^{-2} wt. %), N (to 4×10^{-2} wt. %), and O (to 10^{-3} wt. %). The concentrations of these impurities in single-crystal Cr are an order of magnitude lower.

The materials for the investigations were smelted in a copper water-cooled crucible in a purified-argon atmosphere of a laboratory-electric-arc furnace with a nonconsumable tungsten electrode and then poured into a copper mould. Electrolytic chromium, refined by annealing in hydrogen, served as the initial component. Yttrium or lanthanum (up to 0.1 wt.%) was introduced into the alloys as a reducing agent. The chemical composition of the experimental samples is presented in Table I. This table also contains the peak value of Young's modulus anomaly $(\Delta E/E)_{T_N}$ at the Néel point and the sound damping anomaly $(\Delta_h)_{T_N}$.

Young's modulus $E(T)$ was measured by the resonance method based on the relationship between the modulus of normal elasticity, the characteristic frequency f of bending oscillations of the sample, and the geometric dimensions and mass of the sample (see Ref. 8). The relative change $(\Delta E/E)$ in Young's modulus as a function of temperature T was found from the change Δf in the resonance frequency (according to $E\sim f^2$), which was determined to within 0.05%. The changes were made in vacuum, and the temperature was regulated automatically to within $\pm2°$. The samples were first annealed for 2 h at 1400 K and then cooled at a rate of 1°/s. Chromium single crystals were additionally quenched from 1400 K to the eutectic at 340 K.

The typical measurement of $E(T)\sim f^2(T)$ are presented in Fig. 1. The same behavior of $f^2(T)$ has been observed in Ref. 9. It is evident that in the temperature range from T_N to $1.6T_N$ Young's modulus increases with temperature, i.e., the behavior of $E(T)$ differs from that in paramagnetic crystals as well as in ferro- and antiferromagnets above T_c or T_N.[2] At temperatures $T>2T_N$ Young's modulus, just as in a nonmagnetic crystal (linear continuous asymptote), decreases linearly with increasing temperature. The nonmonotonic behavior of $E(T)$ is attributed to short-range AFM order (see Sec. 4).

Spin density waves in Cr and its alloys have a large period $\sim10a$ (the structure vector $\mathbf{Q}\leqslant0.1$), where a is the period of the bcc lattice. The thermal properties of Cr are also unusual: The nonmonotonic dependence of the elastic $C_{11}(T)$ and other moduli above T_N, and a small entropy difference in the paramagnetic phase of SDW (see Ref. 1). The high Fermi energy $E_F\sim10$ eV suppresses the influence of itinerant electrons on the thermal properties (and on the details of the phase diagram). Fluctuations of the chemical (covalent) bonds should play a very large role.

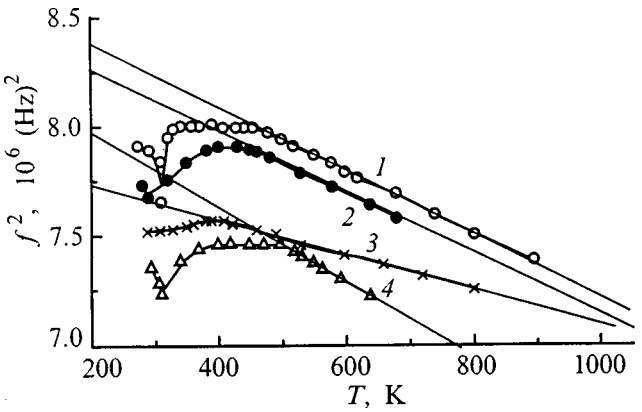

FIG. 1. Temperature dependence of the frequency $f^2(T)$ (elastic modulus $E=Kf^2$) in samples of chromium and its alloys annealed at 1400 K. *1* — Cr polycrystal (No. 9), *2* — the alloy Cr–0.9%Fe, *3* — Cr–5%MgO, *4* — Cr–0.4%Zr–0.5%N (indicated in wt.%).

3. DOMAIN STRUCTURE NEAR T_N AND THE SAFM PHASE ABOVE T_N

3.1. Transitional domain structure

The first-order transition from the SDW to the SAFM phase in Cr and its dilute alloys is accompanied by a transitional domain structure.[2] The transition from the SDW phase (I) to the commensurate (Néel) C phase is similar. For a fixed concentration c_x of the X component (X=Al, Os, Ru, ...) the transition temperature T_{IC} is determined by equality of the energy of the commensurate phase (structure vector $\mathbf{Q}=0$) and that of the SDW phase.

The thermodynamic analysis is based on the variable-valence model of Cr. Chromium ions can have a different number n of covalent electrons. For computational convenience we shall take account of the two possibilities, $n=1$ and 3. We assume the exchange interaction between the spins $\mathbf{S}_n$ of different Cr atoms to be indirect. It is occurs via the covalent electrons, whose polarization $\mathbf{s}_{nj}$ is different for Cr ions in the sublattices $j=1$ (sites of the type (000)) and $j=2$ (sites of the type (1/2 1/2 1/2). The chemical bond $\Gamma_{12}^{(n)}$ between the nearest Cr neighbors determines the dominant intersublattice exchange $A_{12}^{(n)}$. The chemical bond $\Gamma_n(\mathbf{Q})$ inside the sublattices is favorable for SDWs. The spin part of the thermodynamic potential is binary in the vectors $\mathbf{s}_{nj}$ and the average spins $S_{nj}(T)$ of the magnetic ions

$$F=\sum_{nj}\left(\frac{1}{2}U_n\mathbf{s}_{nj}^2-A\mathbf{s}_{nj}\mathbf{S}_{nj}-\Gamma_n(\mathbf{Q})\mathbf{s}_{nj}\mathbf{s}_{nj}\right)$$

$$-\sum_n \Gamma_{12}^{(n)}\mathbf{s}_{n1}\mathbf{s}_{n2}. \tag{1}$$

Here we have introduced the Coulomb parameter (Hubbard) U_n and the Hund exchange A, in terms of which the exchange parameters $\hat{A}^{(n)}$ of the spin lattice are expressed. For example,

$$A_{12}^{(n)}\cong\Gamma_{12}^{(n)}(A/U_n)^2. \tag{2}$$

We vary the potential (1) with respect to the vector variables $\mathbf{s}_{nj}$ assuming $Q\ll 1$. We use

$$\Gamma_n(\mathbf{Q})\cong\Gamma(0)-\Gamma_n'\mathbf{Q}^2,\quad \Gamma_{ij}=\Gamma_i-\Gamma_j. \tag{3}$$

Let

$$U_{13}=U_1-U_3+[\Gamma_{12}^{(1)}(0)-\Gamma_{12}^{(3)}(0)]. \tag{4}$$

For small $c_x\sim 10^{-2}$ we expand the coefficients in the thermodynamic potential (1) in a power series in c_x

$$\Gamma_n'(c_x)=\Gamma_n'(0)+\Gamma_{cn}'c_x, \tag{5}$$

$$A_{12}(c_x)=A_{12}(0)+A_{12}'c_x,\quad A_{12}^{(n)}\cong A_{12}. \tag{6}$$

The variation of the potential (1) using the results of Refs. 10–15 gives an expression for the SDW vector

$$Q^2=[2\Gamma_{13}(0)-U_{13}]/2\Gamma_{13}'>0 \tag{7}$$

and the critical concentration c_x for the I–C transition

$$c_x=[A_{12}(0)+\Gamma_3'(0)]/[\Gamma_{c3}'Q^2(c_x)2A_{12}']>0 \tag{8}$$

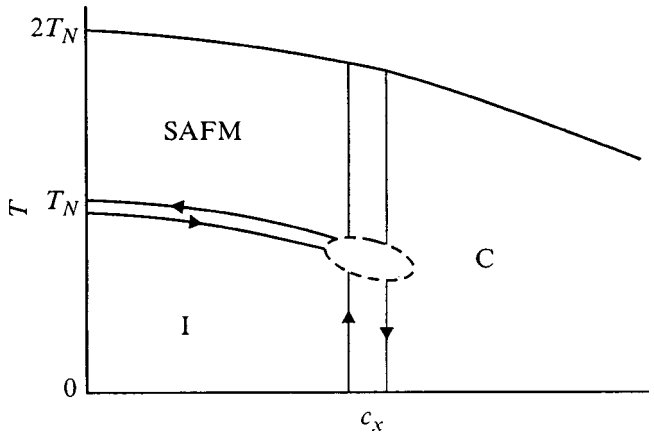

FIG. 2. Phase diagram of the alloy Cr–X (c_X — concentration of the impurity X). Ordinary line — second-order transition, the two lines with the arrows mark first-order transitions with hysteresis.

assuming that in the C phase the Cr ions are in the $n=3$ state with spin $S_3=3/2$.

The result (8) confirms that the spin (exchange) energy A_{12} (2) plays the decisive role in stabilizing SDWs. The SDW structure (the vector $\mathbf{Q}$) is determined by the electronic (covalent in our model) energies $\Gamma_{ij}^{(n)}$. The first-order transitions are shown in the phase diagram (Fig. 2) by two lines (with hysteresis). An ordinary line shows a second-order transition from a commensurate (Néel) C phase to the paramagnetic phase. The dashed line shows a diffuse transition from the SAFM phase to the ordinary paramagnetic phase. The triple point where three first-order transitions cross requires a more extensive analysis, which is not presented here. The inequality (8) determines, specifically, the condition for the existence of an I–C transition.

The domain structure for a SDW–SAFM transition has been calculated in Ref. 2 neglecting the ''attachment'' of AFM clusters to domain walls. We take account of impurities, according to Eqs. (5)–(8), by studying explicitly the dependence of the equations of motion of different types of walls j on the parameters c_x. In matrix form, the equation of motion of an individual wall is

$$m_{\alpha\beta}\ddot{x}+\gamma_{\alpha\beta}\dot{x}_\beta+k_{\alpha\beta}x_\beta=(\hat{P}\otimes\Delta\hat{u})_\alpha,\quad \hat{P}(t)=\hat{P}_\sim e^{i\omega t}, \tag{9}$$

where the mass tensor $\hat{m}$ of a wall, the damping tensor $\hat{\gamma}$, the quasielastic force tensor $\hat{k}$, and the difference $\Delta\hat{u}$ of the spontaneous deformation tensors of neighboring domains determine the displacement vector $\mathbf{x}$ of a flat section of the wall under the action of the external pressure tensor $\hat{P}(t)$. We neglect the nonuniformity of the (acoustic) pressure $\hat{P}$. The uniform periodic solution is

$$\mathbf{x}(t)=\mathbf{x}_0e^{i\omega t}. \tag{10}$$

The vector amplitude

$$\mathbf{x}_0=(\hat{m}\omega^2+i\omega\hat{\gamma})^{-1}(\hat{P}_\sim\otimes\Delta\hat{u}), \tag{11}$$

generally speaking, depends on the position of the given section of the wall. The latter is caused, for example, by the nonuniform impurity distribution $c_x(\mathbf{r})$.

Diagonal tensors $\hat{\gamma}$ and $\hat{k}$ can be studied for a cubic single crystal with symmetric domain walls, but an index j for different types of walls must be introduced.[2] The variable longitudinal deformation of the sample is

$$u(t)=e^{i\omega t}\left\{(P_{\sim}/C_{11})+\sum_j u_j\right\}, \quad u_j=\chi_{0j}\Delta u_j, \qquad (12)$$

whence, substituting Eq. (12), the defect of the complex elastic modulus $C_{11}(T)$ is

$$C_{11}\cong C_{11}^{(0)}-\sum_j C_{11}(\Delta u_j)^2/(k_j^2+i\omega\gamma_j). \qquad (13)$$

The maximum defect of the modulus near T_N (the minimum of $C_{11}(T_N)$; see Table I) equals the real part of Eq. (13)

$$\Delta C_{11}(T_N)=-\sum C_{11}(\Delta u_j)^2 k_j/(k_j^2+\gamma_j^2\omega^2). \qquad (14)$$

The maximum damping ($(\Delta h)_{T_N}$ in Table I) can be expressed in terms of the imaginary part of the expression (13)

$$\mathrm{Im}\, C_{11}(T_N)=\sum C_{11}(\Delta u_j)^2(\omega\gamma_j)/(k_j^2+\omega^2\gamma_j^2). \qquad (15)$$

The dependences of the quantities (14) and (15) on the concentration c_X of the impurity X are determined by $k_j(c_x)$ and $\gamma_j(c_x)$. The values of k_j and γ_j should increase with c_x, which explains the decrease in the damping (15) in the Cr alloys. The different values of the quantity (14) for different samples are explained by the difference of the characteristics Δu_j, k_j, and γ_j of the walls.

3.2. Superantiferromagnetic (SAFM) phase above T_N

The existence of an SAFM phase above T_N of crystals in Cr alloys with SDWs is due to strong intersublattice exchange A_{12}.[4] Its characteristic properties have been calculated in Refs. 4 and 15. The most striking characteristic was the glowing function $C_{11}(T)$ for $T_N<T<2T_N$. The same anomaly has recently been observed in helicoidal Ho,[16] which possesses a periodic spin structure at temperatures $T<T_N=132$ K. The anomalous maximum of the temperature dependence of the longitudinal velocity of ultrasound in Ho is observed at temperatures $T_N<T\leqslant 200$ K for $f=10^7$ Hz.

We assume that in the absence of a magnetic field H the antiferromagnetism vector $\mathbf{l}(T)$ is the main characteristic of the SAFM phase with clusters possessing Néel short-range order. The energy of a cluster is the sum of the magnetic anisotropy energy Φ_A and the magnetoelastic energy $\Phi_{me}(T)$

$$\Phi_A=-K(T)\sum \alpha_j^4, \quad \Phi_{me}=\lambda(T)u_{jj}\alpha_j^2+\ldots,$$

$$\alpha_j=l_j/|\mathbf{l}(T)|. \qquad (16)$$

Only the term responsible for the defect of $C_{11}(T)$ is written out in the expression for Φ_{me}. The partition function of a system of same-size SAFM clusters is

$$Z_0=\int d\alpha \exp\{\{-\beta[\Phi_A+\Phi_{me}(\hat{u})]C_{cl}\},$$

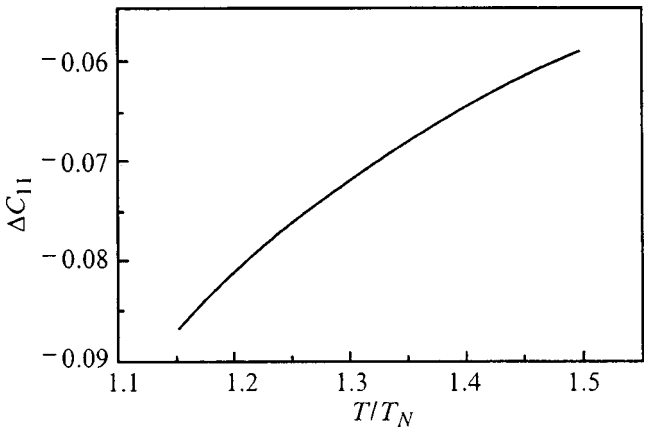

FIG. 3. Computed defect $\Delta C_{11}(T)$ of the elastic modulus of a cubic superantiferromagnet (SAFM) neglecting the dependence of the magnetostriction constant $\lambda(T)$ on the temperature T.

$$\Phi=-\frac{1}{\beta}\ln Z_0+C_{ij}u_{ii}u_{jj}/2, \qquad (17)$$

where V_{cl} is the volume of a cluster and $\beta=1/k_BT$.

We obtain the defect of the elastic modulus (Fig. 3) by varying the expression (17) with respect to $\hat{u}$,

$$\Delta C_{11}(T)=-\beta\lambda^2(T)Z_2,$$

$$Z_2=\partial^2\ln Z_0/\partial B^2, \quad B=\beta K V_{cl}. \qquad (18)$$

The numerical calculation of the function (18) is performed assuming a linear dependence

$$K(T)\cong K_0(1-T/pT_N), \quad p=3/2. \qquad (19)$$

Comparison with experiment, taking $V_{cl}=10^{-20}$ cm^3 and $K_0=10^5$ J/m^3, gives the function $\lambda(T)/\lambda(T_N)$, where $\lambda(T_N)\sim 10^{-2}C_{11}$.

4. COMPARISON OF THEORY WITH EXPERIMENT

We found the defect of Young's modulus as the difference between the extrapolated linear dependence $f^2(T)$ (straight lines in Fig. 1) and the experimentally observed dependence above the Néel point (Fig. 1). The defect of Young's modulus decreases with increasing temperature T (Figs. 4a and 5a). The change in the magnetostriction constant $\lambda(T)$ with increasing T (Figs. 4b and 5b) can be estimated from equation[4]

$$\Delta E^{\exp}=\Delta C_{11}^{(0)}[\lambda(T)/\lambda(T_N)]^2, \qquad (20)$$

where $\Delta C_{11}^{(0)}(T)$ is calculated using Eq. (18) for $\lambda(T)=\mathrm{const}$ (Fig. 3).

The data obtained (Figs. 4 and 5) testify that the content of interstitial impurities in the solid solution, substitutional impurities, and the presence of precipitates of a second phase in some samples, influence the temperature dependences of ΔE and λ. These differences could be due to a different volume V_{cl} of antiferromagnetic clusters in Eq. (18) and a different magnetic anisotropy constant $K(T)$ (19). The experimental curves $\lambda(T)$ obtained are similar to those for the magnetostriction constants of 3*d*-group magnets.[17]

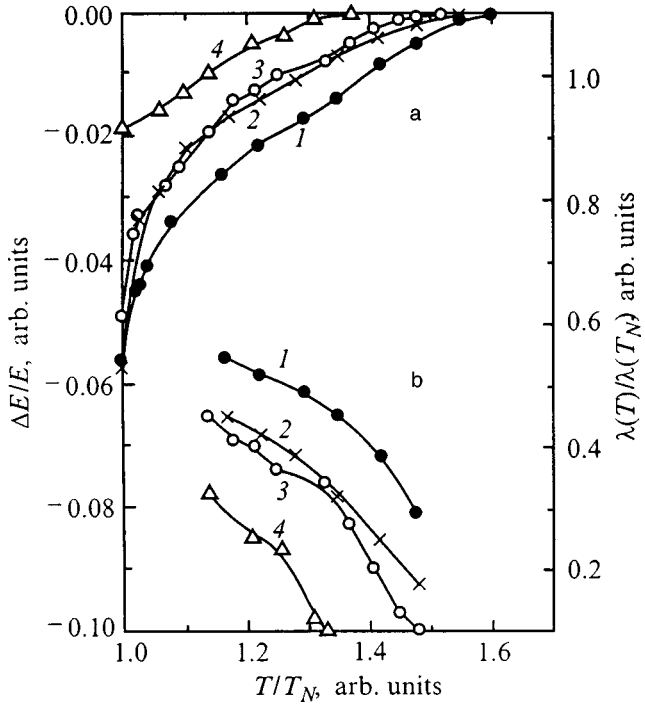

FIG. 4. Temperature dependences of the defect $(\Delta E/E)(T)$ of Young's modulus (a) and the magnetostriction constant $\lambda(T)/\lambda(T_N)$ (b) in a Cr [110] single crystal. *1* — Quenched from 1400 K to the eutectic, *2* — annealed for 2 h at 1400 K, *3* — annealed Cr polycrystal (No. 9), *4* — the alloy Cr–5wt.%MgO.

Comparing the experimental data (Table I and Fig. 1) near T_N in Cr alloys with the theoretical dependences (14) and (15) shows that impurities affect strongly the distribution of domains of the ordered phase. The possible nonuniform distribution of impurities (at the boundaries of crystallites in polycrystals and on dislocations in single crystals) should influence the parameters γ_j and k_j characterizing j-type walls of the transitional domain structure near T_N. The data obtained show that the transitional domain structure near T_N has the dominant effect on the singularity in sound propagation.

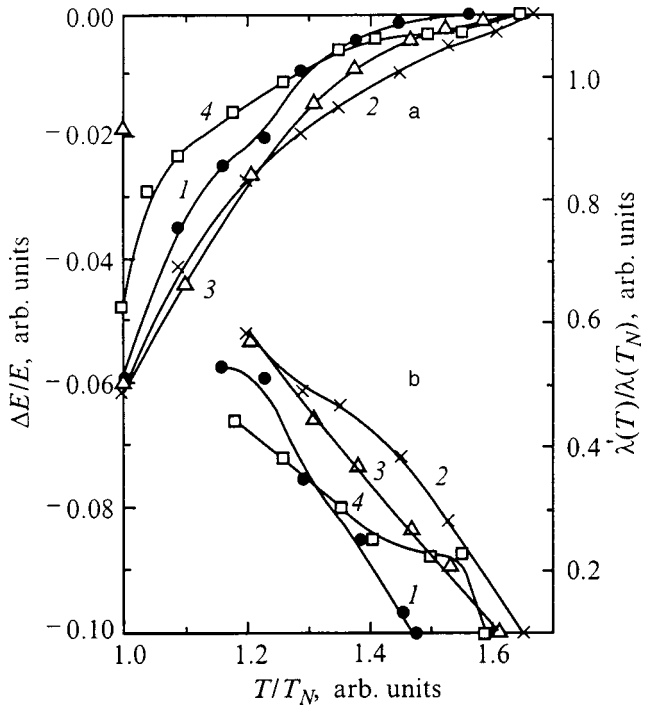

FIG. 5. Same as Fig. 4 for Cr alloys. *1* — Cr–0.5%N, *2* — Cr–0.4%Zr–0.5%N, *3* — Cr–0.9%Fe, *4* — Cr–0.5%Nb.

5. APPLICABILITY OF THE COVALENT MODEL OF CHARGE AND SPIN DENSITY WAVES

The model of localized (covalent and magnetic) electrons has an advantage over the band model of Overhauser *et al.* (see Ref. 1) for detailed description of the charge and spin densities in transition metals with variable valence. The linear relation between the parameters in the covalent and spin Hamiltonians gives the experimentally observed relation between the periods of the charge and spin-density waves. The SDW period is two times smaller. The equation for the SDW vector $2\mathbf{Q}$ leads to the conditions for the existence of SDWs, a first-order transition from SDW into a commensurate (Néel) phase. The phase diagram of Cr alloys containing an SDW phase determines the stability of short-range Néel order.

As soon as the inequality (17) (the condition for the stability of long-range Néel order (C phase) relative to the formation of SDWs) breaks down, the breakdown of SDWs at temperatures $T>T_N$ leads to short-range Néel AFM order. The existence of AFM clusters is manifested as an SAFM phase. The most striking characteristic of the SAFM phase in Cr-type cubic crystals is the anomalous growth of the elastic moduli ($C_{11}(T)$) with increasing T above T_N. A numerical calculation of the defect $\Delta C_{11}(T)$ of the modulus can be checked experimentally. For a fixed volume V_{cl} of AFM clusters and anisotropy constant $K(T)$ of the AFM, the adjustable parameter is the relative magnetostriction constant $\lambda(T)/\lambda(T_N)$. The measured $\lambda(T)$ curves are typical for $3d$ alloys, confirming the applicability of the covalent model of SDWs.

In conclusion, we can draw some specific conclusions.

1) The quasichemical model of the covalent bond of $3d$ ions describes in detail the CDW and SDW state. It is based on the variable valence of $3d$ ions.

2) The CDW period is two times larger than the SDW period. The structure vector $\mathbf{Q}$ is found from the equation relating the dispersion $\Gamma_n(\mathbf{Q})$ of the covalent interaction and the Coulomb integrals U_n. When the dispersion of the exchange integrals $A_{ij}^{(n)}(\mathbf{Q})$ is taken into account, a small peak appears in $\mathbf{Q}(T)$ near T_N.

3) Antiferromagnetic exchange between different sublattices {000} and {1/2 1/2 1/2} plays the dominant role. It determines T_N.

4) The existence of an SAFM phase at temperatures $T_N<T<\lesssim 2T_N$ in Cr and its alloys, which possess SDWs at temperatures $T<T_N$, explains the anomalous growth of the elastic modulus $C_{11}(T)$ with increasing T for $T\lesssim 500$ K.

5) The measured anomalies in sound propagation in Cr and its alloys with Zn, N, Nb, MgO, Fe, ... corroborate the theory. The increase in $C_{11}(T)$ above T_N is not correlated

with the peak anomalies in the defect of C_{11} and the damping of sound near T_N.

6) The interpretation of the experimental data gives the temperature dependences of the magnetostriction constants $\lambda(T)$. Their behavior for $T_N < T \lesssim 2T_N$ agrees with the magnetostriction theory and the experimental data for 3*d*-group magnets.

7) The parameters of the transitional domain structure [quasielastic force k_j and damping γ_j of domain walls of type j) are sensitive to impurities and structural defects (dislocations and boundaries of crystallites)].

8) It can be concluded from the data presented in Table I that the anomalies in sound propagation near T_N are determined by the parameters of the transitional domain structure of a first-order transition. Here:

a) The greatest damping in the transitional region $(\Delta_h)_{T_N}$ is observed in pure Cr. According to Eq. (15), it corresponds to small values of the quasielastic force k_j of the walls j. The latter also determine the largest values of the defects $|\Delta E/E|_{T_N}$ of Young's modulus according to Eq. (14).

b) The smallest damping in the transitional region is observed in Cr alloys with additions of Nb and MgO. According to Eqs. (14) and (15), it correlates with the lowest values of $|\Delta E/E|_{T_N}$ and can be explained by impurity segregation along domain walls, which increases k_j.

c) The large variance in the values of $(\Delta_h)_{T_N}$ as compared to the variance in the data for the defect $|\Delta E/E|_{T_N}$ of the modulus is explained, according to Eq. (15), by the variance of the values of γ_j in the limit $\gamma_j \omega \ll k_j$.

This work was partially supported by grants 2.4/965 and 2.4/993 from the Ukrainian Fund for Fundamental Research.

*)E-mail: golub@imag.kiev.ua

[1] E. I. Kondorskiĭ, *Itinerant Theory of Magnetism, Part 2* [in Russian] (Moscow State University, Moscow, 1977).
[2] A. I. Mitsek and T. V. Golub, Fiz. Met. Metalloved. **66**(1), 95 (1988).
[3] A. J. Kotani, J. Phys. Soc. Jpn. **36**, 103 (1974).
[4] A. I. Mitsek, V. N. Pushkar', and V. A. Mitsek, Metallofizika (Kiev) **18**(5), 37 (1996).
[5] W. C. Muir, E. Fawcett, and J. M. Petz, Phys. Rev. Lett. **59**, 335 (1987).
[6] J. Ziman, *Electrons and Phonons* [Clarendon Press, Oxford, 1960; IIL, Moscow, 1962].
[7] E. A. Turov and A. I. Mitsek, Zh. Éksp. Teor. Fiz. **38**, 1847 (1960) [Sov. Phys. JETP **11**, 1327 (1960)].
[8] A. S. Nowick and B. S. Berry, *Anelastic Relaxation in Crystalline Solids* (Academic Press, New York, 1972; Atomizdat, Moscow, 1975).
[9] T. V. Golub, V. G. Ivanchenko, and O. N. Kashevskaya, Metallofizika (Kiev) **13**(9), 114 (1991).
[10] A. I. Mitsek, Phys. Status Solidi B **152**, 507 (1989).
[11] A. I. Mitsek and V. A. Mitsek, Phys. Status Solidi B **199**, 549 (1997).
[12] A. I. Mitsek and V. N. Pushkar', Fiz. Tverd. Tela (St. Petersburg) **37**, 2865 (1995) [Phys. Solid State **37**, 1581 (1995)].
[13] A. I. Mitsek, Ukr. Fiz. Zh. **41**, 91 (1996).
[14] B. Coqblin, *The Electron Structure of Rare–Earth Metals and Alloys: the Magnetic Heavy Rare–Earths* (Academic Press, San Fransisco, 1977).
[15] A. I. Mitsek, Ukr. Fiz. Zh. **32**, 103 (1987).
[16] P. de V Du Plessis, A. M. Venter, and G. H. F. Brist, J. Phys.: Condens. Matter **7**, 9863 (1955).
[17] R. M. Bozorth, *Ferromagnetism* (Van Nostrand, New York, 1951; IIL, Moscow, 1956).

Translated by M. E. Alferieff

LOW-DIMENSIONAL SYSTEMS AND SURFACE PHYSICS

Theory of Raman light scattering by nanocrystal acoustic vibrations

S. V. Gupalov and I. A. Merkulov

A. F. Ioffe Physicotechnical Institute, Russian Academy of Sciences, 194021 St. Petersburg, Russia
(Submitted December 3, 1998)
Fiz. Tverd. Tela (St. Petersburg) **41**, 1473–1483 (August 1999)

A theory of Raman scattering of light by acoustic phonons in spherical nanocrystals of zinc-blende and wurtzite semiconductors has been developed with the inclusion of the complex structure of the valence band. The deformation-potential approximation was used to describe the exciton-phonon interaction. It is shown that this approximation allows only Raman scattering processes involving spheroidal acoustic phonons with a total angular momentum $F=0$ or 2. The effect of phonon quantum confinement on linewidth in Raman scattering spectra and scattered polarization is analyzed. An expression for the shape of the spectral line corresponding to nonresonant scattering from $F=0$ phonons was obtained. © *1999 American Institute of Physics.* [S1063-7834(99)02508-3]

Raman scattering, in which the frequencies of scattered and incident light differ by a fixed amount corresponding to the characteristic vibrational frequency of the medium, is one of the most informative optical methods to study excitations in solids. This method was used to advantage to investigate the spectra of optical phonons, magnons, etc.

A distinctive feature of light scattering by acoustic phonons in a heterogeneous crystalline medium, for instance, in a bulk semiconductor, is the strong dependence of the frequency difference between the incident and scattered photons on the angle between their wave vectors. This dependence follows from the energy and momentum conservation laws and the linear acoustic-phonon dispersion relation. Note that, because the photon momentum is small, the acoustic phonon involved in a scattering event will have a vanishing wave vector and, hence, a vanishing energy as well (Mandelshtam–Brillouin scattering).

In the case of a spatially inhomogeneous medium, such as a system of spherical semiconductor nanocrystals (quantum dots) distributed randomly in a dielectric matrix, the momentum conservation law for the scattering process breaks down, and one observes instead Raman scattering by acoustic phonons. Raman spectra carry information on the nature of the vibrational modes of nanocrystals, whose study is attracting presently considerable interest.[1–9] Some studies[1–8] propose considering acoustic vibrations of a nanocrystal as vibrational modes of an elastic sphere with a free surface.[1)] The scattering spectrum from such vibrations consists of narrow lines whose position is determined by the condition of vanishing of the forces applied from outside the nanocrystal surface. Similar narrow lines, but with somewhat different frequencies, should arise also in scattering by nanocrystals fixed in an absolutely rigid matrix.[7,8] In this case the acoustic vibrational modes are found by equating to zero the atomic displacements on the nanocrystal surface adjoining the nondeformable matrix.

In the conditions typical of the recent experiments,[8,9] both boundary conditions are far from being realizable. The sound velocities in, and the density of the nanocrystals (CdS) and of the silicate-glass matrix differ only insignificantly. It can be added that the acoustic vibrational modes of a nanocrystal lie within the continuum of the matrix. Interaction between the nanocrystal and matrix phonons should give rise to a substantial broadening of the initially narrow scattering lines from vibrational modes of a single quantum dot. In the limit of equal densities and sound velocities in a nanocrystal and the matrix, sound waves are not reflected from the nanocrystal interface, and there are no phonon-spectrum size-quantization effects. However, a feature in the Raman spectrum at the frequency of acoustic phonons whose wavelength is of the order of the quantum dot diameter appears in this case as well.[9] This feature (phonon pseudoquantization) is due to the fact that the scattering is dominated by processes in which a virtual electron-hole pair with a characteristic wave vector of the order of the reciprocal quantum-dot radius (R^{-1}) is excited in the nanocrystal. Such a pair emits or absorbs most effectively phonons having a wave vector $q\sim\pi/R$. Thus the question of the significance of phonon size quantization in a theoretical description of Raman scattering from nanocrystals still remains open.

The objective of this work was to calculate the line shape and polarization characteristics of Raman light scattering by nanocrystal acoustic vibrations with due inclusion of real boundary conditions and of the real structure of electronic levels in a quantum dot. As a zero approximation, we are going to consider the problem of light scattering from a spherical zinc-blende-lattice nanocrystal with a simple (doubly degenerate in electron spin) conduction band and a complex (consisting of light- and heavy-hole subbands) valence band.

As a result of reflections from the nanocrystal interface, the eigenstates of a size-quantized hole (or of the exciton as

a whole) become superpositions of the states of light and heavy holes (excitons). Similarly, the acoustic eigenmodes of a nanocrystal are superpositions of longitudinal and transverse vibrations. Note that the exciton wave function is affected substantially by the relative magnitude of the quantum-dot radius and the exciton Bohr radius, and the coordinate dependence of displacement in acoustic vibrations, by that of the sound velocities and densities of the nanocrystal and of the matrix in which it is embedded. We shall first discuss the main results of a theoretical calculation of exciton states and acoustic vibrational modes in a quantum dot, then we shall consider the matrix elements of optical and exciton–phonon transitions, and only after that shall we present the results of the calculation of the line shape and polarization characteristics of Raman scattering by quantum-dot acoustic vibrations.

1. GENERAL RELATIONS

To calculate the Raman scattering probability, we shall use the well-known expression[10]

$$W(\hbar\omega_i,\hbar\omega_f)=\frac{2\pi}{\hbar}\sum_{i,f}|M_{fi}|^2\ \delta(\hbar\omega_i-\hbar\omega_f\mp\hbar\Omega), \tag{1}$$

where

$$M_{fi}=\sum_{n,m}\frac{\langle 0|\hat{V}^*|n\rangle\langle n,N\pm1|H_{\text{ex-ph}}|m,N\rangle\langle m|\hat{V}|0\rangle}{(\hbar\omega_i-E_{\text{ex},m}-i\ \Gamma/2)(\hbar\omega_i-E_{\text{ex},n}-i\ \Gamma/2\mp\hbar\Omega)} \tag{2}$$

is the scattering matrix element calculated to third order in perturbation theory, $\langle m|\hat{V}|0\rangle$ and $\langle 0|\hat{V}^*|n\rangle$ are matrix elements of creation and recombination of the exciton in the quantum dot, $\langle n,N\pm1|H_{\text{ex-ph}}|m,N\rangle$ is the matrix element of exciton-phonon interaction, $\hbar\omega_i$ and $\hbar\Omega$ are the energies of the incident photon and emitted (absorbed) phonon, respectively, E_{ex} and $\Gamma/2$ are the real and imaginary parts of the intermediate-state energy of an electron-hole pair, and $N\equiv N(\hbar\Omega)=[\exp(\hbar\Omega/T)-1]^{-1}$ is the occupancy of the phonon state with which the exciton interacts (T is the temperature in energy units). Summation in Eq. (2) is done over all intermediate states (exciton magnetic sublevels), and in Eq. (1), over all initial and final states differing in the presence (absence) of a phonon with energy equal to the Stokes (anti-Stokes) shift.

The scattering matrix elements (2) for identical nanocrystals located at different points in space differ only in the phase advance of the light and acoustic waves. Nanocrystals are usually distributed in a random manner, with their separation exceeding considerably both their size and the wavelength of the emitted or absorbed phonons. In this case there is practically no coherence between photons scattered from different quantum dots so that, when calculating the scattering probability for the total quantum-dot system, the squared modulus of the scattering matrix element in Eq. (1) is equal to the sum of the squared moduli of scattering matrix elements for individual dots.

2. EXCITON QUANTIZATION IN SPHERICAL NANOCRYSTALS

The wave function of the electron-hole pair in a nanocrystal depends substantially on the relative magnitude of the nanocrystal radius (R) and the exciton Bohr radius in a bulk semiconductor (a_B). We shall limit ourselves in what follows to an analysis of the limiting cases $R\ll a_B$ and $R\gg a_B$.

In the first, strong quantization case, the wave function of the electron-hole pair is determined primarily by electron and hole reflections from the dot walls, and their Coulomb interaction is a weak perturbation. Then in zero approximation we shall have

$$\psi^{(\text{ex})}(\mathbf{r}_e,\mathbf{r}_h)\approx\psi^{(e)}(\mathbf{r}_e)\ \psi^{(h)}(\mathbf{r}_h), \tag{3}$$

where $\psi^{(e)}(\mathbf{r}_e)$ and $\psi^{(h)}(\mathbf{r}_h)$ are the wave functions of an electron and a hole localized in a quantum dot. The electron wave function for a spherical quantum dot with infinitely high walls is well known[11]

$$\psi^{(e)}_{n,l,m,\eta}(\mathbf{r}_e)=\frac{\sqrt{2}}{R^{3/2}}\,Y_{l,m}\left(\frac{\mathbf{r}_e}{r_e}\right)\frac{j_l(\phi^{(e)}_{l,n}r_e/R)}{j_{l+1}(\phi^{(e)}_{l,n})}|c,\eta\rangle, \tag{4}$$

where $Y_{l,m}$ are the normalized spherical functions, j_l are the Bessel spherical functions, l is the orbital momentum, m is its projection on the z axis, $\phi^{(e)}_{l,n}$ is the nth root of the j_l function, $|c,\eta\rangle$ are the Bloch functions at the conduction-band bottom, and η is the projection of the electron spin on the z axis. The lowest energy is identified with the electron state described by the usual spherical wave with an angular momentum $l=0$, $n=1$, and an arbitrarily oriented spin $s=1/2$. According to (4), its wave function can be written

$$\psi^{(e)}_{\eta}(\mathbf{r}_e)=\frac{1}{\sqrt{2\pi R}}\,\frac{\sin(\pi r_e/R)}{r_e}|c,\eta\rangle, \tag{5}$$

and its energy

$$E_e=\frac{\hbar^2\pi^2}{2m_eR^2}, \tag{6}$$

where m_e is the effective electron mass in the conduction band.

Because of the strong spin-orbit interaction in the valence band (the hole spin $J=3/2$), the state of a quantum-confined hole is not characterized by a fixed orbital momentum l_h. Neglecting the warping of constant-energy surfaces (spherical approximation), the good quantum number is the total hole momentum $\mathbf{F}_h=\mathbf{J}+\mathbf{I}_h$.[12] This state is $(2F_h+1)$-fold degenerate in the projection of $\mathbf{F}_h$ on the z axis (M). The ground state corresponds to $F_h=3/2$. Note that its wave function[13,14]

$$\psi^{(h)}_M(\mathbf{r}_h)=\sum_{\mu}R_{\mu M}(\mathbf{r}_h)\,|v,\mu\rangle, \tag{7}$$

where $|v,\mu\rangle$ are the Bloch functions at the valence-band top ($\mu=\pm3/2,\pm1/2$),

$$\hat{R}(\mathbf{r})=\frac{1}{\sqrt{4\pi}R^{3/2}}\left\{f_0\left(\frac{r}{R}\right)-f_2\left(\frac{r}{R}\right)\left[\left(\hat{\mathbf{J}}\frac{\mathbf{r}}{r}\right)^2-\frac{5}{4}\right]\right\} \tag{8}$$

is the envelope-function matrix, $\hat{J}_x, \hat{J}_y, \hat{J}_z$ are the 4×4 matrices of the angular-momentum projections corresponding to $J=3/2$, and the f_l functions determine the radial dependence of the envelopes and are linear combinations of the Bessel spherical functions. In the case of infinitely high barriers at the quantum-dot boundary we have[15]

$$f_l(x)=C\left[j_l(\phi^{(h)}x)-(-1)^{l/2}\frac{j_0(\phi^{(h)})}{j_0(\sqrt{\beta}\phi^{(h)})}j_l(\sqrt{\beta}\phi^{(h)}x)\right], \tag{9}$$

where β is the light- to heavy-hole-mass ratio, $\phi^{(h)}$ is the first root of the equation

$$j_0(x)\,j_2(\sqrt{\beta}x)+j_2(x)\,j_0(\sqrt{\beta}x)=0,$$

and the constant C is found from the normalization condition

$$\int_0^1 (f_0^2(x)+f_2^2(x))x^2\,dx=1\,.$$

For the energy of a quantum-confined hole one can write

$$E_h=\frac{\hbar^2\phi^{(h)2}}{2m_{hh}R^2}, \tag{10}$$

where m_{hh} is the heavy-hole effective mass, and the energy of an electron-hole pair under strong quantization is a sum of the energies (6) and (10).

In the second limiting case, $R\gg a_B$ (weak quantization), the exciton binding energy exceeds by far the size-quantization energy of the electron and the hole. In this case the wave function of a size-quantized electron-hole pair can be presented in zero approximation by an expansion in exciton wave functions at the center of the exciton Brillouin zone. Neglecting the exchange interaction between the electron and the hole, we can write the wave function of a fixed exciton in a form similar to Eq. (7)

$$\psi_{m,\eta}(\mathbf{r})=\left[\sum_\mu \varphi_{\mu m}(\mathbf{r})|v,\mu\rangle\right]|c,\eta\rangle\,, \tag{11}$$

where $\mathbf{r}=\mathbf{r}_e-\mathbf{r}_h$ is the position vector of the relative motion of the electron and the hole, and the matrix of the $\hat{\varphi}(\mathbf{r})$ functions describes the relative position of the electron and the hole attracted to one another by the Coulomb field. Similarly to matrix (8), it contains $s(l=0)$- and $d(l=2)$-like terms. It can be added that the latter may be neglected for most direct-band semiconductors.[16] Then $\varphi_{\mu m}(\mathbf{r})\approx\varphi_s(r)\,\delta_{\mu m}$, and

$$\psi_{m,\eta}(\mathbf{r})\approx\varphi_s(r)|v,m\rangle|c,\eta\rangle\,. \tag{12}$$

In this approximation, the wave function of relative motion of the electron and the hole for the exciton ground state can be written

$$\varphi_s(r)=\frac{1}{\sqrt{\pi a_B^3}}\exp(-r/a_B). \tag{13}$$

Taking into account Eq. (12), the wave function of the exciton ground state for a quantum dot of large radius $R\gg a_B$ can be written conveniently in the form

$$\psi_{M,\eta}(\mathbf{R},\mathbf{r})=\sum_m \mathcal{R}_{mM}(\mathbf{R})\,\psi_{m,\eta}(\mathbf{r})$$

$$=\left[\sum_\mu \mathcal{R}_{\mu M}(\mathbf{R})|v,\mu\rangle\right]\varphi_s(r)|c,\eta\rangle\,, \tag{14}$$

where matrix $\hat{\mathcal{R}}(\mathbf{R})$ is expressed, similarly to Eq. (8), through radial functions, which differ from functions (9) only in the light- and heavy-hole masses being replaced by the masses of the light- and heavy-hole exciton. In the weak-quantization conditions, the exciton energy is given by Eq. (10), where the mass of the heavy hole should be replaced by that of the heavy-hole exciton, minus the exciton binding energy in a bulk semiconductor.

3. ACOUSTIC PHONONS IN SPHERICAL NANOCRYSTALS AND THE EXCITON–PHONON INTERACTION

The equation describing propagation of a monochromatic elastic wave in an isotropic medium[17] can be presented in the form

$$[c_l^2\boldsymbol{\nabla}^2+(c_t^2-c_l^2)(\hat{\mathbf{I}}\boldsymbol{\nabla})^2]\mathbf{u}=\frac{\partial^2\mathbf{u}}{\partial t^2}, \tag{15}$$

where c_l and c_t are the longitudinal and transverse sound velocities, respectively, $\hat{I}_x, \hat{I}_y, \hat{I}_z$ are the 3×3 matrices of the angular-momentum projections corresponding to $I=1$, and $\mathbf{u}$ is the displacement vector. The bracketed operator on the left-hand side of Eq. (15) is similar to the Luttinger Hamiltonian in spherical approximation.[18]

Considered within the deformation potential approximation, the interaction of carriers with phonons depends linearly on the strain they produce. It can be added that electrons in a doubly spin-degenerate conduction band interact only with longitudinal phonons. The Hamiltonian of this interaction can be written in the form

$$\hat{\mathcal{H}}_{c,\mathrm{def}}=-a_c(\boldsymbol{\nabla}\mathbf{u}) \tag{16}$$

and does not contain the electron spin operator.[2)]

At the same time holes in a complex valence band are capable of interacting with both longitudinal and transverse acoustic phonons. The operator of this interaction can be written in spherical approximation[20]

$$\hat{\mathcal{H}}_{v,\mathrm{def}}=-a_v\ (\boldsymbol{\nabla}\mathbf{u})+\frac{b_v}{2}\sum_{\alpha,\beta}\left(\hat{J}_\alpha\hat{J}_\beta-\frac{5}{4}\delta_{\alpha\beta}\right)$$

$$\times(\nabla_\alpha u_\beta+\nabla_\beta u_\alpha)\,. \tag{17}$$

The first term on the right of Eq. (17) describes interaction only with longitudinal acoustic phonons, and the second, with longitudinal and transverse ones. The presence of the second term opens a possibility for hole spin-flip transitions. (There is no such interaction for the $s=1/2$ electron.)

3.1 Interaction of quantum-confined carriers with bulk phonons

Sirenko *et al.* calculated the Raman scattering of light in nanocrystals by acoustic vibrations of a homogeneous elastic medium, i.e., neglecting the difference between the elastic

constants of the nanocrystal and of the medium in which it is embedded.[9] The consideration was carried out for a simple band structure, where the interaction with the acoustic vibration of both the electron and the hole is described by Hamiltonian (16). Such an approach allows scattering by longitudinal acoustic phonons only. A comparison of Eqs. (17) and (16) reveals that a complex valence-band structure opens additional Raman scattering channels associated with the hole spin-flip. Such spin-flips should give rise to depolarization of light scattered from longitudinal acoustic phonons, as well as to lifting of forbiddenness from transitions involving transverse acoustic phonons.

Indeed, for a plane acoustic wave corresponding to the displacement[3)]

$$\mathbf{u}(\mathbf{r},t)=\boldsymbol{\nu}(\mathbf{k})\ \exp\ (i(\mathbf{kr}-\Omega t))+\text{c.c.}, \tag{18}$$

where $\mathbf{k}$ is the wave vector, Ω is the frequency, and $\boldsymbol{\nu}(\mathbf{k})$ is the polarization vector of the acoustic wave (for a longitudinal wave $\boldsymbol{\nu}(\mathbf{k})\|\mathbf{k}$), and calculation of the matrix elements of operator (17) using functions (7) yields

$$\hat{H}_{v,\mathrm{def}}(\mathbf{k},\boldsymbol{\nu}(\mathbf{k}),t)=\hat{h}(\mathbf{k},\boldsymbol{\nu}(\mathbf{k}))\exp(-i\Omega t) - \hat{h}(\mathbf{k},\boldsymbol{\nu}^*(\mathbf{k}))\exp(i\Omega t), \tag{19}$$

where

$$\hat{h}(\mathbf{k},\boldsymbol{\nu})=A_v(kR)\,(\mathbf{k}\,\boldsymbol{\nu})+B_v(kR)\,(\mathbf{k}\,\boldsymbol{\nu})\left(\frac{(\mathbf{k}\hat{\mathbf{J}})^2}{k^2}-\frac{5}{4}\right) + C_v(kR)\left[(\mathbf{k}\hat{\mathbf{J}})(\boldsymbol{\nu}\,\hat{\mathbf{J}})+(\boldsymbol{\nu}\,\hat{\mathbf{J}})(\mathbf{k}\hat{\mathbf{J}})-2(\mathbf{k}\,\boldsymbol{\nu})\frac{(\mathbf{k}\hat{\mathbf{J}})^2}{k^2}\right]. \tag{20}$$

The first two terms on the right-hand side of Eq. (20) describe interaction with the longitudinal wave, and the third one that with the transverse one; the actual form of the $\hat{h}(\mathbf{k},\boldsymbol{\nu})$ operator can be found only from symmetry considerations. The coefficients $A_v(kR),B_v(kR)$, and $C_v(kR)$ having the dimensionality of the deformation potential constants a_v and b_v can be written

$$A_v(kR)=i\int_0^1 dx\,x^2\{-a_v\,j_0(kRx)\,[f_0^2(x)+f_2^2(x)] + 2\,b_v\,j_2(kRx)\,f_0(x)\,f_2(x)\}, \tag{21}$$

$$B_v(kR)=i\int_0^1 dx\,x^2\Big\{-2\,a_v\,j_2(kRx)\,f_0(x)\,f_2(x) + b_v\,j_0(kRx)\left[f_0^2(x)-\frac{3}{5}f_2^2(x)\right] - \frac{4}{7}b_v\,j_2(kRx)\,f_2^2(x) + \frac{36}{35}b_v\,j_4(kRx)\,f_2^2(x)\Big\}, \tag{22}$$

$$C_v(kR)=i\int_0^1 dx\,x^2\Big\{\frac{1}{2}b_v\,j_0(kRx)\left[f_0^2(x)-\frac{3}{5}f_2^2(x)\right] - \frac{1}{7}b_v\,j_2(kRx)\,f_2^2(x) - \frac{12}{35}b_v\,j_4(kRx)\,f_2^2(x)\Big\}. \tag{23}$$

For $k\gg R^{-1}$, the integrals in Eqs. (21)–(23) decrease rapidly with increasing k, and for $k\to 0$, $\hat{H}_{v,\mathrm{def}}[\mathbf{k},\boldsymbol{\nu}(\mathbf{k}),t]$ tends to zero as k does. Taking into account the density of phonon states in a bulk semiconductor ($\propto k^2$) and the normalization of displacement ($\propto 1/\sqrt{k}$) obtained by the secondary quantization technique,[21] we obtain that, for $k\to 0$, the hole contribution to the probability of Raman scattering from bulk phonons in a nanocrystal $W^{(h)}(\hbar\omega_i,\hbar\omega_f)\to 0$ as k^3. Thus the hole interacts most strongly with the phonons whose wavelength is of the order of the quantum-dot diameter (phonon pseudoquantization). Obviously enough, the electron contribution has the same property.[9]

3.2 Selection rules

By expanding any solution of Eq. (15) in a Fourier integral, one can use Eq. (19) to obtain the operator for interaction of the acoustic phonon corresponding to this solution with a quantum-confined hole. It would be convenient, however, to construct another basis of solutions which would reflect the symmetry properties of Eq. (15). It was shown[12] that the bracketed operator on the right of Eq. (15) commutes with the operators of the total momentum, $\hat{\mathbf{F}}=\hat{\mathbf{L}}+\hat{\mathbf{I}}$ and of its projection $\hat{F}_z$ ($\hat{\mathbf{L}}$ is the phonon orbital-momentum operator). Therefore, it appears natural to choose for basis functions the following functions

$$\mathbf{u}^L_{F,F_z}(\mathbf{r},t)=\sqrt{\frac{2}{\pi}}j_L(qr)\mathbf{Y}^L_{F,F_z}\left(\frac{\mathbf{r}}{r}\right)\exp(-i\Omega t)+\text{c.c.}, \tag{24}$$

where $\mathbf{Y}^L_{F,F_z}(\mathbf{r}/r)$ are the spherical vectors introduced in Refs. 22 and 23, and L, by the momentum summation rule, can take on the values $L=F,F\pm 1$ for $F\neq 0$ and $L=1$ for $F=0$. The operator in brackets on the left side of Eq. (15) commutes with operators $\hat{\mathbf{F}}$ and $\hat{F}_z$ but does not commute with the $\hat{\mathbf{L}}$ operator. Therefore it has a block-diagonal form in the (24) basis. Taking into account the commutation of this operator with the parity operator as well, it becomes clear that the dimension of the blocks is one or two.[4)] The solutions diagonalizing this operator were constructed by Lamb[26] more than a century ago (see also Refs. 1,2,6,7,27 and 28). Because they are either purely longitudinal or purely transverse in form, they can be expressed through the scalar, φ^s_{F,F_z}, and vector, $\mathbf{A}_{F,F_z}$, potentials

$$\varphi^s_{F,F_z}(\mathbf{r},t)=j_F(q_l r)\,Y_{FF_z}\left(\frac{\mathbf{r}}{r}\right)\exp(-i\Omega t)+\text{c.c.}, \tag{25}$$

$$\mathbf{A}_{F,F_z}(\mathbf{r},t)=j_F(q_t r)\,Y_{FF_z}\left(\frac{\mathbf{r}}{r}\right)\mathbf{r}\exp(-i\Omega t)+\text{c.c.}, \tag{26}$$

where $q_l=\Omega/c_l$ and $q_t=\Omega/c_t$. The corresponding displacement functions are given in Appendix A in an explicit form.

The matrix element for transition of a quantum-confined hole from a state with a total angular-momentum projection M_1 to another state with a total angular-momentum projection M_2 as a result of interaction with an acoustic vibration (24) is given by the expression

$$\langle M_2|\hat{H}^L_{FF_z}(q)|M_1\rangle=\frac{1}{(2\pi)^3}\int d\mathbf{k}\,\langle M_2|\hat{H}_{v,\mathrm{def}} \times(\mathbf{k}\,\boldsymbol{\nu}^L_{F,F_z}(\mathbf{k}),t)|M_1\rangle\,, \tag{27}$$

where

$$\boldsymbol{\nu}^L_{F,F_z}(\mathbf{k})=\sqrt{\frac{2}{\pi}}\int j_L(qr)\mathbf{Y}^L_{F,F_z}\left(\frac{\mathbf{r}}{r}\right)\exp(-i\mathbf{kr})\,d\mathbf{r} =(-i)^L(2\pi)^{3/2}\frac{\delta(k-q)}{k^2}\,\mathbf{Y}^L_{F,F_z}\left(\frac{\mathbf{k}}{k}\right). \tag{28}$$

Substituting (28) and (19) in Eq. (27) yields

$$\begin{aligned}\langle M_2|\hat{H}^L_{FF_z}(q)|M_1\rangle &=(-1)^{3/2+M_2}\left[\begin{pmatrix}\frac{3}{2} & \frac{3}{2} & F\\ M_2 & -M_1 & -F_z\end{pmatrix}\exp(-i\Omega t)\right.\\ &\left.+(-1)^{F_z}\begin{pmatrix}\frac{3}{2} & \frac{3}{2} & F\\ M_2 & -M_1 & F_z\end{pmatrix}\exp(i\Omega t)\right]\frac{iq}{\sqrt{2}\,\pi}\\ &\times\{-2A_\nu(qR)\,\delta_{F0}+[2\sqrt{2/5}\,(B_\nu(qR)-2C_\nu(qR))\\ &+2\sqrt{10}\,C_\nu(qR)]\,\delta_{F2}\,\delta_{L1}+2\sqrt{3/5}\,(B_\nu(qR)\\ &-2C_\nu(qR))\,\delta_{F2}\,\delta_{L3}\}\,.\end{aligned} \tag{29}$$

The Wigner $3j$ symbols entering this equation describe the law of total angular-momentum conservation in interaction with a phonon. The first $3j$ symbol corresponds to absorption, and the second, to emission of a phonon with frequency Ω, total momentum F, and its projection F_z. The Kronecker-δ symbols in the braces determine the selection rules, namely, the matrix element (29) is nonzero only when light is scattered by acoustic phonons with a total angular momentum $F=0,2$ and an odd orbital momentum L.

Note that, as follows directly from the angular momentum and parity conservation laws, only vibrational modes with $F=0,1,2,3$ and an odd L can interact with a hole. The forbiddenness of interaction with acoustic phonons having a total momentum $F=1$ and 3 is not so rigorous. It arises within the deformation potential approximation and is due to time-reversal invariance (see Appendix B).

3.3 Phonon size quantization

We have been considering the interaction of an electron and a hole with acoustic vibrations in a nanocrystal neglecting the difference between the elastic constants inside and outside the latter. It appears substantially more interesting (while more complex too) to take into account the difference between the parameters of acoustic phonons in the nanocrystal and the matrix in which it is embedded which should result in a manifestation of quantum-confinement effects in the acoustic-vibration spectrum. The nanocrystal vibrational modes lie in the continuum of acoustic-phonon states of the matrix. Therefore the levels corresponding to the acoustic vibrational modes of a quantum dot should be broadened substantially. Nevertheless, as this will be shown later, quantum confinement of phonons affects noticeably the line shape in Raman scattering spectra.

In a general case, phonon quantum confinement assumes imposing a boundary condition on the nanocrystal surface. This results in two types of solutions. The first type represents a linear combination of solutions of type (A1) and (A3). They were named[1–6] spheroidal modes.[5)] The solutions of the second type, toroidal[1] or torsional[2–6] modes, are related to displacements of type (A2). Thus the selection rules obtained by us indicate that the above model of exciton-phonon interaction allows only Raman scattering from spheroidal vibrations with momentum $F=0$ or 2. Similarly to observations of such processes, Tanaka *et al.*[5] and Saviot *et al.*[7] interpreted their experimental data of Raman scattering by CdS and CdSe nanocrystals, respectively. The same selection rules were obtained by assuming the polarizability tensor to be symmetrical.[29]

We are going to consider the simplest case of an acoustic vibration of a sphere with $F=0$ (a fully symmetric vibration), which can be presented as a superposition of longitudinal plane waves only. Vector $\mathbf{u}$ of a fully symmetric vibration is directed along $\mathbf{r}$, and inside a quantum dot ($r<R$) can be written in the form

$$\begin{aligned}\mathbf{u}_{in}(\mathbf{r})&=\sqrt{\frac{2}{\pi}}\;\mathcal{A}(\Omega,R)\,j_1(q_{in}r)\,\mathbf{Y}^1_{0,0}\left(\frac{\mathbf{r}}{r}\right)\exp(-i\Omega t)+\text{c.c.}\\ &=-\frac{\sqrt{2}}{\pi}\cos(\Omega t)\,\mathcal{A}(\Omega,R)\,j_1(q_{in}r)\,\frac{\mathbf{r}}{r}\\ &=-\frac{\sqrt{2}}{\pi}\cos(\Omega t)\,\mathcal{A}(\Omega,R)\left[\frac{\sin(q_{in}r)}{(q_{in}r)^2}-\frac{\cos(q_{in}r)}{q_{in}r}\right]\frac{\mathbf{r}}{r},\end{aligned} \tag{30}$$

where $q_{in}=\Omega/c_l^{(in)}$, and $c_l^{(in)}$ is the longitudinal sound velocity in the nanocrystal. Outside the quantum dot ($r>R$), the same solution of Eq. (15) has the form

$$\mathbf{u}_{\mathrm{out}}(\mathbf{r})=-\frac{\sqrt{2}}{\pi}\cos(\Omega t)\,\mathcal{B}(\Omega)\left[\frac{\sin(q_{\mathrm{out}}r+\alpha)}{(q_{\mathrm{out}}r)^2}-\frac{\cos(q_{\mathrm{out}}r+\alpha)}{q_{\mathrm{out}}r}\right]\frac{\mathbf{r}}{r}, \tag{31}$$

where $q_{\mathrm{out}}=\Omega/c_l^{(\mathrm{out})}$, and $c_l^{(\mathrm{out})}$ is the longitudinal sound velocity in the glass matrix. By choosing for the boundary condition on the sphere's surface the continuity of the displacement vector and of the stress tensor, one readily obtains a relation between the vibration amplitudes outside and inside the quantum dot[6)]

$$\mathcal{A}(\Omega,R)=\left(\frac{c_l^{(\mathrm{out})}}{c_l^{(\mathrm{in})}}\right)^2\frac{\mathcal{B}(\Omega)\,(q_{\mathrm{in}}R)^2}{Y(q_{\mathrm{in}}R)}, \tag{32}$$

where

$$Y(x)=\sqrt{\left(\frac{c_l^{(\mathrm{out})}}{c_l^{(\mathrm{in})}x}\right)^2[Z(x)+x^2(x\cos x-\sin x)]^2+Z^2(x)}\,,$$

$$Z(x)=4\left(\frac{c_t^{(\mathrm{in})}}{c_l^{(\mathrm{in})}}\right)^2\left[\frac{\rho_{\mathrm{in}}}{\rho_{\mathrm{out}}}-\left(\frac{c_t^{(\mathrm{out})}}{c_t^{(\mathrm{in})}}\right)^2\right](x\cos x-\sin x)$$
$$+\frac{\rho_{\mathrm{in}}}{\rho_{\mathrm{out}}}x^2\sin x\,, \tag{33}$$

ρ_{in}, ρ_{out}, $[c_t^{(\mathrm{in})}, c_t^{(\mathrm{out})}]$ is the density of the medium [transverse sound velocity] inside and outside the nanocrystal, respectively. [For $c_l^{(\mathrm{out})}=c_l^{(\mathrm{in})}$, $c_t^{(\mathrm{out})}=c_t^{(\mathrm{in})}$, and $\rho_{\mathrm{out}}=\rho_{\mathrm{in}}$, the interface separating the nanocrystal from the surrounding medium is absolutely transparent for acoustic waves, and the vibration amplitudes inside and outside the nanocrystal coincide: $\mathcal{A}(\Omega,R)=\mathcal{B}(\Omega)$].

The relation (32) connecting $\mathcal{A}(\Omega,R)$ and $\mathcal{B}(\Omega)$ remains valid when one crosses over to a quantum-mechanical description. This transition reduces formally to presenting the amplitudes in the form of a product of the sum of the phonon creation and annihilation operators $[\hat{a}^+(\Omega)+\hat{a}(\Omega)]$ by normalization coefficients. Assuming the volume of a quantum dot to be negligible compared to that of the surrounding matrix, we obtain the final expression for the Hermitian operator of the vibration amplitude inside the quantum dot:

$$\hat{\mathcal{A}}(\Omega,R)=\left(\frac{c_l^{(\mathrm{out})}}{c_l^{(\mathrm{in})}}\right)^2\frac{(q_{\mathrm{in}}R)^2}{Y(q_{\mathrm{in}}R)}\sqrt{\frac{\hbar}{2\,\rho_{\mathrm{out}}\Omega}}(\hat{a}^+(\Omega)$$
$$+\hat{a}(\Omega)). \tag{34}$$

As a result, Eq. (31) is replaced by

$$\mathbf{u}_{in}(\mathbf{r})=\sqrt{\frac{2}{\pi}}\hat{\mathcal{A}}(\Omega,R)\,j_1(q_{\mathrm{in}}r)\,\mathbf{Y}^1_{0,0}\left(\frac{\mathbf{r}}{r}\right). \tag{35}$$

In the approximation of an infinite potential barrier for the hole, only displacement inside the nanocrystal provides a contribution to the matrix element of the hole-phonon interaction operator. Then the matrix element of the operator describing interaction of a strongly quantized hole with a fully symmetric phonon can be written [compare Eq. (29) for $F=0$]

$$\langle M_2|\hat{H}_{h-ph}(\Omega)|M_1\rangle=\frac{i\,q_{\mathrm{in}}}{\sqrt{2}\,\pi}\hat{\mathcal{A}}(\Omega,R)\,A_v(q_{\mathrm{in}}R)\,\delta_{M_1,M_2} \tag{36}$$

or, taking into account (21),

$$\langle M_2|\hat{H}_{h-ph}(\Omega)|M_1\rangle=\hat{\mathcal{A}}(\Omega,R)\frac{q_{\mathrm{in}}}{\sqrt{2}\,\pi}\delta_{M_1,M_2}\Big\{a_v\int_0^1[f_0^2(x)$$
$$+f_2^2(x)]j_0(q_{in}Rx)x^2dx-2\,b_v$$
$$\times\int_0^1 f_0(x)f_2(x)j_2(q_{\mathrm{in}}Rx)x^2dx\Big\}\,. \tag{37}$$

In the case of Raman scattering, the matrix element of the exciton–phonon interaction operator is a sum of those of the electron–phonon and hole–phonon interaction operators. Under strong quantization, the matrix element of the electron–phonon interaction operator calculated using functions (5) has the form

$$\langle\eta_2|\hat{H}_{e-ph}(\Omega)|\eta_1\rangle=\hat{\mathcal{A}}(\Omega,R)\frac{q_{\mathrm{in}}}{\sqrt{2}\,\pi}\delta_{\eta_1,\eta_2}a_c$$
$$\times\int_0^1 2\sin^2(\pi x)\,j_0(q_{\mathrm{in}}Rx)dx\,. \tag{38}$$

As shown by direct calculations, the integral entering this expression differs from the first integral in Eq. (37) by less than 10%. Therefore, in the case of strong quantization, one can approximately describe the interaction of an electron-hole pair with a fully symmetric phonon by means of Eq. (37), in which the hole component of the deformation potential a_v is replaced by the sum a_c+a_v.

Under weak quantization, the calculations should also be carried out with Eq. (37). However the parameters a_v and b_v in this expression will now describe the effect of deformation potential on the exciton functions (14).

Thus, under both strong and weak quantization, the electron-hole pair interaction with a fully symmetric phonon is described by the matrix element $\langle M_2,\eta_2|\hat{H}_{\mathrm{ex-ph}}(\Omega)|M_1,\eta_1\rangle$, which coincides to within constants a_v and b_v with Eq. (37) and does not change the exciton spin state. Therefore the matrix element (2) of Raman scattering by a fully symmetric vibration of a spherical quantum dot can be presented in the form

$$M_{fi}=\langle N\pm1,f|\hat{H}_{\mathrm{ex-ph}}(\Omega)|N,i\rangle$$
$$\times\sum_n\frac{\langle 0|\hat{V}^*|n\rangle\langle n|\hat{V}|0\rangle}{(\hbar\omega_i-E_{\mathrm{ex},n}-i\Gamma/2)(\hbar\omega_i-E_{\mathrm{ex},n}-i\Gamma/2\mp\hbar\Omega)}. \tag{39}$$

4. MATRIX ELEMENTS OF OPTICAL TRANSITIONS AND THE POLARIZATION CHARACTERISTICS OF RAMAN SCATTERING

The matrix element of optical excitation of an electron-hole pair localized in a quantum dot in the $|n\rangle\equiv|M,\eta\rangle$ state is given by the expression

$$\langle M,\eta|\hat{V}|0\rangle = i\frac{2e\hbar p_{cv}}{m_0\omega_i}\mathcal{E}_0\,\kappa\,(-1)^{\frac{3}{2}-\eta}\sum_{\alpha}\,e^{\alpha} \times\begin{pmatrix} \frac{1}{2} & 1 & \frac{3}{2} \\ -\eta\alpha & -M & \end{pmatrix}, \tag{40}$$

where $\mathcal{E}_0$ and $\mathbf{e}$ are, respectively, the amplitude and unit vector defining the electric field of the incident light wave, $p_{cv}=\langle S|\hat{p}_x|X\rangle$ is the momentum-operator interband matrix element, and

$$\kappa=\sqrt{2}\int_0^1 f_0(x)\sin\pi x\,x\,dx \tag{41}$$

for the case of strong quantization, and

$$\kappa=2\left(\frac{R}{a_B}\right)^{3/2}\int_0^1 f_0(x)\,x^2\,dx \tag{42}$$

for weak quantization. Whence one obtains

$$\sum_{\eta;\,M}\langle 0|\hat{V}^*|M,\eta\rangle\langle M,\eta|\hat{V}|0\rangle = \frac{4}{3}\left(\frac{e\hbar|p_{cv}|}{m_0}\kappa\right)^2\frac{\mathcal{E}'^*_0\mathcal{E}_0}{\omega_i\omega_s}(\mathbf{e}\mathbf{e}'^*) \tag{43}$$

and, hence, for scattering from a $F=0$ phonon we have

$$|M_{fi}|^2=\frac{16}{9}\left(\frac{e\hbar|p_{cv}|}{m_0}\kappa\right)^4\frac{|\mathcal{E}'_0|^2|\mathcal{E}_0|^2}{\omega_i^2\omega_s^2}|(\mathbf{e}\mathbf{e}'^*)|^2 \times\frac{|\langle N\pm1,f|\hat{H}_{\text{ex-ph}}(\Omega)|N,i\rangle|^2}{|\hbar\omega_i-E_{\text{ex}}-i\Gamma/2|^2|\hbar\omega_i-E_{\text{ex}}-i\Gamma/2\mp\hbar\Omega|^2}. \tag{44}$$

Here $\mathbf{e}$ and $\mathbf{e}'$ are, respectively, vectors characterizing the incident and scattered light polarization, $\mathcal{E}'_0$ is the electric-field amplitude of the scattered wave, and $\omega_s\equiv\omega_i\mp\Omega$ is the secondary-radiation frequency. The exciton level is assumed eightfold degenerate. In this case, as seen from Eq. (44), the scattered light has the same polarization characteristics as the incident one. This coincidence is associated with the exciton-level degeneracy.

Such nanocrystals as CdS have the wurtzite lattice. The lowering of the symmetry produced by taking into account the lattice hexagonality results in a splitting of the exciton ground level into two sublevels, with $M=\pm3/2$ and $M=\pm1/2$, provided the quantization axis is aligned with the C_6 axis. This splitting is small compared to the separation between the quantum-confinement levels and can be taken into account in perturbation theory.[15] The electron-hole exchange interaction produces an additional splitting of the exciton level.[14] We are analyzing below the weak-quantization case, where the exchange splitting is small compared to the crystal-field one and, thus, may be neglected.

Introducing a unit vector $\mathbf{n}$ along the C_6 axis, we obtain for the $M=\pm1/2$ exciton sublevel

$$\sum_{\eta;\,M=\pm1/2}\langle 0|\hat{V}^*|M,\eta\rangle\langle M,\eta|\hat{V}|0\rangle = \frac{1}{3}\left(\frac{e\hbar|p_{cv}|}{m_0}\kappa\right)^2\frac{\mathcal{E}'^*_0\mathcal{E}_0}{\omega_i\omega_s}[(\mathbf{e}\mathbf{e}'^*)+3(\mathbf{e}\mathbf{n})(\mathbf{e}'^*\mathbf{n})], \tag{45}$$

and for the exciton sublevel with $M=\pm3/2$

$$\sum_{\eta;\,M=\pm3/2}\langle 0|\hat{V}^*|M,\eta\rangle\langle M,\eta|\hat{V}|0\rangle = \left(\frac{e\hbar|p_{cv}|}{m_0}\kappa\right)^2\frac{\mathcal{E}'^*_0\mathcal{E}_0}{\omega_i\omega_s}[(\mathbf{e}\mathbf{e}'^*)-(\mathbf{e}\mathbf{n})(\mathbf{e}'^*\mathbf{n})]. \tag{46}$$

Summation of Eqs. (45) and (46) yields Eq. (43), which corresponds to the case of a degenerate level. If there is no degeneracy, the scattering matrix element (39) contains the sum of expressions (45) and (46) with different energy denominators, which can be presented in the form $\Xi_\pm(\mathbf{e}\mathbf{e}'^*)+\Lambda_\pm(\mathbf{e}\mathbf{n})(\mathbf{e}'^*\mathbf{n})$, where

$$\Xi_\pm=4\left(\frac{e\hbar|p_{cv}|}{m_0}\kappa\right)^2\frac{\mathcal{E}'^*_0\mathcal{E}_0}{\omega_i\omega_s}\frac{[\hbar\omega_i-\varepsilon(R)-(i\Gamma\pm\hbar\Omega)/2]^2-(\hbar\Omega/2)^2+\Delta^2-[\hbar\omega_i-\varepsilon(R)-(i\Gamma\pm\hbar\Omega)/2]\,\Delta}{\{[\hbar\omega_i-\varepsilon(R)-i\Gamma/2]^2-\Delta^2\}\{[\hbar\omega_i-\varepsilon(R)-i\Gamma/2\mp\hbar\Omega]^2-\Delta^2\}},$$

$$\Lambda_\pm=12\left(\frac{e\hbar|p_{cv}|}{m_0}\kappa\right)^2\frac{\mathcal{E}'^*_0\mathcal{E}_0}{\omega_i\omega_s}\frac{[\hbar\omega_i-\varepsilon(R)-(i\Gamma\pm\hbar\Omega)/2]\,\Delta}{\{[\hbar\omega_i-\varepsilon(R)-i\Gamma/2]^2-\Delta^2\}\{[\hbar\omega_i-\varepsilon(R)-i\Gamma/2\mp\hbar\Omega]^2-\Delta^2\}}, \tag{47}$$

$\varepsilon(R)$ and Δ are, respectively, the half-sum and half-difference of the energies of the exciton sublevels with $M=\pm1/2$ and $M=\pm3/2$, and Γ is a parameter characterizing their homogeneous broadening caused by various relaxation processes. For resonant scattering from the first pair of sublevels, $3\Xi_\pm=\Lambda_\pm$, and for that from the second pair, $\Xi_\pm=\Lambda_\pm$. Averaging the square of the modulus of this expression in the direction of vector $\mathbf{n}$ for quantum dots of the same size and substituting it in Eq. (39) yields

$$|M_{fi}|^2=\frac{1}{15}\left(\frac{e\hbar|p_{cv}|}{m_0}\kappa\right)^4\frac{|\mathcal{E}_0'|^2|\mathcal{E}_0|^2}{\omega_i^2\omega_s^2}$$
$$\times|\langle N\pm1,f|\hat{H}_{\mathrm{ex-ph}}(\Omega)|N,i\rangle|^2\{[15\,|\Xi_\pm|^2$$
$$+5\,(\Xi_\pm\Lambda_\pm^*+\Lambda_\pm\Xi_\pm^*)+|\Lambda_\pm|^2]\,|(\mathbf{e}\,\mathbf{e}'^*)|^2$$
$$+|\Lambda_\pm|^2[1+|(\mathbf{e}\,\mathbf{e}')|^2]\}\,. \tag{48}$$

We shall write out now the expressions for the polarization of backscattered radiation. If the incident light is linearly polarized, one can readily obtain from Eq. (48) for the scattered linear polarization

$$\rho_L=\frac{15\,|\Xi_\pm|^2+5\,(\Xi_\pm\Lambda_\pm^*+\Lambda_\pm\Xi_\pm^*)+2\,|\Lambda_\pm|^2}{15\,|\Xi_\pm|^2+5\,(\Xi_\pm\Lambda_\pm^*+\Lambda_\pm\Xi_\pm^*)+4\,|\Lambda_\pm|^2}. \tag{49}$$

In the case of circularly polarized incident light, the circular polarization of the scattered radiation can be written

$$\rho_C=\frac{15\,|\Xi_\pm|^2+5\,(\Xi_\pm\Lambda_\pm^*+\Lambda_\pm\Xi_\pm^*)}{15\,|\Xi_\pm|^2+5\,(\Xi_\pm\Lambda_\pm^*+\Lambda_\pm\Xi_\pm^*)+4\,|\Lambda_\pm|^2}. \tag{50}$$

One readily sees that, in the case of resonant scattering from the first or second pair of sublevels (with $M=\pm1/2$ or $M=\pm3/2$, respectively), the backscattered polarization is the same ($\rho_L=7/9$, $\rho_C=5/9$). In the other limiting case where the energy difference between the scattered photon and the virtual electron-hole pair is considerably in excess of the splitting between the $M=\pm1/2$ and $M=\pm3/2$ sublevels, $|\Lambda_\pm|\ll|\Xi_\pm|$,

$$\rho_L\approx1-\frac{2\,|\Lambda_\pm|^2}{15\,|\Xi_\pm|^2}\approx1-\frac{2}{15}\left(\frac{\Delta}{\hbar\omega_i-\varepsilon(R)}\right)^2, \tag{51}$$

$$\rho_C\approx1-\frac{4\,|\Lambda_\pm|^2}{15\,|\Xi_\pm|^2}\approx1-\frac{4}{15}\left(\frac{\Delta}{\hbar\omega_i-\varepsilon(R)}\right)^2, \tag{52}$$

and the scattered polarization is close to 100%.

It should be stressed that 100% polarization of secondary radiation appears only under nonresonant scattering from a fully symmetric $F=0$ vibration. Emission or absorption of an $F=2$ phonon results in a change of the hole spin state and in depolarization of scattered light.

If one neglects the difference between the elastic constants of the nanocrystal and of the matrix, the dependence of the scattered intensity on phonon energy will be determined by pseudo-quantization only. And, due to the contribution of phonons with momentum $F=2$ to scattering, the scattered polarization under nonresonant excitation will be substantially less than 100%.

5. LINE SHAPE IN THE SPECTRUM OF NONRESONANT RAMAN SCATTERING BY A FULLY SYMMETRIC PHONON

For the case of nonresonant scattering by a fully symmetric phonon, the spectral line shape can be described by means of Eq. (44), neglecting in the energy denominators the phonon energy compared to the large phonon-energy detuning $|\hbar\omega_i-E_{ex}|\gg\hbar\Omega$. Then the dependence of the scattered intensity on $\hbar\Omega$ will be determined only by the probability

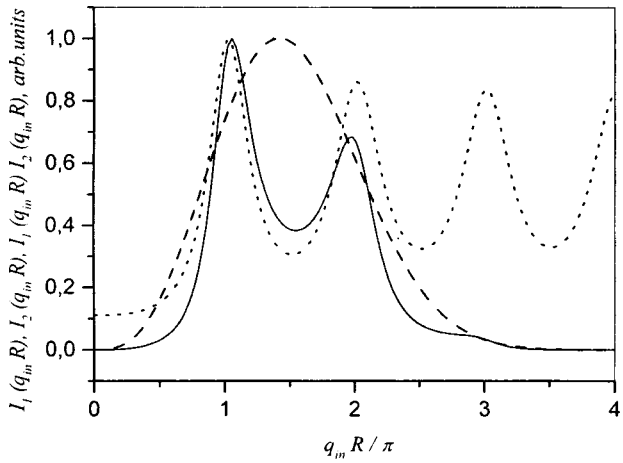

FIG. 1. $I_1(q_{in}R)$ (dashed line), $I_2(q_{in}R)$ (dotted line), and their product, $I_1(q_{in}R)\cdot I_2(q_{in}R)$, calculated using the parameters[30,31] describing a CdS nanocrystal in a silicate-glass matrix: $c_t^{(\mathrm{in})}=1.8\times10^5$ cm/s, $c_l^{(\mathrm{in})}=4.25\times10^5$ cm/s, $c_t^{(\mathrm{out})}=3.77\times10^5$ cm/s, $c_l^{(\mathrm{out})}=5.96\times10^5$ cm/s, $\rho_{\mathrm{in}}=4.82$ g/cm^3, $\rho_{\mathrm{out}}=2.2$ g/cm^3, $\beta=0.23$, and $b_v/a_v=0.13$.

of a virtual electron-hole pair emitting a phonon of the given energy. As discussed in Sec. 3, this dependence originates from two effects, namely, size quantization of acoustic vibrations of the nanocrystal and pseudoquantization, a process in which the phonon wave vector is determined by quantum confinement of the phonon-emitting or absorbing electron-hole pair. According to Eqs. (1), (34), (37), and (44), the line shape is given in this case by the product of several factors corresponding to the contributions of:

(1) quantum confinement of electrons and holes

$$I_1(q_{in}R)=(q_{in}R)^3\left\{\int_0^1[f_0^2(x)+f_2^2(x)]j_0(q_{in}Rx)x^2dx\right.$$
$$\left.-2\,b_v/a_v\int_0^1 f_0(x)f_2(x)j_2(q_{in}Rx)x^2dx\right\}^2, \tag{53}$$

(2) phonon confinement

$$I_2(q_{in}R)=\frac{(q_{in}R)^4}{Y^2(q_{in}R)}, \tag{54}$$

(3) phonon-state filling factor $N(\hbar\Omega)=[\exp(\hbar\Omega/T)-1]^{-1}$

$$\mathcal{I}(\hbar\Omega,R)\propto\frac{\kappa^4}{R^3}I_1\left(\frac{\Omega}{c_l^{(in)}}R\right)I_2\left(\frac{\Omega}{c_l^{(in)}}R\right)$$
$$\times\left(N(\hbar\Omega)+\frac{1\pm1}{2}\right), \tag{55}$$

where the factor $N(\hbar\Omega)+1$ corresponds to the Stokes, and $N(\hbar\Omega)$, to the anti-Stokes component of the scattering line. Figure 1 compares the line-shape contributions due to the phonon quantization and pseudoquantization effects for CdS nanocrystals embedded in a glass matrix. One readily sees that, despite the relatively small difference between the sound velocities in the nanocrystal and the glass matrix, quantum confinement of phonons provides a dominant contribution to the scattering line shape. Pseudoquantization re-

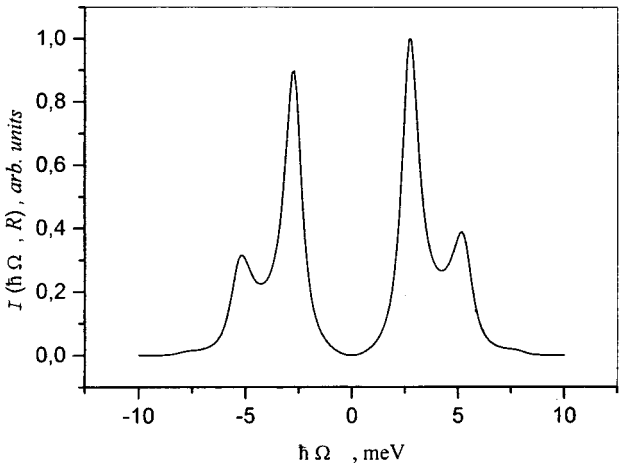

FIG. 2. Spectral line shape for nonresonant Raman light scattering from fully symmetric phonons in a nanocrystal of radius $R=33$ Å measured at $T=300$ K.

sults only in an insignificant additional line narrowing and suppression of the peaks corresponding to phonon resonances with $q_{in}R/\pi \geqslant 2$. Taking into account the dependence of the filling factors $N(\hbar\Omega)$ on phonon energy (Fig. 2) suppresses still more these peaks in scattering spectra while affecting very weakly the line shape. The main effect of this term reduces to a difference in the intensity of the processes involving the emission and absorption of phonons, which account for the Stokes and anti-Stokes spectral line components.

In order to describe quantitatively the experimentally observed spectra of nonresonant Raman light scattering by a system consisting of a large number of quantum dots one should fold the expression for the scattering probability by one quantum dot with the radial distribution function of a nanocrystal.

Let us sum up the above analysis of spectral line shape and polarization characteristics of Raman light scattering by acoustic phonons in a system of semiconductor-crystal quantum dots in a glass matrix. This scattering is dominated by spheroidal acoustic phonons with total momenta $F=0$ and 2.

Scattering by $F=2$ spheroidal phonons gives rise to depolarization of the secondary radiation. The emission or absorption of such a phonon can be accompanied by hole spin-flip. Scattering with electron spin-flip is possible only in weak interaction with phonons whose total momentum is $F=1$. This interaction would require going beyond the deformation potential approximation, and it originates from the mixing of the conduction-band-bottom with valence-band-top wave functions.[19]

In the case of nonresonant scattering by a fully symmetric vibration ($F=0$) the polarization of backscattered light practically coincides with that of the incident radiation.

Even if the sound velocities in CdS nanocrystals and the glass matrix they are embedded in differ very little for quantum dots of the same radius, the scattering line shape is dominated by phonon size quantization. The role of the electron and hole quantum confinement and of the energy dependence of phonon state filling reduces to suppression of the scattering involving absorption or emission of phonons with wave vectors exceeding noticeably π/R.

We owe our thanks to A. I. Ekimov who stimulated this work, and to O. G. Lyublinskaya, without whose stimulating discussions its completion would hardly have been possible. We are grateful also to E. I. Ivchenko who suggested to us the idea of the proof presented in Appendix B, and to V. I. Perel' and M. I. D'yakonov for fruitful discussions.

Support of the Russian Fund for Fundamental Research (Grants 96-02-16941 and 98-02-18267), Volkswagen Stiftung, as well as of the Young Scientists' Support Program, Russian Academy of Sciences, is gratefully acknowledged.

APPENDIX A: BASIS DISPLACEMENT FUNCTIONS

Basis displacement functions, which are eigenvectors of the operator in the brackets on the right side of Eq. (15), represent one longitudinal ($\mathbf{u}^{s}_{F,F_z}$) and two transverse ($\mathbf{u}^{v1}_{F,F_z}$ and $\mathbf{u}^{v2}_{F,F_z}$) solutions

$$\mathbf{u}^{s}_{F,F_z}(\mathbf{r},t)=\nabla\varphi^{s}_{F,F_z}\propto\left[\sqrt{F+1}\,j_{F+1}(q_l r)\,\mathbf{Y}^{F+1}_{F,F_z}\left(\frac{\mathbf{r}}{r}\right)+\sqrt{F}\,j_{F-1}(q_l r)\,\mathbf{Y}^{F-1}_{F,F_z}\left(\frac{\mathbf{r}}{r}\right)\right]\times\exp(-i\Omega t)+\text{c.c.}, \tag{A1}$$

$$\mathbf{u}^{v1}_{F,F_z}(\mathbf{r},t)=\nabla\times\mathbf{A}_{F,F_z}\propto j_F(q_t r)\,\mathbf{Y}^{F}_{F,F_z}\left(\frac{\mathbf{r}}{r}\right)\times\exp(-i\Omega t)+\text{c.c.}, \tag{A2}$$

$$\mathbf{u}^{v2}_{F,F_z}(\mathbf{r},t)=\nabla\times\nabla\times\mathbf{A}_{F,F_z}\propto\left[\sqrt{F}\,j_{F+1}(q_t r)\,\mathbf{Y}^{F+1}_{F,F_z}\left(\frac{\mathbf{r}}{r}\right)-\sqrt{F+1}\,j_{F-1}(q_t r)\,\mathbf{Y}^{F-1}_{F,F_z}\left(\frac{\mathbf{r}}{r}\right)\right]\times\exp(-i\Omega t)+\text{c.c.}. \tag{A3}$$

APPENDIX B: SELECTION RULES ASSOCIATED WITH TIME-REVERSAL INVARIANCE

Consider a vibration with a total angular momentum $F=1$ and an orbital momentum $L=1$. The displacement vector of such vibrations can be presented in the form of an expansion $\mathbf{u}(\mathbf{r},t)\propto\Sigma_{F_z=\pm1,0}(C_1^{F_z}\mathbf{Y}^1_{1,F_z}(\mathbf{r}/r)\exp(-i\Omega t)+\text{c.c.})$. The spherical vectors $\mathbf{Y}^1_{1,F_z}(\mathbf{r}/r)$ are covariant components of a first-rank irreducible tensor and transform through one another under rotation of the coordinate frame by means of Wigner's D function, $D^1_{F_z'F_z}(\alpha,\beta,\gamma)$, where α,β,γ are Euler's angles characterizing the rotation.[23] The $C_1^{F_z}$ coefficients are contravariant components of a first-rank irreducible tensor and transform through one another under rotation of the coordinate frame by means of $D^{1*}_{F_z'F_z}(\alpha,\beta,\gamma)$.

Because the displacement vector is real, one can conveniently operate in place of the cyclic components of first-rank tensors with their Cartesian components and write $\mathbf{u}(\mathbf{r})$ as an expansion $\mathbf{u}(\mathbf{r})\propto\Sigma_{\alpha=x,y,z}(C_{1\alpha}\mathbf{Y}^1_{1,\alpha}(\mathbf{r}/r)\exp(-i\Omega t)$

+c.c.). The deformation potential approximation assumes that the hole interacts at each instant of time with a quasistatic deformation field. The variation of this field in time enters the final expressions only through the phonon frequency determining the energy conservation law. Therefore the $C_{1\alpha}$ coefficients are real and $\mathbf{u}(\mathbf{r},t) \propto 2\cos\Omega t \Sigma_{\alpha=x,y,z} C_{1\alpha} \mathbf{Y}^1_{1,\alpha}(\mathbf{r}/r)$.

The operator describing interaction of a quantum-confined ground-state hole with the vibration under study is proportional to the scalar, which is made up of the $C_{1\alpha}$ coefficients and $\hat{J}_\alpha$ matrices and is linear in $C_{1\alpha}$: $\Sigma_{\alpha=x,y,z} C_{1\alpha} \hat{J}_\alpha$. The time reversal operation does not change the displacement and, hence, the $C_{1\alpha}$ coefficients, while the $\hat{J}_\alpha$ matrices reverse their sign. This accounts for the forbiddenness of hole interaction with vibrations having a total angular momentum $F=1$. In a similar way one can prove the impossibility of interaction of a ground-state hole with an $F=3$ vibration.[7)]

[1)]Determination[2–5] of the vibrational modes of an elastic sphere with a free surface was made with an error corrected subsequently in Refs. 6–8.

[2)]Terms containing the electron spin operator appear in the electron-phonon interaction Hamiltonian when the interaction between the valence and conduction bands is taken into account. Generally speaking, such terms result in electron spin-flip.[19]

[3)]For the sake of simplicity, we use here the classical expression for displacement. The transition to quantum-mechanical description is effected through secondary quantization.[21]

[4)]We have already pointed out the analogy between the bracketed operator on the left in (15) and the Luttinger Hamiltonian in the spherical approximation. Formulation of the latter in a block-diagonal form in a basis similar to (24) was used[24,25] in constructing the wave function of a quantum-confined hole.

[5)]More rigorously, one calls spheroidal only the vibrations of a sphere of this type with the total momentum $F=2$.[27] Such vibrations deform the sphere into an ellipsoid of revolution, which may have an either prolate, or oblate shape, depending on the vibration phase.

[6)]The same boundary conditions are used to determine the phase α in Eq. (31).

[7)]Vibrations with a total angular momentum $F=3$ cannot become involved in Raman scattering processes also for the reason that only the exciton state with a total angular mimentum $\mathcal{F}_{ex}=1$ is optically active in the dipole approximation. Therefore, according to the summation rule for angular momenta, the exciton scattered by light into an intermediate state interacts only with vibrations having $F=0, 1$, and 2.

[1] N. Nishiguchi and T. Sakuma, Solid State Commun. **38**, 1073 (1981).
[2] A. Tamurar, K. Higeta, and T. Ichinokawa, J. Phys. C **15**, 4975 (1982).
[3] E. Duval, A. Boukenter, and B. Champagnon, Phys. Rev. Lett. **56**, 2052 (1986).
[4] M. Fujii, T. Nagareda, S. Hayashi, and K. Yamamoto, Phys. Rev. B **44**, 6243 (1991).
[5] A. Tanaka, S. Onari, and T. Arai, Phys. Rev. B **47**, 1237 (1993).
[6] T. Takagahara, J. Lumin. **70**, 129 (1996).
[7] L. Saviot, B. Champagnon, E. Duval, I. A. Kudryavtsev, and A. I. Ekimov, J. Non-Cryst. Solids **197**, 238 (1996).
[8] L. Saviot, B. Champagnon, E. Duval, and A. I. Ekimov, J. Cryst. Growth **184/185**, 370 (1998).
[9] A. A. Sirenko, V. I. Belitsky, T. Ruf, M. Cardona, A. I. Ekimov, and C. Trallero-Giner, Phys. Rev. B **58**, 2077 (1998).
[10] V. B. Berestetskiĭ, E. M. Lifshits, and L. P. Pitaevskiĭ, *Quantum Electrodynamics* [in Russian] (Nauka, Moscow, 1989).
[11] Al. L. Efros and A. L. Efros, Fiz. Tekh. Poluprovodn. **16**, 1209 (1982) [Sov. Phys. Semicond. **16**, 772 (1982)].
[12] D. Schechter, J. Phys. Chem. Solids **23**, 237 (1962).
[13] E. L. Ivchenko and G. E. Pikus, *Superlattices and Other Heterostructures. Symmetry and Optical Phenomena* (Springer, Berlin, 1997), p. 133.
[14] S. V. Goupalov and E. L. Ivchenko, J. Cryst. Growth **18/185**, 393 (1998); Acta Phys. Pol. A **94**, 341 (1998).
[15] Al. L. Efros, Phys. Rev. B **46**, 7448 (1992).
[16] U. Rössler, ''Fine structure, line shape, and dispersion of Wannier excitons,'' in *Festkörperprobleme/Advances in Solid State Physics*, Vol. XIX, edited By J. Treusch (Vieweg, Braunschweig, 1979), p. 77.
[17] L. D. Landau and E. M. Lifshits, *Theory of Elasticity* (Pergamon Press, Oxford, 1970; Nauka, Moscow, 1987, p. 126).
[18] J. M. Luttinger, Phys. Rev. **102**, 1030 (1956).
[19] G. E. Pikus and A. N. Titkov, in *Optical Orientation/Modern Problems in Condensed Matter Sciences*, Vol. 8, edited by F. Meier and B. Zakharchenya (North-Holland, Amsterdam, 1984; Nauka, Leningrad, 1989).
[20] G. L. Bir and G. E. Pikus, *Symmetry and Strain-Induced Effects in Semiconductors* (Wiley, New York, 1974; Nauka, Moscow, 1972).
[21] C. Kittel, *Quantum Theory of Solids* (Wiley, New York, 1964; Nauka, Moscow, 1967).
[22] A. I. Akhiezer and V. B. Berestetskiĭ, *Quantum Electrodynamics* (Interscience, New York, 1985; Nauka, Moscow, 1981).
[23] D. A. Varshalovich, A. N. Moskalev, and V. K. Khersonskiĭ, *Quantum Theory of Angular Momentum* (World Scientific, Singapore, 1988; Nauka, Leningrad, 1975).
[24] P. C. Sercel and K. J. Vahala, Phys. Rev. B **42**, 3690 (1990).
[25] T. Richard, P. Lefebvre, H. Mathieu, and J. Allègre, Phys. Rev. B **53**, 7287 (1996).
[26] H. Lamb, Proc. London Math. Soc. **13**, 187 (1882).
[27] A. E. H. Love, *A Treatise on the Mathematical Theory of Elasticity* (Cambridge University Press, 1927; ONTI, Moscow, 1935).
[28] P. M. Morse and H. Feshbach, *Methods of Theoretical Physics* (McGraw-Hill, New York, 1953; IL, Moscow, 1960), Vol. 2.
[29] E. Duval, Phys. Rev. B **46**, 5795 (1992).
[30] Landolt-Börnstein, *Numerical Data and Functional Relationships in Science and Technology* (Springer, Berlin, 1982) Vol. 17b, p. 166.
[31] N. P. Bansal and R. U. Doremus, *Handbook of Glass Properties* (Academic Press, New York, 1986).

Translated by G. Skrebtsov

Structural study of nanoporous carbon produced from polycrystalline carbide materials: small-angle x-ray scattering

R. N. Kyutt, É. A. Smorgonskaya, and A. M. Danishevskiĭ

A. F. Ioffe Physicotechnical Institute, Russian Academy of Sciences, 194021 St. Petersburg, Russia

S. K. Gordeev and A. V. Grechinskaya

Central Materials Research Institute, 121014 St. Petersburg, Russia
(Submitted February 8, 1999)
Fiz. Tverd. Tela (St. Petersburg) **41**, 1484–1488 (August 1999)

An x-ray small-angle scattering study is reported of the structure of nanoporous carbon prepared by chlorinating carbide compounds having different crystal structures (SiC, TiC, Mo_2C). The measurements were carried out both in reflection and transmission. The angular dependences of the scattering intensity obtained are treated as a result of scattering from nanoparticles of different size. By unfolding the experimental curves into components corresponding to particles with different gyration radii R_g, scatterer distribution functions in gyration radius $m(R_g)$ were found. It is shown that, irrespective of the type of the starting carbide, particles with $R_g \sim 5$ Å make up the largest fraction in porous carbon. Samples prepared from different carbides differ in the degree of nanoparticle uniformity in size. The most uniform in size are nanoparticles in the samples prepared from SiC, in which the average value $R_g^{av} < 6$ Å. Nanoparticles in the porous carbon produced from Mo_2C are about twice larger. © *1999 American Institute of Physics.* [S1063-7834(99)02608-8]

Carbon prepared from polycrystalline carbides of silicon or metals by chemical removal of other than carbon atoms represents a highly porous system.[1–3] A distinctive feature of a carbon material of this type is the presence of a large number of nanopores characterized by a narrow size distribution. New techniques permitting production of mechanically strong products of a given shape from carbon with nanoporous structure by pretreatment of carbide materials were developed in recent years.[4] This has opened up new prospects for the use of nanoporous carbon in technology, for instance, as an efficient adsorbent in molecular filters or as electrode material for superhigh-capacitance electrolytic capacitors.[5,6]

Until recently, investigation of bulk nanoporous carbon materials was limited to measuring the degree of porosity and pore size, as well as to studying the relations governing the formation of the porous structure by physicochemical methods. In particular, an experimental study of the adsorption of nitrogen molecules showed that nanopores in the carbon prepared from polycrystalline SiC are typically 8.2 ± 0.2 Å wide (an estimate made in the crack-pore model) and fairly uniform in size, with the degree of sample porosity reaching as high as 70–75 vol.%. At the same time information on the structure of the carbon framework in materials of this kind is lacking. It may be expected that, if the starting carbides differ in the type of the carbide-forming element and, besides, possess different crystal structures, the carbon materials prepared from them would also differ in structure from one another. This difference may become manifest on both a short-range scale and on length scales considerably in excess of interatomic distances. This should, in its turn, entail differences in the physical and physicochemical properties as well. In this connection it appears of interest to carry out a comparative analysis of the nanostructure of carbon materials prepared in chemical reaction of the same type from polycrystalline materials of different types, such as SiC (hexagonal or cubic sphalerite structure), TiC (NaCl-type cubic), or Mo_2C (hexagonal).

The small-angle x-ray scattering method is known to be widely employed in studies of nm-scale structural nonuniformities in disperse systems, including porous materials.[7,8] Interpretation of small-angle scattering data within reasonable models offers a possibility of estimating the average size of the scattering fragments (clusters or pores), as well as of inferring in some cases their shape or size distribution, as this was done, for instance, in studies[9,10] of porous coals or aluminum oxide. This work presents the results of an experimental small-angle x-ray scattering study and characterization of the nanostructure of bulk samples of nanoporous carbon prepared from polycrystalline SiC (with hexagonal structure), TiC, and Mo_2C.

1. SAMPLE PREPARATION AND EXPERIMENTAL TECHNIQUES

The starting samples based on polycrystalline carbide materials were prepared of the corresponding carbide powder with particle size below 40 μm by molding it to desired size using a temporal binder. After this, pyrocarbon was synthesized in the pores of the stock thus produced in an amount of 7–8 vol.% to bind the carbide particles in a composite. This intermediate product was treated with chlorine at a temperature of 700–100 °C until complete removal of the carbide-forming element. After completion of the reaction, the

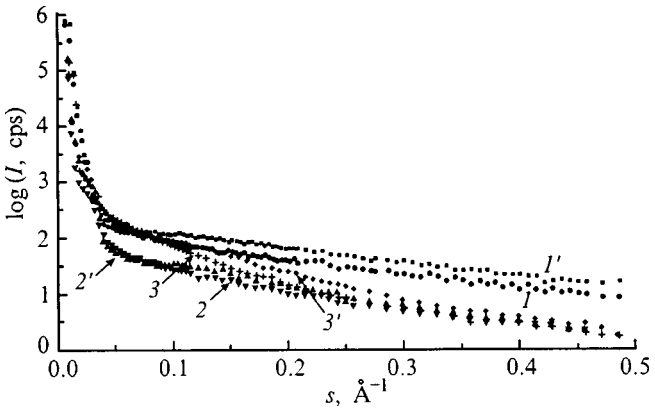

FIG. 1. Experimental small-angle x-ray scattering curves obtained in transmission (*1,2,3*) and reflection (*1′,2′,3′*) on samples of nanoporous carbon of different types. Starting material: *1,1′*—SiC; *2,2′*—TiC; *3,3′*—Mo_2C.

sample was maintained in an argon flow to remove the chlorine excess. The samples of nanoporous carbon were shaped as 0.11-cm thick wafers with a diameter of about 2 cm.

The small-angle x-ray scattering measurements were carried out on a two-crystal diffractometer with a perfect Ge-crystal monochromator [the (111) reflection]. This arrangement provided an angular divergence of the incident beam of 20 arcsec. The small-angle scattering was measured in two sample geometries, namely, in reflection from the sample surface (the reflectometry mode) and in transmission of the beam through the sample. In the first case, $\theta/2\theta$ scanning was used, which yields intensity distribution in the scattering plane in the direction of the scattering vector $\mathbf{s}=\mathbf{k}_1-\mathbf{k}_0$, which is parallel to the sample surface normal. Here $\mathbf{k}_0$ and $\mathbf{k}_1$ are wave vectors of the incident and scattered wave, respectively, and 2θ is the scattering angle. In the second case, the sample was mounted at right angles to the incident beam, and the scattered intensity was measured under rotation of the detector (2θ scanning). One obtains in this way the distribution of scattered intensity in the plane perpendicular to the $\mathbf{k}_1$ vector, i.e. also practically along the **s** vector, but the latter lies here parallel to the sample surface. The slits in front of the sample and of the detector were 0.25 and 0.5 mm wide, respectively, thus providing a resolution of 0.16° in the scattering angle 2θ.

Because of the low absorption of porous carbon (the linear absorption coefficients measured on the sample under study were 1.8–2.4 cm^{-1}), the effective scattering volume and, accordingly, the scattered intensity in the two measurement geometries were practically the same.

2. RESULTS AND DISCUSSION

Standard x-ray diffractograms measured on all samples within a broad angular range did not exhibit reflections corresponding to the starting materials. In the vicinity of the angles $2\theta=26$ and 44° one observed weak diffuse maxima close in position to the (0002) and (110) graphite reflections.

Figure 1 shows on a semilog scale experimental small-angle x-ray scattering curves, i.e. dependences of the scattered intensity I on the modulus of the scattering vector $s=4\pi\sin\theta/\lambda$, which were obtained in the transmission mode (curves *1*, *2*, *3*) and in the reflection mode (curves *1′*, *2′*, *3′*) from porous-carbon samples prepared from polycrystalline SiC (*1,1′*), TiC (*2,2′*), and Mo_2C (*3,3′*). We readily see that while the $I(s)$ curves for the samples prepared from different carbides differ somewhat in pattern, their character is similar for all types of samples. One can isolate in all curves a section of steep decay in $I(s)$ for small s ($s<0.02\,Å^{-1}$) and an extended portion of slow falloff for large s ($s>0.06Å^{-1}$), which bound a region with a relatively smooth transition from the fast to slow decline ($0.02<s<0.06\,Å^{-1}$). One should also point out that the $I(s)$ curves measured on the same sample in transmission and reflection are fairly close in shape. For SiC samples, the $I(s)$ curves obtained in transmission and reflection exhibit a noticeable difference primarily in the region of comparatively slow decay, for $s>0.04\,Å^{-1}$. For TiC samples, the difference between the two curves is less pronounced. While the difference between the data obtained for Mo_2C samples in transmission and reflection is weaker than that for SiC samples, it also is seen predominantly for large s.

The close similarity between the data obtained in two different experimental geometries indicates apparently that the conditions of beam interaction with the sample are similar in both cases. Note that for 2θ angles close to zero ($0-0.2°$) the unabsorbed part of the incident beam becomes superimposed on the scattered intensity measured in transmission. In reflection measurements performed at the smallest θ angles chosen the beam is almost parallel to the sample surface, and the sample does not interrupt completely the incident beam (the sample is flown around, as it were, by the latter). However at these angles part of the beam cross section is obstructed by the end face of the sample and interacts with the layer near the sample surface. The radiation scattered by this volume at the 2θ angle is also detected by the receiver, so that it can be assumed that when working in the reflectometry mode the scattering curve $I(s)$ characterizes practically the same scattering volume throughout the scattering-angle range measured. But then the $I(s)$ curves in both experimental configurations should be similar to within the difference between the scattering volumes and the corresponding beam attenuation due to absorption in different paths, exactly what is observed for all the samples investigated. This gives us grounds to consider the measured data as resulting from scattering associated with electronic-density inhomogeneities in the bulk of porous carbon.

An important feature of all $I(s)$ curves is the absence of an interval of s within which the well-known Porod's law, $I(s)\propto s^{-4}$, determining the asymptotic behavior of scattering from a smooth surface of particles with linear size R for $s\gg R^{-1}$, would hold. The pattern of the experimental $I(s)$ scattering curves suggests that the samples under study contain scattering particles (of the material or pores) varying in size, from small-scale ones contributing to scattering for large s to large-scale particles dominating scattering for small s. Note that interparticle interference effects are practically not seen in scattering; indeed, there is essentially no structure in the $I(s)$ curves for any sample. The weakly pronounced shoulder in the $I(s)$ curves obtained for TiC and Mo_2C samples (curves *2,2′* and *3,3′*) is related to the small

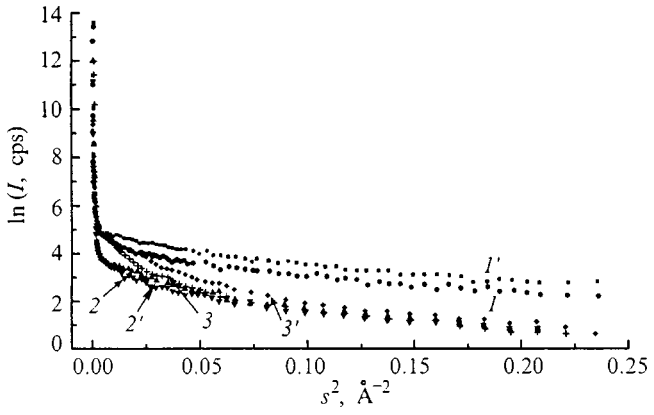

FIG. 2. Experimental small-angle x-ray scattering curves of Fig. 1 redrawn in Guinier's coordinates. Same notation as in Fig. 1.

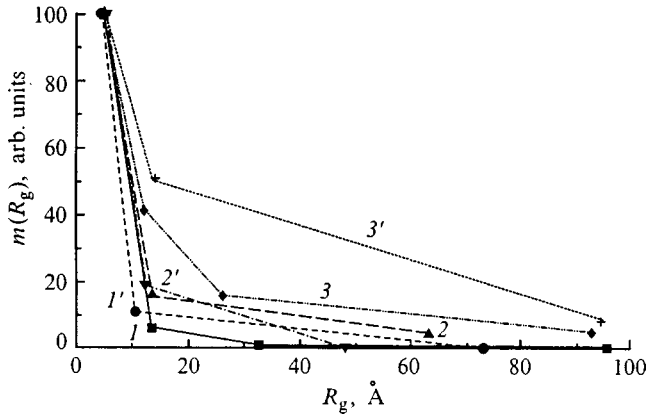

FIG. 3. Distribution functions of scattering nanoparticles in gyration radii derived from small-angle x-ray scattering data, which were obtained in transmission (*1*,*2*,*3*) and in reflection (*1′*,*2′*,*3′*) on nanoporous-carbon samples of different types. Same notation as in Fig. 1.

shoulder in the distribution of the primary x-ray beam intensity in radial direction, which is normal to the beam direction. For SiC samples (curves *1*, *1′*), this true shape of the primary-beam cross section turns out to be masked by the stronger scattering from these samples within the corresponding angular region.

Because the shape of the scattering particles is not known in advance, we shall use in the analysis of small-angle x-ray scattering the classical approach of Guinier,[7] which characterizes the particle size by one universal parameter, the gyration radius R_g. According to this approach, for small s ($sR_g \gg 1$) the scattering intensity can be presented in the form

$$I(s)=I(0)\exp[-(s\,R_g^2)/3].$$

Having redrawn the $I(s)$ curves in the form $\ln(s)=f(s^2)$ and obtained a straight-line section, one can determine from its slope the gyration radius R_g.

Figure 2 shows experimental small-angle x-ray scattering curves in the Guinier coordinates, $\ln(s)=f(s^2)$, obtained in the reflection and transmission modes, respectively. One readily sees that none of the $I(s)$ relationships can be fully fitted by Guinier's expression. In this connection, and taking into account the above considerations, we shall assume the system to consist of particles with different gyration radii. In particular, if these particles are approximately homogeneous in electronic density and have the same or similar shape, this simply means that the system is made up of particles of different dimensions. Based on this model, we shall look for an approximate particle-distribution function in gyration radii using the experimental small-angle x-ray scattering curves in the Guinier coordinates (Fig. 2) and invoking a simple idea put forward by Kitaĭgorodskiĭ.[8]

We assume the system to contain a small number of species of independently scattering particles differing in size. Then the $I(s)$ curve may be considered as a sum of components $I_k(s)$ corresponding to species k. Next we choose a straight-line section in the most remote part of the $\ln I(s)=f(s^2)$ curve (for the largest s), or draw a tangent to this part of the curve. The slope of this straight line will yield the gyration radius R_{g1} of the smallest particles which still provide a measurable scattering contribution in our experiment ($R_{g1}=R_{g\,\min}$). The intercept of this straight line on the vertical axis, $I_1(0)$, gives the contribution of these particles to the scattered intensity, thus offering a possibility to determine their fraction. Now we subtract from the experimental $I(s)$ curve the part $I_1(s)$ which is accounted for by the smallest particles, i.e. which corresponds to the above-mentioned straight line. We obtain a difference curve $I(s)-I_1(s)$, in which (after redrawing it in the Guinier coordinates) we also isolate a rectilinear portion in s^2 far from the origin or draw a tangent corresponding to the smallest particles providing a contribution to this difference curve. The slope of this line will likewise yield the gyration radius for these particles, R_{g2}, and the intercept on the vertical axis, $I_2(0)$, the fraction of such particles. After this, the next difference curve is constructed, and the procedure is continued until successive subtractions yield a straight line from the origin of the curve in the $\ln I(s)=f(s^2)$ coordinates (close to $s=0$). Its slope determines the maximum gyration radius $R_{g\,\max}$ of the particles detected in the experiment, and its extrapolation to $s^2=0$, the relative number of these largest particles. The fraction of the volume or of the mass (for uniform density) of particles of a given size can be estimated as

$$m_k \propto I_k(0)/R_{gk}^3.$$

Figure 3 shows with points the values of $m_k(R_{gk})$ in arbitrary units found by the above procedure of deconvoluting the small-angle x-ray scattering curves for two experimental configurations in all the samples studied. The curves drawn through these points are essentially the approximate distribution functions of scattering particles as functions of gyration radii, $m(R_g)$ we have been looking for. As seen from Fig. 3, the distribution functions $m(R_g)$ exhibit the same feature for all samples of porous carbon, irrespective of the starting material, namely, the most probable size [the maximum value of $m(R_g)$] corresponds to the smallest scattering particles (with the gyration radius $R_{g\,\min}$). For $R_g > R_{g\,\min}$, the distribution function falls off more or less steeply, making the region of the maximum in $m(R_g)$ fairly narrow. In the case of porous carbon prepared from polycrys-

TABLE I. Parameters of the distribution function of scattering particles in gyration radii in nanoporous carbon.

Starting material	SiC		TiC		Mo_2C	
Measurement mode	Transmission	Reflection	Transmission	Reflection	Transmission	Reflection
$R_{g\,\min}$, Å	4.8	4.3	4.9	5.2	4.7	5.1
ΔR_g, Å	3.4	3.5	5.1	4.4	6.1	7.9
R_g^{av}, Å	5.8	5.2	8.1	6.6	11.4	12.8

talline SiC, this result (curves *1*, *1′* in Fig. 3) correlates well with the already mentioned data on the high uniformity of nanopore sizes.

In our case, the degree of uniformity of scatterer sizes can be characterized conveniently by the dispersion in the distribution function $\Delta R_g \equiv R_g - R_{g\,\min}$, where the value of R_g satisfies the condition of decay of the distribution function to one half its maximum value: $m(R_g) = m(R_{g\,\min})/2$. Small-angle x-ray scattering measurements made on a SiC sample in transmission and reflection permit one to estimate the dispersion ΔR_g as ~ 3.5 Å, with the most probable value $R_{g\,\min} = 4.8$ and 4.3 Å, respectively. The estimates of the parameters $R_{g\,\min}$ and ΔR_g of the distribution function $m(R_g)$ for all the samples studied are listed in Table I, which contains also the average values of the gyration radius R_g^{av} of the scatterers estimated by the expression

$$R_g^{av} = \frac{\Sigma_k R_{gk} m_k}{\Sigma_k m_k}$$

As seen from Table I, while the scatterer distribution functions in size have the same pattern, quantitatively the characteristics of this distribution differ noticeably for samples of different types. Indeed, although most of the volume of each sample is occupied by the smallest nanoparticles, the relative contribution of larger particles in samples of different types is different. One readily sees that the fraction of large particles increases in the series of materials prepared from SiC, TiC, and Mo_2C, which makes the average particle size increase too. Porous carbon prepared from SiC is characterized by the most narrow distribution in size and by the smallest particles. By contrast, the average particle size in samples prepared from Mo_2C is about twice that for samples from SiC. The samples fabricated from TiC occupy an intermediate position in particle size and size scatter and in this respect lie closer to those prepared from SiC.

It should be noted that both the most probable (minimal) and average gyration radius of particles found for samples prepared from SiC from measurements in transmission are larger than the value determined from reflectometric studies. For samples from TiC and Mo_2C, however, the reverse is true for $R_{g\,\min}$. At the same time the value of R_g^{av} for the sample from TiC was estimated to be larger from transmission data, and for the Mo_2C sample, from reflectometric measurements. The slight difference between the small-angle x-ray scattering data obtained in different experimental geometries evidences, in our opinion, the presence of a transverse-longitudinal macroanisotropy in the sample structure. Because, as already mentioned, the scattering vector in reflection has a single component directed along the surface normal, and in transmission measurements, only a component parallel to the surface, it appears that the scattering nanoparticles have a nonspherical (oblate or prolate) shape and, on average, not equally probable spatial orientation in the sample. As follows from our data, nanoparticles in the samples prepared from SiC and TiC are oriented parallel to the surface, on the average, with a slightly higher probability than along its normal, whereas in the samples from Mo_2C, on the contrary, orientation along the normal is, on the average, more probable. The transverse-longitudinal anisotropy in samples obtained from macroscopically isotropic starting materials can be expected if one takes into account that the frontline of chemical reaction involved in the formation of porous carbon propagates primarily from the surface along the normal into the starting sample. The resulting difference between the formation conditions of nanoparticles and nanopores in the longitudinal and transverse directions may account to a considerable extent for the nonspherical shape and dominant orientation of the nanoparticles. The type of the starting material apparently determines the degree and character of the observed longitudinal-transverse anisotropy. One also cannot rule out the possibility that the conditions at the reaction frontline itself change as it moves into the starting sample. Besides, during the time the newly formed carbon material spends in the reactor it may undergo structural rearrangement. For these reasons the character of the porous nanostructure of a sample may vary with depth. In this case the results of reflectometric measurements relating primarily to the near-surface region of a sample up to a few hundred μm in thickness may differ from those obtained in transmission, when the entire volume is studied. The transverse-longitudinal structural anisotropy, if it indeed does exist in the porous-carbon samples under study, should be apparent in the physicomechanical properties of material. This problem requires a dedicated investigation.

Thus small-angle x-ray scattering measurements made on all nanoporous carbon samples studied indicate a high uniformity of the scattering particles in size. The maximum fraction of the volume is occupied by the smallest nanoparticles, whose size ($\sim 2R_g$) is ~ 10 Å and was found to be approximately the same for samples prepared from starting composites differing in composition and in structure. As follows from small-angle x-ray scattering data, the nanoporous carbon obtained from Mo_2C contains, compared to samples of other types, a substantially larger fraction of scattering particles with sizes above 20–25 Å, so that on the average particles in the material of this type are about twice larger than those in the SiC-based material. According to preliminary data on molecular adsorption, pores in Mo_2-based

samples are also approximately twice larger (~20 Å) than those measured on samples prepared from SiC.

Support of the Russian Fund for Fundamental Research (Grant 99-02-17984) and of the Foundation of Intellectual Cooperation within the ''Fullerenes and Atomic Clusters'' program is gratefully acknowledged.

[1] US Patent No. 3066099 (1962).
[2] FRG Patent No. 1185163 (1966).
[3] N. F. Fedorov, G. K. Ivakhnyuk, D. N. Gavrilov, V. V. Tetenov, G. N. Smetanin, V. V. Samonin, O. É. Babkin, and Yu. A. Zaĭtsev, in *Carbon-Based Adsorbents and Their Industrial Applications* [in Russian], edited by T. G. Plachenov (Nauka, Moscow, 1983), p. 20.
[4] S. K. Gordeev and A. V. Vartanova, Zh. Strukt. Khim. **66**, 1080 (1994); *ibid.*, 1375 (1994).
[5] S. K. Gordeev, A. V. Vartanova, S. G. Zhukov, I. N. Gran', V. V. Sokolov, T. I. Mazaeva, and R. G. Avarbé, RF Patent No. 2026735 (1995).
[6] R. G. Avarbé, S. K. Gordeev, A. V. Vartanova, *et al.*, RF Patent No. 2084036 (1997).
[7] D. I. Svergun and L. A. Feĭgin, *Small-Angle X-Ray and Neutron Scattering* [in Russian] (Nauka, Moscow–Leningrad 1986).
[8] A. I. Kitaĭgorodskiĭ, *X-Ray Structural Analysis of Fine-Grained and Amorphous Bodies* [in Russian] (GITTL, Moscow, 1952).
[9] P. W. Schmidt, J. Appl. Crystallogr. **15**, 367 (1982).
[10] T. N. Vasilaevskaya and R. I. Zakharchenya, Inorg. Mater. **31**, No. 4, 1 (1995).

Translated by G. Skrebtsov

Surface diffusion of Ni on Si(111) with coadsorption of Co

A. E. Dolbak, B. Z. Ol'shanetskiĭ,*) S. A. Tiĭs, and R. A. Zhachuk

Institute of Semiconductor Physics, Siberian Branch of the Russian Academy of Sciences, 630090 Novosibirsk, Russia

(Submitted September 15, 1998)
Fiz. Tverd. Tela (St. Petersburg) **41**, 1489–1494 (August 1999)

The effect of the coadsorption of Co and Ni on an Si(111) surface structure and on the diffusion of adsorbed atoms is investigated by low-energy electron diffraction and Auger electron spectroscopy. It is established that surface structures similar to those formed with the adsorption of Co alone are formed with the Ni and Co coadsorption on an Si(111) surface. It is found that the contribution of surface diffusion to the transport of Ni atoms is sharply higher on an Si(111) surface with submonolayer Co concentrations in the temperature range 500–750 °C than for a pure surface, where the main mechanism of Ni transport along the surface is diffusion of Ni atoms through the bulk of Si. © *1999 American Institute of Physics.* [S1063-7834(99)02708-2]

Surface diffusion plays an important role in atomic processes on solid surfaces. It can depend on the surface orientation and structure, atomic steps present on the surface, applied external fields, the chemical nature and concentration of the adsorbed atoms, and other factors.[1,2]

Interest in the coadsorption of the atoms of two elements on crystal surfaces has been increasing in recent years because such studies open up new possibilities for producing surfaces with the required properties. Coadsorption of the atoms of two elements can increase the stability of the surface phases induced by one of the elements,[3] and result in the formation of surface phases that are not formed when only one element is adsorbed.[4–7] The coadsorption of atoms should affect atomic processes occurring on the surface, such as the surface diffusion of adsorbed atoms. The interest in the coadsorption of transition-metal atoms on Si surfaces stems from, specifically, investigations of ternary transition-metal silicides (see, for example, Refs. 8–11).

Our objective in the present work is to study the effect of the coadsorption of Ni and Co atoms on the Si(111) surface structure and to investigate the surface diffusion of atoms of one element in the presence of adsorbed atoms of the other element.

1. EXPERIMENTAL PROCEDURE

Samples of *p*-type silicon with Si(111) orientation, resistivity 5–10 $\Omega\cdot$cm, and dimensions $22\times5\times0.3\,\mathrm{mm}^3$ were investigated. A clean surface was obtained by heating at a temperature of about 1200 °C for 1–2 min by passing an ac current through the sample at $(1-2)\times10^{-8}$ Pa pressures. After cleaning, Auger electron spectroscopy (AES) with a signal/noise ratio $>2\times10^3$ for the Si LVV (92 eV) peak of silicon showed no impurities on the surface. The temperature of the sample was monitored with an optical pyrometer.

Nickel and cobalt plates welded to a tantalum ribbon were used as the sources of Ni and Co atoms. The impurity concentration in Ni was less than 0.1% and it did not exceed 0.02% in Co. The ribbon was heated by passing an electric current along it. The atomic flux was calibrated before each experiment. The deposition rates of the metal atoms were 0.01–0.1 ML/min (ML — monolayer). The Ni and Co concentrations were measured by AES using the Ni LMM (848 eV) and Co LMM (775 eV) Auger peaks, respectively. The elemental sensitivity coefficients from the atlas of Auger spectra[12] were used to calculate the concentrations. Since Ni and Co form compounds with silicon, the AES method does not permit measuring directly the thickness of the coatings deposited. For this reason, the coating thicknesses were determined using the relation between the measurements on the coatings with quartz balances and AES after deposition of Ni[13] and Co[14] on Si(111) at room temperature.

The spatial resolution of the Auger spectrometer (ASC-2000, Riber) was 10 μm. The surface structure was determined by low-energy electron diffraction.

To investigate surface diffusion of the adsorbed atoms, a several-nm-thick metal strip having a sharp boundary was deposited on the sample surface perpendicular to the long side of the sample. The strip served as a source of diffusing atoms. Each sample was annealed at a definite temperature T for a time t and cooled to room temperature at a rate of at least 100 °C/s, after which the resulting concentration distributions $C(x)$ of the metal atoms along the surface were measured by AES (x — distance from the edge of the deposited metal strip) and the diffusion coefficients D were calculated from these distributions. The anneal time t was chosen so that the metal atoms diffused over a substantial distance within the length of the sample.

2. EXPERIMENTAL RESULTS AND DISCUSSION

2.1. Surface phases on Si(111) with Ni and Co coadsorption

Ni and Co adsorption on silicon surfaces have been investigated by LEED and AES previously and described in Refs. 15 and 16.

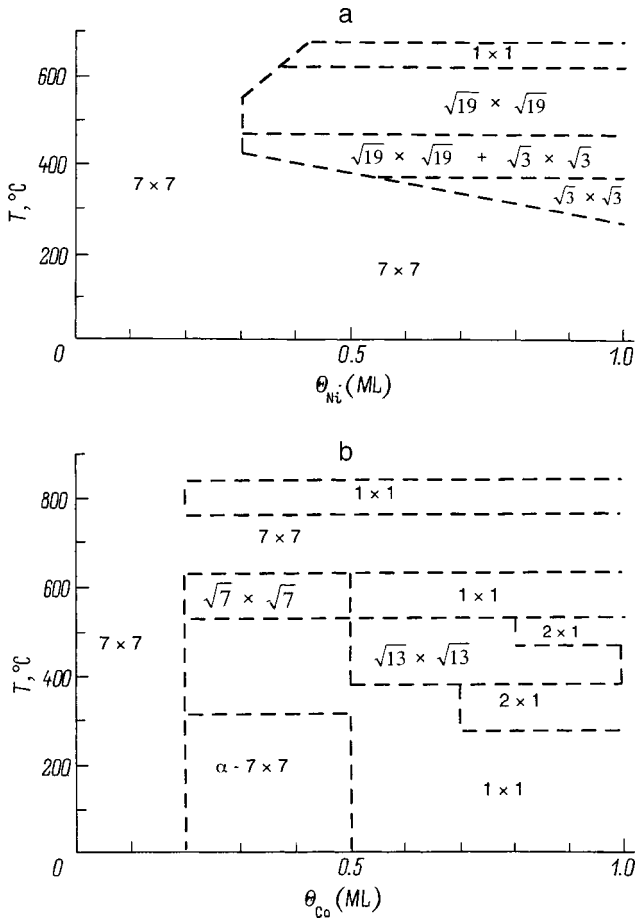

FIG. 1. Relation between the Si(111) surface structure, the thickness of the coating deposited at room temperature, and the annealing temperature of the sample: a — Ni adsorption, b — Co adsorption.

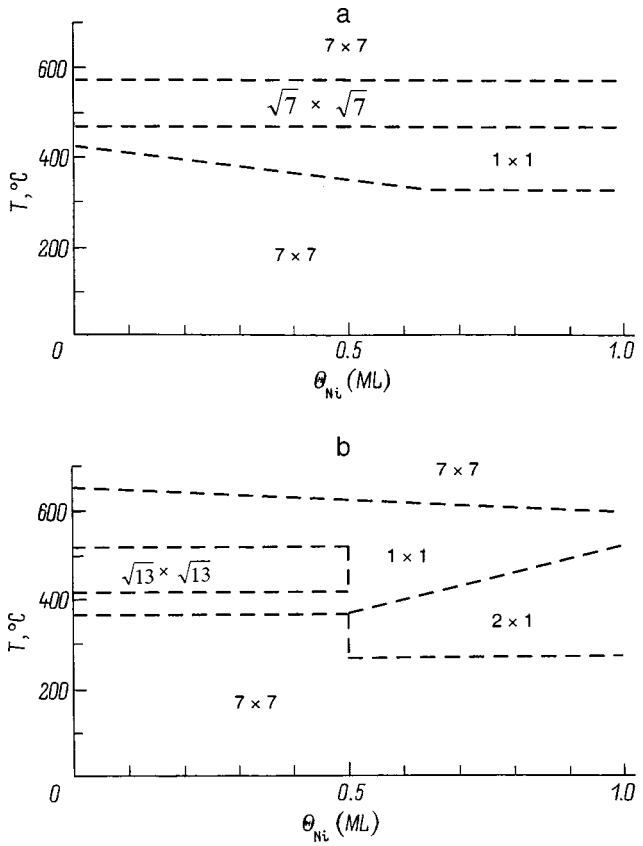

FIG. 2. Relation between the Si(111) surface structure, the Ni and Co coatings deposited at room temperature, and the annealing temperatures of the sample: a — Ni adsorption on a surface with adsorbed Co with $\Theta_{Co}=0.3$ ML, b — Ni adsorption on a surface with adsorbed Co for $\Theta_{Co}=0.7$ ML.

The Ni-induced surface structures formed on Si(111)after the sample is cooled from a temperature above 900 °C at a rate exceeding 100 °C/s have been described in Ref. 15, where the corresponding results obtained by other authors are reviewed. As a supplement to this, in the present work a relation was established between the thickness of the Ni coating deposited at room temperature, the temperature of subsequent annealing of the sample, and the surface structure (Fig. 1a). The formation of an Si(111)—$\sqrt{3}\times\sqrt{3}$–Ni structure, which was first described in Ref. 17 but is not formed when samples heated above 900 °C are rapidly cooled, was observed in these experiments.

The results of our investigations of the influence of Co adsorption on the Si(111) surface structure[16] are presented in Fig. 1b.

Figures 2a and 2b show the dependences of the Si(111) surface structure, formed with coadsorption of Ni and Co on Si(111), on the thickness of the Ni coating, and the annealing temperature of the sample for fixed values of the Co coating, equal to 0.3 and 0.7 ML, respectively. These coatings were chosen because, as is evident from Fig. 1b, after such quantities of Co are adsorbed on an initially clean Si(111) surface and after the corresponding annealing, Si(111)—$\sqrt{7}\times\sqrt{7}$–Co, Si(111)—$\sqrt{13}\times\sqrt{13}$–Co, and Si(111)—1×1–Co structures are formed. To obtain these dependences, which are presented in Fig. 2, a uniform Co coating and a series of 20–30 0.5-mm-wide Ni strips with coatings increased to 1.0 ML were deposited on the Si(111) surface at room temperature. Then the sample was annealed for 20 min with increasing temperatures at intervals of 50 °C in the range 200–700 °C. The surface structure was studied at room temperature by LEED. It is evident that the surface structures formed in these experiments are similar to the structures formed with Co adsorption on a clean Si(111) surface (Fig. 1b). The $\sqrt{3}\times\sqrt{3}$ and $\sqrt{19}\times\sqrt{19}$ structures (Fig. 1a), characteristic for Ni adsorption on a clean Si(111) surface[17,18,15] do not form with coadsorption of Ni and Co. The surface structures obtained were independent of the order of deposition of Ni and Co.

2.2. Surface diffusion of Ni and Co on Si(111) with Ni and Co coadsorption

According to current ideas, the migration rates of atoms on a surface are higher and the activation energy of surface diffusion is lower than the corresponding values in the interior of a solid. But, according to our previous investigations, surface diffusion does not always play the main role in the transport of adsorbed atoms on a surface. Previous AES and LEED investigations of Ni diffusion on clean Si surfaces[15] have shown that the diffusion of Ni atoms through the interior bulk of silicon followed by segregation on the surface as

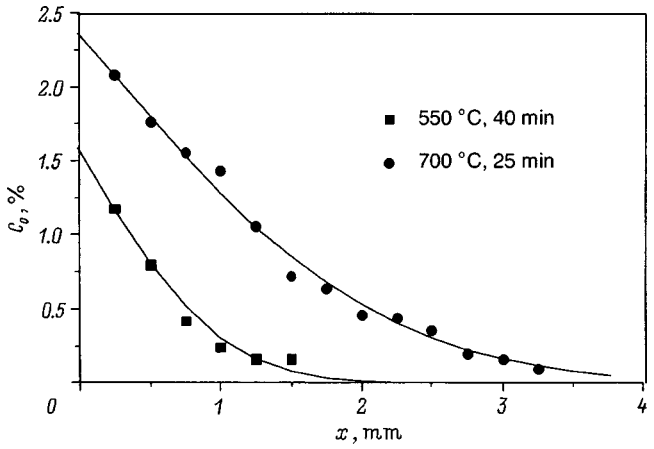

FIG. 3. Typical concentration distributions $C_{Ni}(x)$ on an Si(111) surface. The solid line shows the dependence described by the expression (1).

a result of a decrease in the solubility of Ni in Si with decreasing temperature making the main contribution to Ni transport along a surface.[19]

Our problem in the present work was to investigate the possible influence of adsorption of atoms of a second element on Co and Ni transport on an Si(111) surface. But, just as for a clean surface,[15] we were not able to detect by LEED and AES the diffusion of Co at temperatures 600–1000 °C on a surface containing adsorbed Ni. At the same time, we did observe that the presence of adsorbed Co strongly influences the surface transport of Ni.

Ni diffusion was studied on clean Si(111) surfaces and on surfaces with adsorbed Co.[20] The influence of adsorbed Co on the diffusion of Ni was investigated after Co was predeposited at room temperature on a clean Si(111) surface and the samples were annealed at the corresponding temperatures. In this manner, surface phases could be formed on the surface in accordance with the diagram in Fig. 1b.

The temperature dependences of the Ni surface diffusion coefficients were measured on 7×7–Co ($\Theta_{Co}=0.4$ and 0.8 ML, respectively), 1×1–Co ($\Theta_{Co}=0.6$ ML) and $\sqrt{7}\times\sqrt{7}$–Co ($\Theta_{Co}=0.2$ ML) surfaces. The measurements of the diffusion coefficients on a Co surface showed poor reproducibility and are not presented in this paper. We were not able to measure the temperature dependences of the Ni diffusion coefficients on the $\sqrt{13}\times\sqrt{13}$–Co surface because this surface exists only in a narrow temperature range.

We calculated the temperature dependence of the Ni diffusion coefficients $D(T)$ on a Si(111) surface using the concentration distributions $C_{Ni}(x)$ that appeared after the samples containing a deposited Ni strip were annealed. Examples of the concentration distributions $C_{Ni}(x)$ observed on an Si(111) surface in our experiments are shown in Fig. 3. Just as the distributions obtained on clean surfaces, they satisfied the relation

$$C(x)=C_0\mathrm{erfc}(x/2\sqrt{Dt}). \quad (1)$$

Such distributions are characteristic for one-dimensional diffusion from a constant-intensity source.

The temperature dependences obtained for the Ni diffusion coefficients on clean Si(111) surfaces and surfaces containing adsorbed Co are presented in Fig. 4. The accuracy of the calculation of the diffusion coefficients using the distributions $C_{Ni}(x)$ was $\pm30\%$. The temperature dependence of the Ni diffusion coefficients on Si(111) surfaces with adsorbed Co in the coordinates chosen in Fig. 4 contain two linear sections corresponding to diffusion with different activation energies: at temperatures 500–750 °C and above 750 °C. Compared with a clean surface, coadsorption of Co substantially expanded the temperature range where Ni diffusion can be detected by LEED and AES.

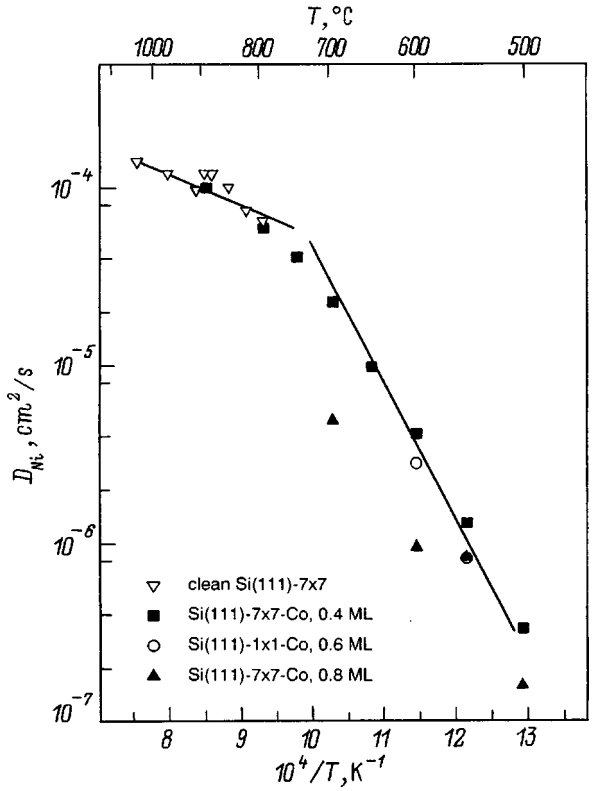

FIG. 4. Temperature dependences of the Ni diffusion coefficients on a clean Si(111) surface and an Si(111) surface containing adsorbed Co.

At temperatures above 750 °C the Ni diffusion coefficients agree with good accuracy with the coefficients measured on an initially clean Si(111)–7×7 surface. Hence it can be concluded that at temperatures above 750 °C the same mechanism makes the main contribution to Ni transport on a clean Si(111) surface and on a Si(111) surface with adsorbed Co. It follows from out experiments that Ni transport along clean Si surfaces occurs by diffusion via the interior volume followed by segregation on the surface as a result of a decrease of Ni solubility in silicon as the crystal cools. This result is based on the facts that there is no Ni Auger signal in the Auger spectra from the sample surface during Ni diffusion and that an Ni Auger signal from a surface with an Ni strip and an Si Auger signal from the rest of the surface were observed during annealing of the sample. The concentration distributions $C_{Ni}(x)$ on a clean Si surface appeared only after the sample was cooled. Ni transport on an initially clean Si(111)—7×7 surface was observed only at temperatures above 750 °C. At temperatures below 750 °C the amount of nickel dissolved in the silicon decreased, and the sensitivity

of the Auger spectrometer was inadequate to detect the concentration distributions $C_{Ni}(x)$. We were not able to observe such distributions after 60-min anneal at 700 °C. The result for Ni transport by diffusion via the interior agrees with the absence of a dependence of the Ni diffusion coefficients on the surface orientation and structure,[15] which one would expect if Ni diffusion proceeded along the surface. Moreover, the diffusion coefficients calculated from our experimental data agree with the values obtained in Refs. 21 and 22 for coefficients of Ni diffusion along interstices in silicon, $10^{-4}-10^{-5}\,cm^2\cdot s^{-1}$ at 1100 °C. But Ni surface diffusion on a clean silicon surface still occurs. It is manifested in the formation of nickel-induced ordered structures and in the formation of epitaxial islands of nickel disilicide $NiSi_2$. However, the contribution of surface diffusion to nickel transport is negligibly small compared with the diffusion via the interior volume of silicon.

Our conclusion concerning the mechanism of Ni transport on clean Si surfaces has been confirmed in Ref. 23.

In experiments on Si surfaces with adsorbed Co the Ni Auger signal could be observed during diffusion of Ni, and this means that the Ni atoms diffuse along the silicon surface. At temperatures 500–750 °C the Auger signal from Ni, measured at a certain point of the sample, is identical in magnitude to the signal measured after the sample is cooled to room temperature. Therefore Co adsorption on silicon surfaces sharply increases the contribution of surface diffusion to the transport of Ni atoms, and the contribution of surface diffusion to Ni transport in the temperature range 500–750 °C is determining.

An Ni Auger signal on surfaces with adsorbed Co could also be observed in the process of Ni diffusion at temperatures above 750 °C, but we were not able to measure the Ni surface diffusion coefficients proper at these temperatures because the measurement of the concentration distributions $C_{Ni}(x)$ under these conditions required a much longer time than the time in which the Ni atoms diffused over a distance comparable to the length of the sample. This made it impossible to separate the contributions of surface diffusion and diffusion through the interior to Ni transport.

The computed activation energy of the surface diffusion of Ni on an Si(111)—7×7–Co surface in the temperature range 500–750 °C is 1.3 eV, and the temperature dependence of the surface diffusion coefficients can be expressed as $D=1\times10^2\exp(-1.3/kT)\,cm^2\cdot s^{-1}$ (Fig. 5). The corresponding expression at temperatures above 750 °C is $D=2.4\times10^{-3}\exp(-0.32/kT)\,cm^2\cdot s^{-1}$ (data from this work and Ref. 15).

Therefore, when Co coadsorption occurs, in addition to Ni transport on clean silicon surfaces by diffusion via the interior volume, Ni atoms are transported by surface diffusion.

To explain the mechanism of Ni surface diffusion it is necessary to take account of the properties of a Si surface containing adsorbed Co. The adsorption of Co on a clean silicon surface results in the formation of a variety of surface structures that depend on the cobalt concentration and the annealing temperature (Fig. 1b).[16] These structures are due to the presence of Co atoms uniformly arranged in an ordered

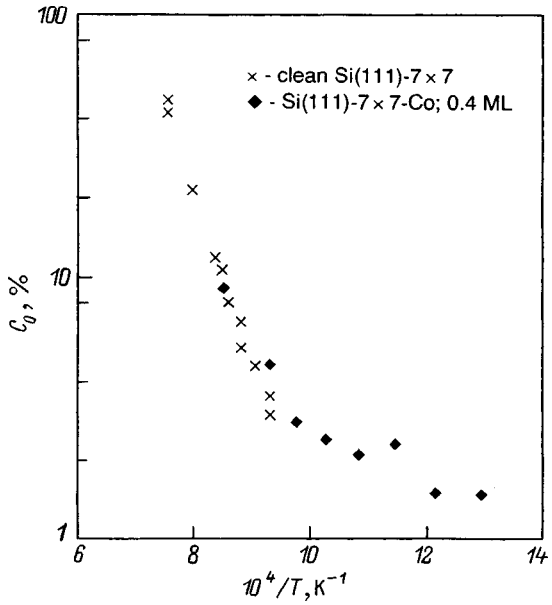

FIG. 5. The preexponential factor C_0 from Eq. (1) measured as a function of the reciprocal of the temperature for an Si(111)—7×7 surface with $\Theta_{Co}=0.4$ ML.

fashion on the surface and incorporated in the composition of the unit cell of the surface structure. The excess Co atoms that have not been incorporated in the unit cell interact with the silicon, as a result of which nuclei of the cobalt disilicide $CoSi_2$ phase in the form of epitaxial islands are formed.[16] During annealing at temperatures above 600 °C, cobalt atoms diffuse to these islands from adjoining regions of the surface, the concentration of the uniformly arranged Co atoms on these sections of the surface decreases, and the Si(111)—7×7 structure characteristic of a clean surface is restored. The total surface area occupied by the $CoSi_2$ islands is a small fraction of the entire area, and the structure of the surface between the islands determines the form of the LEED patterns. Therefore the 7×7–Co surface contains $CoSi_2$ islands surrounded by sections of clean surface with 7×7 structure. Since Ni diffusion on a clean silicon surface is not detected by AES, it is logical that it should appear accompanying Co adsorption with the epitaxial $CoSi_2$ islands which are formed.

The preexponential factor C_0 in Eq. (1) as a function of the reciprocal of the temperature for a clean Si(111) surface and the same surface containing adsorbed Co are presented in Fig. 5. The coefficient C_0 characterizes the amount of Ni participating in diffusion. To explain the temperature dependence $C_0(T)$ at 500–750 °C, where Ni transport occurs by means of surface diffusion, it is necessary to take into consideration the fact that the source of Ni atoms in the experiments was a strip of nickel disilicide $NiSi_2$,[24] which forms as a result of the Ni–Si interaction at temperatures above 300–350 °C. The number of Ni atoms released from $NiSi_2$ and participating in surface diffusion increases with temperature. At temperatures above 750 °C Ni transport occurs by diffusion of Ni via the interior volume, and the increase in C_0 is due to the increase in the solubility of Ni in Si[19] and therefore an increase in the total number of Ni atoms that have

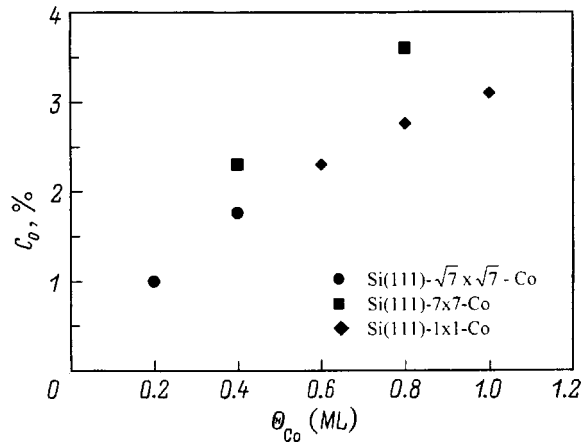

FIG. 6. The preexponential factor C_0 from Eq. (1) measured as a function of Θ_{Co} after samples are annealed at a temperature near 600 °C.

diffused through the interior volume of silicon.

It follows from the dependence of the preexponential factor C_0 (Eq. (1)) on the Co coating measured after the samples are annealed at 600 °C (Fig. 6) that the amount of Ni which has diffused along the surface on the same sample increases with the Co coating.

The following conclusions can be drawn from the results obtained.

Ni transport on a Si(111) surface containing adsorbed cobalt can occur by two mechanisms: diffusion through the interior of Si followed by segregation on the surface, as a result of a decrease in Ni solubility in Si with decreasing temperature, and surface diffusion.

The contribution of each mechanism to Ni transport on a silicon surface depends on the temperature. At temperatures above 750 °C diffusion through the interior makes the main contribution while at temperatures in the range 500–750 °C surface diffusion makes the main contribution.

Surface diffusion of Ni is due to the presence of cobalt disilicide islands.

When Ni and Co are coadsorbed on a Si(111) surface, surface structures with periods characteristic for structures formed as result of the adsorption of Co alone are formed.

This work was supported by the Russian Fund for Fundamental Research (grant No. 98-02-17843) and the Russian government program ''Surface Atomic Structures'' (project No. 95-1.17).

*)E-mail: olshan@isp.nsc.ru

[1] B. I. Boltaks, *Diffusion and Point Defects in Semiconductors* [in Russian] (Nauka, Leningrad, 1972).
[2] Ya. E. Geguzin and Yu. S. Kaganovskiĭ, *Diffusion on Crystal Surfaces* [in Russian] (Energoatomizdat, Moscow, 1984).
[3] J. Yuhara, R. Ishigami, and K. Morita, Surf. Sci. **326**, 133 (1995).
[4] H. Daimon, C. Chung, S. Ino, and Y. Watanabe, Surf. Sci. **235**, 142 (1990).
[5] I. Homma, Y. Tanishiro, and K. Yagi, Surf. Sci. **242**, 81 (1991).
[6] Y. L. Gavrilyuk, V. G. Lifshits, and N. Enebish, Surf. Sci. **297**, 345 (1993).
[7] A. V. Zotov, S. V. Ryzhkov, and V. G. Lifshits, Surf. Rev. Lett. **1**, 285 (1994).
[8] A. Vantomme, M. F. Wu, G. Langouche, J. Tavares, and H. Bender, Nucl. Instrum. Methods Phys. Res. B **106**, 404 (1995).
[9] S. Hong, C. Porri, P. Wetzel, and G. Gewinner, Phys. Rev. B **55**, 13040 (1997).
[10] X. N. Li, Z. Zhang, C. Dong, Z. X. Gong, T. C. Ma, and S. Jin, Thin Solid Films **304**, 196 (1997).
[11] D. Mangelinck, L. Wang, C. Lin, P. Gas, J. Grahn, and M. Oestling, J. Appl. Phys. **83**, 4193 (1998).
[12] P. W. Palmberg, G. E. Riach, R. E. Weber, and N. C. Mac-Donnald, *Handbook of Auger Electron Spectroscopy* (Phys. Elek. Ind. Inc., Minnesota, 1972).
[13] J. W. Ridgway and D. Haneman, Surf. Sci. **26**, 687 (1971).
[14] N. Cherief, R. Cinti, M. De Crescenzi, J. Derrien, T. A. Nguyen Tan, and J. Y. Veuillen, Appl. Surf. Sci. **41/42**, 241 (1989).
[15] A. E. Dolbak, B. Z. Olshanetsky, S. I. Stenin, S. A. Teys, and T. A. Gavrilova, Surf. Sci. **218**, 37 (1989).
[16] A. E. Dolbak, B. Z. Olshanetsky, and S. A. Teys, Surf. Sci. **373**, 43 (1997).
[17] J. G. Clabes, Surf. Sci. **145**, 87 (1984).
[18] A. J. Van Bommel and F. Meyer, Surf. Sci. **8**, 467 (1967).
[19] Eicke R. Weber, Appl. Phys. A: Solids Surf. **30**, 1 (1983).
[20] A. E. Dolbak, B. Z. Ol'shanetskiĭ, S. A. Tiĭsa, T. A. Zhachuk, JETP Lett. **66**, 643 (1997).
[21] M. K. Bakhadyrkanov, B. I. Boltaks, and G. S. Kulikov, Fiz. Tverd. Tela (Leningrad) **12**, 181 (1970) [Sov. Phys. Solid State **12**, 144 (1970)].
[22] H. Kitagava and K. Hashimoto, Jpn. J. Appl. Phys. **16**, 173 (1977).
[23] M. Y. Lee and P. A. Bennett, Phys. Rev. Lett. **75**, 4460 (1995).
[24] A. E. Dolbak, B. Z. Olshanetsky, S. I. Stenin, and S. A. Teys, Surf. Sci. **247**, 32 (1991).

Translated by M. E. Alferieff

Raman scattering in a near-surface *n*-GaAs layer implanted with boron ions

L. P. Avakyants, V. S. Gorelik, É. M. Temper, and S. M. Shcherbina

P. N. Lebedev Physics Institute, Russian Academy of Sciences, 117924 Moscow, Russia
(Submitted July 13, 1998; resubmitted December 4, 1999)
Fiz. Tverd. Tela (St. Petersburg) **41**, 1495–1498 (August 1999)

Structure in the Raman scattering spectra of near-surface *n*-GaAs layers ($n=2\times10^{18}\,\mathrm{cm}^{-3}$) implanted with 100 keV B^+ ions in the dose range $3.1\times10^{11}-1.2\times10^{14}\,\mathrm{cm}^{-2}$ is investigated. The qualitative and quantitative data on the carrier density and mobility and on the degree of amorphization of the crystal lattice and the parameters of the nanocrystalline phase as a result of ion implantation are obtained using a method proposed for analyzing room-temperature Raman spectra. © *1999 American Institute of Physics.* [S1063-7834(99)02808-7]

Ion implantation is now widely used to obtain low-resistance conducting and high-resistance insulating semiconductor layers with a specified doping profile. Investigations of the characteristics of the Raman spectra in implanted layers are important for monitoring and optimizing the indicated processes. Previously, Raman scattering has been used successfully for quantitative analysis of structural disordering[1–4] and of the electric activation of impurities[3,4] implanted in GaAs. Ion implantation ws found to change the parameters of the Raman line corresponding to the longitudinal optical (LO) phonons. Thses changes were attributed to partial amorphization of a near-surface layer of the crystal during the implantation process and to phonon localization in nanocrystals less than 20 nm in size. Characteristic features resulting from thermal annealing of ''implanted'' samples and electric activation of the impurity were found in the Raman spectrum, and they were attributed to scattering by coupled phonon–plasmon modes (CPPMs).

In the present work Raman scattering was used to investigate the characteristic features of the formation of insulating layers implanted with B^+ ions in low-resistance *n*-type gallium arsenide.

1. EXPERIMENTAL PROCEDURE

The experimental samples consisted of GaAs films obtained by vapor-phase epitaxy and silicon-doped during the growth process. High-resistance GaAs (100) served as the substrate. The film thickness was 0.5 μm. Before implantation, the films were characterized by *n*-type conductivity with carrier density $n=2\times10^{18}\,\mathrm{cm}^{-3}$. Implantation was performed with 100 keV B^+ ions and doses in the range $3.1\times10^{11}-1.2\times10^{14}\,\mathrm{cm}^{-2}$. The penetration depth of the B^+ ions was 370 nm. The ion current density did not exceed $10\mathrm{nA/cm}^2$, which made it possible to avoid overheating the sample.

The Raman spectra were recorded with an automated Raman scattering spectrometer in backscattering geometry $S(YZ)\overline{X}$. An argon laser with 514.5 nm wavelength was used as the source of excitation radiation. The power of the excitation radiation did not exceed 100 mW, so as to avoid heating the sample. The spectral width of the slit was 2 cm^{-1}.

2. EXPERIMENTAL RESULTS AND DISCUSSION

The Raman spectra obtained with implantation doses up to $6.2\times10^{12}\,\mathrm{cm}^{-2}$ are displayed in Fig. 1. The bottom spectrum (Fig. 1a) corresponds to the high-resistance GaAs substrate ($n<10^{16}\,\mathrm{cm}^{-3}$). As one can see from this figure, a sharp Raman peak corresponding to LO phonons in GaAs is observed in the spectrum in accordance with the selection rules for (100) orientation. In addition, a weak Raman peak appears at 268 cm^{-1}, corresponding to the TO mode that is forbidden in this geometry. This line is present because the finiteness of the entrance aperture of the spectrometer destroys the backscattering symmetry. Figure 1b shows the Raman spectrum of the initial *n*-GaAs epitaxial film with carrier density $n=2\times10^{18}\,\mathrm{cm}^{-3}$. This spectrum contains a weakened LO peak, whose intensity becomes comparable to

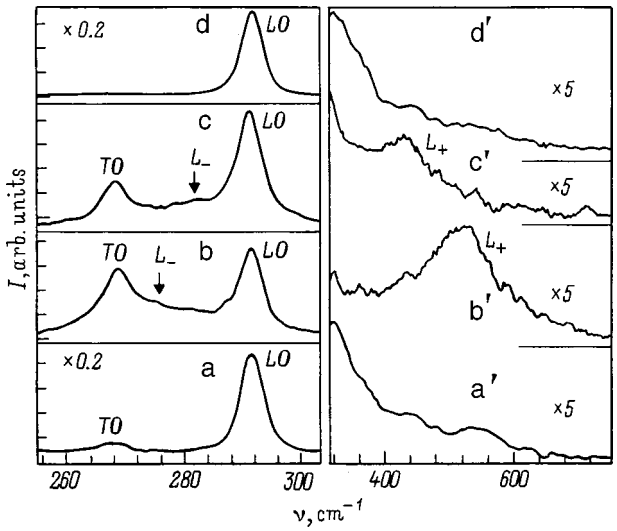

FIG. 1. Raman spectra of *n*-GaAs: a — high-resistance substrate ($n<10^{16}\,\mathrm{cm}^{-3}$); b — low-resistance film before implantation ($n=2\times10^{18}\,\mathrm{cm}^{-3}$); c — film after implantation of B^+ ions with dose $3\times10^{11}\,\mathrm{cm}^{-2}$; d — film after implantation of B^+ ions with dose $6.2\times10^{12}\,\mathrm{cm}^{-2}$.

that of the forbidden TO Raman component, and a characteristic feature (designated below as L_-) in the range of the TO and LO phonon frequencies. A wide band (L_+), comparable intensity to the second-order Raman spectrum, is also observed in the high-frequency region (Fig. 1b′). The use of crossed polarization for the incident and scattered light makes it possible to decrease the intensity of the second-order Raman spectrum and distinguish the signal from L_+. For implantation dose $D=3.1\times10^{11}\,\mathrm{cm}^{-2}$ (Fig. 1c) the center of gravity of the feature L_- and the high-frequency band L_+ shift in the direction of the LO component. The observed contour was decomposed into three Lorentzians (Fig. 2), corresponding to the Raman lines of the TO and LO photons and the L_- mode, for detailed analysis of the Raman spectra under discussion.

3. LIGHT SCATTERING BY COUPLED PHONON–PLASMON MODES IN *n*-GaAs

The implantation-induced changes in the spectrum of low-resistance GaAs can be explained on the basis of a double-oscillator model of CPPMs.[5] As a result of the interaction of the free-carrier charge-density fluctuations with the macroscopic longitudinal electric field of the LO phonons, coupled modes of a mixed plasmon–phonon character (so-called L_+ and L_- modes) arise in the Raman spectrum. The Raman scattering intensity is determined by the imaginary part of the dielectric response function

$$I\sim\mathrm{Im}\left(-\frac{1}{\varepsilon(\omega,q)}\right). \tag{1}$$

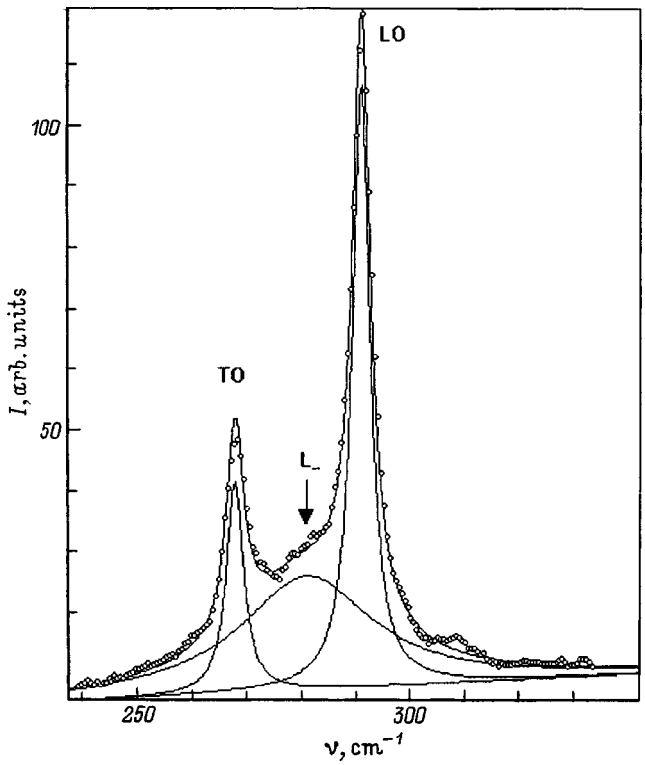

FIG. 2. Fit of Lorentzians to the Raman spectrum of an *n*-GaAs film after implantation of B^+ ions with dose $3\times10^{11}\,\mathrm{cm}^{-2}$.

For small wave numbers q, which is ordinarily the case for light scattering, where Landau damping is weak, the total longitudinal dielectric function $\varepsilon(\omega,q)$ is

$$\varepsilon(\omega,q)=\varepsilon_\infty\left(1+\frac{\omega_{\mathrm{LO}}^2-\omega_{\mathrm{TO}}^2}{\omega_{\mathrm{TO}}^2-\omega^2-i\omega\gamma}-\frac{\omega_p^2}{\omega(\omega+i\Gamma_p)}\right), \tag{2}$$

where the last two terms in parentheses describe, respectively, the contribution of the polar lattice and the contribution of plasmons to the permittivity, the plasma frequency is

$$\omega_p^2(0)=\frac{ne^2}{\varepsilon_0\varepsilon_\infty m^*},$$

m^* is the effective mass, ε_∞ is the relative permittivity, ε_0 is the permittivity of vacuum, and e is the electron charge.

Neglecting the phonon γ and plasmon $\Gamma_p\ll\omega_p$ damping, we obtain an expression for the frequencies of the coupled modes L_+ and L_-

$$\omega_\pm^2=\frac{1}{2}[(\omega_p^2+\omega_{\mathrm{LO}}^2)\pm\{(\omega_p^2-\omega_{\mathrm{LO}}^2)^2\pm4\omega_p^2(\omega_{\mathrm{LO}}^2-\omega_{\mathrm{TO}}^2)\}^{\frac{1}{2}}]. \tag{3}$$

Analysis of the relation (1) shows that there exist three variants of the apperaance of plasmon–LO-phonon oscillations. In the first one, $\Gamma_p\ll\omega_p$, two peaks with frequencies $\omega_+>\omega_{\mathrm{LO}}$ (L_+ mode) and $\omega_-<\omega_{\mathrm{TO}}$ (L_- mode) should be expected in the spectrum. In the second one, $\Gamma_p\gg\omega_p$, a single maximum is observed in the region of the LO phonons. Finally, for $\Gamma_p\simeq\omega_p$ the position of the L_- peak corresponds to the frequency range between TO and LO phonons. According to Figs. 1 and 2, the latter case occurs in the experiment. The solid lines in Fig. 2 correspond to the best approximation of the experimental results by Lorentzians corresponding to the TO, LO, and L_- modes of GaAs.

For densities $n\geqslant2\times10^{18}\,\mathrm{cm}^{-3}$ the L_- mode can be treated as a free-electron plasmon. The carrier mobility $\mu=e/m^*\Gamma_p$ and the carrier density can be estimated from the width and position of the line. For the initial film with free-electron density $n=2\times10^{18}\,\mathrm{cm}^{-3}$ the computed value is $\omega_+=500\,\mathrm{cm}^{-1}$, which is close to the observed value 510 cm^{-1} (Fig. 1b). Even though the frequency of the L_+ mode with this carrier density falls in the region of the second order spectrum of GaAs, it is visible in Fig. 1b. The facts that the frequency of the L_+ mode decreases to 420 cm^{-1} and the L_- mode is shifted into the region of the LO component with implantation dose $D=3.1\times10^{11}\,\mathrm{cm}^{-2}$ (Fig. 1c′) indicate that the carrier density n and the carrier mobility μ decrease as a result of implantation. As the implantation dose increases to $6.2\times10^{11}\,\mathrm{cm}^{-2}$, the L_+ and L_- modes no longer appear in the Raman spectrum (Fig. 1d) because of the low carrier density.

Measurements of the Hall coefficient and electric conductivity of the films showed that implantation of B^+ ions decreases the carrier density n and the carrier mobility $\mu=e/m^*\Gamma_p$. This should decrease the frequency of plasma oscillations and increase the plasmon damping Γ_p, which

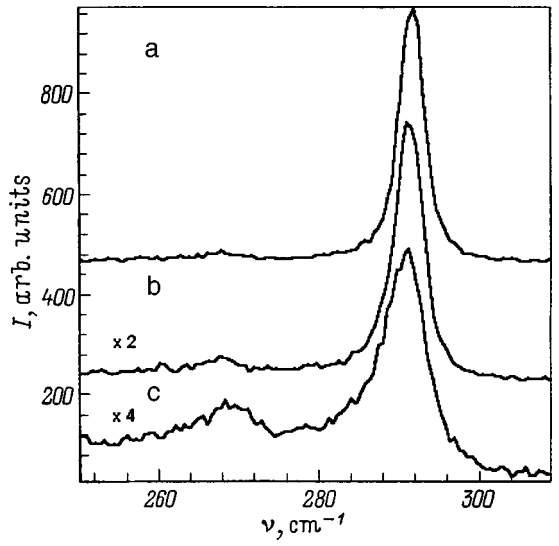

FIG. 3. Raman spectra of an *n*-GaAs film after implantation of B^+ ions with dose: a — $6.2\times10^{12}\,cm^{-2}$, b — $3\times10^{13}\,cm^{-2}$, c — $1.2\times10^{14}\,cm^{-2}$.

explains the differences in the spectra in Fig. 1. An interesting feature of the spectra (Figs. 1 and 2) is the position of the L_- line, located in the frequency range between the TO and LO oscillations. This situation could be due either to the dependence of Γ_p on the contribution of resonant plasmon–phonon interactions to the damping or to the fact that the L_- mode falls in the frequency range where Landau damping is present.

The presence of the LO mode together with the coupled modes in the Raman spectra of *n*-GaAs and the change in the intensity of this mode can be explained by the existence of a depleted layer — a surface-charge region whose thickness d depends on the carrier density[5]

$$d=\left(\frac{2\varepsilon_s\varepsilon_0\Phi_b}{e^2n}\right)^{\frac{1}{2}}, \tag{4}$$

where Φ_b is the height of the potential barrier at the surface and ε_s is the static permittivity.

At implantation dose $\sim10^{12}\,cm^{-2}$ the carrier density $N<10^{16}\,cm^{-3}$. The thickness of the depleted region is much greater than the penetration depth of light and Raman scattering by LO phonons, which do not interact with free carriers, is detected (Figs. 1a and 1d).

4. DISORDERING OF A NEAR-SURFACE LAYER OF GaAs AS RESULT OF THE IMPLANTATION OF B^+ IONS

As the implantation dose increases to $6.2\times10^{12}\,cm^{-2}$, the L_+ and L_- modes vanish and the spectrum (Fig. 1d) becomes identical to the Raman spectrum of the high-resistance sample (substrate). As the implantation dose increases further, the intensity of the LO component decreases in the Raman spectrum and this component shifts by a small amount in the direction of low frequencies and exhibits asymmetric broadening (Fig. 3a–c), which, as shown previously,[1–4] testifies to the presence of a nanocrystalline phase. At dose $1.2\times10^{14}\,cm^{-2}$ a wide continuum characteristic for amorphous GaAs appears in the spectrum (Fig. 3c). The presence of both a shifted and broadened LO component and lines of amorphous GaAs in the spectra of ''implanted'' samples indicates that the near-surface layer is an amorphous matrix containing microcrystals whose average size depends on the implantation dose.

For quantitative analysis of the experimental results following Richter's model,[6] we shall take account of phonon localization by multiplying the phonon wave function by the weighting function $W(r,L)=\exp(-2r^2/L^2)$, describing the decrease in the phonon amplitude at the boundary of a spherical region with diameter L. For this choice of the function $W(r,L)$, which gives the best agreement between theory and experiment in studying Raman spectra in GaAs microcrystals,[1] the intensity of the first-order Raman line is described by the expression

$$I(\omega)\sim L^3\int_0^1\exp\left(-\frac{q^2L^2}{4}\right)\frac{d^3q}{[\omega-\omega(q)]^2+(\Gamma_0/2)^2}, \tag{5}$$

where $\omega(q)$ is the phonon dispersion curve, Γ_0 is the width of the LO component of an infinite single crystal, the values of q are expressed in units of $2\pi/a$, and a is the lattice constant.

The value $\Gamma_0=3\,cm^{-1}$ was used in the calculations, and the dispersion curve was approximated as $\omega(q)=A+B\cos(\pi q)$, where $A=269.5$ and $B=22.5\,cm^{-1}$.[1] Analysis of the relation (5) shows that as L decreases, an appreciable low-frequency shift and asymmetric broadening of the Raman line first appear at $L\approx20$ cm. The experimentally observed frequency shifts for implantation doses 6.2×10^{12}, 3.0×10^{13}, and $1.2\times10^{14}\,cm^{-2}$ are 0.7, 1.0, and 1.7 cm^{-1}. The corresponding values of L calculated using Eq. (5) are 17, 12, and 8 nm.

It should be noted that the indicated mechanism does not change the total intensity of the Raman lines. The observed decrease of the intensity of the LO Raman component for implantation doses $>6.2\times10^{12}\,cm^{-2}$ can be explained by a decrease of the relative amount of the crystal fraction and an increase in the absorption coefficient α of the implanted layer as a result of amorphization of the layer.[2] The effective thickness $l=1/2\alpha$ of the layer investigated in Raman scattering is 44 nm for crystalline and 11 nm for completely amorphized GaAs,[2] which is almost an order of magnitude smaller than the average thickness of the implanted layer. Therefore it can be assumed that the implanted layer is a uniform two-phase medium with absorption coefficient for light $\alpha=\alpha_Cf_C+\alpha_Af_A$, where α_C and α_A are, respectively, the absorption coefficients of the crystalline and amorphous GaAs, and f_C and f_A are the relative amounts of the crystal

TABLE I. The dependence of the degree f_C of crystallinity and the size L of nanocrystals in *n*-GaAs films versus the implantation dose Φ.

Φ, cm^{-2}	f_C	L, nm
3×10^{11}	1	–
6.2×10^{12}	0.90	17
3×10^{13}	0.86	12
1.2×10^{14}	0.8	8

and amorphous fractions, where $f_C + f_A = 1$. In this case the ratio of the total intensities of the LO components of the ''implanted'' and ''nonimplanted'' samples (substrates) is given by

$$\frac{I'}{I_0} = \frac{f_C \alpha_C}{f_C \alpha_C + f_A \alpha_A}. \tag{6}$$

The dose dependences of F_C calculated using this formula are presented in Table I.

In summary, the structure in the Raman spectra of near-surface layers of *n*-GaAs implanted with B^+ ions were established. Qualitative and quantitative data on the carrier density and mobility and the degree of amorphization of the crystal lattice and the parameters of the nanocrystalline phase in the process of ion implantation were obtained on the basis of a method proposed for analyzing room-temperature Raman spectra.

This work was supported by the Russian Fund for Fundamental Research (project No. 98-02-18372).

[1] K. K. Tiong, P. M. Amirtharaj, F. H. Pollak, and D. E. Aspnes, Appl. Phys. Lett. **44**, 122 (1984).
[2] M. Holtz, R. Zallen, O. Brafman, and S. Matteson, Phys. Rev. B **37**, 4609 (1987).
[3] M. Gargouri, B. Prevot, and C. Schwab, J. Appl. Phys. **62**, 3902 (1987).
[4] L. P. Avakyants, V. S. Gorelik, I. A. Kitov, and A. V. Chervyakov, Fiz. Tverd. Tela (St. Petersburg) **35**, 1354 (1993) [Phys. Solid State **35**, 684 (1993)].
[5] *Light Scattering in Solids*, Vol. IV, edited by M. Cardona and M. Güntherodt (Springer-Verlag, New York, 1986; Mir, Moscow, 1986).
[6] H. Richter, Z. P. Wang, and L. Ley, Solid State Commun. **39**, 625 (1981).

Translated by M. E. Alferieff

FULLERENES AND ATOMIC CLUSTERS

Characteristic features of the melting of two-dimensional mesoscopic Wigner clusters

Yu. E. Lozovik*) and E. A. Rakoch

Institute of Spectroscopy, Russian Academy of Sciences, 142092 Troitsk, Moscow District, Russia
(Submitted October 20, 1998)
Fiz. Tverd. Tela (St. Petersburg) **41**, 1499–1504 (August 1999)

Two-dimensional Wigner microclusters in a semiconductor dot are studied. Their melting is investigated in detail and it is shown that, for typical mesoscopic clusters possessing a shell structure, melting occurs in two stages: orientational melting (rotation of the shells relative to one another) and total melting, where the shells start to overlap with one another and exchange particles. An example of a ''magic'' microstructure which has a triangular structure and melts in a single stage is presented. For this, the temperature dependences of various quantities characterizing cluster structure are investigated. The change in the distribution of cluster configurations over local minima of the potential energy with increasing temperature is investigated. At temperatures below the temperature of total melting, a cluster is always located near the configuration of a global minimum and, at temperatures above the temperature of complete melting, a cluster can be located with finite probability near configurations corresponding to various local minima of the potential energy. © *1999 American Institute of Physics.* [S1063-7834(99)02908-1]

In the last few years, a great deal of attention has been devoted to the study of systems consisting of a finite number of particles having a repulsive interaction potential confined by an artificial or natural external potential.[1–6] Systems consisting of a small number of confined particles with physical properties that are different (as a result of their small size) from those of crystals are called clusters. It is impossible to distinguish ''volume'' and ''surface'' particles inside a mesoscopic cluster. Adding only a single particle can produce a large rearrangement of the structure of a mesoscopic cluster. The reverse situation occurs in a macrocluster (however, in contrast to a microparticle, the number of particles in the volume phase is of the same order of magnitude as the number of particles on the surface in a macrocluster).

Two-dimensional dipole and vortex clusters and their melting have been investigated in detail in Refs. 3 and 4, respectively. Specifically, it has been shown that, depending on the number of particles, dipole clusters can melt in one or two stages[3] while vortical clusters (for $N<200$ particles) can melt only in two stages. For two-stage melting, orientational melting occurs at a lower temperature, and then total melting occurs at a higher temperature (see Ref. 4). The term ''orientational melting'' is used in the following sense: At a certain temperature certain shells start to rotate relative to one another, retaining their crystallinity, but the shell structure of the cluster remains.

The structure and melting of two-dimensional Coulomb clusters have been studied in Refs. 2, 5, and 6. One of the most interesting physical realizations of Coulomb clusters are electrons in semiconductor dots.[7] Crystallized mesoscopic Coulomb clusters possess a shell structure,[2,5,6] as a rule differing substantially from the structure of an extended Wigner crystal, approaching the latter only if the number of particles is sufficiently large (and in the rare case — for magic clusters, see below). It has been shown that in classic Coulomb mesoscopic clusters orientational melting occurs for all pairs of shells, while in macroclusters it occurs only for the outer pairs of shells (see Ref. 5). However, the more detailed investigation performed in the present work has shown that there exist ''magic clusters'' that possess at a global minimum a high-symmetry structure and melt in a single stage (i.e., orientational melting is absent).

For this reason, our objective in the present work is to investigate in detail the change in characteristics and the melting of two-dimensional ''crystalline'' electronic (Wigner) microclusters. We shall study the classic regime, where the de Broglie thermal wavelength of the electrons is

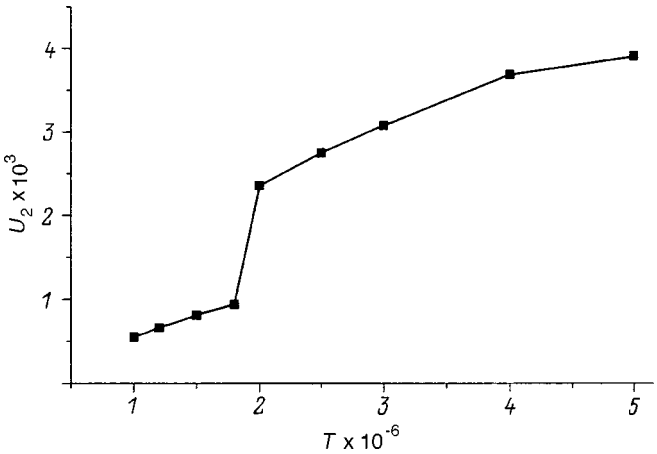

FIG. 1. Relative angular displacement U_2 versus the temperature T. $N=20$.

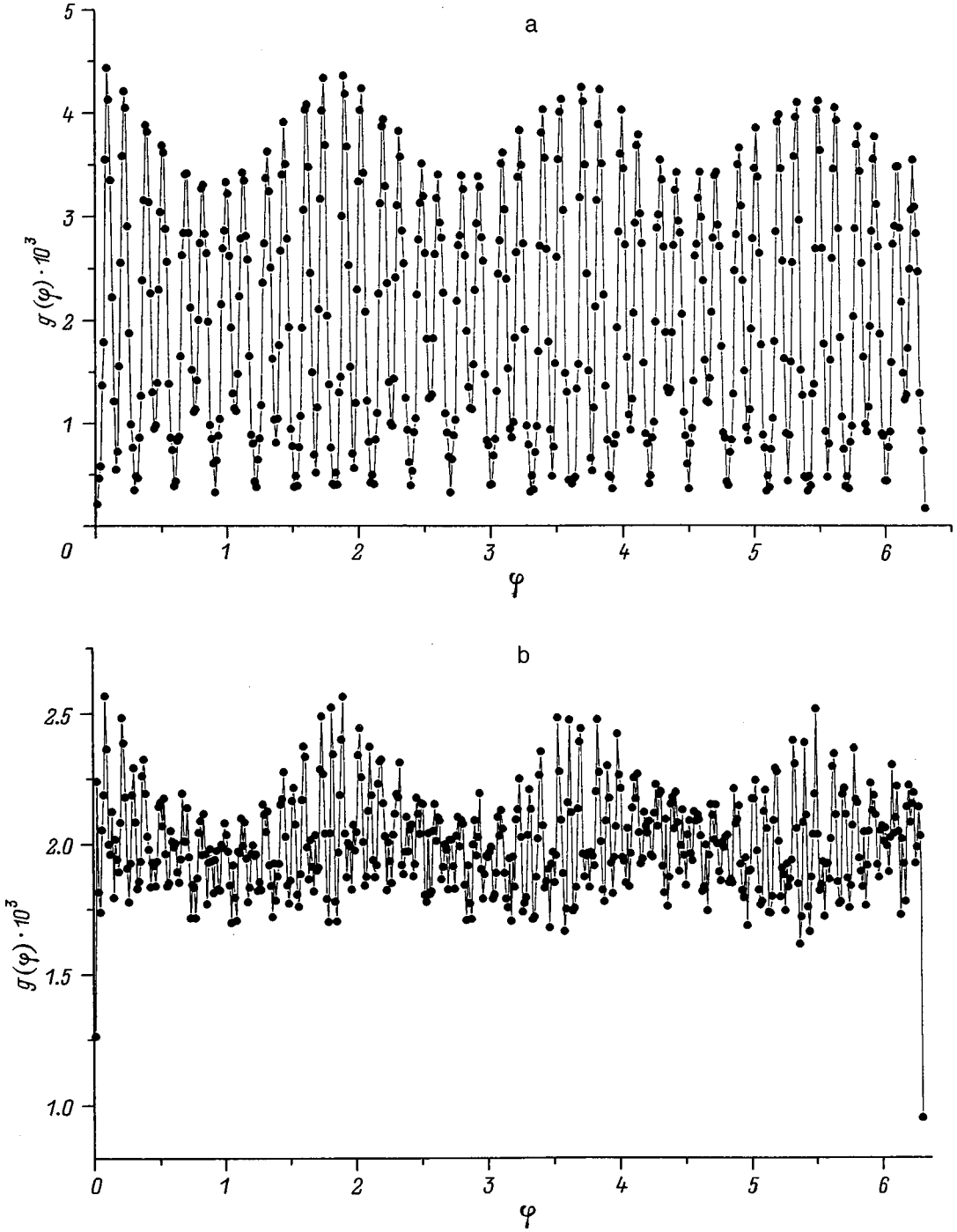

FIG. 2. Distribution function $g(\varphi)$ of the angles between the particles of two shells. $N=20$. a — $T=1\times10^{-6}$; b — $T=4\times10^{-6}$.

much longer than the average distance between electrons. To describe the orientational melting of a cluster, the temperature dependence of the parameter characterizing the relative orientational order of the shell pair under study is investigated. The analysis is performed for clusters with different shell structure. Moreover, it will be shown that at a temperature below the temperature of complete melting (but even at a temperature above the temperature of orientational melting) a cluster is located near a configuration of a single (global) minimum of the energy, and at temperature aboves the temperature of complete melting a cluster ''hops'' between different minima.

The physical model of the system is described in Sec. 1. A numerical method for solving the problem and the physical quantities investigated are described in Sec. 2. The computational results for melting are presented in Sec. 3.

1. PHYSICAL MODEL

A physical realization of two-dimensional Coulomb clusters are electrons in a semiconductor dot[7] (this model also describes electrons in a well on a liquid He surface[8] or laser-cooled ions in a flat Penning or Polya type trap).

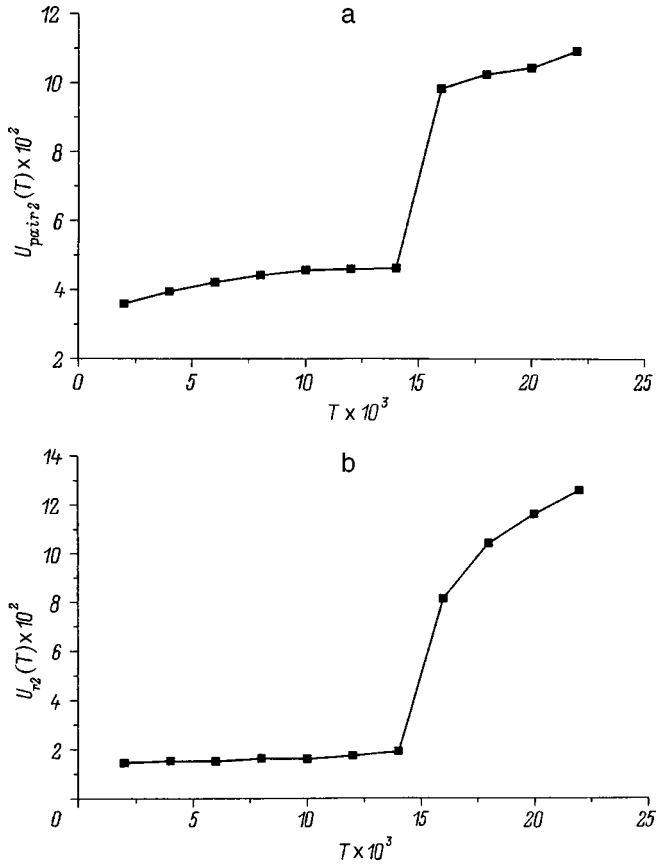

FIG. 3. Temperature dependence of the quantities characterizing radial displacement. $N=20$. a — Relative radial displacement $U_{\text{pair2}}(T)$; b — absolute radial displacement $U_{r2}(T)$.

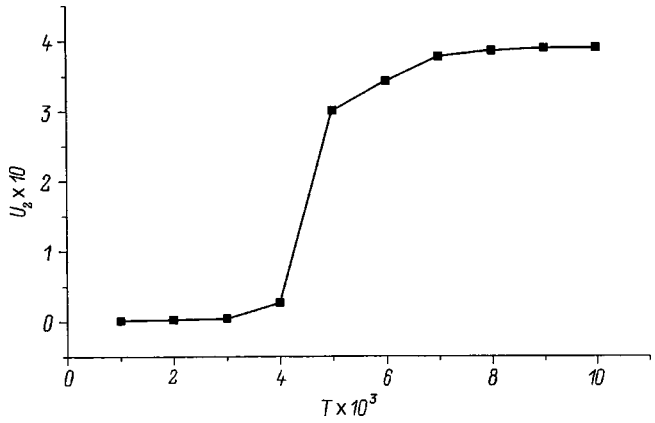

FIG. 4. Relative angular displacement U_2 versus the temperature T. $N=19$.

We shall investigate a two-dimensional system with a finite number N of charged particles repelling one another according to the Coulomb law $U_{ij}=e^2/r_{ij}$, where $r_{ij}=r_i-r_j$ and r_i is the radius vector of particle i. A parabolic confining potential $U_i=\alpha r_i^2$ is considered.

In thermal equilibrium theclassic Coulomb clusters studied here are characterized by a single dimensionless parameter $1/T'=\Gamma=(e^{4/3}\alpha^{1/3})/k_BT$. The potential energy in dimensionless form is

$$U=\sum_{i<j}^{N}\sum_{i=1}^{N}\frac{1}{r_{ij}}+\sum_{i=1}^{N}(r_i)^2. \tag{1}$$

Numerical estimates of the parameter α for certain experimental systems are presented in, for example, Refs. 9 and 10.

2. NUMERICAL METHOD

The Monte Carlo method with two different algorithms was used to investigate melting. The first algorithm implemented random motion of one (randomly chosen) particle and random motion of one (randomly chosen) shell (see Refs. 3–5). The second algorithm employed a multigrid method (V cycle): first $1=2^0$ particle, then $2=2^1$, then $4=2^2$ particles, and so on move, after which all particles, half of the particles, and so on down to one particle move. Numerical calculations showed that the second method is 2.5 times more efficient than the first one (i.e. 2.5 times more iterations in the first method than the second method are required to achieve the same accuracy). To achieve good accuracy the system at each temperature was heated for 3×10^4 iterations, and then the system was investigated for $5\times 10^6-10^7$ iterations.

We calculated the following physical quantities:

1) The total potential energy U_{pot} of the system according to Eq. (3);

2) the specific heat $C=(\langle E^2\rangle-\langle E\rangle^2)/T$, where $E=U$; here and below the averaging $\langle\ldots\rangle$ is performed over the number of measurements with different Monte Carlo configurations (10^3 iterations each);

3) the relative radial displacement

$$U_{\text{pair}}=\frac{2}{N(N-1)}\sum_{i<j}^{N}\sum_{i=1}^{N}\sqrt{\frac{\langle r_{ij}^2\rangle}{\langle r_{ij}\rangle^2}-1} \tag{2}$$

or

$$U_{\text{pair2}}=\frac{2}{N(N-1)}\sum_{i<j}^{N}\sum_{i=1}^{N}\left(\frac{\langle r_{ij}^2\rangle}{\langle r_{ij}\rangle^2}-1\right); \tag{3}$$

4) the radial Lindeman coefficient

$$U_r=\frac{1}{N}\sum_{i=1}^{N}\sqrt{\frac{\langle r_i^2\rangle}{\langle r_i\rangle^2}-1} \tag{4}$$

or the quantity

$$U_{r2}=\frac{1}{N}\sum_{i=1}^{N}\frac{\langle r_i^2\rangle}{\langle r_i\rangle^2}-1; \tag{5}$$

5) the radial distribution function

$$g_r(r)=\left\langle\sum_{i=1}^{N}\delta(r_i-r)\right\rangle; \tag{6}$$

6) the radial correlation function

$$g_{\text{pair}}(r)=\left\langle\sum_{i<j}^{N}\sum_{i=1}^{N}\delta(r_i)\,\delta(r_j-r_i+r)\right\rangle; \tag{7}$$

7) the relative mean-square angular displacement

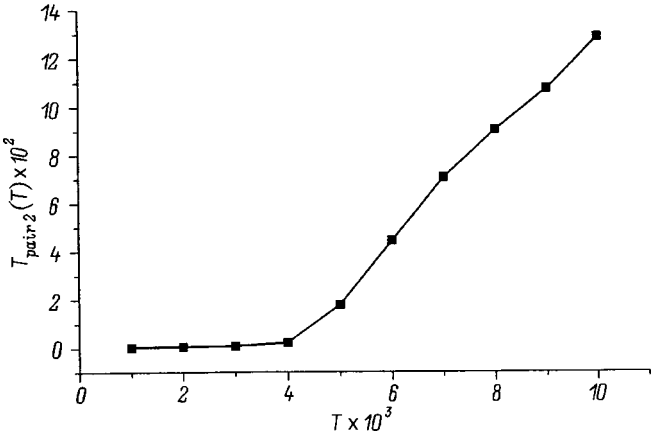

FIG. 5. Relative radial displacement $U_{\text{pair2}}(T)$ versus the temperature. $N=19$.

$$U_2=\frac{2}{N_1N_2}\sum_{i=1}^{N_1}\sum_{j=1}^{N_2}\langle(\varphi_i-\varphi_j)^2\rangle-\langle(\varphi_i-\varphi_j)\rangle^2; \tag{8}$$

8) the relative orientational order parameter of the shells l_1 and l_2

$$\rho_{l_1l_2}=\langle\Psi_{l_1},\Psi^*_{l_2}\rangle, \tag{9}$$

where $\Psi_l=\frac{1}{N_l}\Sigma_{i=1}^{N_l}\exp(iN_l\varphi_{il})$ is the angular order parameter of the shell l and N_l is the number of particles in the shell l; the relative orientational order parameter of the shells should vanish when orientational melting of the shells occurs;

9) the angular correlation function of two shells

$$g(\varphi)=\left\langle\sum_{i=1}^{N_1}\sum_{j=1}^{N_2}\delta(\varphi_i)\,\delta(\varphi_j-\varphi_i+\varphi)\right\rangle; \tag{10}$$

10) the distribution of particles over local minima — the probability $P_{\min}$ of observing the system near different minima of the potential energy. To calculate this probability the system was periodically (once in 10^5 iterations) rapidly cooled to a temperature (1×10^{-7}) several orders of magnitude lower than all melting temperatures for 2×10^4 iterations. Then the minimum value of the energy was compared with the value of the energy in different local minima and, if it was close to the energy in a certain minimum, then the system was assumed to fall into this minimum (the local and global minima of the total potential energy were calculated beforehand).

3. MELTING OF TWO-DIMENSIONAL COULOMB CLUSTERS

Clusters with a close number of particles $N=19$ and $N=20$ but with substantially different structures in the global minima of the potential energy were chosen to calculate the melting. In addition, the cluster with $N=19$ possesses the configuration (1, 6, 12) and is almost an exact fragment of a triangular lattice, while the cluster with $N=20$ has the configuration (1, 7, 12) and a distinct shell structure. For this reason, the difference in the characters of melting of these clusters is of interest. It was found that the $N=20$ cluster melts in two stages, the temperature of orientational melting being very different from the temperature of total melting,

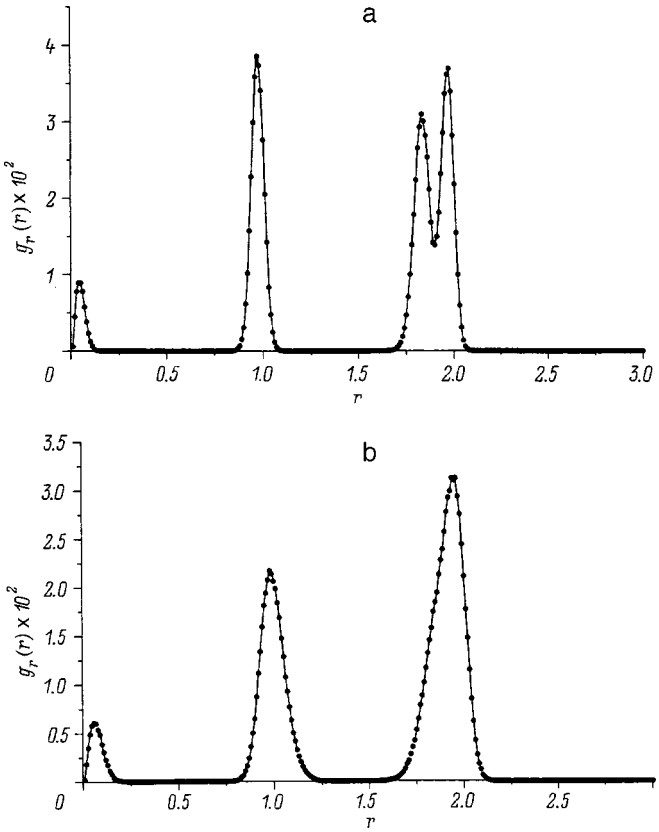

FIG. 6. Radial distribution function $g_r(r)$. $N=19$. a — $T=3\times10^{-3}$; b — $T=7\times10^{-3}$.

while the cluster with $N=19$, because of its high symmetry, melts in a single stage, which is unique for Coulomb microclusters. Previously it was assumed[1–6] that all Coulomb clusters melt in two stages, and in mesoscopic clusters (or microclusters) orientational melting of all pairs of shells occurs, while in macroclusters only the outer pairs of shells melt.

Orientational melting of the $N=20$ cluster occurs at a very low temperature $T_{c_2}=1.8\times10^{-6}$. The relative angular displacement U_2 undergoes a sharp jump (Fig. 1), and the relative orientational order parameter $\rho_{l_1l_2}$ of the shells drops to zero. For $T<T_{c_2}$ the function $g(\varphi)$ possesses zeros (see Fig. 2a), and for $T>T_{c_2}$ the zeros in the function $g(\varphi)$ vanish (see Fig. 2b), confirming the presence of orientational melting at $T=T_c$ in the cluster $N=20$. The very low orientational melting temperature is due to the fact that the numbers of particles in the shells 7 and 12 are incommensurate (they do not have common divisors), and therefore the relative potential energy of the ''frozen'' shells possesses very shallow minima as a function of the rotation angle. The period of the function $g(\varphi)$ for $T<T_{c_2}$ is inversely proportional to the lowest common multiple of the numbers of particles in the shells $P=(2\times2\pi)/(\text{LCM}[l_1,l_2])=4\pi/12\times7=2\pi/42$ (the factor of 2 in the numerator is due to the corresponding symmetry of the cluster); see Fig. 2a.

The temperature of complete melting of a cluster is somewhat higher $T=T_{c_1}=1.4\times10^{-2}$. The following quantities have kinks: the radial relative displacement U_{pair} and

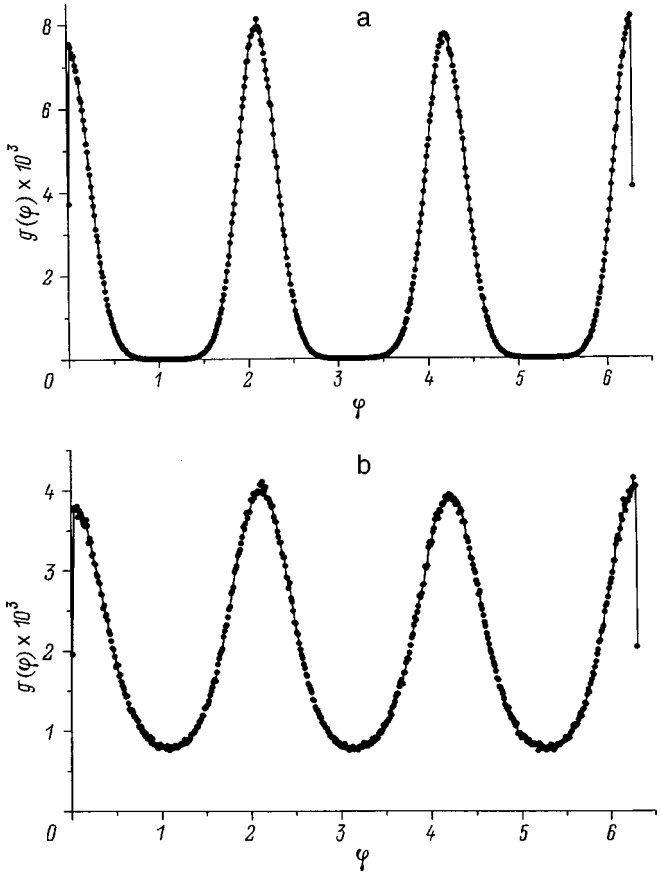

FIG. 7. Distribution function $g(\varphi)$ of the angles between the particles of two shells. $N=19$. a — $T=3\times10^{-3}$; b — $T=7\times10^{-3}$.

U_{pair2}, the radial Lindeman coefficient U_r, and the variation U_{r2} of the radial distances (see Fig. 3).

In the $N=19$ cluster U_2 undergoes a jump at the same temperature $T_c=4\times10^{-3}$ as U_{pair}, U_{pair2}, U_r, and U_{r2} (compare Figs. 4 and 5). At $T=T_c$ the two maxima of the outer shell merge in the function $g_r(r)$, and the shells are strongly smeared in the radial direction (see Fig. 6); the zeros in the function $g(\varphi)$ vanish (see Fig. 7). All this shows that orientational melting is absent in the $N=19$ cluster, and total melting of a cluster occurs immediately at $T=T_c$. In Fig. 7 the period of the function $g(\varphi)$ is $42\pi/12=2\pi/3$ (the coefficient 4 in the numerator is due to the corresponding symmetry of the cluster).

It should be noted that the potential energy and specific heat as functions of temperature have no characteristic features in both clusters, and therefore these dependences cannot be used to determine the melting temperatures. Strictly speaking, orientational and total melting in microclusters can be called phase transitions only conditionally, since the system is finite.

We also investigated the distribution of the system over local minima with increasing temperature. It was found that for $N=19$ and 20 a cluster at a temperature less than the temperature of complete melting is always near a configuration corresponding to a global minimum of the potential energy. At a temperature above the temperature of total melting the probability of a cluster being near a configuration corresponding to a global minimum decreases and becomes constant; the probabilities that a cluster is found near a configuration corresponding to a local minimum of the potential energy increase and also saturate at a constant value. Figure 8 shows the changes in the probabilities of finding an $N=20$ cluster in a global minimum of the potential energy with the shell structure (1, 7, 12) and in the local minimum with structure (1, 6, 13) closest to it. The cluster hops between the configurations corresponding to different local minima.

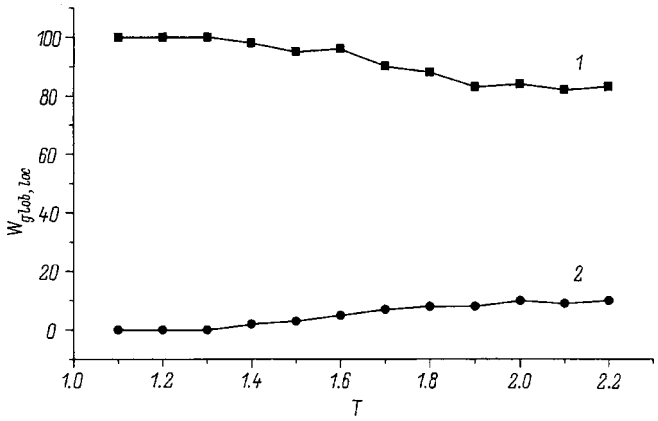

FIG. 8. Probability $W(T)$ of finding a cluster near a global minimum (1) and a local minimum (2) of the potential energy as a function of temperature T. $N=20$.

In conclusion, we note that certain results of the present work pertain not only to mesoscopic electronic clusters but also an extended Wigner crystal in semiconductors with defects, structural roughness, and so on. Indeed, in the presence of random potential wells, an electronic crystal can, under certain conditions, break up into individual clusters near these wells as the clusters ''melt'' as described above.

This work was supported by the Russian Fund for Fundamental Research, INTAS, and the program ''Physics of Nanostructures.''

*)E-mail: lozovik@isan.troitsk.ru

[1] Yu. E. Lozovik, Usp. Fiz. Nauk **153**, 356 (1987) [Sov. Phys. Usp. **30**, 912 (1987)]; Izv. Ross. Akad. Nauk, Ser. Fiz. **60**, 72 (1996).
[2] Yu. E. Lozovik and V. A. Mandelshtam, Phys. Lett. A **145**, 269 (1990); Yu. E. Lozovik, V. A. Mandelshtam, Phys. Lett. A **165**, 469 (1992).
[3] Yu. E. Lozovik and E. A. Rakoch, Phys. Lett. A **235**, 55 (1997); Yu. E. Lozovik and E. A. Rakoch, Fiz. Tverd. Tela (St. Petersburg) **40**, 1379 (1998) [Phys. Solid State **40**, 1255 (1998)]; A. I. Belousov, Yu. E. Lozovik, cond-mat/9806108.
[4] Yu. E. Lozovik and E. A. Rakoch, JETP Lett. **65**, 282 (1997); Yu. E. Lozovik and E. A. Rakoch, Fiz. Tverd. Tela (St. Petersburg) **39**, 1005 (1997) [Phys. Solid State **39**, 901 (1997)]; Yu. E. Lozovik and E. A. Rakoch, Phys. Rev. B **57**, 1214 (1998).
[5] Yu. E. Lozovik and E. A. Rakoch, Phys. Lett. A **240**, 311 (1998).
[6] F. M. Peeters, V. A. Schweigert, and V. M. Bedanov, Physica B **212**, 237 (1995).
[7] M. A. Read and W. P. Krik, *Nanostructure Physics and Fabrication* (Academic Press, Boston, 1989).
[8] P. Leiderer, W. Ebner, and V. B. Shikin, Surf. Sci. **173**, 405 (1987).
[9] F. Diedrich, E. Peik, J. M. Chen, W. Quint, and H. Walther, Phys. Rev. Lett. **59**, 2931 (1988).
[10] S. L. Gilbert, J. J. Bollinger, and D. J. Wineland, Phys. Rev. Lett. **60**, 2022 (1988).

Translated by M. E. Alferieff

Quantum confinement in CdS_xSe_{1-x} spherical nanocrystals in a fluorophosphate glass matrix

V. A. Gaĭsin, S. V. Karpov,*) E. V. Kolobkova, B. V. Novikov, V. D. Petrikov, A. A. Lipovskiĭ, D. L. Fedorov, and M. A. Yastrebova

Institute of Physics, St. Petersburg State University, 198904 St. Petersburg, Petrodvorets, Russia
(Submitted December 24, 1998; resubmitted January 29, 1999)
Fiz. Tverd. Tela (St. Petersburg) **41**, 1505–1510 (August 1999)

Differential (wavelength-modulated) absorption of sulfoselenide solid-solution nanocrystals has been studied in a glassy fluorophosphate matrix near the fundamental absorption edge at 360–620 nm. The observed oscillations in the absorption are attributed to size quantization of electrons and holes under strong quantum-confinement conditions. The sulfur content in the mixed semiconductor has been refined from Raman scattering spectra in CdS_xSe_{1-x} samples with $x=0.30$, and the nanocrystal size ($R\cong 30$ Å) has been derived from low-frequency Raman scattering spectra. These data were used to calculate the energies of electron-hole transitions in nanocrystals of mixed composition, and their subsequent comparison with experiment. The calculations were found to be in a good agreement with the observed experimental absorption spectrum for nanocrystals about 45 Å in size. The applicability of band-structure simulation for a nonspherical nanocrystal grown in a fluorophosphate glass matrix is discussed.
 [S1063-7834(99)03008-7]

Self-organization of a physical system is intimately connected with transformation of its energy states, and investigation of its eigenstates is of considerable importance for the understanding of the processes governing structural arrangement of atoms in nanocrystalline objects. As is well known, these processes culminate in the formation in periodic crystalline solids with an electronic-band structure. At the same time the contribution of both periodic and random potentials to a concrete band structure remains not quite clear. On the other hand, the technology of preparing semiconductor nanoobjects (quantum dots) developed recently permits one to vary the size of such nanocrystals and, hence, their energy spectrum and optical properties, which is already finding application in nanoelectronics devices.[1,2] This accounts for the increased interest in nanoobjects by both theorists and experimenters.[3–7]

Decreasing the size of a periodic system, i.e. transition to a nanoobject, entails both renormalization of the eigenstates of the system and discretization of the observed transitions corresponding to quasicontinuous states of the valence and conduction band of a semiconductor. Such a discrete manifestation of individual quantum transitions depends on the size of the crystalline object and is called a size-quantization effect. It results from the quantum confinement of motion of the exciton quasiparticle in a nanoobject and gives rise to quantization of its energy; it may be added that the energy levels of a nanostructure depend strongly on the size and shape of the nanocrystal.

Most of studied semiconductor nanocrystals are embedded in a borosilicate matrix, where the concentration of the II–VI semiconductors prepared by conventional technology is usually not in excess of 0.1–0.2 wt.%. Phosphate systems are more flexible in this respect and permit increasing the content of a semiconductor in a glass to 1–1.5%. On the whole, the nature of the size quantization of excitonic states in CdS_xSe_{1-x} mixed crystals grown in a fluorophosphate glass matrix is clear.[4–8] However quite frequently the model of a simple exciton band with a parabolic dispersion law does not fit adequately to the real structure of these crystallites and describes only approximately the experiment. This is particularly true of mixed nanocrystals. Besides, synthesis of mixed nanocrystals in a fluorophosphate matrix results in formation of nonspherical nanoparticles, whereas the theory relates to spherical objects. Moreover, spin-orbit splitting in the valence-band structure, whose parameters depend on the relative contents of sulfur and selenium in the cadmium sulfoselenide solid solution, makes the absorption spectrum in the excitonic region still more complex.

This paper reports on a comprehensive study of the spectrum of excitonic absorption of mixed cadmium sulfoselenide nanocrystals and compares it with a spectrum calculated in the approximation of a parabolic band and of a spherical nanoparticle, in order to reveal the parameters of its band structure. A Raman study of the optical-phonon frequencies and low-frequency scattering in the 5–50 cm^{-1} interval were used to derive refined values of the relative sulfur and selenium concentrations in the sample under consideration and the size of the nanocrystalline formations.

1. EXPERIMENT

Nanocrystals of cadmium sulfoselenide were grown within a volume of glass where CdS and CdSe were added. We used the P_2O_5–Na_2O–ZnO–AlF_3 glass-forming system permitting preparation of glasses with increased semiconductor contents. The synthesis was carried out at a temperature about 1100 °C. The characteristic temperature T_l for these

glasses is 410 °C. An analysis of the composition of the glasses thus produced, made with an electron-beam microprobe, yielded a maximum cadmium sulfoselenide concentration of about 1.2%.[9] The nanocrystals were grown at glass treatment temperatures above T_l in the course of diffusive phase decomposition of a supersaturated solid solution. Annealing the glasses resulted in their coloring, which varied from light yellow to dark red (which corresponded to the optical absorption edge positions of 0.4 to 0.7 μm). A TEM study of the annealed samples demonstrated the presence of inclusions varying in size from 2 to 6 μm, while unannealed glass samples did not reveal the existence of grains. An interesting feature of the inclusions thus formed is their clearly pronounced nonsphericity.[9]

Differential absorption spectra of the mixed semiconductor samples were studied near the absorption edge in the 360–620-nm spectral region. The spectral equipment used, a DFS-12 spectrometer modified to perform wavelength modulation, permitted detection of weak lines against a strong absorption background continuum with a resolution of 0.01 eV. An incandescent lamp with an effective thermal temperature of 3200 K was used as a source of continuum radiation, which did not produce any features in the region under study. The measurements were carried out at room- and liquid-nitrogen temperatures. The Raman scattering spectra were studied with an automated DFS-24-spectrometer-based arrangement provided with a step motor, a photon counting system, and a computer-controlled MS-0511 mass spectrometer. The light source was an LGN-503 argon-ion laser ($\lambda_0 = 488.0$ nm, $W = 300$ mW) and an LG-75 helium-neon laser ($\lambda_0 = 632.8$ nm, $W = 20$ mW). All Raman spectral measurements were performed in the 180° geometry.

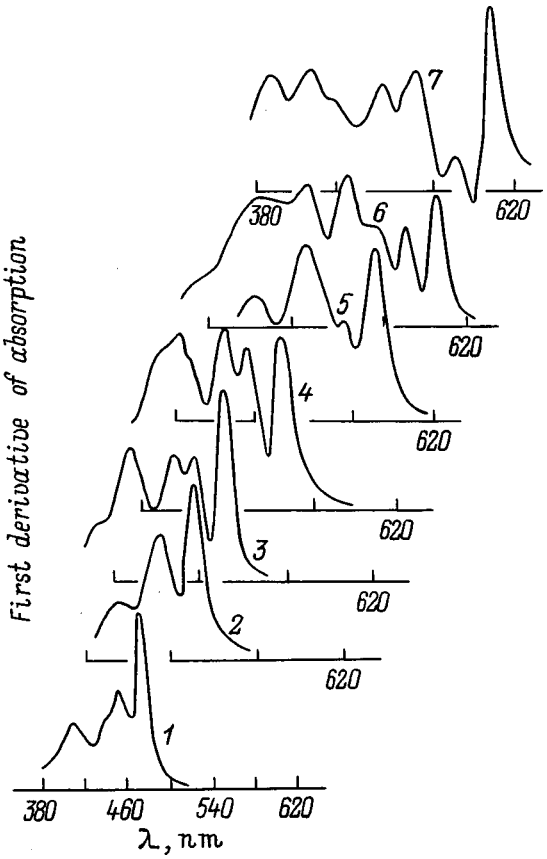

FIG. 1. Wavelength-modulated light transmission spectra of cadmium sulfoselenide nanocrystals in fluorophosphate glassy matrices. $T = 77$ K. Sulfur concentration in the CdS_xSe_{1-x} mixed nanocrystal (%): *1* — 100, *2* — 90, *3* — 76, *4* — 60, *5* — 40, *6* — 20, *7* — 0.

2. INTERBAND ABSORPTION

The light transmission spectra of the cadmium sulfoselenide solid solution measured for different sulfur and selenide concentrations are displayed in Fig. 1. The wavelength modulation technique employed in this work permitted isolation of weak features associated with discrete absorption lines against the strong absorption background. To compare the spectra with calculations, one can conveniently use the second-derivative absorption spectra (see Fig. 4), whose minima lie exactly at the positions of the absorption spectral lines. As the temperature decreases from 300 to 77 K, the intensity of the lines increases, and their halfwidth decreases to make the whole spectrum more contrasting, and all features move toward higher energies. The aperiodic oscillations clearly visible in interband absorption are associated with transitions between the hole and electron quantum-confined levels.[10,11]

The pattern of an absorption spectrum depends essentially on the sulfur and selenium concentrations in a mixed nanocrystal, because the semiconductor absorption edge varies from 1.8 eV for pure CdS to 2.5 eV for pure CdSe (at 77 K). Besides, the change of the spin-orbit splitting Δ_{so} from 62 to 420 meV for the extreme compositions also affects strongly size quantization spectra, which, according to literature data,[10,11] can be associated with the contribution of the spin-orbit-split valence band Γ_7 to the formation of the fundamental absorption edge in a mixed nanocrystal. However no complete assignment of the mixed cadmium-sulfoselenide line spectrum is presently available.

The quantum-confined optical properties of nanocrystals become manifest when the quantum dot is comparable in size to or less than the exciton Bohr radius. In this limit, defined as the strong confinement regime,[3] the wave functions of the nanoobject undergo three-dimensional quantization as a result of taking into account the quantum-dot boundaries and can be described through the individual electron and hole wave functions.

The electronic and hole states are described by the wave-function envelope method,[9] which takes into account the effect of the periodic potential in the region of the crystalline phase by introducing effective particle masses described by Bloch functions, and the finiteness of the nanocrystal size R, by using an envelope (apodizing) function. For a simple parabolic band (with an effective mass m^*) approximating the real valence band of the II–VI-type semiconductors and a spherical particle the electron wave function can be written

$$|nlm\rangle = \sqrt{\frac{1}{4\pi R^3}}\,\frac{J_l\left(\alpha_{nl}\dfrac{r}{R}\right)}{J_{l+1}(\alpha_{nl})}\,Y_l^m(\theta,\varphi),$$

where $Y_l^m(\theta,\varphi)$ is a spherical harmonic, $J_l(z)$ are lth order Bessel functions, and α_{nl} is the nth root of the Bessel function of order l. The eigenenergies can be expressed in the form

$$E_l=\frac{\hbar^2}{2m^*}\left(\frac{\alpha_{nl}}{R}\right)^2.$$

Thus the solutions have convenient quantum numbers n, l, and m, and, similar to atomic spectroscopy, eigenstates with quantum number n differing in the quantum number of the orbital momentum $l=0,1,2,\ldots$, are denoted by symbols s, p, d, etc.

Therefore the electronic ground state in CdS- and CdSe-type semiconductors is well known — it is the $1S$ state (with the orbital momentum $l=0$).

The valence band consisting of a fourfold degenerate Γ_8 subband with light and heavy holes and of a twofold degenerate Γ_7 subband presents a more complex situation. It is described by a six-band Luttinger Hamiltonian[12] with more complex corresponding wave functions, but the hole quantum-confined eigenvalues are also inversely proportional to the squared nanocrystal size $1/R^2$. Experimental values for pure CdSe fit well to the calculated spectrum.[13,14] The situation is more complex for mixed nanocrystals. An interesting calculational feature for CdSe is the specific transformation of the hole quantum-confined levels occurring when the spin-orbit split valence-subband Γ_7 forms near the energy $\Delta_{so}=420$ meV.[13] Such a transformation is associated with the forcing apart of hole quantum-confined states with the same symmetry, and it results in anticrossing of these levels (Fig. 5). At the same time the wave-function symmetry, i.e., the mixing of the valence-band S and D states, changes depending on nanocrystal size and gives rise to a change in the intensity of transitions to these states. This complicates unambiguous assignment of the line structure in the absorption spectra of cadmium sulfoselenide nanocrystals, particularly of the corresponding solid solutions. According to Ref. 6, a quasi-line spectral structure can also appear due to several transitions of comparable intensity from different quantum-confined light- and heavy-hole levels at the valence-band top, without a clearly pronounced contribution of the spin-orbit split Γ_7 valence band. This conjecture was partially refuted by the discovery[10,15] that in a set of glass samples with nanocrystals having different relative sulfur and selenium contents (but with selenium concentrations not above 40%) one can always isolate absorption lines separated from the lowest excited state by the amount of the spin-orbit splitting in macrosamples of the same composition. Therefore, when attempting interpretation of experimental data, one should always also take into account transitions from the Γ_7 spin-orbit split band. There are doubts, however, as to whether the spin-orbit splittings Δ_{so} in a macro- and nanocrystal behave in the same way. The more so that the frequently used linear interpolation of the quantity Δ_{so} from 62 meV in CdS to 420 meV in CdSe does not find experimental confirmation.[15]

Therefore we used excitonic absorption spectra to choose a sample, from those available, having an extensive line structure and calculated its electron-hole transition states. Because the result of a calculation depends substantially on the magnitude of the spin-orbit splitting Δ_{so} and nanocrystal size R, we carried out, in order to determine these quantities, independent studies of Raman scattering spectra in the phonon frequency region of crystalline cadmium sulfide and selenide, as well as at low frequencies near the Rayleigh line.

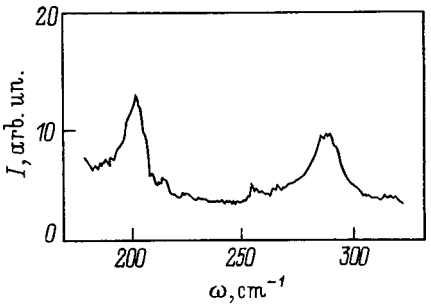

FIG. 2. Raman scattering spectrum of CdS_xSe_{1-x} nanocrystals in fluorophosphate glass in the region of cadmium sulfide and selenide fundamental modes.

3. RAMAN SPECTRA

The bimodal behavior of the phonon spectrum of a mixed nanocrystal permits one to derive the real sulfur (selenium) concentration in the samples from experimental values of the frequencies of the CdS and CdSe optical modes (close to 300 and 200 cm^{-1}, respectively), whose position as a function of sulfur concentration x is well known both for bulk and nanocrystal samples.[16] The phonon mode of CdSe yields a better agreement of the concentration with x-ray structural data. Raman scattering spectra of a glass sample containing cadmium sulfoselenide nanocrystals obtained in the region of CdS and CdSe fundamental vibrations are shown in Fig. 2. The experimental positions of the phonon modes, $\omega_1=203$ cm^{-1} and $\omega_2=297$ cm^{-1}, yield 0.30 ± 0.05 for the sulfur concentration in the sample under study. The same result is derived from measurements of the intensity ratio of these lines, which can also provide information on the relative concentration of sulfur and selenium.

The size of the nanocrystalline formations can be determined spectroscopically by investigating the Raman scattering of samples near the Rayleigh line. It is known[17,18] that nanocrystalline formations give rise to the appearance in the scattering spectrum of an additional peak, whose frequency is directly related to the nanocrystal radius R. This is also a consequence of size quantization, and it implies that the vibrational spectrum of an object of a finite size lies in the region bounded by the minimum frequency $\omega_{\min}=\nu_s/dc$ and the Debye frequency $\omega_{\max}=\nu_s/ac$, where d is the crystal size, a is the lattice constant, and ν_s and c are the velocities of sound and light, respectively. Because one has to take into account the existence of one longitudinal and two transverse sound waves in a real crystal, for spherical particles one usually takes the expression $\omega=0.9\,\nu_s/2Rc$. In this expression, ν_s is the velocity of the longitudinal acoustic wave, and R is the radius of a spherical nanocrystal. For a mixed

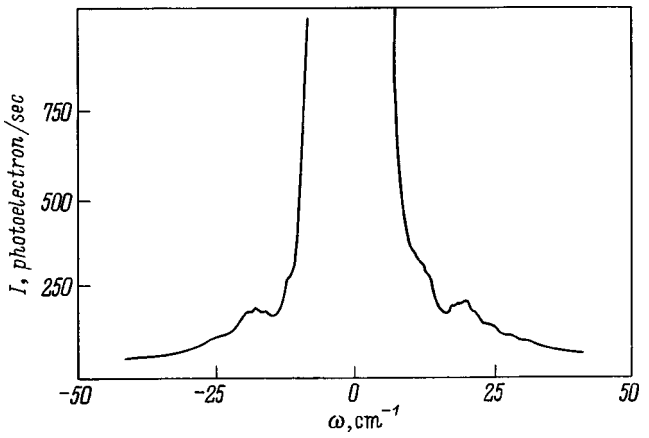

FIG. 3. Raman scattering spectrum of CdS_xSe_{1-x} nanocrystals in fluorophosphate glass near the Rayleigh line.

cadmium-sulfoselenide nanocrystal with a sulfur concentration $x=0.30$, the velocity of the longitudinal wave obtained by linear interpolation between the corresponding values for pure crystals was found to be 4062 m/s. In this case, the low-frequency feature in the Raman spectrum observed near 19 cm^{-1} (Fig. 3) yields $R=32$ Å for the average nanocrystal radius.

4. DISCUSSION OF RESULTS

The optical transition energies between quantum-confined levels in mixed nanocrystals were calculated using a program similar to the one in Ref. 6. The energies were obtained for the $x=0.30$ sulfur concentration in the nanocrystals studied, which, taking into account available data,[15] corresponds to a spin-orbit splitting $\Delta_{so}=0.360$ eV. This value correlates well with the position of a strong absorption line (2.51 eV) observed in the experimental spectrum (Fig. 4) and separated from the lowest excited state (2.14 eV) by 0.37 eV, which, according to Ref. 10, may be related to the spin-orbit-split band. The electron effective mass was chosen 0.137 m_e, and the Luttinger parameters determining the light- and heavy-hole masses were taken to be $\gamma=0.697$ and

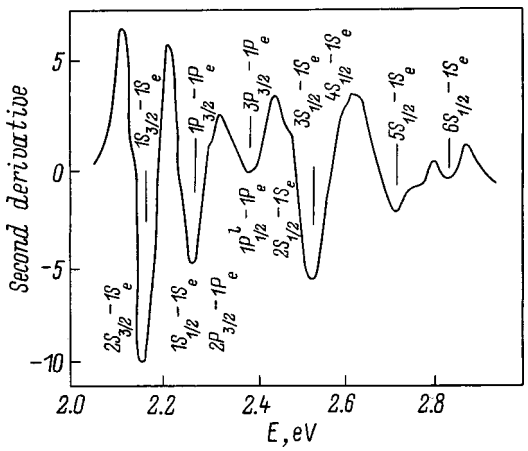

FIG. 4. Second-derivative absorption spectra of CdS_xSe_{1-x} nanocrystals in a glass matrix with sulfur concentration $x=0.3$. The spectrum is given by curve 6 in Fig. 1.

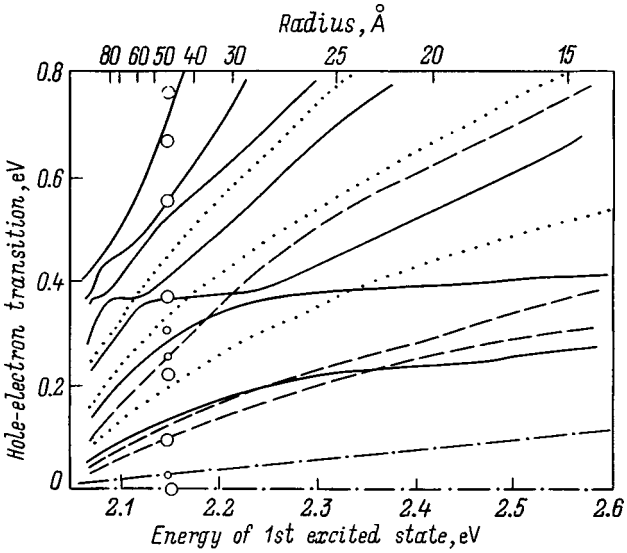

FIG. 5. Calculated electron-hole transition energies in nanocrystals vs the position of the first (ground) excitonic state. Solid lines — $nS_{1/2}$-nS_e-type transitions, dashed lines — $nP_{1/2}$-nP_e-type, dot-and-dash lines — $nS_{3/2}$-nS_e transitions, dotted lines — $nP_{3/2}$-nP_e transitions. The experimental values obtained in this work are shown with circles corresponding to the 48-Å nanocrystal radius. The smaller circles refer to the weak features observed in the experiment.

$\gamma_1=2.216$, which are close to the corresponding parameters[13] for CdSe. Figure 5 shows the energy difference between quantum-confined levels as a function of the energy of the first excited state, i.e., actually of the inverse square of the nanocrystal radius R.

The intensities of optical transitions connecting quantum-confined states depend both on the symmetry of the electronic and hole states and on the actual form of the wave functions. Transitions from quantum-confined levels with an orbital quantum number $l=0$ (i.e., the S states) and a total momentum $j=1/2$ (denoted by solid lines in Fig. 5) lie higher in energy than those from the $j=3/2$ state, although their order depends on both the light- to heavy-hole mass ratio and nanocrystal size.[4] The two lowest confined levels of a conduction-band electron are $1S_e$- and $1P_e$-type states. Therefore the main strong transitions to the lowest quantum-confined level $1S_e$ will be only the $1S_{3/2}-1S_e$ and $2S_{3/2}-1S_e$ transitions[4] specified in Fig. 5 by dot-and-dash lines. Holes containing the P type in their representation can participate in transitions to the second quantum-confined level $1P_e$. These are $1P_{3/2}-1P_e$, $2P_{3/2}-1P_e$ etc. (shown by dotted lines). Calculations of the intensities of these transitions in CdSe shows[13] that the transitions from the $n=1$ level, i.e. $1S_{3/2}-1S_e$ and $1P_{3/2}-1P_e$, should be stronger than those starting from the $n=2$ level. This offers a possibility for comparing the observed experimental spectrum, presented in Fig. 4 in the form of a second-derivative absorption spectrum, to the calculations. The strongest line (2.14 eV), which is seen as a poorly resolved doublet in the experiment, corresponds to the $1S_{3/2}-1S_e$ (and $2S_{3/2}-1S_e$) transition. The higher-frequency strong component at 2.250 eV (also possibly a doublet) can be assigned to the $1P_{3/2}-1P_e$ (and $2P_{3/2}-1P_e$) transition. Then the spin-orbit split state (2.51 eV)

separated by $\Delta_{so}=0.370$ eV from the first excitonic level originates from transitions to the quantum-confined level $1S_e$ from the $3S_{1/2}$ and $4S_{1/2}$ states, which undergo anticrossing resulting in the mixing between *S*- and *D*-type valence-band states.[13] The magnitude of this mixing depends on nanocrystal size and determines the intensity of the corresponding transitions, which apparently accounts for the complex structure of the spin-orbit split band. This interpretation permits a fairly reliable fit of the experimental spectrum to calculations made for a nanocrystal radius of about 48 Å. The experimental values of the frequencies corresponding to this nanocrystal size are identified in Fig. 5 with circles. A satisfactory agreement is obtained in this case also for the absorption lines lying at 2.37, 2.70, and 2.82 eV, which can be assigned with a certain confidence to the $3P_{3/2}$–$1P_e$ transition and, possibly, to $7S_{1/2}$-$1S_e$. The fine structure of the band observed near 2.37 eV is possibly due also to the $1P^{l}_{1/2}$–$1P_e$ transition. Besides, transitions to the higher-lying quantum-confined electronic states $2S_e$ and $1D_e$, whose intensity should be considerably weaker, also fall into this spectral region. The corresponding transitions in the calculated spectrum (Fig. 5) are shown with smaller circles.

The coincidence of the main features in the experimental spectrum with calculated energies observed over a broad spectral region evidences a satisfactory agreement with theory for spherical cadmium sulfoselenide nanocrystals. The main parameters of the calculation coincide satisfactorily with the values known for mixed-composition single crystals. Nevertheless a good agreement with theory is reached for nanocrystals of about 48 Å in radius, which exceeds practically by a factor 1.5 the dimensions of the nanoformations derived from Raman scattering experiments. However, when using Raman scattering data, one should bear in mind that the inhomogeneous broadening of quantum-dot excitonic states may play an important role for correct interpretation of experimental results,[19] because one has to take into account the increase in Raman scattering intensity due to a part of crystals of a certain size which cause resonant excitation of scattering.[20] If we accept the above calculation, then the 488.0-nm excitation used in Raman scattering experiments (2.53 eV) falls into the absorption band associated with transitions from the spin-orbit split subband Γ_7. It is essential that as a result of anticrossing (see the $3S_{3/2}$-$1S_e$ transition in Fig. 5) the energies of electron-hole quantum-confined transitions depend only very weakly on nanocrystal radius. Therefore even a very small variation of the laser frequency may affect strongly the conditions of resonant excitation of crystallites of various dimensions.[20] Besides, the disagreement in crystallite size between the experimental and calculated spectra can be a consequence of the approximations associated with nanocrystal sphericity which were used for the description of both the quantum-confined electron-hole states of nanocrystals and of their acoustic low-frequency vibrations.

*)E-mail: karpov@snoopy.niif.spb.su

[1] N. Peyghambarian, H. Tajalli, E. M. Wright, S. W. Koch, S. I. Najafi, D. Hulin, and J. MacKenzie, Crit. Rev. **53**, 211 (1994).
[2] J. Yumoto, S. Fukushima, and K. Kubodera, Opt. Lett. **12**, 832 (1987).
[3] Al. L. Efros and A. A. Efros, Fiz. Tekh. Poluprovodn. **16**, 1209 (1982) [Sov. Phys. Semicond. **16**, 772 (1982)].
[4] G. B. Grigoryan, E. M. Kazaryan, Al. L. Efros, and T. V. Yazeva, Fiz. Tverd. Tela (Leningrad) **32**, 1772 (1990) [Sov. Phys. Solid State **32**, 1031 (1990)].
[5] A. I. Ekimov, Al. L. Efros, and A. A. Onushchenko, Solid State Commun. **56**, 921 (1985).
[6] A. I. Ekimov, F. Hache, M. C. Schanne-Klein, D. Ricard, C. Flytzanis, A. I. Kudryavtsev, T. V. Yazeva, A. V. Rodina, and Al. L. Efros, J. Opt. Soc. Am. B **10**, 100 (1993).
[7] C. B. Murray, D. J. Norris, and M. G. Bawendi, J. Am. Chem. Soc. **115**, 8706 (1993).
[8] A. A. Lipovskii, E. V. Kolobkova, and V. D. Petrikov, J. Cryst. Growth **184/185**, 365 (1998).
[9] E. V. Kolobkova, A. A. Lipovskii, N. V. Nikonorov, and A. A. Sitnikova, Phys. Status Solidi A **147**, K65 (1995).
[10] V. A. Gaisin, B. V. Novikov, D. L. Fedorov, M. A. Jastrebova, E. V. Kolobkova, A. A. Lipovskii, and V. D. Petrikov, in *Proceedings of the 2nd International Conference on Excitonic Processes in Condensed Matter* (Dresden, 1996), p. 135.
[11] V. A. Gaĭsin, E. V. Kolobkova, A. A. Lipovskiĭ, B. V. Novikov, V. D. Petrikov, D. L. Fedorov, and M. A. Yastrebova, *Abstracts of the 1st International Conference on Highly-Organized Compounds* (St. Petersburg, 1996), p. 53.
[12] J. M. Luttinger, Phys. Rev. **102**, 1030 (1956).
[13] D. J. Norris and M. G. Bawendi, Phys. Rev. B **53**, 16338 (1996).
[14] D. J. Norris, A. Sacra, C. B. Murray, and M. G. Bawendi, Phys. Rev. Lett. **72**, 2612 (1994).
[15] K. L. Stokes, H. Yukselici, and P. D. Persans, Solid State Commun. **92**, 195 (1994).
[16] A. Tu and P. D. Persans, Appl. Phys. Lett. **58**, 1506 (1991).
[17] B. Champagnon, B. Andrianasolo, A. Ramos, M. Gandais, M. Allais, and J.-P. Benoit, J. Appl. Phys. **73**, 2775 (1993).
[18] E. Duval, A. Boukenter, and B. Champagnon, Phys. Rev. Lett. **56**, 2052 (1986).
[19] T. Bischof, M. Ivanda, G. Lermann, A. Materny, W. Keifer, and J. Kalus, J. Raman Spectrosc. **27**, 297 (1996).
[20] A. V. Baranov, Ya. S. Bobovich, and V. I. Petrov, J. Raman Spectrosc. **24**, 767 (1993).

Translated by G. Skrebtsov

Auger and emission spectra of carbon nanotubes

M. M. Brzhezinskaya,*) E. M. Baĭtinger, and V. I. Kormilets

Chelyabinsk State Pedagogical University, 454080 Chelyabinsk, Russia
(Submitted July 2, 1998; resubmitted November 12, 1998)
Fiz. Tverd. Tela (St. Petersburg) **41**, 1511–1514 (August 1999)

The Auger and x-ray emission spectra of carbon nanotubes are calculated by the FP-LMTO method. The computed spectra for nanotubes are compared to the analogous spectra for a graphite monolayer, which is used as a test object, and to the experimental curves for graphite. It is concluded that the Auger-characteristic emission can be used to identify carbon nanotubes.
 [S1063-7834(99)03108-1]

The synthesis of new framework structures consisting of carbon[1] has stimulated the investigation of their physicochemical properties. Specifically, carbon nanotubes exhibit unusual electric conductivity,[2] magnetic properties,[3] and other characteristics.

The prediction of the emission characteristics of nanotubes is very important for diagnostics purposes, especially during synthesis, as well as at subsequent technological stages. For this reason, an attempt is made in the present investigation to calculate the Auger electron and x-ray emission spectra of a small-diameter carbon nanotube.

The calculations are based on the calculation of the energy bands and the density of states by a nonempirical method. The results obtained are compared to the results for a test object, which was a graphite monolayer in the present work, often called graphene.

1. COMPUTATIONAL PROCEDURE

A nanotube is based on a graphene fragment, twisted during synthesis in a definite manner.[4]

Two factors, specifically, the diameter and direction of twist (in other words, the chirality), determine the nature of the symmetry describing the structure of nanometer-size carbon tubes and, correspondingly, determine their electronic properties. The energy gap in the electronic spectrum of a nanotube, if a gap exists, should decrease with increasing tube diameter according to calculations performed in Ref. 5 and reach zero if the tube diameter is very large. In this case the properties of the tube approach those of graphene.

In the present paper we report the results of calculations of the Auger and x-ray spectra for a (4, 4) nanometer-size carbon tube. The tube studied is zig-zag-shaped, and its diameter is 5.46 Å. The number of hexagons along the perimeter of the tube is 8. The z axis is chosen along the tube axis, and the x axis is chosen along the radius within the tube.

The energy bands of the nanotube were calculated by the self-consistent method of linear muffin-tin (MT) orbitals with a ''full'' potential[6] (the English acronym is FP–LMTO). The method is based on the density functional theory and is a first-principles method. The exchange-correlation potential was chosen in the local density approximation (LDA) in the Ceperley–Alder form[7] with Perdeu–Zunger parameterization.[8]

To use the band method of calculation, a nanotube fragment was placed in an expanded cell, whose height z was taken to be the same as the period of the zig-zag-type nanotube ($3\sqrt{a_{\text{graph}}}$; $a_{\text{graph}}=1.42$ Å). In the xy plane, perpendicular to the nanotube axis, the form of the expanded cell was chosen so as to correspond to the rotational symmetry of the tube. Specifically, a square was taken for the (4, 4) structure, in which four links (16 atoms in all) are placed on a circle. Symmetric cells make it possible to attain self-consistency and to calculate the density of states on a more dense grid in k space. In our calculation self-consistency was attained with 18 special points in 1/8-th of the Brillouin zone of a (4, 4) nanotube. The density of states was calculated by the method of tetrahedra on 325 points in 1/8-th of the Brillouin zone (12 steps along the z axis). The energy step was $\Delta E=0.002$ Ry $=0.027$ eV.

To calculate the band energies, the maximum orbital angular momentum was taken to be 2 in the MT spheres and 3 to calculate the structural constants and wave functions. In the intersphere space the calculation was performed for three values of the critical energies: -0.7, -1.0, and -2.3 Ry. The first value is close to the center of the valence band of the nanotube (and graphite), which the LMTO method requires.

The distances between the carbon atoms in the nanotubes were taken to be the same as in graphite, specifically, 1.42 Å . The MT spheres of carbon atoms were taken almost to be touching, with radii $R_{\text{MT}}=1.340$ a.u. With only carbon atoms the filling of the cell volume with spheres (the cell parameter was $a=15.0$ a.u.) is $\sim 10\%$. For this reason, several other types of MT spheres of different MT radius were introduced into the cell. The largest empty spheres were placed at the center and at the corners of the cell, and the small spheres were placed in the gap between the carbon atoms in the nanotube walls and in the voids remaining between the large spheres outside the tube. In this manner the filling of the cell with spheres was increased to 37.8%.

Calculations of the band structure of graphene, which in the present case is a test object, were performed beforehand.

The intensity of the Auger spectrum is proportional to the convolution of the valence states (only $k\nu\nu$ transitions

are possible in carbon) and to the cross section of the Auger process which, taking account of only the Coulomb channel for transferring interaction within an atom with the core of a vacancy, can be represented by[9]

$$|M_{12fs}|^2=|\langle 1,2|\mathbf{r}|f,s\rangle|^2+|\langle 2,1|\mathbf{r}|f,s\rangle|^2 - \mathrm{Re}(\langle 1,2|\mathbf{r}|f,s\rangle\langle 2,1|\mathbf{r}|f,s\rangle). \quad (1)$$

Here 1, 2, *f*, and *s* are the symbolic designations of the wave functions of the two excited electrons in the valence band (1 and 2) and an electron in the final state *f* and the core electron *s*.

According to Eq. (1), the cross sections of the Auger process for different groups of valence electrons were chosen in our calculations as[10]

$$|M_{pp}|^2=1, \quad |M_{ps}|^2=0.5, \quad |M_{ss}|^2=0.8. \quad (2)$$

The indices *p* and *s* in Eq. (2), as usual, denote two groups of valence wave functions in the carbon atom. The parameters (2) remained unchanged in calculating the Auger spectrum of the test object and the nanotube.

The total Auger spectrum was calculated as

$$I(E)=|M_{ss}|^2(N_s^*N_s)+2|M_{sp}|^2(N_s^*N_p)+|M_{pp}|^2(N_p^*N_p), \quad (3)$$

where N_s and N_p are the partial densities of the *s* and *p* states and * denotes a convolution operation.

For convenience in analysis, the last term is divided into two components including separately the π component and the remaining *p* function.

Taking account of the optical selection rules and the polarization of the characteristic radiation, the emission spectrum is determined only by the partial density of *p* states in the valence band. The probability of emission of photons (which for carbon is almost 100 times smaller than the probability of the Auger process (1)) does not change the form of the emission band, which extends into the wavelength range 4.3–4.7 nm. As a result, we identified the intensity distribution in the emission spectrum with the analogous distribution $N_p(E)$. It was assumed that the instrument analyzing the radiation collects not only rays emitted from the sample perpendicular to the graphene or tube but also grazing along them.

2. DESCRIPTION OF THE RESULTS

The basic computational results are presented in Figs. 1 and 2. For visual clarity, the convolutions of the partial densities of states, multiplied by the coefficients (2) for the test object (bottom) and tubulet (top), are presented in Fig. 1. It is evident that in both cases the formation of a central Auger peak is due only to the self-convolution of the N_p states in the valence band of graphene and the tubulet. The contribution of the $N_p^*N_s$ cross states determines the characteristic features near the edge of the Auger spectrum, and the self-convolutions $N_\pi^*N_\pi$ and $N_s^*N_s$ have virtually no effect on the shape of the spectrum. Moreover, we noticed that the π-electron contribution in the test spectrum of the graphite monolayer is even smaller than the calculation predicts. This

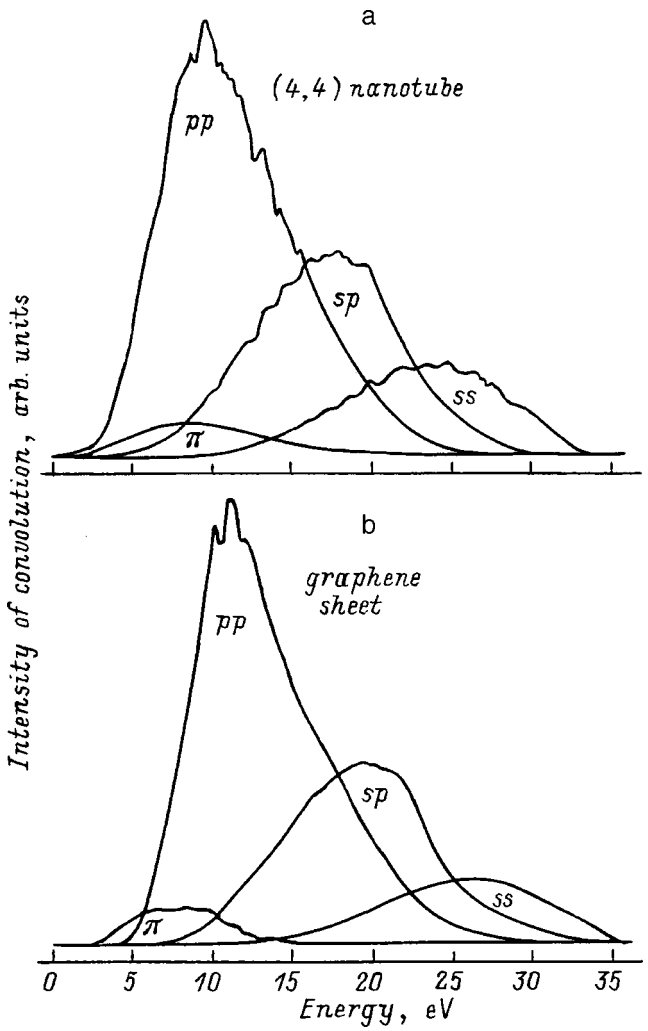

FIG. 1. Inverted Auger spectra (*4, 4*) of a nanotube (a) and graphene (b).

is most likely because in flat structures (and, probably, in tubulets also) there is one (or even less) π electron per atom.

The integral $N_p^*N_p$ self-convolution in the nanotube is very similar to the analogous convolution for graphene: The central peak is split and the intensity drops off smoothly at high binding energies.

To compare with experiment, it is convenient to differentiate the total spectra (Fig. 2). The result of differentiating the data presented in Fig. 1 is presented in Fig. 2 together with the published spectrum of a graphite monolayer on iridium.[11] We note that, to make a better comparison with the experimental spectrum, the binding energy scale is turned in the opposite direction compared to Fig. 1. Thus the large negative excursion in the differential spectra is due to the region of a steep rise of the function $N_p^*N_p$ and the contribution of the π states ($N_\pi^*N_\pi$). In this region of the spectrum the computed and experimental results for the test object agree well with each other. This gives confidence in the objectivity of the Auger spectrum of a nanotube, for which we were not able to find experimental results in the literature.

The agreement between experiment and calculations for high binding energies is also good for the test object. The two positive peaks at ~15 and 22 eV are reproduced in the calculations. As usual, the computed spectra contain fine

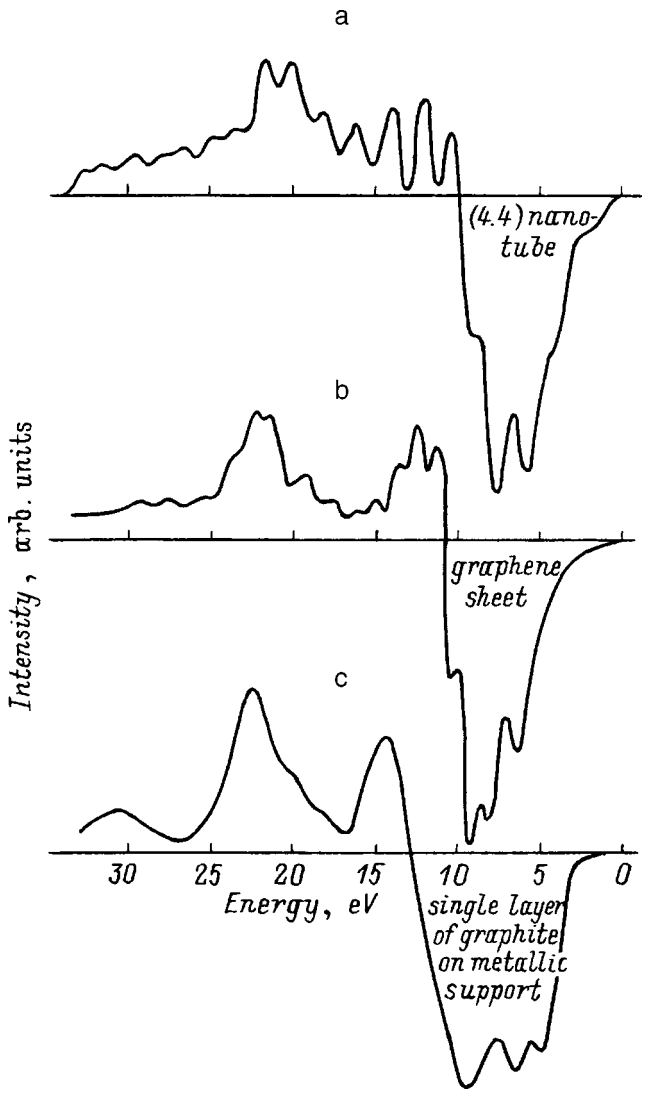

FIG. 2. Computed (a, b) and experimental (c) Auger spectra of a (*4*, *4*) nanotube (a) and graphene (b, c).

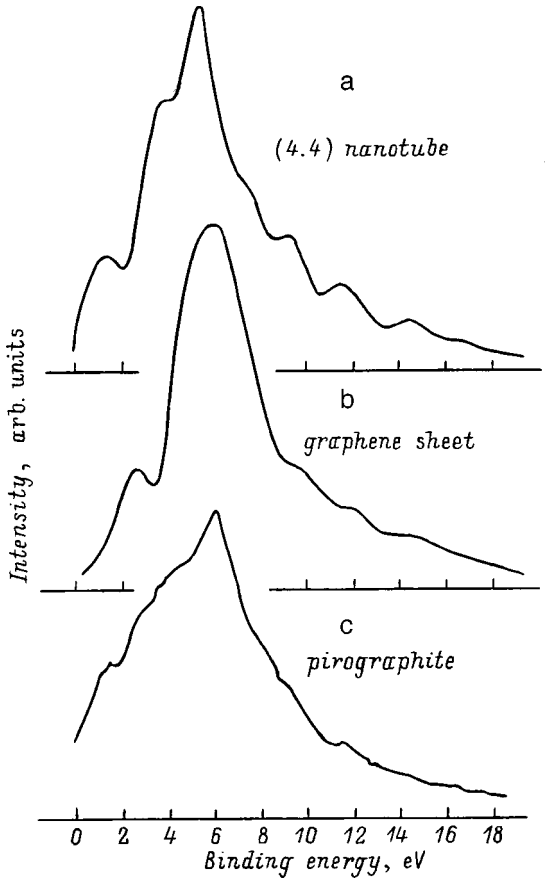

FIG. 3. Computed (a, b) and experimental (c) emission spectra of a (*4*, *4*) nanotube (a), graphene (b), and pyrolytic graphite (c).

structure (for example, the splitting of the peak at the binding energy 15 eV is visible), which is not observed in experiment, possibly because of experimental difficulties. For this reason not all characteristic features of the tubulet spectrum appear in the experiment. The main ones are the splitting of the large negative extremum and the positive extremum at the binding energy 22–23 eV.

Figure 3a shows the x-ray emission spectrum of a nanotube, which, to facilitate identification, is compared not only to the spectrum obtained for the test object (Fig. 3b) but also to the publihsed experimental spectrum for pyrolytic graphite (Fig. 3c). As one can see from Fig. 3, there is a negligible difference between the computed curve, which we obtained for the test object, and the experimental curve. However, an extremum at 2.5 eV, whose direct presence in the experimental curve is not observed, is clearly seen in the computed curve. The emission spectrum of a nanotube is identical to the experimental curve for graphite. A characteristic feature of all three spectra presented in Fig. 3 is their smooth merging at high binding energies.

To a first approximation, the computed spectra due to valence states of carbon nanotubes are similar to the graphite spectra. For this reason, the main objective in performing experiments is to study certain characteristic features that could distinguish the results obtained with tubes and graphite. In the present paper computational data showing that spectroscopic methods (Auger spectra and characteristic radiation) can be used to identify nanotubes were presented for a zig-zag small-diameter nanotube.

*)E-mail: bmm@cspi.urc.ac.ru

[1] S. Iijima, Nature (London) **354**, 56 (1991).
[2] Y. Nakayama, S. Akita, and Y. Shimada, Jpn. J. Appl. Phys., Part 1 **234**, L10 (1995).
[3] S. N. Song, X. K. Wang, R. P. H. Chang, and J. B. Ketterson, Phys. Rev. Lett. **72**, 697 (1994).
[4] J. W. Mintmire and C. T. White, Carbon **33**, 893 (1995).
[5] R. A. Jishi, D. Inomata, K. Nakao, M. S. Dresselhaus, and G. Dresselhaus, J. Phys. Soc. Jpn. **63**, 2252 (1994).
[6] K. H. Weyrich, Phys. Rev. B **37**, 10269 (1988).
[7] D. M. Ceperley and B. J. Alder, Phys. Rev. Lett. **45**, 566 (1980).
[8] J. P. Perdeu and A. Zunger, Phys. Rev. B **23**, 5048 (1981).
[9] Yu. N. Kucherenko and V. T. Alëshin, Fiz. Met. Metalloved. **63**(1), 4 (1982).
[10] J. E. Houston, J. W. Rogers, and R. R. Rye, Phys. Rev. B **34**, 1215 (1986).
[11] E. M. Baĭteinger, N. R. Gall', S. A. Orlov, E. V. Rut'kov, and A. Ya. Tontegode, Izv. Vyssh. Uchebn. Zaved. Fiz. **10**, 84 (1997).

Translated by M. E. Alferieff

Tamm states and quantum dots in carbon and heteroatomic nanotubes

I. V. Stankevich*)

Institute of Hetero-Organic Compounds, Russian Academy of Sciences, 117813 Moscow, Russia

L. A. Chernozatonskiĭ

Institute of Biochemical Physics, Russian Academy of Sciences, 117334 Moscow, Russia
(Submitted November 12, 1998)
Fiz. Tverd. Tela (St. Petersburg) **41**, 1515–1519 (August 1999)

The electronic structure of C–BN nanotubes is discussed in the π approximation. Two types of such structures with $(n,0)$-tubulet topology are investigated: 1) semiinfinite C–BN and C nanotubes and 2) C–BN nanotubes, consisting of two semiinfinite BN nanotubes coupled by a ring-shaped carbon fragment C_{mn}. It is shown that, in the first case, energy levels (Tamm levels) whose wave functions are localized on the terminal fragment can exist under certain conditions. In the second case, bound states localized on atoms of the carbon fragment exist. It is established that if a quite extended, cylindrical, carbon cluster is present at the end of a semiinfinite BN nanotube, then such a system can be viewed as a very simple model of a quantum dot. C–BN nanotubes where the carbon fragment couples two semiinfinite BN nanotubes can also be interpreted similarly. A simple analytic method is proposed for finding the Tamm energy levels in heteroatomic nanotubes.
[S1063-7834(99)03208-6]

Among nanotubes obtained thus far, tubular structures consisting of atoms of two or more elements are especially interesting. The electronic properties of such heteroatomic tubular forms depend on their length and diameter, the relative arrangement of the atoms, and the structure of the terminal fragments, which can be closed or open. Typical examples of heteroatomic structures are tubular forms of boron nitrides and boron carbonitrides.[1–4] It should be noted that the band gap separating the valence and conduction bands in the electronic spectra of tubular boron nitrides is quite large (in some estimates the band gap reaches 5–6 eV) and is essentially independent of the tubulet diameter. In carbon tubulet, however, the band gap depends strongly on the tubulet diameter and ranges from 0 to 2–3 eV. In addition, the ionization potential of the carbon atom is close to the average value of the ionization potentials of the N and B atoms. Therefore it should be expected that when carbon clusters are embedded in a hexagonal boron nitride lattice on a cylindrical surface, either discrete energy levels (Tamm levels) or minibands can appear in the band gap of such systems. In the present paper the electronic spectra of certain such tubular forms of carbon and boron nitride are simulated. Tubulenes of two types are considered: 1) semiinfinite C–BN or C nanotubes (Fig. 1a) and 2) C–BN nanotubes consisting of two semiinfinite BN nanotubes coupled by a graphitic cylindrical carbon fragment (Fig. 1b).

1. COMPUTATIONAL PROCEDURE

The electronic structure of a fairly long tubulet having regular structure (but finite size) can be investigated in two approximations: in terms of an infinite periodic translationally-symmetric model or using a semiinfinite model. The first approach makes it possible to find the bands in the continuous spectrum and to calculate the dispersion curves and the various average characteristics of the tubulet which are associated with them (for example, the density of states, the average total energy, the effective charges on atoms of an elementary fragment, and others). In a semiinfinite model, finer details of the spectrum can be investigated, specifically, the discrete spectrum appearing as a result of the finiteness of clusters or the presence of terminal groups. The existence of discrete energy levels and the corresponding localized wave functions (or local states) in one-dimensional crystals was first proved by Tamm in 1932.[5] We shall not get into the more detailed terminology used for classifying such states in crystals, and we shall simply call them Tamm energy levels.[6]

We shall confine our attention to the spectra of tubular nanostructures whose topology is based on that of $(n, 0)$ tubes.

We shall examine in detail the case of semiinfinite C–BN or C tubulets. We shall illustrate the method used below to find local states for the example of a boron carbonitride $(n, 0)$ tubulene, where the terminal fragment is a cylindrical carbon cluster, consisting of $s=2t$ cyclic carbon chains C_{2n} coupled with one another and with the atoms of the boron nitride by chemical bonds forming a hexagonal network on a cylindrical surface (Fig. 1a).

We shall use a topological approximation (the Hückel method) in which only atomic π orbitals and π electrons are taken into account; the interaction between nonneighboring centers is neglected. We note that each C atom

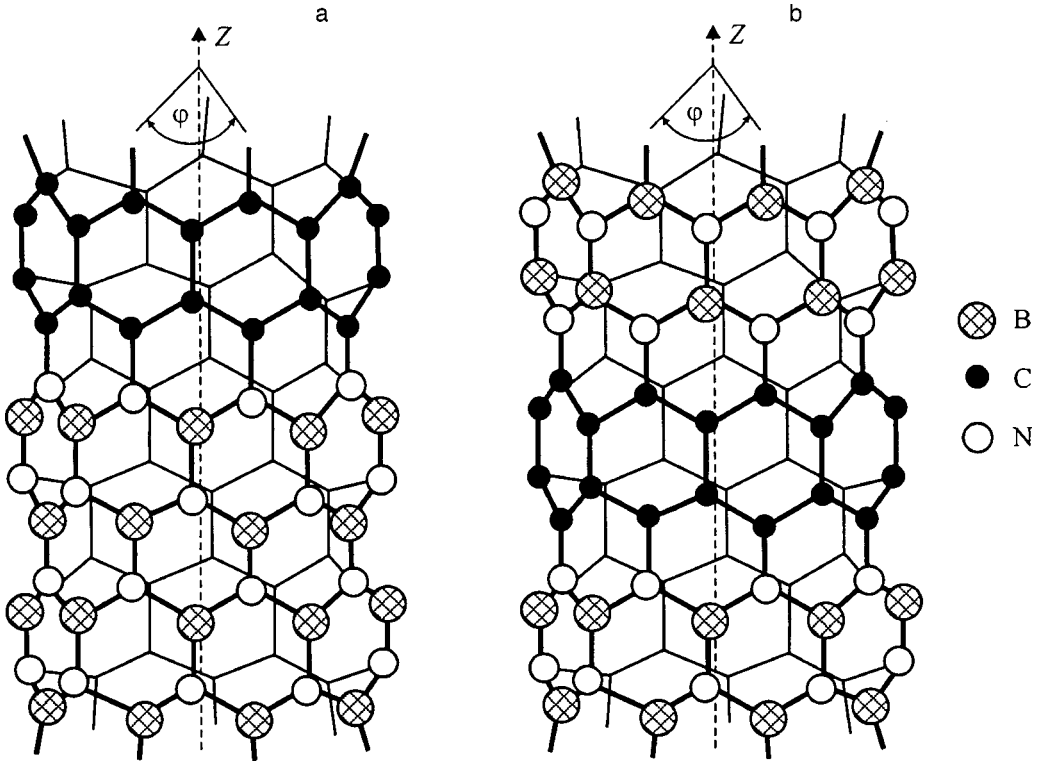

FIG. 1. Structure of two types of boron carbonitride $(n, 0)$ tubulets: a — a carbon cluster is located at the end of tubular boron nitride with an open end (type-1 tubulet); b — a cylindrical carbon cluster connects two semiinfinite fragments of tubular boron nitride (type-2 tubulet); $\varphi = 2\pi/n$.

supplies one electron to the π electron system of a tubulet, whereas nitrogen supplies two such electrons while boron has no π electrons but it does have a vacant π orbital that can accept π electrons from neighboring atoms. As a result, the effective charges on the atoms alternate in boron nitrides.

Only the following types of parameters of the Coulomb α_x and resonant β_{xy} integrals characterizing the energy of the atomic orbitals and their interaction energy are possible in boron carbonitride tubulenes: $\alpha_C = \alpha$, $\alpha_N = \alpha + h_N\beta$, $\alpha_B = \alpha + h_B\beta$, $\beta_{BN} = k_{BN}\beta$, $\beta_{BC} = k_{BC}\beta$, $\beta_{CC} = \beta$, and $\beta_{NC} = k_{NC}\beta$. In what follows, the value of the Coulomb integral for the C atom is taken as the reference point, and the modulus of the resonance integral $\beta_{CC} = \beta$ is taken as the unit of energy. The values of the parameters k_{xy} and h_{xy} used below to calculate specific systems correspond to the data presented in Ref. 7, specifically, $k_{BN} = 0.9$, $h_B = -1.0$, $h_N = 1.5$, $k_{BC} = 0.7$, and $k_{NC} = 1.0$. In the Hückel topological approximation, the electronic structure of a heteroatomic tubulet is described by a matrix Hamiltonian $\mathbf{H}$ written in the basis of atomic π orbitals. The numbers of the rows and columns of this operator are the numbers of the atoms. The diagonal elements of the Hamiltonian $\mathbf{H}$ equal the corresponding values of the parameters h_x, and the off-diagonal elements $\mathbf{H}_{i,j}$ differ from zero only if the i and j atoms lie next to one another, in which case $\mathbf{H}_{i,j} = k_{i,j}$. We assume that the symmetry group of the tubulene under study is C_n. Using group theory representations, the matrix Schrödinger equation

$$\mathbf{H}\phi = E\phi \tag{1}$$

can be factored. As a result, Eq. (1) decomposes into n equations with effective Hamiltonians $\mathbf{H}^{(j)}$ $(j = 0,1,\ldots, n-1)$ having a block structure

$$H^{(j)} = \begin{Vmatrix} H_{11}^{(j)} & H_{12}^{(j)} \\ H_{21}^{(j)} & H_{22}^{(j)} \end{Vmatrix}.$$

In this equation $\mathbf{H}_{11}^{(j)}$ and $\mathbf{H}_{22}^{(j)}$ are Jacobi matrices

$$\mathbf{H}_{11}^{(j)} = \begin{Vmatrix} 0 & b_1 & 0 & & & & & & \\ b_1^* & 0 & 1 & 0 & & & & & \\ 0 & 1 & 0 & b_1 & 0 & & & & \\ & 0 & b_1^* & 0 & 1 & & & & \\ & & & 1 & & & & & \\ & & & & \cdots & & & & \\ & & & & & \cdots & & & \\ & & & & & & \cdots & & \\ & & & & & & & 0 & b_1 \\ & & & & & & & b_1^* & 0 \end{Vmatrix},$$

$$\mathbf{H}_{22}^{(j)} = \begin{Vmatrix} h_x & k_{\mathrm{BN}} & 0 & & & & & & \\ k_{\mathrm{BN}} & h_v & b_2 & 0 & & & & & \\ 0 & b_2^* & h_x & k_{\mathrm{BN}} & 0 & & & & \\ & 0 & k_{\mathrm{B}} & h_v & b_2 & 0 & & & \\ & & 0 & b_2^* & h_x & k_{\mathrm{BN}} & & & \\ & & & & & \cdots & & & \\ & & & & & & \cdots & & \\ & & & & & & & \cdots & \\ & & & & & & & h_v & b_2 \\ & & & & & & & b_2^* & h_x \end{Vmatrix}.$$

The matrix $\mathbf{H}_{11}^{(j)}$ is of order s; the matrix $\mathbf{H}_{12}^{(j)}$ contains an infinite number of elements, the only nonzero element being the element located at the intersection of the s-th row and $(s+1)$-st column of the matrix $\mathbf{H}^{(j)}$; this element is k_{CX}, where X is either a B or N atom. The matrix $\mathbf{H}_{21}^{(j)}$ is the transpose of the matrix $\mathbf{H}_{12}^{(j)}$; $b_1=1+\exp(i2\pi j/n)$ and $b_2=k_{\mathrm{BN}}(1+\exp(i2\pi j/n))$; an asterisk denotes complex conjugation. The matrix $\mathbf{H}_{11}^{(j)}$ can be viewed as an energy matrix of a finite homoatomic linear chain of s atoms with alternating bond lengths characterized by resonance integrals equal to 1 and $|b_1|$. The matrix $\mathbf{H}_{22}^{(j)}$ is of infinite order and can be interpreted as the Hamiltonian of a semiinfinite BN heteroatomic system with alternating bond lengths, which are characterized by the resonant integrals k_{BN} and $|b_2|$. The symbols X(Y) denote B or N depending on the structure of the terminal part of BN tubulene.

We note that each matrix $\mathbf{H}^{(j)}$ is a semiinfinite Jacobi matrix and can be regarded as the effective Hamiltonian of a linear chain of atoms which consists of two fragments: a semiinfinite part having a periodic structure, formed by B and N atoms with an effective interaction, and a terminal homoatomic fragment with s atoms, likewise having a linear structure. The spectral theory of such Jacobi matrices has been developed in detail and we shall employ the results of Ref. 8. The following follow from this work:

1) The continuous spectrum of the Hamiltonian $\mathbf{H}^{(j)}$ is identical to the continuous spectrum of the operator $\mathbf{H}_{22}^{(j)}$ describing a periodic one-dimensional system characterized by the Coulomb parameters h_{N} and h_{B} and the two resonant integrals k_{BN} and $|b_2|$.

2) The operator $\mathbf{H}^{(j)}$ can possess a discrete spectrum. It is located at the zeros of the following polynomial:

$$\mathbf{F}^{(j)}(x)\equiv\mathbf{P}_{1+s}^{(j)}(x)\mathbf{P}_s^{(j)}(x)-\mathbf{P}_{2+s}^{(j)}(x)\mathbf{P}_{s-1}^{(j)}(x)=0. \qquad (2)$$

Here $\mathbf{P}_k^{(j)}(x)$ is the characteristic polynomial of the truncated Hamiltonian $\mathbf{H}_k^{(j)}$ whose elements are located in the first k rows and k columns of the matrix $\mathbf{H}^{(j)}$.

3) The condition

$$|\mathbf{P}_{2+s}^{(j)}(x)|<|b_2k_{\mathrm{BN}}||\mathbf{P}_s^{(j)}(x)|. \qquad (3)$$

is sufficient for a zero of the polynomial $\mathbf{F}^{(j)}(x)$ to be an eigenvalue of the Hamiltonian $\mathbf{H}^{(j)}$. The equations (2) and (3) have a simple interpretation. It follows from Eq. (2) that under a translation by one period the components of the solution ψ of the equation $\mathbf{H}^{(j)}\psi=E\psi$ that correspond to the periodic part of the system are multiplied by a constant. It follows from Eq. (3) that this constant is less than 1.

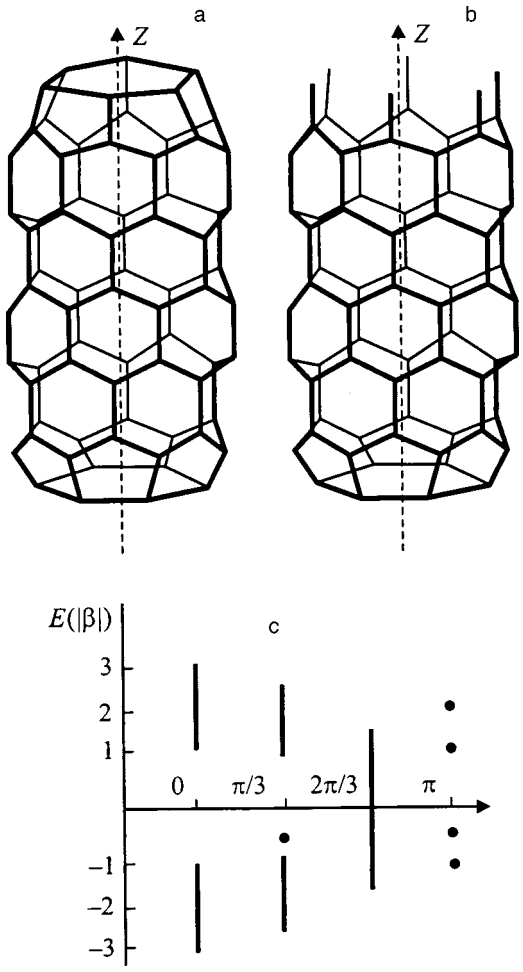

FIG. 2. a — Structure of a cluster of a D_{6d}-C_{72} precursor of a (6, 0) tubulene; b — fragment of a semiinfinite (6, 0) tubulet with a closed end; c — schematic of the spectrum of a semiinfinite (6, 0) tubulet with a closed end; the spectrum components corresponding to angles $\varphi=\pi j/3$ with $j=0,1,2,3$ are indicated.

If $s=0$, i.e., the system under study consists only of repeating fragments, the equations presented above simplify. For example, Eq. (2) becomes $\mathbf{P}_1^{(j)}(x)=0$.[9]

We note that the procedure described above can be used to find the local states for semiinfinite C–BN tubulenes of the first type, where the number s of terminal carbon chains is odd (in this case ''dangling'' C–C, C–B, or C–N bonds exist). Moreover, it can be used for tubulenes of the second type (Fig. 1b), which possess a symmetry plane perpendicular to the axis of the cylinder.

We shall examine two examples illustrating the approach presented above.

1) A C_{72} cluster with D_{6d} symmetry is displayed in Fig. 2a. This cluster is the second term in the row of barrelene-type polyhedral carbon clusters C_{60+12m}, $m=1,2,\ldots$, with a six-fold symmetry axis.[10] In the limit $m\to\infty$ such a cluster becomes either a translationally-symmetric (6, 0) tubulet or a semiinfinite (6, 0) tubulet closed at one end (Fig. 2b). In the case of a semiinfinite cluster, the application of the method

described above shows that the spectrum of the Hamiltonian **H** of such a system is a union of the spectra of six Hamiltonians $H^{(j)}$ $(j=0,\ldots,5)$ of the type described above. Figure 2c shows the components of the spectrum of the operators $\mathbf{H}^{(j)}$ with $j=0,1,2,3$ (they correspond to the angles $\varphi=0,\pi/3,\ 2/3\pi$, and π). For $j=3$ the spectrum of the operator $\mathbf{H}^{(3)}$ is purely point-like and consists of four eigenvalues: ± 1 and -0.4142 and 2.4142. The first two eigenvalues are infinitely degenerate. Together with a continuous component, the spectrum of the Hamiltonian **H** contains eigenvalues. However, these energy levels lie in the continuous spectrum. It is interesting to note that one such energy level, -0.4142, exists for all values of m. The corresponding wave function is localized only on atoms of a six-member ring of the cover and the atoms in the layer closest to it. For $m<5$ this energy level is doubly degenerate and is an upper level, occupied by two electrons. For large values of m, it is absorbed by the quasicontinuous spectrum.

We note that various functional groups can be located at the end of an open $(n,\ 0)$ tubulet. The method described above makes it possible to find easily the local states generated by them and the corresponding energy levels. The detailed structure of the spectra of some systems of this type is discussed in detail in Ref. 11. (See also Ref. 12, where a different approach is used to find the Tamm energy levels in carbon nanotubes.)

2) As a second example, we shall consider a semiinfinite linear chain of the form X–Y–X–Y–...X–Y–..., formed by two types of atoms X and Y with Coulomb integrals h_x and h_y and with alternating neighboring-bond lengths, so that the resonance integrals take on two different values (k_1 and k_2). It should be noted that the investigation of spectra of the operators $\mathbf{H}^{(j)}$ $(j=0,1,\ldots,n)$ engendered by $(n,\ 0)$ tubular boron nitride with an open end reduces to this model. In this case the spectrum consists of two bands

$$[-(h_x+h_y)\pm 0.5((h_x-h_y)^2+4(k_1+k_2)^2)^{1/2};$$
$$-(h_x+h_y)\pm 0.5((h_x-h_y)^2+4(k_1-k_2)^2)^{1/2}],$$

where the plus signs correspond to the valence band. The band gap $\Delta\varepsilon$ is given by

$$\Delta\varepsilon=((h_x-h_y)^2+4(k_1-k_2)^2)^{1/2}. \quad (4)$$

In addition, a discrete energy level, coinciding with the value $E=h_x$, can appear in the band gap. This energy level corresponds to a wave vector Z with the components $Z=(1,0,(-k_1/k_2),0,(k_1/k_2)^2,0,\ldots)$. If $|k_1/k_2|<1$, then the point $E=h_x$ is a discrete energy level whose wave function is localized mainly on the terminal atom X. It follows from Eq. (4) that $\Delta\varepsilon=(h_x-h_y)$ for $k_1=k_2$. For X = B and Y = N $\Delta\varepsilon=2.5|\beta|$. For $\beta=-2.4$ eV we find $\Delta\varepsilon=6.0$ eV.

2. NUMERICAL RESULTS

In this section we present the results of computer simulation of the π-electron spectra of certain tubulets of the types 1 and 2 presented in Figs. 1a and 1b.

2.1. Type-1 tubulets

Systems with N–C or C–C ''dangling bonds'' at the end were studied. It was assumed that the order n of the symmetry axis of the tubulet takes on thevalues 5, 6, 9, and 27, and the number s of cyclic layers consisting of carbon clusters is 1 or 5. It was established that for $s=1$ three local states appear in such nanotubes with small diameter D ($n=5,6$ and $D=0.78n$). The energies of two of them lie in the continuous spectrum of the corresponding boron nitride, and the energy of the third state lies in the band gap below the value of the Coulomb integral α_c, whose value was chosen to be 6.2 eV (the spectroscopic value of the resonance integral $\beta=-2.4$ eV was used in the calculations). As the tubulet diameter increases, a 0.5 eV wide quasi-miniband displaced from the conduction band of the BN nanotube by 1.7 eV tends to form in the band gap.

For $s=5$ the number of local states whose energy lies in the band gap of the BN tubulet increases. For a 21 Å diameter tubulet (27, 0), the spectrum of local states consists of three minibands. One minihand is filled; it lies near the valence band and is displaced from the nearest vacant miniband by 2 eV.

2.2. Type-2 tubulets

We analyzed only the π-electron spectrum of a finite (6, 0) cluster $[C_4B_{16}N_{16}]_6$ with D_{6h} symmetry. It was established that six discrete energy levels, whose wave functions are localized on the carbon fragment, appear in the band gap in this case corresponding to (6, 0) boron nitride; four of the energy levels, -1.39, -1.15, and -0.50 (in units of $|\beta|$), are filled and two, 0.36 and 0.35 (in units of $|\beta|$) are vacant. For $\beta=-2.4$ eV the energy difference between the bottom vacant and top occupied levels is 1.7 eV. We note that, in Ref. 13, it is shown that the spectrum of the tubular clusters $[(BN)_3C_2(BN)_3]_n$ with $n=9$, 24, and 72 has a similar structure.

It follows from the results presented above that, in heteroatomic tubular structures of the types 1 and 2, consisting of quite extended fragments of boron nitride and finite carbon clusters, discrete energy levels corresponding to wave functions localized on ring-shaped carbon fragments appear in the band gap of boron nitride; the occupied energy levels are displaced from the vacant levels by approximately 1.5 eV. For this reason, the type-1 and -2 systems should exhibit properties characteristic for quantum dots. We also note that localization of the wave functions can be encountered in tubular C–BN superlattices having a regular structure and in quasi-one-dimensional systems consisting of C_{60} fullerenes. It is shown in Refs. 4 and 13 that the dispersion curves for some of these systems do not depend on the wave vector. This attests to the existence of localized wave functions. The successes achieved in obtaining C–BN nanotubes give hope that in the near future the quantum particles similar to type-1 and type-2 systems will be synthesized and investigated experimentally.

We thank E. G. Gal'pern for performing the calculations.

This work was supported by Russian Fund for Fundamental Research (Grants Nos. 96-02-18445 and 98-03-33016) and the Russian government program ''Fullerenes and Atomic Clusters'' (Project No. 98061).

*)E-mail: stan@ineos.ac.ru

[1] O. Stephan, P. M. Ajayan, C. Colliex, Ph. Redlich, J. M. Lambert, P. Berkier, and P. Lefin, Science **226**, 1683 (1994).
[2] H. Y. Zhu, D. J. Klein, W. A. Seitz, and N. H. March, Inorg. Chem. **34**, 1377 (1995).
[3] Y. Miyamoto, A. Rubio, M. L. Cohen, and S. G. Louie, Phys. Rev. B **50**, 4976 (1994).
[4] E. G. Galpern, V. V. Pinyaskin, I. V. Stankevich, and L. A. Chernozatonskii, Phys. Chem. B **101**, 705 (1997).
[5] I. E. Tamm, Zs. Sowjet. **1**, 733 (1932).
[6] S. Davison and J. Levine, *Surface (Tamm) States* (Mir, Moscow, 1973).
[7] A. Streiwieser Jr., *Molecular Orbital Theory for Organic Chemists* (Wiley, New York, 1962; Mir, Moscow, 1965).
[8] Ya. L. Geronimus, Zap. Matem. Otd. Fiz.-Mat. Fakulteta Khar'kovskogo Universiteta i Khar'kovskogo Matem. Obshchestva **25**, 87 (1957).
[9] I. V. Stankevich, Mat. Zametki **8**, 297 (1970).
[10] E. G. Gal'perin, I. V. Stankevich, A. L. Chistyakov, and L. A. Chenozatonskiĭ, JETP Lett. **55**, 483 (1992).
[11] I. V. Stankevich and L. A. Chernozatonskiĭ, JETP Lett. **63**, 621 (1966).
[12] R. Tamura and M. Tsukada, Phys. Rev. B **52**, 6015 (1995).
[13] E. G. Galpern, I. V. Stankevich, A. L. Chistyakov, and L. A. Chernozatonskii, Fullerene Sci. Technol. **6**, 499 (1998).

Translated by M. E. Alferieff

Crystalline fullerene deuteride $C_{60}D_{24}$: Spectral investigation

Yu. M. Shul'ga*)

Institute of Chemical Physics, Russian Academy of Sciences, 142432 Chernogolovka, Moscow District, Russia

B. P. Tarasov and V. M. Fokin

Institute of New Chemical Problems, Russian Academy of Sciences, 142432 Chernogolovka, Moscow District, Russia

N. Yu. Shul'ga

Moscow Physicotechnical Institute, 141700 Dolgoprudnyĭ, Moscow District, Russia

V. N. Vasilets

Affiliate of the Institute of Energy Problems of Chemical Physics, Russian Academy of Sciences, 142432 Chernogolovka, Moscow District, Russia

(Submitted July 2, 1998; resubmitted November 17, 1998)
Fiz. Tverd. Tela (St. Petersburg) **41**, 1520–1526 (August 1999)

X-ray diffraction patterns, infrared and x-ray photoelectron spectra, and electron energy-loss spectra are obtained for fullerene deuteride $C_{60}D_{24}$ prepared by treating solid C_{60} with D_2 gas. It is established that the deuteride is a polycrystalline powder with an fcc lattice ($a_0 = 14.55$ Å). The product of thermal decomposition of the deuteride consists mainly of fullerene molecules separated by a distance much greater than in the initial fullerite. © *1999 American Institute of Physics.* [S1063-7834(99)03308-0]

Fullerenes and their derivatives are attracting intense attention because of their unique structural, dynamic, and electronic properties. Of fullerene derivatives, compounds with alkali metals, for which a superconducting transition has been established,[1] and the ferromagnet TDAE-C_{60}, where TDAE is tetrakis(dimethlyamino)ethylene,[2] are being most intensively investigated. The hydrides of fullerenes are also being actively investigated, evidently, because of the possibility of producing hydrogen cells based on them (see, for example, the review in Ref. 3). At the same time, thus far it has proved impossible to obtain single crystals of fullerene hydrides. For polycrystalline $C_{60}H_{36}$, obtained by hydrogenization of fullerene at high pressure, it has been established that the packing of the molecules is body-centered cubic (bcc).[4] No other information about the crystal structure of fullerene hydrides has been found in the literature. The induced electron emission spectra of $C_{60}H_x$ have been little studied, especially for samples with $x<36$.

It has been reported[5] that hydrides with $10<x<26$, which retain the face centered cubic (fcc) structure of the initial fullerene, can be obtained by vapor-phase hydrogenization of solid fullerene (fullerite) C_{60}. It was of interest to investigate the x-ray photoelectron (XPE) spectra and the electron energy-loss (EEL) spectra of fullerene deuteride $C_{60}D_{24}$ obtained by the method described in Ref. 5 and to compare them to the spectra of other structurally characterized fullerene compounds.[6–8] The infrared (IR) spectra of deuteride are also of great interest, since the IR spectra of C_{60} and the hydride $C_{60}H_{36}$ are well known (see, for example, Refs. 3, 9, and 10); possible adsorption of hydrocarbons from the atmosphere does not affect the structure of the absorption bands (ABs) due to vibrations of the C–D bonds.

1. EXPERIMENTAL FEATURES

In the present work we used 99.8 mass% crystalline fullerene C_{60}. Deuteration was conducted at pressures 1.0–2.5 MPa and temperature 673 K in a standard high-pressure apparatus. The fullerene was degassed beforehand as it was heated to 500 K in vacuum (~ 1 Pa). To increase the efficiency, the deuteration process was conducted in a cyclic thermal regime, i.e., the sample was heated to 673 K under deuterium pressure and held at this temperature for 1 h, after which the reaction mixture was cooled to room temperature. The cycle was repeated at least five times, which promoted greater completion of the process and made it possible to obtain samples with a homogeneous distribution of the components. The samples were unloaded in an inert atmosphere after being cooled in an autoclave to 300 K.

The IR spectra were recorded with a Perkin Elmer 1720X Fourier spectrometer. The samples for investigating the IR spectra were prepared in the form of tablets with KBr (2 mg of the experimental substance per 300 mg KBr). An ADP-1 diffractometer (Cu $K\alpha$ radiation) was used to record the x-ray diffraction patterns (XDPs). Chemical analysis of the deuterium content was performed by the standard method of burning the sample in an oxygen stream in an apparatus for performing organic semi-microanalysis. The deuterium content of the experimental sample was found to be 6.2 ± 0.1 mass%, which corresponds to the empirical formula $C_{60}D_{24}$. Investigation of the decomposition of this sample

TABLE I. Description of the C 1*s* spectra of the experimental compounds by Gaussian curves.

Sample	Peak	Assignment	Area, %	Width, eV	Center, eV	Energy loss, eV
C_{60}	1	C 1*s*	73	1.63	285.02	–
	2	π-plasmon	27	6.70	287.80	2.87
$C_{60}D_{24}$	1	C 1*s*	80	1.94	284.74	–
	2	π-plasmon	20	5.85	286.84	2.10
PTDD	1	C 1*s*	73	1.72	285.09	–
	2	π-plasmon	25	5.31	287.69	2.60

Note. PTDD — product of thermal decomposition of the deuteride.

showed that approximately 6 mass% are lost at temperatures 800–823 K. We attribute this loss to the release of deuterium, since after such heating the intense absorption bands corresponding to stretching vibrations of the C–D bonds virtually vanish in the IR spectrum of the sample, and chemical analysis showed that the deuterium content of the sample does not exceed the measurement error (± 0.1 mass%).

The XPE spectra were excited with Al $K\alpha$ radiation ($h\nu = 1486.6$ eV). The preparation of samples for investigation of the XPE spectra is described in detail in Ref. 11. The spectra were calibrated according to the C 1*s* (285.0 eV) peak. This value corresponds to the position of the peak on the binding-energy scale for pure C_{60} for the method used in the present work to prepare the sample and is identical to the published data for C_{60} films on different substrates.[12] It is obvious that for compounds with small charge transfer this value will differ negligibly from 285.0 eV. The quite narrow energy distribution of C 1*s* photoelectrons (see Table I) made it possible to consider them also as a source for excitation of the EEL spectra.

2. EXPERIMENTAL RESULTS AND DISCUSSION

Diffraction patterns of the initial C_{60} powder, the deuteride $C_{60}D_{24}$, and the product of thermal decomposition of the deuteride are presented in Fig. 1. As noted in Ref. 5, vapor-phase hydrogenization (deuteration) preserves the fcc lattice of the initial solid C_{60} fullerene, and the increase in the hydrogen content results in a larger lattice constant a_0. The diffraction pattern of the deuteride investigated is indeed different from that of the initial fullerene, not only by the shift of the peaks but also by the asymmetric broadening of the peaks (Fig. 2). The broadening of the lines in the diffraction patterns is ordinarily attributed to an increase in the dispersity of the powder investigated or to a decrease in the sizes of the constituent crystallites. The effective size of the crystallites estimated from the half-widths of the three strongest lines is 510–560 Å . The appearance of asymmetry in the lines of the diffraction patterns of the fcc lattice signifies the appearance of stacking faults. For this reason, the crystallite sizes in the deuteride investigated can actually be greater than the estimates presented above.

The fcc lattice constant in $C_{60}D_{24}$ is 14.55 Å . For solid

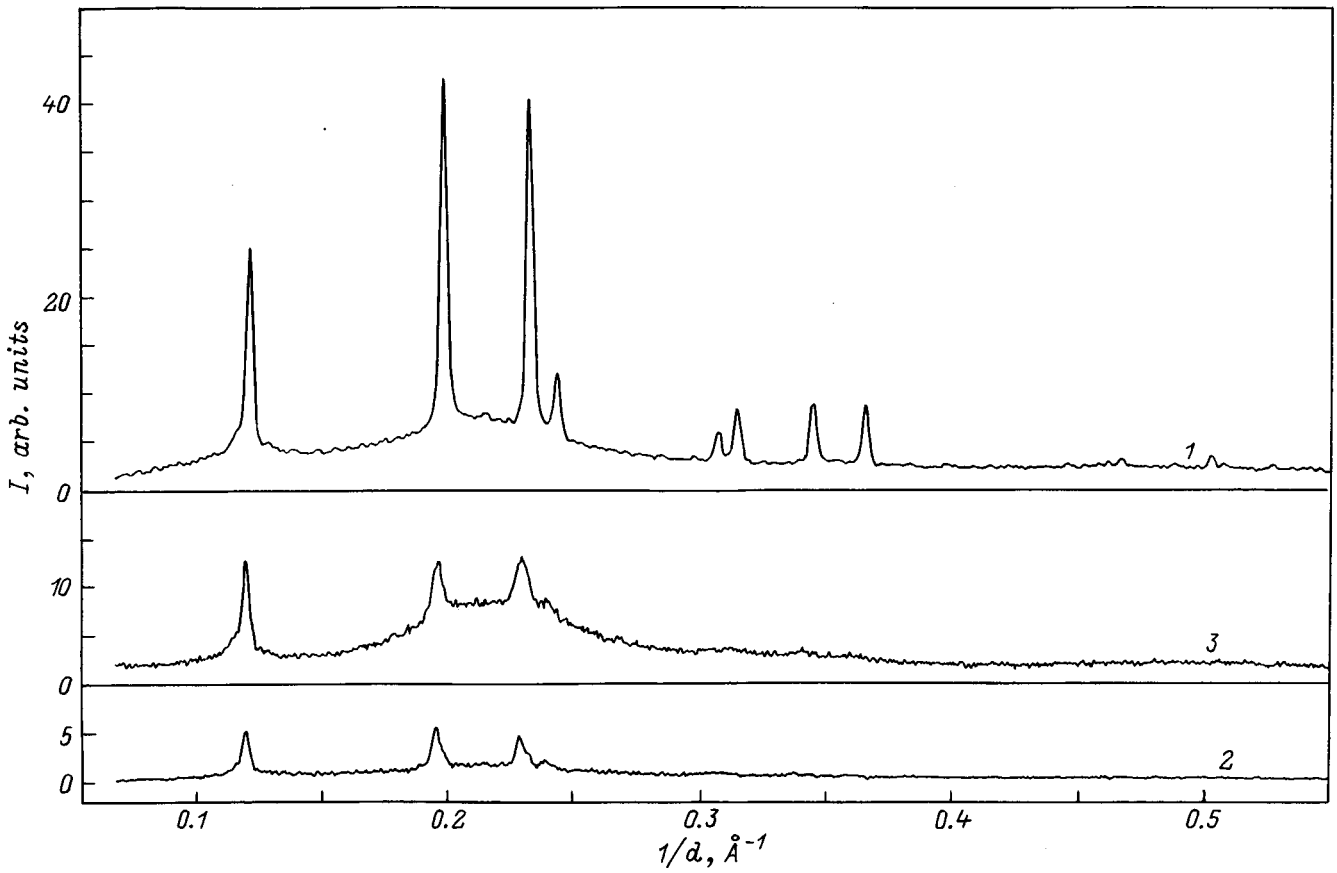

FIG. 1. Powder diffraction patterns of the initial fullerene (*1*), fullerene deuteride $C_{60}D_{24}$ (*2*), and product of thermal decomposition of the deuteride (*3*).

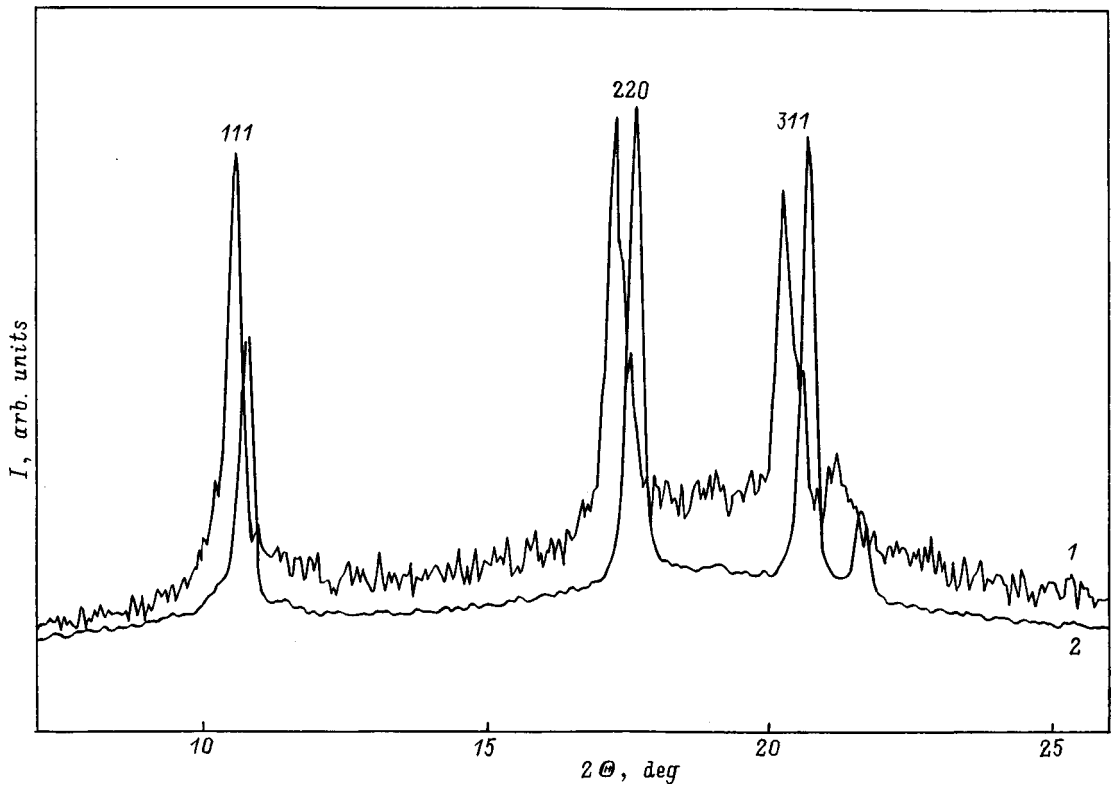

FIG. 2. Superposition of the diffraction patterns of $C_{60}D_{24}$ (*1*) and C_{60} (*2*) in the region of the strongest peaks.

C_{60} $a_0 = 14.17$ Å .[13] The values of a_0 obtained for the hydrides $C_{60}H_{10}$ and $C_{60}H_{18}$ in a similar manner were also determined. The dependence of a_0 on the hydrogen (deuterium) content is described quite well by the straight line

$$a_0 = 14.17 + 0.015x \text{ (Å)}, \quad (1)$$

where x is the number of deuterium (hydrogen) atoms per fullerene molecule (Fig. 3). However, it is possible that the deuterium atoms at low concentrations are located in the pores between fullerene spheres and have little effect on the structure parameter of the initial fullerene and, as x increases, the deuterium atoms increase the distance between the centers of the carbon framework of deuteride molecules, and the stacking faults accumulated in the process decrease the region of coherent scattering and the crystallite sizes. The fcc lattice is destroyed possibly because the bcc lattice becomes more favorable at high deuterium concentrations.[4]

According to the literature,[14,15] the hydride $C_{60}H_{36}$ heated in vacuum (823–923 K) completely converts to the initial fullerene. Because the experimental deuteride undergoes thermal decomposition at 823 K in 10 min, the intensi-

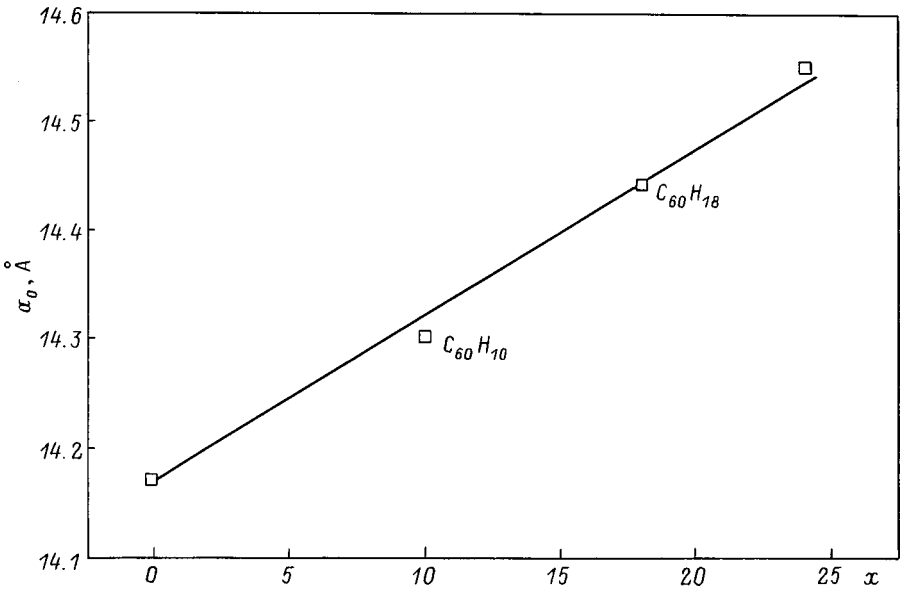

FIG. 3. The parameter a_0 of the fcc lattice of deuteride (hydride) versus x — the number of deuterium (hydrogen) atoms per fullerene molecule.

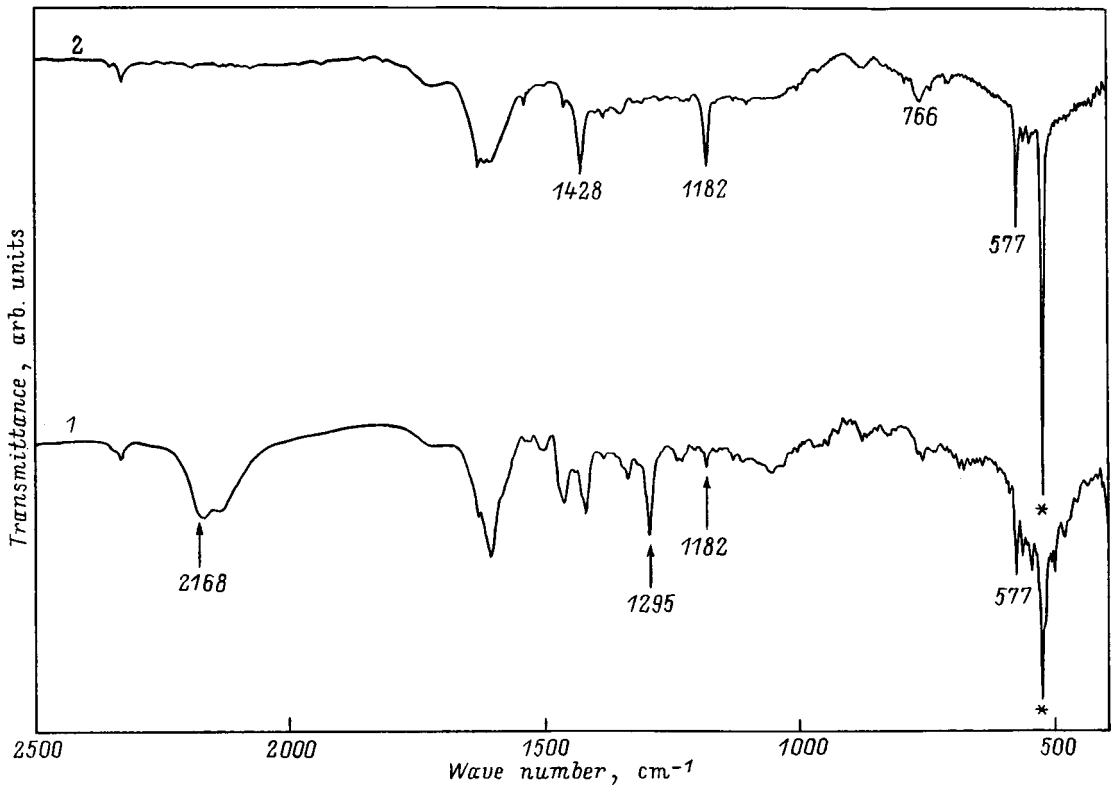

FIG. 4. IR spectra of the deuteride $C_{60}D_{24}$ (*1*) and the product of its thermal decomposition (*2*). The asterisk marks the absorption band at 527 cm^{-1}.

ties of the peaks in its diffraction pattern increase somewhat, the asymmetry of the peak decreases, and the center of gravity of the lines shifts in the direction of the interplanar distances. However, the diffraction pattern of the product of thermal decomposition of deuteride (PTDD) is substantially different from the diffraction pattern of the initial fullerene (Fig. 1). The value of a_0 for PTDD still remains quite large (14.52 Å). It can be inferred that doping of this sample with alkali metals could be quite successful. Specifically, an attempt can be made to obtain a lithium superconductor Li_3C_{60} in this way. The diffraction pattern of PTDD also shows a wide line with center of gravity at $d \cong 4.57$ Å , and for the time being it is unknown how this structural feature will influence the formation of the superconductor.

The main absorption bands in the PTDD spectrum [527 (marked by an asterisk in Fig. 4), 577, 1182, and 1428 cm^{-1}] have the same position and shape as the IR-active vibrational modes (F_{1u}) of the high-symmetry (I_h) C_{60} molecule. This confirms the results of Ref. 14 and 15 that fullerene hydrides transform into fullerene on heating. However, the IR spectrum of PTDD also contains a quite intense absorption band with a maximum at 766 cm^{-1} that is absent in the IR spectrum of the initial fullerene. The presence of a series of bands in the range 700–800 cm^{-1} is often attributed to the formation of fullerene polymers. It is evident from the spectra presented in Ref. 16 that the polymers obtained as a result of photopolymerization and by subjecting C_{60} to high pressures and temperatures have an entire series of absorption bands in this range, the positions of some of which being close to the absorption band at 766 cm^{-1} and to other weaker absorption bands present in the designated region in the PTDD spectrum. Investigation of the solubility confirmed the presence of polymer in PTDD. It was found that only half the PTDD dissolves in toluene, giving a violet color characteristic for C_{60} solutions, while the control, initial fullerite charge dissolved completely under similar conditions.

Comparing the spectra of the deuteride and its products of thermal decomposition makes it possible to assign the absorption bands of the deuteride. Thus, the absorption band at 527 cm^{-1} has the same nature as the absorption band in C_{60} whose position is close. Deuteration sharply decreases the relative intensities of the absorption bands at 577 and 1182 cm^{-1}, but the bands can also be seen in the deuteride spectrum. Instead of the absorption band at 1428 cm^{-1}, two absorption bands, at 1419 and 1462 cm^{-1}, can be seen in the spectrum. These absorption bands are due to vibrations of the carbon framework, since they can also be seen in the spectrum of the similarly obtained hydride (Fig. 5). The absorption band at 1428 cm^{-1} evidently split as a result of the hindered rotation of the deuteride (hydride) molecule around the center of gravity. The origin of the absorption bands at 1295 and 1607 cm^{-1} remains unclear. A wide absorption band at $\sim$1630 cm^{-1}, which is due to water molecules adsorbed on the KBr tablet, is superposed on the absorption band at 1607 cm^{-1}. Finally, the wide absorption band with a maximum at 2168 cm^{-1} and a shoulder at $\sim$2130 cm^{-1} is due to stretching vibrations of the C–D bonds. We note that, among the works known to us reporting measurement of IR spectra of fullerene deuterides, only one absorption peak, which was located at 2128 cm^{-1} (Ref. 17) or 2153 cm^{-1} (Ref. 18), was noted in the region of the stretching vibrations

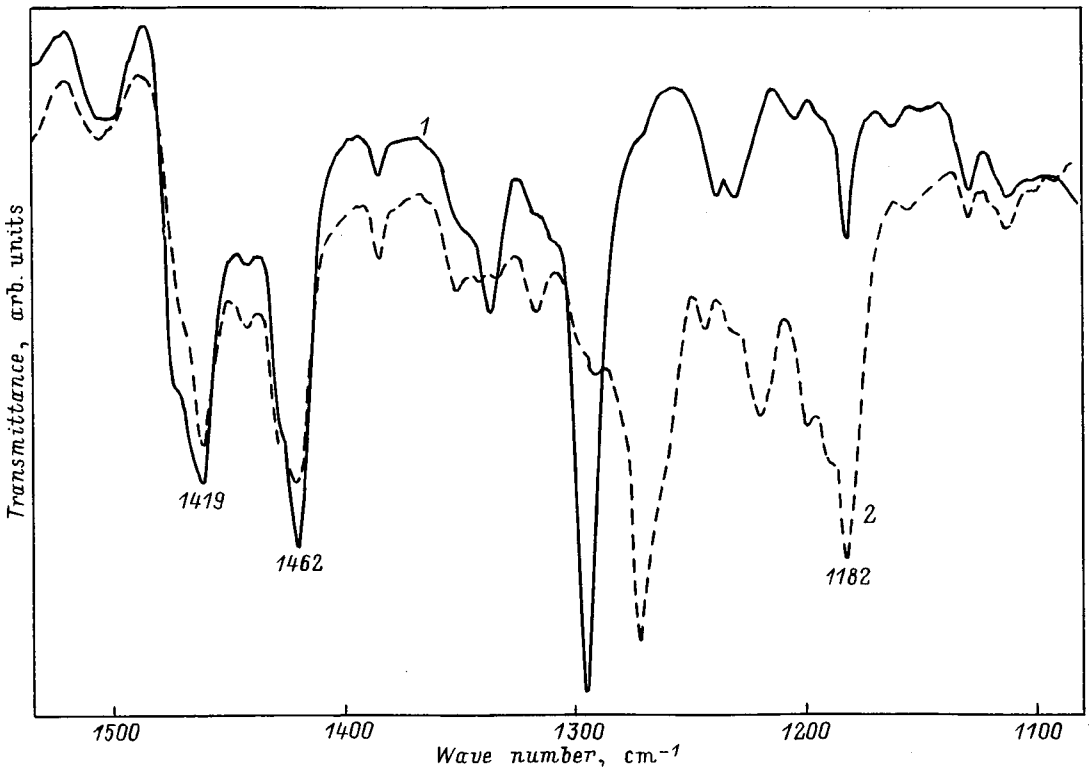

FIG. 5. IR spectra of the deuteride $C_{60}D_{24}$ (*1*) and hydride $C_{60}H_x$ (*2*) in the region of the $F_{1u}(4)$ and $F_{1u}(3)$ modes of the C_{60} molecule.

of the C–D bonds. At the same time, either two[9,17,19,20] or three[10,17,18] peaks in the region of the stretching vibrations of C–H bonds were observed for the hydrides $C_{60}H_x$. Evidently, the reason for this difference between the deuterides and hydrides cannot be explained simply by instrumental resolution.

The XPE spectra of $C_{60}D_{24}$, the product of its thermal decomposition, and pure C_{60} are presented in Fig. 6. The

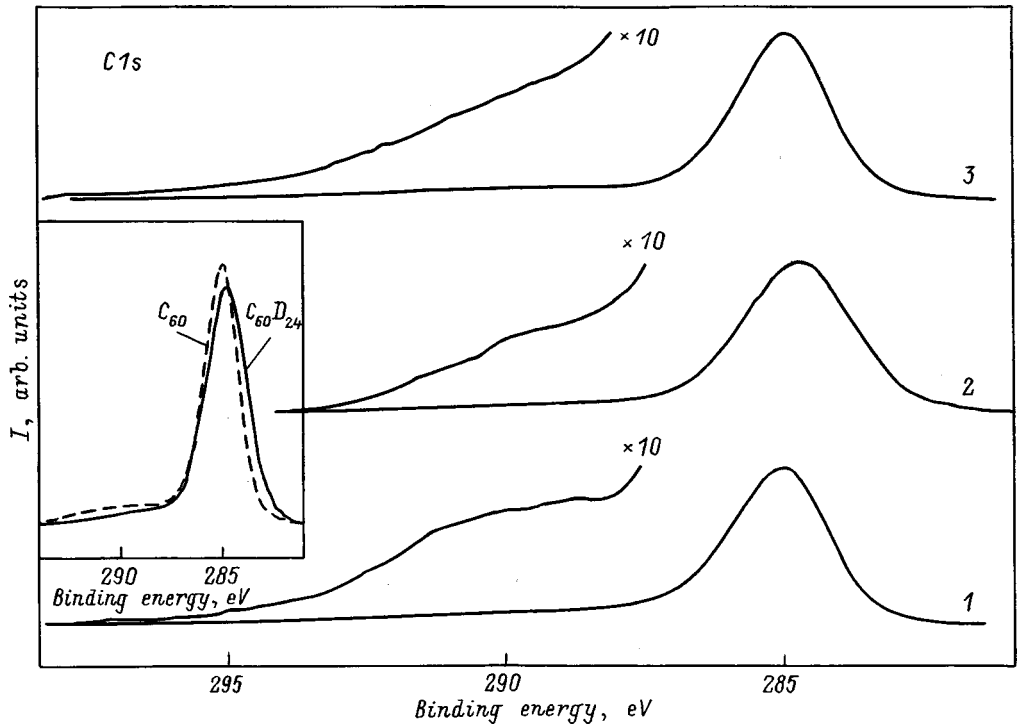

FIG. 6. XPE spectra of C_{60} fullerene (*1*), the deuteride $C_{60}D_{24}$ (*2*), and the product of decomposition of the deuteride (*3*). Inset: Superposition of $C_{60}D_{24}$ and C_{60} spectra.

basic parameters obtained by analyzing the spectra are presented in Table I. It is evident that the position of the maximum of the main peak in the case of the deuteride is shifted in the direction of lower binding energies compared with the peak for pure C_{60}. The half-width of the C 1*s* peak in the deuteride is greater than in pure C_{60}. Hence it follows that a small positive charge is present on the deuterium in $C_{60}D_{24}$. (For this reason, the compound investigated should not be called fullerene deuteride but rather deuterofullerene, but in the present paper we knowingly adhere to the established terminology.) When the deuteride undergoes thermal decomposition, the C 1*s* peak becomes narrower and its center of gravity shifts in the direction of higher binding energies.

A satellite is present in the spectra of all compounds on the high-binding-energy side of the main C 1*s* peak. For pure C_{60} this satellite is ordinarily attributed to losses due to the excitation of plasma oscillations of π electrons (π plasmons). A fit of two Gaussian curves the spectra presented shows that deuteration shifts the satellite peak in the direction of the main photoelectron peak and decreases the intensity of the satellite. The intensity decrease correlates with a decrease in the number of π electrons per carbon atom. As a result of thermal decomposition, the intensity of the satellite increases to virtually the initial state. However, the shape of the satellite in PTDD is different from that in pure C_{60} (Fig. 5). Moreover, for PTDD the fit of two Gaussian functions to the spectrum is less satisfactory than for C_{60} or $C_{60}D_{24}$.

The $\sigma+\pi$ plasmon energy ($\hbar\omega_p(\sigma+\pi)$), determined by the method described in Ref. 21, it 25.0 eV for the deuteride studied. For C_{60} $\hbar\omega_p(\sigma+\pi)=26.1$ eV, if similar measurements are performed. A calculation of the $\sigma+\pi$ plasmon energy on the basis of the free-electron model using the formula

$$\hbar\omega_p(\sigma+\pi)=\hbar(4\pi ne^2/m)^{1/2} \tag{2}$$

(where n is the density of valence electrons and m and e are the electron mass and charge) gives $\hbar\omega_p(\sigma+\pi)=21.74$ and 21.57 eV for $C_{60}D_{24}$ and C_{60}, respectively. The valence-electron density was calculated from the measured values of the fcc lattice constant a_0 using the relation

$$n=4Z/a_0^3, \tag{3}$$

where Z is the number of valence electrons per $C_{60}D_x$ molecule ($Z=240+x$). The values of the parameter δ ($\delta=1-\hbar\omega_p(\text{calc})/\hbar\omega_p(\text{exp})$), which shows the degree to which the computed values of the $\sigma+\pi$ plasmon energy deviate from the measured values are 0.18 and 0.13 for C_{60} and $C_{60}D_{24}$, respectively. This means that the plasma oscillations of all valence electrons in the deuteride are less localized than the oscillations in solid fullerene. We note here that for molecular complexes such as DBTTF C_{60} C_6H_6 (DBTTF =dibenzotetratiafulvalene),[7] C_{60} $2PPh_3AuCl$ $0.1C_6H_5CH_3$,[8] $(C_{60})_2$ (TPDP) $(CS_2)_4$ (TPDP=tetraphenyldipyranylidene),[22] and C_{60} $(TMDTDM-TTF)_2$ $(CS_2)_3$ (TMDTDM – TTF = tetramethylenedithiodimethyl – tiafulvalene)[23] the values of δ fall in the range 0.16–0.18. The structure of the vibrational absorption bands of the fullerene molecule in the IR spectra of these complexes is essentially the sme as that for pure C_{60}.

In summary, our investigations have established that the deuteride $C_{60}D_{24}$, obtained by deuteration of solid fullerene with D_2 gas, is a polycrystalline powder with an fcc lattice ($a_0=14.55$ Å) and crystallite sizes 510–560 Å . The stretching vibrations of the C–D bonds appear in the IR spectrum as a wide absorption band with a peak at 2168 cm^{-1} and a shoulder at $\sim$2130 cm^{-1}. Deuteration broadens the C 1*s* photoelectron peak and shifts its center of gravity in the direction of lower binding energies. This corresponds to a small positive charge on the deuterium atoms. It was established for the photoelectron spectra of $C_{60}D_{24}$ that the intensity of the peak due to the excitation of plasma oscillations of the π electrons is lower than that for the spectra of the initial C_{60}. It was also established that the $\sigma+\pi$ plasmon energy for the deuteride is 25.0 eV, which is less than the analogous energy for C_{60}. The product of thermal decomposition of $C_{60}D_{24}$ at 823 K is mainly fullerene, the distance between the C_{60} spheres in it being much greater than the distance in the initial fullerite.

We thank A. P. Moravskiĭ for providing the initial fullerite.

This work was supported by the Russian government program ''Surface Atomic Structures,'' the Russian Fund for Fundamental Research (Project No. 96-03-33586), and the Russian Science and Technology Program ''Fullerenes and Atomic Clusters.''

*)E-mail: shulga@icp.ac.ru

[1] A. F. Hebard, M. L. Rosseinsky, R. C. Haddon, D. W. Murphy, S. H. Glarum, T. T. M. Palstra, A. P. Ramirez, and A. R. Kortan, Nature (London) **350**, 900 (1991).
[2] P.-M. Allemand, K. C. Khemani, A. Koch, F. Wudl, K. Holczer, S. Konovan, G. Gruner, and J. D. Thompson, Science **253**, 301 (1991).
[3] N. F. Gol'dshleger and A. P. Moravskiĭ, Usp. Khim. **66**, 353 (1997).
[4] L. E. Hall, D. R. McKenzie, M. I. Attalla, A. M. Vassallo, R. L. Davis, J. B. Dunlop, and D. J. H. Cockayne, J. Phys. Chem. **97**, 5741 (1993).
[5] B. P. Tarasov, V. P. Fokin, A. P. Moravskiĭ, and Yu. M. Shul'ga, Izv. Ross. Akad. Nauk, Ser. Khim., No. 10, 2093 (1998).
[6] Yu. M. Shul'ga, V. I. Rubtsov, and A. S. Lobach, Z. Phys. B **93**, 327 (1994).
[7] D. V. Konarev, Y. V. Zubavichus, Yu. L. Slovokhotov, Yu. M. Shul'ga, V. N. Semkin, N. V. Drichko, and R. N. Lyubovskaya, Synth. Met. **92**, 1 (1998).
[8] Yu. M. Shul'ga, N. Yu. Shul'ga, and A. Graja, Solid State Commun. **105**, 491 (1998).
[9] R. E. Haufler, J. Conceicao, L. P. F. Chibante, Y. Chai, N. E. Byrne, S. Flangan, M. M. Haley, S. C. O'Brien, C. Pan, Z. Xiao, W. E. Billups, M. A. Ciofolini, R. H. Hauge, J. L. Margrave, L. J. Wilson, R. F. Curl, and R. E. Smalley, J. Phys. Chem. **94**, 8634 (1990).
[10] M. I. Attalla, M. A. Vassallo, B. N. Tattam, and J. V. Hanna, J. Phys. Chem. **97**, 6329 (1993).
[11] V. I. Rubtsov and Yu. M. Shul'ga, Zh. Éksp. Teor. Fiz. **103**, 2065 (1993) [JETP **76**, 1026 (1993)].
[12] M. B. Jost, N. Toullier, D. M. Poirier, J. L. Martins, J. H. Weaver, L. P. F. Chibante, and R. E. Smalley, Phys. Rev. B **44**, 1966 (1991).
[13] P. A. Heinev, G. B. M. Vaughan, J. E. Fischer, N. Coustel, D. E. Cox, J. R. D. Copley, D. A. Neumann, W. A. Kamitakahara, K. M. Greegan, D. M. Cox, J. P. McCauley, and A. B. Smith III, Phys. Rev. B **45**, 4544 (1992).
[14] C. Jin, R. L. Hettich, R. N. Compton, D. Jouce, J. Blencoe, and T. Burch, J. Phys. Chem. **98**, 4215 (1994).
[15] A. G. Avent, P. R. Birkett, A. D. Darwish, H. W. Kroto, R. Taylor, and D. R. M. Walton, *Proceedings of the International Workshop on Fullerene and Atomic Clusters, IWFAC'95* (St. Petersburg, 1995), p. 7.

[16] A. M. Rao, P. C. Eklund, L. L. Hodeu, L. Marques, and M. Nunez-Regueiro, Phys. Rev. B **55**, 4766 (1997).
[17] C. Ruchardt, M. Gerst, J. Ebelhoch, H.-D. Beckhaus, E. E. B. Campbell, R. Tellgmann, H. Schwarz, T. Weiske, and S. Pitter, Angew. Chem. Int. Ed. Engl. **32**, 584 (1993).
[18] M. Gerst, H.-D. Beckhaus, C. Ruchardt, E. E. B. Campbell, and R. Tellgmann, Tetrahedron Lett. **34**, 7729 (1993).
[19] A. D. Darwich, A. K. Abdul-Sada, G. J. Langley, H. W. Kroto, R. Taylor, and D. R. M. Walton, J. Chem. Soc., Perkin Trans. 2, 2359 (1995).
[20] K. Shigematsu, K. Abe, M. Mitani, and K. Tanaka, Fullerene Sci. Technol. **1**, 309 (1993).
[21] Yu. M. Shul'ga, A. P. Moravskiĭ, A. S. Lobach, and V. I. Rubtsov, JETP Lett. **55**, 132 (1992).
[22] D. V. Konarev, O. S. Roschupkina, M. G. Kaplunov, Yu. M. Shul'ga, E. I. Yudanova, and R. N. Lyubovskaya, Mol. Mater. **8**, 83 (1996).
[23] D. V. Konarev, E. F. Valeev, Yu. L. Slovokhotov, Yu. M. Shul'ga, O. S. Roschupkina, and R. N. Lyubovskaya, Synth. Met. **88**, 85 (1997).

Translated by M. E. Alferieff